8th Numerical Towing Tank Symposium

2.-4. October 2005

Varna/Bulgaria

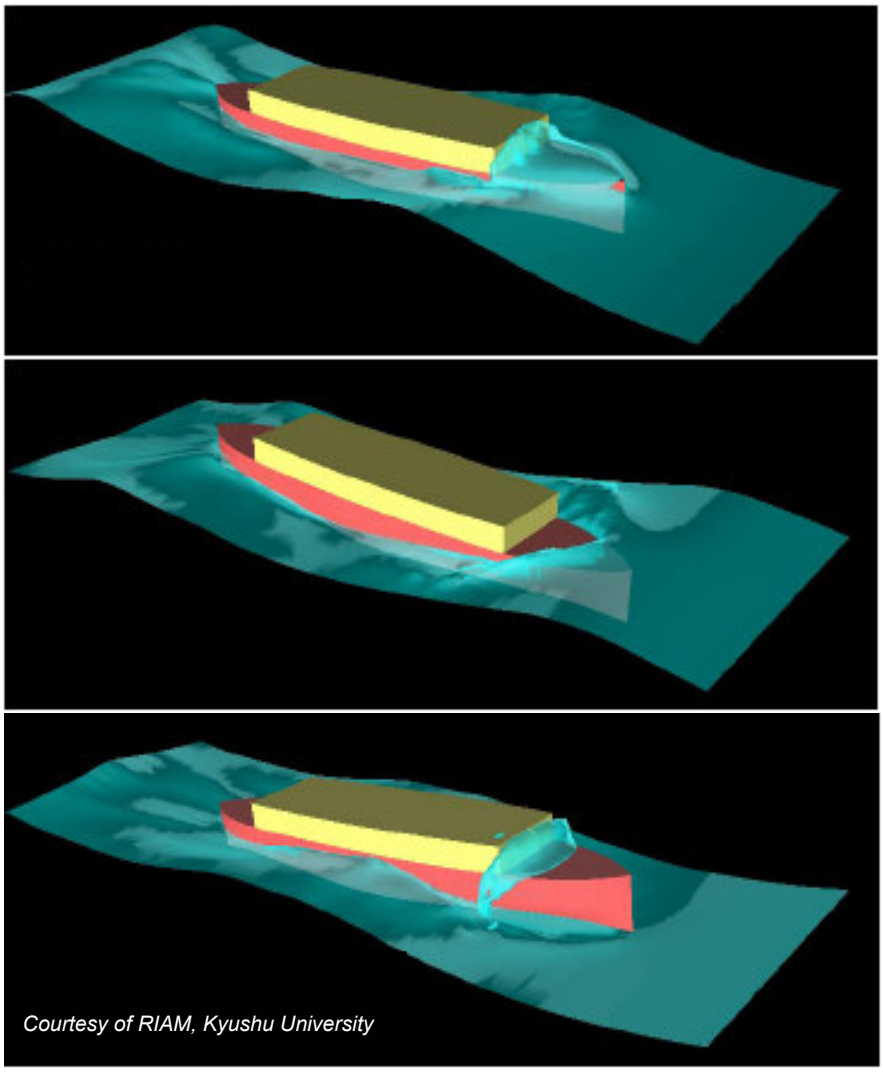

Volker Bertram, Stefan Kyulevcheliev (Ed.)

BULGARIAN SHIP HYDRODYNAMICS CENTRE

Sponsored by

5th Framework Programme of EC

CD adapco Group

HYDROREMONT I&G Ltd.

Varna Scientific and Technical Unions

CB Allianz Bulgaria

ODESSOS Shipreapir Yard S.A.

STRAIN TEST INSTRUMENTS VARNA CO.

P&S Project GmbH

INSTITUTE OF OCEANOLOGY

Technical University of Varna

Sirius Beach Hotel

Printed and bound by :

Copy Centers PAUS Ltd.

TABLE OF CONTENTS

(in alphabetical order by first author)

Experimental and Numerical Studies of Sloshing Flows in Three-Dimensional Rectangular Tanks

Hakan AKYILDIZ
Istanbul Technical University, Naval Architecture and Ocean Eng. Faculty,
34469, Maslak, Istanbul, Turkey
Email: akyildiz@itu.edu.tr
URL: www.gidb.itu.edu.tr/staff/akyildiz

Introduction

The liquid sloshing in a moving partially filled ractangular tank have been investigated. A numerical algorithm based on the Volume of Fluid technique (VOF) is used to study the non-linear behaviour of liquid sloshing. A moving coordinate system is used to include the non-linearity and avoid the complex boundary conditions of moving walls. The numerical model solves the complete Navier-Stokes equations in primitive variables by using of the finite difference approximations. In order to mitigate a series of discrete impacts, the signal computed is averaged over several time steps. The numerical method also allows interaction of the fluid with the tank top. In order to assess the accuracy of the method used, computations are compared with the experimental results. Both several configurations of baffled and unbaffled tanks are studied.

Liquid sloshing in a moving container constitutes major components in a number of dynamical systems such as aerospace vehicles, road tankers, liquified natural gas carriers and elevated water towers. Fluid motion in partially filled tanks may cause large structural loads if the period of tank motion is close to the natural period of fluid inside the tank. This phenomenon is called sloshing. Sloshing means any motion of a free liquid surface inside a container. The amplitude of the slosh, in general, depends on amplitude and frequency of the tank motion, liquid-fill depth, liquid properties and tank geometry. These parameters have direct effect on the dynamic stability and performance of moving containers.

The dynamic behavior of a free liquid surface depends on the type of excitation and its frequency content. The excitation can be impulsive, sinusoidal, periodic and random. Its orientation with respect to the tank can be lateral, parametric, pitching/yaw or roll and a combination. Under lateral harmonic excitation, the free liquid surface may exhibit two types of non-linearity: The first is large amplitude response and the second involves different forms of liquid behavior produced by coupling or instabilities of various sloshing modes. The most important of these is the rotary sloshing or swirl motion. This type of motion usually occurs very near the lowest liquid natural frequency.

A liquid's motion inside a container has an infinite number of natural frequencies, but it's the lowest few modes that are most likely to be excited by the motion of a vehicle. However, non-linear effects result in the frequency of maximum response being slightly different from the linear natural frequency and dependent on amplitude. Non-linear effects include amplitude jump, parametric resonance, chaotic liquid surface motion and non-linear sloshing mode interaction (internal resonance among the liquid sloshing modes).

Tanks with two-dimensional flow are divided into two classes: low and high liquid fill depths. d/L <0.2, where d is the still liquid depth and L is the tank width in the direction of the motion represents the low fill depth case. The low fill depth case is characterized by the formation of hydraulic jumps and traveling waves for excitation periods around resonance. At higher fill depths, large standing waves are usually formed in the resonance frequency range. When hydraulic jumps or traveling waves are present, extremely high impact pressures can occur on the tank walls
When the frequency of the tank motion is close to one of the natural frequencies of the tank fluid, large sloshing amplitudes can be expected. If both frequencies are reasonably close to each other, resonance will occur. The question is how close both frequencies should be to excite sloshing. Under

free oscillations, the motion of the free liquid surface decays due to damping forces created by viscous boundary layers. Basically, the damping factor depends on the liquid height, liquid kinematics viscosity and tank diameter width. From this point of view, we varied tank fill levels, tank excitation frequency and amplitude to study effects on pressure response. The tank was excited rotationally about a transverse axis through the tank center. There are two major problems arising in a computational approach to sloshing; these are the moving boundary conditions at the fluid tank interface, and the non-linear motion of the free surface. Therefore, in order to include the non-linearity and avoid the complex boundary conditions of moving walls, a moving coordinate system is used.

Mathematical Formulation

The fluid is assumed to be homogenous, isotropic, viscous and Newtonian. Tank and fluid motions are assumed to be three- dimensional. The domain considered here is a rigid rectangular container with and without baffle configuration partially filled with liquid, Fig.1. In the coordinate system, x_0-y_0-z_0 is the equilibrium position and x-y-z is the instantaneous position.

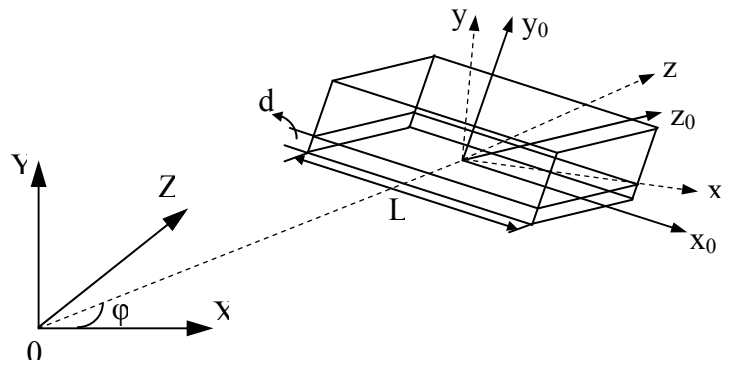

Fig.1: The moving coordinate system

The governing equations namely Navier-Stokes and continuity equations are solved simultaneously with the corresponding boundary conditions and free surface kinematics and dynamic boundary conditions.

$$\nabla \vec{U}(u,v,w) = 0, \text{ In the fluid domain}$$

$$\frac{\partial \vec{U}}{\partial t} + \vec{U} \cdot \nabla \vec{U} = -\frac{1}{\rho} \cdot \nabla \vec{P} + \vec{F} + \nu \nabla^2 \vec{U}, \text{ In the fluid domain}$$

Where, $\vec{U}(u,v,w)$ is the velocity vector defined in the tank fixed coordinate, and ρ, P, ν and F are the liquid density, pressure, kinematics viscosity and external forces respectively. In order to include the non-linearity and avoid the complex boundary conditions of moving walls, the moving coordinate system is used. The origin of the coordinate system is in the position of the center plane of the tank and in the undisturbed free surface. The moving coordinate is translating and rotating relative to an inertial system, Fig.1. The equilibrium position of the tank relative to the axis of rotation is defined by ϕ. For instance, the tank is rotating about a fixed point on the y-axis at $\phi = 90^o$. Thus the moving coordinate system can be used to represent general roll (displayed by θ) or pitch of the tank.

Numerical Computation

For analysis of the sloshing flow inside a partial filled tank, a finite difference method is applied to the governing equations. A FDM (finite difference method) is useful when there are internal structures inside the tank or the fluid contacts the tank ceiling frequently. As the internal structures exist, the viscous effects may be dominant. In this study, the method concentrates on the global fluid motion, so some local effects, such that turbulence and wave breaking have been ignored. In some cases, these

local effects are important, but the simulation of global flow plays a more critical role in many sloshing problems. The scheme adopted in this study is the SOLA method. Tank volume is discretized into Cartesian stagger grids, Fig.2.

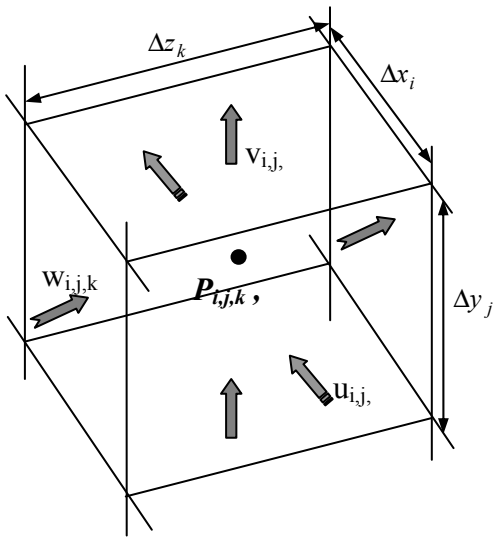

Fig.2: Three-dimensional Cartesian staggered grid

Fluid velocities are located at the centers of the cell boundaries and pressure (P) and the volume of fluid function (F) are also computed at the center of the cell. The solution algorithm works as a time cycle or 'movie frame'. The results of the time cycle act as initial conditions for the next one. At each time step the following computations are performed;

(a) Explicit approximations of the velocity field from the momentum equations use old time level values for the advective, viscous, Coriolis terms and time centered values for the other apparent body forces. Since the pressure is evaluated implicitly, the new velocities can then be obtained.

(b) For each cell, the change of pressure δP is calculated and added to the old pressure. This pressure is found by driving the velocity divergence to zero in each cell. Therefore, the continuity equation is first satisfied, then the new pressure field is calculated and the additional pressure contribution is added into the velocity field. Iteration is required since adjacent cells are coupled. After completion of this step, the new pressure and velocity field is known. At each step, suitable boundary conditions must be imposed at all boundaries.

Experimental studies

The objectives of the experimental studies are:

- To develop an experimental system accounting for the effects of large tank motions, large amplitude wave motions, fluid viscosity and baffle arrangements,
- To understand the fluid dynamics of liquid inside an unbaffled and baffled tanks,
- To provide useful information for the design of liquid cargo transport systems,
- To demonstrate the verification of the validity and the accuracy of the numerical model.

For a given rectangular prismatic tank, the natural frequencies of the fluid depending on the fill depth are given by:

$$\omega_n^{\,2} = g\,\frac{n\pi}{L}\tanh\left(\frac{n\pi}{L}d\right)$$

Where **L** is the tank width and **d** is the water depth and n is the mode number. Because of the non-linear feature of the sloshing problem, resonance does not occur exactly at the natural frequency of the fluid as computed from the above equation taking the mode number n=1, but at a frequency very close

to that value. The liquid resonance frequency shifts for different baffle arrangements, excitation amplitudes, liquid densities and viscosities.
The severity of sloshing and its accompanying dynamic pressure loads depend on the tank geometry, the depth of the liquid, the amplitude and nature of the tank motions. They also depend on the frequency of excitation over a range of frequencies close to the natural frequency of the fluid. For shallow liquid depths, the sloshing is characterized by a hydraulic jump. Under roll excitation, the liquid depth influences the frequency at which a jump will occur and it decreases as liquid depth is increased. The range of frequencies where jumps will exist is also influenced by the location of the roll axis. For roll oscillations about a fixed axis, the sloshing wave amplitude increases linearly with the excitation amplitude of the tank. The rate of increase is slower at the higher excitation amplitudes of the tank. The effect of the fluid viscosity is present and but more uncertain. However, viscosity does affect the sloshing wave amplitude at the resonance frequency. It also has a pronounced effect on surface waves such as spray and breaking.
In this study, the problem was restricted to liquid sloshing in rectangular tank under pitch oscillations. Many series of physical model investigations were carried out. A wide model tank was built for the experiments in order to allow for three-dimensional liquid motion. Thus, a 92 cm by 62 cm model tank, width of 46 cm and of 1.5 cm Plexiglas was built. The tank was designed with interchangeable internal structure arrangements. These internal structure members were bottom transverse and side stringers. A larger baffle (15.24 cm high) made of 1.5 cm Plexiglas plate was used for the bottom transverse and the left side stringer. A smaller baffle (7.62 cm high) was also used for the right side stringer with the same thickness. Nine pressure transducers were installed to monitor pressure distributions at various locations. The locations of the pressure transducers and the baffle configurations tested are shown in Fig 3.

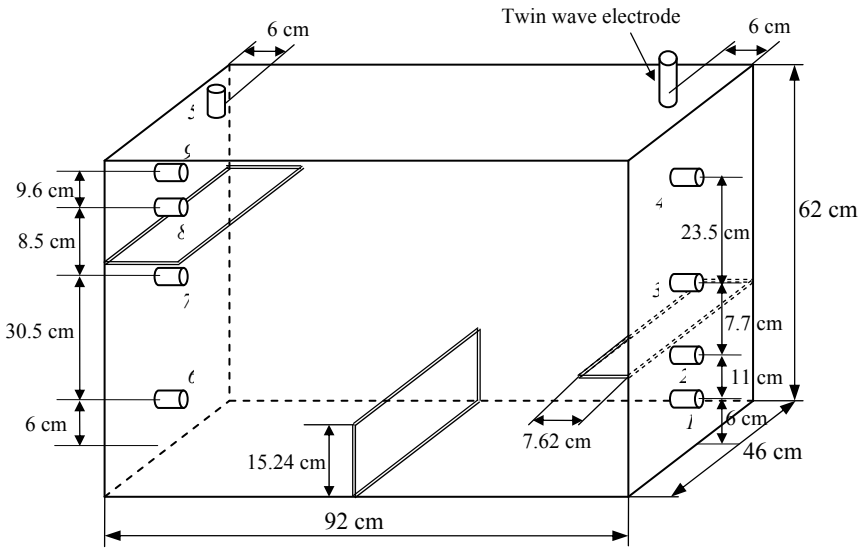

Fig.3: The locations of the pressure transducers and the baffle configurations

The tank is allowed to rotate freely about a transverse axis through the tank center. The tank platform on the base frame and the testing system consist of a DC motor controlling the rotational oscillations, an amplifier with analog-digital converter card for wave probe and a data logger type 34970 A for pressure transducers which were installed on the end bulkhead of the model tank at various locations. These gauge type transducers have sensitivity ranges from 0 to 1 bar G. Waves produced in the model tank were transformed to the system using a twin wave electrode. For each test run, the tank was always started from an upright position with predetermined frequency and excitation amplitudes and the tank was rotated for 2 minutes.

Conclusions

The sloshing liquid can create two types of dynamic pressure: They are called non-impulsive and impulsive pressures. Impulsive pressures are rapid pressure pulses due to the impact between the liquid and the solid surface. Such impulsive pressures are much localized and extremely high pressures. They are usually associated with hydraulic jumps and traveling waves. Non-impulsive pressures are the ordinary dynamic pressures in an oscillating fluid. They are slowly varying pressures that result from standing waves. The most severe impact pressures occur near the still water level or at the abrupt intersections of the tank walls. The variation of these pressures is neither harmonic nor periodic, even though the external excitation is harmonic. For a given liquid depth / tank width ratio and frequency of oscillation, sloshing pressure is in general proportional to the specific weight of the liquid, linear dimension of the tank and amplitude of excitation of the tank. At high excitation amplitudes of the tank, sloshing pressure is less sensitive to the excitation amplitude because of a non-linear softening effect. Sloshing in a three dimensional rectangular tank at a model scale was experimentally and numerically investigated. For an example, results at a snapshot for rolling frequency of 3.0 rd/s and rolling amplitude of 8^0 are presented in Figure 4. The instant of time corresponds to t=2.19 s after the start of the simulation and free surface positions are shown.

The following conclusions are made:

- Increasing the excitation amplitude and frequency increased the pressure response both unbaffled and baffled cases. It can be concluded that baffles significantly reduce the fluid motion and consequently the pressure response.
- As the amplitude of excitation is increased, the liquid responds violently such as occurrence of turbulence, hydraulic jump, wave breaking and three-dimensional effects. Therefore, the rolling amplitude and frequency of the tank directly affected the degrees of non-linearity of the sloshing.
- Increasing fill depth results in much more slamming pressures, because the horizontal baffles on the sides represent a shallow water effects and consequently enhance the travelling characteristics of the sloshing wave. It is concluded that energy dissipated by forming a hydraulic jump and a breaking wave. As the amplitude of excitation and the forcing frequency are increased, the liquid responds violently due to the three-dimensional effects.

The Navier – Stokes equation was solved using the SOLA scheme with staggered grids. Based on the numerical computations, some very strong non-linear flows and some local impact pressures on the tank top have been ignored. In this case, using the baffle seems to be useful when the fluid generates impulsive pressures on the tank top and these pressures depends on the size of the baffle. The pressure signals computed have showed a favourable agreement with the experimental data. It can be concluded that more experimental investigations are needed to validate with experimental data. Furthermore, the computer code developed should be extended to more complicated tank geometry using the curvilinear coordinate system and the simulation of hydraulic jump and multi-component random excitations with phase difference should be carried out more validation with experimental data.

References

1. Akyıldız H., Ünal E. Experimental Studies on Liquid Sloshing. Department Report TR 04 / 03, Department of Ocean Eng., Faculty Of Naval Arch. and Ocean Eng., I.T.U., Turkey, 2004.

2. Akyıldız H., Çelebi M.S. A Liquid Sloshing in a Moving Rectangular Tank. Department Report TR 01 / 02, Department of Ocean Eng., Faculty Of Naval Arch. and Ocean Eng., I.T.U., Turkey, 2001.

3. Akyıldız H., Çelebi M.S. Numerical Computation of Pressure in a Rigid Rectangular Tank Due to Large Amplitude Liquid Sloshing. Turkish Journal of Engineering and Environmental Sciences 2001; 25(6): 659-674.

4. Çelebi M.S., Akyıldız H. Nonlinear Modelling of Liquid Sloshing in a Moving Rectangular Tank. Ocean Engineering Journal 2002; 29(12): 1527-1553.

5. Akyıldız H., Çelebi M.S. Numerical Computation of Hydrodynamics Loads on Walls of a Rigid Rectangular Tank Due to Large Amplitude Liquid Sloshing. Turkish Journal of Engineering and Environmental Sciences 2002; 25(6): 659-674.

6. Faltinsen O.M., Timokha A.N. An adaptive Multimodal Approach to Nonlinear Sloshing in a Rectangular Tank. Journal of Fluid Mechanics 2001; 432: 167-200.

7. İbrahim R.A., Pilipchuk V.N., Ikeda T. Recent Advances in Liquid Sloshing Dynamics. Applied Mechanical Review 2001; 54(2): 133-199.

8. Lou Y.K., Su T.C., Flipse J.E. A Nonlinear Analysis of Liquid Sloshing in Rigid Containers. US Department of Commerce, Final Report, MA-79-SAC-B0018, 1980.

9. Lou Y.K., Wu M.C., Lee C.K. Further Studies on Liquid Sloshing. US Department of Transportation, Final Report, MA-RD-760-85009, 1985.

10. Lui A.P., Lou J.Y.K. Dynamic Coupling of a Liquid Tank System Under Transient Excitations. Ocean Engineering Journal 1990; 17(3): 263-277.

11. Su T.C., Lou Y.K., Flipse J.E., Bridges T.J. A Numerical Analysis of Large Amplitude Liquid Sloshing in Baffled Containers. US Department of Transportation, Final Report, MA-RD-940-82046, 1982.

12. Kim Y. Numerical Simulation of Sloshing Flows with Impact Load. Applied Ocean Research 2001; 23: 53-62.

13. Kim Y. A Numerical Study on Sloshing Flows Coupled with Ship Motion – The Anti-Rolling Tank Problem. Journal of Ship Research 2002; 46(1): 52-62.

14. Lou Y.K., Choi H. Spatial Pressure Variations and Three-Dimensional Effects on Liquid Sloshing Loads. US Department of Transportation, Report No. MA-RD-760-87039, 1987.

15. Hirt C.W., Nichols B.D. Volume of Fluid Method for the Dynamics of Free Boundaries. Journal of Computational Physics 1981; 39: 201-225.

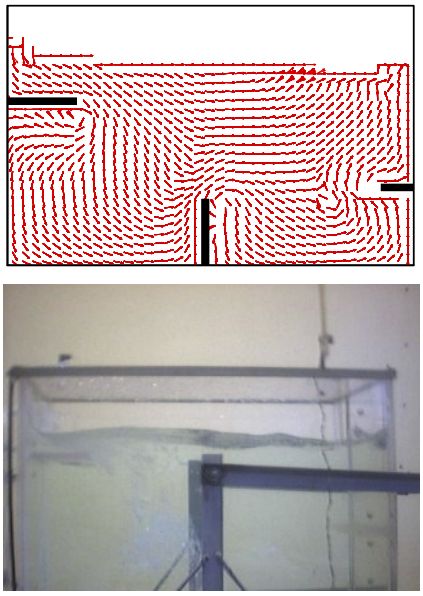

Figure 4. Position of free surface at t = 2.19 s.

CAVITATING HYDROFOILS INSIDE A NUMERICAL WAVE TANK

Sakir Bal Istanbul Technical University, sbal@itu.edu.tr

Introduction

It is very-well known that the effects of the walls of a wave tunnel are substantial in determining the lift and drag values and the cavity characteristics on cavitating hydrofoils and/or bodies. This paper addresses the steady cavitating flows around three-dimensional hydrofoils inside a numerical wave tank (NWT) by an iterative boundary element method (IBEM) and some numerical results are given.

The flow around three-dimensional cavitating hydrofoils has been modeled successfully in an unbounded fluid domain in (Kinnas and Fine, 1991) and (Kinnas and Fine, 1993). They applied a nonlinear theory by employing a low-order potential based boundary element method. Their method was later extended to predict face cavitation and search for cavity detachment on three-dimensional hydrofoils and propellers (Kinnas, 1998). A localized finite element method was described for nonlinear free surface condition in (Bai and Han, 1994). An iterative panel method has been applied for surface piercing hydrofoils without cavitation in (Hsin and Chou, 1998). (Kim, 1992) and (Ragab, 1998) solved the submerged high-speed hydrofoil problem without cavitation. (Mainar, Newman and Xu, 1990) used Havelock type of singularities to treat the flow around yawed surface piercing plates. On the other hand, the tunnel wall effects on cavitating hydrofoils without free surface have been calculated by iterative methods based on Green's theorem in (Kinnas, Lee and Mueller, 1998) and (Choi and Kinnas, 1998). The tunnel problem and the hydrofoil (or propeller) problem were solved separately, with the effects of one on the other being accounted for in an iterative method. The hydrofoil problem was solved in the context of nonlinear cavity theory by employing a low-order potential-based boundary element method, (Kinnas and Fine, 1993). Normal dipole and source distribution both on the cavity surface and on the hydrofoil surface were used. The tunnel problem was solved by applying the zero normal velocity condition. An IBEM was described for both two-dimensional and three-dimensional cavitating hydrofoils under the linearized free surface condition in (Bal and Kinnas, 2000) and (Bal, Kinnas and Lee, 2001). An integral equation obtained by applying Green's theorem on the surfaces of the problem was divided into two parts; the cavitating hydrofoil part and the free surface part. The cavitating hydrofoil influence on the free surface and the free surface influence on the cavitating hydrofoil were considered via potential. Some convergence tests carried out and extensive results of this IBEM were given in (Bal and Kinnas, 2002). The effects of walls (side and bottom) of the NWT on both 2-D and 3-D cavitating hydrofoils were also included into the calculations (Bal and Kinnas, 2003). The integral equation based on Green's theorem is divided into five parts: (i) The cavitating hydrofoil part, (ii) The free surface part, (iii) The right side wall of the tunnel, (iv) The left side wall of the tunnel and (v) The bottom surface of the tunnel. These five problems are solved separately, with the effects of one on the others being accounted for in an iterative manner. It can be said that these five problems communicate or "talk to" each other via potential. The cavitating hydrofoil part in 3-D is modelled with constant strength dipole and source panels. The free surface part and the side and the bottom walls of NWT are also modelled with constant strength dipole and source panels. The source strengths on the free surface are proportional to the derivative of the perturbation potential with respect to the vertical (z) axis. They are expressed by using the linearized free surface condition, in terms of the second derivative of the perturbation potential with respect to the horizontal (x) axis (Bal, Kinnas and Lee, 2001). The corresponding second order derivative on the free surface is calculated via application of Dawson's backward finite difference scheme (Dawson, 1977). In order to prevent upstream waves the first and second derivatives of the perturbation potential with respect to horizontal axis are enforced to be equal to zero (Nakos and Sclavounos, 1990). No radiation condition is enforced at the downstream boundary or at the transverse boundary (in the case of the three-dimensional problem) (Sclavounos and Nakos, 1988) and (Nakos and Sclavounos, 1994). The source strengths on the walls of NWT are zero due to the vanishing normal velocity. The potential induced by cavitating hydrofoil on the free surface and on the tunnel walls; the potential induced by right side wall on the other walls (left side wall and bottom surface), on the free surface and on the hydrofoil surface; the potential induced by left wall on the other walls (right side wall and bottom surface), on the free surface and on the hydrofoil surface; etc. are considered on the right hand side of each corresponding integral equation. The IBEM is applied to a rectangular cavitating hydrofoil which has NACA0012 constant sections along its spanwise direction. It is found that the Kelvin wave pattern started to be transformed into a regular waves on the free surface due to walls of NWT. It is shown that the present IBEM converged after several iteration steps.

Numerical Implementation

Consider a cavitating hydrofoil moving inside NWT subject to a uniform inflow, as shown in Figure 1. The x-axis is positive in the direction of uniform inflow, the z-axis is positive upwards while the y-axis completes the right-handed system. The calm free surface is located at z=h, while the finite bottom surface at z=-d. The distance between left and right walls of NWT is b. The mathematical formulation of the problem is given

in (Bal and Kinnas, 2003) in detail. The numerical implementation is just summarized below in a very short form for the completeness of the paper.

According to the Green's third identity the perturbation potential on the hydrofoil surface (including the cavity surface) and on the free surface can be expressed as,

$$2\pi\phi = \int_{S_{FS}+S_H+S_{LW}+S_{RW}+S_B} \left(\phi \frac{\partial G}{\partial n} - \frac{\partial \phi}{\partial n} G \right) dS + \int_{S_W} \Delta\phi_W \frac{\partial G}{\partial n^+} dS \tag{1}$$

where S_H, S_W, S_{FS}, S_{LW}, S_{RW} and S_B are the boundaries of the hydrofoil surface (including the cavity surface), wake surface, the free surface, left wall, right wall and bottom surface, respectively. G is the Green function (G=1/r), (r is the distance between the singularity point and field point). $\Delta\phi_W$ is the potential jump across the wake surfaces, and n^+ is the unit vector normal to the wake surfaces pointing upwards. In the present study, the iterative method presented in (Bal, Kinnas and Lee, 2001) and (Bal and Kinnas, 2000) is applied to solve Equation (1). The iterative method in general is composed of five parts: (i) the hydrofoil and cavity part which solves for the unknown perturbation potential on the hydrofoil and cavity surface, (ii) the free surface part, which solves for the unknown perturbation potential on the free surface, (iii) the bottom surface part of NWT, which solves for the unknown perturbation potential on the bottom surface, (iv) the left wall part of NWT, which solves for the unknown perturbation potential on the left wall surface, and, (v) the right wall part of NWT, which solves for the unknown perturbation potential on the right wall surface. The potential in the fluid domain due to the influence of the hydrofoil, ϕ_H, can be given as,

$$2\pi\phi_H = \int_{S_H} \left(\phi \frac{\partial G}{\partial n} - \frac{\partial \phi}{\partial n} G \right) dS + \int_{S_W} \Delta\phi_W \frac{\partial G}{\partial n^+} dS \tag{2}$$

The potential in the fluid domain due to the influence of the free surface, ϕ_{FS}, the left wall, the right wall and the bottom surface, however, can be given as,

$$2\pi\phi_{FS} = \int_{S_{FS}} \left(\phi \frac{\partial G}{\partial n} - \frac{\partial \phi}{\partial n} G \right) dS \tag{3}$$

$$2\pi\phi_{LW} = \int_{S_{LW}} \left(\phi \frac{\partial G}{\partial n} - \frac{\partial \phi}{\partial n} G \right) dS \tag{4}$$

$$2\pi\phi_{RW} = \int_{S_{RW}} \left(\phi \frac{\partial G}{\partial n} - \frac{\partial \phi}{\partial n} G \right) dS \tag{5}$$

$$2\pi\phi_B = \int_{S_B} \left(\phi \frac{\partial G}{\partial n} - \frac{\partial \phi}{\partial n} G \right) dS \tag{6}$$

,respectively. By substituting Equations (3-6) into Equation (1), the following integral equation for the flow on the hydrofoil can be written as,

$$2\pi\phi = \int_{S_H} \left(\phi \frac{\partial G}{\partial n} - \frac{\partial \phi}{\partial n} G \right) dS + \int_{S_W} \Delta\phi_W \frac{\partial G}{\partial n^+} dS + 4\pi (\phi_{FS} + \phi_{LW} + \phi_{RW} + \phi_B) \tag{7}$$

and by substituting Equations (2, 4-6) into Equation (1) similarly, the following integral equation for the flow on the free surface can be written as,

$$2\pi\phi = \int_{S_{FS}} \left(\phi \frac{\partial G}{\partial n} - \frac{\partial \phi}{\partial n} G \right) dS + 4\pi \ (\phi_H + \phi_{LW} + \phi_{RW} + \phi_B) \tag{8}$$

Similarly, the following integral equations can be written for the left wall, right wall and bottom surface as,

$$2\pi\phi = \int_{S_{LW}} \left(\phi \frac{\partial G}{\partial n} - \frac{\partial \phi}{\partial n} G \right) dS + 4\pi \ (\phi_H + \phi_{FS} + \phi_{RW} + \phi_B) \tag{9}$$

$$2\pi\phi = \int_{S_{RW}} \left(\phi \frac{\partial G}{\partial n} - \frac{\partial \phi}{\partial n} G \right) dS + 4\pi \ (\phi_H + \phi_{LW} + \phi_{FS} + \phi_B) \tag{10}$$

$$2\pi\phi = \int_{S_B} \left(\phi \frac{\partial G}{\partial n} - \frac{\partial \phi}{\partial n} G \right) dS + 4\pi \ (\phi_H + \phi_{LW} + \phi_{RW} + \phi_{FS}) \tag{11}$$

After applying the kinematic condition on the hydrofoil, free surface condition and the wall conditions, Equations (7-11) can be reduced to,

$$2\pi\phi = \int_{S_H}\left(\phi\frac{\partial G}{\partial n} + Un_x G\right)dS + \int_{S_W}\Delta\phi_W\frac{\partial G}{\partial n^+}dS + 4\pi\left(\phi_{FS}+\phi_{LW}+\phi_{RW}+\phi_B\right) \tag{12}$$

$$2\pi\phi = \int_{S_{FS}}\left(\phi\frac{\partial G}{\partial n} + \frac{\partial^2\phi}{\partial x^2}\frac{G}{k_0}\right)dS + 4\pi\left(\phi_H+\phi_{LW}+\phi_{RW}+\phi_B\right) \tag{13}$$

$$2\pi\phi = \int_{S_{LW}}\left(\phi\frac{\partial G}{\partial n}\right)dS + 4\pi\left(\phi_H+\phi_{FS}+\phi_{RW}+\phi_B\right) \tag{14}$$

$$2\pi\phi = \int_{S_{RW}}\left(\phi\frac{\partial G}{\partial n}\right)dS + 4\pi\left(\phi_H+\phi_{LW}+\phi_{FS}+\phi_B\right) \tag{15}$$

$$2\pi\phi = \int_{S_B}\left(\phi\frac{\partial G}{\partial n}\right)dS + 4\pi\left(\phi_H+\phi_{LW}+\phi_{RW}+\phi_{FS}\right) \tag{16}$$

Integral Equations (12-16) can be solved iteratively by a low-order panel method with the potentials ϕ_H, ϕ_{FS}, ϕ_{LW}, ϕ_{RW} and ϕ_B being updated during the iterative process. Here, the hydrofoil, the free surface, the left and right walls and bottom surface communicate, or "talk to", each other via potential. The hydrofoil surface, the free surface, the left and right walls and the bottom surface are discretized into panels with constant source and dipole distributions. The discretized integral equations provide five matrix equations with respect to the unknown potential values and can be solved by any matrix solver. In equation 13, the second derivative of perturbation potential term can be expressed in terms of the potentials on the free surface by applying Dawson's original fourth-order backward finite difference scheme (Dawson, 1977). The first and the second derivatives of potential with respect to x at point i are given in (Bal and Kinnas, 2002). In order to prevent upstream waves, the first derivative of potential with respect to x (which corresponds to the wave deformation) and the second derivative of potential with respect to x (which corresponds to first derivative of wave deformation) are enforced to be equal to zero (Nakos and Sclavounos, 1990). The source strengths from some distance (radiation distance) in front of the hydrofoil to the upstream truncation boundary of the free surface are set to zero, and this forces the first derivative of potential with respect to z to be equal to zero. The details of the numerical procedure can be found in (Bal and Kinnas, 2003).

Results

The present IBEM is applied to a rectangular planform hydrofoil with span/chord=5 and NACA0012 profiles along the span-wise direction. The angle of attack is chosen as $\alpha=5^0$ and the cavitation number as $\sigma=0.2$. The Froude number based on chord (c) is $F_c=1.0$ and the ratios of the submergence depth of the hydrofoil from free surface, h/c and of the height of the hydrofoil from bottom surface, d/c are equal to 1.0 and 1.0, respectively. A general view of panelling of the walls of NWT and the hydrofoil and its wake is shown in Figure 2. (40x20) panels (along chordwise and span-wise direction) are used on the hydrofoil surface. In Figure 3, the perspective views of the cavity shapes with and without (unbounded flow case) NWT effect (b/s=2.0) are shown for half of the hydrofoil. Note that the cavity lengths and volume decreased for this case. The side and bottom walls of NWT caused shorter cavity lengths for almost all strips of the hydrofoil. This can be seen much clearly in Figure 4 that the cavity planforms for different b/s ratios are shown. In Figure 5, for the mid-strip (the strip in the middle of the hydrofoil), the effect of the side walls of NWT on the cavity shape is shown. In Figures 6 and 7, the perspective views of wave elevations and wave contours are shown for both b/s=3.0 and 2.0 cases, respectively. It can easily be seen that the Kelvin wave pattern for b/s=3.0 case is started to be transformed into a regular wave pattern due to the effect of side walls of NWT. In Figures 8, the convergence history of the cavity planform is shown. Note that the IBEM converged at the 8th iteration.

Conclusions

An IBEM for cavitating hydrofoils moving with a constant speed inside NWT was described and applied to a rectangular cavitating hydrofoil. The iterative nonlinear method is based on the Green's theorem, which is applied to the surfaces of the hydrofoil, NWT and the free surface. The hydrofoil part, the free surface part and the wall parts of the NWT were solved separately, with the effects of one on the others taken into account iteratively. It can be said that all these parts of the problem communicate to each other via their potential. The cavitating three-dimensional hydrofoil surfaces, the free surface and all thw walls are modeled

with constant strength dipole and constant strength source panels, distributed all over surfaces, including the cavity and wake surfaces of the hydrofoil. The IBEM was applied to the three-dimensional cavitating hydrofoil problem. It was found that the Kelvin wave pattern is started to be transformed into a regular wave pattern (wave train) due to the effect of NWT. The method converges after several iteration steps. The method can be applied to the surface piercing hydrofoils, struts and ship hulls (with and without cavitation). The IBEM can also be extended to the case of multi-hydrofoils (bodies).

References

Bai, JK, and Han, JH (1994). "A localized finite element method for the nonlinear steady waves due to a two-dimensional hydrofoil," *Journal of Ship Research,* Vol 38, pp 42-51.

Bal, S, and Kinnas, SA (2000). "A bem for cavitating hydrofoils under a free surface," *Proc. IABEM-2000 Symp.*, Brescia, Italy, pp 13-17.

Bal, S, and Kinnas, SA (2002), "A Bem for the prediction of free surface effect on cavitating hydrofoils", *Computational Mechanics*, 28, 3, pp: 260-274.

Bal, S, and Kinnas, SA (2003), "A Numerical wave tank model for cavitating hydrofoils", *Computational Mechanics*, 32, 4-6, pp: 259-268.

Bal, S, Kinnas, SA, and Lee, H (2001). "Numerical analysis of 2-D and 3-D cavitating hydrofoils under a free surface," *Journal of Ship Research*, 45,1, pp 34-49.

Choi, JK, and Kinnas, SA (1998). "Numerical water tunnel in two- and three-dimensions," *Journal of Ship Research,* Vol 42, pp 86-98.

Dawson, DW (1977). "A practical computer method for solving ship-wave problems," *Proc. 2nd Int. Conf. Numerical Ship Hydro.*, USA.

Hsin, CY, and Chou, SK (1998). "Applications of a hybrid boundary element method to the analysis of free surface flow around lifting and nonlifitng bodies," *Proc. 22nd Symposium on Naval Hydrodynamics*, Washington DC, USA.

Kim, BK (1992). "Computation of hydrodynamic forces on a submerged lifting body," *Proc. 2nd Int. Offshore and Polar Engn. Con.*, ISOPE, San Francisco, USA, June 14-19, pp 367-374.

Kinnas, SA (1998). "The prediction of unsteady sheet cavitation",*3rd Int. Symp. on Cavitation*, Grenoble, France.

Kinnas, SA, and Fine, NE (1991). "Nonlinear analysis of the flow around partially or supercavitating hydrofoils by a potential based panel method," *Proc. IABEM-90 Symp.,* Rome, Italy, pp 289-300.

Kinnas, SA, and Fine, NE (1993). "A numerical nonlinear analysis of the flow around two- and three-dimensional partially cavitating hydrofoils," *Journal of Fluid Mechanics*, Vol 254, pp 151-181.

Kinnas, SA, Lee, H, and Mueller, AC (1998). "Prediction of propeller blade sheet and developed tip vortex cavitation," *Proc. 22nd Symposium on Naval Hydrodynamics*, Washington DC, USA.

Maniar, H, Newman, JN, and Xu, H (1990). "Free surface effects on a yawed surface piercing plate," *Proc. 18th Symposium on Naval Hydrodynamics*, Ann Arbor, Michigan, USA.

Nakos, DE, and Sclavounos, PD (1990). "On steady and unsteady ship wave patterns," *Journal of. Fluid Mechanics,* Vol 215, pp 263-288.

Nakos, DE and Sclavounos, PD (1994) "Kelvin wakes and wave resistance of cruiser and transom stern ships", *Journal of Ship Research*, 38,1, pp 9-29.

Ragab, SA (1998). "Inviscid Non-Cavitating Flow Over Shallowly Submerged Swept Hydrofoils," *Proc. 8th Int. Offshore and Polar Engn. Con.*, ISOPE, Montreal, Canada, May 24-29, pp 253-259.

Sclavounos, PD, and Nakos, DE (1988). "Stability analysis of panel methods for free surface flows with forward speed," *Proc. 17th Symposium on Naval Hydrodynamics*, Netherlands.

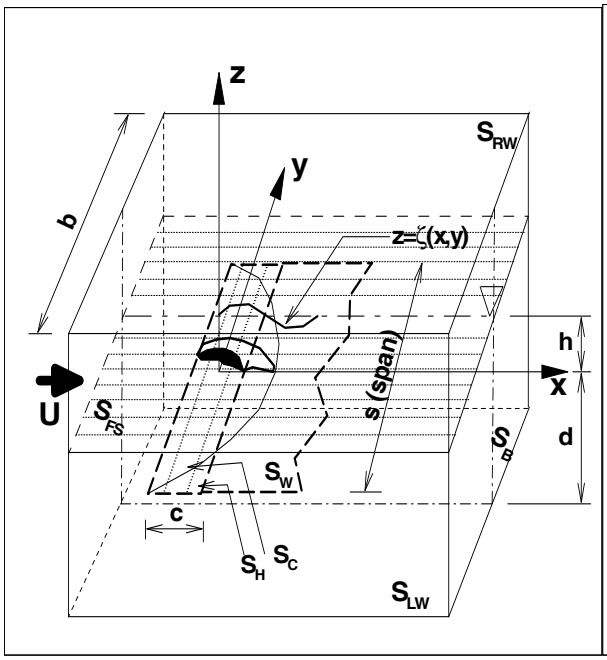

Figure 1. Definition of Coordinate System.

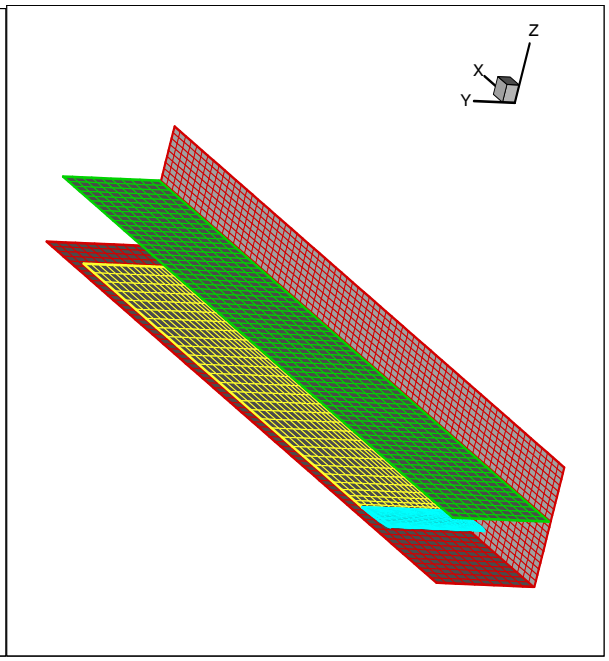

Fig. 2. Half of Perspective View of Tunnel, Hydrofoil and Wake.

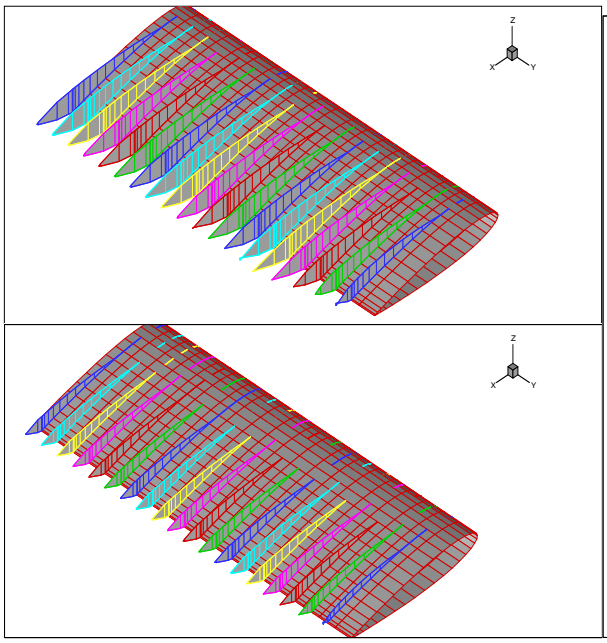

Figure 3. Cavity Patterns in Unbounded Domain (Top) and with NWT (b/s=2.0) Effect (Bottom).

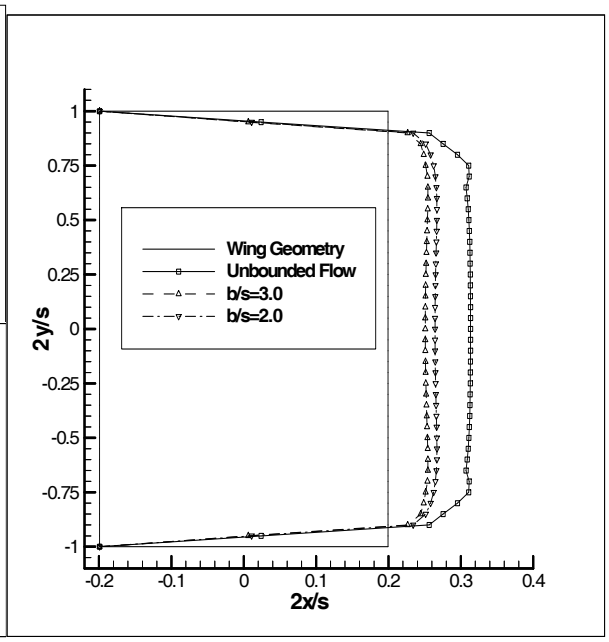

Figure 4. Cavity Planforms with and without NWT Effect.

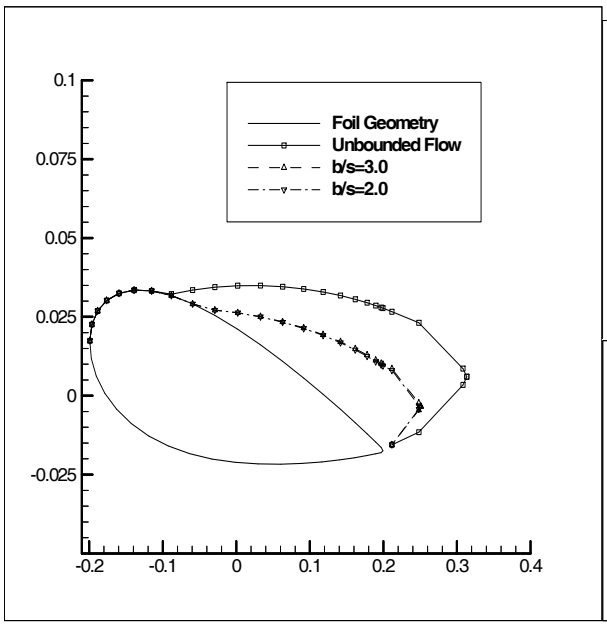

Figure 5. Cavity Shape for the Mid-Strip with NWT and without NWT Effect.

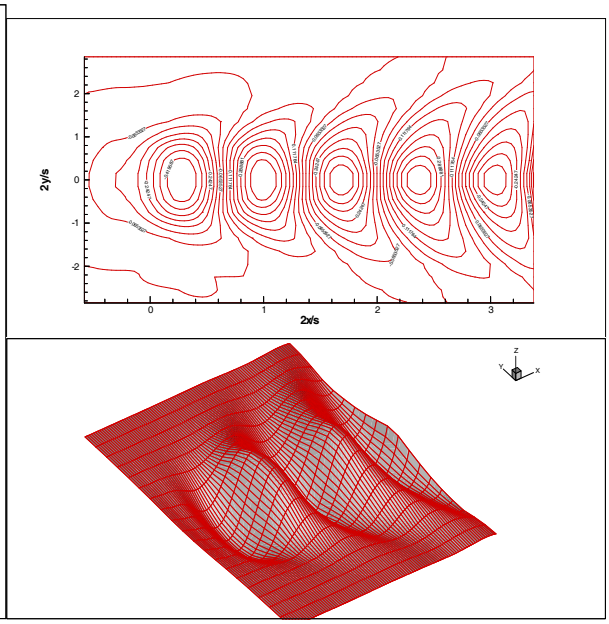

Figure 6. Wave Contours and Deformation for b/s=3.0.

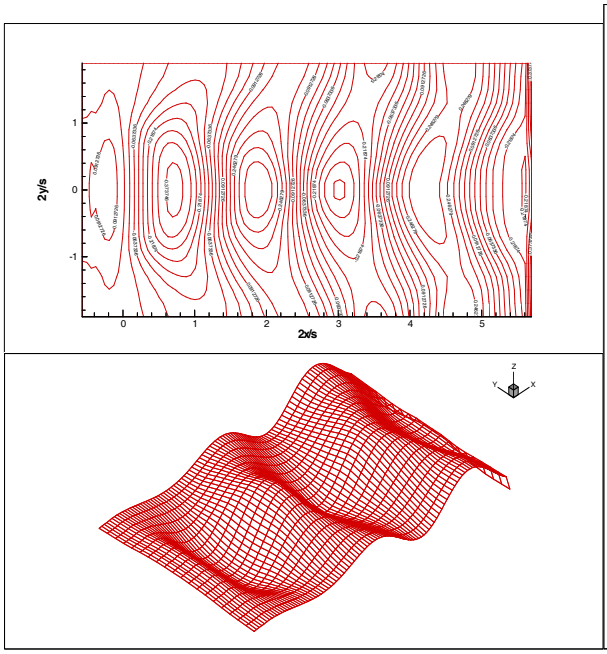

Figure 7. Wave Contours and Deformation for b/s=2.0.

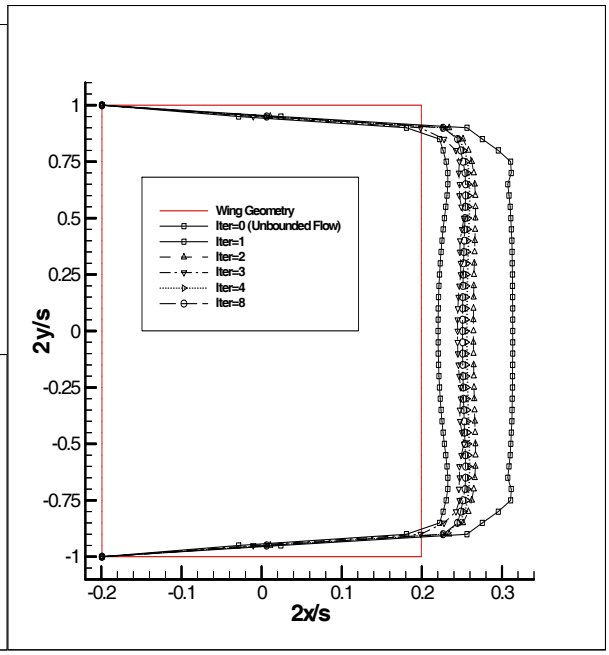

Figure 8. History of Cavity Planform with Iteration Numbers.

Effects of Vortex on Submarine Maneuverability at Angle of Drift

Ali Raza Bashir[1], Hafiz Rafi[2], S.Bilal[3], S.Zahir[4], M.A.Khan[5]

1. Asst. Manager (Tech), ealiraza@hotmail.com
2. Senior Engineer, hafiz_rafi@yahoo.com
3. Senior Engineer, bukharibilal@hotmail..com
4. Member AIAA, s.zahir@ccsspak.org
5. Member AIAA, rana_mahmood@hotmail.com
(Computational Modeling, Control & Simulation Society of Pakistan)

When a submarine executes a high speed turn, the sail experiences a crossflow velocity component, creating a vortex at the sail tip. The flowfield induced by the vortex creates higher pressure on the hull deck(top) and lower pressure on the keel(bottom), leading to the nose-up pitching moment. CFD computations were performed on a submarine at drift angles of 0, 5 and 9.5 deg, with the sail on and off, speed upto 14.9 m/s, and the Vorticity, Circumferential pressure distributions, Forces and Moments results were obtained. An analysis was done to demonstrate the change in pressure distribution, forces and moments when the sail is on and off.
The results then compared with the experimental data and a good agreement was found between them.

INTRODUCTION

The pitching moment is created when a body is at angle of attack, and there is no such a large effect on pitching moment with change in angle of drift or side angle. But this is not in the case of submarine with sail. When a submarine executes a high speed turn, a nose up pitching moment is created. When a submarine executes a high speed turn, the sail of the submarine is placed at angle of attack. Because the sail in this condition is essentially a low aspect ratio, finite-span wing, a tip vortex is created that trails aft the sail. This vortex modifies the pressure distribution on the rear of the submarine, due to which a net force created on the hull aft the sail and because this force acts aft the center of gravity of the submarine, thus contributes to a nose up pitching moment.
When a submarine is in a turning maneuver, there is a distribution of angle of drift developed along the length of the hull. The local angle of drift is relatively small along the forebody, but is relatively large along the afterbody. Lift is developed on the hull due to the local angle of drift. Actually there is a vortex system, in which a bound vortex is also created with the trailing vortex. An image vortex is located inside the hull. This system of vorticity sets up circulation around the hull and there is also a circulation of the trailing vortex, which in combination with the local crossflow causes a hydrodynamic pressure difference to occur between the deck and keel. Thus a net downward force is occurred on the submarine resulting in nose up pitching moment.
A mathematical concept commonly associated with vortex is that of circulation. Circulation is a term defined as the line integral of the tangential component of the velocity taken around a closed curve in a flow field. This force is due to the combined effects of the trailing vortex, bound vortex and the cross flow velocity component. We can think vorticity attached to submarine is like a horseshoe vortex, where the base of horseshoe is bound to the sail, one leg is sail tip vortex, and the other is actually enlarged and wrapped around the submarine hull.

In this paper, an attempt is done to solve the 3D Reynolds Average Navier Stokes equations with standard k- epsilon model for a structured grid around a submarine using *Fluent 6.1* at 0, 5 and 9.5 drift angles and calculate the vorticity, pressure distributions, net downward force, and pitching moment when sail is Off and On. The circumferential pressure distribution is taken at axial location of 0.47 of the total length, and then compared the results with experimental data and a good agreement is found between them.
Downward force and pitching moment is increased with increase in drift angle when the sail is On whereas there is no such effect on downward force and pitching moment when the sail is Off. So all of the downward force is due to the sail tip vortex.

GEOMETRY

The model used in this paper is standard submarine with axisymmetric hull and four cruciform stern appendages.
With the definition of θ, the region 0 deg < θ < 180 deg corresponds to the "deck" or "top" of the submarine hull, and the region 180 deg < θ < 360 deg corresponds the "keel" or "bottom" of the submarine hull as shown in Fig:1.

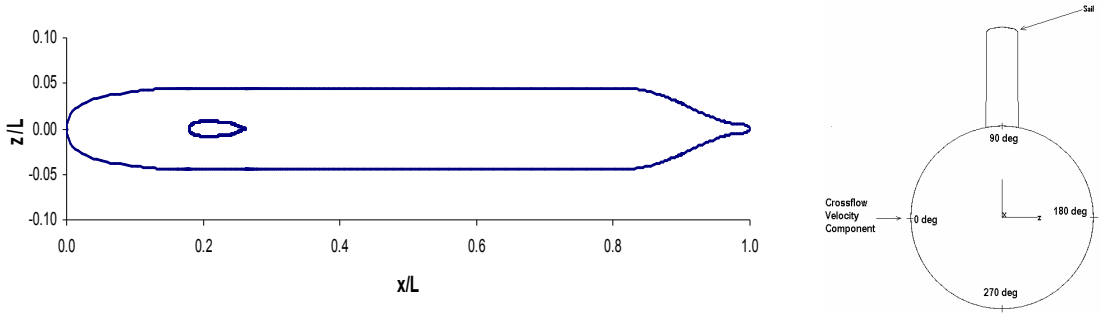

Fig: 1

GRID GENERATION

A 3D structured grid with clustering near model is made by using *Gridgen 15.04* as shown in the fig:2. Constructed grids satisfy the requirement of grid independence.

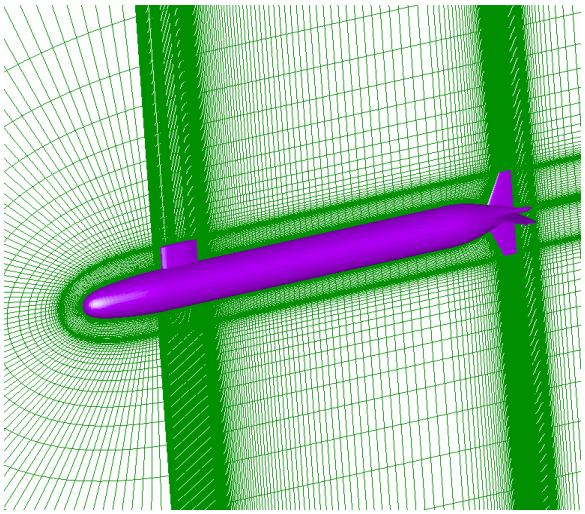

Fig: 2

BOUNDRY CONDITIONS AND SOLVER PARAMETERS

Solver	3d, segregated, steady
Turbulence Model	*k-Epsilon*
Free stream Velocity	14.8 m/s
Discretization Scheme	2nd Order
Average Wall Y+ Value	80
Surface of submarine	No slip adiabatic wall

RESULTS AND DISCUSSIONS

Vorticity Measurements

Vorticity is the measure of rotation of a fluid element as it moves in the flow field, as it is defined as a curl of velocity vector.

$$Vorticity = \nabla \times V$$

Although there is a low pressure in the vortex center as shown in Fig: 8, but the net effect is that low pressures occur on the side of the submarine opposite to the sail tip vortex and high pressure on the side adjacent to the tip vortex. This is because that there is a vortex system, in which there is also a bound vortex with the trailing vortex. This system of vorticity sets up circulation around the hull, which in combination with the local crossflow causes a hydrodynamic pressure difference to occur between the deck and keel.

This is a flow phenomena [2] that rotation of vortex aligns with the direction of free stream, therefore outside of vortex moves in the same direction as the free stream, so the vortex is in clockwise direction, while the circulation around hull is anti clockwise, thus at the lower side of submarine the crossflow velocity components of free stream are added by the circulation velocities and at the upper side free stream crossflow velocity components are subtracted due the clockwise circulation of the trailing vortex .This force is something like a Magnus force where lift is produced due to the circulation velocities are added with free stream velocities. According to the Bernoulli's Theorem pressure increases where velocity decreases and vice versa , so on the upper side pressure increases due to decrease of velocity and on the lower side pressure decreases due to increase of velocity.Fig: 3 shows the streamlines around the submarine at drift angle 9.5 and a vortex is clearly shown behind the sail.

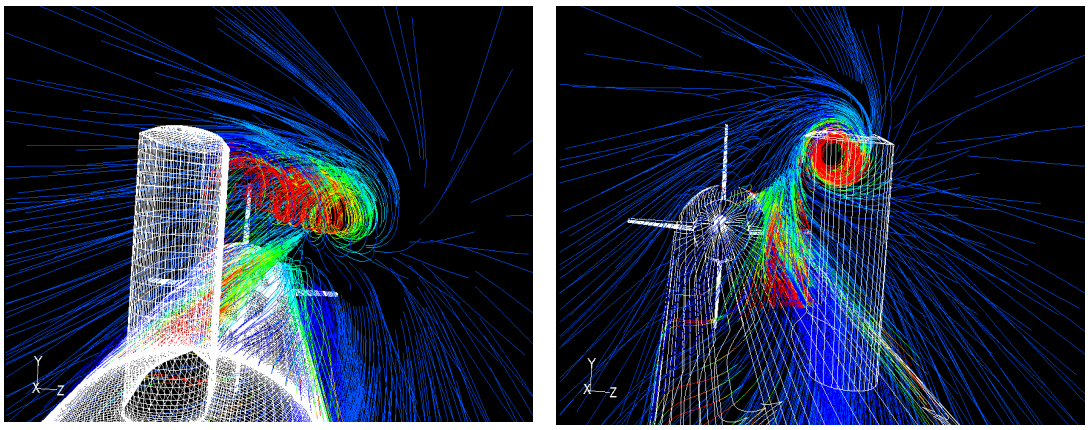

Fig: 3 Streamlines behind the Sail at drift angle 9.5.

Actually vortex motion is a circularly or rotary movement of a liquid about a line or axis. This trailing vortex is in helical motion just like the wing tip vortex around an aircraft wing. The helicity is the dot product of vorticty and velocity vector.

$$Helicity = (\nabla \times V) \bullet V$$

The helicity contours are shown at different cross sections as shown in the Fig: 4, and from this we estimated that vortex starts just behind the sail and ended at approximately 3.95 m , where the total length is 6.92 m.

Fig: 5. clearly show the strong helicity contours located above the submarine behind the sail.

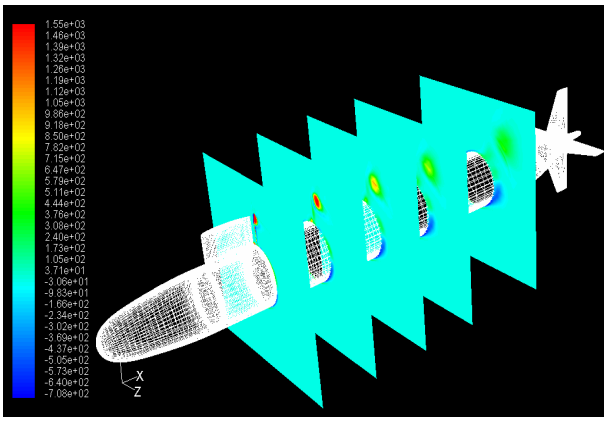

Fig:4 Helicity Contours at different x-sections

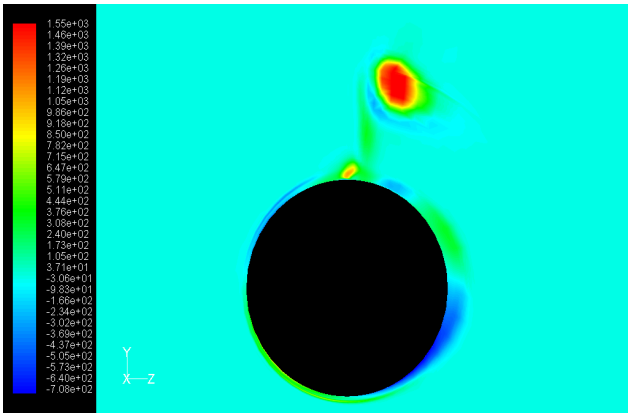

Fig:5 Helicity Contours (m/s^2)at x/L=0.36

Pressure Measurements

The pressure distributions obtained in this investigation were perhaps the most important results because they would provide evidence that would help confirm the postulated mechanisms for the creation of pitching moment. Fig: 6 shows the circumferential pressure coefficient at axial location of x/L=0.47 with experimental results for the model at 9.5-deg drift and with the sail attached and Fig: 7 shows the pressure distributions without sail with experimental results. Contours of pressure with sail on and off are shown in Fig: 8 and Fig: 9. It is obvious from Fig: 6 that the pressures are higher on the deck than they are on the keel. This would create a net downward force on the hull aft of the sail and generally aft the center of gravity of the submarine. The pressure distribution results are consistent with the experimental results of D.H.Bridges[1].

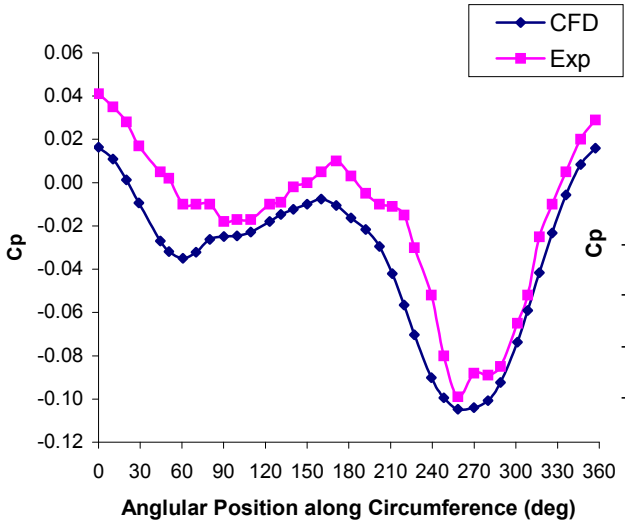

Fig: 6 Circumferential pressure distribution: β =9.5, sail On (x/L=0.47)

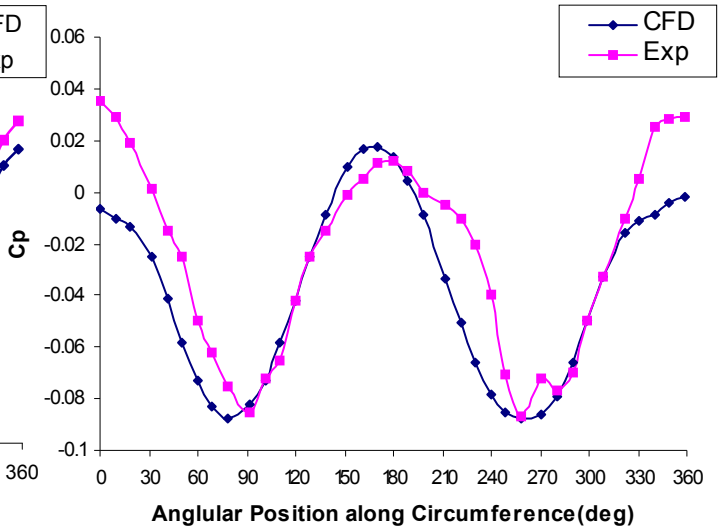

Fig:7 Circumferential pressure distribution β =9.5, sail Off (x/L=0.47)

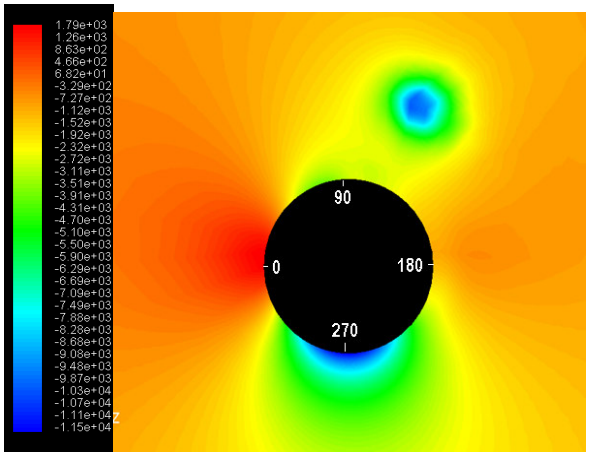

Fig: 8 Contours of Pressure(Pa) at section β =9.5, sail On (x/L=0.47)

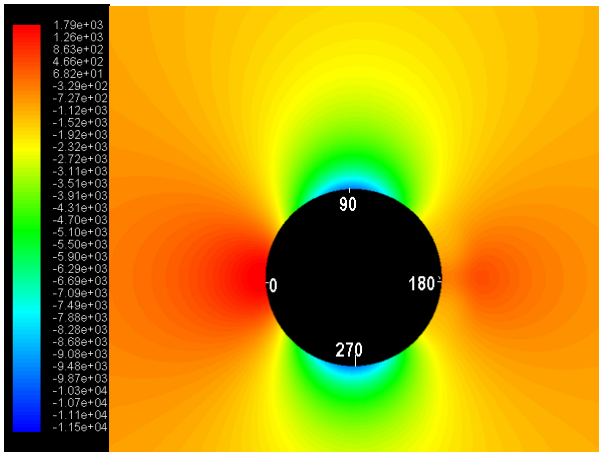

Fig: 9 Contours of Pressure(Pa) at section β =9.5, sail Off (x/L=0.47)

There is low pressure in the vicinity of vortex as shown Fig: 8 .
Fig: 10 demonstrate that what is effect on pressure by adding the sail at x/L=0.47. In this figure, the first distribution is for the submarine at zero drift and with no sail attached, which is essentially an axisymmetric configuration with respect to oncoming flow. There is no any pressure variation along the circumference at such a condition. The second distribution is for drift angle 9.5 but with no sail attached. Here the distribution is what one would expect for the flow past an inclined cylinder, with two suction peaks on the sides of the model corresponding to the regions of the maximum flow acceleration, this is also shown in Fig: 9. The third distribution repeats pressure shown in Fig: 6, for the same angle of drift but with sail attached. It is clear in comparing the second and third distribution that the addition of the sail has caused an increase in the pressure on the deck and decrease in pressure on keel.

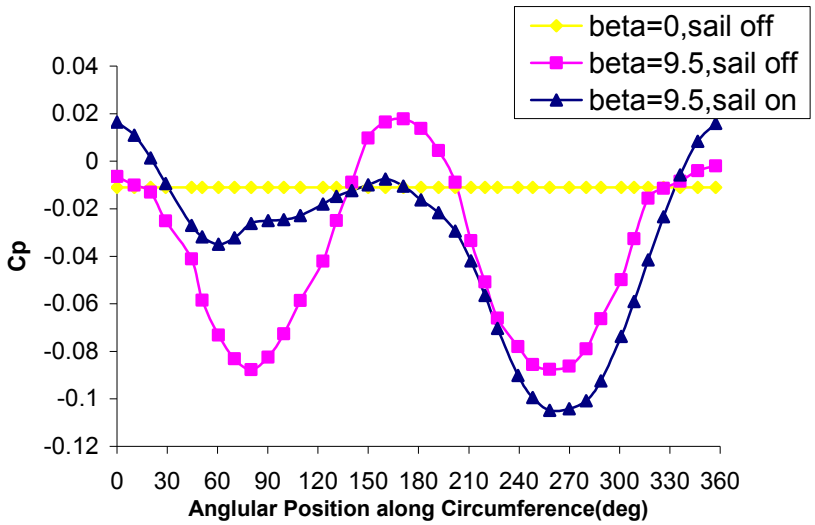

Fig:10 Demonstration of the effect on Pressure by adding the Sail at x/L=0.47

Force and Pitching Moment Measurements

The results of downward force and pitching moment are shown in Fig: 15. These results are obtained at different drift angles 0, 5 and 9.5. All moment results shown here are with reference to force balance center, located at x/L=0.271

It has been found that downward force and pitching moment is increased with increase in drift angle when the sail is on whereas there is no such effect on downward force and pitching moment when the sail is off. So all of the down ward force is due to the sail tip vortex. Because these forces are located aft portion of the submarine, they yield the positive or nose-up pitching moment. It has been also found that both of these coefficients demonstrate the nonlinear variation with the change in drift angle when sail is on. This is also consistent with description of D.H. Bridges[1] and Feldman[5] that pitching moment demonstrate nonlinear increase with angle of drift.

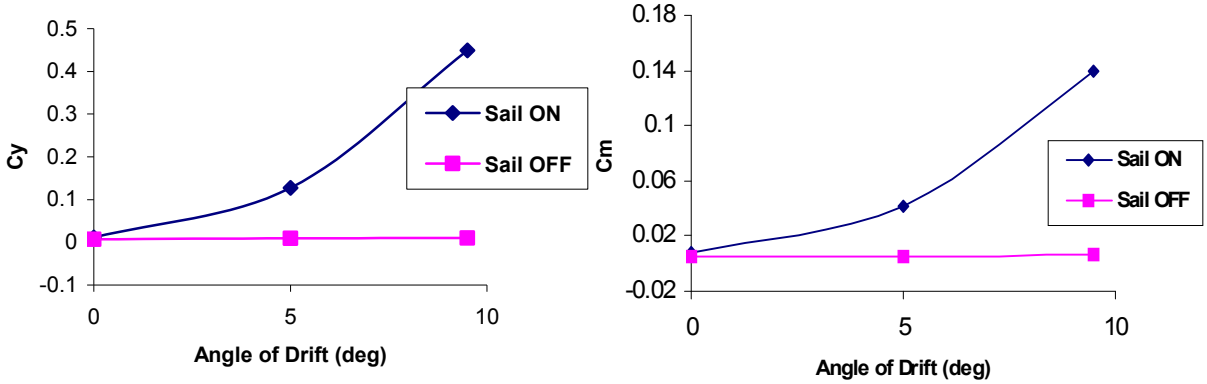

Fig: 15 Downward Force & Pitching Moment Variations with change in Angle of Drift

CONCLUSIONS

The tip vortex shed from sail at angle of drift during high speed turn causes an out of plane pitching moment. The circulation associated with the vortex creates an equal and opposite circulation around hull and with the combination with cross flow velocity component, results in shifting the pressure distribution, increasing the pressure on the deck and decreasing the pressure on the keel. Pressure distribution results are consistent with the experimental results of D.H.Bridges.[1]. Because this net downward force acts primarily on the rear of the submarine, the net result is nose-up pitching moment.

From helicity contours it is rough estimated that vortex starts just behind the sail and diffused at x/L=0.57.

The downward force and pitching moment show a non-linear variation with the change in drift angle when the sail is on. This is also consistent with Bridges[1] and Feldman[5], and when sail is off, there is no such effect on downward force and pitching moment with the change in drift angle.

Flow simulation of a propeller in open water condition and experimental validation

N. BERCHICHE
nabila.berchiche@chalmers.se

C-E. JANSON
carl-erik.janson@chalmers.se

Department of Shipping and Marine Technology of Chalmers University
412 96 Göteborg, Sweden.

INTRODUCTION

During the past few years, a large number of studies related to numerical simulation of propeller flow demonstrated the ability of Reynolds Averaged Navier-Stokes codes in predicting the performance and the overall features of the flow of marine propellers. Hsio and Pauly [4] studied the tip vortex flow generated by a propeller using RANS calculations with the Baldwin-Barth turbulence model. The general characteristics of the tip vortex flow were well predicted. However, the strength of the vortex was slightly underestimated mainly due to the one-equation turbulence model. In their paper, Rhee and Joshi [6] have used an unstructured grid and the k-ω turbulence model to simulate the flow around a highly skewed propeller. The forces and the circumferentially averaged velocity components were in a good agreement with the measured values, whereas the velocity and the turbulence quantities in the highly concentrated tip vortex region were under-predicted.
In the present study, three-dimensional steady RANS computations were carried out to simulate the flow around a conventional propeller operating in open water conditions. The main objective of this study is to predict the flow around the propeller blade particularly around the blade tip. Computational results, which consist of the forces acting on the propeller and velocity distributions close to the trailing edge of the blade are illustrated and compared with the experimental data obtained from open water tests and PIV measurements for the design advance coefficient J.
This study was performed within the framework of the EU-project "Leading Edge".

NUMERICAL METHOD

The computations were carried out in a single rotating reference frame using the commercial Navier-Stokes code Fluent version 6.1.22 [3].
A segregated solver with absolute velocity formulation was used in the present computations. The Pressure and the pressure-velocity coupling were discretized with the second order and SIMPLE schemes respectively, and the second order upwind scheme was selected for the momentum, turbulence kinetic energy and dissipation rate.

COMPUTATIONAL GRID

The propeller model investigated in this paper is a four-bladed, fixed-pitch propeller of conventional shape, manufactured by MARIN. The diameter D of the propeller is 0.28086 m.
Since the flow in the actual propeller configuration is periodical and stationary, only one blade was modeled. The computational domain was thus reduced to one blade passage with: the inlet at 2D upstream from the propeller center, the outlet 3 D downstream, the outer boundary at 2D from the hub axis and two periodic boundaries on each side of the blade. The hub section was extended in both upstream and downstream boundaries.
The computational grid is generated in ICEM CFD. The calculation domain, Figure 1, consists of 28 blocks, 9 blocks were used to capture the blade geometry. To ensure good quality mesh and resolve the boundary layer on the solid surface, an O-type grid topology was applied around the propeller blade. The first cell height near the wall is 0.003mm which corresponds to $y^+ \approx 1$. In the rest of the domain around the propeller, an H-type grid was applied. The total number of grid cells is 1401388.
Figure 2 illustrates the surface mesh on the blade; the grid was refined on the blade near the zones of strong gradients in particular close to the leading edge and the trailing egde. A close up view of the surface mesh on the hub near the leading edge is shown in Figure 3.

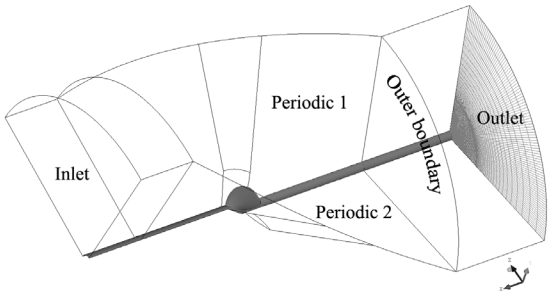

Figure 1. View of the computational domain.

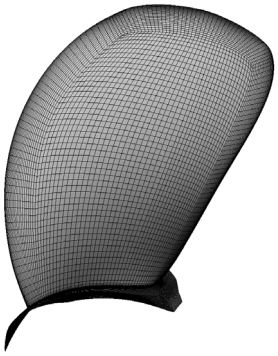

Figure 2. Surface mesh on the blade.

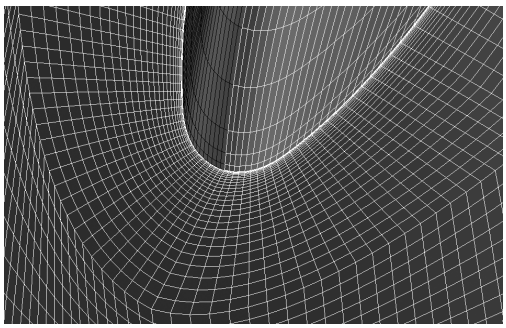

Figure 3. Surface mesh on the hub.

BOUNDARY CONDITIONS & TURBULENCE MODEL

The boundary conditions were the following: a uniform velocity inlet assigned at the upstream boundary; a pressure outlet at the downstream boundary; a no-slip solid wall condition was applied on the blade and hub surface, and rotational periodicity was specified on the periodic boundaries. For the outer radial boundary, a slip condition is imposed.

The effects of turbulence were modeled using the shear stress transport SST k-ω model [5]. The influence of the turbulence model was also investigated by using the realizable k-ε model [8] in combination with enhanced-wall treatment as an alternative. The standard and SST k-ω models have shown good potential to compute the flow around marine propellers [6], [7] and [9]. In the computations, the inlet turbulence intensity was considered to be 1%.

COMPUTATIONAL RESULTS & VALIDATION

The flow condition investigated in this study was based on the experimental condition at J= 0.4, which is also the design condition of the propeller.

Thrust and torque coefficients

Table 1 compares the predicted thrust and torque coefficients obtained using the SST k-ω and the k-ε Realizable turbulence models with the experimental values.

Table 1. Computed and experimental values of K_T and K_Q

	K_T	$10\,K_Q$
Computations with *SST k-ω* model	0.1662	0.2114
Computations with *k-ε* Realizable model	0.1680	0.2183
Experiments	0.165	0.195

The error in the prediction of K_T was less than 1% and 2% for the SST k-ω and the k-ε Realizable models respectively. However, K_Q was over-predicted by about 8 % for the SST k-ω model and 12% for the k-ε Realizable. Consequently, the performances of the propeller seem to be better predicted with the SST k-ω model.

The over-prediction of K_Q was observed in many papers [6], [7] and [9]. Recently in their paper, Bulten and Oprea [1] pointed out that the over-prediction of the torque is related to an over-estimation of the total drag force due to an error in the evaluation of the pressure at the stagnation point.

Additional computations were also performed at different J values. The numerical results, shown in Figure 4, seem to agree well with the measured data especially for the prediction of K_T, but for the K_Q the difference increases as the advance coefficient is increased. This behavior might be related to the grid resolution near the wall region since the same grid was used in the calculations. This leads to an increase of the y^+ value when the inflow velocity is increased.

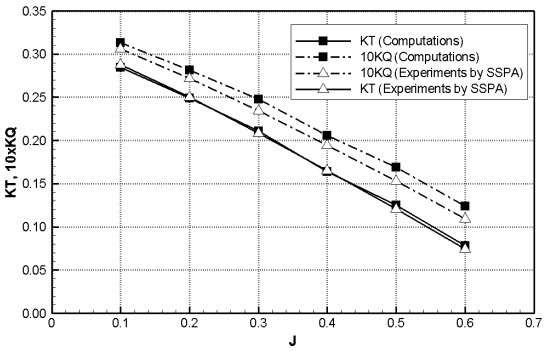

Figure 4. Comparison of the calculated and experimental values of K_T and K_Q for several J.

Pressure distributions on the blade

Figure 5 shows the pressure coefficient contours on the suction and pressure sides of the blade. A low-pressure area is visible on the suction side along the leading edge and in the tip region of the blade indicating a roll-up of the flow in this area. Cavitation tests performed by SSPA and Marin, on the model

propeller at the same design condition, showed a clear vortex at the blade tip.

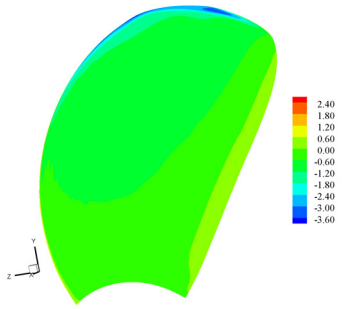

(a) Suction side

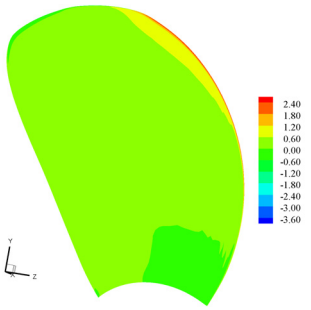

(b) Pressure side

Figure 5. Pressure coefficient contours on the suction and pressure sides of the blade.

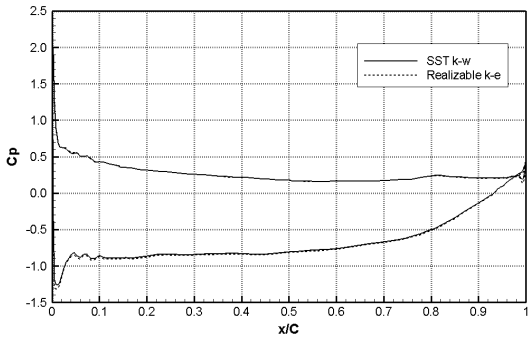

(a) r = 0.7R

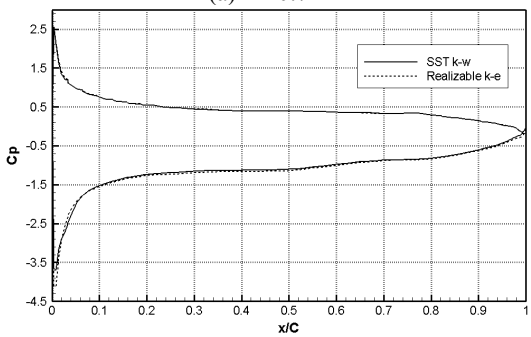

(b) r = 0.95R

Figure 6. Pressure coefficient distributions along the chord length at r/R = 0.7 and r/R = 0.95.

The pressure coefficient distributions along the chord length of the blade, obtained with the SST k-ω and the k-ε Realizable turbulence models, are illustrated in Figure 6 for two sections: r = 0.7R and 0.95R. In this figure, the pressure coefficient is plotted along the chord length from the leading edge (x/c = 0) to the trailing edge (x/c = 1) of the blade. The Cp profiles are similar except near the leading edge of the suction side where the minimum value of Cp is lower for the k-ε Realizable turbulence model. The predicted minimum values of the pressure coefficient Cp_{min} were –3.73 and -4.16 for the SST k-ω and the k-ε Realizable models respectively and in both cases Cp_{min} occurred near the leading edge of the blade close to the section 0.95R.

Flow investigation and validation

The computed flow field was compared to the measured PIV data [2] at a plane located downstream of the propeller, Figure 7. Shown in this figure are also the coordinate systems (xyz) and ($x_p y_p z_p$) used in the numerical computations and the PIV measurements respectively. The three velocity components measured at the measurements plane were averaged over about 200 revolutions and were defined as follow:

- The axial in-plane velocity is in the x_p-direction, parallel to the inflow and is positive in the main flow direction. Note that the inflow velocity is subtracted from the axial in-plane velocity.
- The vertical in-plane velocity is in the y_p-direction, which is also perpendicular to x_p-direction. Its positive direction is pointing from the propeller center towards the tip.
- The out-of-plane velocity is in the z_p-direction and is positive towards the leading edge.

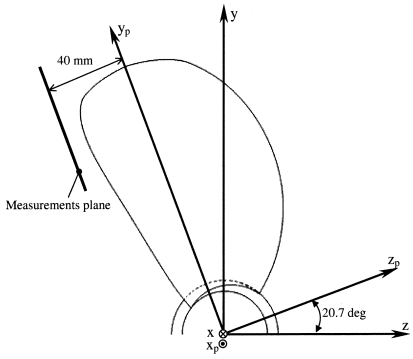

Figure 7. Location of the measurements plane.

Figures 8-10 show a comparison of the non-dimensional velocity components (axial in-plane velocity, vertical in-plane velocity and the out-of-plane velocity) between the present numerical solution and the PIV data at the measurements plane downstream of the propeller. The numerical and measured values of the velocities were made non-dimensional by the tip speed.

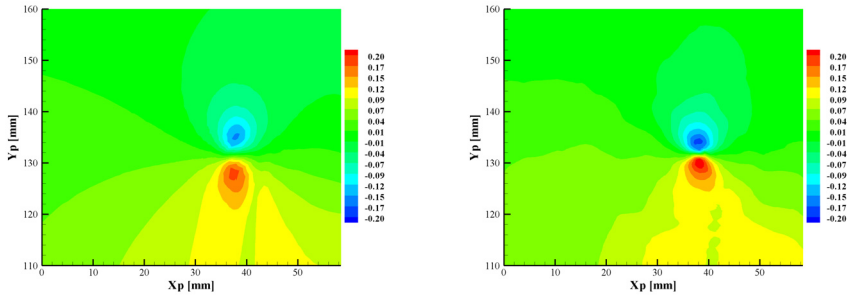

Figure 8. Comparison of the non-dimensional axial in-plane velocity between numerical (left) and experimental (right) results at the measurements plane.

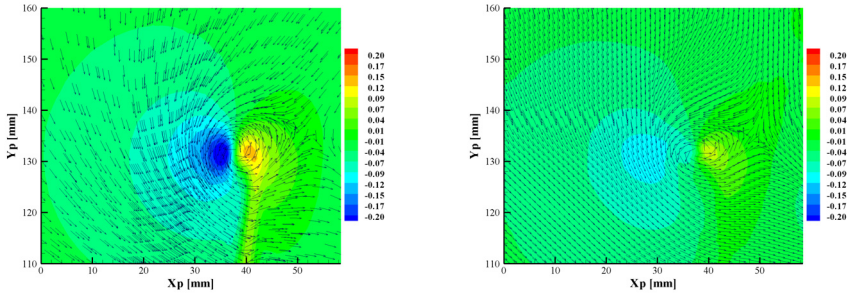

Figure 9. Comparison of the non-dimensional vertical in-plane velocity and the in-plane velocity vector between numerical (left) and experimental (right) results at the measurements plane.

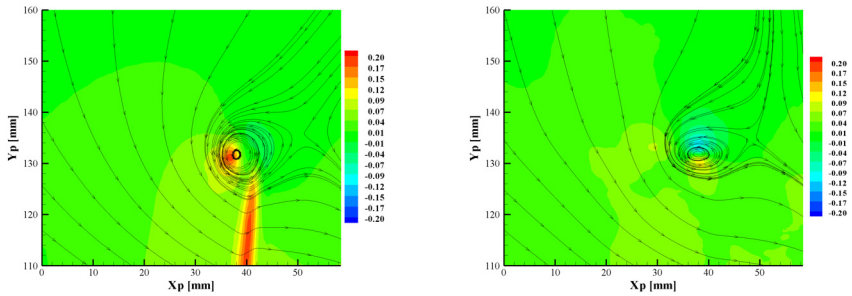

Figure 10. Comparison of the non-dimensional out-of-plane velocity and the streamlines between numerical (left) and experimental (right) results at the measurements plane.

The overall structure of the tip vortex in the measurements plane appear to be reasonably well predicted. The two components of the in-plane velocity vector have similar patterns for both numerical and experimental results, whereas for the out-of-plane velocity, the narrow wake of the blade is captured in the CFD data but it is not visible in the PIV results. This discrepancy can be attributed to the measuring accuracy of the PIV method, which depends on a large variety of parameters and the PIV set-up used during the measurements. The uncertainty of the out-of-plane component was about a factor two higher than the uncertainty of the in-plane component. A detailed analysis of the PIV measurements is required in order to investigate the differences in the out-of-plane component of the CFD-data and the PIV-data. Despite these differences, the numerical results show a rather good correlation with the experimental PIV data.

Propeller flow patterns

Streamlines on the suction side of the blade are shown in Figure 11 for different J values. This type of illustration is very useful to locate the origin of the tip vortex on the blade and its development. For the design advance coefficient J = 0.4, it was found that the vortex starts at the leading edge of the blade close to 0.95 non-dimensional radius of the propeller blade. As the loading of the propeller decreases, i.e. advance coefficient increases, Cp_{min} increases, the strength of the tip vortex decreases and the origin of the leading edge vortex moves towards the tip of the propeller blade. At high J values only a weak tip vortex is observed on the suction side of the blade.

Figure 12 illustrates the predicted pressure coefficient along the tip vortex core obtained with the SST k-ω and the k-ε Realizable turbulence models for the design advance coefficient. In this figure, the pressure

coefficient is plotted along a number of planes parallel to the measurements plane, starting from plane ($x_p y_p$) at z_p = 0 to a plane located at z_p = -100 mm downstream the blade. Downstream the propeller blade (-z_p >35 mm), the values of the pressure coefficient along the tip vortex core are similar for the two models, but close to the propeller blade, the k-ε Realizable turbulence model resulted in higher values of the pressure coefficient. Figure 13 shows that the pressure coefficient along the tip vortex core is decreased as the advance coefficient is decreased, and for all the J values, the minimum pressure coefficient in the tip vortex core occurred near the propeller blade tip.

From the pressure coefficient distributions, Figure 6, and the streamlines plots on the blade, Figure 11, it is possible to estimate the location and extent of the moderate cavitation that may develop on the propeller blade in a cavitating flow conditions i.e. at conditions for which the local cavitation number σ is lower than $-Cp_{min}$.

For a cavitation number corresponding for example to Cp=-2.5 at J=0.4, Figure 6b indicates that a narrow sheet cavity can be expected along the leading edge close to the blade tip at r = 0.95R. However, Figure 6a indicates that the cavity will not extend to r = 0,7R, since σ is higher than $-Cp_{min}$ at this radius. Cavitation in the tip vortex is also expected for this condition, as the minimum pressure in the vortex core is lower than the vapor pressure, Figure 13. From the Cp distribution, it is also clear how changes in σ will result in different cavitation extents. Cavitation tests performed at the design condition have shown the existence of a tiny sheet cavity and a tip vortex cavity on the propeller blade.

For higher J values, for instance J= 0.6, Figure 11 indicates a distinct vortex from the suction side but with a moderately low pressure, Figure 13. In cavitating conditions, this would result in a thin tip vortex cavity. Furthermore, on the pressure side of the blade, if the Cp is low enough, a sheet face cavitation starting at the leading edge is likely to occur due to the unfavorable inflow.

CONCLUSIONS

This paper presents RANS computations of the flow around a conventional propeller in open water condition.

It was found that the performance of the propeller is better predicted with the SST k-ω model than the k-ε Realizable model. The computed thrust and torque coefficients at various J values agreed well with the measured data especially for the prediction of K_T. Furthermore, the predicted velocity distributions at a plane downstream the propeller blade were well correlated with the PIV measurements results.

The results obtained in this study are very promising and indicate that RANS codes are very useful tools to investigate the flow around marine propellers provided that a good quality grid is used and suitable turbulence model is selected.

ACKNOWLEDGMENTS

This study was sponsored by The European Commission and is a part of the EU-project “Leading Edge” being a project within the Fifth (EC) FRAMEWORK PROGRAMME Promoting Competitive and Sustainable Growth. The authors would like to express their acknowledgments to the project partners for the permission to publish this paper.

REFERENCES

1. Bulten; N.W.H., Oprea, I.A., Consideration on deviations in torque prediction for propellers and waterjets with RANS codes, Marine CFD 2005, Southampton, UK.

2. Dautel; J., Martigny, D., Corrignan, PH. and Tukker, J., Development and application of a new three components PIV system (3c-PIV) designed for towing tank applications, 10th Days of Hydrodynamics, Ecole de Nantes, Nantes, March 2005.

3. FLUENT 6.1 User's Guide.

4. Hsiao, C-T. and Pauley, L.L., Numerical computation of tip vortex flow generated by a marine propeller, ASME Fluids Engineering Division Summer Meeting FEDSM’98, June 21-25, 1998, Washington D.C.

5. Menter, F.R., Two-Equation Eddy-Viscosity Turbulence Models for Engineering Applications, *AIAA Journal*, 32(8): 1598-1605, August 1994.

6. Rhee, S.H. and Joshi, S., CFD validation for a marine propeller using an unstructured mesh based RANS method, Proceedings of FEDSM’03, 4th ASME-JSME Joint Fluids Engineering Summer Conference, Honolulu, Hawaii, USA, July 6-11, 2003.

7. Rhee, S.H. and Kawamura, T., A study of propeller cavitation using a RANS CFD method, 8th International Conference on Numerical Ship hydrodynamics, September 22-25, 2003, Busan, Korea.

8. Shih, T-H., Liou, W.W., Shabbir, A., Yang, Z. and Zhu, J., A New k-ε Eddy-Viscosity Model for High Reynolds Number Turbulent Flows - Model Development and Validation. *Computers Fluids*, 24(3): 227-238, 1995.

9. Watanabe, T. et al., Simulation of unsteady cavitation on a marine propeller using a RANS CFD code, 5th International Symposium on Cavitation (CAV2003), Osaka, Japan, November 1-4, 2003.

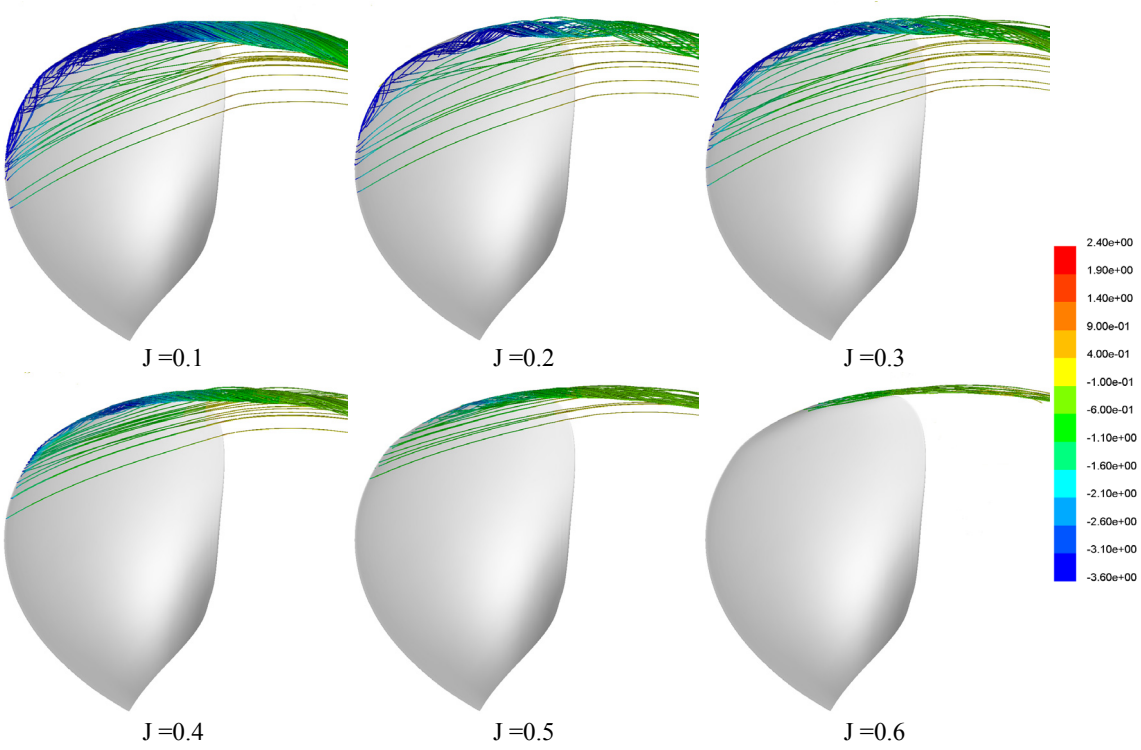

Figure 11. Streamlines on the suction side of the blade, colored by the pressure coefficient, for different J values.

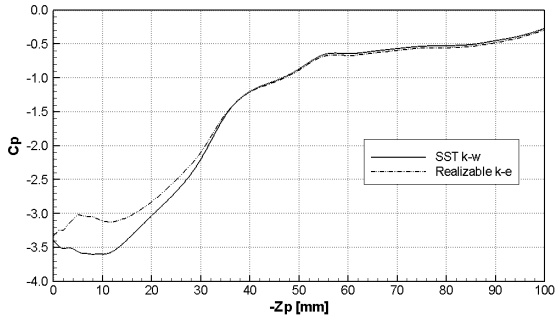

Figure 12. Pressure coefficient distribution along the tip vortex core for J= 0.4.

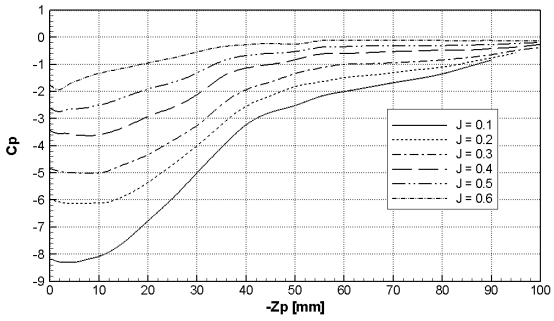

Figure 13. Pressure coefficient distribution along the tip vortex core for different J values.

Issues on Nonlinear Programming for Multidisciplinary Design Optimization (MDO) in Ship Design Framework

Emilio F. Campana[1], Giovanni Fasano[1,2] and Daniele Peri[1]

(1) Istituto Nazionale per Studi ed Esperienze di Architettura Navale INSEAN,
via di Vallerano 139, 00128 Roma, ITALY
E-mail: (e.campana,g.fasano,d.peri)@insean.it.

(2) Istituto di Analisi dei Sistemi ed Informatica 'A. Ruberti' - IASI, CNR,
viale Manzoni 30, 00185 Roma, ITALY
E-mail: fasano@iasi.rm.cnr.it.

Abstract

This work is concerned with the study and the evaluation of formulations for Multidisciplinary Design Optimization (MDO) problems. The latter topic includes very difficult computational aspects, naturally arising from the simultaneous solution of several related optimization problems. In particular, in the naval applications deep interaction among different *disciplines* (i.e. optimization/feasibility problems) is claimed, in order to provide the solution. Each discipline concurs to give intermediate results to other disciplines, until the convergence of the overall framework is reached. The usual nonlinear programming techniques, including multiobjective optimization methods, seem still inadequate to cope with most of these challenging applications. In this work we first consider some relevant formulations proposed in the literature for MDO. Then, we consider the relationship between MDO and NonLinear Programming (NLP), with specific reference to feasibility and convergence analysis. Preliminary numerical results on a ship design application are included.

Keywords: Multidisciplinary Design Optimization, Nonlinear Programming, Formulation and Feasibility issues, Convergence analysis.

1 Introduction

In the last decades a large number of industrial applications claimed for complex optimization approaches, in order to obtain reliable and effective solutions. Several of these applications (e.g. aircraft and spacecraft engines design) provide challenging problems which have been formulated within MDO frameworks [9, 1]. The latter methodologies substantially include both parallelization and coupling of different optimization or feasibility schemes, i.e. the *disciplines*, involved in the application. This kind of approach is still missing in the framework of the marine design, while the design activities in this field involve naturally several different disciplines, with an high degree of coupling. Under this perspective, marine design would be taking an enormous advantage by the application of MDO.

Unfortunately, the interaction among the standard optimization techniques used within the respective disciplines is non-trivial. This requires a special care for the overall resulting formulation. Nevertheless, the formal and accurate coupling among disciplines is essential, in order to guarantee both the *convergence* and *satisfactory performance* of the overall framework [1]. On one hand, specific attention has to be paid in order to ensure the *correctness* of the MDO formulation in hand. Indeed, a single application often allows different

MDO formulations. However, some of them are *naive* or permit only a poor convergence analysis; hence they should be discarded if theoretical achievements are sought [9]. On the other hand, nonlinear programming often provides powerful and reliable techniques for the solution of standard optimization problems. This suggests that those MDO formulations, which rely on the abilities of optimization methods, may efficiently gain advantage from conventional optimization algorithms [3, 4]. Observe that most of the usual ingredients considered for nonlinear programming (e.g. feasibility, optimality conditions, sensitivity analysis, duality, etc.), are not immediately applicable and require a suitable adaptation to MDO frameworks.

On these guidelines, the first classifications proposed in the literature for MDO problems, often relied on the possibility of managing standard and simple nonlinear programming schemes. This was partially imposed by the huge computational burden usually involved in large scale design problems. In addition, whenever coarse solutions where allowed, for extremely tough practical problems, the coupling among disciplines was weakened. Thus, independent optimization methods could be autonomously applied, so that MDO frameworks reduced to a sequence of mere nonlinear programming schemes, adaptively coordinated by some rules [3]. Unfortunately, the resulting scenarios poorly described several non-convex real problems, which tried engineers' abilities and efforts [16].

In this work we review some issues related to the current formulation of MDO problems. Then we consider more recent papers, where novel MDO formulations are studied. In particular we focus on *bilevel programming* methods, where the original MDO formulation is decomposed into a *system level* problem and a set of *lower level* subproblems. The master (i.e. the system level) problem depends on the optimal solutions of subproblems; conversely each subproblem includes a set of unknowns provided by the master level. We specifically review some theoretical difficulties related to the convergence of MDO bilevel formulations.

Then, we apply our preliminary conclusions to the formulation of a small scale ship design problem, where PDE solvers are included. We finally give evidence that the solution of the resulting optimization problem requires efficient techniques from nonconvex Nonlinear Programming.

2 Preliminaries

In this paper[1] we indicate with

$$\min_{x \in \mathcal{A}} \; f(x) \tag{2.1}$$

the general mathematical programming problem, where $\mathcal{A} \subseteq \mathbb{R}^n$, $n \geq 1$, is the *feasible set* and $f : \mathbb{R}^n \to \mathbb{R}^q$ is the *objective function*. If $q > 1$ then (2.1) is a *multiobjective* problem, while $f(x) = const.$ for any $x \in \mathcal{A}$, transforms (2.1) into a *feasibility* problem.

A *local minimum* of $f(x)$ on the set $\mathcal{A}$ is a point $x^* \in \mathbb{R}^n$ such that:

$$f(x^*) \leq f(x), \qquad \forall x \in \mathcal{A} \cap B(x^*, \rho),$$

where $B(x^*, \rho) \subset \mathbb{R}^n$ is a ball with center in x^* and radius $\rho > 0$. Similarly, a *global minimum* of $f(x)$ on the set $\mathcal{A}$ is a point $x^* \in \mathbb{R}^n$ such that:

$$f(x^*) \leq f(x), \qquad \forall x \in \mathcal{A}.$$

We define a set of *optimality conditions* for (2.1) as a set of analytical relations satisfied by the so called *stationary points* of $f(x)$ in (2.1). The set of stationary points includes the minima of $f(x)$ on $\mathcal{A}$, but in general may also include other points like local maxima, inflection points, etc. Then, when we report that the point $x^* \in \mathcal{A}$ simply satisfies some optimality conditions, we mean that the latter conditions are only *necessary* for x^* to be a local minimum.

Then, we say that an algorithm for solving (2.1) is *globally convergent* when it generates the (possibly infinite) sequence $\{x_k\} \subset \mathcal{A}$, converging to a *stationary point* of (2.1), regardless of the choice for the initial point x_0. For instance, when $\mathcal{A} \equiv \mathbb{R}^n$ and $f(x)$ is continuously differentiable, the latter definition corresponds to an algorithm which generates the sequence $\{x_k\}$, such that $\liminf \|\nabla f(x_k)\| \to 0$. When further (stronger) assumptions are considered (e.g. the convexity of $f(x)$ in (2.1), the convexity of $\mathcal{A}$, etc.),

[1] The following notation is adopted: $\mathbb{R}^n$ is the real n-dimensional space. We indicate the Euclidean norm of vector x as $\|x\| \doteq < x, x >^{1/2}$, while $\|x\|_\alpha$ represents the general α norm, for any $\alpha > 0$.

it is possible to ensure also *sufficient* conditions for the convergence to a minimum point.
Observe that despite the misleading use of the term '*global*', the definition of global convergence and global minimum are independent, i.e. a globally convergent method could in general yield a local minimum [7].

Without loss of generality we consider in the paper only *minimization problems*. This is not a limitation; indeed, suppose for instance that we have to maximize the objective function $f : \mathbb{R}^n \to \mathbb{R}$ over the set $\mathcal{A}$. Then, by means of the identity $\max_{x\in\mathcal{A}} f(x) = -\min_{x\in\mathcal{A}}[-f(x)]$ we can immediately transform the maximization into an equivalent minimization. On this guideline, we remark that the optimality conditions can be intended for both minimization or maximization problems[2].

3 General aspects of an MDO formulation

As the Section 1 suggests, in general the MDO formulation of a real problem may be not unique. Indeed, an MDO formulation is characterized by the following ingredients:

- each discipline contributes to describe the overall problem;
- each discipline represents an independent problem with its own formulation. This formulation and its solution rely on theoretical results (e.g. optimality conditions, sensitivity analysis, convergence analysis), solution techniques (e.g. solution methods, heuristics, etc.) and possibly use software codes arising from within that discipline;
- the independent formulations of the different disciplines require a suitable unification, to form an overall MDO formulation, which claims for its own theory, solution methods and software packages.

From this scenario several theoretical difficulties naturally arise when dealing with MDO, not to mention severe *feasibility issues*, which arise in different forms for both the discipline and the MDO level (see Section 3.2). Let us describe now a formal representation of an MDO formulation.

Some variables of the overall formulation, which comprehends the formulations of the disciplines, are *design unknowns*, i.e. they have a physical meaning related to real parameters of the ship. On the other hand, in the formulation associated with each discipline, other variables are in general introduced, e.g. *state unknowns* of the discipline, auxiliary parameters, etc., and do not play a direct role in the design problem.
More formally, consider the discipline D_i, $i = 1, \dots, p$, and let the pair of vectors $(x_i, s_i) \in \mathbb{R}^{n_i \times m_i}$ be associated with D_i. In particular, s_i is the subvector of unknowns representing the *state* of that discipline D_i (e.g. variables generated by the discretization of a PDE solver), while x_i is the subvector of design unknowns included in the formulation of D_i. With these positions, and including the subvector x_0 of design unknowns shared by the p disciplines, we want to address a formal definition for MDO formulations, by considering the vectors: $x^T = (x_0^T \; x_1^T \; \cdots \; x_p^T) \in \mathbb{R}^n$, $n = n_0 + n_1 + \cdots + n_p$ (design variables), and $s^T = (s_1^T \; \cdots \; s_p^T) \in \mathbb{R}^m$, $m = m_1 + \cdots + m_p$ (state vector).

Assumption 3.1 *Consider a real problem and suppose it involves the disciplines D_i, $i = 1, \dots, p$. Let $x^T = (x_0^T \; x_1^T \; \cdots \; x_p^T) \in \mathbb{R}^n$, $n = n_0 + n_1 + \cdots + n_p$, and $s^T = (s_1^T \; \cdots \; s_p^T) \in \mathbb{R}^m$, $m = m_1 + \cdots + m_p$, suppose that*

1. *the set $B_i \subseteq \mathbb{R}^{n_0 \times n_i \times m}$ exists for the discipline D_i, such that it is defined by the block of nonlinear constraints*
$$B_i = \{(x_0, x_i, s) \in \mathbb{R}^{n_0 \times n_i \times m} : \; g_i(x_0, x_i, s) \geq 0, \quad A_i(x_0, x_i, s) = 0\};$$
2. *the nonlinear function $f_i(x_0, x_i, s)$ exists, with $f_i : \mathbb{R}^{n_0 \times n_i \times m} \to \mathbb{R}^{q_i}$, such that it is always possible to associate the formulation*
$$\min_{(x_0, x_i, s) \in B_i} f_i(x_0, x_i, s_i)$$
to each discipline D_i, $i = 1, \dots, p$;

[2]Note that the Karush-Kuhn-Tacker (KKT) conditions are among the most adopted optimality conditions for nonlinear optimization. However, in the literature they are often referred to minimization problems, so that their application to a maximization problem requires some simple but *careful* changes.

3. *the functions* $f(x,s) = \varphi[f_1(x_0,x_1,s),\ldots,f_p(x_0,x_p,s)]$ *and* $g_0(x,s)$ *exist, with* $f : \mathbb{R}^{n\times m} \to \mathbb{R}^q$ *and* $g_0 : \mathbb{R}^{n\times m} \to \mathbb{R}$, *such that if* $B = \{(x,s) \in \mathbb{R}^{n\times m} : g_0(x,s) \geq 0,\ (x,s) \in B_1 \cap \cdots \cap B_p\}$ *the real problem may be formulated as*

$$\min_{(x,s)\in B} f(x,s). \tag{3.2}$$

□

We are now ready to give the following general definition for MDO formulations, which will be adopted in this paper, unless differently specified.

Definition 1 *Consider a real problem and suppose the Assumption 3.1 holds; then, we say that (3.2) is a* `nonlinear MDO formulation` *for that problem.* □

Observe that the previous definition is necessary, in order to distinguish between *tractable* MDO problems (i.e. those problems whose formulation can take advantage from the nonlinear programming techniques), and *intractable* MDO problems, whose formulation is unclear or it is not a mathematical program.
If the formulation (3.2) were treated as a nonlinear program, the usual techniques from numerical optimization could be adopted for its solution. Unfortunately, the specific difficulty of (3.2) is in the equality constraints, the so called *MultiDisciplinary Analysis (MDA)* of the feasible set B, given by

$$MDA = \begin{cases} A_1(x_0,x_1,s) = 0 \\ \vdots \\ A_p(x_0,x_p,s) = 0. \end{cases}$$

Indeed, the i-th block of equalities $A_i(x_0,x_i,s) = 0$ may not correspond exactly to a set of nonlinear equations; though it may be a black-box, which only implicitly defines a nonlinear relation among the variables x_0, x_i and s. Moreover, the MDA often corresponds to the discretization of PDE systems, so that the *implicit function theorem* cannot be exploited to retrieve $s = s(x)$. Thus, (3.2) can be hardly reformulated as a nonlinear program uniquely dependent on the design vector x.

We say that an algorithm for solving the formulation (3.2) is *convergent* if it is globally convergent, so that a stationary point (x^*, s^*) is given for (3.2), which satisfies some optimality conditions. The *Karush-Kuhn-Tacker (KKT) conditions* are the most common optimality conditions adopted for the nonlinear program (3.2): they may involve the use of first and second order derivatives [14]. We avoid a detailed description of KKT conditions [6], nonetheless we remind that they often provide analytical conditions which can be fruitfully implemented within convergence frameworks of optimization algorithms. On the other hand, KKT conditions require some assumptions on both the objective function and the feasible set in (3.2). It is not difficult to find simple examples of MDO problems where the latter assumptions do not hold. Hence, this proves the intrinsic difficulty of providing both a complete convergence analysis and effective algorithms for the formulation (3.2).

Finally, we remark that most of the real problems implicitly require box constraints, at least for a subset of the design unknowns. The block of inequalities $g_0(x,s) \geq 0$ in (3.2) also includes the latter constraints.

3.1 MDO reformulations: issues on classification

In order to provide a general classification for nonlinear MDO formulations, a further set of constraints and unknowns has to be introduced in (3.2). In particular, suppose we modify (3.2) as [4]

$$\min_{(x,s,t)\in B'\cap\mathbb{R}^{n\times m\times m}} f'(x,s,t), \qquad B' = \Gamma_1 \cap \Gamma_2 \cap \Gamma_3, \tag{3.3}$$

where the sets of constraints Γ_1, Γ_2, Γ_3 are defined by

$$\textit{Design Constraints}: \quad \Gamma_1 = \begin{cases} g_0(x,s) \geq 0 \\ g_1(x_0,x_1,s) \geq 0 \\ \quad \vdots \\ g_p(x_0,x_p,s) \geq 0 \end{cases}$$

$$\textit{Disciplinary Analysis Constraints (MDA)} \quad \Gamma_2 = \begin{cases} A_1(x_0,x_1,s_1,t_2,\ldots,t_p) = 0 \\ \quad \vdots \\ A_p(x_0,x_p,s_p,t_1,\ldots,t_{p-1}) = 0 \end{cases}$$

$$\textit{Interdisciplinary Consistency Constraints} \quad \Gamma_3 = \begin{cases} t_1 = \mathcal{C}_1(s_1) \\ \quad \vdots \\ t_p = \mathcal{C}_p(s_p). \end{cases}$$

The Interdisciplinary Consistency Constraints are assumed nonlinear and introduce with respect to (3.2) the new set of unknowns $t^T = (t_1^T \cdots t_p^T)$. For each block $A_i(x_0, x_i, s)$, $i = 1, \ldots, p$ in (3.2), they weaken the dependency from the entire vector s of the state unknowns. The latter modification may be suitably appreciated by recalling that in this way, the general blocks $A_i(x_0, x_i, s) = 0$ and $A_j(x_0, x_j, s) = 0$, in the MDA, only share the subvector of unknowns x_0. This particular structure of the formulation could be used to apply optimization algorithms for the nonlinear program (3.3). In particular, either *decomposition techniques* or *multilevel methods* could be advisable in this case. According with a common terminology within the MDO literature, we can say that the set t of auxiliary variables is introduced in order to *decouple the interdisciplinarity* among disciplines.
As previously reported, the formulation (3.3) can be hardly solved with a direct application of standard mathematical programming techniques. Most of the times, optimality conditions, as KKT conditions, cannot be directly used and (3.3) must be reformulated into *more* tractable alternative problem(s), were nonlinear algorithms may be adopted.

Definition 1 *Let the set B' in (3.3) be nonempty, let Z^* be the solution set of the MDO formulation (3.3). We say that $\hat{\mathcal{F}}$ is a* reformulation *of (3.3) if a smooth nonlinear function $\varphi_{\hat{\mathcal{F}}}$ exists such that $\varphi_{\hat{\mathcal{F}}}(\hat{z}^*) \in Z^*$, for any $\hat{z}^* \in \hat{Z}^*$, where $\hat{Z}^*$ is the solution set of $\hat{\mathcal{F}}$.* □

Note that any MDO formulation is also an MDO reformulation with φ given by the identity. Furthermore, the solution(s) obtained for the reformulated problem *are not* in general optimal solutions of (3.3). This opens a serious discussion on all the possible and reliable reformulations for (3.3). Anyway, this is far beyond the purposes of the present paper; thus, we simply introduce the following definition of *equivalence among reformulations*.

Definition 2 *Let $\tilde{\mathcal{F}}$ and $\bar{\mathcal{F}}$ be reformulations of the MDO formulation (3.3). Let $\tilde{Z}^*$ and $\bar{Z}^*$ be the solutions sets of $\tilde{\mathcal{F}}$ and $\bar{\mathcal{F}}$. We say that $\tilde{\mathcal{F}}$ is* equivalent *to $\bar{\mathcal{F}}$ (i.e. $\tilde{\mathcal{F}} \sim \bar{\mathcal{F}}$) if the nonlinear functions $\varphi_{\tilde{\mathcal{F}}}$, $\varphi_{\bar{\mathcal{F}}}$ exist such that $\varphi_{\tilde{\mathcal{F}}}(\tilde{x}^*, \tilde{s}^*, \tilde{t}^*) \in \bar{Z}^*$ and $\varphi_{\bar{\mathcal{F}}}(\bar{x}^*, \bar{s}^*, \bar{t}^*) \in \tilde{Z}^*$, for any $(\tilde{x}^*, \tilde{s}^*, \tilde{t}^*) \in \tilde{Z}^*$ and $(\bar{x}^*, \bar{s}^*, \bar{t}^*) \in \bar{Z}^*$.* □

The latter definition[3] is evidently inoperative, due to the difficulty in computing all the solutions $(\tilde{x}^*, \tilde{s}^*, \tilde{t}^*)$ and $(\bar{x}^*, \bar{s}^*, \bar{t}^*)$ of the MDO reformulations $\tilde{\mathcal{F}}$, $\bar{\mathcal{F}}$. Then, a more qualitative (and realistic) classification for the reformulations of (3.3), may be given according with either of the following *general criteria* (see also [3]).

- *Structural (or Analytical) Perspective*: we give a reformulation of (3.3) which meets a suitable nice structure. On this guideline we usually consider a structure where each discipline may be treated approximately as independent with respect to the others, so that some known results from nonlinear programming may be usefully applied. Consequently, the resulting reformulation is partially decomposed with respect to the disciplines: this requires a *globalization method* for analytically coordinate the intermediate results from each discipline.

[3]It is easy to prove that the equivalence of reformulations introduced in Definition 2 satisfies the standard *Reflexive*, *Symmetric* and *Transitive* properties. Thus, the equivalence relation induces a suitable partition of the set of all possible reformulations for MDO formulation (3.3).

- *Algorithmic Perspective*: the reformulation of (3.3) is aimed at using as many results, algorithms and packages as possible, from nonlinear programming. For instance, convex or continuously differentiable reformulations would be in general preferable to respectively nonconvex or nonsmooth ones.

Another possible criterion, for classifying the reformulations of nonlinear MDO formulation (3.3), is hinted by the following definition (see [2]).

Definition 3 *Consider the reformulation $\hat{\mathcal{F}}$ of the nonlinear MDO formulation (3.3). We say that $\hat{\mathcal{F}}$ is* closed [open] *with respect to the block Γ_i, $i = 1, 2, 3$, of constraints, if the structure of $\hat{\mathcal{F}}$ assumes that the block Γ_i is* satisfied [not satisfied]*, regardless of the optimization algorithm(s) used to solve $\hat{\mathcal{F}}$.* □

Note that in the previous definition, the classification does not rely on the optimization technique(s), which can be used to approach the set of solutions of the MDO reformulation. From Definition 3 we associate to the MDO reformulation $\hat{\mathcal{F}}$ the label

$$\hat{\alpha}\text{D} \ / \ \hat{\beta}\text{DA} \ / \ \hat{\gamma}\text{IC}, \qquad \hat{\alpha}, \hat{\beta}, \hat{\gamma} \in \{\text{O}, \text{C}\}, \tag{3.4}$$

where the possible entries $\{\text{O}, \text{C}\}$ for $\hat{\alpha}$, $\hat{\beta}$ and $\hat{\gamma}$ stand respectively for '*OPEN*' and '*CLOSE*'. As an example, an MDO reformulation with the label OD/CDA/CIC is *OPEN* with respect to the Design Constraints and *CLOSED* with respect to both the Disciplinary Analysis and the Interdisciplinary Constraints.

3.2 Relevant MDO reformulations from the literature

This section reviews some specific MDO reformulations of (3.3), which are also MDO formulations and are widely adopted in the applications. We urge to remark that the structure of both the objective function and the constraints in (3.3) is strongly dependent on the application in hand. This suggests that a reformulation may be suitable for a specific real problem though, it might be completely inadequate for another application. The latter drawback is intuitively a consequence of the general complexity of nonlinear MDO formulations, where the interdisciplinarity represents both a theoretical and a computational challenge. Here we consider the following MDO reformulations of (3.3), according with the classification suggested by Definition 3.

- *MultiDisciplinary Feasible (MDF).* It is an MDO reformulation of (3.3) also known as *FIO* or *AIO* [9], which represents the most trivial approach to the solution. It consists of using the implicit function theorem to explicit the vectors $s = s(x)$ and $t = t(x)$ from the Disciplinary Analysis and the Interdisciplinary Constraints. Then, the resulting MDO reformulation is simply

$$\begin{aligned} \min_{x} \quad & f'(x, s(x), t(x)) \\ & g_0(x, s(x)) \geq 0 \\ & g_1(x_0, x_1, s(x)) \geq 0 \\ & \qquad \vdots \\ & g_p(x_0, x_p, s(x)) \geq 0, \end{aligned} \tag{3.5}$$

  which may be treated as a nonlinear program in the unknown $x \in \mathbb{R}^n$. As previously said, the equality constraints in (3.3) often represent the state equations of the disciplines, hence they strongly affect the difficulty to get a solution. Therefore, the equality constraints in (3.3) can be hardly inverted to provide $s = s(x)$, so that the reformulation (3.5) is quite unlikely in general for the MDO formulation (3.3). According with the pattern (3.4), the MDF scheme is an OD/CDA/CIC reformulation.

- *Simultaneous Analysis and Design (SAD).* Also known with the acronyms *AAO* or *SAND* [11], may be considered as the counterpart of MDF. Indeed, here x, s and t are all variables of the reformulation,

so that the overall optimization problem to be solved is

$$\begin{aligned}
\min_{x,s,t} \quad & f'(x,s,t) \\
& g_0(x,s) \geq 0 \\
& g_1(x_0,x_1,s) \geq 0 \\
& \qquad \vdots \\
& g_p(x_0,x_p,s) \geq 0 \\
& A_1(x_0,x_1,s_1,t_2,\ldots,t_p) = 0 \\
& \qquad \vdots \\
& A_p(x_0,x_p,s_p,t_1,\ldots,t_{p-1}) = 0 \\
& t_1 = \mathcal{C}_1(s_1) \\
& \qquad \vdots \\
& t_p = \mathcal{C}_p(s_p).
\end{aligned} \tag{3.6}$$

Observe that the number of unknowns for SAD may be relatively larger than in the case of MDF. However the reformulation (3.6) may be treated as a unique nonlinear program, implying the use of theory and algorithms from optimization. From (3.4) and the Definition 3 the SAD scheme is an OD/ODA/OIC reformulation.

- *Distribute Analysis Optimization (DAO).* This is an intermediate approach between the previous two (indeed it is often addressed as the *In Between* [9, 12] reformulation, or alternatively it is the *IDF* approach [9]). Here, a subset of the equality constraints is used to explicit a subvector of the unknowns in terms of the remaining variables. Considering the following partition of vectors $s^T = (\tilde{s}^T \quad \hat{s}^T)$ and $t^T = (\tilde{t}^T \quad \hat{t}^T)$, the resulting optimization problem becomes (for simplicity we have compounded the Disciplinary Analysis and the Interdisciplinary Consistency constraints)

$$\begin{aligned}
\min_{x,\tilde{s},\tilde{t}} \quad & f'\left[x,(\tilde{s}^T \quad \hat{s}^T(x,\tilde{s}))^T,(\tilde{t}^T \quad \hat{t}^T(x,\tilde{s}))^T\right] \\
& g_0\left[x,(\tilde{s}^T \quad \hat{s}^T(x,\tilde{s}))^T\right] \geq 0 \\
& g_1\left[x_0,x_1,(\tilde{s}^T \quad \hat{s}^T(x,\tilde{s}))^T\right] \geq 0 \\
& \qquad \vdots \\
& g_p\left[x_0,x_p,(\tilde{s}^T \quad \hat{s}^T(x,\tilde{s}))^T\right] \geq 0 \\
& A\left[x,(\tilde{s}^T \quad \hat{s}^T(x,\tilde{s}))^T,(\tilde{t}^T \quad \hat{t}^T(x,\tilde{s}))^T\right] = 0 \\
& \tilde{t} = \tilde{\mathcal{C}}(\tilde{s}).
\end{aligned} \tag{3.7}$$

Finally observe that the DAO scheme is an OD/CDA/OIC reformulation.

- *Optimization by Linear Decomposition (OLD).* Despite the previous MDO reformulations, this is a *bilevel reformulation* [10]. Here the first (*upper*) level of minimization has the role of coordinating the results coming from the second (*lower*) level of minimization, which is the disciplines level. The overall nonlinear program is

$$\begin{aligned}
\min_{x_0,t} \quad & f'\left[x_0,x_1,\ldots,x_p,s_1(x_0,x_1,t),\ldots,s_p(x_0,x_p,t)\right] \\
& g_0\left[x_0,x_1,\ldots,x_p,s_1(x_0,x_1,t),\ldots,s_p(x_0,x_p,t)\right] \geq 0 \\
& m_i(x_0,x_i,t) \leq 0, \qquad i \leq p \\
& \min_{x_i} \quad m_i(x_0,x_i,t) \\
& \qquad t_i = C_i\left[s_i(x_0,x_i,t)\right], \qquad i \leq p
\end{aligned} \tag{3.8}$$

where

$$m_i(x_0, x_i, t) = \left\| g_i^+ \left[x_0, x_i, s_i(x_0, x_i, t) \right] \right\|^2$$

$$g_i^+ \left[x_0, x_i, s_i(x_0, x_i, t) \right] = \min \left\{ 0, g_i \left[x_0, x_i, s_i(x_0, x_i, t) \right] \right\},$$

and the last equality is intended componentwise. Observe that here the subvector $s_i(x_0, x_i, t)$ is made explicit from the i-th block of constraints $A_i(x_0, x_i, t_1, \ldots, t_{i-1}, s_i, t_{i+1}, \ldots, t_p) = 0$. The function $m_i()$ (*discrepancy function* [4]) in both the upper and lower level of (3.8) substantially measures a penalization of the infeasibility. Moreover, the exponent 2 in its definition yields a continuously differentiable objective function for the lower level.

- *Collaborative Optimization (CO).* Likewise the previous case, CO provides a multilevel optimization reformulation [8], where it is more clear the different role played by the system level and the disciplines level. In the following scheme we allow the dependency of the Interdisciplinary Constraints from both the design variables and the state variables. The final nonlinear program is given by introducing a sequence $\{y_1, \ldots, y_p\}$ of the so called *surrogates* of vector x_0. For each discipline the latter unknowns have substantially a role similar to that of vector t, i.e. they are used to decouple the upper level and the lower level in the following MDO reformulation.

$$\begin{aligned}
\min_{x_0, t} \quad & f'(x_0, x_1, \ldots, x_p, t) \\
& \left\| t_i - C_i \left(y_i - x_0, s_i(y_i, x_i, t) \right) \right\|_* = 0, \qquad i \leq p \\
\min_{y_i, x_i} \quad & \frac{1}{2} \left[\|y_i - x_0\|^2 + \|s_i(y_i, x_i, t) - t_i\|^2 \right] \\
& g_i \left(y_i, x_i, s_i(y_i, x_i, t) \right) \geq 0, \qquad i \leq p
\end{aligned} \tag{3.9}$$

where the explicit availability of the subvector $s_i = s_i(y_i, x_i, t)$, by the implicit function theorem applied to the i-th block of constraints $A_i(y_i, x_i, t_1, \ldots, t_{i-1}, s_i, t_{i+1}, \ldots, t_p) = 0$, is a strong prerequisite. Observe that also in this case the MDO reformulation is quite articulate, however the bilevel structure may be fruitfully exploited by suitable techniques [10] of nonlinear programming. The choice of the norm '$*$' is substantially arbitrary. However, common choices are '$*$'$= 2$ (which yields CO_2) and '$*$'$= 1$ (which yields CO_1).

The first one is appealing because it gives a smooth feasible region of the upper level in (3.9). Unfortunately, in case the feasible region of the upper level is open, the KKT optimality conditions may fail, since the Jacobian matrix (of the upper level constraints) vanishes in any feasible point. Thus, the Lagrange multiplier rule [7] may not be satisfied, unless the solution is also an unconstrained stationary point of the upper level objective function.
The choice '$*$'$= 1$ in (3.9) may be also troublesome, inasmuch as the constraints of the upper level are not differentiable. This again implies that the Lagrange multiplier rule may fail. Numerical results give evidence of the shortcomings described for the MDO reformulations CO_1 and CO_2 [17].

4 A case study: sail boat keel design

The theory described in Sections 2-3, though not immediately applicable, must be considered for any MDO problem. We describe here an application on ship design, where unfortunately the discussion above has not a straightforward application. The design optimization of a fin of a sailing yacht is here described. This particular device is often used in race yacht to sustain the bulb, a faired object whose weight is able to give stability to the yacht itself. The bulb sometimes represents a large portion of the ship's displacement, around 80% in the America's Cup sailing yachts. A "pure" fluid dynamic approach will simply consider the hull, the fin and the bulb as rigid, connected bodies. Unlikely, as a consequence of the weight of the bulb and of its position, the shape of the fin is largely modified by the bending moments and stresses arising from

the different sailing positions plus the dynamic pressure field, and the final performances of the yacht are undoubtedly influenced by the structural behavior of the fin.

In the following an extremely simplified case will be considered, which however contains all the fundamental elements of a typical MDO problem: an immersed, isolated fin moving at constant speed at a yaw and heel angle. The objective function is to maximize the efficiency of the fin (i.e. the ratio between the horizontal lift and the drag) The fin is assumed to have a constant horizontal section. Only the hydrodynamic actions are take into account and will be responsible for the bending of the fin which is assumed to be fixed at a certain level. This simplified problem will be solved by using a limited number of design variables and a single constraint is imposed, that is, a prescribed volume must be contained into the fin body.

The multidisciplinary equilibrium can be obtained in an iterative way. A non-linear BEM solver is adopted for the determination of the hydrodynamic loads: once these are computed, the deformed shape is obtained by the FEM solver and then passed back to the BEM solver, and so on until convergence. Convergence check is performed by monitoring the difference of the objective function value of the fin between two successive iterations j and $j+1$. When the difference is less than a cut-off threshold the equilibrium is assumed to be reached. The optimizer has then the task of finding a better shape, which at the beginning will not satisfy the multidisciplinary equilibrium. This basic approach is however well suited to test different reformulations and degrees of coupling among the disciplines, the focus of the present paper, which may be enforced by simply changing the convergence cut-off parameter.

In this preliminary application, a MDF reformulation and a suite of different DAO reformulations are solved and compared. In the following, $\mathbf{H}, \mathbf{S}$ indicate the hydrodynamic and the structural simulations, respectively, u is the vector of the disciplinary variables, $\mathbf{x}$ is the vector of the design variables identifying the shape of the fin and f is the objective function (here we drop the $'$ for simplicity). The basic algorithm at the step k is the following:

$\mathbf{H} : x^k, \tilde{u}_S^0 \Longrightarrow u_H^j, f^j$

$\mathbf{S} : x^k, u_H^j \Longrightarrow \tilde{u}_S^j$

$\mathbf{H} : x^k, \tilde{u}_S^j \Longrightarrow u_H^{j+1}, f^{j+1}$

$\mathbf{S} : x^k, u_H^{j+1} \Longrightarrow \tilde{u}_S^{j+1}$

Then convergence is checked: if $|\frac{f^{j+1}-f^j}{f^j}| \leq \epsilon$ then $\left\{ \begin{array}{ll} \tilde{u}_S^{j+1} & \rightarrow u_S^k \\ f^{j+1} & \rightarrow f^k \end{array} \right.$

Once the new multidisciplinary equilibrium has been found, the optimizer play the role of finding the new shape $\mathbf{x}^{k+1}$ and the cycle is ready to continue. In a MDF-type reformulation, the initial guess for the disciplinary variables is $\tilde{u}_S^0 = 0$, whereas in a DAO reformulation, the initial guess is $\tilde{u}_S^0 = u_S^k$. The latter choice ensures a faster convergence of the disciplinary variables once we are in the nearby of the optimal solution, because the initial values are nearly the convergent ones.

As a preliminary example, the standard (single-discipline) non-MDO reformulation can be compared with one MDO result. In figure 1, the objective function and the second design variable values provided by the single discipline optimization problem (hydrodynamic only) and the MDF reformulation of the coupled hydroelastic problem are reported. The same optimization algorithm has been adopted in both the numerical experiments. The difference in the objective function values is evident: the objective function value provided by the non-MDO reformulation is better than the one of the MDO problem. However, we should keep in mind that the non-MDO reformulation consider the body as rigid, *which in this case is rather far from the reality*. The hydroelastic approach is the only way to correctly consider (and try to solve) the design problem at hand. Differences in the results are indirect indicators of the inaccuracy in the solution of the problem if the hydroelastic coupling is not taken into account via an MDO approach.

The second example of the paper is introduced in the attempt of detecting some of the pros and cons coming out from the application of different reformulations and optimization algorithms. In the following, two different reformulations (MFD and DAO) and two different optimization algorithms will be applied to the same optimization problem. The coupling between the disciplines is modulated by means of the differences in the objective function value between two successive iterations: in this particular application,

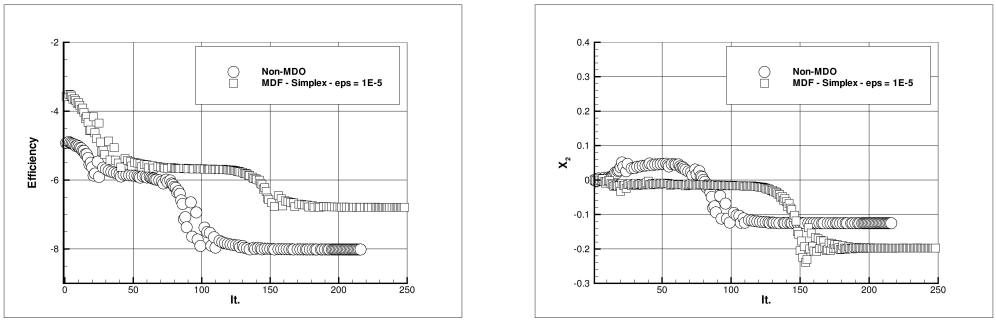

Figure 1: Comparison between the standard non-MDO reformulation and an MDO reformulation. The pure hydrodynamic non-MDO reformulation consider the body as rigid, whereas the more realistic hydroelastic approach take into account the deformation of the fin due to the hydrodynamics loads. **On left**: history of the objective function value during the iterations. **On right**: history of the second design variable value during the iterations. The other variables behave similarly.

the threshold value ϵ for the equilibrium constraints is set to 10^{-5} (see the above convergence condition).

Both the MDO reformulation have been tested with two different optimization algorithms: a standard Simplex Method [15] and a Derivative-Free Method [13]. In figure 2 the history of the design variables for the four different numerical experiments are reported.

A first comment about the influence of the MDO reformulation of the problem is nearly straightforward. In fact, no real differences are observed between the solutions provided by the Derivative-Free algorithm when changing the MDO problem reformulation, whereas only small differences are observed when using the Simplex algorithm. This behavior could be interpreted as a sign of the weak influence of the reformulation on the numerical solution of the MDO problem: the final solution does not change with the reformulation, which in turn means that the two reformulations can be considered as totally equivalent.

In table 1, the number of objective function evaluations and the number of inner iteration to achieve the convergence are also presented; in the last column, the average of the cost of the single objective function evaluation in terms of inner iterations is computed. It is evident how the DAO reformulation gives advantages in terms of the convergence of the disciplinary variables, decreasing the unit cost of the single multidisciplinary analysis.

On the other hand, different reformulations have a higher impact on the overall cost of the solution. In table 1, the number of objective function evaluations (i.e. the total number of CFD solution required which in more general terms are the number of disciplinary analyzes) and the number of inner iteration to achieve the convergence are presented; in the last column, the average cost of the single objective function evaluation in terms of inner iterations is computed. The DAO reformulation gives a slightly advantage in terms of convergence of the disciplinary variables, decreasing the unit cost of the single multidisciplinary analysis.

On the other hand, an increase in the number of iterations is observed. Moreover, the difference in the adopted algorithm results in different detected local minima. Both these features could be partly explained in a similar way. In fact, due to the adopted approach of considering the disciplines coupling convergence, we are introducing a numerical noise, i.e. a feasibility error when attempting at satisfying the equilibrium constraints. When the MFD reformulation is applied, the starting value for the disciplinary variables is set to zero and this is true for every single computation. On the contrary, for the DAO reformulation, the initial guess depends from the last computed configuration. Since the objective function $f' = f'(x, s(x), t(x))$ depends on the disciplinary variables $s(x)$, a different coupling parameter ϵ in the convergence check and/or a different initial guess for $s(x)$ could result in different final values of $s(x^*)$ and $f'(x^*, s(x^*), t(x^*))$. The coupling parameter ϵ was set quite low in this test and with an expected weak influence on the objective function value, but one must keep in mind that optimization algorithms are in general highly sensitive to this feature. As a consequence, the algorithm could perform poorly till convergence.

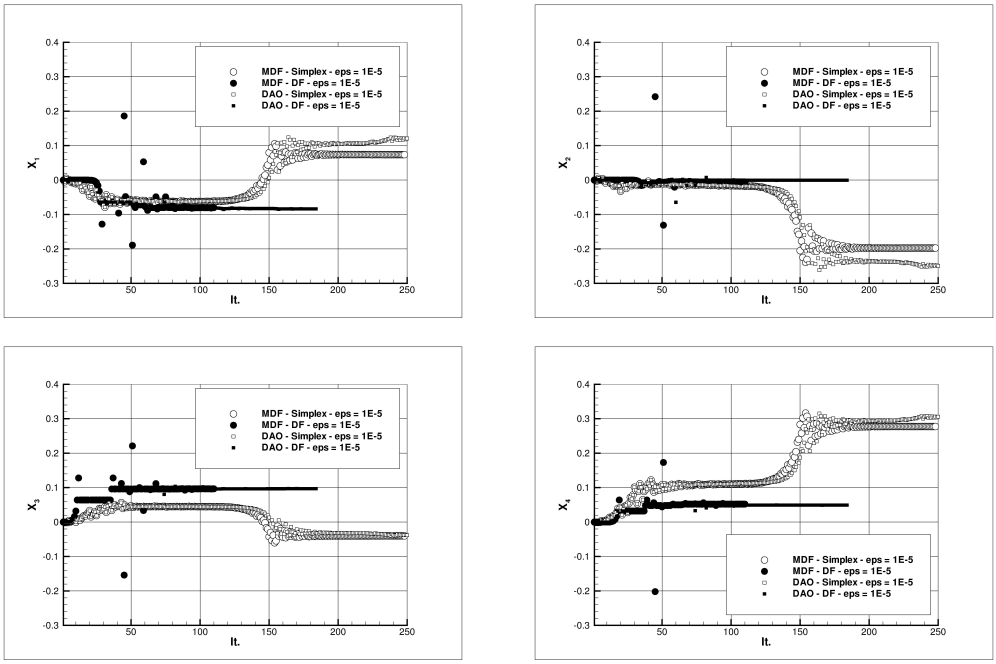

Figure 2: History of the design variables during the optimization process. Full symbols refer to the Derivative-Free algorithm, empty symbols refer to the Simplex algorithm. Circles indicate the MDF reformulation, squares the DAO. From top to bottom, left to right, variables 1, 2, 3 and 4.

A second simpler explanation for the different solutions detected is probably the fact that different algorithms have different selection strategy for the new iterate, and possibly this concurs in the selection of different local minima. This explains the difference in the optimal solution detected by the different algorithms.

It is finally fundamental here to stress that by changing the ϵ value in the convergence check, the advantage of the DAO w.r.t the MDF reformulation will probably increase greatly. In other terms, ϵ play the role of control over computational burden and by relaxing its value a substantial reduction in the total time is expected. The verification of this feature will represents the next step of this work.

5 Conclusions

This paper partially surveys some introductory aspects of renowned MDO formulations from the literature. Furthermore, specific emphasis is devoted to the relation between MDO problems and Nonlinear programming. A numerical experience is finally provided, in order to start the exploration of some of the main features of the problem reformulations. Numerical results demonstrate both the usefulness and the complexity of the problem.

Acknowledgments

This work has been supported by the *Ministero delle Infrastrutture e dei Trasporti* in the framework of the research plan "Programma di Ricerca sulla Sicurezza", Decreto 17/04/2003 G.U. n. 123 del 29/05/2003.

Reformulation	Algorithm	Total calls	Iterations	Unit cost
MDF	Simplex	2597	248	10.5
MDF	Derivative Free	1303	110	11.9
DAO	Simplex	2832	290	9.8
DAO	Derivative Free	1710	184	9.3

Table 1: Cost of the optimization problem solution as a function of the adopted reformulation and algorithm. *Total calls* indicates the total number of disciplinary calls: total elapsed time is proportional to this value.*Iteration* represents the number of solutions required by the algorithm to achieve convergence. *Unit cost* is the ratio between the total calls and the iterations number and gives the average number of solver calls per each multidisciplinary analysis.

References

[1] Natalia M. Alaxandrov, M. Y. Hussaini (Eds.), 1997, "*Multidisciplinary Design Optimization - state of the art*", Proceedings of the ICASE/NASA Langley Workshop on Multidisciplinary Design Optimization, SIAM Proceedings Series.

[2] Natalia M. Alaxandrov, Robert M. Lewis, 1999, "*Comparative properties of Collaborative Optimization and other approaches to MDO*", Proceedings of the First ASMO UK/ISSMO CONFERENCE on Engineering Design Optimization, July 8-9, 1999, MCB Press.

[3] Natalia M. Alexandrov, Robert M. Lewis, 2000, "*Algorithmic Perspectives on Problem Formulations in MDO*", AIAA 2000-4719.

[4] Natalia M. Alexandrov, Robert M. Lewis, 2000, "*Analytical and Computational Properties of Distributed Approaches to MDO*", NASA Langley Research Center, Hampton, Virginia, AIAA 2000-4718.

[5] Natalia M. Alexandrov, Robert M. Lewis, 2000, "*Analytical and Computational Aspects of Collaborative Optimization*", NASA Langley research Center, Hampton, Virginia, NASA/TM 2000-210104.

[6] Moktar S. Bazaraa, Hanif D. Sherali, C.M. Shetty, 1993 "*Nonlinear Programming: Theory and Algorithms - second edition*", John Wiley and Sons, Inc., Canada.

[7] Dimitri P. Bertsekas, 1995, "*Nonlinear Programming*", Athena Scientific, Belmont, Massachusetts.

[8] Robert D. Braun, 1996 "*An architecture for large-scale distributed design*". PhD thesis, Stanford University, May 1996. Department of Aeronautics and Astronautics.

[9] Evin J. Cramer, J.E. Dennis Jr., Paul D. Frank, Robert M. Lewis, Gregory R. Shubin, 1994 "*Problem Formulation for Multidisciplinary Optimization*", SIAM Journal on Optimization, Vol. 4., Issue 4, pp. 754-776.

[10] Stephan Dempe, 2002, "*Foundations of Bilevel Programming*", Kluwer Academic Publishers, Dordrecht, Boston, London, The Netherlands.

[11] Raphael T. Haftka, Zafer Gurdal, Manoharp P. Kamat, 1990 "*Elements of Structural Optimization*", Kluwer Academic Publishers, Dordrecht, The Netherland.

[12] Robert M. Lewis, 1997 "*Practical aspects of variable reduction formulations and reduced basis algorithms in Multidisciplinary Design Optimization*", in Natalia M. Alaxandrov, M. Y. Hussaini (Eds.), 1997, *Multidisciplinary Design Optimization - state of the art*, Proceedings of the ICASE/NASA Langley Workshop on Multidisciplinary Design Optimization, SIAM Proceedings Series.

[13] Stefano Lucidi, Marco Sciandrone, 2002 "*On the Global Convergence of Derivative Free Methods for Unconstrained Optimization*", SIAM Journal on Optimization, Vol. 13, issue 1, pp. 97-116.

[14] Olvi L. Mangasarian, 1994 "*Nonlinear Programming*", SIAM Classic in Applied Mathematics, Philadelphia, PA.

[15] J. L. Nelder, R. Mead, 1965 "*A Simplex Method for Function Minimization*", Computer Journal, Vol.7, pp. 308-313.

[16] Jaroslaw Sobieszczanski-Sobieski, Raphael T. Haftka, 1997 "*Multidisciplinary aerospace design optimization: Survey of recent developments*", Structural Optimization, Vol. 14, no. 1, pp. 1-23.

[17] Rajiv Thareja, Raphael T. Haftka, 1986, "*Numerical Difficulties associated with using equality constraints to achieve multi-level decomposition in structural optimization*", AIAA Paper 86-0854.

Flow at a ship-hull and free-surface contact curve at a ship bow and overturning bow wave

Gérard Delhommeau[1], Michel Guilbaud[2] and Francis Noblesse[3]
[1] Laboratoire de Mécanique des Fluides (UMR CNRS n°6598), Ecole Centrale, Nantes, France
[2] Laboratoire d'Etudes Aérodynamiques (UMR CNRS n°6609), Université de Poitiers, Poitiers, France
[3] David Taylor Model Basin, NSWC-CD, West Bethesda, Maryland, USA
gerard.delhommeau@ec-nantes.fr; michel.guilbaud@lea.univ-poitiers.fr; francis.noblesse@navy.mil

Introduction

The flow at the contact curve between the hull of a ship that advances at constant speed V_S in calm water and the free surface is analysed. The flow at the contact curve is assumed to be steady (in a frame of reference attached to the moving ship), and effects of surface tension and viscosity are ignored. Thus, the flow is governed by the Euler equations and the mass-conservation equation for incompressible flows. However, neither these field equations nor far field radiation conditions are considered in the local-flow analysis that is considered here.

Specifically, this local-flow analysis considers the dynamic and kinematic boundary conditions at the free surface and the ship-hull boundary condition, which are presumed to hold at the ship-hull and free-surface contact curve. These three boundary conditions are satisfied exactly at the contact curve between the actual free surface and ship hull (not the mean free-surface plane and/or the ship centerplane). Thus, a fully-nonlinear flow analysis is performed here. This analysis extends the analysis previously reported in [1].

A main result of the nonlinear local flow analysis given in [1] is that the waterline at a ship bow is tangent to the ship stem line, i.e. is nearly vertical for typical ship hulls. This theoretical result is confirmed experimentally in [2], and also appears to be in agreement with the wave-profile measurements reported in [1] for the Wigley hull. The bow-flow analysis given in [1] is not reconsidered here. However, the analysis of the flow at the ship-hull and free-surface contact curve given in [1] is considered further using a local system of coordinates attached (normal and tangent) to the ship hull. This analysis yields a simple analytical expression that defines the flow velocity at the ship-hull and free-surface contact curve in terms of the ship speed, the (flare) angle between the ship hull and the vertical plane, the elevation of the contact curve above the mean free-surface plane, and the angle between the free surface and the horizontal plane. This analytical expression for the flow velocity at the contact curve is equivalent to the results given in [1], but simpler and more practical.

The analytical expression for the flow velocity at a ship-hull and free-surface contact curve is used to predict the detached flow and related spray sheet that leaves the ship hull at the contact (flow separation) curve. This analysis, based on elementary considerations within the Lagrangian flow-representation framework, yields simple analytical expressions that define the spray sheet. These analytical results are combined with the simple analytical expressions for the height and location of a ship bow wave given in [3] to obtain analytical approximations that explicitly determine the spray sheet generated at a ship bow in terms of the ship speed, draft, waterline-entrance angle, and flare angle. Thus, a simple theory of the spray sheet that is commonly observed at the bow of a ship advancing in calm water is given below.

Nonlinear boundary conditions

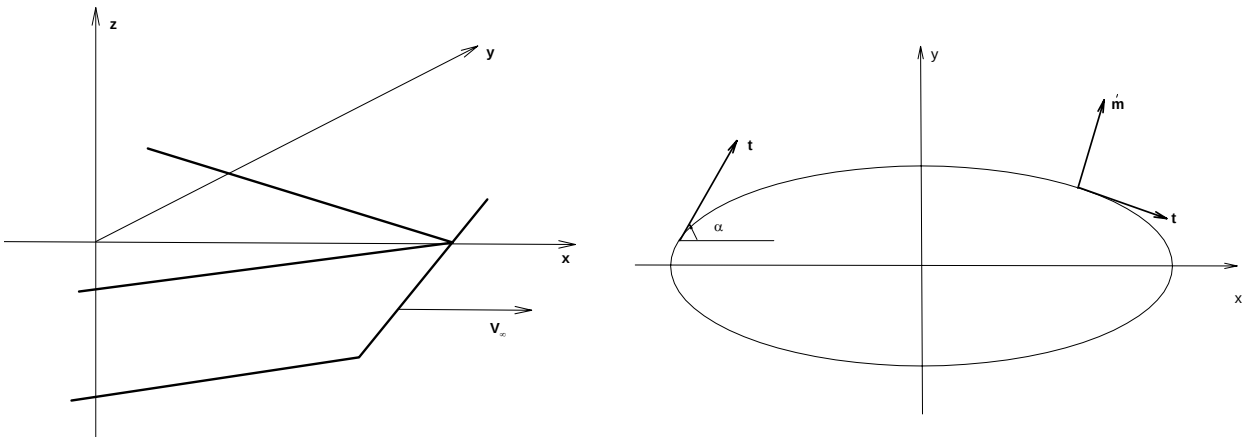

Figure 1 Definition sketches

Steady inviscid flow about a ship advancing at constant speed V_S in calm water is observed from a system of dimensional coordinates (X,Y,Z) or non dimensional coordinates (with respect to V_S^2/g) attached to the moving ship, as shown in figure1 (left); the z axis is vertical and points upward and the mean free surface is the plane z=0. Non dimensional velocities due to the ship are defined as (u,v,w)=(U,V,W)/V_s. The non dimensional velocity of the total flow is $(u\text{-}1,v,w)$. At the free surface, defined by $z=\zeta(x,y)$, the dynamic and kinematic boundary conditions:

$$(u-1)^2+v^2+w^2=1-2\zeta;\ w=(u-1)\zeta_x+v\zeta_y \tag{1}$$

must be satisfied. The boundary conditions (1) are applied here without approximation, at the actual location of the free surface. At the ship hull, the boundary condition:

$$n^x(u-1)+n^y v+n^z w=0 \tag{2}$$

holds. Here, $\mathbf{n}=(n^x,n^y,n^z)$ is a unit vector that is normal to the ship hull and points outside the ship.

Boundary conditions in system of coordinates attached to ship hull

It is possible to express the previous boundary conditions (1) and (2) in terms of a local system of coordinates attached to the hull. Two unit orthogonal vectors lying in a horizontal plane, **t** and **m**, shown on figure 1 (right), are used. The vector **t** is tangent to the ship hull surface and the vector **m** is colinear with the projection of the unit normal vector **n** to the ship hull onto the mean free-surface plane z=0. On the positive half $y\geq 0$ of the ship hull, **t** points toward the ship bow. The unit vectors **t**, **m** and **n** are given by:

$$\mathbf{t}=(\cos\alpha,-\sin\alpha,0);\ \mathbf{m}=(\sin\alpha,\cos\alpha,0);\ \mathbf{n}=(\sin\alpha\cos\gamma,\cos\alpha\cos\gamma,-\sin\gamma) \tag{3}$$

where $-\pi/2\leq\alpha\leq\pi/2$ is the angle between the unit vector **t** and the x axis (positive in the bow region, and negative in the stern region) and $-\pi/2\leq\gamma\leq\pi/2$ is the angle between the normal vector **n** to the ship hull and the mean free-surface plane z=0. The flare angle γ is positive for a typical hull form, and negative for a tumble hull. The unit vector $\mathbf{s}=\mathbf{t}\times\mathbf{n}=(\sin\alpha\sin\gamma,\cos\alpha\sin\gamma,\cos\gamma)=\mathbf{m}sin\gamma+\mathbf{k}\cos\gamma$ is tangent to the ship hull and points upward, **k**=(0,0,1). Let μ stand for the angle between the free surface and the mean free-surface plane z= 0. One then has $\zeta_m=\tan\mu$ with $-\pi/2-\gamma\leq\mu\leq\pi/2-\gamma$. Figure 2 shows a plot of a cut of figure 1 by a vertical plane parallel to x axis. Angles γ and μ and unit vectors **m, n** and **s** are also shown in figure 2.

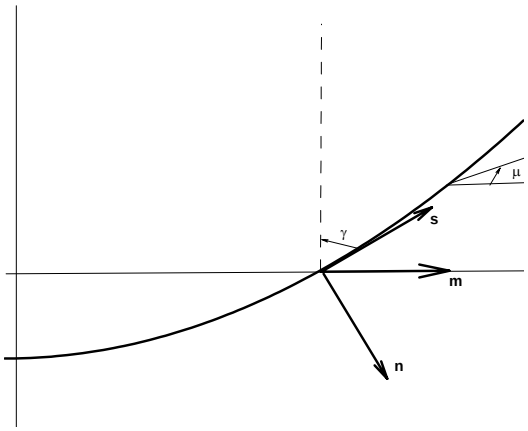

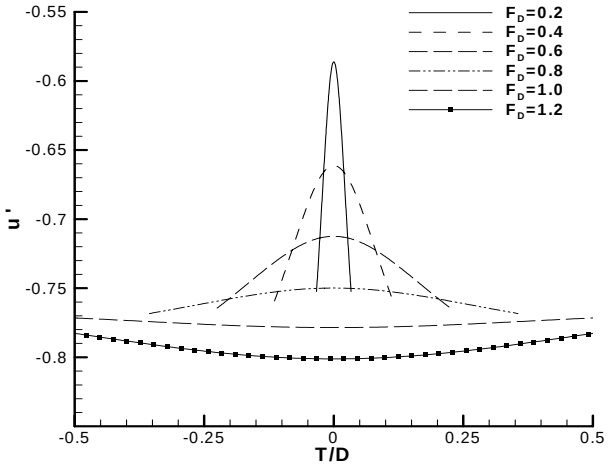

Figure 2 Unit vectors **m**, **n** and **s** and angles γ, μ Figure 3 Horizontal velocity component u' versus T/D for F_D=0.2, 0.4,0.6,0.8, 1.0 and 1.2 with α_E=10° and γ=30°

The components $(u\text{-}1,v,w)$ of the total flow velocity $\boldsymbol{v}_{\text{total}}$ along the unit vectors ***(i,j,k)*** attached to the (x,y,z) axes and the corresponding velocity components (u',v',w') along the unit vectors (**t,n,s**) are related by:

$$u-1=w'\sin\alpha\sin\gamma+v'\sin\alpha\cos\gamma+u'\cos\alpha;v=w'\cos\alpha\sin\gamma+v'\cos\alpha\cos\gamma-u'\sin\alpha;w=w'\cos\gamma-v'\sin\gamma \tag{4}$$

As expected, expressions (2) to (4) yield the hull boundary condition:

$$v'=0 \tag{5}$$

The velocity component along the unit vector **n** normal to the ship hull is null, and the flow velocity is given by:

$$\mathbf{v}_{total} = u'\mathbf{t} + w'\mathbf{s} = u'\mathbf{t} + w'\mathbf{t}\times\mathbf{n} \tag{6}$$

The velocity components u' and w' along the unit vectors **t** and **s** tangent to the hull are determined by the dynamic and kinematic free-surface boundary conditions, now considered. Expressions (1), (4) and (5) yield the dynamic free-surface boundary condition:

$$(u')^2 + (w)'^2 = 1 - 2\zeta \tag{7}$$

The free surface is defined by $z=\zeta(x,y)=\zeta(t,m)$. The identity $\zeta_x dx+\zeta_y dy=\zeta_t dt+\zeta_m dm$ and expressions (3) yield $\zeta_x=\zeta_t cos\alpha+\zeta_m sin\alpha$ and $\zeta_Y=\zeta_m cos\alpha-\zeta_t sin\alpha$. These relations, (4) and (5), show that the kinematic free-surface boundary condition (1) becomes:

$$w'\left(\cos\gamma - \zeta_m \sin\gamma\right) = u'\zeta_t \tag{8}$$

Thus, the velocity components u' and w' in (6) satisfy the dynamic and kinematic free-surface boundary conditions (7) and (8).

Flow at contact curve

From the previous equations, it can be shown that the total flow velocity at the contact curve is:

$$\mathbf{v}_{total} = -\sqrt{\frac{1-2\zeta}{\cos^2(\gamma+\mu) + \zeta_t^2\cos^2\mu}}\left[\cos(\gamma+\mu)\mathbf{t} + \zeta_t\cos\mu\ \mathbf{t}\times\mathbf{n}\right] \tag{9}$$

Here, the condition $cos(\gamma+\mu) \geq 0$, which follows from the relation $\zeta_m=tan\mu$, and the condition $u' \leq 0$ (no flow reversal allowed) were used. Thus, the total flow velocity $\mathbf{v}_{total}$ at the contact curve between a ship hull and the free surface is defined by the simple analytical expression (9) in terms of the ship speed V_s, the flare angle γ, the elevation ζ of the contact curve, and the angle μ between the free surface and the horizontal plane. Expression (9) is equivalent to the expressions for the velocity components u,v,w given in [1]. Expression of w' in (9) and the relations $u' \leq 0$ and $cos(\gamma+\mu) \geq 0$ then yield $sign(w')=-sign(\zeta_t\ cos\mu)$. This relation yields $sign(w')=-sign(\zeta_t)$, for $-\pi/2 \leq \mu \leq \pi/2$, and one then has $w'>0$ in the region between a ship stem and a ship bow-wave crest where $\zeta_t<0$. So, it can be shown that if $tan\gamma\ tan\mu<<1$ then $w'cos\gamma \approx u'\zeta_t$.

This previous approximation may be expected to hold except near a ship stem or stern where μ or γ can be large. So, using the dynamic free-surface boundary condition (7) yield:

$$\mathbf{v}_{total} \approx -\sqrt{\frac{1-2\zeta}{\cos^2\gamma + \zeta_t^2}}\left[\cos\gamma\mathbf{t} + \zeta_t\mathbf{t}\times\mathbf{n}\right] \tag{10}$$

This approximation defines the flow velocity at the free-surface and ship-hull contact curve in terms of the ship speed V_s and flare angle γ, and the elevation ζ of the contact curve.

Bow wave

The height $z_b=Z_b g/V_s^2$ and the location $x_b=X_b g/V_s^2$ of the bow wave generated by a ship that advances at constant speed V_s in calm water are approximately determined in terms of the ship speed V_s, draft D, and waterline entrance angle $2\alpha_E$ by the analytical expressions, with $F_D=V_s/\sqrt{gD}$ and $C^Z \approx 2.2$ and $C^x \approx 1.$:

$$z_b \approx \frac{C^Z}{1+F_D}\frac{\tan\alpha_E}{\cos\alpha_E};\ x_b \approx \frac{C^X}{1+F_D} \tag{11}$$

Expressions (11) are shown in [3] to be in very good agreement with experimental measurements for wedge-like ship bows, and for other ship-bow forms if the simple procedure given in [3] is used to define an effective draft D and an effective waterline entrance angle $2\alpha_E$. A ship bow wave can then be realistically approximated by (using $t=Tg/V_s^2$):

$$\frac{Z}{D}\frac{\cos\alpha_E}{\tan\alpha_E} = \frac{C^Z F_D^2}{1+F_D}\left(1 - \left[\left(1+F_D\right)^2 T^2 / \left\{D^2\left(C^X F_D^2\right)^2\right\}\right]\right) for\ \frac{|T|}{D} \leq \frac{F_D^2}{1+F_D} \tag{12}$$

The crest of the bow wave is chosen as the origin t=0 of the axis associated with the previously-defined unit vector **t** tangent to the ship hull. Expressions (12) show that the normalized bow-wave elevation $(1+F_D)(Zg/V_s^2)cos\alpha_E/tan\alpha_E$ only depends on the normalized horizontal distance $(1+F_D)Xg/V_s^2$ from the bow-wave crest. This similarity rule implies that all bow-wave profiles (for every ship speed, draft, and waterline

entrance angle) approximately coalesce into a single curve if represented in terms of the foregoing normalized variables, [3].

Flow velocity at bow-wave contact curve

The ship-hull and free-surface contact curve in the vicinity of the bow-wave crest is approximately given by $\zeta=z$ with z defined by expression (12). Thus, it is possible to determine easily the values of ζ and ζ_t in expressions (9) and (10) for the flow velocity at the contact curve within the bow region:

$$\zeta = \frac{C^Z}{1+F_D}\frac{\tan\alpha_E}{\cos\alpha_E}\left(1-\frac{\left(1+F_D\right)^2 t^2}{\left(C^X\right)^2}\right);\ \zeta_t = \frac{-2C^Z}{\left(C^X\right)^2}\frac{\tan\alpha_E}{\cos\alpha_E}\left(1+F_D\right)t \tag{13}$$

Expressions (10) and (13) provide a simple analytical approximation that explicitly defines the flow velocity at a ship-hull and free-surface contact curve in the vicinity of the ship bow-wave crest in terms of the ship speed, draft, waterline entrance angle and flare angle. The flare angle is not restricted to be constant (and indeed typically varies) within the bow region $|t|\le 1/(1+F_D)$. The approximation (10) defines the velocity components, with ζ and ζ_t given by (14) and $|t|\le 1/(1+F_D)$, as:

$$(u', w') = -\sqrt{\frac{1-2\zeta}{\cos^2\gamma+\zeta_t^2}}\left(\cos\gamma, \zeta_t\right) \tag{14}$$

Figure 3 illustrates the variation of the velocity components u' along a ship-hull and free-surface contact curve, in the vicinity of the bow-wave crest, as the ship speed varies. It can be observed that u' (always <0) has a parabolic shape and presents a maximum for F_D<1.0 and a minimum otherwise, showing a change of the sign of the curvature for F_D between 0.8 and 1.0. The value of the extremum (max or min) of u' decreases when the Froude number increases. The amplitude of the variation increases for vary low or high values of the Froude number and is weak around $F_D\approx 1.0$.

The effect of the angle between the sea surface and the horizontal plane is illustrated in Figure 4, for two values of the flare angle γ=20°, 40°. Specifically, these figures depict the velocity components u' and w' for α_E=10 and F_D=1. The angle μ is given by $\mu=\mu_{max}(1+F_D)t$, $|t|\le 1/(1+F_D)$, for μ_{max}=10°; u' is quite constant with *T/D* while w' has quite a linear variation. The effect μ_{max} is weak and can be seen only for high values of $|T|/D$. The effect of μ_{max} is quite weak for a flare angle γ=20° but increases with this angle (γ=40°).

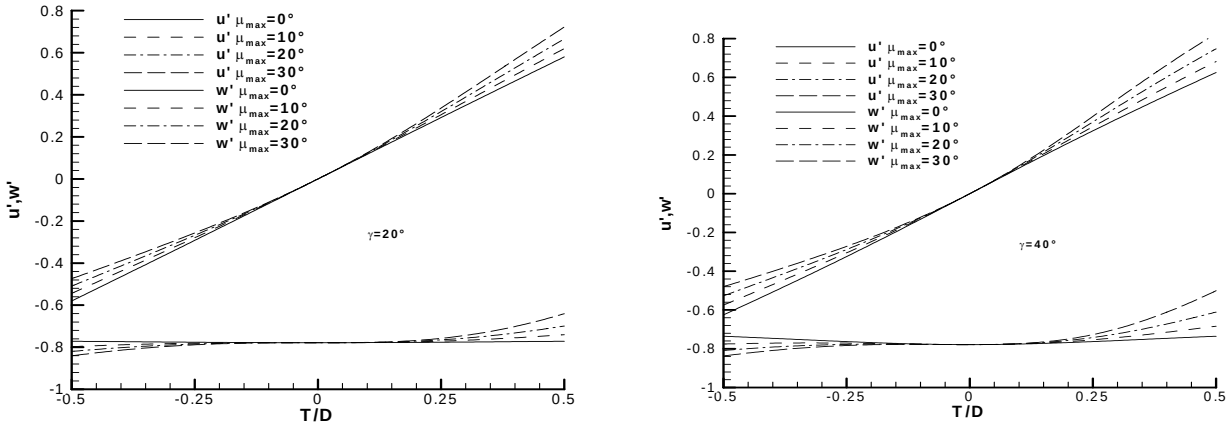

Figure 4 Effect of angle μ on velocity components α_E=10°; F_D=1 with $\mu=\mu_{max}(1+F_D)t$

Detached flow and bow sheet

If the flow is detached along a portion of the ship-hull and free-surface contact curve, equations (6) show that water particles leave the ship hull at the contact (flow-separation) curve with velocity:

$$u'\mathbf{t} + w'\mathbf{s} = u'\mathbf{t} + w'\left(\mathbf{m}\sin\gamma + \mathbf{k}\cos\gamma\right)$$

with u' and w' given by (9) or the related approximation (10). The nondimensional time $\theta=\Theta g/V_s$ and coordinates show that the path of a water particle is determined by Newton's equations $d^2t/d\theta^2=0$, $d^2m/d\theta^2=0$ and $d^2z/d\theta^2=-1$ where $t=Tg/V_s^2$ and $m=Mg/V_s^2$ are the nondimensional horizontal

distances along the unit vectors **t** and **m** tangent and normal to the ship hull in the horizontal plane $z = 0$. Thus, a water particle that leaves a point (t_0, m_0, ζ) of the contact (flow-separation) curve at time $\theta = 0$ follows the path:

$$t = t_0 + \theta u'; \quad m = m_0 + \theta w' \sin\gamma; \quad z = \zeta + \theta w' \cos\gamma - \theta^2/2 \tag{15}$$

Equations (15) yield:

$$m = m_0 + \frac{t - t_0}{u'} w' \sin\gamma;\ z = \zeta + \frac{t - t_0}{u'} w' \cos\gamma - \frac{(t - t_0)^2}{2(u')^2};\ z = \zeta + \frac{m - m_0}{\tan\gamma}\left(1 - \frac{m - m_0}{(w')^2 \sin(2\gamma)}\right) \tag{16}$$

Thus, the projections of the paths of water particles on the horizontal plane (**m**, **t**) and the vertical planes (**k**, **t**) and (**k**, **m**) are a straight line and parabolas, respectively. The relation $m_0 = \zeta \tan\mu$ may be used in (15)–(16) if the ship hull surface can be defined as $m = z\tan\gamma$ in the vicinity of the mean waterline, which corresponds to $m = 0$. The water trajectory defined by (16) intersects the mean free-surface plane $z = 0$ for:

$$(t_{z=0} - t_0)/u' = w' \cos\gamma + \sqrt{(w')^2 \cos\gamma + 2\zeta} = (m_{z=0} - m_0)/(w' \sin\gamma) \tag{17}$$

If $w' > 0$, the water trajectory reaches a top height for $(t_{top} - t_0)/u' = w' \cos\gamma = (m_{top} - m_0)/(w' \sin\gamma)$ with $z_{top} - \zeta = (w' \cos\gamma)^2/2$. The approximation $w' \cos\gamma \approx u'$ if $\tan\gamma \tan\mu << 1$ yields $z_{top} - \zeta = (u'\zeta_t)^2/2$. Thus, the maximum height z_{top} reached by water particles that leave the ship-hull and free-surface contact curve at a height $z = \zeta$ is significantly larger that ζ only if $|\zeta_t|$ is large, e.g. near a ship stem where the ship-hull and free-surface contact curve is tangent to the ship stem, [1].

Spray sheet in bow-wave region

It is possible to express equations (16) as:

$$\frac{M}{D} = \frac{M_0}{D} + \left(\frac{T}{D} - F_D^2 t_0\right)\frac{w'_0}{u'_0}\sin\gamma;\ \frac{Z}{D} = F_D^2\zeta + \left(\frac{T}{D} - F_D^2 t_0\right)\frac{w'_0}{u'_0}\cos\gamma - \frac{\left(T/D - F_D^2 t_0\right)^2}{2F_D^2 (u'_0)^2} \tag{18}$$

where t_0 is the point of contact line as in (16). u'_0 and w'_0 are the velocity component at t_0 on the contact line This change in notation is used here to combine expressions (18) with expressions (14) and (13), in the manner shown further on. The variable T/D in (18) varies within the range: $T_{z=0}/D \le T/D \le F_D^2 t_0$ The variable M/D varies within the range:

$$M_0/D \le M/D \le M_{z=0}/D \ \text{if}\ w'_0 > 0 \ \ or \ \ M_{z=0}/D \le M/D \le M_0/D \ \text{if}\ w'_0 < 0$$

Here, $T_{z=0}/D$ and $M_{z=0}/D$ are defined as:

$$\frac{T_{z=0}/D - F_D^2 t_0}{u'_0} = F_D^2\left[w'_0 \cos\gamma + \sqrt{(w'_0)^2 \cos^2\gamma + 2\zeta}\right] = \frac{M_{z=0}/D - M_0/D}{w'_0 \sin\gamma} \tag{19}$$

If the ship hull surface can be defined as $M = Z \tan\gamma$ in the vicinity of the mean waterline, which corresponds to $M = 0$, it is possible to show that the relation $M_0/D = F_D^2\zeta$ may be used in (18).

Equations (17) and equations (14) and (13) can be used to determine the spray sheet generated along a ship-hull and free-surface contact curve within the bow-wave region:

$$\frac{-F_D^2}{1 + F_D} \le F_D^2 t_0 \le \frac{F_D^2}{1 + F_D} \tag{20}$$

Equations (18) define the projection onto the horizontal plane (*T/D, M/D*) of the path followed by a water particle after it leaves the ship hull, at a point of the contact curve identified by a value of $F_D^2 t_0$ within the range (20). Similarly, equations (18) define the projections of a water-particle path onto the vertical planes (*T/D, Z/D*) and (*M/D, Z/D*), respectively. Equations (18), where $F_D^2 t_0$ varies within the range defined previously, provide parametric equations that define the intersection of the spray sheet with the mean free-surface plane $z=0$.

Results

Figures 5 show the comparison between numerical results of calculation of the spray sheet and experiment made in a water circulation channel at Ecole Centrale de Nantes with a flat plate of 0.38m draft and 0.782m long graduated every 10 cm. The channel is 2 meter wide with a water height of 1 m. The flare angle $\gamma = 10°$ and the half waterline-entrance angle $\alpha_E = 10°$. The figure shows the spray sheet for a velocity of 1.3 m/s.

The results are in reasonable agreement. Further experiments will be conducted in a towing tank to have a better resolution on measurements and avoid flow unsteadiness.

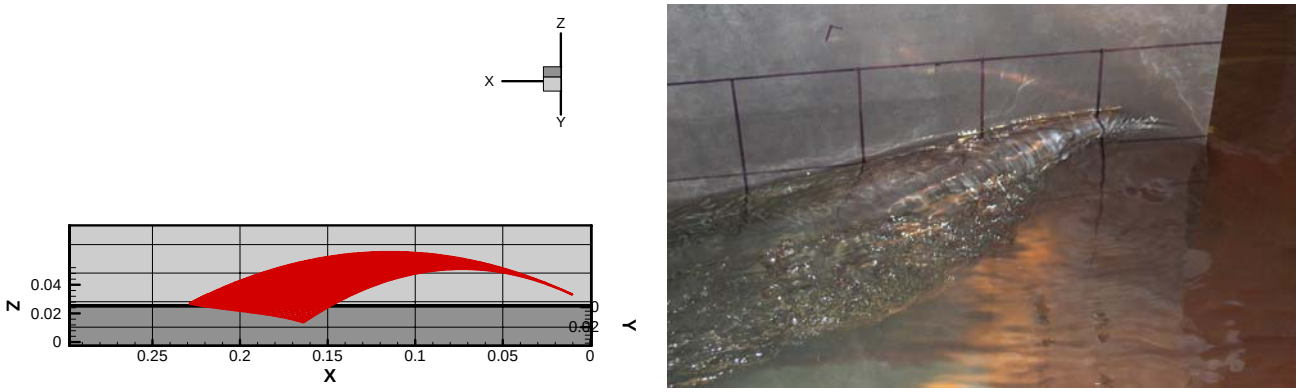

a) Calculations b) Measurements

Figure 5 Spray sheet for γ=10°, α_E=10°, U=1.3m/s and F_D=0.67

Conclusion

A main result of the foregoing local analysis of the fully-nonlinear steady flow along the contact curve between a ship hull and the free surface is expression (9). This simple analytical expression defines the total flow velocity $\mathbf{v}_{\text{total}}$ at the contact curve in terms of the ship speed V_s, the flare angle γ between the ship hull and the vertical plane, the elevation ζ of the contact curve above the mean free surface, and the angle μ between the sea surface and the horizontal plane. The related approximation (10) defines $\mathbf{v}_{\text{total}}$ in terms of V_s, γ and ζ. These analytical expressions for the flow velocity at the contact curve are equivalent to the expressions given in [1], but simpler and more practical.

The analytical expression for the flow velocity $\mathbf{v}_{\text{total}}$ at a ship-hull and free-surface contact curve have been used to determine the detached flow (spray sheet) that leaves the ship hull at the contact (flow-separation) curve. The main result of this elementary analysis is the simple analytical expressions (16) and (17), which define the spray sheet in terms of V_s, γ, ζ, and the flow velocity $\mathbf{v}_{\text{total}}$ at the contact curve.

These analytical results have been combined with expressions (11), given in [3], for the height and the location of a ship bow wave to obtain analytical approximations that explicitly determine the flow velocity $\mathbf{v}_{\text{total}}$ at a ship-hull and free-surface contact curve in the bow-wave region and the spray sheet generated at a ship bow in terms of V_s, D, α_E and γ. Specifically, these results are expressions (14) and (13) for the flow velocity $\mathbf{v}_{\text{total}}$ and equations (18)-(19) for the spray sheet. These analytical expressions provide a simple theory of the spray sheet that is commonly observed at the bow of a ship advancing in calm water.

The foregoing simple analytical results, and the results already given in [1], provide insight that may be useful to guide numerical calculations, experimental measurements, and hull-form design. In particular, these results explicitly define important aspects of the flow at a ship bow, including the spray sheet, in terms of major design parameters (V_S, D , 2 α_E, and γ). The analysis presented in this study can be extended in several directions, briefly noted below.

For purposes of illustration, the bow wave and related spray sheet has only been considered here in the vicinity of the bow-wave crest. However, the analysis can easily be extended up to the ship stem, where the wave profile is known to be tangent to the stem line, [1]. Thus, the spray sheet generated by a ship can be fully determined, by remarkably simple analytical expressions, over the whole bow region. Preliminary experimental results to validate these calculations are presented and other tests have planned in a towing tank. Furthermore, the analytical expressions for the flow velocity at a ship-hull and free-surface contact curve given here provide a theoretical basis for a rational expression for the spray drag of a ship, which is known to be an important (even dominant) component of the drag of a ship at high Froude number. Finally, the analysis can be extended to unsteady free-surface flows about ships (or offshore structures) in waves. This extension may be useful for determining deck wetness.

References

[1] Noblesse, F.; Hendrix, D.M.; Khan, L. (1991) “Nonlinear local analysis of steady flow about a ship”, *J. Ship Research,* 35:288–294

[2] Waniewski, T.A.; Brennen, C.E.; Raichlen, F(2002) “Bow wave dynamics”, *J. Ship Research,* 46:1–15

[3] Noblesse, F.; Hendrix, D.: Faul, L.; Slutsky, J. (2005) “Bow-Wave Height, Location, and Steepness”, *J. Ship Research,* in review.

Numerical Computation of Hydrodynamic Forces on Hydrofoil. Prediction of Cavitation Phenomenon

Paweł Dymarski
padym@cto.gda.pl

Ship Design and Research Centre S.A.
Poland

Introduction

This paper presents results obtained from SOLAGA computer program which is developed in the frame of project supported by Polish Ministry of Science and Information Society Technologies (number of the project is 5 T12C 012 22). The main purpose of the project was to develop the computer program to calculate viscous flow around hydrofoil and ship propellers. Additionally the program can be used for a cavitation phenomena prediction. Theoretical bases of the model and numerical methods applied in the computer program will be briefly described below. The article contains example of computations of viscous flow around rectangular hydrofoil NACA66-9 with aspect ratio $\lambda = 6$ and computation of cavitation phenomenon on rectangular hydrofoil with profile NACA16

1. Theoretical Model

The closed equations system of motion derived for incompressible fluid is based on the law of momentum conservation and on the mass conservation principle. In the case of turbulent flow the averaged form of both equations is applied.
For such flow we express the instantaneous velocity $u_i(\mathbf{x},t)$ as the sum of a mean $U_i(\mathbf{x})$ and fluctuating part $u'_i(\mathbf{x},t)$, so that $u_i(\mathbf{x},t) = U_i(\mathbf{x}) + u'_i(\mathbf{x},t)$
The Reynolds averaged equations for conservation of mass and momentum are

$$\frac{\partial U_i}{\partial x_i} = 0 \tag{1}$$

$$\rho \frac{\partial U_i}{\partial t} + \rho U_i \frac{\partial U_i}{\partial x_j} = -\frac{\partial P}{\partial x_i} + \frac{\partial}{\partial x_j}\left(2\mu S_{ji} - \rho \overline{u'_j u'_i}\right) \tag{2}$$

Vector x_i is position, t is time, P is mean pressure, ρ is density, μ is molecular viscosity S_{ij} is the mean strain-rate tensor,
The quantity $-\rho \overline{u'_i u'_j}$ is the Reynolds stress tensor. In order to calculate the Reynolds stress tensor we must introduce additional equations, which are called turbulence model.

Turbulence model

In the present program one-equation Spalart-Allmaras turbulence model was applied [Wilcox, 2002]. The model is especially suitable for the hydrofoil and wing applications, because of the type of objects it has been calibrated for.
The Reynolds stress tensor is calculated using Bossinesq approximation

$$\tau_{ij} = -\rho u'_i u'_j = \rho \nu_T \left(\frac{\partial U_i}{\partial x_j} + \frac{\partial U_j}{\partial x_i} \right) \tag{3}$$

where ν_T is kinematic eddy viscosity, given by:

$$\nu_T = \tilde{\nu} f_{v1} \tag{4}$$

$$\frac{\partial \tilde{\nu}}{\partial t} + U_j \frac{\partial \tilde{\nu}}{\partial x_j} = c_{b1} \tilde{S} \tilde{\nu} - c_{w1} f_w \left(\frac{\tilde{\nu}}{d} \right)^2 + \frac{1}{\sigma} \frac{\partial}{\partial x_k} \left[\left(\nu + \tilde{\nu} \right) \frac{\partial \tilde{\nu}}{\partial x_k} \right] + \frac{c_{b2}}{\sigma} \frac{\partial \tilde{\nu}}{\partial x_k} \frac{\partial \tilde{\nu}}{\partial x_k} \tag{5}$$

Closure coefficients and auxiliary relations are given below:

$$c_{b1} = 0.1355, \quad c_{b2} = 0.622, \quad c_{v1} = 7.1, \quad \sigma = 2/3 \tag{6}$$

$$c_{w1} = \frac{c_{b1}}{\kappa^2} + \frac{\left(1 + c_{b2}\right)}{\sigma}, \quad c_{w2} = 0.3, \quad c_{w3} = 2, \quad \kappa = 0.41 \tag{7}$$

$$f_{v1} = \frac{\chi^3}{\chi^3 + c_{v1}^3}, \quad f_{v2} = 1 - \frac{\chi}{1 + \chi f_{v1}}, \quad f_w = g \left[\frac{1 + c_{w3}^6}{g^6 + c_{w3}^6} \right]^{1/6} \tag{8}$$

$$\chi = \frac{\tilde{\nu}}{\nu}, \quad g = r + c_{w2} \left(r^6 - r \right), \quad r = \frac{\tilde{\nu}}{\tilde{S} \kappa^2 d^2} \tag{9}$$

$$\tilde{S} = S + \frac{\tilde{\nu}}{\kappa^2 d^2} f_{v2}, \quad S = \sqrt{2 \Omega_{ij} \Omega_{ij}} \tag{10}$$

$$\Omega_{ij} = \frac{1}{2} \left(\frac{\partial U_i}{\partial x_j} - \frac{\partial U_j}{\partial x_i} \right) \tag{11}$$

where *d* is the distance from the closest surface.

The initial and boundary conditions. The initial and inlet value of $\tilde{\nu}$ is taken as $0.1\nu_L$. At solid walls $\tilde{\nu}$ is set to zero [Blazek J., 2001].

Cavitation

The cavitation model is based on travelling bubble method. Behaviour of a single bubble is described by Raileigh-Plasset equation:

$$R \frac{\mathrm{d}^2 R}{\mathrm{d}t^2} + \frac{3}{2} \left(\frac{\mathrm{d}R}{\mathrm{d}t} \right)^2 + 4 \frac{\mu}{\rho R} \frac{\mathrm{d}R}{\mathrm{d}t} = - \frac{p_\infty + \frac{2A}{R} - p_v - p_g}{\rho} \tag{12}$$

where R is a radius of the bubble, t is time, p_∞ is pressure far from the bubble, p_v -vapour pressure, p_g - pressure of the gas in the bubble.

When spectrum of nuclei at inflow is given one can calculate nuclei distribution in every point inside the domain. Probability of cavitation phenomenon is approximated by:

$$P_{CAV} = cut\left(\sum_i \frac{4}{3}\Pi R_i^3 n_i\right) \tag{13}$$

where n_i is the number of nuclei of size R_i in the unit volume,

$cut(x) = \{x \quad \text{for} \quad x \le 1\,;\, 1 \quad \text{for} \quad x > 1\}$

2. Numerical methods. Discretization approach

Discretization of domain is carried out using Finite Volume (FV) Method .The FV method is based on integral form of conservation equation. The solution domain is subdivided into a finite number of control volumes, and the conservation equations are applied to each of them. At the centroid of each control volume (CV) lies the computational node at which field values are to be calculated.

The integral form of conservation equation of quantity ϕ reads:

$$\int_S \rho\phi \boldsymbol{v}\cdot\boldsymbol{n}\,\mathrm{d}S = \int_S \Gamma \operatorname{grad}\phi\cdot\boldsymbol{n}\,\mathrm{d}S + \int_\Omega q_\phi\,\mathrm{d}\Omega \tag{14}$$

where $\boldsymbol{v}$ is velocity vector, ρ is density, q_ϕ source of ϕ, Γ is the diffusivity for ϕ , $\boldsymbol{n}$ is normal vector.

To express value of each field quantity on CV surface S suitable interpolation methods are used. In the present program two methods are applied: *upwind UDS* (first order) and *linear interpolation CDS* (second order). Surface and volume integral are approximated using midpoint quadrature [Ferziger J.H., Peric M., 1999].

As a result of FV discretization approach one obtains an algebraic equation for each CV.

The system of equations (after linearisation) is solved using iterative method. In present program two algorithms are used: ICCG for symmetric systems and CGStab for nonsymmetric systems [Ferziger J.H., Peric M., 1999] .

3. Testing calculations

Example 1. Calculations of lifting and drag force coefficients.

Computational data and model details

The geometry of hydrofoil:	chord c=0.2 m;
	span w=1.2 m;
	profile geometry NACA 66-9.

Angles of attack:	0, 2, 4, 6, 8, 10, 12 degrees
Inflow velocity:	v=5 m/s
Turbulence model:	Spalart-Allmaras (see eqns (3) – (11))
Interpolation scheme:	UDS and CDS (blending factor B=0.5)
Time integral approximation scheme:	Implicit Euler (first order)
Number of control volumes:	600 000

Results

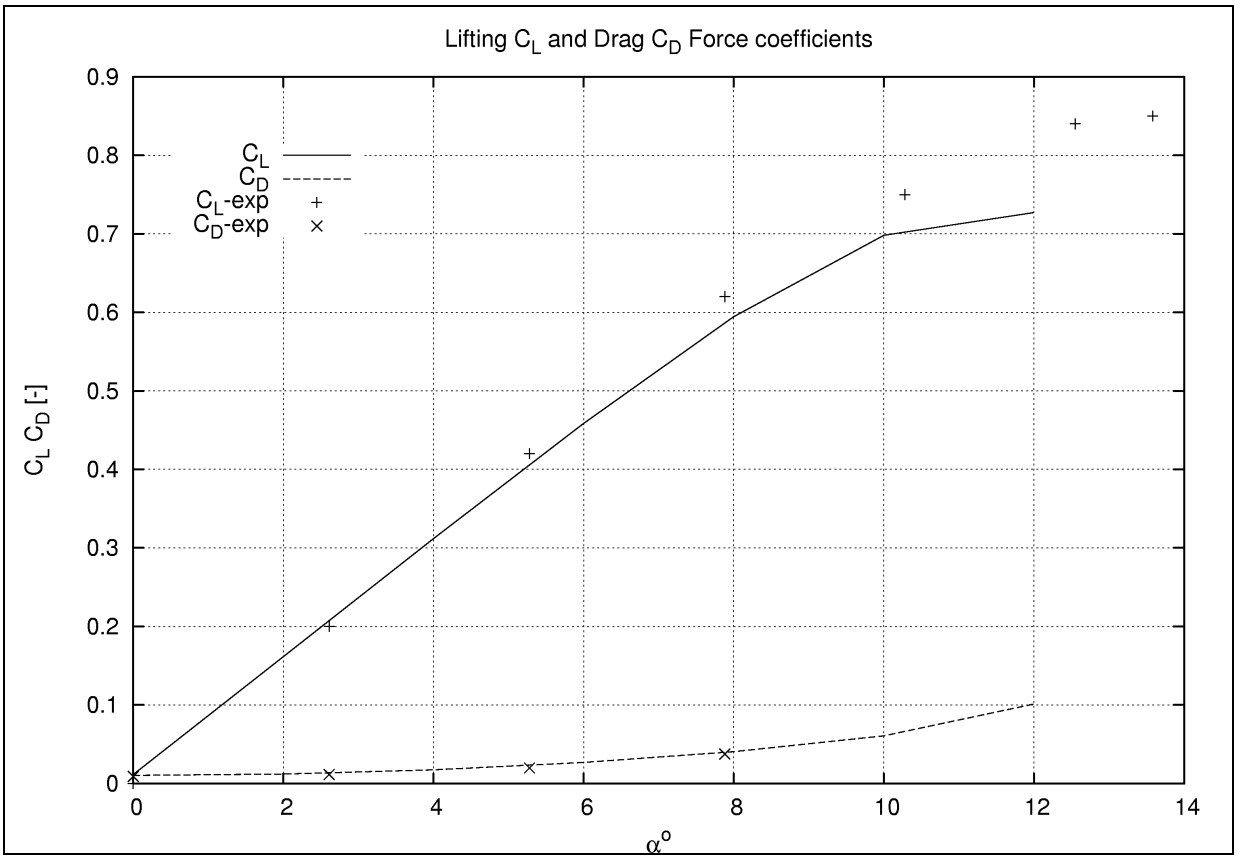

Fig.1. Comparison of the calculated characteristics of lifting C_L and drag C_D force coefficients and characteristics obtained from experimental data [Abbott, 1959].

Example 2. Calculations of cavitation phenomenon.

Computational data

The geometry of hydrofoil: Profile: - suction side: NACA16 - pressure side: flat	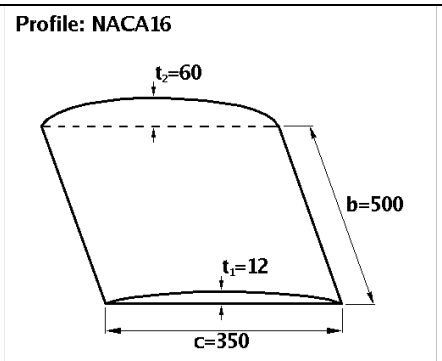
Angles of attack:	0, 5, 10 degrees
Inflow velocity:	v=5 m/s
Size and number of nuclei at inflow:	$R_0 = 10.0 \cdot 10^{-6} m$; $n = 0.1 \cdot 10^6$

Results

angle of attack	pressure p [bar]	Experimental data	Computational results
5^o	0.08	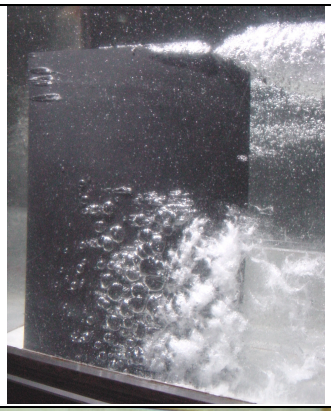	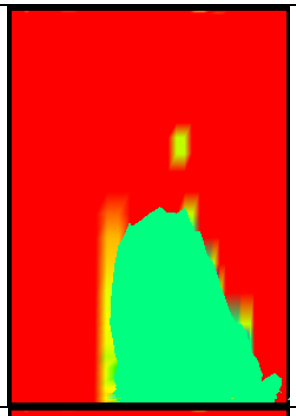
5^o	0.10		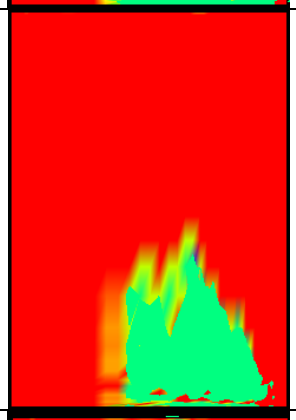
10^o	0.10	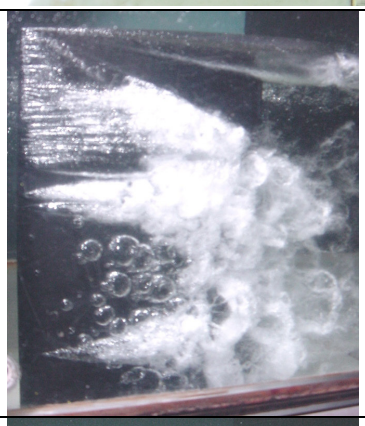	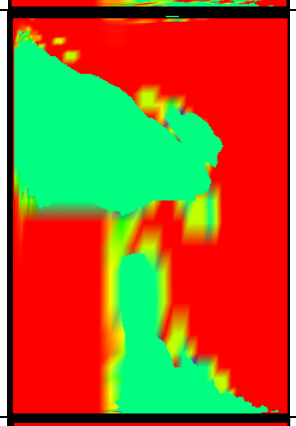
10^o	0.15	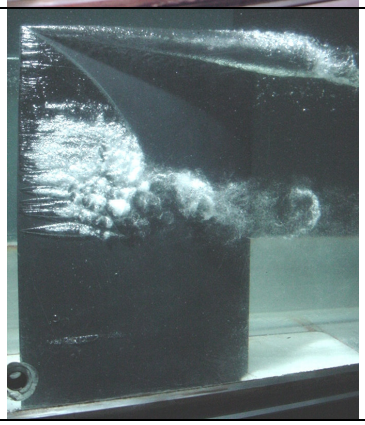	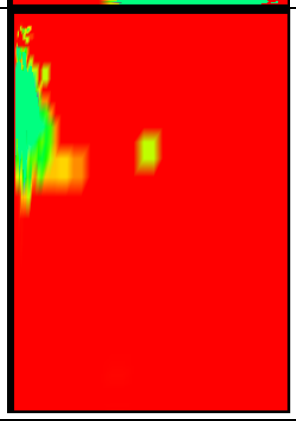

Fig. 2. Simulation of cavitation: experimental data and computational results.

Experimental data are taken from tests, which were carried out in cavitaion tunnel in Ship Design and Research Centre S.A. (CTO).

5. Conclusions

The computational results presented in this paper may be summarised in the following conclusions:

- Lifting force and drag force coefficients have a good conformity with experiment especially in the range of angle of attack from 0 to 6 degrees. The critical point of lifting force coefficient characteristic is predicted with accuracy of about 1 degree.
- The cavitation computation gives reliable results for the prediction of laminar and bubble cavitation, however the model fails to predict the tip vortex cavitation phenomenon.

6. Bibliography

Abbott I.H., von Doenhoff A.E. (1959): Theory of Wing Sections, New York, Dover Publications, inc.

Blazek J. (2001): Computational Fluid Dynamics: Principles and Applications, ELSEVIER.

Ferziger J.H., Peric M. (1999): Computational Methods for Fluid Dynamics, Berlin, Springer.

Koronowicz T. (2002): Rationality of Solving 3D Circulation Problems Exclusively with the Use of Navier-Stokes Equation, Task Quarterly No 1, pages 217-221

Lecoffre Y. (1999): Cavitation. Bubble Trackers, A.A.Balkema

Wilcox D.C. (2002): Turbulence Modeling for CFD, DCW Industries.

Applying Neural Networks to Predict Ship Turning Manoeuvre Track

Adel Ebada[1] and Moustafa Abdel-Maksoud[2]
Institute for Ship Technology und Transport Systems
University Duisburg-Essen, Germany

Introduction

The development of Recursive Neural Networks (RNN) as a simulation tool for submarine manoeuvring was documented in (Faller, *et al*., 1997) and (Faller, *et al*., 1998a). A recursive network is one that employs feedback; namely, the information stream issuing from the outputs is redirected to form additional inputs to the network. RNN simulations were carried out by using manoeuvre data from both model and full-scale submarine. In the later case, incomplete data measured on the full-scale vehicle was augmented by using feed forward neural networks as virtual sensors to estimate the missing data (Hess, *et al*., 1999). The creation of simulations at both scales permitted the exploration of scaling differences between the two vehicles (Faller, *et al*., 1998b). An initial formulation of the problem using an RNN model for ships is described in (Hess, *et al*., 1998).

The technique was further developed for accurate prediction of tactical circle and horizontal overshoot manoeuvres (Hess, *et al*., 2000). The implementations and techniques to predict the submarine manoeuvres were published (Hess and Faller 2002). Different applications of ANN can be found in [1, 2, and 6].

Applied ANN mathematical model

For developing the ANN-mathematical model, the following assumptions are made in the present study: single screw ship, right handed propeller, calm sea condition and deep water depth.

The main data of the investigated ships and the input parameters for ANN are given in table 1. Ship speed (U) is measured relative to the fluid. Control data for propulsion and manoeuvrability of the vessel are propeller rotation speed (n), rudder deflection angle (δ_r), rudder area (A_R) and rudder angle ordered (δ_{RO}). Trim angle is neglected due to even keel-loaded condition. Draft, block coefficient and displacement were modified to meet the actual loaded condition.

The required results for training the system were generated using a navigation simulator. Trajectory is defined as x-, y-coordinates. The surface motions are presented by the longitudinal axis x. It is positive towards the bow. y is the transverse axis and is positive to starboard. The angular motion takes place around the vertical z-axis. The trails were carried out according to the IMO requirements. In each run, the ship started with steady course ahead.

The action of the rudder angles was ordered (δ_{RO}) at time (t_o) and in the same time the ship position and all required data for such type of manoeuvre were saved. Eighty-two runs were recorded and documented. Fifty-nine of such data files were provided for training the system. Twenty-three runs were used as input data for blind manoeuvres and for validation.

The time interval for recording data was 5 or 10 seconds. The following items were recorded: simulation time (t), starting position as latitude and longitude, speed (U), number of revolution per minute (RPM), ship's ground course ($\Psi - \beta$), ship heading (Ψ), turn rate ($d\Psi/dt$), rudder angle (δ_r), distance travel, and acceleration. During a turning manoeuvre, the rate of turn increases gradually till reaches a certain amount. All the data were recorded till the manoeuvre ceased after one complete turn, which is a track course of 360 degrees plus the actual drift angle (β).

Parallel Neural Networks (PNN) Architecture

Multi-layer networks were built. All layers are called hidden layers except the first and the last layers. The first layer is defined as an input one. The last layer produces the network output and is called output layer.

Many numbers of ANNs are used in parallel to describe the different positions of the ship track during its motion. The number of ANNs depends on distance travel, time travel, track and application purposes.

Figure 1 shows one of these architectures, which use the back propagation feed forward neural network form. The developed structure has four layers (one input layer, two hidden layers and one output layer) where the inputs are fed to the neurons, which are constructed before the hidden layer number one. Each layer has a weight matrix W, a bias vector b, and an output vector z. To distinguish between the weight matrices, output vectors,

[1] ebada@nav.uni-duisburg.de
[2] maksoud@nav.uni-duisburg.de

etc., for each of these layers in the built system, the number of the layer is appended as a super script to the variable of interest shown in figure 1 and in equations 1, 2 and 3.

The nodes in the input layer serve as a summation to couple the inputs to the designed net. The calculations are performed in the hidden layers and the output layer. The nodes in the four layers are fully connected by weighted links. Most nodes have a bias and this is implemented as an additional input multiplied by the weight associated with the link and then summed along with the other inputs to the node, further details can be found in (Hirose, 2003).

The network shown above has M^1 inputs that could be so many inputs for wider applications of motion prediction. The inputs were reduced to be twenty-one which are adequate for this application, see table 1. The network in figure 1 has N^1 neurons in the first layer, N^2 neurons in the second layer, etc. A constant input of one is fed to the biases for each neuron to reflect the correct magnitude with any decision output value applying the sigmoid form of activation function.

The outputs of each intermediate layer are the inputs of the next layer. One of the intermediate layers such as layer two can be analysed as a one-layer network. The vectors and matrices of layer two can be identified as N^1 that represents the input to each neuron; N^2 is the number of neurons in this layer. The multiplication of N^2 and N^1 is the weight matrix W^2 while the input to layer two is z^1 and the output is z^2. Each layer can be treated as a single-layer network on its own using the similar notation. The three layers notation can be articulated by the following equations:

$$z^1 = f^1 (IW_{1,1} p + b_1) \tag{1}$$

$$z^2 = f^2 (LW_{2,1} z^1 + b_2) \tag{2}$$

$$z^3 = f^3 (LW_{3,2} z^2 + b_3) \tag{3}$$

Equivalent of z^3 is as follows:

$$z^3 = f^3 (LW_{3,2} f^2 (LW_{2,1} f^1 (IW_{1,1} p + b_1) + b_2) + b_3) \tag{4}$$

Each layer has neurons, which contain a non-linear transfer function that processes the input to the node and produces decision outputs. The binary sigmoid functions were used for this study:

$$g = f(net) = \frac{A}{1+e^{(-\lambda\, net)}} - D \tag{5}$$

Where: A and D are constants. A can be equal 2 or 1 and D is equal 0 or 1. The value A or D depends on the pattern problem and the desired decision outputs. f is a non-linear function and λ is the neuron input.

Training Procedures

It is common to normalize all variables (inputs and outputs). It is also possible to combine two or more inputs together to form one input after normalization, which has the advantage of reducing the number of inputs while their effect on the results is taken into account.

The inputs of the network are processed by the presence of weights and by the non-linear functions as outputs of each of the various nodes until they arrive at the output layer of the network. The difference between the target and predicted output is a measure of the error of the prediction, see equation 6.

$$E_p = \frac{1}{2} \sum_j (t_{pj} - o_{pj})^2 \tag{6}$$

Where:
- E : error function (least squares)
- P : pattern index
- j : index of output neuron
- t_{pj} : target output for pattern p on node j
- o_{pj} : actual output at that node.

The purpose of training is to reduce gradually the error on subsequent iterations. The training algorithm used in this study is called back propagation feed forward which is a gradient descent algorithm. Back-propagation is the most commonly used training algorithm for neural networks. For minimizing the error from hidden-to-output neurons, the weights were updated using the delta rule (steepest descent):

$$\triangle w_{ij}(t) = -\eta \frac{\partial E(t)}{\partial w_{ij}(t)} + \alpha \triangle w_{ij}(t-1) \qquad (7)$$

Where $-\eta$ is the learning rate, α is the momentum and t is the iteration number.

The Batch Gradient Descent is used in the current training. The weights and biases are updated in the direction of the negative gradient of the performance function.

In the present study, the ANNs need about 6148 epochs for the initial points of the patterns just after the first action of the manoeuvres and about 150 000 epochs to reach the specific goals. An epoch is defined as the presentation of the time series for the inputs and outputs for one specific case in the training set. The numbers of trained epochs for the networks are chosen depending on realistic and probability aspects according to the worst condition. The worst condition is the case where the measurement error is added to the error in the ANN and hence the overall error is maximized. i.e. the two errors have the same signs. The results in this case have to remain within acceptable level to increase the reliability of the process.

For one of the cases, 89603 epochs were needed to train the network until reaching best performance of the architecture, see figure 2 and 3. The network was tested for its ability to generalize during the training process and paused every 200 epochs. Consequently, the weights were written to a data file every 200 epochs.

Results

All manoeuvring files delivered to the built system and the twenty-three blind manoeuvres were used to prove the liability and validity of the method applied. The only information provided to the network by carrying out of blind manoeuvres was initial conditions and ship parameters. Figure 4 shows some of the predicted manoeuvres in twelve subfigures. The results of four of the training tests are shown in (4.1-4.4) while the subfigures (4.5 - 4.10) include the testing results for the blind manoeuvres.

The study was conducted for four different ships (two container ships, one bulk carrier and one VLCC). For both training and testing manoeuvres, the rudder angles were varied from 5^0 to 35^0 to port and to starboard side. The predicted turning manoeuvre tracks with small and maximum angles of rudder have been tested for the four ships, see figure 4.

The results show that the applied method is able to predict the different behaviour of the turning manoeuvres of the ship investigated. Not only the advance distance and turning diameter agree well with the experimental data but also the coordinates of the complete turn.

Figure 5 shows the behaviour of the tanker ship when it turns to port and to starboard with same rudder angle. The test conditions were 269 869 tones displacement weight, starting speed 14.7 knots and rudder angle of 25 degrees.

Conclusion

The presented work is a step to accomplish the building of an architecture system of PNN that can meet the marine operation needs for sea units. It gives the opportunity also to analyse different ship motion under different operation conditions.

Further work is under consideration to categorize the strengths and weaknesses of the presented method to take into account the real operation conditions of ships. One of the main aims of the future research is to provide guidance for ships' Master, which allows the auto control system to estimate the safe modes of navigation with high accuracy. Ship control system needs an accurate and reliable tool to predict the motion in advance at any loaded draft and speed.

Bibliography

[1] Aleksander M. Stankovic, Andrija T. Saric and Mirjana Milosevic (2003), Identification of nonparametric dynamic power system equivalents with artificial neural network, IEEE Transactions on Power Systems, Volume: 18, Issue: 4, Page(s): 1478-1486.

[2] Charytoniuk, W. and Mo-Shing Chen., (2000), Very short-term load forecasting using artificial neural network, IEEE transactions on Power Systems, Vol. 15, No.1.

[3] Faller, W.E., Smith, W.E., and Huang, T.T., (1997), Applied Dynamic System Modelling- Six Degree-Of-Freedom- Simulation Of Forced Unsteady Manoeuvres Using Recursive Neural Networks, 35th AIAA Aerospace Sciences Meeting, Paper 97-0336, pp. 1-46.

[4] Faller, W.E., Hess, D.E., Smith, W.E. and Huang, T.T., (1998a), Full-Scale Submarine Manoeuvre Simulation, 1st Symposium on Marine Applications of Computational Fluid Dynamics, U.S. Navy Hydrodynamic / Hydro-acoustic Technology Centre, McLean, Va. .
[5] Faller, W.E., Hess, D.E., Smith, W.E., and Huang, T.T., (1998b), Applications of Recursive Neural Network Technologies to Hydrodynamics", Proceedings of the Twenty-Second Symposium on Naval Hydrodynamics, Washington, D.C., Vol. 3, August, pp. 1-15.
[6] Fukukda, T. and Shibata, T. (1992), Theory and applications of Neural Network for industrial control systems, IEEE Trans. on Industrial Electronics, vol. 39, No. 6, pp. 472-489.
[7] Hess, D. & Faller, W. (13 July 2002), Using Recursive Neural Networks for Blind Predictions of Submarine Manoeuvres, 24th Symposium on Naval Hydrodynamics Fukuoka, JAPAN.
[8] Hirose, (2003), A Complex-Valued Neural Networks, Theories and Applications. World Scientific Publishing Co. Pte. Ltd.

Table 1 Main Ship Data and input data.

Type of ship **Condition** Ship No.		**Container 1** **Loaded** **1281**	**Container 2** **Loaded** **3011**	**Bulk Carrier** **Loaded** **1225**	**Tanker** **Loaded** **1223**	**Input Data (*)**
Displacement	m^3	42275	65,366	73096	269869	*
L. B.P.	m	230,5	280.00	219.0	310	*
Length overall	m	241.10	294.06	234	322	
Breadth moulded	m	32.20	32.20	32.2	56	*
Draught fore	m	10.15	11.45	12.8	20	*
Draught aft	m	10.15	11.45	12.8	20	*
Wetted Surface	m^2	8021	11,436	10153	17721	
Wind area, side	m^2	4633	1,004	2043	7101	
Wind area, front	m^2	872	6,800	648	1706	*
Block coefficient	---	.561	0.63	.810	.7905	
Trim by the stern	%	0	0	0	0	
LCB for. from of LBP/2	% of LBP	.06	-3.27	2.42	-1.13	
Radius of inertia	% of LBP	24	24	24	24	
Type of Engine		Diesel	Diesel	Diesel	Diesel	
Number of propellers		1	1	1	1	
Type of propellers		FP	FP	FP	FP	
Direction of rotation		R. Handed	R. Handed	R. Handed	R. Handed	
Propeller diameter	m	8.0	8.40	6.15	9.35	*
Pitch ratio at 0.7R	--	1.187	0.95	.766	.738	*
Propeller area ratio	--	.79	0.50	.447	.580	*
Shaft Power (Ahead)	MW	37.08	36.80	5.00	17.87	*
Shaft Power (Astern)	MW	37.08	36.80	5.00	17.87	
Number of rudders		1	1	1	1	
Type of rudders		Semi- Spade	Semi-Spade	Spade	Semi-	
Position		In CL	In CL	In CL	Spade	
Area of each rudder,	(m^2)	52.6	74.60	45.5	In CL	
incl. ½ horn					82.9	*
total rudder area	%	2.25	2.35	1.62		
/LBP x T⊗					3.07	*
Turning velocity of	°/sec	2.50	2.80	2.50		
rudder.					2.50	
Max. rudder angle	°	35	35	35		
					35	
Number of bow thrusters		1	1	0	0	
Nom. bow-thruster force	kN	147	2.000	-	-	
Numbers of stern thrusters		1	-	0	0	
Nom. stern thruster force	kN	98	-	-	-	

In addition to the input data mentioned above, the following data is used as input to ANN:
Ship parameters:

Lateral area, water plan area (A_w), water plan area coefficient, rudder angle (δ_r) and ship's speed (U).

Propeller parameters:
Number of blades (z), Revolution per minute (RPM) or (n),

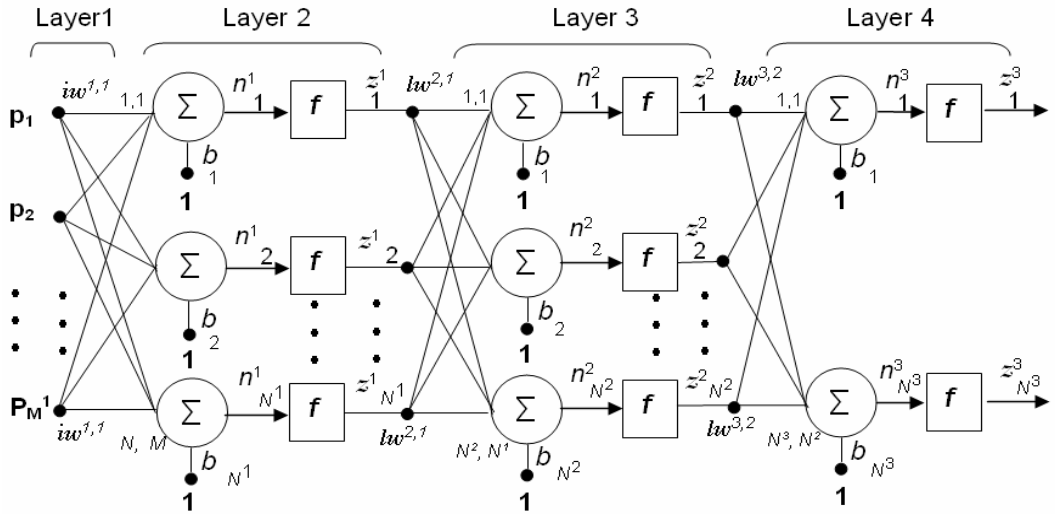

Figure 1: Architecture of multiple-layer PNN

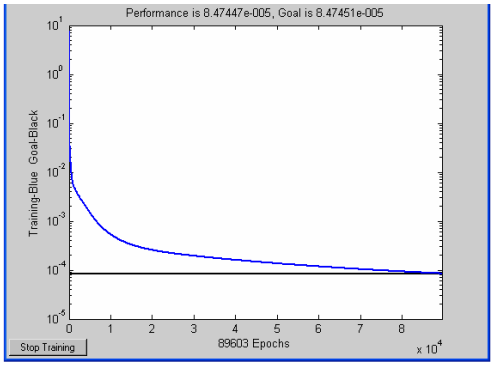

Figure 2: Epochs and goal of one case of PNN

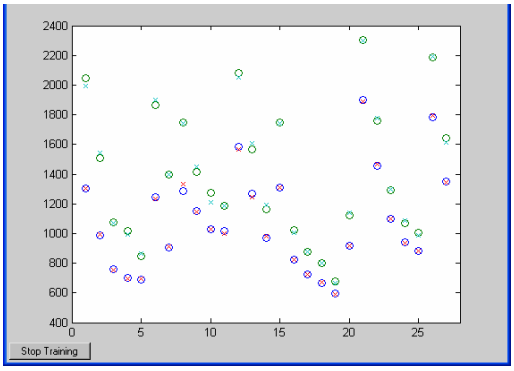

Figure 3: Results of training goal for one case

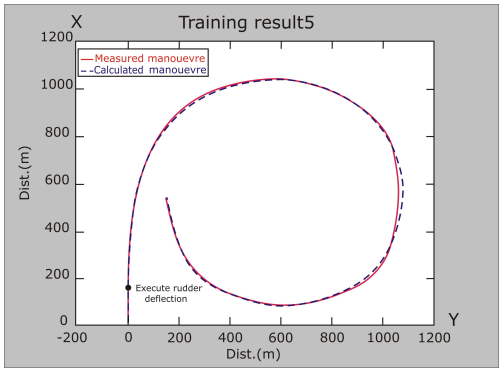

Figure 4.1: Container ship 1, δ_r= 35° to starboard

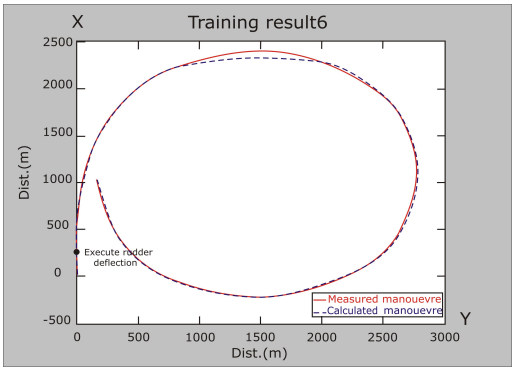

Figure 4.2: Container ship 2, δ_r= 5° to starboard

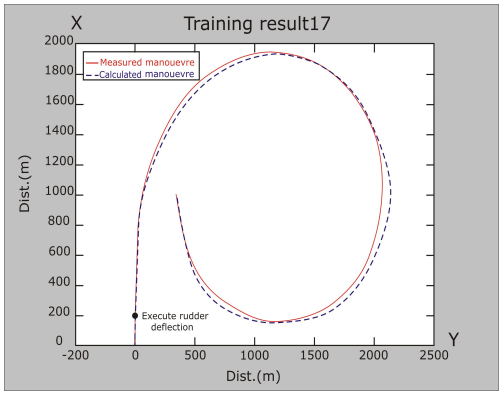

Figure 4.3: VLCC, δ_r= 10° to starboard

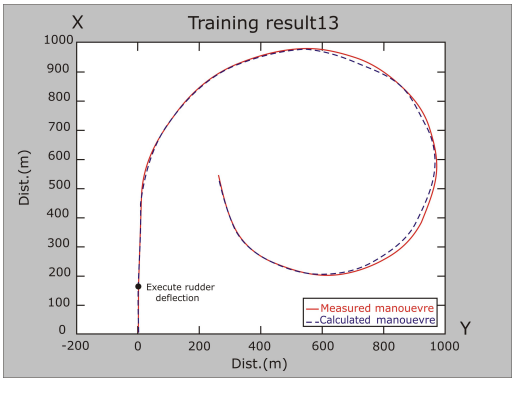

Figure 4.4: Bulk carrier, δ_r=20° to starboard

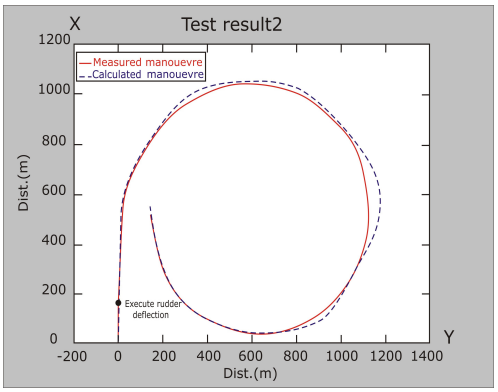

Figure 4.5: Container ship 1, δ_r =30° to starboard

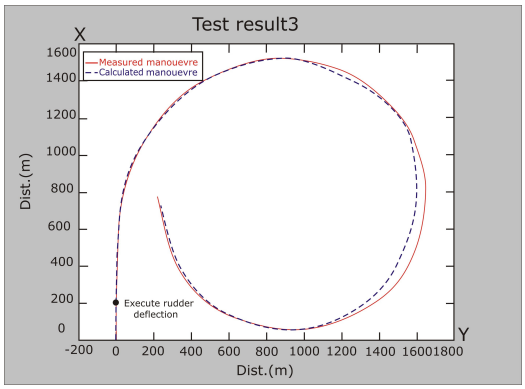

Figure 4.6: Container ship 2, δ_r= 20° to starboard

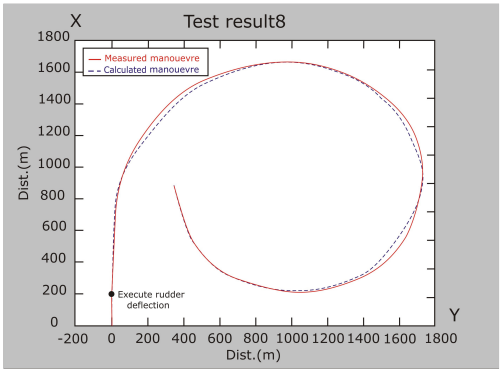

Figure 4.7: VLCC, δ_r=15° to starboard

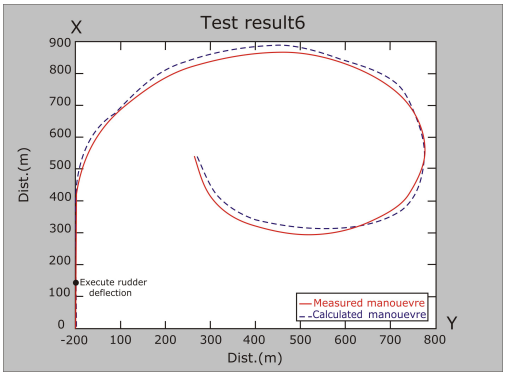

Figure 4.8: Bulk carrier, δ_r=30° to starboard

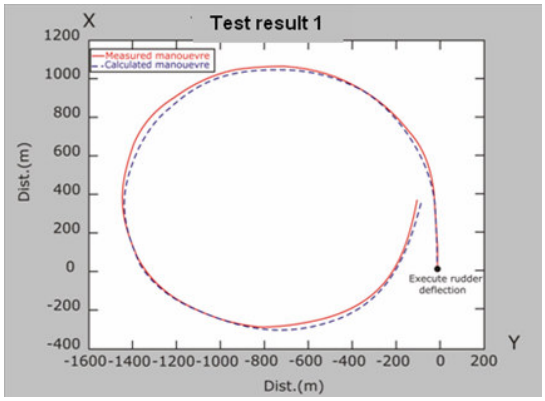

Figure 4.9: Container ship 1, δ_r= 15° to port side

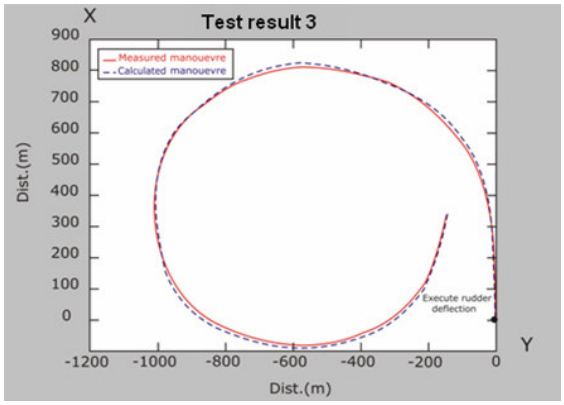

Figure 4.10 Container ship 1, δ_r= 33° to port side

Figure 4 Turning manoeuvre tracks of different ships at various rudder angles

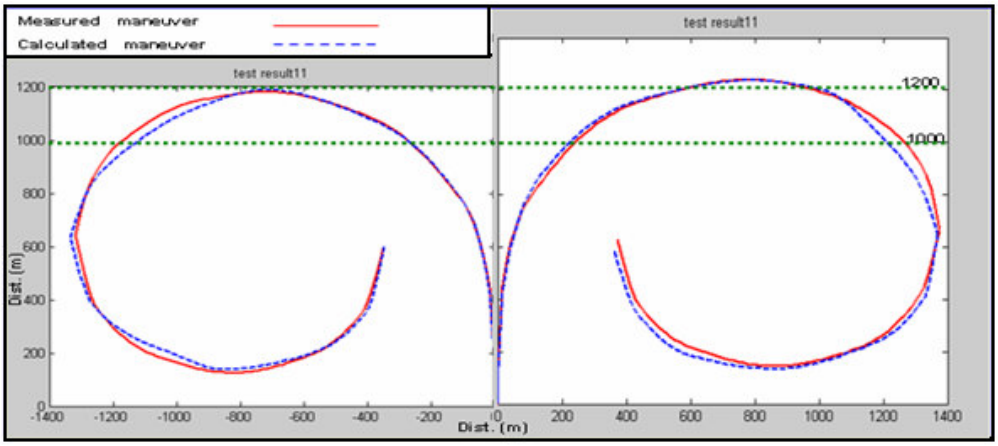

Figure 5: Turning manoeuvre tracks of VLLC, δ_r= 25° degrees to both sides

RANSE Simulation of Ship Ventilation for a Navy Vessel

François Grosjean, Steven Kerampran
ENSIETA, 2 Rue F. Verny, F-29806 Brest, France, grosjefr@ensieta.fr

Introduction

Two new warships are currently built by DCN-Brest for the French Navy represented by DGA (Délégation Générale de l'Armement). These warships have to host two landing craft air cushion (LCAC) vehicles in their docks.

We employed the RANSE solver Fluent 6.1 to investigate the ventilation configuration of the landing dock, specifically to determine the temperature distributions inside the dock. Some specific locations have to be protected since they will host people or temperature-sensitive devices. Some steady intake and outlet devices provide a basic ventilation. Some additional ventilation systems are available. These are reversible systems, able to act as intake or outlet within a given range of flow rates. The aim of this study was to test several configurations of these additional systems, to determine the best suited to the docking of an LCAC.

Problem formulation

Before including any LCAC movement, the temperature state of the docking area has to be computed. The object of this first calculation is to obtain the stationary pressure, velocity and temperature distribution in the dock with the LCAC dormant. In the simplified model used for the computations, the motor is started before the LCAC gets in motion, and air is taken in by 2 admission holes and blown out of 4 exhaust holes. The problem is now unstationary, and the computation is run 80 s. Eventually, the LCAC moves and the 2 main propellers and the 2 stem propellers are activated. In the simulations, it is assumed that the LCAC needs 10 s to exit the docking area. To simplify the computations, the actual movement of the LCAC is not taken into account (although possible, this would require some remeshing at each time step and would be too time-consuming). This leads to an over-estimation of the peak temperatures observed in the dock, which is acceptable from a safety point of view.

Fluent 6.1 solves the Reynolds averaged Navier Stokes Equations (RANSE) using a finite volume method. We add the energy equation and a multi-species model to take into account the exhaust gas. Turbulence was modeled by the standard k-ε model. Two types of boundary conditions are imposed :

1. in the presence of open air, the pressure is set to atmospheric pressure and the temperature to 35° C.
2. in the case of a suction or a blowing device, the mass flow rate and the temperature are set.

For each boundary condition the values for the turbulent energy and dissipation rate are calculated, using empirical formulas [1].

Numerical simulations

The docking floor geometry is directly imported from a CAE file, with minor adjustments in order to use Gambit, Fluent's pre-processor. In particular, some very narrow spaces had to be removed, such as the metallic sheets around the blowing systems, Fig.1. Numerous tests resulted in a rather fine grid, Fig.1, to take into account the wide range of characteristic dimensions. The dock is approximately 100 m long, but some holes with diameter 0.23 m needed to be meshed with several cells. The LCAC shape is also simplified, the roundness is removed in favor of straight lines. This results in a parallel-epipedic shape, Fig.2. The LCAC rests on the ship dock during all the computation.

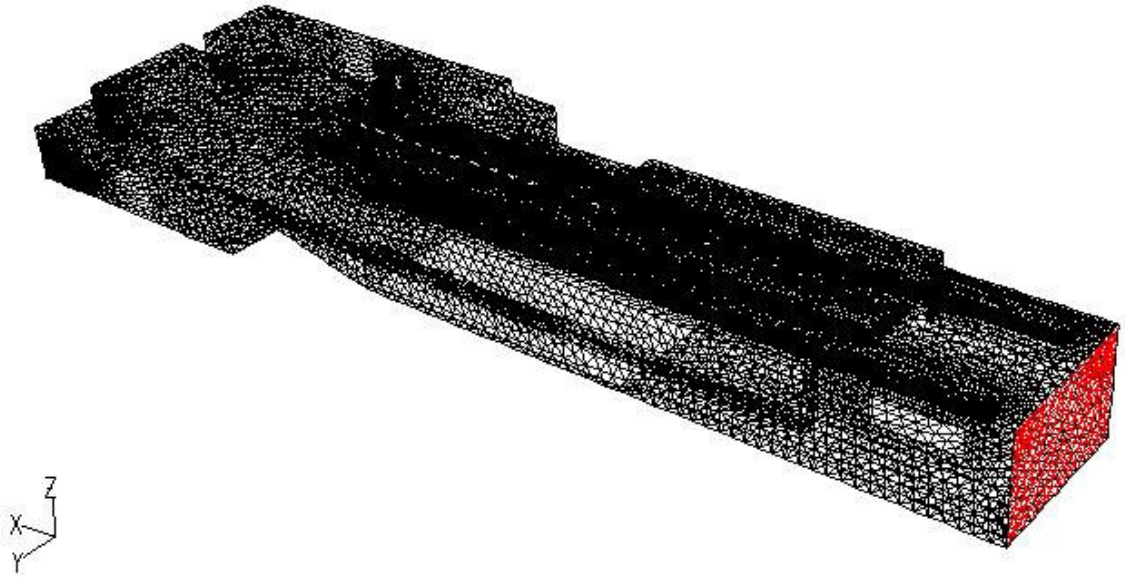

Fig.1: Global mesh with 1.1 million cells

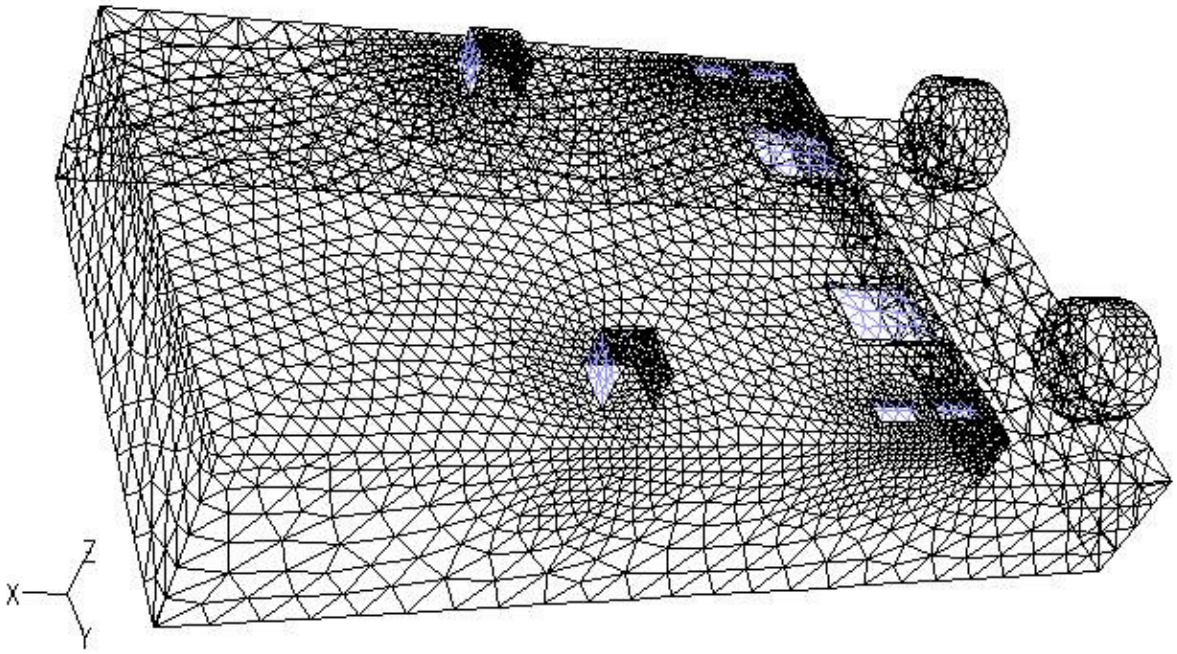

Fig.2: Zoom on LCAC grid

The dock is equipped with several intake, outlet and double-purpose ventilation devices. For details see [2] *Grosjean and Kerampran (2005)*. Boundary conditions can change during the LCAC take-off. The exhaust gas is a combination of several simple gases and assimilated to a single species. Classical laws are used to determine its physical properties, such as the Sutherland law for the dynamical viscosity.

First simulation: Exhaust

The first part of the calculation is performed to know the stationary state of the dock, the LCAC being still at rest. The boundaries conditions are imposed as follows for the mass flows (Kg/s) :

zone 4 (ventilation_port): 20.400011
zone 5 (ventilation_stb): 15.300001
zone 6 (extraction_stb): -51
zone 6 bis (extraction_port): -50.999992
zone 7 (reversible_stb): 20.4
zone 8 (reversible_fond): 10.3
zone 9 (reversible_port): 10.3

For the outlets, the computed results are :
zone 10 (ouverture_2_port): 4.1372075
zone 10 (ouverture_2_stb): 4.5593686
zone 10 (porte): 16.613634

The balance sheet is $0.01 kg.s^{-1}$, the equilibrium is therefore obtained.

The second operation begins: the LCAC motors are switched on. During 80 s, the LCAC motors take air in, but they also blow burnt gas at very high temperature (~550°C). The boundary conditions for the dock do not change. Now the problem becomes unstationary and we change the solver to add the time-dependent terms to the equations. The residuals of these equations all have to be less than 1E-3, except for the energy equation, where a value of 1E-6 is required. The time step is 1 s. Fig.4 shows the temperature for two vertical planes, in the vicinity of the LCAC (which can be guessed in the figure). Fig.5 gives the temperature for an horizontal plane, just above the LCAC. The highest temperatures are recorded just above the exhaust pipes of the LCAC. We can distinguish the line where the exhaust gas are taken in by all the holes along the roof of the dock. We can see the fresh air coming from the extremities of the dock, one is open to the atmosphere, and at the bottom of the dock, where the space is larger, fresh air is breathed. In the third stage, the LCAC begins to move. The fans are started and the LCAC breathes more fresh air. This phase lasts only 10 s. The time step does not change. There is a noticeable drop of temperature is recorded by the various gauges around the dock, compare Figs.5 and 6. This is mainly due to the additional flow through the fans.

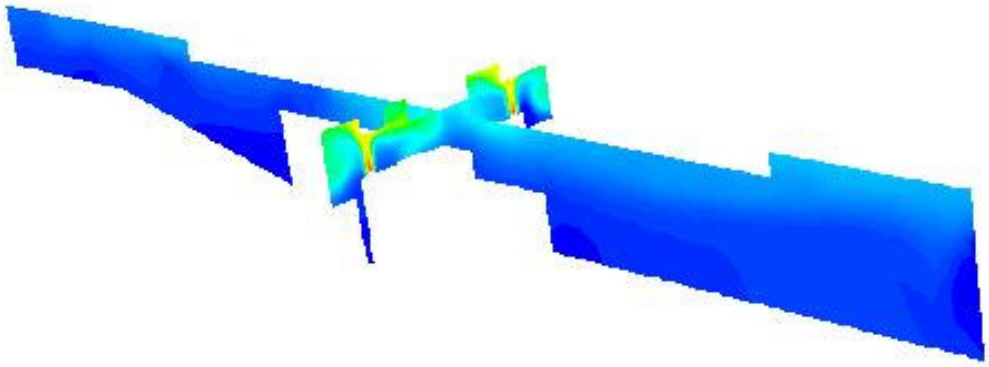

Fig.4: Temperature planes near LCAC

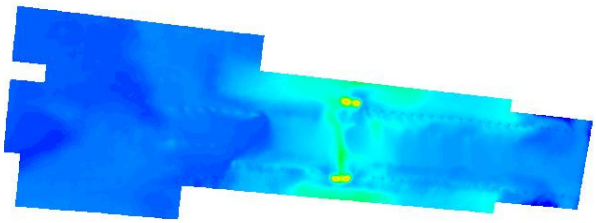

Fig.5: Temperature in horizontal plane above LCAC (starting stage)

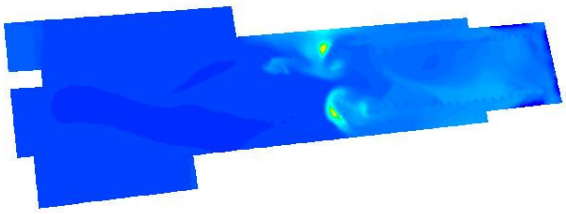

Fig.6: Same horizontal plane with LCAC, fans started (moving stage)

Second simulation: Intake

The boundaries conditions are imposed as follows for the mass flows (Kg/s) :

zone 5 (ventilation_stb): 15.300001
zone 6 (extraction_stb): -51
zone 6 bis (extraction_port): -50.999992
zone 7 (reversible_stb): -20.4
zone 8 (reversible_fond): -10.3
zone 9 (reversible_port): -10.3
zone 10 (ouverture_2_port): 23.844944
zone 10 (ouverture_2_stb): 22.530842
zone 10 (porte): 60.919636

Thus the signs for three boundary conditions change in this case. This results in a much larger mass flow through the openings. The balance sheet is -0.004558 $kg.s^{-1}$. The equilibrium is obtained at the end of this stationary stage. Fig.7 shows the temperature field in the same plane as Fig.6. The average temperature is higher than in the previous case. In particular, higher temperatures are recorded in critical places, such as the positions of the people guiding the LCAC during its entrance or exit. When the LCAC begins to move, the fans have a strong effect, as in the previous case. Over 10 s, the temperature decreases in approximately the same proportions as in the first case, Fig.8.

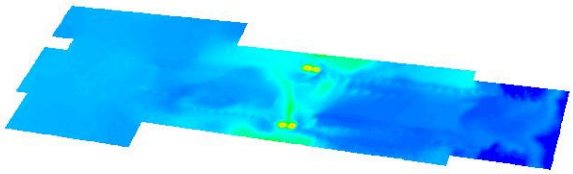

Fig.7: Temperature in horizontal plane above LCAC (starting stage)

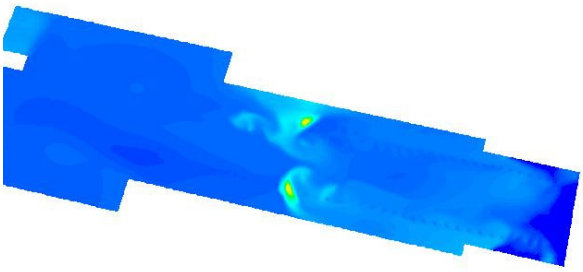

Fig.8: Temperature in horizontal plane above LCAC (moving stage)

Third simulation : Front intake

Another option was tested, by creating a larger flow when the LCAC propellers are used, even before any other operation. In the same time, we change the flow rate of the reversible fans. The equilibrium state is obtained and the flow rates are :

zone 4 (ventilation_port): 20.400011
zone 5 (ventilation_stb): 15.300001
zone 6 (extraction_stb): -51
zone 6 bis (extraction_port): -50.999992
zone 7 (reversible_stb): -34.
zone 8 (reversible_fond): -17.2
zone 9 (reversible_port): -17.2
zone 10 (ouverture_2_port): 27.55
zone 10 (ouverture_2_stb): 25.89
zone 10 (porte): 81.26
zone 19 (lcac_helices): 18.73

The balance sheet is - 0.0013 $kg.s^{-1}$. In this second phase, the LCAC is started but does not move. The hot gas invade the upper region and in 80 s the roof is full of hot gas. Yet, the average temperature is lower than in the second case almost everywhere in the docking area. Only some locations close to the dock roof have a higher temperature, Fig.9. This is not a concern since these locations do not hold sensitive devices. When the LCAC begins to move, the fans continue to have a powerful action as in the previous cases, but the temperature keeps increasing in some pockets where the air is trapped, Fig.10.

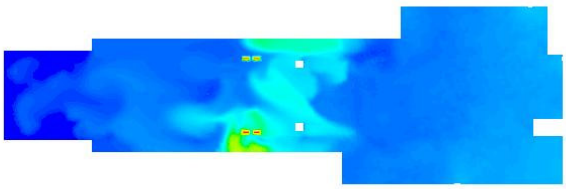

Fig.9: Temperature in horizontal plane above LCAC (starting stage)

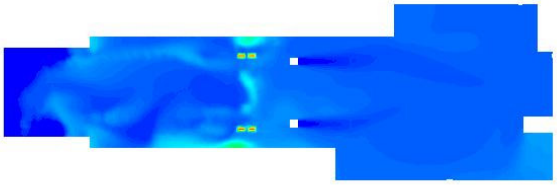

Fig.10: Temperature in horizontal plane above LCAC (moving stage)

Fourth simulation: Mixed formula

Finally, we test the possibility to create a flow between the reversible fans in the back of the docking area. The flow rates henceforth show a transverse flow at the left end of the deck:

zone 4 (ventilation_port): 20.400011
zone 5 (ventilation_stb): 15.300001
zone 6 (extraction_stb): -51
zone 6 bis (extraction_port): -50.999992
e 7 (reversible_stb): -34.
zone 8 (reversible_fond): 10.3
zone 9 (reversible_port): 10.3
zone 10 (ouverture_2_port): 17.88
zone 10 (ouverture_2_stb): 17.63
zone 10 (porte): 44.14
zone 19 (lcac_helices): 12.03

The balance sheet is 0.0017 $kg.s^{-1}$.

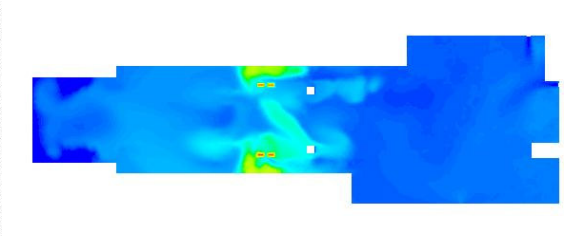

Fig.11: Temperature in horizontal plane above LCAC (starting stage)

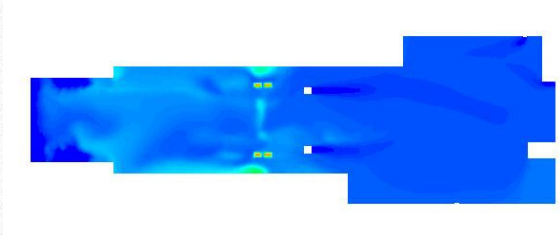

Fig.12: Temperature in horizontal plane above LCAC (moving stage)

In the starting stage, the hot gas invades the bottom of the dock, but owing to the flow created at the back of the dock, the flow is maintained in the larger area, and the temperatures do not change too much, Fig.11. People standing at the locations by the maneuvering of the LCAC are safer than in all the other cases. The temperature strongly decreases almost everywhere, except in the right part of the dock where it was quite moderate during the previous stage, Fig.12.

Comparison

Fig.13 shows the reduced temperature $\tau = (T-T_0)/(T_{max}-T_0)$ temporal evolution at three locations around the LCAC. T_{max} is the maximum temperature recorded during the simulations and T_0 is the ambient temperature. The first location will be manned during LCAC operation. Temperature recording at this position is therefore crucial. The other locations correspond to temperature sensitive devices (fire detector, light). As regards the first location, the minimal temperature is recorded for case n°2. Unfortunately, this case is quite detrimental to the two other locations considered. Case n°4 could prove a good compromise, showing that resorting to the LCAC fans during the warm-up stage to provide an additional ventilation could be an idea worth considering.

Acknowledgments

We would like to thank DCN Brest and its correspondent Thierry Barale for giving us the opportunity to test our knowledge.

References

[1] Fluent 6, user's guide (2001)

[2] GROSJEAN, F.; KERAMPRAN, S. (2005), Numerical simulation of a ship ventilation to collect landing craft air cushion, FAST'2005, St.Petersburg

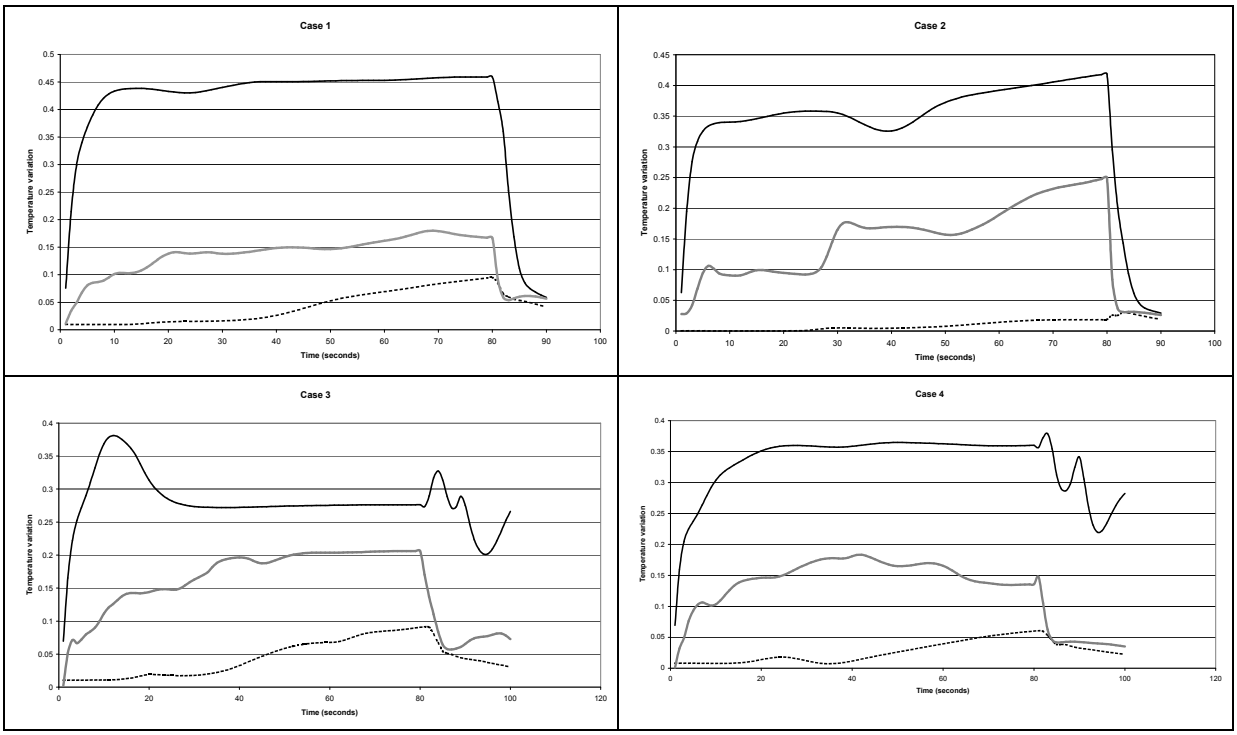

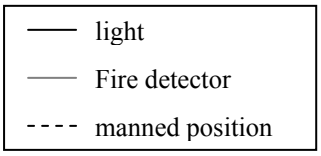

Fig.13: Temperature on 3 captors

Sensitivity Tests of a Steady Euler Solver For Prediction of Ship Effective Wake

Henri Haimov , *e-mail*: haimov@cehipar.es

1. Introduction

The effective inflow is a necessary input data for any propeller design and should be taken into account in the analysis of the propeller behaviour in non-uniform flow. Simple correction of the nominal wake flow behind the ship had been used by the designers before more elaborate methods of prediction appeared. In the pioneering works of Huang & Cox (1977), Nagamatsu & Tokunaga (1978), Goodman (1979), Dyne (1980) etc. it has been shown that the resulting flow to the propeller is mainly due to the interaction of the rotational non-uniform stern flow and the propeller. It is assumed that this interaction is mainly of inviscid character, being the nominal wake flow a consequence of the viscous flow around the ship. The nominal flow distribution is usually known from model tests or can be calculated using viscous CFD codes. The strictly viscous interaction is neglected and this assumption seems to be confirmed by experiments not to introduce, in general, excessive errors. The hydrodynamic theories of momentum (actuator disk) and inviscid fluid flow with vorticity have been applied successfully to account for the interaction, representing the propeller as an actuator disk or as a lifting-line model in rotational inflow.

Since then, although the basic assumptions have not changed, more elaborate solutions based on the solutions of the Euler equations for rotational flows have been developed and combined with more precise modelling of the propeller.

As a member (until Phase 3) of the Consortium on Cavitation Performance of High Speed Propulsors, CEHPAR (El Pardo Model Basin) has received and implemented the Euler solvers (steady and unsteady) developed by Choi and Kinnas (1998, 2000) from the University of Texas at Austin. The research in this area still continues within Phase 4 of the Consortium.

The present study is limited to the axisymmetric solver GBFLOW-3X, version 1.1.1, although the full 3D solver GBFLOW-3D is also implemented.

As the authors of the solver reported verification and partial validation of the programs and our experience confirms this, the present work concentrated only on evaluating the sensitivity of the codes to some physical parameters of the propeller design of interest to applications.

2. The 3-D Steady Euler Solver

The steady incompressible Euler equations are:

$$\nabla.\vec{v} = 0$$

$$\nabla.(\vec{v}\vec{v}) = -\nabla p + \vec{f}$$

where $\vec{v}$ is the velocity vector, p – the pressure and $\vec{f}$ - the external body force, formulated in the finite volume method. The artificial compressibility method similar of that of Chorin is applied for the computation of pressure. The region concerned is discretized into hexahedral cells and the equation is applied to each cell. The external force term in the Euler equations represents the so called body forces acting on the flow, in this case due to the propeller action. The body force is a function of space, although its variation in axial direction is neglected, as suggested by the numerical tests. The body force is distributed over the disk area of the propeller within two cell thickness axially and simulates the time averaged spatially varying loading calculated by the propeller lifting-surface analysis code MPUF-3A, version 2.1.1 developed by S. Kinnas et al. (1998). The circulation distribution is used to obtain the axial and tangential body force related to the thrust and torque of the propeller. The axisymmetric Euler solver called GBFLOW-3X is described in more details in Choi & Kinnas (1998,2001) .

An iterative VMS procedure is established between programs GBFLOW-3X and MPUF-3A, where the former uses as input the propeller loading distribution and the latter - the calculated effective wake. The convergence is usually obtained in few iterations (4 used here). The computer is a HP Alpha Station DS15 of 1GHz CPU and 4 GB RAM and the computer time for a meridional mesh of 70x50 is about 7 minutes.

The authors reported extensive verification and some validation of the programs. Especially, the influence of the parameters of the method like number of internal iterations, artificial compressibility and viscosity, time step size, positions of the boundaries of the flow and the plane where the effective wake is evaluated. Also convergence and mesh size tests resulted in recommendations to the use.

Nevertheless, the process of validation of the computer codes includes more necessary steps, among them the not easily obtained uncertainty analysis to be done by the user in order to evaluate the tool before using it confidently in practice.

3. Sensitivity Tests

The tests presented here are based on the Huang & Groves (1980) calculation samples with **J** propulsor and **A** nominal wake. The same grid of 76 cells axially and 50 radially, generated by GRID-R3 program is used for all tests, as shown on Figure 1. The nominal wake velocity is denoted by **Vn** and the effective velocity - **Ve**, the radius of the propeller **Rp**.

The first test consisted in introducing three more nominal wakes having the same mean volumetric value but different radial distribution. The nominal and the corresponding effective velocity distribution obtained are shown in Figure 2, the latter being represented by black filled symbols. The results confirm the expected behaviour of more pronounced difference between the effective and the nominal wake when the gradient of the incoming flow is higher, i.e. carrying more vorticity. The case **Vnm** – **Vem** is an uniform flow with velocity equal to the volume-mean value. The deviation of about 3% is observed from the expected uniform effective wake, as reported by Choi and Kinnas. This numerical error affects the total forces on the propeller blade less than 1.5% and thus is inside the precision of the prediction.

Conserving the same basic nominal wake flow the following tests aimed at to changing some of the parameters of the propeller design and its working regime.

In Figure 3 the squares correspond to advance coefficient 0.416 and the triangles to J=0.666. As expected, the higher loading results in a more pronounced effective wake.

Another parameter that is expected to affect the distribution of the effective wake is the radial loading distribution on the blades of the propeller. The propeller **Jmod** has the same mean loading as the basic propeller **J** calculated in nominal wake, but is unloaded towards the tip. The small influence on the distribution of the effective wake is detected, as seen in Figure 4. The corresponding circulation **G** is non-dimensional to its maximum value.

Figure 5 is obtained calculating four propellers of different number of blades and equal mean total loading. The result is that the increase of the number of blades (form 3 to 6) reduces the effective velocity. For more than five blades an asymptotic behaviour is observed.

4. Conclusions

The tests performed with the steady Euler solver for the prediction of the ship effective wake field from given nominal wake, propeller geometry and regime data showed the good sensitivity of the codes to the variations of the basic physical parameters of the design.

Nowadays, the RANS methods advance considerably and could be useful to predict the wake of the moving body as well as the effective wake of the ship. As the prediction of the effective wake requires an iterative procedure, due to the unknown propeller loading, which is computer time consuming, the Euler solvers will still play a basic role in this matter.

5. Acknowledgments

This work is a part of a contract of the author with the Canal de Experiencias Hidrodinámicas de El Pardo (CEHIPAR) whose support is highly appreciated.
I take this opportunity to recall the late Professor Kiril Varsamov for the inspiration given to me in this field, years ago.

6. References

-Huang T.T., B.D.Cox (1977) " Interaction of Afterbody Boundary Layer and Propeller." Symposium on Hydrodynamics of Ship and Offshore Propulsion Systems, Hovik outside Oslo.

-Nagamatsu T., K.Tokunaga (1978) " Prediction of Effective Wake Distribution for a Body of Revolution. JSNAJ, vol.143.

-Goodman Th. (1979) " Momentum Theory of a Propeller in a Shear Flow", Journal of Ship Research, vol.23,No.4.

-Huang T.T, N.C.Groves (1980) "Effective Wake: Theory and Experiment". 13th Symposium on Naval Hydrodynamics, Tokyo.

-Dyne G. (1980) "A Note on the Design of Wake-Adapted Propellers". Journal of Ship Research,vol.24,No.4.

-Haimov A.,(1983) "Calculation of Effective Wake Distribution in Axisymmetric Shear Flow." Intern.Symp. on Ship Hydrodynamics and Energy Saving, ElPrado, Madrid.

-Choi J.K., S.Kinnas, (1998) " A 3-D Euler Solver and its Application of Cavitationg Propellers." 25th ATTC, Iowa City.

-Choi J.K, S.Kinnas, (2001) "Prediction of Non-Axisymmetric Effective Wake by a Three-Dimensional Euler Solver.", Journal of Ship Research, vol.45,No.1.

-Kinnas, S.,P.Griffin, J.K.Choi and E.Kosal, (1998) "Automated design of propulsor blades for high-speed ocean vehicle applications." Trans. SNAME, vol.106.

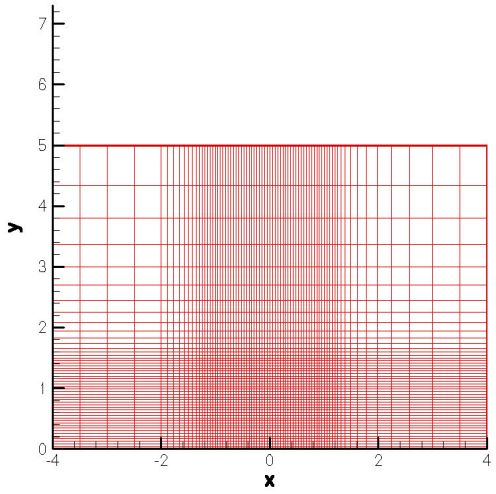

Figure 1.

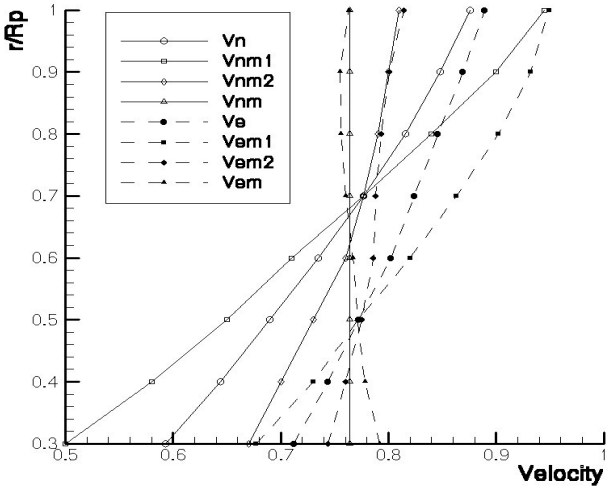

Figure 2.

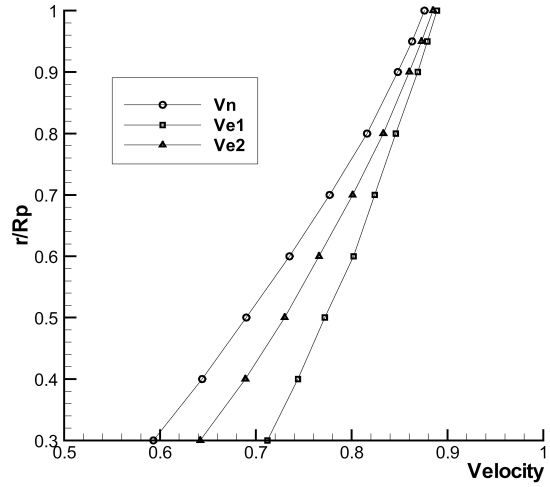

Figure 3.

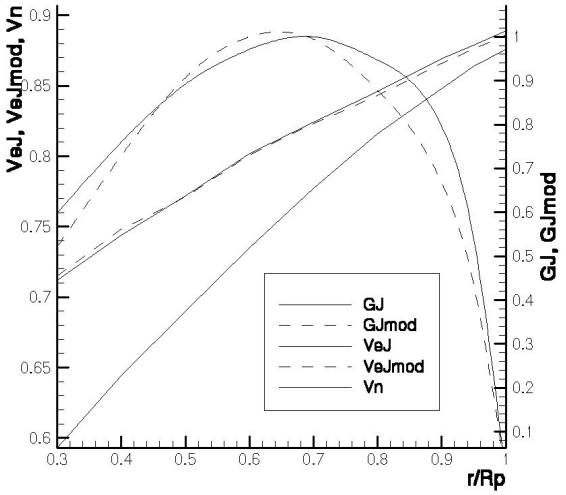

Figure 4.

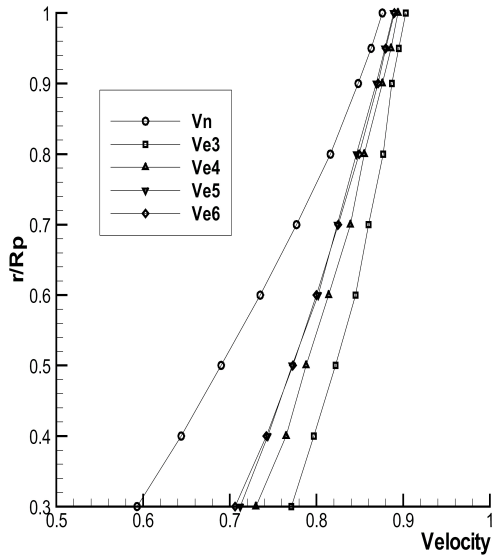

Figure 5.

A Procedure for Optimizing Cavitating Propeller Blades in a Given Wake

K-J Han[1], G. Bark[2], L. Larsson[3], B. Regnström[4]
[1]Chalmers University of Technology, kaijia@na.chalmers.se
[2]Chalmers University of Technology, bark@na.chalmers.se
[3]Chalmers University of Technology, larsl@na.chalmers.se
[4]Flowtech International AB, Sweden, regnstrom@flowtech.se

Introduction

With more understanding and research on the prediction of propeller performance, it is natural for propeller designers to try to find an optimum design propeller. This problem was addressed already by Betz in 1919[1]. Glauert [2] combined the momentum theory and blade element theory for predicting and optimizing the efficiency of a propeller. Adkins et al [3] extended Glauert's propeller theory by eliminating the light loading and small angle assumptions in the optimization design theory and calculated the vortex displacement velocity accurately. De Jong [4] carried out an optimization including the viscosity effects of ship propellers with end plates. Rizk [5] developed a scheme to update design parameters and flow variables iteratively. The accuracy, efficiency and sensitivity of the computational parameters were tested with a single equality constraint. It is possible to extend this method to solve more general optimization problems with more constraints, even of the inequality types. Triantafyllou [6] formulated a preliminary B-series design process considering the interaction of engine, hull, wake and propeller, the fuel consumption being the optimization objective. The blade number, expanded area ratio and advance coefficient were investigated. A similar but more recent method for propeller optimization is presented by Benini [7]. In this research a multi-objective evolutionary algorithm was used for preliminary design of a B-Screw propeller. Kinnas and Mishima [8] applied a numerical optimization method for designing both partial and super-cavitating sections. The drag was minimized with given cavitation number and lift force. They coupled a numerical optimization technique with MPUF for the analysis and optimization of a cavitating propeller. The objective and constraints were expressed in terms of design parameters, which are movements of B-Spline control points. The method was applied on 2D partially and supercavitating hydrofoil sections, 3D propeller blades in uniform flow and cavitating blades in non-uniform flow.

In the present work, we optimize a cavitating propeller in a given wake by coupling an optimization framework SOFT [9] with the numerical propeller performance prediction code MPUF, satisfying both thrust and cavitation constraints. The Dynamic Hill Climbing method is chosen as the optimization algorithm after comparison of four different optimization methods. The efficiency of the propeller, or both the efficiency and the propeller induced pressure fluctuation at a point on the ship hull are set as single or multiple objectives respectively. Design parameters are the cubic B-Spline control points for span-wise pitch ratio, chord length ratio, camber ratio and skew distribution curves. Thrust is set as an equality constraint. The Keller criterion, the maximum cavity volume, the cavity length, the cavity area and the face side pressure are all set as constraints or outputs. Optimizations starting both from a near optimum propeller and from an off-design propeller are tested. Results show that the present optimization method can be used for preliminary design of a cavitating propeller in a given wake.

Optimization models

The cavitation related quantities, i.e. cavity volume, cavity area, cavity length, first harmonic pressure pulse and root mean square of the first three order harmonic pressure pulse amplitudes are all interrelated and partly overlapping. All are however useful, simultaneously. For example, the cavitation length indicates the risk of shedding of a cavity and the thickness is an indication of the risk of powerful re-entrant jets and thick cloud formations resulting in noise and/or erosion. Reduction of pressure pulses often means unloading the blade tip or at least reducing the tip pitch and increasing the tip section camber, the later approach to save efficiency. Both cases may however result in blade tip erosion on the suction or pressure sides, or both. It may also result in erosion at lower radii on the suction side if the load there is increased to keep thrust and efficiency and the sheet therefore becomes too convex in this region. In some cases the pressure pulses are important; in others the erosion can be more critical. It is also noted that the influence on these quantities by wake distribution, pitch distribution, camber distribution, skew distribution, chord length distribution and blade area is complex and that

some of the parameters force the results in different directions. To this adds also the fact that other aspects than cavitation have to be taken into account.

With this review as a background we have given some reasons for using the following cavitation data in objective functions and constraints:

- CL : The cavity chord-wise length at a number of radii and at the blade position where the maximum cavity volume on the single blade occurs. The quantity of cavity length is nondimensionalized by local chord length. Usually the longest cavity length value occurs near the blade tip. Here we limit the length to 1.0. At the other radii the length must be smaller than a user selected value CLMAX
- CV : The maximum cavity volume over a single blade, nondimensionalized by R^3
- CA : The maximum cavity area at the blade position where the maximum cavity volume on the single blade exists. The cavity volume is nondimensionalized by the blade expanded area
- p_{rms} : The rms value of the three lowest harmonic pressure pulse components, including the non-cavitating contribution
- p_1 : The rms amplitude of the first harmonic component, the blade frequency component, of the pressure pulse
- c : Safety factor defined by the ratio of face side pressure coefficient and cavitation number
- Keller criterion [10]: A criterion used to control minimum blade area. Based on the blade number, thrust, cavitation number and a user defined constant

Present optimization models

It is assumed that the propeller is working in a given non-homogeneous effective wake. The diameter, revolution speed, blade number and some flow variables are fixed as constants.

Objective: To maximize propeller efficiency and minimize pressure pulses

In this work, we select efficiency of propeller and pressure pulse amplitude induced by propeller as our objective functions. In order to deal with two objective functions, we use a weighted sum of the two functions. The same priority is set for efficiency and first order harmonic pressure pulse amplitude, which means their weighs are both 0.5. The objective function then can be formulated as

$$\max \qquad \eta \cdot \omega_1 - p_1 \cdot \omega_2 \qquad \omega_1 = \omega_2 = 0.5$$

Pressure pulses are computed at a set of points, a level 0.66D above the shaft centre. To represent a solid surface the pressure pulses are multiplied by an empirical solid boundary factor equal to 1.9.

Design parameters:

B-Spline Control points of span-wise P/D , C/D F/D and $Skew$ curves whose variation ranges are all $\pm 10\%$ around the initial control points obtained from original propeller

Constraints:

Constant thrust force: $K_T = K_{T_0}$

Keller criterion: $\left(\frac{A_E}{A_O}\right)_{\min} = \left(\frac{A_E}{A_O}\right) - \frac{(1.3+0.3Z)T}{(P_0 - P_v)D^2} + k, \qquad \mathrm{k} = 0.05$

Maximum cavitation volume: $CV \le CVMAX$

Maximum cavity area: $CA \le CAMAX$

Maximum cavity length: $CL \le CLMAX$

Face pressure: $c \ge c_{\min}$

Case studies

Optimization of a near optimum propeller

In this case, we optimize the propeller blade geometry of a near optimum propeller. The blade geometry comparison between the original propeller and the optimized propellers are illustrated in Fig.2-7.

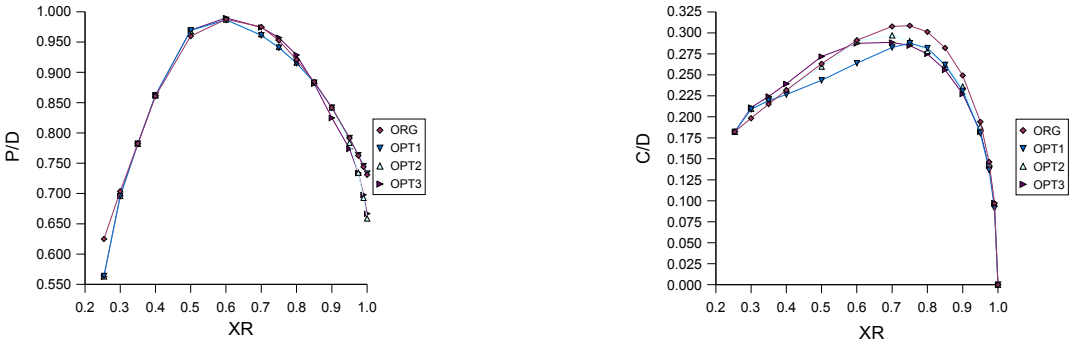

Fig. 2 Span-wise pitch ratio and chord length ratio distribution comparison of ORG and OPT1-3

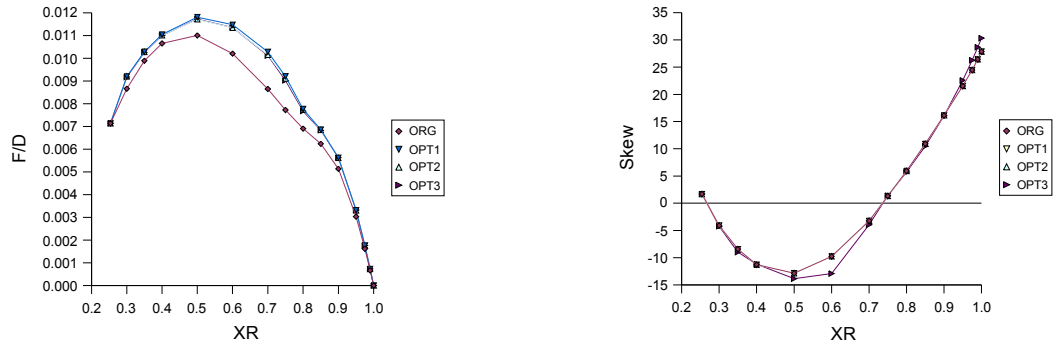

Fig. 3 Span-wise camber ratio and skew distribution comparison of ORG and OPT1-3

ORG--- Original propeller from which we start our optimization.

OPT1---Single objective optimization of the efficiency η. The pitch ratio P/D is slightly lower than for ORG, especially near the root, as shown in Fig. 2. The blade area is decreased, which improves the efficiency and the camber ratio F/D is increased almost to the constraint limit to compensate for the reduced pitch. The efficiency η is increased from 0.8493 to 0.8568 but the first order harmonic pressure amplitude p_1 is increased from 5.039 Mpa to 5.097Mpa. The cavity volume CV, cavity length CL and cavity area CA as outputs are all higher than those from original propeller ORG.

OPT2---Multi-objective optimization of the efficiency η and the pressure amplitude p_1. The tip pitch is smaller than for OPT1 and ORG but not much difference is shown between OPT1 and OPT2 at other radii. Low tip pitch decreases tip loads and there is the contribution from the tip region to the pressure fluctuation. A larger blade area is produced compared with OPT1 which can be useful for improvement of cavitation performance. The camber is almost the same for OPT1 and OPT2 though higher than for ORG. The efficiency η is little lower than for OPT1 but still higher than the original propeller ORG. The pressure pulse amplitude is lower than OPT1. Cavity volume CV, cavity length CL and cavity area CA are all greatly decreased compared with OPT1. The face side cavitation margin is safe enough.

OPT3---Multi-objective optimization of the efficiency η and the pressure amplitude p_1 with account of also the design parameter Skew. Like for OPT2, tip pitches of OPT3 are reduced compared with ORG and OPT1. OPT1-3 all have smaller blade areas than ORG but with different chord length distributions. The cambers of OPT2 and OPT3 show little difference. Tip skews have been increased also to the constraint limit which shows the optimization tendency of increasing the tip skews. The pressure pulse amplitude p_1 is decreased from the original 5.039 to 4.649. At the same time efficiency η has increased slightly compared with ORG. However, cavitation results show the highest cavity volume CV (Fig. 4), the longest cavity length CL and the largest cavity area CA.

Figure 5-6 show further variation cases of OPT3. OPT31 has the constraint of cavity length CL. OPT32-33 have the constraint of the cavity area CA. OPT34 has the constraint of the risk of face side cavitation. OPT35 has the constraints of CL, CA and c applied simultaneously. In Fig. 5, OPT35 shows smaller pitches near 0.3R-0.6R

but higher near 0.7R-0.8R. OPT32-35 all show lower tip pitches corresponding to reduced tip loads. OPT31-35 all have larger blade areas than OPT3. And among them OPT33 and OPT35 have the largest blade areas, even larger than original propeller. The tip skew of OPT3 has increased from 28.87 to 30.33 together with decreased tip pitch and lower pressure amplitude. For other test cases, OPT31-35, skews have no change near the tips but show different distributions between 0.3R and 0.75R. The largest difference of skew distribution happens at 0.5R and 0.6R.

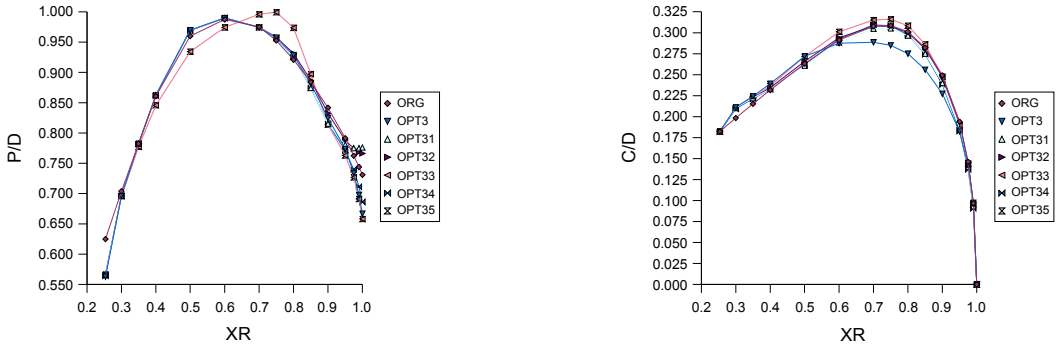

Fig.4 Span-wise pitch ratio and chord length ratio distribution comparison of ORG, OPT3 and OPT31-35

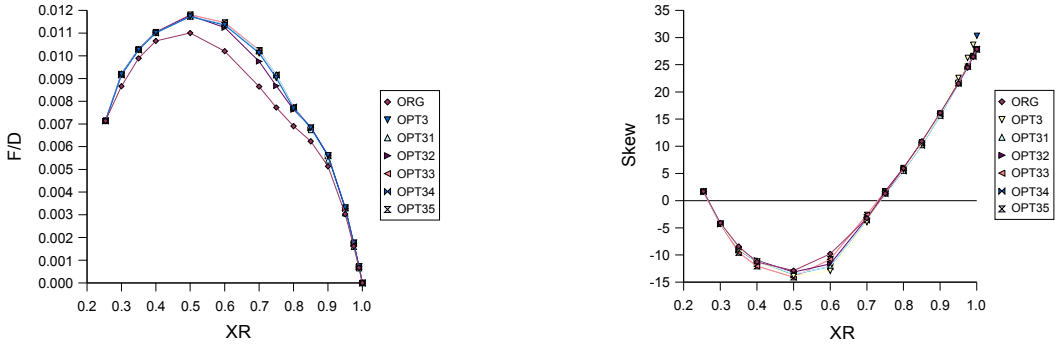

Fig.5 Span-wise camber ratio and skew distribution comparison of ORG, OPT3 and OPT31-35

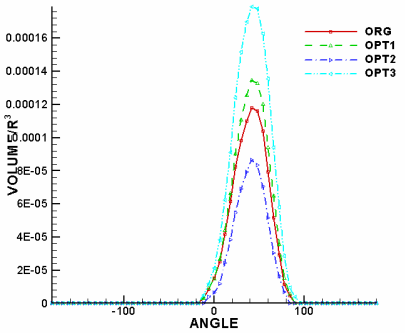

Fig. 6 Cavity volume comparison of ORG and OPT1-3

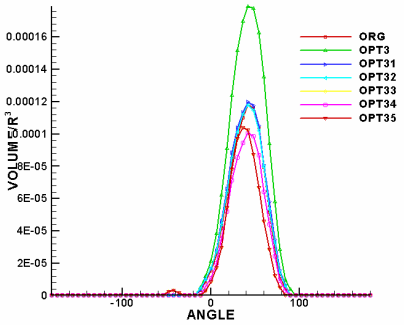

Fig. 7 Cavity volume comparison between ORG, OPT3 and OPT31-35

Optimization starting from an off-design propeller

As the optimization is multi-objective, with multi-design parameters and non-linear relations, differences of the initial starting guess and constraints can lead the optimizer into different directions and it may finally get stuck in some local optimum. In this part, we begin our optimization from an off-design propeller. Based on the previously used original propeller ORG, we decrease P/D by 50% and C/D by 80% except the root and tip points. Other geometries, such as camber and skew, are kept the same as original propeller ORG. This new propeller is

called Ini_OFF2. In order to make names compatible with Ini_OFF2, we call ORG propeller in this optimization as Ini_OFF1. With only pitch ratio and chord ratio as design parameters, OFF1 is the multi-objective optimization starting from Ini_OFF1 and OFF2 the multi-objective optimization starting from Ini_OFF2. The optimized blade geometry is illustrated in Fig.8.

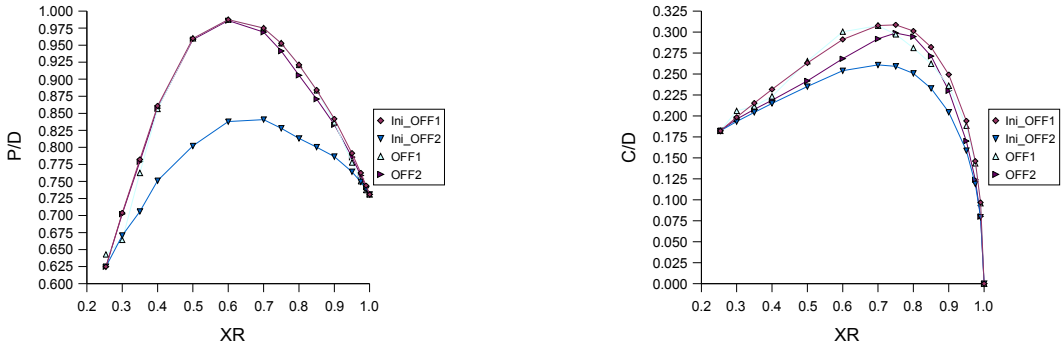

Fig. 8 Comparison of original, off-design and optimum propeller shape

It is observed from Fig. 8 that the pitch distributions of both OFF1 and OFF2 converge to almost the same shape. The chord lengths are distributed spanwise in different ways. OFF1 as a near optimum propeller shows better cavitation performance than OFF2.

It is noted from the evolution history that at the beginning of the optimization, the Keller criterion plays an important role in filtering out the propeller blades with serious cavitation and helps the optimizer to jump over some unacceptable local optima. Once the Keller criterion is satisfied, both cavity volume and the thrust equality constraint are the most dominating factors to get a final optimum.

Conclusions, Discussions and Suggestions

An optimization model is build up for optimizing cavitating propeller blades in a given wake. The model is first applied to a near-optimum cavitating propeller in a given wake. The optimal blade geometry including pitch ratio, chord length ratio, camber ratio and skew distributions along the radius direction is obtained with required constraints. The Keller criterion and maximum cavity volume are mainly used to control minimum blade area and tolerable amount of cavitation. Another three cavity constraints are switched on separately or simultaneously to find their influence on the objectives and cavitation performance. Higher efficiency is obtained by reducing blade area, increasing tip skew and controlling cavitation parameters.

The method is also applied for an optimization starting from an off-design propeller with the same given wake and the required thrust. The same constraints are used in this case. Optimization starting from different initials are made and compared. Results show good convergence of blade geometry to the original propeller and the improvement margin of the original propeller. Like in the first case, higher efficiency is obtained by reducing blade area, cavity area, cavity volume and controlling face side pressure.

It is worth mentioning that cavitation effects such as cavity volume, cavity length, cavity thickness, cavity area, face cavitation are working dependently and simultaneously. The present work compares the influence from different cavitation factors on efficiency and pressure pulse amplitudes only in a schematic and qualitative way. The flexibility of the present optimization model is shown by allowing users to switch some variables on as constraints or off as outputs. According to the different aims and backgrounds of users and designers, the present optimization model can be used to set up different new optimization models conveniently.

It is suggested that convex cavity shape and cavity detachment could be other constraints or outputs to control cavity shape and mid-chord cavity. To fully exploit such knowledge some further improvements of the cavitation simulation would be beneficial. More careful tuning of objective functions and constraints are needed for off-design propellers.

The present work will be extended at the next stage of the work to optimize a cavitating propeller behind a ship.

Acknowledgements

It is greatly appreciated that this research work has been supported by following companies and researchers:

VINOVA, Rolls-Royce Group plc in Derby of United Kingdom, Rolls-Royce AB in Kristinehamn of Sweden, Shahrokh Shahpar, Patrik Kron, Göran Pettersson and Dan Johansson.

Reference

1. Betz,A. and Prandtl, L., Screw Propellers with minimum Energy Loss, Gottinger Reports, 1919
2. Glauert, H., Airplane propellers, Ed. by Durand, W., Aerodynamic Theory, Div. L, Vol.4, 1976
3. Adkins, C.N., Church, VA and Liebeck, R.H., Design of optimum propellers, AIAA paper 83, AIAA-83-0190. 1983
4. de Jong, K., On the optimization including viscosity effects of ship screw propellers with optional end plates, Eighteenth Symposium on Naval Hydrodynamics, Natinonal Academic Press, Washinton, D.C. 1991
5. Rizk M. H., Optimizing advanced propeller designs by simultaneously updating flow variables and design parameters, AIAA Journal V24, No 9. 1986
6. Triantafyllou, M., Computer-aided propeller preliminary design using a B-Series, Marine Technology. Vol. 16, No.4. 1979
7. Benini E., Multiobjective design optimisation of B-Screw series propellers using evolutionary algorithms, Marine technology, Vol.40, No.4.2003
8. Kinnas S.A., Mishima S., Application of a numerical optimization technique to the design of cavitating propellers in non-uniform flow, Journal of Ship Research, Vol.41, No.2, 1997
9. Shahpar, S., Technical report of SOFT, Rolls-Royce Group plc, United Kingdom, 2000
10. Carlton J.S., Marine Propellers and Propulsion, , Butterworth-Heinemann,1994

NUMERICAL INVESTIGATION OF THE SCALE EFFECT ON THE FLOW AROUND A SHIP HULL

Satu Hänninen[1]
Ship Laboratory, Helsinki University of Technology

1 INTRODUCTION

The hydrodynamic characteristics of a new ship are usually predicted at model scale, either by performing model tests for a physical model or by numerical simulations. Over the last years, the increased computing capacities have enabled computations of viscous flows also at ship-scale Reynolds numbers. Full-scale computations of ship-hull flows using a moving-grid technique have been presented by *Schweighofer (2003)*, *Tzabiras (2004)*, *Raven et al. (2004)*, who all computed the flow past the Series-60 ship. In each study, turbulence was treated differently and different methods were used to evaluate the shape of the free surface.

As the hydrodynamic ship design is based on the model-scale results which are scaled to full scale, it is essential to understand the physics of the scaling. The previous numerical studies on the subject mainly focussed on the viscous effects without evaluating the wave pattern simultaneously: *Eça and Hoekstra (1996,2001)*, *Watson and Bull (1999)*, *Choi and Min (2003)*. *Tzabiras (2004)* presents a study of the scale effect on the resistance and propulsive characteristics of a slender ship (Series-60) including the interactive evaluation of the free surface. In this extended abstract, the scale effect on the flow around a typical container ship, the Hamburg Test Case, is studied. The computations were performed using a moving-grid technique. A comprehensive description of the investigation is given in *Hänninen (2005)*.

2 NUMERICAL METHOD

The Reynolds-averaged Navier-Stokes solver FINFLO-SHIP is used as the flow solver, *Matusiak and Lehtimäki (2001)*. The solution process during one iteration cycle consists of two steps. First, the bulk flow of the initial grid is computed, *Siikonen (1998)*. The convective fluxes are approximated by an upwind-type spatial discretisation of third-order accuracy without flux limitation. The turbulence is treated using Menter's Shear-Stress Transport (SST) turbulence model, *Menter (1993)*. Then, the new wave heights are computed, *Mikkola (1999)*, and the grid is deformed to follow them, *Lehtimäki (2000)*.

3 COMPUTATIONS

The flow field around the container ship Hamburg Test Case (HTC), Table I, is computed both at model and full scale. The corresponding Reynolds numbers are $R_n = 1.0 \cdot 10^7$ and $R_n = 1.2 \cdot 10^9$, respectively. The Froude number is $F_n = 0.238$. The scale of the model is 1/24.

Table I: Principal parameters of the Hamburg Test Case at full scale

Length between perpendiculars	L=153.7m
Width	B= 27.5m
Draught at forward perpendicular at zero speed	T_f=9.20m
Draught at aft perpendicular at zero speed	T_a=10.30m
Block coefficient	C_B=0.645

The running trim measured in the model tests is 9.5 minutes by bow for the $F_n = 0.238$. The trim is taken into account when generating the grids. The movements of the hull are prevented during the computations. In the model tests, the measured sinkage was equal to 15.8 mm for $F_n = 0.238$, but it was not taken into account in the computations.

[1]Ship Laboratory, Helsinki University of Technology, Tietotie 1, FIN-02015 Espoo, Finland – E-Mail: Satu.Hanninen@tkk.fi
The computations of this work are part of the European-Union project EFFORT - European Full-Scale Flow Research and Technology

At model scale, the initial values of the turbulence level and the free-stream turbulence level are set to $5.721 \cdot 10^{-5}$. The initial values of the nondimensional turbulence coefficient and the nondimensional free-stream turbulence coefficient are set to 0.01 at model and full scale. At full scale, the initial value of the turbulence level is set to $7.27 \cdot 10^{-5}$. The free-stream turbulence level is set to $5.265 \cdot 10^{-6}$. As the development of the turbulent boundary layer depends on the free-stream turbulence quantities, the suitability of the chosen quantities is validated by a flat plate computation, *Hänninen (2005)*.

Each simulation case is computed three times using different grid resolutions in order to evaluate the grid influence on the results. The result of the computation with a coarser grid is given as an initial value to the next finer grid.

The grids consist of one block in O-O-topology. On the fine grids, there are 140 cells along the hull both at model and full scale. The total number of cells is 788480 at model scale and 985600 at full scale. The distance of the first node from the wall is set to $2.06 \cdot 10^{-5}$ m at model scale and $7.8 \cdot 10^{-6}$ m at full scale. The average of the nondimensional distances from the wall is 1.2 at model scale and 3.1 at full scale. The coarser grids are obtained from the finer ones by merging four cells into one.

4 RESULTS

4.1 CONVERGENCE

At model scale, the computations converged for the three grids used. At full scale, only the computation with the finest grid is fully converged. Using the second finest grid, the residuals are converged. However, the deformation of the free surface at the stern area was restricted at a certain stage of the computations due to the continuous appearance of negative cells. The computations were performed until the resistance coefficient did not change more than 1% and the L_2-norms of the pressure and momentum residuals reached the order 10^{-6}.

4.2 INFLUENCE OF THE GRID

Table II: Resistance coefficients at model scale.

Case	C_T	C_F	C_P
Fine grid	$3.93 \cdot 10^{-3}$	$2.98 \cdot 10^{-3}$	$0.95 \cdot 10^{-3}$
Medium grid	$3.95 \cdot 10^{-3}$	$2.95 \cdot 10^{-3}$	$1.00 \cdot 10^{-3}$
Coarse grid	$7.40 \cdot 10^{-3}$	$3.35 \cdot 10^{-3}$	$4.05 \cdot 10^{-3}$

Table II compares the resistance coefficients computed with the different grids at model scale. The total resistance coefficient C_T consists of the frictional and pressure resistance coefficients. The frictional resistance coefficient C_F obtained with the medium grid is 11.9% smaller than the one obtained with the coarse grid. The result computed on the fine grid is 1.0% larger than the one on the medium grid. Thus, the final result may be considered independent of the grid density. The pressure resistance coefficient C_P computed on the medium grid is 75.3% smaller than the one on the coarse grid. The result computed on the fine grid is 5.0% smaller than the one on the medium grid.

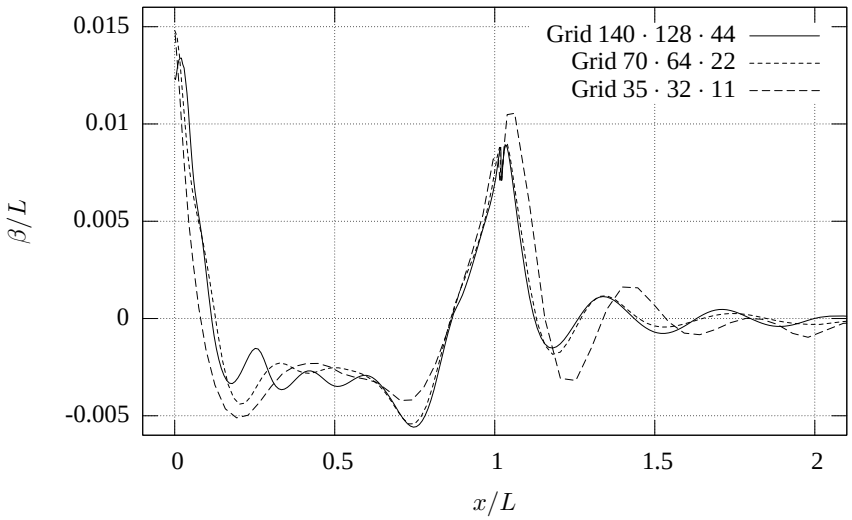

Fig.1: Nondimensional wave profiles obtained at model scale with three different grid resolutions. The fore perpendicular is located at x/L=0.0. β denotes the wave height.

The influence of the grid resolution on the evaluation of the free surface is studied by comparing the wave profiles and patterns. The wave profiles computed on the two finest grids agree well, Fig.1, except at the fore shoulder. The wave patterns obtained with the two finest grids hardly differ near the hull, Fig.2. The differences in the wave patterns further away from the hull are a consequence of the different numerical damping caused by the different grid densities.

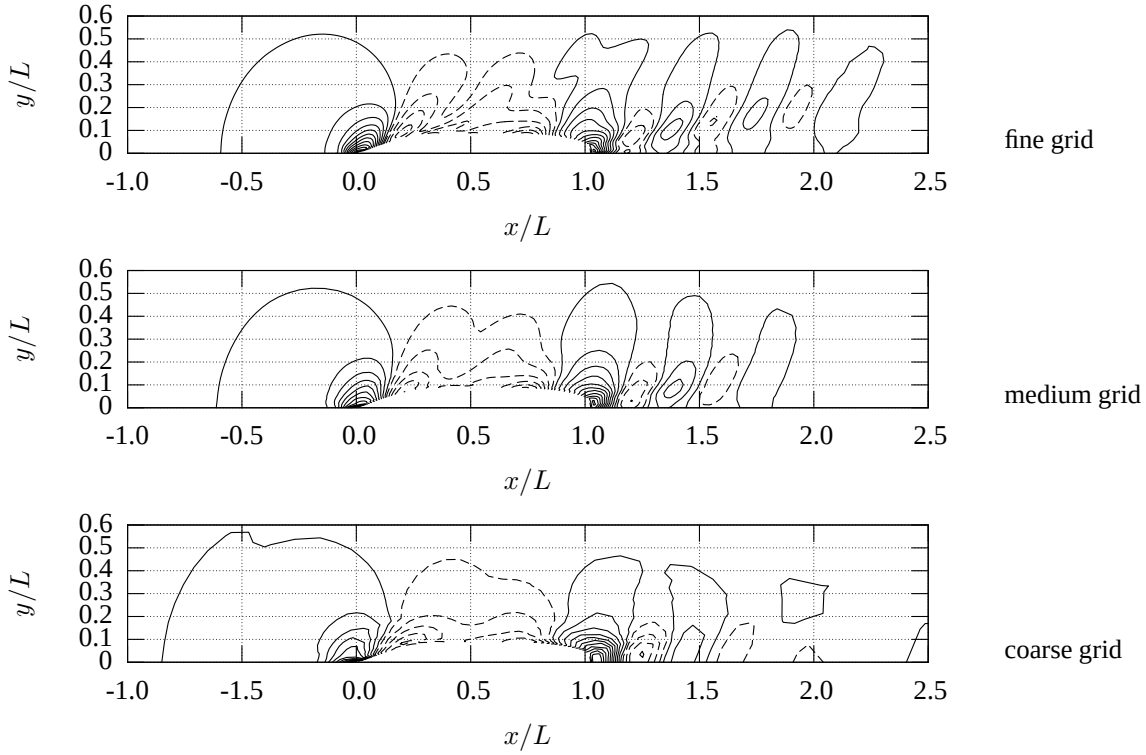

Fig.2: Contours of the wave pattern computed with the different grid resolutions at model scale. Positive contours: solid line; negative contours: dashed line. Contour interval is 0.006 m, zero line omitted.

At full scale, an extensive comparison of the resistance coefficients is not reasonable, as the result is fully converged with respect to the wave elevation only on the fine grid. The frictional resistance coefficient may be assumed to be converged for both the fine and medium grids. The result obtained with the fine grid is 5.7% smaller than the one obtained with the medium grid.

The influence of the grid resolution on the evaluation of the free surface is demonstrated by comparing the wave patterns obtained with the two finest grids, Fig.3. The wave pattern computed with the medium grid is not fully developed in the wake, since the movements of the grid were restricted there.

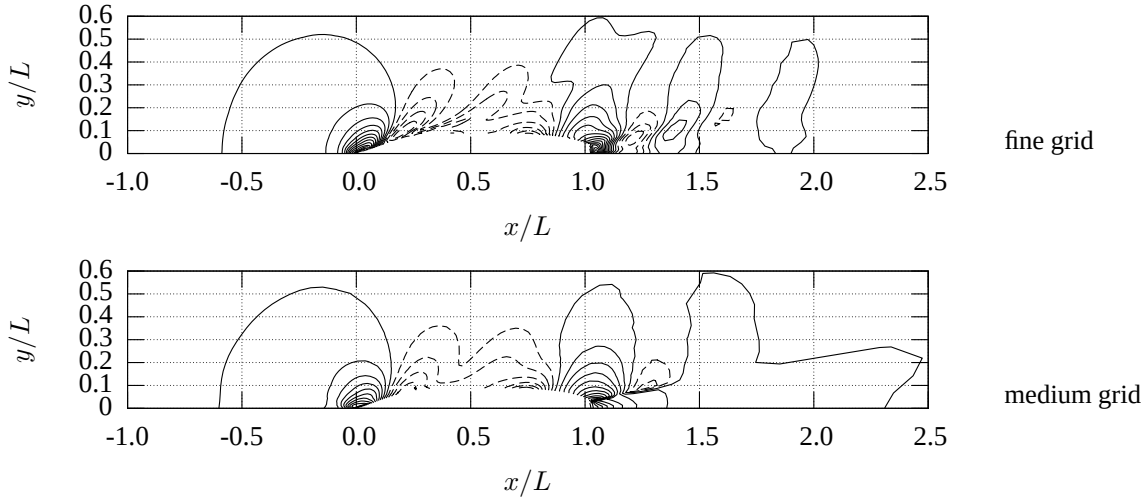

Fig.3: As Fig.2, but for full scale and contour interval 0.15 m

4.3 VALIDATION

The model test results presented in *Bertram et al. (1994)* are used for the validation of the computations. The total resistance coefficient at model scale is compared with the measured one. The computed frictional resistance coefficients both at model and ship scale are compared with the estimate given by the ITTC 1957 model-ship correlation line

$$C_{F_{ITTC-57}} = \frac{0.075}{(\log Re - 2)^2} \tag{1}$$

The computed pressure resistance coefficients are compared with the residual resistance coefficient which is the difference between the total resistance coefficient measured in the model tests and the frictional resistance coefficient of the model calculated with the ITTC 1957 model-ship correlation line. The residual resistance coefficient is assumed to have the same value both at model and ship scale.

At model scale, the computed total resistance coefficient is 5.1% smaller than the measured one. By using the correct sinkage in the computations, a reduced deviation of the computed resistance coefficient from the measured one may be expected. The computed frictional resistance coefficient is 0.3% smaller than the estimate given by the ITTC 1957 model-ship correlation line. The computed pressure resistance coefficient is 17.4% smaller than the residual resistance coefficient. At full scale, the frictional resistance coefficient is 2% smaller than the estimate given by the ITTC 1957 model-ship correlation line. The pressure resistance coefficient is 38% smaller than the residual resistance coefficient.

5 SCALE EFFECT REVEALED BY THE COMPUTATIONS

5.1 RESISTANCE

Table III compares the computed resistance coefficients. It is reasonable to study the frictional and pressure resistance coefficients separately, as they are supposed to be affected differently by the Reynolds number.

Table III: Computed resistance coefficients of the model and the ship

	C_P	C_F	C_T	$C_{F_{ITTC-57}}$
Model	$0.95 \cdot 10^{-3}$	$2.98 \cdot 10^{-3}$	$3.93 \cdot 10^{-3}$	$2.99 \cdot 10^{-3}$
Ship	$0.71 \cdot 10^{-3}$	$1.47 \cdot 10^{-3}$	$2.18 \cdot 10^{-3}$	$1.50 \cdot 10^{-3}$

The computed frictional resistance coefficients seem to follow the ITTC 1957 model-ship correlation line. To obtain the total frictional resistance coefficient at full scale, the effect of the hull roughness need to be added to the computed value afterwards. If the effect of the rough surface is not included, the difference between the results of the C_F at model and full scale is $\sim 50\%$. The difference becomes smaller, if an estimate of the effect of the hull roughness is added to the frictional resistance coefficient. It is possible that a numerical simulation including the effect of hull roughness could affect the other results than the frictional resistance coefficient as well.

The computed pressure resistance coefficient is about 25% smaller at full scale than at model scale. The result is inconsistent with Froude's scaling law which requires the same pressure resistance coefficient for model and full scale in this case. *Tzabiras (2004)* presents the computed pressure resistance coefficients of the Series-60 ship for three Froude numbers both at model and ship scale. He reports that the coefficients obtained at full scale are less than 4% smaller than the ones at model scale. In this respect, it might be possible that the different numerical errors in the computations at model and full scale may cause the different pressure resistance coefficients in this study. However, this seems not to be the case as the agreement between the grid independent solution at model scale and the solution at full scale is good and meaningful. Further, the hull forms of the Series-60 ship and the Hamburg Test Case are different causing also different viscous effects. The result of this study may explain why the actual total resistance of some ships has been overestimated. As the pressure resistance may be divided into the wave-making resistance and the viscous pressure resistance, the viscous pressure resistance may cause the total pressure resistance to be different at different scales.

5.2 FREE SURFACE

The wave profiles on the hull of the ship and the model look quite similar, Fig.4. The most important differences concerning the evaluation of the resistance appear at the bow ($x/L \approx 0$) and at the stern ($x/L \approx 1$). The wave profile of the ship is higher in those domains. The reason for the difference at the bow may be explained by the different grid qualities. It was noticed afterwards that the grid at model scale was unorthogonal and unfavourably

stretched at the bow. This has probably caused the pressure and thereupon the wave profile to be too low at the bow of the model. The higher wave at the stern of the ship is likely to be a consequence of different viscous damping at model and full scale, since the viscous effects are larger at model scale.

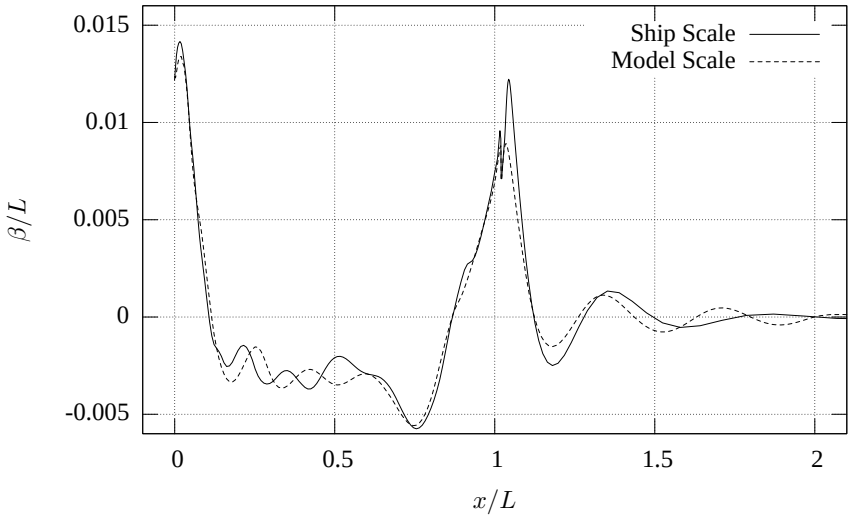

Fig.4: Nondimensional wave profiles on the hull at ship and model scale

The wave patterns agree well, Fig.5. The most important differences are in the wake. The wave is higher at the stern of the ship, as already observed in Fig.4. The wave pattern further from the ship is not as well developed as the one of the model. This can be explained by the better resolution of the model-scale grid. These results show that the scale has an important effect on the wave pattern at the stern.

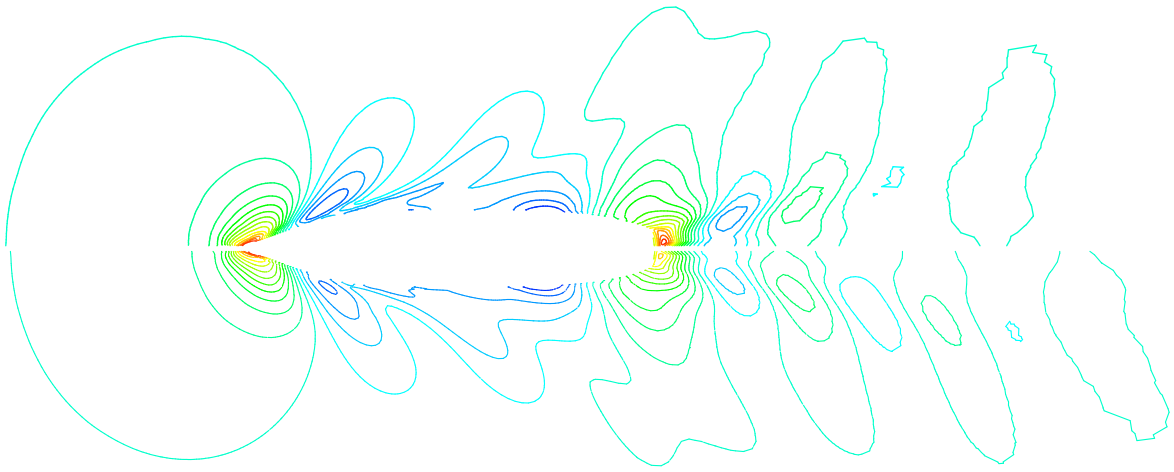

Fig.5: Nondimensional wave patterns of ship (above) and model (below)

5.3 STREAMLINES

The differences between the streamlines on the aft hull of the model and the ship are significant, Fig.6. At model scale, the vertical convergence line near the stern frame indicates line separation. Near the upper end of the vertical convergence line, there is a saddle point where the flow is divided into two branches. A horizontal convergence line is situated close to the bottom of the hull where the bottom flow merges with the flow on the side of the hull. It indicates that a strong bilge vortex possibly appears. There is also a second horizontal convergence line between the vertical convergence line and the hub. At ship scale, the situation is totally different. The flow follows the hull surface until the stern frame of the hull.

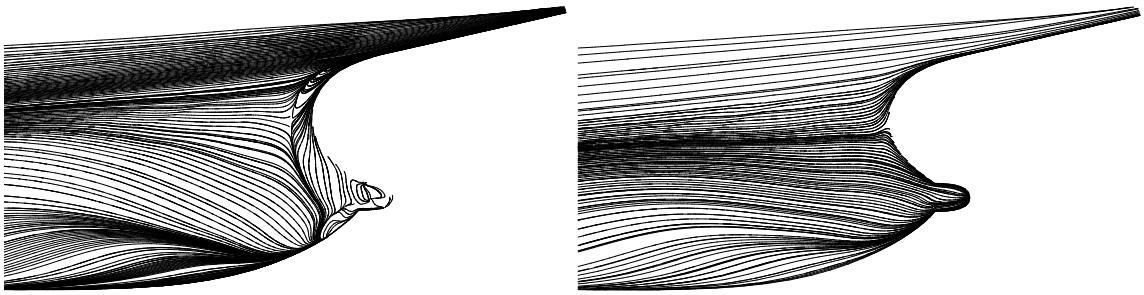

Fig.6: Streamlines on the hull at the stern, model scale (left) and ship scale (right)

References

BERTRAM, V., CHAO, K.Y., LAMMERS, G. AND LAUDAN, J. (1994), *Experimental validation data of free-surface flows for cargo vessels*, CFD Workshop Tokyo 1994, pp.311-320

CHOI, J.E. AND MIN, K.S. (2003), *Study on the scale effect on the flow characteristics around a full slow-speed ship*, 8^{th} Int. Conf. Num. Ship Hydrodynamics, Busan

ECA, L. AND HOEKSTRA, M. (1996), *Numerical calculations of ship stern flows at full-scale Reynolds numbers*, 21^{st} Symp. Naval Hydrodyn., Trondheim, pp.377-391

ECA, L. AND HOEKSTRA, M. (2001), *Numerical prediction of scale effects in ship stern flows with eddy-viscosity turbulence models*, 23^{rd} Symp. Naval Hydrodyn., Val de Reuil, pp.553-568

HÄNNINEN, S. (2005), *Evaluation of the scale-effect on the flow around a ship hull using CFD*, Master's Thesis, Ship Laboratory, Helsinki Univ. of Technology

LEHTIMÄKI, R. (2000), *On Structured Grid Generation*, Ph.D. Thesis, Helsinki University of Technology, Laboratory of Aerodynamics.

MATUSIAK, J. AND LEHTIMÄKI, R. (2001), *Numerical simulation of viscous flows with free surface around realistic hull forms with transom*, Int. J. Numerical Methods in Fluids 37, pp.601-624

MENTER, F.R. (1993), *Zonal two equation k-ω turbulence models for aerodynamic flows*, AIAA 93-2906, 24^{th} Fluid Dynamics Conf., Orlando

MIKKOLA, T. (1999), *Testing of two FINFLO-based free-surface codes using Eulerian flow over a Gaussian ground elevation*, Ship Laboratory, Helsinki Univ. of Technology

RAVEN H.C., VAN DER PLOEG, A. AND STARKE, B. (2004), *Computation of free-surface viscous flows at model and full scale by a steady iterative approach*, 25^{th} Symp. Naval Hydrodyn., St. John's

SCHWEIGHOFER, J. (2003), *Viscous-flow computations at full-scale ship Reynolds numbers using the RANS solver FINFLO*, 6^{th} Num. Towing Tank Symp., Rome

SIIKONEN, T. (1998), *FINFLO user guide, version 3.0*, Laboratory of Applied Thermodynamics, Helsinki Univ. of Technology

TZABIRAS, G.D. (2004), *Resistance and self-propulsion simulations for a Series-60, C_B = 0.6 hull at model and full scale*, Ship Techn. Res. 51, pp.21-34

WATSON, S.J.P. AND BULL, P.W. (1999), *The scaling of high Reynolds numbers viscous flow predictions using CFD techniques*, 3^{rd} Osaka Coll. Advanced CFD Applications to Ship Flow and Hull Form Design, Osaka

3-D Computation of Ship-Wave Interaction by CIP / Cartesian Grid Method

Changhong Hu[*], *Masashi Kashiwagi*[*] *and Odd Faltinsen*[+]

*Research Institute for Applied Mechanics, Kyushu University
6-1 Kasuga-koen, Kasuga, Fukuoka 816-8580, JAPAN
+ Department of Marine Technology, NTNU, Trondheim, Norway

INTRODUCTION

The current research is a step towards developing a CFD method to predict hydrodynamic loads for strongly nonlinear ship-wave interactions. Our challenge is to incorporate the local slamming and green water impact predictions in the global ship motion calculations. The motivation is that such local loads can be sensitive to the inflow conditions, which need to be determined from the calculation of ship-wave interactions. For several years researches have been done to develop a 3-D CFD code that can be both robust and efficient to compute complicated interactions of a freely moving ship with ambient free surface flow.

Our numerical model is a Cartesian grid approach coupled with an interface capturing method. The CIP (Constrained Interpolation Profile) algorithm[1] is adopted as the base scheme. As the underlying Cartesian grid does not depend on the body boundary and the free surface, the computation of a strongly nonlinear problem, which may require treatment of both complicated free surface deformation and violent body motion, can be more efficient and robust than conventional body fitted approach.

The accuracy of the CIP based method for 2-D problems such as dam breaking[2], forced oscillation of a floating body[2,3], sloshing in tanks[4], water entry[5,6], have been validated. 3-D code development and its applications are ongoing[7,8]. A lot of efforts have been done by the authors to make the method be not only able to handle complicated flow phenomena but also relatively simple in scheme which can perform three-dimensional simulations in an acceptable spatial and temporal resolution at reasonable cost. In this extended abstract we will describe some new improvements on 3-D code development and an application example of 3-D NWT for demonstrating the capability of the proposed numerical model.

NUMERICAL APPROACH

The details of the CIP based method can be found in the authors' previous papers for two-dimensional case[2]. The wave-body interaction problem in our numerical model is treated as a multiphase problem, which includes a liquid phase (water), a gas phase (air) and a solid phase (floating body). A CIP based finite difference calculations are carried out in a regular computation domain with a Cartesian grid system. The free surface and the body boundary are treated as immersed interfaces to be determined by an interface capturing method. To recognize different phases we define a density function ϕ_m, as shown in Fig.1, m=1, 2, 3 denotes liquid, gas, and solid phase, respectively. The density functions for each computational cell have the relation of $\sum \phi_m = 1.0$ and satisfy the following equation:

$$\frac{\partial \phi_m}{\partial t} + u_i \frac{\partial \phi_m}{\partial x_i} = 0 \tag{1}$$

There are two kinds of the interface in the problem of interest: the gas-liquid interface (free surface) and

the solid-fluid interface (body boundary). Different interface capturing methods are designed for them.

The motion of the free surface is determined by solving Eq. (1) for the density function of liquid ϕ_1. We have developed a CIP coupled with function-transformation method for capturing the free surface. It has been shown that the method works well for violent free surface.

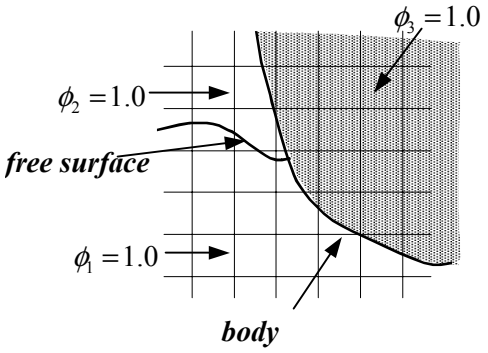

Fig.1 Density functions for multi-phase problems.

For the calculation of floating body such as a ship, the use of Cartesian grid approach makes it possible to treat violent ship motions and its complicated interactions with free surface in a relatively easy manner. However, the use of Cartesian grid usually has the disadvantage of its low order accuracy near the body boundaries because the grids generally do not conform to those boundaries. Efforts must be made to improve the accuracy near the body surface. In our method, the solid body is represented by distributing virtual particles on the surface in which the boundary condition is satisfied at these particles. One of the advantages of the method is that extension from two-dimensional to three-dimensional is straightforward. Furthermore, both non-slip and slip condition for velocity can be achieved by this method.

Governing Equations for Incompressible Flow

We use unsteady, viscous, incompressible Navier-Stokes equations as the governing equations for fluid.

$$\partial u_i / \partial x_i = 0 \tag{2}$$

$$\frac{\partial u_i}{\partial t} + u_j \frac{\partial u_i}{\partial x_j} = -\frac{1}{\rho}\frac{\partial p}{\partial x_i} + \frac{1}{\rho}\frac{\partial \sigma_{ij}}{\partial x_j} + f_i \tag{3}$$

where σ_{ij} is the viscous stress tensor. The last term on the right-hand side of Eq. (3) denotes the internal force, e.g., a gravity force, etc.

In order to apply CIP scheme, Eq. (3) is differentiated with respect to the spatial coordinates. Defining $\partial_\xi u_i = \partial u_i / \partial \xi$ $(\xi = x_1, x_2, x_3)$, we obtain:

$$\frac{\partial \left(\partial_\xi u_i\right)}{\partial t} + u_j \frac{\partial}{\partial x_j}\left(\partial_\xi u_i\right) = -\left(\partial_\xi u_j\right)\frac{\partial u_i}{\partial x_j} + \frac{\partial H}{\partial \xi} \tag{4}$$

where *H* represents the right hand term of the Eq. (3). Time evaluation of (3) and (4) are made by a fractional step method in which these equations are divided into an advection step and two non-advection steps. In one of the non-advection steps, the coupling of velocities and pressure is conducted by solving the following Poisson equation:

$$\frac{\partial}{\partial x_i}\left(\frac{1}{\rho}\frac{\partial p^{n+1}}{\partial x_i}\right) = \frac{1}{\Delta t}\frac{\partial u_i^*}{\partial x_i} \tag{5}$$

where the superscript '*' denotes the time level after the advection step. Note that this equation is valid for liquid and gas phases, and is computationally possible to apply to solid phase. Therefore, by solving Eq. (5),

the pressure in the whole computation domain can be obtained.

The advection phase calculation is performed by CIP method, which is described as follows.

CIP for Advection Computation

By CIP scheme, the profile inside a computation cell is approximated by an interpolation function. For three-dimensional case, a cubic polynomial can be used to approximate the spatial profile of a function χ inside a computational cell, and the following formulation is used for our code.

$$\begin{aligned} \mathrm{X}^n(\eta_1,\eta_2,\eta_3) = \; & C_{300}\eta_1^3 + C_{030}\eta_2^3 + C_{003}\eta_3^3 + C_{111}\eta_1\eta_2\eta_3 \\ & + C_{210}\eta_1^2\eta_2 + C_{021}\eta_2^2\eta_3 + C_{102}\eta_3^2\eta_1 + C_{120}\eta_1\eta_2^2 + C_{012}\eta_2\eta_3^2 + C_{201}\eta_3\eta_1^2 \\ & + C_{200}\eta_1^2 + C_{020}\eta_2^2 + C_{002}\eta_3^2 + C_{110}\eta_1\eta_2 + C_{011}\eta_2\eta_3 + C_{101}\eta_1\eta_3 \\ & + C_{100}\eta_1 + C_{010}\eta_2 + C_{001}\eta_3 + C_{000} \end{aligned} \tag{6}$$

where $\eta_1 = x_1 - x_{1_i}$, $\eta_2 = x_2 - x_{2_j}$ and $\eta_3 = x_3 - x_{3_k}$. $\left(x_{1_i},\ x_{2_j},\ x_{3_k}\right)$ is the coordinate for the grid point of interest. Eq. (6) contains 20 unknown coefficients, C_{lmn}, which can be determined by using the known values of χ^n and $\left(\partial_\xi \chi\right)^n$ at the surrounding grid points of the computational cell. Here the superscript '*n*' denotes the current time level.

Once the interpolation function is determined, the advection phase calculation is carried out by a semi-Lagrangian procedure as

$$\chi^*(\mathbf{x}) = \mathrm{X}^n\left(\mathbf{x} - \mathbf{u}^n\Delta t\right) \qquad \left(\partial_\xi \chi\right)^*(\mathbf{x}) = \frac{\partial \mathrm{X}^n}{\partial \xi}\left(\mathbf{x} - \mathbf{u}^n\Delta t\right) \tag{7}$$

Treatment of Free Surface and Body Boundary

The free surface is captured by solving Eq. (1) about the density function of liquid ϕ_1 with CIP method. By using a selected transformation function $\Phi = \Phi(\phi_1)$ the sharpness of the interface can be enhanced[1], i.e., instead of Eq. (1) we solve the following equation with CIP method.

$$\frac{\partial \Phi}{\partial t} + u_i \frac{\partial \Phi}{\partial x_i} = 0 \tag{8}$$

For the solid body boundary, we only consider the rigid body case and we can use a Lagrangian method to directly calculate the density function for the solid phase ϕ_3 and the local velocity at the body surface. To numerically realize this for three-dimensional case, we use particles to approximate the body geometry. Fig. 2 shows an example in which a ship model is represented in the computation by distributing virtual particles on the body surface. The pressure at a particle can be obtained by interpolation among the surrounding grid pressures. The hydrodynamic forces on the body are then calculated by integrating the pressure at wet particles. According to Newton second low, it is not difficult to calculate translational and rotational velocities at the gravity center of the rigid body, and the velocity for new time step at any particle $\mathbf{U}_P^{n+1}$ can therefore be obtained by interpolation. As shown in Fig. 3, $\mathbf{U}_P^{n+1}$ will be distributed to the surrounding grid points as $\hat{\mathbf{U}}^{n+1}$, which is the enforced velocity at a body boundary cell that is required to specify as the boundary condition.

For non-slip boundary condition, the following updating is done after the computation of Eq. (3).

$$\mathbf{u}^{***} = \phi_3 \hat{\mathbf{U}}^{n+1} + (1-\phi_3)\mathbf{u}^{**} \tag{9}$$

Here, $\mathbf{u}^{**}$ stands for the velocity computed by Eq. (3). In boundary cell Eq. (9) is a volume fraction weighting treatment for velocity interpolation. In this treatment, the method of imposing the velocity distribution inside and on the body boundary is considered equivalent to apply a forcing term to the momentum equation.

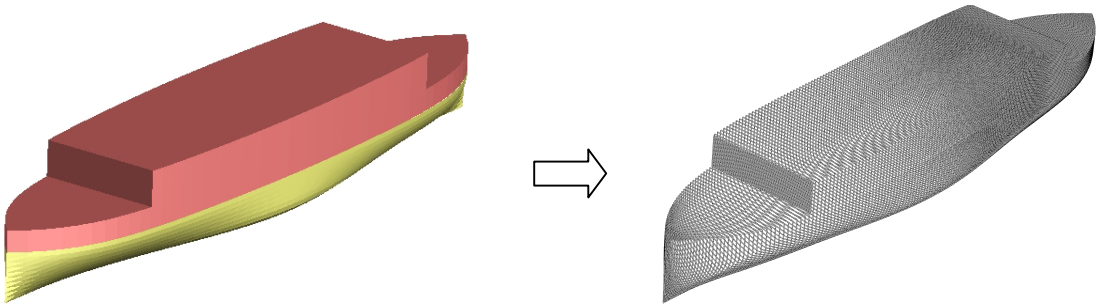

Fig. 2 A ship model represented by particles at body surface

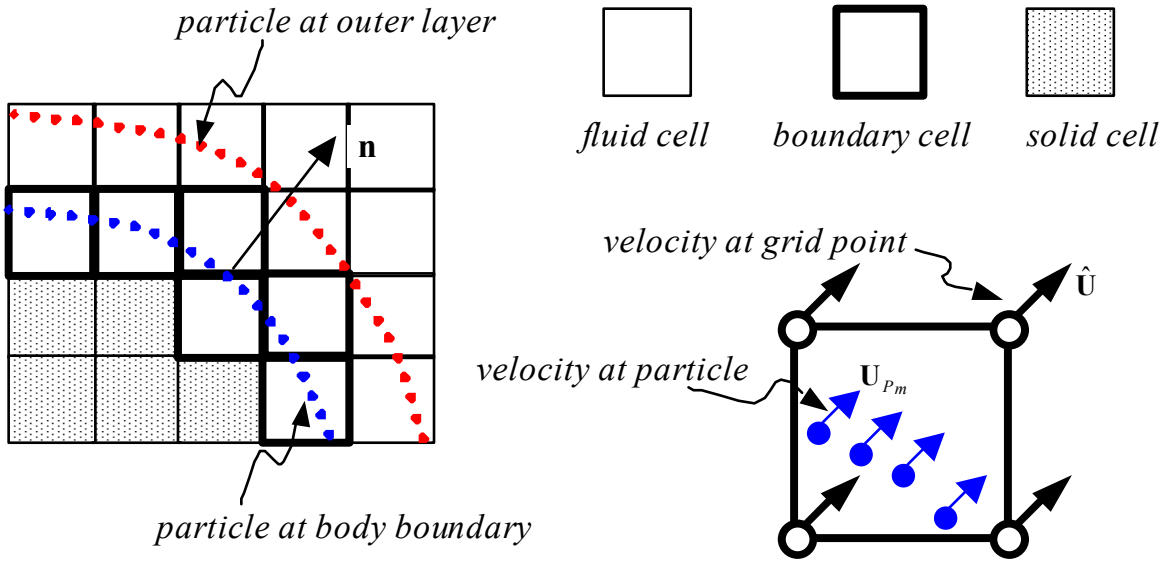

Fig. 3 Treatment of BC for velocity at body boundary

For a slip or a partial slip velocity condition, the equation (9) can also be used but the particle velocity $\mathbf{U}_P^{n+1}$ need to be determined in a different way. In the case, the particle velocity should satisfy that the normal velocity is the same with the surrounding flow while the tangential velocity is either equal to that of the neighboring flow (slip condition) or between the body velocity and the flow velocity (partial slip condition). Then we need to know the normal and tangential velocities of the nearby flow. This can be done by introducing an outer layer of particles as shown in Fig. 3. The particles at the two layers are in one-to-one correspondence and distance between them is generally chosen to be equal to the order of cell size. The

velocity at outer layer particles is calculated by interpolation among the flow velocity at surrounding grid points.

NUMERICAL RESULTS

A numerical wave tank (NWT) for strongly nonlinear ship-wave interactions is computed as the first application. By strongly nonlinear we mean a ship model may perform large amplitude motion in relatively large incident waves. Some typical phenomena, e.g., water on deck and slamming, are expected in the simulation results by the CIP method.

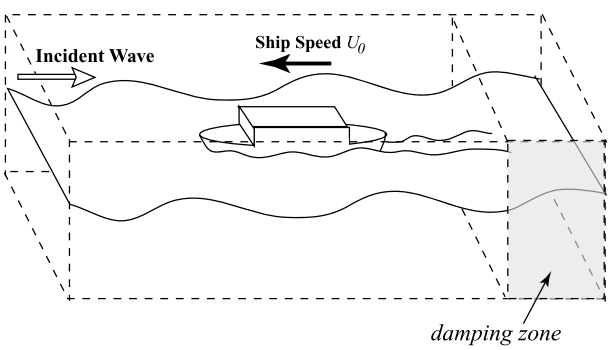

Fig.4 Sketch of the 3-D numerical wave tank

The numerical wave tank is constructed in a way shown in Fig. 4. The ship model is a Wigley model with an upstructure as shown in Fig. 2. The ship is free in pitch and heave but restrained in other motions. The ship moves with a constant forward speed U_0.

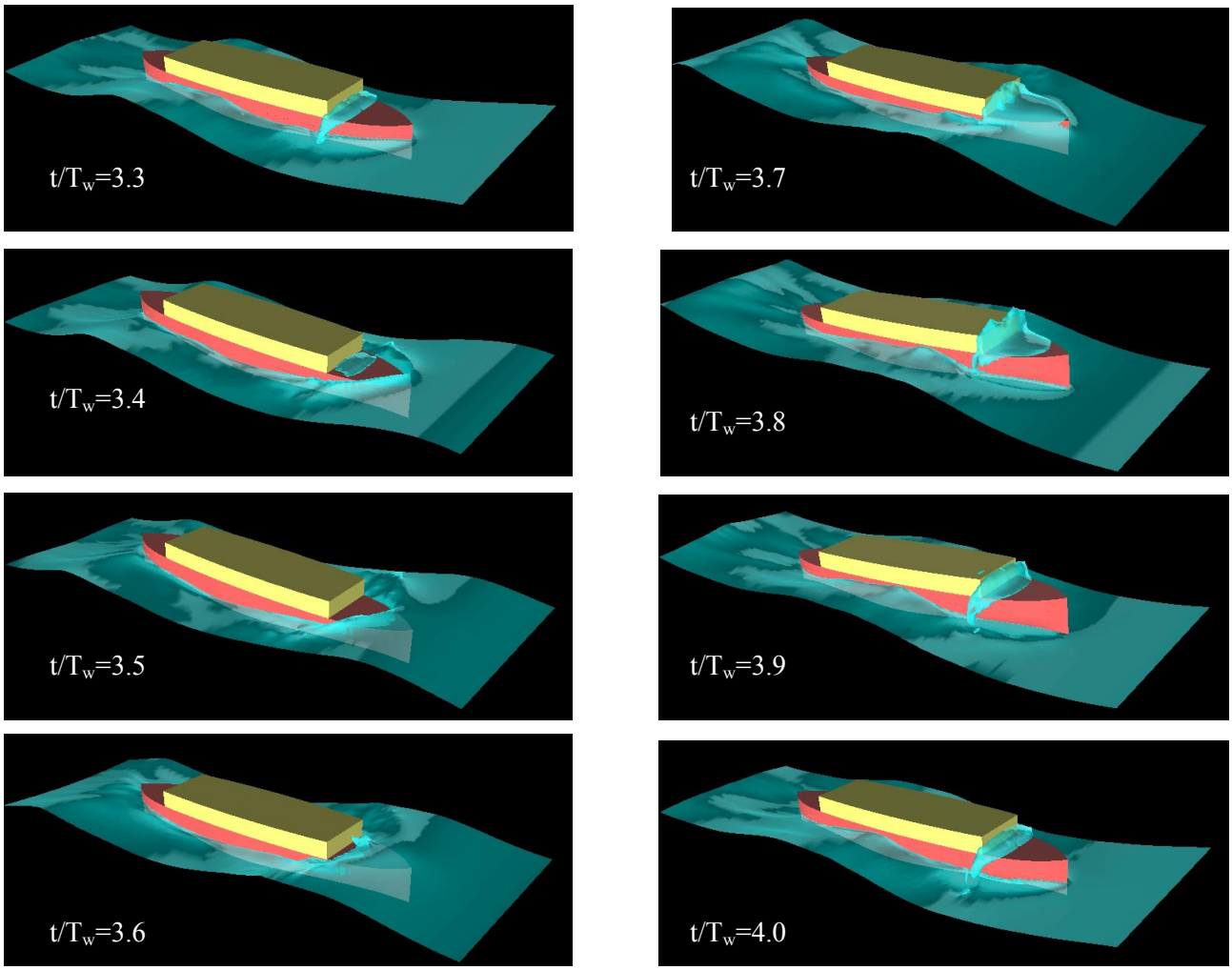

Fig. 5 Computed snap shots of a Wigley hull in large-amplitude waves

Fig. 5 shows one computation result. The computation condition is shown in Table 1. The slip boundary condition is used for velocity at the ship surface. The water on deck, slamming and large amplitude motion of the ship can be seen in the computed snap shots. Quantitative comparison of computation to experiments on ship motion and forces acting on the ship will be made in the near future.

Table 1 Computation details for NWT

Ship model	Length at waterline	L =2.5 m	Incident waves	Wave theory	Stokes Second-order
	Beam at midship	0.2 L		Wave length L_w	L
	Draft	0.07 L		Wave height H_w	L_w /15
	Displacement	0.13877m^3		Water depth d	4 L_w
	Free board	0.03 L	Grid	Grid number $165(x)\times80(y)\times80(z)$	
	Froude number	0.15		Min grid space $0.006L(x)\times0.005L(y)\times0.005L(z)$	
	Reynolds number	1.856x10^6	Time step	T_w /2000	

CONCLUSION AND PERSPECTIVES

A CIP/Cartesian grid method has been developed for 3-D numerical simulation of strongly nonlinear ship-wave interactions. Qualitatively correct result has been obtained for calculation of 3-D water on deck problem. We have had a big success with this method but there is still a long way to go. Validation of the 3-D code by experiment is ongoing. Some questions remain and improvement of the code will continue. Researches have also to be done to increase the computation efficiency of the present method.

REFERENCES

1. Yabe T, Xiao F and Utsumi T (2001) The Constrained Interpolation Profile Method for Multiphase Analysis. J Comput Phys 169:556-593
2. Hu, CH. & Kashiwagi, M. (2004). A CIP method for numerical simulation of violent free surface flows. J. Mar Sci Tecnol. 9, pp. 143-157.
3. Hu, CH., Faltinsen, O.M. and Kashiwagi, M. (2004) Development and Validation of CIP based Cartesian Grid Method for Nonlinear Wave-Body Interactions, Proc. of 8th NuTTS, Hamburg, Germany
4. Hu, CH., Kashiwagi, M. and Kishev Z. (2004) Numerical Simulation of Violent Sloshing by CIP Method, Proc. of 19th IWWWFB, Cotona, Italy.
5. Zhu, XY., Faltinsen, O.M. and Hu, CH. (2005) Water entry and exit of a horizontal circular cylinder, Proc. OMAE2005, Halkidiki, Greece.
6. Zhu, XY., Faltinsen, O.M. and Hu, CH. (2005). Water entry loads on heeled ship sections, Proc. HYDMAN05, Gdańsk, Poland.
7. Hu, CH., Kashiwagi, M. and Faltinsen, O.M. (2005). 3-D Numerical Simulation of Water-Entry Problem by CIP based Cartesian Grid Method, Proc. of 20th IWWWFB, Longyearbyen, Norway.
8. Hu, CH., Kashiwagi, M. and Faltinsen, O.M. (2005). 3-D Numerical Simulation of Freely Moving Floating Body by CIP Method, Proc. ISOPE2005, Seoul, Korea, V4, 674-679.

Multi-dimensional free surface flow simulation using two-phase Navier-Stokes solver

Ebrahim Jahanbakhsh, Roozbeh Panahi, Mohammad S. Seif
Sharif University of Technology
Ebrahim_Jahan@mehr.sharif.ir

1. Introduction

Continuous growth of computer power, strongly encourages engineers to rely on Computational Fluid Dynamics (CFD) for designing and testing new technological solutions. In addition, simulation of incompressible, viscous flows with moving free surface is very important in marine science, environmental engineering, die-casting, injection molding process and many others. Accurate and conservative simulation of such flows requires a compatible couple of primitive governing equations (momentum and continuity) with a free surface modeling scheme. This case is always divided into two main sub-problems as: a) Navier-Stokes equations and b) free surface modeling.

Methods for solving the Navier-Stokes equation are typically categorized as: a) Pressure-corrector schemes and b) Projection or fractional step schemes.

In pressure corrector methods like SIMPLE [1] and PISO [2, 3], a pressure correction equation is solved for several times in each time step to reach a divergence free velocity field. In contrast with such iterative methods, in fractional step schemes a pressure or pseudo-pressure poisson equation is solved once in each time step to enforce continuity. Therefore, using of such schemes is preferable, especially in unsteady problems [4].

Fractional step methods which have been used widely over past two decades, pioneered by Chorin [5, 6] based on Hodge decomposition. In the 1980s, several second-order projection methods are proposed by Goda [7], Bell et al. [8], Kim and Moin [9] and Van Kan [10]. Accuracy of such methods are discussed by Brown et al. [11], resulted in introducing a modified scheme based on Bell et al. [8]. This method has second-order time accuracy for both pressure and velocity.

On the other hand, the existing approaches for handling fluids interface are: a) interface tracking or surface methods and b) interface capturing or volume methods [12]. The interface tracking methods are characterized by an explicit representation of the interface. In other words, the computational grid is moved and updated in each time step to have no flow across it while satisfying force equilibrium on fluid at interface [4] (respectively interface kinematic and dynamic conditions). The common drawback of this category is the inability to handle complex geometries and overturning waves. This leads to interface capturing methods where the interface is captured as a part of the physical domain. One of the most interesting approach in volume methods is to solve an additional convection equation. This results in volume fraction which implies the availability of two phases in each computational cell for whole domain. Discretisation of such an equation encounters face values which must be estimated using an appropriate interpolation scheme. This interpolation must ensure boundedness and availability criteria [13] to have physical volume fraction values. It means the value of a flow property in the absence of source or sink can not be higher or lower than prescribed on the boundaries of a cell. In addition, the amount of flow convected over a face during a time step should be less than or equal to the amount available in donner cell. Simple interpolations have some problem with transitional area between two phases while introducing numerical diffusion [14] or disobeying the local boundedness [15]. There are some composite schemes which switch between their options according to the received signals about current, to have physical distribution of fluids in whole domain [16, 17]. CICSAM (Compressive Interface Capturing Scheme for Arbitrary Meshes) [13] is one of these methods which appropriately retains the changing region between two fluids while establishing all criteria.

Integrated numerical solution for simulation of multi-dimensional interfacial flows will be described in this paper. It includes reviewing the governing equations and their discretisation, fractional step method, CICSAM interpolation and the connection between these parts. Finally, the developed program is verified using Raleigh-Taylor instability and broken dam problem in two- and three-dimensions.

2. Numerical Method

There is an approach in simulating two-phase flow, where different fluids are modeled as a *single fluid* obeying the same set of governing equations, with the different local identified volume fraction values α. Incompressible Navier-Stokes equations and the continuity equation are well-known and given by the equations:

$$\frac{\partial u_i}{\partial t} + u_j \frac{\partial u_i}{\partial x_j} = -\frac{1}{\rho}\frac{\partial p}{\partial x_i} + \nu \frac{\partial^2 u_i}{\partial x_j \partial x_j} + g_i \tag{1}$$

$$\frac{\partial u_i}{\partial x_j} = 0 \tag{2}$$

Where u_i is the velocity, p is the pressure, and ν is the kinematic viscosity.

Local density ρ and viscosity ν of the single fluid are defined as:

$$\rho_{cell} = \alpha \rho_1 + (1-\alpha)\rho_2$$
$$\nu_{cell} = \alpha \nu_1 + (1-\alpha)\nu_2 \quad (3)$$

Subscripts 1 and 2 yield two fluids (e.g. water and air), where α (volume fraction) is the percentage of fluid 1 (e.g. water) available in cell and defined as follow:

$$\alpha = \begin{cases} 1 & for\ cells\ inside\ fluid\ 1 \\ 0 & for\ cells\ inside\ fluid\ 2 \\ 0 < \alpha_0 < 1 & for\ transitional\ area \end{cases} \quad (4)$$

Reformulating the continuity equation (eq.2) [18] and using the definition of single fluid density results in extracting a scalar transport equation for volume fraction α :

$$\frac{\partial \alpha}{\partial t} + div(\alpha \vec{u}) = 0 \quad (5)$$

Appropriate discretisation of governing equations is an important step in CFD, especially in two-phase flows where fluids have significant differences in their densities and viscosities. By Integration of the governing equations over the control volume it results in finite volume formulation. Here the convection term (the second term in lhs of eq.2), is discretised using Gamma interpolation scheme [19] based on NVD (Normalized Variable Diagram) [14] concept. To discretise the diffusion term (the second term in rhs of eq.2), the Central Differencing Scheme (CDS) is applied. In addition, the Crank-Nicholson scheme is implemented to discretise eq.2 in time. To couple the velocity and the pressure fields (solving the Navier-Stokes and continuity equations), fractional step method of Brown et al. [11] which is the modified scheme of Bell et al. [8], is selected. This procedure is completed by determination of the *single fluid* physical properties in the computational domain. To discretise the volume fraction α transport equation, the CICSAM scheme is implemented [13,17]

3. Test Cases and Numerical Results

In order to assess the feasibility, a computer program is written according to above mentioned procedure. This is summarized in some conclusion about the accuracy, efficiency and robustness of such an algorithm.

3.1. The Two-dimensional Rayleigh-Taylor Instability

When a horizontal layer of heavy fluid overlies a layer of light fluid in the presence of vertical gravitational field, the interface between the two fluids is unstable. If the interface is perturbed, buoyancy forces will cause the amplitude of perturbation to grow with time. This phenomenon is known as the Rayleigh-Taylor instability and related computations have been performed by Puckett et al. [20, 21] and later by Popinet and Zaleski [22]. A one meter wide, four meter high rectangular domain is discretised using 64*256 grids. Fig.1 shows the initial perturbation and fluids properties.

The numerical results have been compared to other one, obtained by Popinet and Zaleski [22] and it show a good concordance [Fig 2.]. In addition Rayleigh-Taylor problem is an unstable one and time advancement apparently shows this phenomenon [Fig.3].

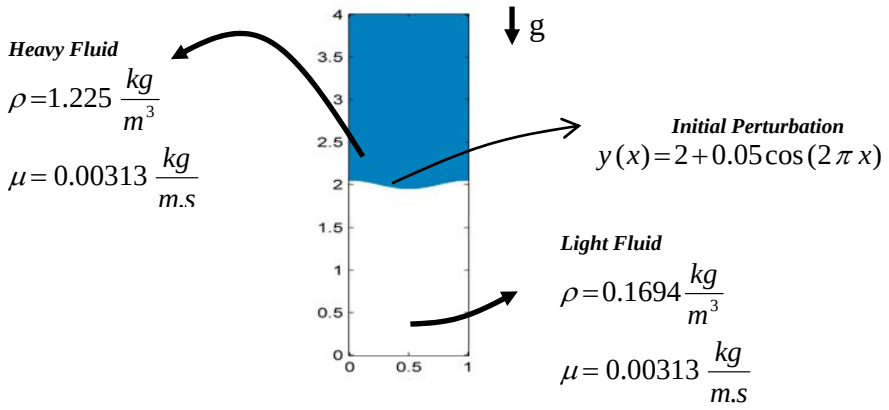

Fig.1. Illustration of Rayleigh-Taylor instability problem

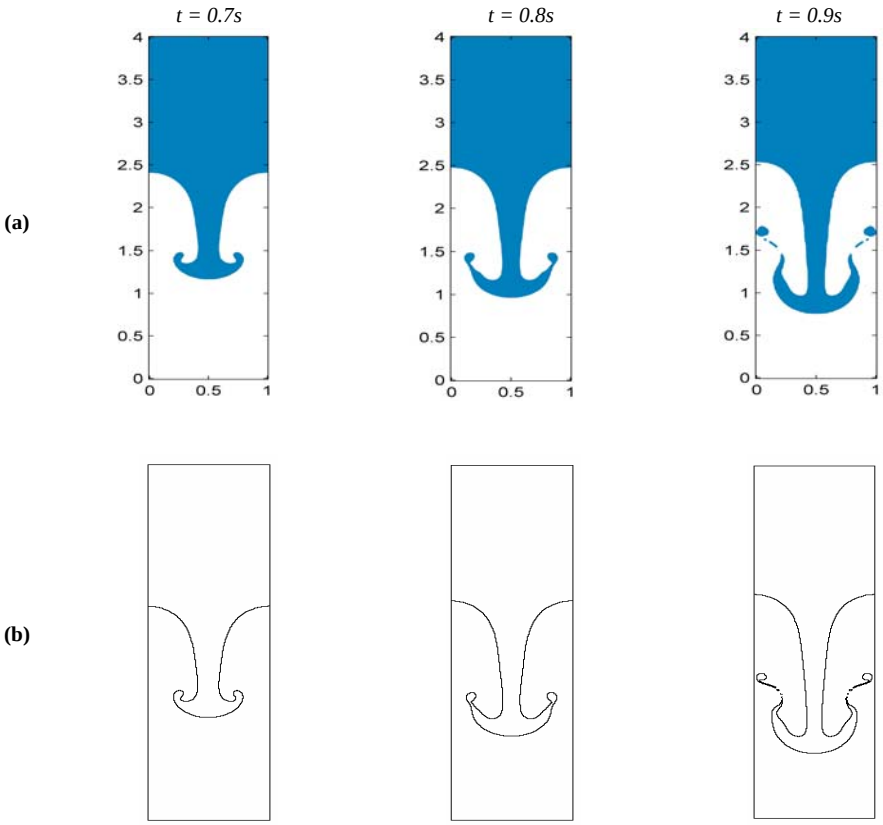

Fig2. Rayleigh-Taylor instability at different times; (a): present work, (b): Popinet and Zaleski [22]

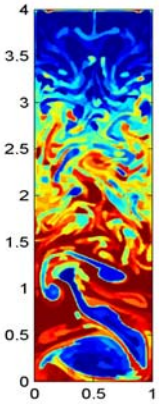

Fig.3. Rayleigh-Taylor instability in t = 5.6 s

3.2. Two-Dimensional Broken Dam

A classical experiment used in the validation of mathematical modeling of two-fluid system, is the collapse of liquid column. Fig.4 shows the sketch of primary experimental setup [23]. There are some secondary data such as reduction of the column height (y) and progression of column front (x) to validate numerical calculations. The specific geometry employed in the present work is illustrated in Fig.5 where $a = 0.05715$ m. Free surface motion is captured in times and plotted in Fig.6 as snapshots. The interface movement seems to have a natural deformation. Anyway, to validate these data the computed surge front (x) and column height positions (y) are plotted in Fig.7 and Fig.8. The data of Martin and Moyce [23] are also plotted for comparison and it shows that the numerical results are in good agreement with experiment. However, the simulation seems to be ahead of the physical data with respect to the position of the leading edge. Someone implies that the unsynchronized start of simulation and physical data leads to such a shift [24]. In addition, it must be remembered that the current simulation ignores the effect of surface tension which exists in physics.

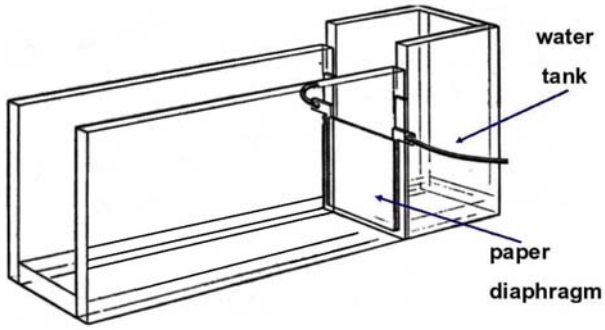

Fig.4. Diagram of a typical apparatus in dam breaking experimental setup [23]

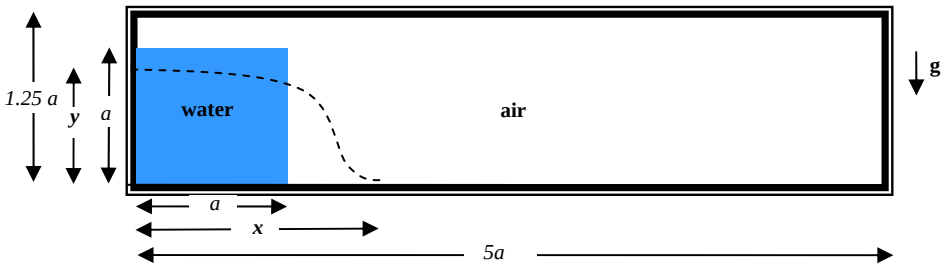

Fig.5. Illustration of two-dimensional broken dam problem

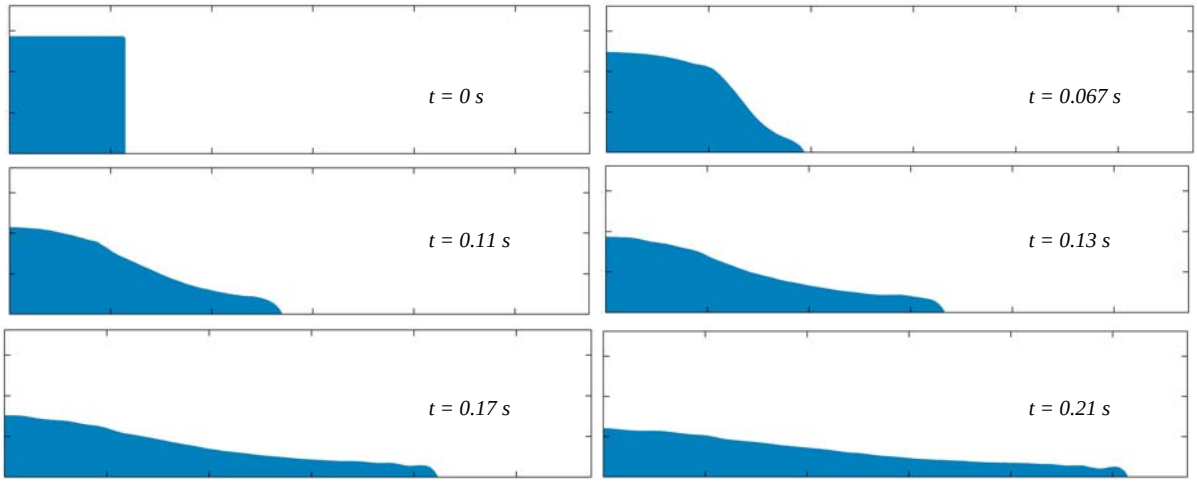

Fig.6. Free surface motion

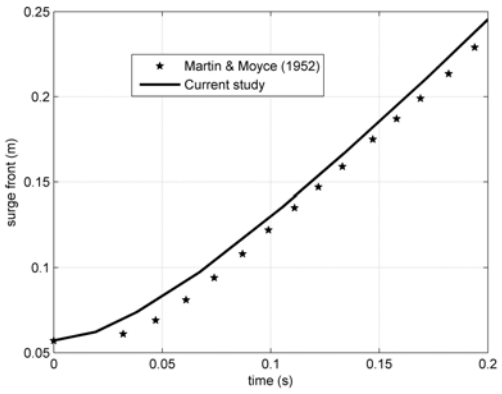

Fig.7. Surge front position

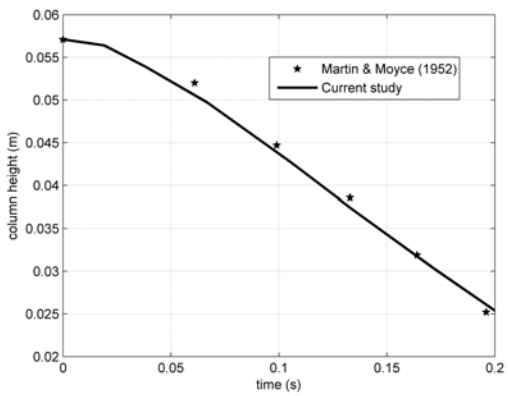

Fig.8. Column height

3.3. Three-Dimensional Broken Dam

To test the three-dimensional free surface flow solver, the broken dam is modeled. Its geometry and specifications is same as two-dimensional case with finite thickness of *0.05715* m. The calculation is made using a uniform grid of 80*20*20 control volumes.

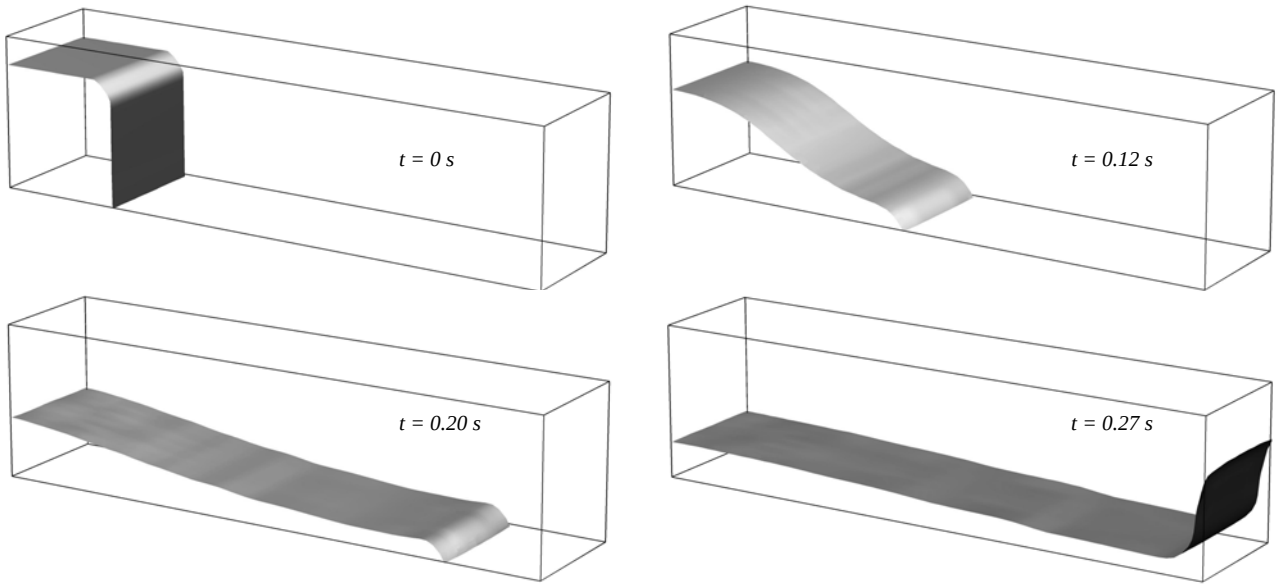

Fig.9. Free surface motion

The snapshots of free surface motion are plotted in Fig.9. By measurement of surge front and column height at the symmetry plane, they are plotted in Figs. 10 and 11. Also plotted in this figures are the experimental data of Martin and Moyce [23] and the corresponding results for the two-dimensional broken dam problem. There is very little difference between two- and three-dimensional simulations, which is clear in such plots. That is probably due to the high Reynolds number for this particular case, which reduces the influence of side walls on the flow field at the symmetry plane.

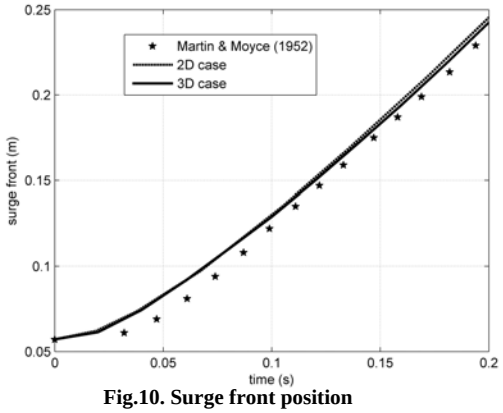

Fig.10. Surge front position

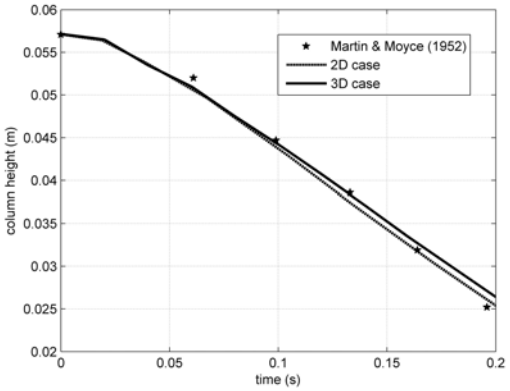

Fig.11. Column height

4. Conclusion

The preceding sections have described the development of a free surface flow solver. The algorithm employs the fractional step method to couple both velocity and pressure. To simulate the free surface, an appropriate surface capturing scheme is selected. To discretise the free surface scalar transport equation which calculates the volume fraction distribution, a high resolution differencing scheme is applied. The use of a consistent formulation in both the liquid and gas regions permits the free surface to be automatically captured as a discontinuity in the density and viscosity, and thereby eliminates the need for special free surface tracking procedure, although this discontinuity must be treated in a special manner.

An extensive set of validation calculations were carried out for two and three dimensional test cases and comparison of the results shows a reasonably good agreement between numerical and experimental data.

Although the presented method has been tested using simple geometries, the discretisation scheme is of sufficient generality to permit free surface flows in more complex geometries to be computed.

5. References

1. Patankar, S.V., Spalding, D.B., *A calculation procedure for heat, mass and momentum transfer in three dimensional parabolic flows*, Int. J, Heat Mass Transfer, vol. 15, p. 1787, (1972)
2. Issa, R.I., Solution of the implicitly discretised fluid flow equations by operator-splitting, J. Comput. Phys. Vol. 62(1),p. 40-65, (1986)
3. Versteeg, H.K., Malalasekera, W., *An introduction to computational fluid dynamics, the finite volume method*, Hrlow; Longman scientific & Technical, (1995)
4. ferziger, J. H., Peric, M. *Computational methods for fluid dynamics*, 3rd ed., Springer, 2002.
5. Chorin, A.J., *Numerical solution of the Navier-Stokes equations*, Math. Comput. 22, 745, (1968)
6. Chorin, A.J., *On the convergence of discrete approximations to the Navier-Stokes equations*, Math. Comput. 23, 341, (1969)
7. Goda, K., *A multiphase technique with implicit difference schemes for calculating two- or three- dimensional cavity flows*, J. Comput. Phys. 30, 76, (1979)
8. Bell, J.B., Collela, P., Howell, H., *An efficient second-order projection method for viscous incompressible flow*, in proceeding of tenth AIAA Computational Fluid Dynamics Conference, AIAA, p.360, (1991)
9. Kim, J., Moin, P., *Application of a fractional-step method to incompressible Navier-Stokes equations*, J. Comput. Phys. 59, 308, (1985)
10. Van Kan, J., *A second-order accurate pressure-correction scheme for viscous incompressible flow*, SIAM, J. Sci. Comput. 7, 870, (1986)
11. Brown, D.L., Cortez, R. Minion, M.L., *Accurate projection methods for the incompressible Navier-Stokes equations*, J. Comput. Phys. 168, 464-499, (2001)
12. Muzaferija, S., Peric, M., *Computation of free surface flows using interface tracking and interface capturing methods*, chap. 2 in O. Mahrenholtz and M. Markiewicz (eds.), Nonlinear Water Waves Interaction, computational Mechanics Publications, Southahmpton, (1998)
13. Ubbink, O., *Numerical Prediction of two fluid systems with sharp interfaces*, PhD thesis, Imperial College, Department of Mechanical engineering, (1997)
14. Leonard, B.P., *The ULTIMATE conservation difference scheme applied to unsteady one dimensional direction*, Computational methods in applied mechanic and engineering, (1991)
15. Leonard, B.P., *Stable and accurate convective modeling procedure based on quadratic upstream interpolation*, Comp. Methods in Applied Mechanics and Engineering, vol. 19, pp. 59-98, (1979)
16. Nielsen, K. B., *Numerical prediction of green water loads on ships*, PhD thesis, Technical University of Denmark, Department of mechanical engineering, (2003)
17. Ubbink, O., Issa, R. I., A *method for capturing sharp fluid interfaces on arbitrary meshes*, J. comput. Phys. 153, 26-50, (1999)
18. Spalding, D.B., *A method for computing steady and unsteady flows possessing discontinuities of density*, CHAM Report 910/2, (1974)
19. Jasak, H. *Error analysis and estimation for finite volume method with application to fluid flows*, PhD Thesis, University of London, (1996)
20. Puckett, E.G., Almgren, A.S., Bell, J.B., Marcus D.L., Rider, W.J., *A second order projection method for tracking fluids interfaces in variable density incompressible flows*, submitted to J Comp. Phys.
21. Puckett, E.G., Almgren, A.S., Bell, J.B., Marcus D.L., Rider, W.J., *A high order projection method for tracking fluids interfaces in variable density incompressible flows*, J Comp. Phys. 100:269-282, (1997)
22. Popinet, S., Zaleski, S., *A front tracking algorithm for accurate representation of surface tension*, Int. J. Num. Methods Fluids, vol. 30, pp. 775-793, (1999)
23. Martin, J.C., Moyce, W.J., *An experimental study of the collapse of liquid columns on a rigid horizontal plane*, Philos. Trans. Roy. Soc. London, Vol. A244, p.312-324, (1952)
24. Croce, R., Griebel, M., Schweitzer, M. A., *A parallel level-set approach for two-phase flow problems with surface tension in three space dimensions*, Preprint 157, Sonderforschungsbereich 611, Universitat Bonn, (2004)

CIP Method for Numerical Simulation of Violent Sloshing

Zdravko R. Kishev
Interdisciplinary Graduate School of Engineering, Kyushu University
Kasuga, Fukuoka, Japan

Changhong Hu, Masashi Kashiwagi
RIAM, Kyushu University
Kasuga, Fukuoka, Japan

INTRODUCTION

Liquid sloshing is an important problem in several fields of modern hydrodynamic and engineering research, such as marine industry, space technology and civil engineering. In this paper, violent liquid motion inside partially filled ship tanks is particularly addressed. The phenomenon is known as provoker of local structural deformations and even damage, i.e. on board LNG carriers (membrane type), where the tanks have no internal structure, thus providing only little damping of the liquid motion and increasing probability of violent sloshing occurrence.

Liquid motion inside the tank is strongly coupled with ship motion. The liquid not only responds to the motion of the ship, but also has a great effect on it. This means that a coupled sloshing model should be used in principle. However, due to the high complexity of the coupled problem, ship motion and tank liquid motion are often considered separately. In the current paper, the same approach is adopted and ship motion is prescribed beforehand.

Depending on tank geometry, frequency and amplitude of oscillation and filling height, different modes of sloshing can be observed. As a good example, the case of liquid motion at shallow tank water depth can be provided. In the low frequency range, a flat standing wave is observed, which changes to a train of small amplitude travelling waves at higher frequencies. At resonance, a hydraulic jump evolves, and at above-resonance frequencies the profile changes to a solitary wave. Different modes are observed at finite liquid depths in the tank. Flat standing waves can be observed below resonance with their amplitude increasing when approaching resonance frequency. At resonance, the typical response is a combination between standing and large amplitude travelling waves. Liquid motion becomes gradually less violent at higher frequencies. At some special frequencies non-symmetrical cases can also be observed. Roof impacts can occur with very high impulsive pressures acting, which could provoke structural damage on tank ceiling.

It is usually difficult to predict the correct sloshing loads and motions theoretically, due to the strong non-linearity of the problem and the large number of parameters involved. Experiments are useful, but are time- and cost-consuming. Many different numerical solutions have been proposed so far, but as a rule, they assume incompressible flow and exclude the gas phase from the computations. Taking into account gas compressibility is, however, important for violent sloshing simulations, especially high filling levels. Moreover, most of the conventional numerical schemes often have problems with highly distorted free-surfaces, such as those occurring during violent sloshing. Therefore, a new approach needs to be applied for this problem.

NUMERICAL METHOD

General

In Hu and Kashiwagi (2003) and (2004-2), the authors recently proposed a new CFD simulation approach for extremely nonlinear wave-body interactions. The method is a finite difference scheme based on the CIP (Constrained Interpolation Profile) algorithm. The advantages of the method are that it can treat easily multiphase flows by using a simple rectangular grid even in the case of rather complex geometries. It also can easily be applied to any kind of excitation. The boundaries between phases (liquid and gas) are treated as inner interfaces. A unified pressure-based flow solver, the CCUP scheme (CIP-Combined and Unified Procedure), is used to treat both phases simultaneously and describe their motion by one set of equations. The CIP scheme was applied for interface capturing. However, this interface capturing scheme may suffer from interface smearing due to numerical diffusion. The interface may become too thick and an unphysical mass change may occur especially in long-term computations. Even though this smearing is smaller then the smearing of many of the conventional numerical schemes, it can become a problem in the simulation of violent sloshing, as will be shown later on. Therefore the authors decided to improve the situation by applying a conservative form of the CIP algorithm, the CIP-CSL3 scheme (CIP-Conservative Semi-Lagrangian with cubic interpolation polynomial) of Xiao and Yabe (2001) for interface capturing. The scheme keeps the computed interface very compact and has an excellent mass conservation property.

The basic idea of the method is to use some additional constraint when constructing the interpolation function inside the computational cell. This makes it possible to preserve information about the behaviour of the variable inside the computational cell and thus reduce diffusion. Therefore, the CIP method is considered to have sub-cell resolution, which makes it superior to other finite difference schemes. Yabe et al. (2001) showed that the CIP method could successfully capture a wave between

three grid points only. All other methods used in the comparison failed to reproduce the same result.
The different phases are identified by a density function equal to unity, if the cell is occupied by the respective phase and to zero in the opposite case. That function is calculated by an advection equation of the type bellow:

$$\frac{\partial \phi_l}{\partial t} + u_i \frac{\partial \phi_l}{\partial x_i} = 0 \tag{1}$$

As discussed in Hu and Kashiwagi (2003), owing to the sub-cell resolution feature of the CIP scheme, for many cases the gas-liquid interface can be successfully determined by solving Eq. 1 for the density function of liquid ϕ_l.

A description of the method is given below.

Governing Equations

The governing equations are the conservation of mass equation and Navier-Stokes equations for compressible fluid flows. Under the assumption that no temperature changes are present, the complete set of equations can be given as:

$$\frac{\partial \rho}{\partial t} + \sum_i u_i \frac{\partial \rho}{\partial x_i} = -\rho \sum_i \frac{\partial u_i}{\partial x_i} \tag{2}$$

$$\frac{\partial u_i}{\partial t} + \sum_j u_j \frac{\partial u_i}{\partial x_j} = \frac{1}{\rho} \sum_j \frac{\partial \sigma_{ij}}{\partial x_j} + f_i \tag{3}$$

$$\frac{\partial p}{\partial t} + \sum_i u_i \frac{\partial p}{\partial x_i} = -\rho C_S^2 \sum_i \frac{\partial u_i}{\partial x_i} \tag{4}$$

C_S is the speed of sound and σ_{ij} is the total stress for a Newtonian fluid, defined as:

$$\sigma_{ij} = -p\delta_{ij} + 2\mu S_{ij} - 2\mu\delta_{ij} \sum_k \frac{S_{kk}}{3} \tag{5}$$

$$S_{ij} = \frac{1}{2}\left(\frac{\partial u_i}{\partial x_j} + \frac{\partial u_j}{\partial x_i} \right) \tag{6}$$

Conventional CIP Scheme

Originally the CIP algorithm was developed for pure advection equation, which for a function χ can be written as:

$$\frac{\partial \chi}{\partial t} + u_i \frac{\partial \chi}{\partial x_i} = 0 \tag{7}$$

It was generalized for solving an equation with non-zero right-hand side by the use of a fractional step approach. The solution of Equations 2-4 within one time step is divided into several phases. Firstly, pure advection is solved by the CIP method. Then solution is updated with diffusion and external force terms by use of an explicit finite difference algorithm. At last, a Poisson-type equation is solved iteratively by means of some iterative method, such as SOR, ICCG or other.
For advection phase calculations, a semi-Lagrangian procedure is used. The solution of equation (7) is given by equations (8) and (9). The value after advection is calculated by shifting the profile before advection by $u_i.\Delta t$ to the upwind direction. Spatial gradient is calculated in a similar way:

$$\chi^*(x_1, x_2) = X^n(x_1 - u_1\Delta t, x_2 - u_2\Delta t) \tag{8}$$

$$\varphi^*_{1,2}(x) = \frac{\partial X^n}{\partial x_{1,2}} \tag{9}$$

Here φ^* is the spatial gradient of χ^* and X is the interpolation function. A cubic polynomial with 10 coefficients as given by Eq. (10) is used in the present calculation:

$$\begin{aligned} X^n(\xi,\eta) &= C_{30}\xi^3 + C_{21}\xi^2\eta + C_{12}\xi\eta^2 + C_{03}\eta^3 \\ &+ C_{20}\xi^2 + C_{11}\xi\eta + C_{02}\eta^2 + C_{10}\xi + C_{01}\eta + C_{00} \end{aligned} \tag{10}$$

For a grid point of interest with coordinates (x_{1k}, x_{2m}) ξ and η are defined as:

$$\xi = x_1 - x_{1k}$$

$$\eta = x_2 - x_{2m}$$

Expressions for the coefficients together with their derivation can be found in an earlier paper by the authors (Hu and Kashiwagi 2004-2) and will not be repeated here.

Conservative CIP-CSL3 Scheme

Xiao and Yabe (2001) suggested several conservative modifications of the conventional CIP method, one of which was the CIP-CSL3 scheme. To start, we rewrite equation (7) in conservative form and, without loss of generality, we add a right hand side term. In 2D the basic equation can then be written in the form:

$$\frac{\partial \chi}{\partial t} + \frac{\partial (u_i \chi)}{\partial x_i} = H_1 \tag{11}$$

Instead of using spatial gradients as additional constraints, the CIP-CSL3 scheme adopts surface and volume integrated averages. For a computational cell with a volume V and surrounded by surfaces ${}^{\pm l}S$, l=1-3, they are given as:

$${}^{l}\overline{\chi} = \frac{1}{{}^{l}S} \oint_{{}^{l}S} \chi \, dS$$

$$\overline{\overline{\chi}} = \frac{1}{V} \oint_V \chi \, dV$$

For a 2D case, the following equations are obtained by surface averaging and volume averaging Eq. 11:

$$\frac{\partial {}^{l}\overline{\chi}}{\partial t} + u_i \frac{\partial {}^{l}\overline{\chi}}{\partial x_i} = H_1' \tag{12}$$

$$\frac{\partial \overline{\overline{\chi}}}{\partial t} + \frac{1}{V} \sum_{l=1}^{2} \left({}^{+l}\overline{u_i \chi}\, {}^{+l}S - {}^{-l}\overline{u_i \chi}\, {}^{-l}S \right) = \frac{1}{V} \oint_V H_1 dV \tag{13}$$

Eqs. 12 and 13 will be solved by a fractional step approach, similar to that used in the CIP method.
Another difference between the conventional and the conservative CIP schemes is that the later adopts a directional splitting technique. A 1D cubic polynomial in each direction and a successive interpolation is used to perform the 2D calculation. For details, please refer to the paper of Xiao and Ikebata (2003)
The 1D polynomial is given by the following expression:

$$X_1^n(\xi) = C_3\xi^3 + C_2\xi^2 + C_1\xi + C_0 \tag{14}$$

When performing calculation in x_1-direction, the coefficients will be determined by the following constraints:

$$
\left.
\begin{aligned}
&X_1^n(x_{1\,k+1/2}) = \bar{\chi}_{k+1/2\,j} \\
&X_1^n(x_{1\,k-1/2}) = \bar{\chi}_{k-1/2\,j} \\
&\frac{1}{\Delta x}\int_{x_{1\,k-1/2}}^{x_{1\,k+1/2}} X_1^n(x_1)dx = \bar{\bar{\chi}}_{k\,j} \\
&\frac{dX_1^n(x_{1k})}{dx_1} = \lambda_{1\,k}
\end{aligned}
\right\} \qquad (15)
$$

In the last line of Eq. 15, λ_{1k} is the slope of X_1^n at cell center. It is determined separately as a free parameter. Modifying this parameter provides us with the possibility to reduce numerical diffusion at the interface, which is in fact done in the present computations to reduce interface smearing.

It should be noticed that although the CIP-CSL3 scheme can be applied to a general advection equation, at the present stage of our research it is only applied as an interface-capturing procedure.

NUMERICAL RESULTS

Results by both numerical schemes have been compared with experimental results. Excitation periods covered a wide range near the first natural period of the tank. A comparison was made for free-surface profiles and pressure time histories. Transfer functions for maximum pressures and for pressure impulses were also built. Examples for such transfer functions for 12 cm filling height are shown at Figure 1.

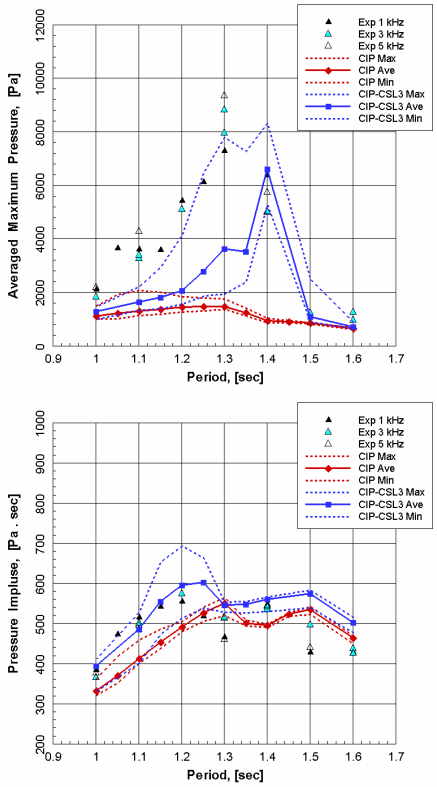

Fig. 1. Transfer functions for the average maximum pressure and for the pressure impulse. H=12 cm, y_P=10 cm

It is obvious that results, obtained when using the CIP-CSL3 scheme as interface capturing method, results for maximum pressure predictions are much better then those obtained when conventional CIP scheme is used instead. However, results for pressure impulse by both schemes are in good agreement with experimental measurements. This can be explained by looking at Figure 2, where pressure time-histories are compared. It is obvious that the conservative scheme successfully simulates the maximum values and the general tendency, while the conventional scheme predicts well only the general tendency, but fails to predict the first sharp peak of the time-history.

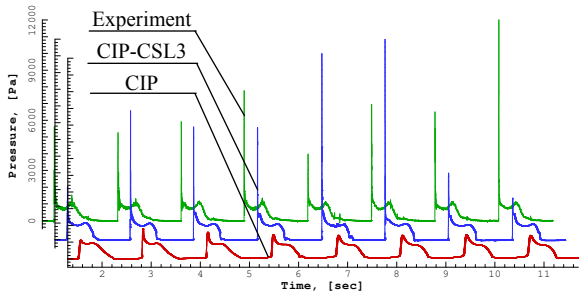

Fig. 2. Comparison of pressure time-histories for T = 1.30 sec. From back to front – experimental results, CIP-CSL3 and CIP simulation; y_P=10 cm

Comparison of free-surface profiles at several time-instants is made in Figure 3. Solid line corresponds to density function values ϕ_l = 0.50, which is considered to be the interface. Dashed contour lines for ϕ_l = 0.01 and ϕ_l = 0.99 are also shown in order to provide a basis for qualitative comparison of numerical diffusion. Results from CIP-CSL3 are in perfect agreement with experiments, while results from conventional CIP show a very thick transition zone, even though general shape of the profiles is also relatively good. The large transition zone between gas and liquid phases observed in the conventional CIP results doesn't have a physical meaning and is a sign for large numerical diffusion of the scheme. This is also the reason why this version becomes unreliable after some time and the main reason for developing a conservative form of the method.

CONCLUSIONS

Here, numerical results for interface profiles as well as pressure time histories by both methods for a resonance excitation case have been compared with experimental measurements.

The presented numerical schemes agree well with each other and with experimental measurements, except for the simulation of maximum pressures, which are largely underestimated by the conventional CIP scheme. The results by the conservative CIP-CSL3 scheme give predictions, much closer to experimental values. The only difference between them from numerical point of view is the interface capturing method, while the flow solver is exactly the same in both schemes. Therefore it seems that good prediction of the interface is also crucial for good prediction of impact pressures. The numerical diffusion of the CIP method, applied to simulation of velocities and pressure in the advection phase of each time step is not so important and the method can be used, when conservation is not a key-factor in the solution. However, if the CIP-CSL3 scheme is applied also to velocities, probably a further refinement of the results can be obtained. This remains to be verified in near future.

It must be noted that the code is under development and much work remains to be done in future. For example,

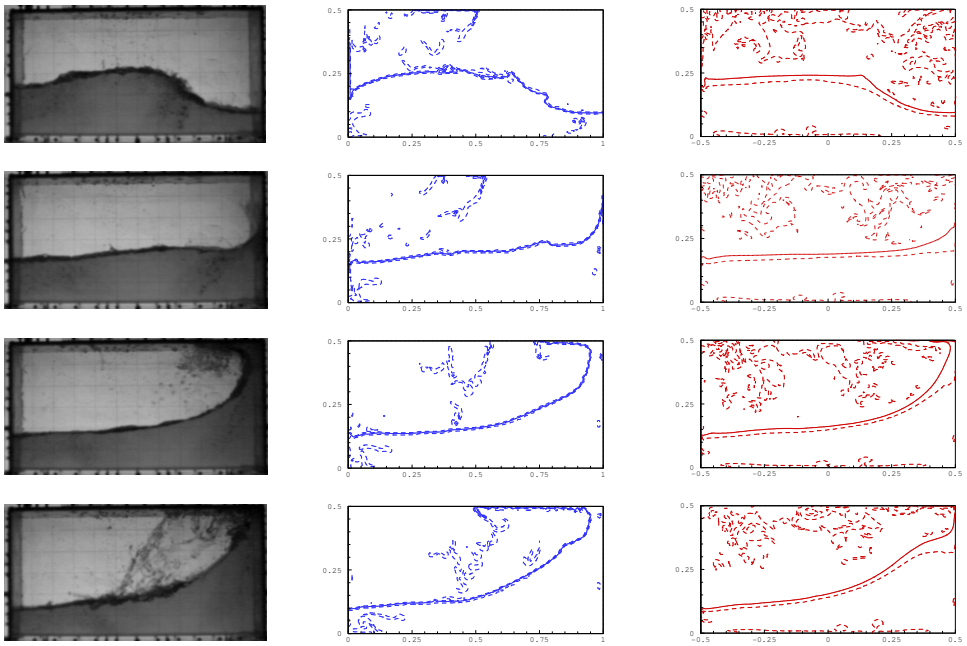

a) b) c)

Fig. 3. Comparison of gas-liquid interface profiles observed during experiments (a) and obtained by the CIP-CSL3 (b) and CIP (c) methods. T = 1.30 sec. From top to bottom time instants are T/10, 2T/10, 3T/10 and 4T/10.

so far only a rectangular tank has been used, while real tanks have often more complex geometries. Also real phenomena, such as wave breaking, jet formation, splashes and other complicated phenomena, occurring during violent sloshing, are three-dimensional, while the model so far is only two-dimensional. This causes some problems at high filling levels and therefore a 3D formulation is highly desirable. This is also left for future work.

REFERENCES

Faltinsen, OM (1978) - A Numerical Nonlinear Method of Sloshing in Tanks with Two-dimensional Flow, *J. Ship Research*, Vol 22, No 3, pp 193-202

Faltinsen, OM, Timokha, AN (2001) - Adaptive Multi-modal Approach to Nonlinear Sloshing in a Rectangular Tank, *J. Fluid Mech.* Vol 432, pp 167-200

Hu, CH and Kashiwagi, M (2003) - Development of a CFD Simulation Method for Extreme Wave-Body Interactions, *Proc. 8-th Int. Conf. on Numerical Ship Hydrodynamics*, 22-25 September 2003, Busan, Korea, Vol 2, pp 50-57

Hu, CH, Kashiwagi, M and Kishev, ZR (2004-1) - Numerical Simulation of Violent Sloshing by CIP Method, *Proc. 19 IWWWFB*, Italy

Hu, CH, Kashiwagi, M (2004-2) - A CIP-based method for Numerical Simulation of Violent Free-Surface Flows, *J Mar Sci Technol,* Vol 9, No 4, pp 143-157

Kim, Y (2001) - Numerical Simulation of Sloshing Flows with Impact Load, *Applied Ocean Research*, Vol 23, No 1, pp 53-62

Kishev, Z, Hu, C, Kashivagi, M (2005) - Numerical Simulation of Violent Sloshing by CIP Method with Experimental Validation, *Proc. ISOPE'05, Seoul,* Korea, June 2005

Mikelis, NE, Miller, JK, Taylor, KV (1984) - Sloshing in Partially Filled Liquid Tanks and its Effect on Ship Motions: Numerical Simulations and Experimental Verification, *RINA spring meeting 1984*, paper No. 7

Tanaka, R, Nakamura, T, Yabe, T (2000) - Constructing exactly conservative scheme in a non-conservative form, *Comp Phys Communications*, Vol 126, pp 232-243

Xiao, F, Ikebata, A (2003) - An Efficient Method for Capturing Free Boundaries in Multi-fluid simulations, *Int J Numer Meth Fluids*, Vol 42, pp 187-210

Xiao, F, Yabe, T (2001) - Completely Conservative and Oscillationless Semi-Lagrangian Schemes for Advection Transportation, *J Comp Phys*, Vol 170, pp 498-522

Yabe, T, Xiao, F, Utsumi, T (2001) - The Constrained Interpolation Profile Method for Multiphase Analysis, *J Comp Phys*, Vol 169, pp 556-593

Yabe, T et al. (1991) - Unified Numerical Procedure for Compressible and Incompressible fluid, *J Phys Society of Japan*, Vol 60, pp 2105-2108

RANS Based Analysis of Roll Damping Moments at Bilge Keels

Florian Kluwe (kluwe@tu-harburg.de), Daniel Schmode, Gerhard Jensen

Introduction

The simulation of ship motions in seaways gets increasing relevance for the evaluation of ship safety. Usually the hydrodynamic forces are calculated with potential flow methods. The damping forces of the roll motion, in particular those of the bilge keels can be considered only by empirical methods. These are based on experiments and estimations, for example obtained by using plates in transverse flow. In this paper various results of instationary flow calculations by means of RANS-simulations are presented for different bilge keel configurations. Using these results regression formulas for the damping work can be determined. Subsequently the nonlinear damping coefficients can be gained.

Model

In order to find results, which are not influenced by a specific hullform, a simple cylindrical hull section was used for the parameter studies. Using such a form furthermore omits all interactions between the forces at the bilgekeel and the forces on the main hull. Additionally a parallel midship section was used to investigate the influence of different bilge radii on the damping forces. Another practical advantage of these simple models is that they are easy and quickly to variate. All numerical models have full scale size. The length of the computational domain is 60 meters. The Radius of the cylindrical cross section is 13 meters, whereas the outer boundary of the computational grid extends to a radius of 53 meters. This gives a 40-meter water layer above the hull surface. No free surface is considered in the simulation, assuming that the bilge keels are always sufficiently submerged.

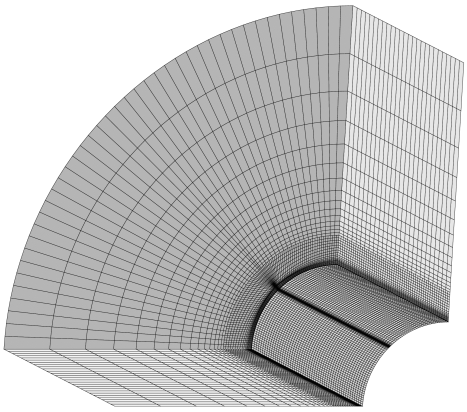

Figure 1: Perspective view of the model with cylindrical cross section

Therefor the water surface is treated as symmetry plane. Also symmetry can be found at the ship's centre plane. For the models with a cylindrical cross section these two symmetry planes

are identical, which reduces thecomputational domain to a quarter of the full model. Figure 1 shows the numerical grid of such a variation.For the ship-like cross sections one half of the full model has to be calculated, because the four symmetry planes differ from each other. Therefor only the water plane is used as a symmetry-boundary. Figure 2 for example shows such a numerical grid for a hull section with a 4m bilge radius.

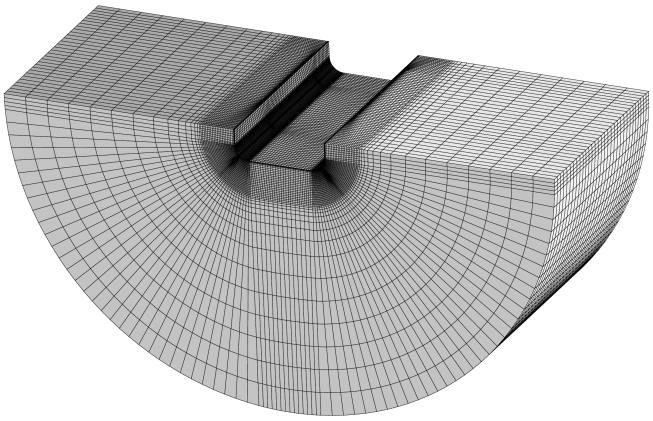

Figure 2: Finite Volume grid of hull section with 4m bilge radius

The hull sections described above, are fitted with various different bilge keels.Three main types of bilge keels are investigated (Figure 3): One type consists of a continuous bilge keel throughout the whole domain. In this case no leading and trailing edges exist within the model. The second type contains a continuous bilge keel, which starts and ends within the boundaries of the computational domain. The third type consists of two consecutively placed bilge keels.This type is used to investigate the effects of a interrupted bilge keel on the roll damping, because this type of bilge keels is widely used by shipyards. Within these three main types the length, height and gap width of the bilge keels are systematically variated. The calculations for the different bilge keels are repeated with various roll periods and roll amplitudes. A block-structured grid

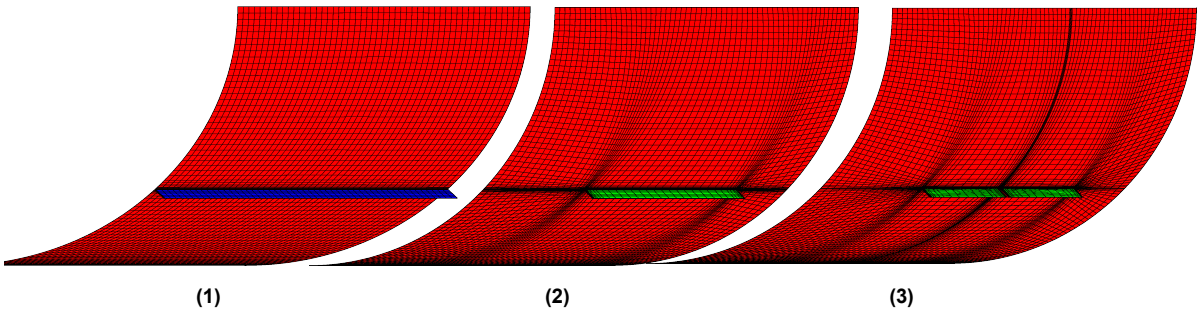

Figure 3: The three main types of bilge keels investigated

with refinement towards the hull surface is used. The highest grid resolution is concentrated around the bilge keels, because it is important to capture the flow in this area as detailed as possible in order to get satisfying results for the calculated forces. The overall number of

cells is limited by the computation time needed, as a large number of variations has to be investigated for the parameter studies.The rotational axis is fixed amidships in the waterplane level andoriented along the global x-axis. The roll motion of the ship (rotation around x-axis) is achieved by body forces, which lead to a periodic acceleration of the water in the computational domain.All borders of the numerical grid must be treated with boundary conditions, which have to be specified.Figure 4 shows the boundary conditions which are applied to themodel borders.If the ship moves with forward speed the forward and backward ends of the hullsection are modeled as Inlet, respectively Outlet boundaries. Otherwise Symmetry Planes on each end are used. The hull surface and the bilge keels are coveredwith a Noslip Wall boundary, which considers that there is no flow through thesurface. Additionally this boundary type considers the friction between wall and fluid (no tangential velocity on the surface). The outer border ismodeled with a Slip Wall.Due to the roll motion of the model and the resulting circular flow, the watersurface and the midship plane are connected as Cyclic Couples with each other.Turbulence is considered by a standard κ-ϵ-model. Due to the limited number of cells, the velocity distribution within the boundary layer near to the hull surface is modeled with a wall function.In order to consider the influence of the foreship, which is not included in the numerical grid, a logarithmic velocity profile, representing the foreship's boundary layer, is introduced at the inlet boundary.

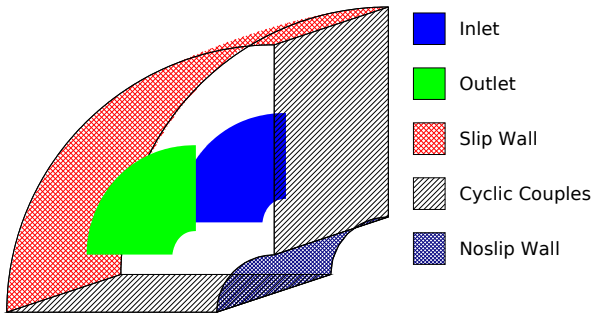

Figure 4: Boundary Conditions

Parameter Identification and Regression Model

The damping work is used as an integral value for the roll damping. To obtain the damping work the moments are integrated over a half period. Period and amplitude are the two characterising values for an oscillating motion, they determine the rotational velocity of the body. These two closely connected parameters are investigated together. Using the calculation results a nonlinear regression based on the least squares method delivers the following formula for the damping work:

$$W_D = c \cdot \frac{\hat{\varphi}^{2.51}}{T^{1.92}} \tag{1}$$

This relationship is valid, if the amplitude is given in degrees and the period in seconds.The correlation coefficient c is dependent on the bilge keel geometry. Figure 5 compares the calculated

values with the regression function for a bilge keel of 30 m length and 0.63 m height.

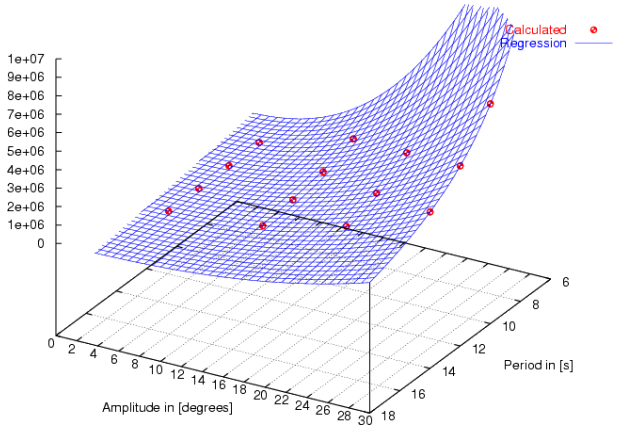

Figure 5: Damping Work in dependency of Amplitude and Period

As can be seen a good correlation is achieved. The average error is about 4 %, whereas the calculation results for small amplitudes and periods are met worse than in the medium and upper range.

Besides the kinematic factors amplitude and period the forces produced by a bilge keel are influenced by its geometry. First of all the geometry is described by the main parameters length and height. The results obtained from the RANS simulations approximately show a linear relationship between length and damping work (see Figure 6). Different lengths with and without forward speed are tested. The gradient is approximately the same for both cases, but the bilge keel with a forward speed component produces a larger damping work than without.

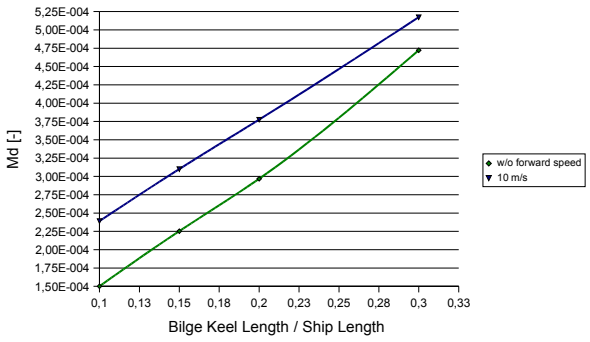

Figure 6: Damping Work in dependency of the bilge keel length

As for the length, the dependence of the damping work on the height is expected to be linear as well. This proves to be correct for moderate heights. The resultant damping work is significantly higher for large bilge keels than expected from the linear relationship. Therefore a potential regression function is applied to consider the bilge keel height in the overall regression model:

$$W_{D\,Sk} = c \cdot h_{Sk}^{1.5} \tag{2}$$

c again is the correlation coefficient.

Furthermore the relationship between the damping work on the one side and the bilge radius, the distance to the rotational axis and the forward speed on the other side are investigated.

All the relationships are composed to one overall regression formula. With this formula (Equation 3) it is possible to approximate the damping work for any given parameter configuration within a certain range of values.

$$W_D = 1.82E-3 \cdot \left(\frac{\hat{\varphi}^{2.51}}{T^1, 92}\right) \cdot l\, h^{1.5} \cdot r^{2.6} \cdot (13416 - 738 r_{Kimm}) + \left(8159.6 hv^{1.5}\right) \tag{3}$$

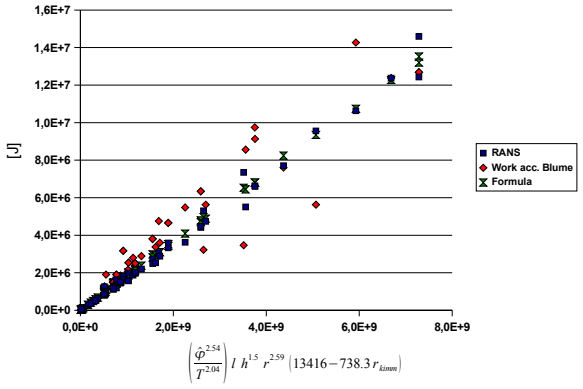

Figure 7: Damping Work obtained with RANS simulation compared with empirical methods

The influence of forward speed is considered as additive term due to two reasons. Firstly the damping work must not be zero for the cases without forward speed and secondly the forward speed causes lift at the leading edge of the bilge keel and thus is independent of other geometry parameters except the height. The part in the brackets containing r_{Kimm} represents the linear dependence on the bilge radius. The factors further left consider the geometric dependences and finally the relationship between amplitude and period. All parameters must be put into the formula with dimensions. Geometric values in meters, speed in meters per second, the amplitude in degrees and time dependent values in seconds. The damping work then is obtained in Joule. Figure 7 compares the results from the RANS simulations with those calculated with the regression formula and those delivered by another empirical prediction method, which is used by *Blume* [1]. The error between the regression formula and the RANS results averages 10%.

References

[1] Blume, P.: *Experimentelle Bestimmung von Koeffizienten der wirksamen Rolldämpfung und ihre Anwendung zur Abschätzung extremer Rollwinkel*, Schiffstechnik Band 26, 1979

[2] Kumar B. Salui, Vladimir Shigunov, Dracos Vassalos: *A RANS Based Prediction Method of the Ship Roll Damping with Forward Speed*, 6th NuTTS, Rome 2003

[3] Kumar B. Salui, Tanmay Sarkar, Dracos Vassalos: *An Improved Method for Determining Hydrodynamik Coefficients in Roll Motion Using CFD Techniques*, Schiffstechnik Bd. 47, 2000

[4] O. Grim, P. Blume, H.G. Hattendorff: *Ermittlung der Rolldämpfung von Schiffen*, Hamburgische Schiffbau - Versuchsanstalt, Bericht Nr. S 97/76, 1976

[5] Kröger, Peter:*Simulation der Rollbewegung von Schiffen im Seegang*, Institut für Schiffbau der Universität Hamburg, Bericht Nr.: 473, 1987

[6] Müller, Volker: *Theoretische und experimentelle Untersuchungen zur Zähigkeitsbedingten Rolldämpfung an Spantformen mit Schlingerkielen*, Schiffbauforschung, Heft 1, pp. 14-24, 1987

Flow simulation around ship hulls with appendages in towed and self-propelled conditions

Hiroshi KOBAYASHI, National Maritime Research Institute, hiroshi@nmri.go.jp
Takanori HINO, National Maritime Research Institute, hino@nmri.go.jp
Munehiko HINATSU, National Maritime Research Institute, hinatsu@nmri.go.jp

Modern ship hulls have a complicated shape and their geometry becomes more complex with the presence of propeller shaft, rudders and various appendages. Unstructured grid based methods are expected to be one of the most powerful approaches for a practical design application because of its flexibility to cope with such complex geometry. In the present paper, an unstructured grid based Navier-Stokes solver is presented and it is applied to the flow simulations around two different ships with appendages in towed and self-propelled conditions. Numerical results of both ships are compared with experimental data and the applicability of the present method to practical ship hull form designs is examined.

1. Introduction

Modern ship hull forms equipped with bulbous bow and/or transom stern have a complicated shape and their geometrical complexity is further increased with the presence of propeller shaft and rudders together with various appendages. Therefore, ship hull design tools should be able to cope with bodies of complex geometry.

In various fields of fluid engineering, CFD (Computational Fluid Dynamics) is extensively used both for researches and for designs. However, it is difficult to generate a single structured grid that can cope with such complex geometry. Multiblock structured grid methods, the Chimera overlapping grid method or unstructured grid methods are proposed to solve the problem. Among them Unstructured grid methods are expected to be one of the most powerful CFD approaches for use of practical design application due to its flexibility of handling complex geometry.

In the ship design process, it is very important to determine the specification of engines. Thus, tank tests not only in towed condition but also self-propelled condition are usually performed to estimate the powering performance. It is required for CFD software to be able to deal with both conditions so that it occupies the firm position in the ship design process.

In view of these situations, the unstructured grid based Navier-Stokes solver for computing turbulent viscous flows, called **SURF** [1] is under development at National Maritime Research Institute (NMRI).

Outline of the numerical method is described first. Numerical simulations are carried out for two different types of hull forms in towed and self-propelled conditions. Numerical results are compared with the experimental data.

2. Numerical Procedure

The Navier-Stokes solver **SURF** is under development at National Maritime Research Institute. The governing equations are the three dimensional Reynolds averaged Navier-Stokes equations for incompressible flows. Coupling between pressure and velocity is made by artificial compressibility approach.

The Spalart-Allmaras model with the axial vortex correction [2] is adopted as a turbulence model. A body force model is adopted for propeller effects, and a multigrid method is used for getting fast convergence.

2.1 Governing Equations

The governing equations can be written in a vector form as

$$\frac{\partial \boldsymbol{q}}{\partial t} + \frac{\partial (\boldsymbol{e} - \boldsymbol{e}^v)}{\partial x} + \frac{\partial (\boldsymbol{f} - \boldsymbol{f}^v)}{\partial y} + \frac{\partial (\boldsymbol{g} - \boldsymbol{g}^v)}{\partial z} = 0 \quad (1)$$

where

$$\boldsymbol{q} = [p \quad u \quad v \quad w]^T$$

is the vector of flow variables which consist of p, pressure and (u, v, w) , the (x, y, z)-components of velocity. The inviscid fluxes $\boldsymbol{e}$, $\boldsymbol{f}$, and $\boldsymbol{g}$ are defined as

$$\boldsymbol{e} = \begin{bmatrix} \beta u \\ u^2 + p \\ uv \\ uw \end{bmatrix}, \boldsymbol{f} = \begin{bmatrix} \beta v \\ vu \\ v^2 + p \\ vw \end{bmatrix}, \boldsymbol{g} = \begin{bmatrix} \beta w \\ wu \\ wv \\ w^2 + p \end{bmatrix}$$

where β is a parameter for artificial compressibility. $\boldsymbol{e}^v$, $\boldsymbol{f}^v$, and $\boldsymbol{g}^v$ are the viscous fluxes:

$$\boldsymbol{e}^v = \begin{bmatrix} 0 \\ \tau_{xx} \\ \tau_{xy} \\ \tau_{zx} \end{bmatrix}, \quad \boldsymbol{f}^v = \begin{bmatrix} 0 \\ \tau_{xy} \\ \tau_{yy} \\ \tau_{yz} \end{bmatrix}, \quad \boldsymbol{g}^v = \begin{bmatrix} 0 \\ \tau_{zx} \\ \tau_{yz} \\ \tau_{zz} \end{bmatrix}$$

where

$$\tau_{ij} = \left(\frac{1}{R} + \nu_t \right) \left(\frac{\partial u_i}{\partial x_j} + \frac{\partial u_j}{\partial x_i} \right) \quad (2)$$

R is the Reynolds number defined as $R = \frac{U_0 L_0}{\nu}$ where ν is the kinematic viscosity. ν_t is the non-dimensional kinematic eddy viscosity which is determined by the Spalart-Allmaras one equation model.

2.2 Spatial Discretization

Spatial discretization is based on a finite volume method for an unstructured grid. In the present approach, a cell centered layout is adopted in which flow variables $\boldsymbol{q}$ is defined at the centroid of each cell and a control volume is a cell itself. Cell shapes the present solver can cope with are tetrahedron, prism, pyramid, or hexahedron and face shapes are either triangular or quadrilateral. These four types of cells give larger flexibility in handling complex geometries.

Volume integration of Equation(1) over a cell yields

$$\iiint_{V_i} \left(\frac{\partial \boldsymbol{q}}{\partial t} + \frac{\partial (\boldsymbol{e} - \boldsymbol{e}^v)}{\partial x} + \frac{\partial (\boldsymbol{f} - \boldsymbol{f}^v)}{\partial y} + \frac{\partial (\boldsymbol{g} - \boldsymbol{g}^v)}{\partial z} \right) dV = 0 \quad (3)$$

The first term in the integral can be expressed as the time derivative of the product of the cell volume V_i and the cell averaged value of flow variables $\boldsymbol{q}_i$, since the grid is stationary in the current applications. The remaining terms are converted into surface integration over cell faces using the divergence theorem. This yields the semi-discrete form of the governing equation as follows,

$$\frac{\partial (V_i \boldsymbol{q}_i)}{\partial t} + \sum_j \boldsymbol{F}_{(i+j)/2} - \sum_j \boldsymbol{R}_{(i+j)/2} = 0 \quad (4)$$

where i is a cell index and j is the index of neighboring cells of the cell i. $(i+j)/2$ denotes the face between cells i and j.

$\boldsymbol{F}$ and $\boldsymbol{R}$ are the inviscid and viscous fluxes defined as follows.

$$\boldsymbol{F} = \boldsymbol{e} S_x + \boldsymbol{f} S_y + \boldsymbol{g} S_z$$
$$\boldsymbol{R} = \boldsymbol{e}^v S_x + \boldsymbol{f}^v S_y + \boldsymbol{g}^v S_z$$

where (S_x, S_y, S_z) are the (x, y, z)-components of the area vector of a cell face in the direction from the cell i to the cell j.

2.3 Time Integration

The backward Euler scheme is used for the time integration in which the governing equation is written as

$$V_i \frac{\Delta \boldsymbol{q}_i}{\Delta t} + \sum_j \boldsymbol{F}^{n+1}_{(i+j)/2} - \sum_j \boldsymbol{R}^{n+1}_{(i+j)/2} = 0 \quad (5)$$

where

$$\Delta \boldsymbol{q} = \boldsymbol{q}^{n+1} - \boldsymbol{q}^n$$

and the superscripts denote the time step. Δt is time increment for local time stepping in which Δt is determined cell by cell in such a way that the CFL number is globally constant.

2.4 Turbulence Model

A turbulence model is essential for simulating high Reynolds number flows of practical interests. The simplest among various turbulence models are algebraic models or zero-equation models in which eddy viscosity can be computed with algebraic formula using velocity profile information. However, implementation of this kind of models on unstructured grids encounters difficulties because velocity profile is not easily defined without inherent grid structure.

One- and two-equation models are more suitable for unstructured grid methods although they require solution of one or two field equations which are an advection-diffusion equation with source term in addition to flow equations.

The Spalart-Allmaras model is a relatively recent one-equation eddy viscosity model and is local, in the sense that the equation at the point does not depend on the solution at other points, except for the near wall term. The model is derived from empiricism and arguments of dimensional analysis, Galilean invariance and selective dependence of the molecular viscosity. The empirical results used in its development are two-dimensional mixing layers, wakes and flat plate boundary layer flows, which can be considered to be the building blocks for aerodynamic flows. The model does not give good predictions in jet flows, but gives reasonably good predictions of the above calibrated flows and shows improvements in the prediction of flows with adverse pressure gradients compared with the k - ϵ and k - ω models.

The turbulent eddy viscosity production term in the Spalart-Allmaras model should be corrected to simulate the damping effect of the turbulence in the core of axial vortices. In a paper of Dacles-Mariani et al. [2], on an investigation for a rear-field of wingtip vortex, a newly proposed evaluation of the vorticity in the production term, is suggested. The advantage of this modification is that the eddy visocousity is reduced in the regions where the magnitude of the vorticity exceeds that of the strain rate, such as in the vortex core. This modified Spalart-Allmaras model is used in the present work.

2.5 Propeller Model

A body force model is employed to take into account a propeller effect in the Navier-Stokes computations. Body force distibutions are calculated using a simplified propeller theory [3] in which a propeller effect is represented by the vortices distributed on the panels tessellated on the whole propeller disc where the number of propeller blades is assumed to be infinite. Thrust and torque of a propeller are calculated from the vortex distributions as follows:

$$T = \int_{R_b}^{R_p} \left(\int_0^{2\pi} \Gamma(r,\theta)[V_\theta]_{(SP)} d\theta - \frac{1}{2} C_{PD} N \cdot c(r) \sqrt{1 + \left(\frac{h}{r}\right)^2} [V_{0x}]_{(SP)} [V_{0\theta}]_{(SP)} \right) dr \quad (6)$$

$$Q = \int_{R_b}^{R_p} \left(\int_0^{2\pi} \Gamma(r,\theta)[V_x]_{(SP)} d\theta - \frac{1}{2} C_{PD} N \cdot c(r) \sqrt{1 + \left(\frac{h}{r}\right)^2} ([V_{0\theta}]_{(SP)})^2 \right) r dr \quad (7)$$

where R_p and R_b are the radii of a propller and propeller boss, respectively. $[V_x]_{(SP)}$ and $[V_\theta]_{(SP)}$ are the inflow velocity components in x- and θ- directions and $[V_{0x}]_{(SP)}$ and $[V_{0\theta}]_{(SP)}$ are values averaged in θ direction. C_{PD} is the sectional drag coefficient of a propeller blade and N is the number of blades. $c(r)$ is a chord length at the radius $r = r$ and h is the pitch ratio fo the free vortices at $r = 0.7R_p$. $\Gamma(r, \theta)$ is the strength of bound vortices on the propeller panels which are obtained by solving the simultaneous equations derived from the propeller inflow velocities and a propeller operating condition.

The body force distributions are then obtained by

$$fb_x = \frac{\Gamma(r,\theta)[V_\theta]_{(SP)}}{r\Delta x} - \frac{\frac{1}{2}C_{PD}N \cdot c(r)\sqrt{1+\left(\frac{h}{r}\right)^2}[V_{0x}]_{(SP)}[V_{0\theta}]_{(SP)}}{2\pi r\Delta x} \tag{8}$$

$$fb_\theta = \frac{\Gamma(r,\theta)[V_x]_{(SP)}}{r\Delta x} - \frac{\frac{1}{2}C_{PD}N \cdot c(r)\sqrt{1+\left(\frac{h}{r}\right)^2}([V_{0\theta}]_{(SP)})^2}{2\pi r\Delta x} \tag{9}$$

y- and z- components of the body force can be computed from fb_θ above. In case a propeller is attached with a rake, an appropriate coordinate transformation is applied.

2.6 Multigrid

A multigrid method is known as the extremely efficient way to get fast convergence. The concept of a multigrid time stepping applied to the solution of hyperbolic equations is to compute corrections to the solution on a fine grid by the time-stepping on a coarser grid.

The multigrid for unstructured grids is not so trivial as its counterpart for structured grids, since the coarser grids cannot be generated easily. There are several ways to implement multigrid on unstructured grids. The one is an algebraic multigrid, in which coarse grid operators are constructed based on the algebraic equations of the finer grids and actual coarser grids are not required. In the other approaches, the coarser grids should be generated in one way or another. Several methods have been proposed for grid coarsening. In the present study, the agglomeration multigrid method [4] is adopted in which the coarse grids are generated by the agglomeration of the fine grid cells. The grid coarsening is performed using the algorithm similar to the one proposed in Okamoto et al. [5].

3. Computational Conditions

For high speed ships with twin propellers shafts and brackets configurations are commonly used stern layout. Hydrodynamic performances of such ships are largely dependent on the arrangement of appendages and CFD analysis is expected to give detailed flow field data required for optimal hull designs.

Table. 1: Principal particulars of Ship Models

Name	MS No. 635 (original)	MS No. 737 (modified)
L_{PP}	6.6560	6.6560
L_{DWL}	6.8695	6.8583
$B[m]$	0.9966	0.9410
$d[m]$	0.2492	0.2492
$D[m]$	0.3915	0.4627
C_b	0.4815	0.5053

Table. 2: Number of grid points and cells

Name		MS No. 635		MS No. 737	
		bare	appended	bare	appended
vertices		177K	925K	276K	1007K
cells	hexahedra	-	67K	-	66K
	prism	245K	1385K	414K	1547K
	pyramid	-	7K	-	8K
	tetrahedra	239K	820K	302K	804K
	total	484K	2279K	716K	2425K

Two ship models used in the present work are called "MS No. 635" and "MS No. 737" respectively. They are models of fast coastal ferries and principal particulars of them are listed in Table 1. "MS No. 737" is a modified hull form of "MS No. 635" with the aim of improving propulsive performance.

Following three cases are analyzed for both two models.

- bare hull in towed condition
- appended hull with shaft brackets and twin rudders in towed condition
- appended hull with shaft brackets and twin rudders in self-propelled condition

Free surface is not taken into account in the present study and Reynolds number based on L_{PP} of a ship is set 2.1×10^7.

Number of vertices and cells are shown in Table 2. A solution domain is a box shape which covers the left half of a whole domain since a flow field can be assumed to be symmetric. The inflow is one ship length in front of FP(bow) and the outflow is two ship lengths behind AP(stern). Both width and depth of the domain is two ship length. Thus, the solution domain is

$$-1.0 < x < 3.0, \quad -2.0 < y, z < 0.0$$

where the ship's FP on a water plane is the origin and (x, y, z), which is nondimensionalized by

L_{PP}, denotes downstream, starboard, and upward direction respectively. In case of a hull with appendages, the number of grid points and cells increase due to the complexity of a body. The grid for MS No. 737 with appendages is shown in Fig. 1.

4. Results and Discussions

4.1 Unpropelled conditions

Unpropelled conditions are simulated for both the bare hull and the appended hull. Surface pressure distribution of appended hulls of both MS No. 635 and MS No. 737 are shown in Fig. 2. Presence of rudders and brackets causes complicated pressure patterns on the hull surface. The form of appendages is changed from MS No. 635 to MS No. 737 in addition to the main hull modification. The computed results show the change of the surface pressure distribution due to the difference of the forms between two hulls.

In Fig. 3, computed nominal wakes at the propeller plane ($x = 0.98235$) are compared with the measured data in case of MS No. 737 with appendages. Although the actual propeller are attached with the rake angle of 2 degrees, the propeller plane here is defined as the vertical plane at the center of propellers. Note that measurements is carried out at the design Froude number of 0.3833, while the computations neglects the free surface effect($F_n = 0.0$).

The wake inside brackets is observed clearly and the cross flow vectors show a flow surrounding the propeller boss for both computed and measured results. There is a region where the axial velocity is over 1.0 outside the boss in the measurement. However, the corresponding high speed region in the computation is much smaller. The fact that rudders are not equipped in the measurement while the computation is with rudders may be the reason for this discrepancy. Detailed analysis of both numerical and measured data is required for full understanding of this discrepancy.

The form factors which correspond to viscous resistance are compared in Tables 3 and 4. For the bare hulls, the computed values of $1 + k$ of MS No. 635 and 737 give good agreements with the measured ones. For the appended hulls, although the computed values of $1 + k$ of both MS No. 635 and MS No. 737 are larger than the measured data, the resistance increase due to the appendages and the tendency of the resistance variaton due to the difference of the hull form are predicted reasonably Note that the grids for MS No. 635 and those for MS No. 737 are gen-

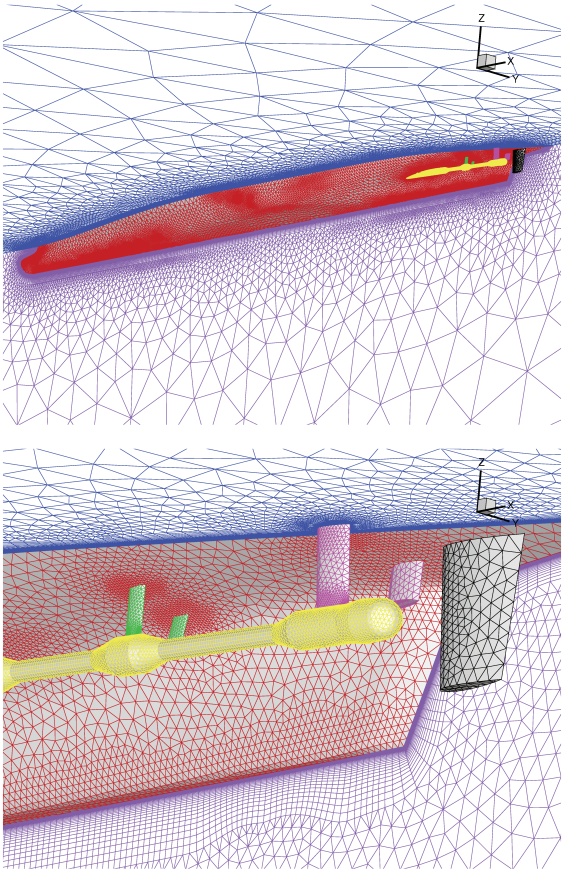

Fig. 1: Computational grid around MS No. 737 with appendages

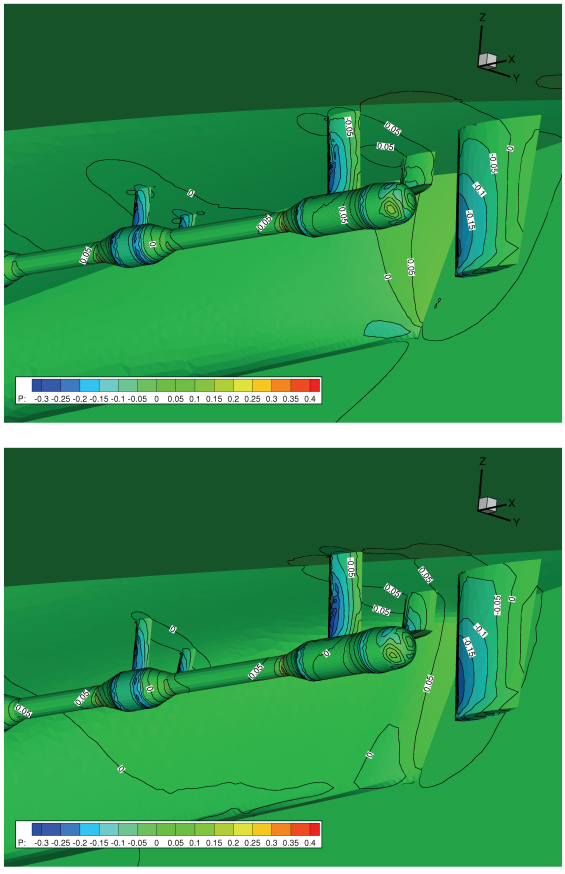

Fig. 2: Surface pressure distribution Top: MS No. 635, Bottom: MS No.737 ($\Delta\left(p/\rho U^2\right) = 0.1$)

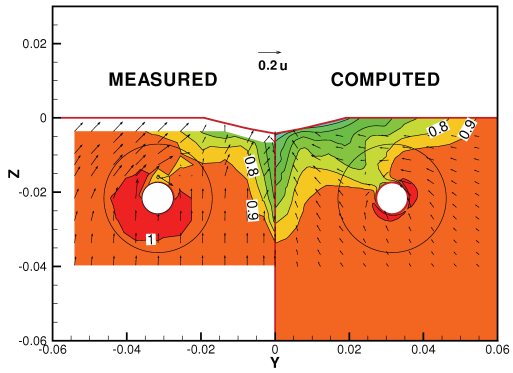

Fig. 3: Comparison of nominal wake at the propeller plane ($x = 0.98235$) for MS No. 737 appended hull ($\Delta u = 0.1$)

Table. 3: Comparison of form factors and nominal wake fractions about the bare hulls

	MS No. 635		MS No. 737	
	Measured	Computed	Measured	Computed
$1+k$	1.10	1.11	1.10	1.12
$1-w_n$	0.95	0.93	0.97	0.94

Table. 4: Comparison of form factors and nominal wake fractions about the appended hulls

	MS No. 635		MS No. 737	
	Measured	Computed	Measured	Computed
$1+k$	1.34	1.38	1.27	1.36
$1-w_n$	0.98	0.92	0.98	0.93

erated independently and the characteristics of grids are not necessarily the same.

Nominal wake fractions, which are the ratio of axial velocity inside the propeller disc to uniform flow are also compared in Tables 3 and 4. Tendency of nominal wake fractions between a bare and an appended hulls is not consistent between the measurements and the computations for both types of ships, because the high velocity region in a propeller disc is not reproduced in the computation as described earlier.

4.2 Self-propelled conditions

For the self propulsion conditions, the Reynolds number is set to be the same as the unpropelled condition. The computational grids are as same as unpropelled since flow is still symmetric due to the twin propellers.

The computation of a self propulsion condition uses the results of an unproplled condtion as an initial flow data. Then the propeller revolution number is changed automatically in order to match the propeller thrust to the ship drag at the ship point. Iterations are preformed until the propeller reolution number and the flow field converge. Self propultion factors are computed by the thrust identity method. In the simulations, the propeller rake angle of 2 degrees is taken into account and the body force components are transformed appropriately. Propeller shafts are fixed and the effects of their rotation are neglected. The principal particulars of the model propellers MP No. 411 and 412 are list in Table 5 .

Table. 5: Principal particulars of propeller model MP No. 411 and 412

MP No.	411	412
Diameter [m]	0.1944	
Boss Ratio	0.3	
Pitch Ratio at $0.7R$	1.4787	
Expanded Area Ratio	0.73	
Number of Blades	4	
Skew Angle [deg]	25.0	
Direction of Rotation	Right	Left
Blade Section	NACA	

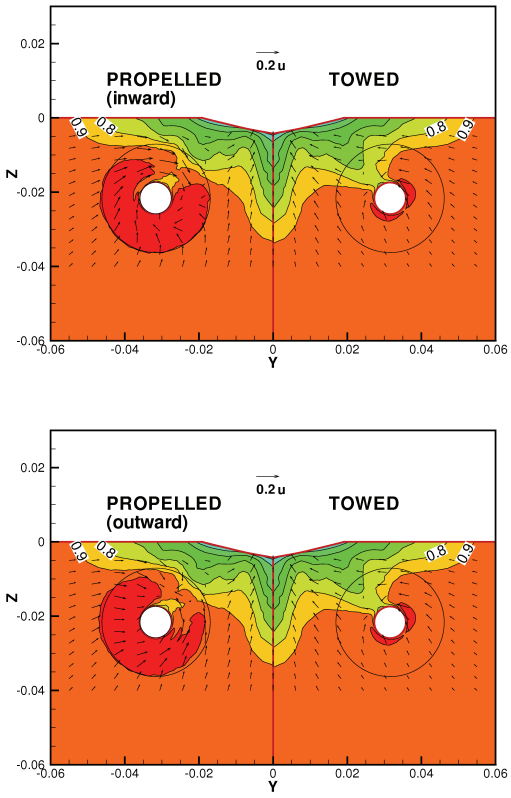

Fig. 4: Effective wake at the propeller plane ($x = 0.98235$) for MS No. 737. Top: inward, Bottom: outward ($\Delta u = 0.1$)

Two types of propeller operation models, the inward rotation mode and the ourward rotation mode, are simulated and the results are compared with the measurements.

Table. 6: Comparison of self propulsion factors MS No. 635

	Measured($Fn = 0.24$)		Computed	
	Inward	Outward	Inward	Outward
$1-t$	0.926	0.954	0.892	0.909
$1-w_t$	0.957	0.890	0.872	0.889
η_r	0.937	0.930	1.004	1.008
η_o	0.708	0.706	0.720	0.721

Table. 7: Comparison of self propulsion factors MS No. 737

	Measured($Fn = 0.24$)		Computed	
	Inward	Outward	Inward	Outward
$1-t$	0.909	0.960	0.894	0.921
$1-w_t$	0.952	0.911	0.886	0.914
η_r	0.942	0.973	1.002	1.033
η_o	0.705	0.707	0.721	0.722

The computed wake fields of MS No. 737 of both inward and outward modes at the propeller plane are shown in Fig. 4. Again, propeller plane is the vertical plane at $x = 0.98235$. The acceleration in the axial velocity in a propleller disc are apparent. Although swirling velocities due to propeller effects can be found to some extent, the vortical flow of the nominal wake (shown on a right side) is dominant and it compensates rotational motions of the propellller slipstreams.

Computed self propulsion factors of both MS No. 635 and 737 are compared with the measured data in Tables 6 and 7 . The measured data is for $F_n = 0.24$, while the computations assume $F_n = 0.0$. Therefore, the computed values of thrust required for self propulsion are different from those at the measurement. It yields that the computed thrust deduction factors $1-t$ are lower than the mesured ones. Also, as seen in the nominal wake comparison in Fig. 3, the wake fields of unpropelled conditions already show some differences. These differences may cause the inconsitent tendencies of inward and outward modes, or of two models MS No. 635 and 737 between computations and measurements.

5. Concluding Remarks

The unstructured grid based Navier-Stokes solver is applied to the flow simulations around ships with appendages. The numerical simulations can estimate surface pressure distribution on the hull and the appendages. Nominal wakes at the propeller plane can be obtained corresponding to the results of measurements. The computed values of the form factor are larger than the measured data especially in the case of the hulls with appendages, however the increase of resistance due to appendages are reasonably predicted by the computations.

The body force model is introduced to represent a propeller effect and it gives the results of self-propelled conditions for complex geometries and demonstrates its usability.

It can be concluded that use of unstructured grids allows the applications to the practical geometry such as a ship with shaft brackets and twin rudders. For future work, it is required to improve overall accuracy especially of nominal wake, and to perform combination tests for the propeller model and free surface model.

References

(1) Hino T., A 3D Unstructured Grid Method for Incompressible Viscous Flows, Journal of the Society of Naval Architects of Japan, Vol.182, pp.9 –15, (1997)

(2) Dacles-Mariani, J. et al, Numerical/experiment study of a wingtip vortex in the near field, AIAA J., Vol. 33 No. 9, pp. 1561-1568, (1995)

(3) Moriyama, F., On an Approximate Numerical Method for Estimating the Performance of Marine Propellers(in Japanese), Papers of Ship Research Institute, Vol. 16, No. 6, pp. 361-376 (1979)

(4) Mavriplis, D. J. and Venkatakrishnan, V., A 3D Agglomeration Multigrid Solver for the Reynolds Averaged Navier-Stokes Equations on Unstructured Method, AIAA Paper 95-0345, 33rd Aerospace Sciences Meeting and Exhibit, (1995)

(5) Okamoto, N., Nakahashi, K. and Obayashi, S., A Coarse Grid Generation Algorithm for Agglomeration Multigrid Method on Unstructured Grids, AIAA Paper 98-0615, 36th Aerospace Sciences Meeting and Exhibit, 1998

(6) Hirata,N. and Hino,T., A Comparative Study of Zero- and One-Equation Turbulence Models for Ship Flows, Journal of Kansai Society of Naval Architects, Japan, No.234, pp.1-8. (2000)

(7) Hino, T., Ohashi, K. and Ukon, Y., Flow computations around a ship with appendages by an unstructured grid based NS solver, Proc. The 8^{th} International Conference on Numerical Ship Hydrodynamics, Volume II, pp. 1-11., (2003)

Computation of the Viscous Free-Surface Flow around the Ship Model Free to Trim and Sink.

Marek Kraskowski,
Ship Design and Research Centre S.A., Poland.
marek.kraskowski@cto.gda.pl

The following paper describes an attempt on the RANSE computations of the viscous, free-surface flow around the free model in calm water, with the dynamic trim and sinkage taken into account. The COMET flow solver was used with some additional user coding which enabled evaluating the running attitude of the hull.

Computations including evaluation of the running attitude of the hull require higher computational effort than the computations for fixed model and thus, for low and moderate Froude numbers it is reasonable to neglect the dynamic trim and sinkage, especially in cases of comparing different versions of the same shape. For high Froude numbers, in order to estimate the resistance and the wave pattern properly, the running attitude of the hull should be taken into account. The presented computations were performed for the Froude number value range 0.3 – 0.6.

There are different methods for evaluation of the running attitude of the hull; one of them is to apply the moving mesh in the RANSE solver. The displacement of the hull is computed basing directly on the forces acting on the hull, obtained from the flow solver, and the entire mesh is moving together with the hull. The presented computations were focused on the steady-state solution for the fast ship in calm water, not on the exact simulation of the motion in time. In such case, some modifications of the motion equations could be done in order to improve the stability of the computation and to speed up reaching the steady running attitude by the hull.

A few methods of computing the position of the hull were tested; two of them were presented here. Before performing the computation for the ship hull model, the 2D test case was investigated in order to check out the correctness of the user coding: the solid body was submerged in the flowing water with some imposed initial trim and draught (the shape of the body and its initial position were shown in Fig. 1). The initial position of the body caused the unbalanced force and torque.

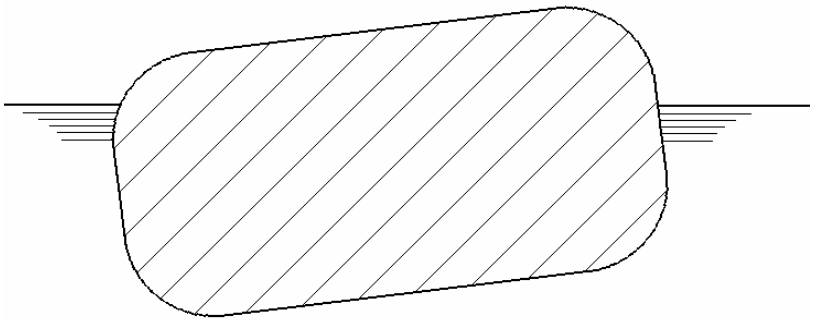

Fig. 1 2D test case.

The first procedure of evaluating the steady position of the body, tested for this case, could be shortly described as follows:

- The acceleration values, computed basing on the Newton's equations, were reduced by applying the artificial damping force, proportional to the velocity value.
- To improve the stability of the motion, two limitations of the acceleration were applied: first of them limits the maximum absolute value of the acceleration, the second one sets the acceleration to zero each time when it changes its sign in two subsequent time steps.

- The velocity increments in each time step was computed simply as $\Delta v = \Delta t \cdot a$, $\Delta \omega = \Delta t \cdot \varepsilon$, where v and ω were the translational and rotational velocities, a and ε were the accelerations and Δt was the time step.
- The translation and rotation increments were computed as $\Delta Z = \Delta t \cdot v$, $\Delta \varphi = \Delta t \cdot \omega$.

The second procedure could be summarized in following:
- The acceleration in each time step was computed as the arithmetic mean of the value from the previous time step and the value computed for the current time step. The maximum absolute value was limited.
- The velocity increments were computed as: $\Delta v = \alpha \cdot \Delta t \cdot a$, $\Delta \omega = \beta \cdot \Delta t \cdot \varepsilon$, where α and β are the factors between 0 and 1 [1]. If the absolute value of acceleration was smaller than some threshold value, the velocity increment was zero.
- The velocity value was set to zero each time when the acceleration value reached zero. This meant that the velocity was a discontinuous function of time.
- The translation and rotation increments were computed as in the previous method.

The time history of the rotational motion for these two methods (accelerations, velocities and translations) were presented in the Tab. 1.

Tab. 1 Motion history for two methods of evaluating the running attitude.

Procedure 1	Procedure 2
Rotational acceleration	
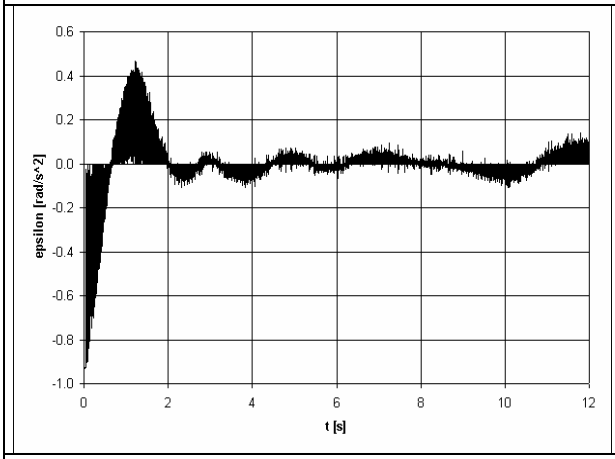	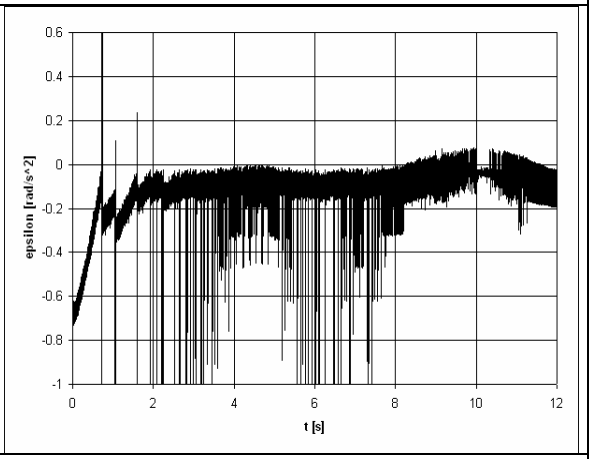
Rotational velocity	
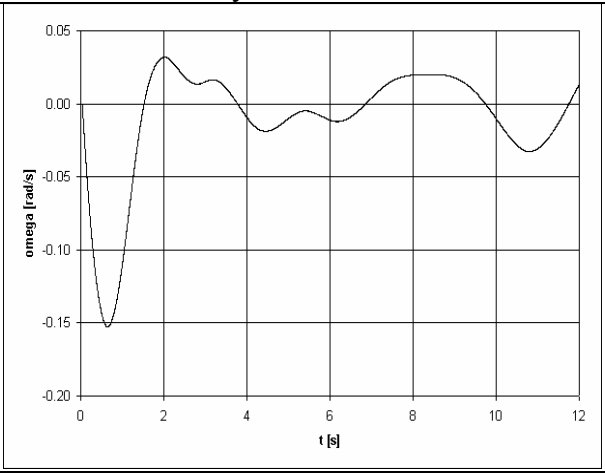	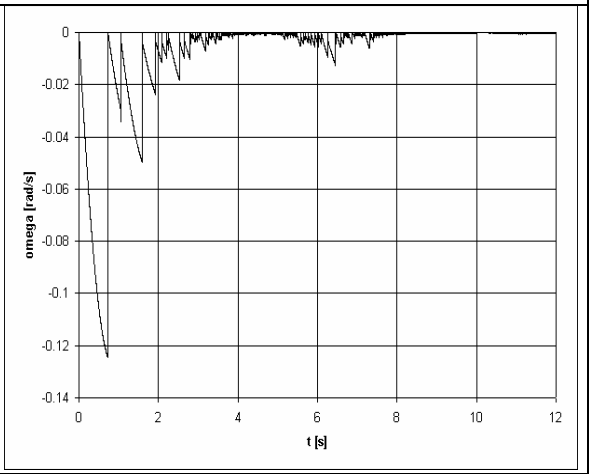

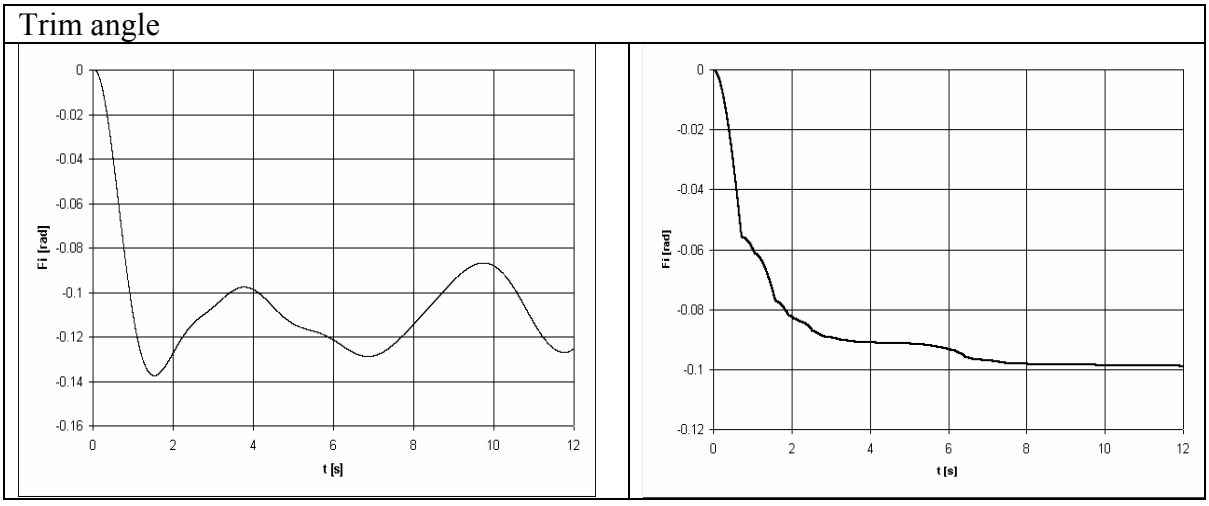

Based on the results of the test case computations, the second procedure of evaluating the running attitude was chosen for the computations of the ship hull model. The main particulars of the ship were summarized in Tab. 2.

Tab. 2 Main particulars of the ship.

Length b.p.	L_{PP}	135.250	m
Breadth	B	16.900	m
Draught	T	4.140	m
Block coefficient	C_B	0.443	-

The body lines of the ship were presented in Fig. 2.

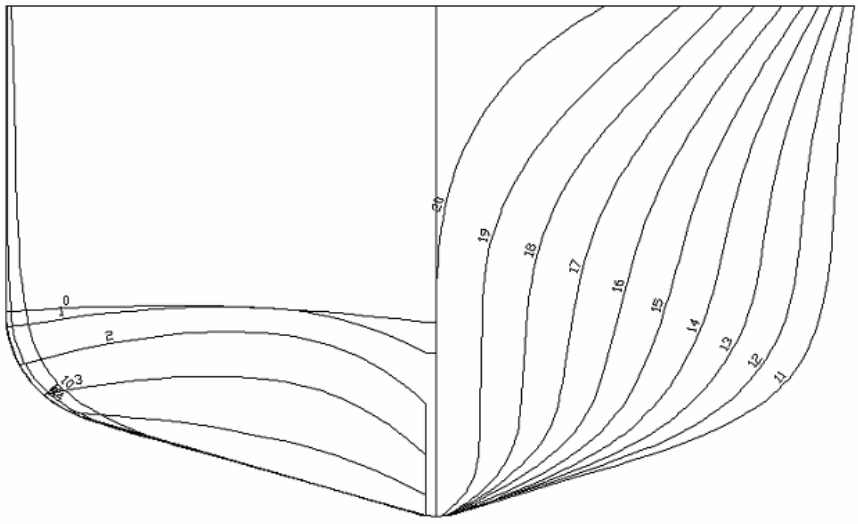

Fig. 2 Body lines of the hull.

The computations were carried out in model scale 1:20.92. The following procedure of computations was applied:

- The flow was initialized with uniform velocity, equal to the model speed.
- The calculation was started for the fixed model, one iteration per time step was performed.
- After stabilizing the wave pattern and forces for the fixed model, the model motion was released and the computation was carried on until stabilizing the ship attitude. The number of iterations per time step was increased to 5.

The time step value was about 0.001 – 0.002 s, depending on the Froude number. The RNG $k-\varepsilon$ turbulence model with standard wall functions was used, the $y+$ value on the hull surface was about 60.
The discretization scheme for the convective terms in momentum equations was First Order Upwind, after stabilizing the hull attitude it was switched to Second Order Central, blended with First Order upwind with the blending factor 0.9. It was found that the influence of the discretization scheme for momentum on the wave pattern shape decreased with increasing Froude number. The choice of the computation parameters was done on the basis of the results of earlier works [2].

The mesh was generated with ICEM CFD-Hexa generator. The mesh consists of 860 000 elements, the computational domain was rectangular and ranged 1L (model length) upstream, 2L downstream, 2L to the side and 1L below the hull. Because no drift was taken into account, only one half of the hull was considered. The surface mesh on the hull and the sections of the mesh interior were shown in figures 3, 4 and 5.

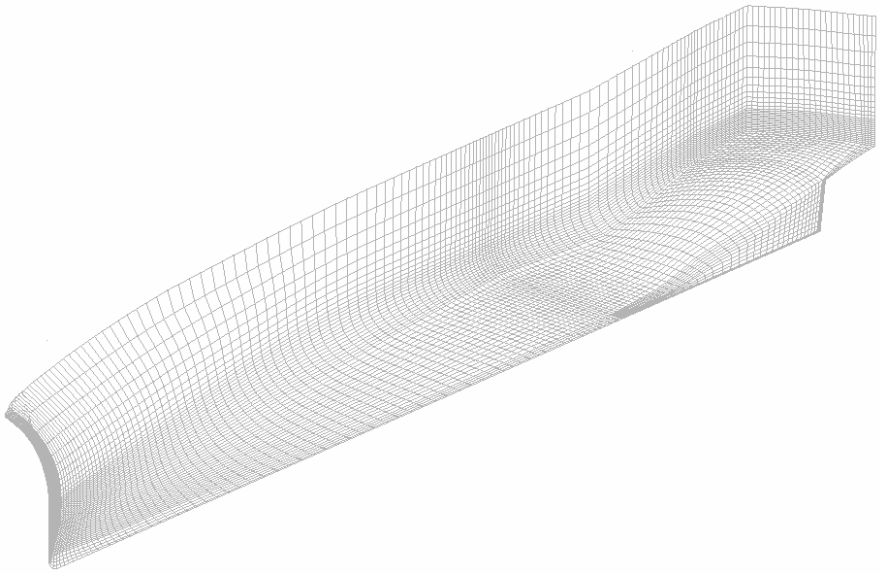

Fig. 3 Surface mesh on the hull.

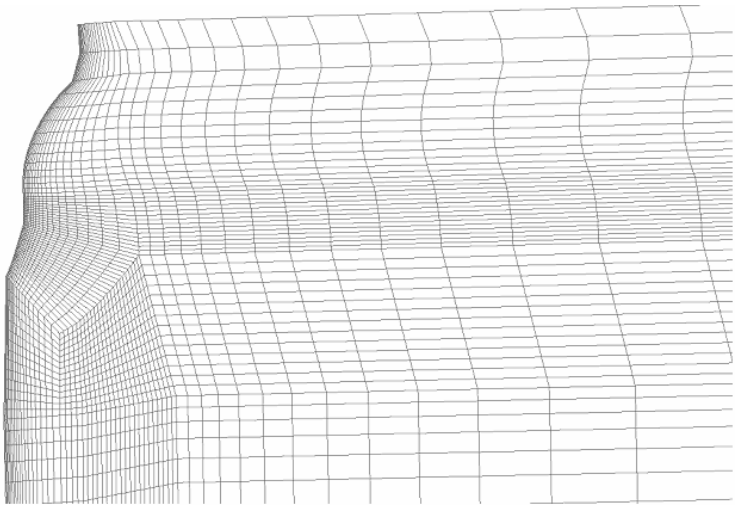

Fig. 4 Mesh interior – transversal section close to the model bow.

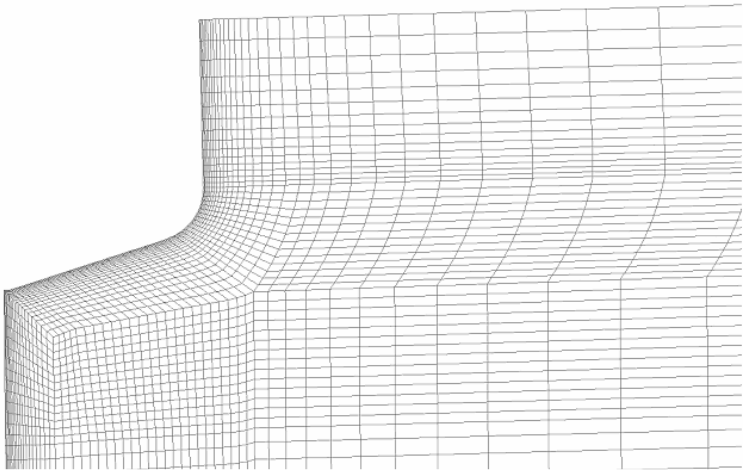

Fig. 5 Mesh interior – transversal section close to the midship.

The following boundary conditions were applied:

- Upstream and lower boundary of the domain: uniform velocity inlet, water volume fraction equal to 0 or 1 depending on the location of the initial free surface. The velocity vector direction depended on the trim angle.
- Downstream and upper boundary of the domain: given pressure value.
- Lateral boundary of the domain: slip wall.
- Hull surface: no-slip wall.
- Symmetry plane: zero normal velocity and normal gradients.

The computed wave patterns for particular values of Froude number are presented in Tab. 3.

Tab. 3 Computed wave pattern.

$F_n = 0.3$ 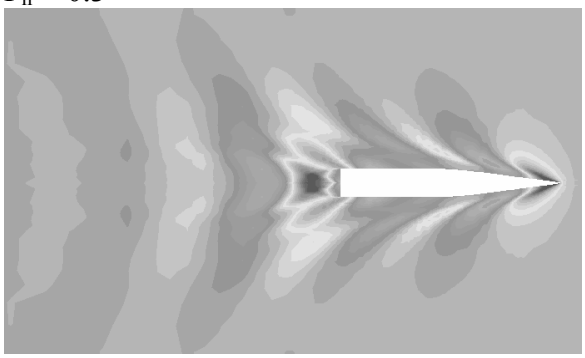	$F_n = 0.4$ 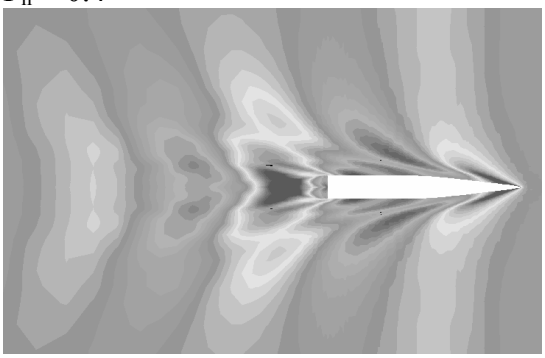
$F_n = 0.5$ 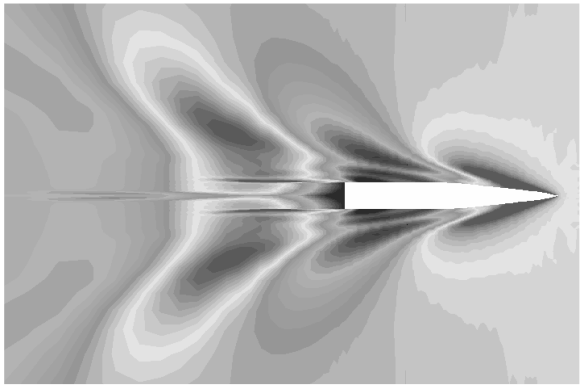	$F_n = 0.6$ 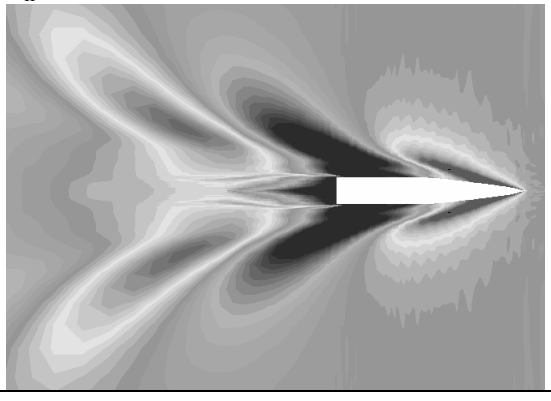

The convergence of the running attitude for the ship model was much worse than for the 2D body. There were no problems for the Froude number equal to 0.3 and 0.4, however, for larger values, the following problems were observed:

- Generating the additional wave of large length in the entire domain.
- Uplift of the water in the middle part of the domain.
- No convergence of the translational motion.

The further work' which is planned to be done, will be focused on the improvement of the method by applying the locally refined mesh, much denser in the hull surrounding and coarser in the outer parts of the domain. It is expected to obtain better accuracy of computing the hull attitude without significant increase of the overall number of cells.

References:

[1] Azcueta R., 2001, *"Computation of Turbulent Free-Surface Flows Around Ships and Floating Bodies"*, PhD thesis

[2] Kraskowski M., Bugalski T., 2005, *"Study of the computation parameters influence on the free-surface RANS computation results"*, NuTTS'05.

Study of the computation parameters influence on the free-surface RANS computations results.

Marek Kraskowski, Tomasz Bugalski

Ship Design and Research Centre S.A., Poland
marek.kraskowski@cto.gda.pl , tomasz.bugalski@cto.gda.pl

The Reynolds Averaged Navier-Stokes (RANS) equations are very useful in numerical analysis of the ship flow because of the accuracy of evaluating the wave pattern, ability to handle the complexity of the flow in the stern region and reasonable computational effort. However, some experience is necessary to minimize the influence of the mesh and the computational parameters on the results. The present paper shows the results of the computations carried out with the use of relatively coarse mesh (about 500 000 elements) and different values of parameters like time step, number of iterations per time step and under-relaxation factors in order to check their influence on the convergence and the results. The COMET flow solver was used for the computations.

The basic characteristics of the computational mesh were as follows:

- One half of the hull was considered due to flow symmetry.
- The computations were performed in model scale because of lower computational effort in comparison with full scale computations.
- The flow was computed in the rectangular domain surrounding the hull. The dimensions of the domain were shown in Fig. 1.

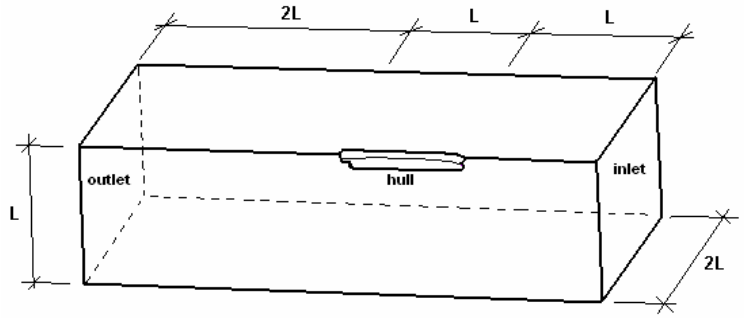

Fig. 1 Domain of the flow – shape and dimensions.

- Hexahedral mesh generated with ICEM CFD-Hexa was used.

The number of mesh cells was about 500 000. The surface mesh on the hull was shown in Fig.2. Main dimensions of the ship were given in Tab. 1.

Tab. 1 Main dimensions of the hull.

L_{PP} [m]	69.55
B [m]	6.58
T [m]	1.86
Model scale	1:10

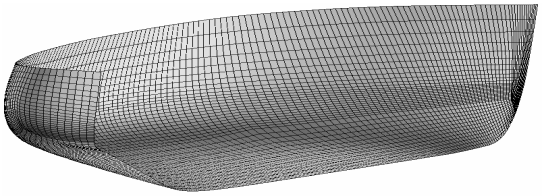

Fig. 2 Surface mesh for "Wrangel".

The computations were carried out for three values of the time step δt . These values were presented in Tab. 2, together with the non–dimensional values of the time step δt , defined as: $\delta t = \frac{\delta t \cdot V}{L}$ (V is the hull speed, and L is the hull length).

Tab. 2 Time step values.

δt [s]	δt [-]
0.01	0.002811
0.005	0.001405
0.0025	0.000703

The hull speed at model scale was set to $V = 1.955$ [m/s]

In general, the computations were performed with only one iteration per time step, with the exception of one computation, in which five iterations per time step were done.
The figures below show the time history of the forces acting on the ship hull for different time step values. Two components of the force were investigated: the friction force and the pressure force. The friction force showed minimal dependency on the time step (Fig. 3), thus only the pressure force was taken into account in further investigation.
The figures in Tab. 3 show the time history of the pressure force convergence for the specified values of the time step. One can see that, regardless of the time step value, no full convergence of the pressure force was obtained and thus, in the case like this, the constant oscillation of the pressure force must be treated as the converged solution.

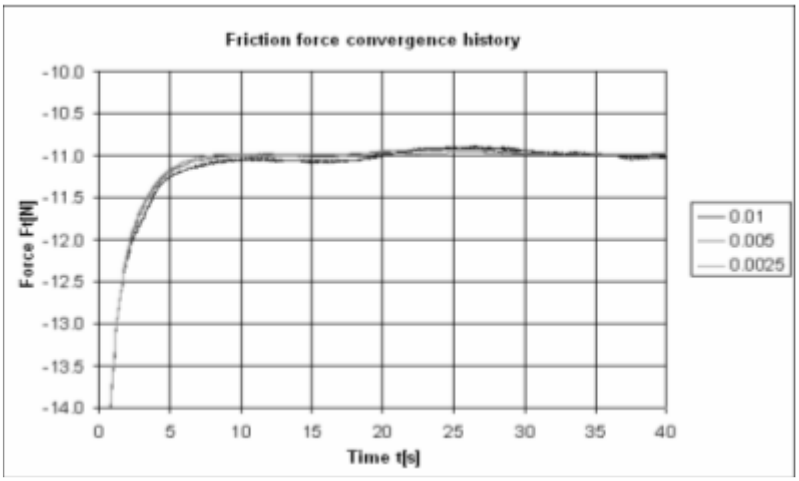

Fig. 3 Friction force convergence history for different time step values.

Tab. 3. Pressure force convergence for different time steps.

δt [s]	History of the pressure force convergence.
0.01	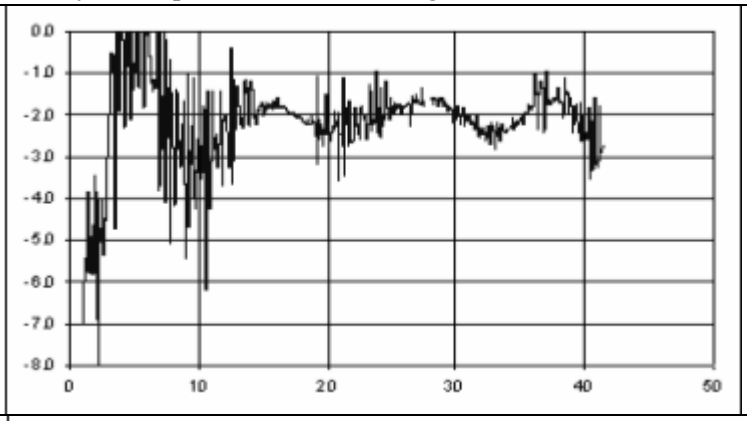
0.005	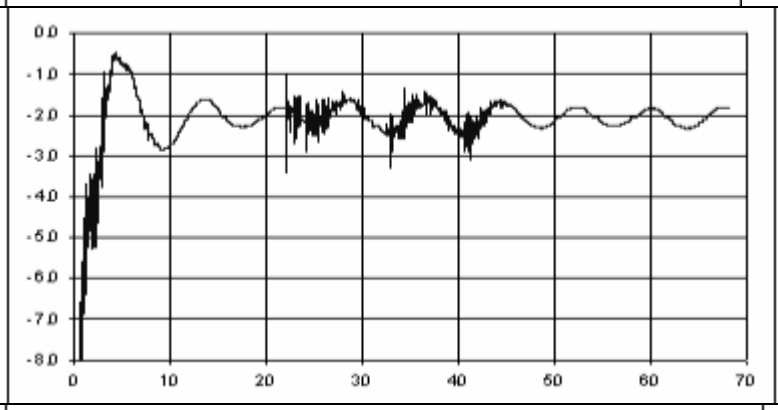
0.0025	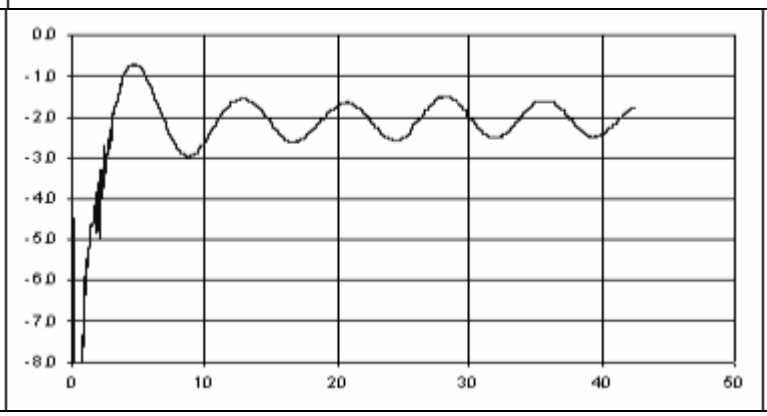

The table below present the CPU time for different time steps.

Tab. 4 Computation time for different time steps.

Time step δt [s]	Non-dimensional time step $\bar{\delta t}$ [-]	Time to simulate 40 s of the flow [h]
0.01	0.002811	7.87
0.005	0.001405	14.43
0.0025	0.000703	26.54

For the presented case, the lowest value of the time step seems to be the most appropriate, because the pressure force oscillations became constant after about 20 seconds of simulation and thus the computational time is shortest, although more time steps must be calculated to simulate the same flow time.

No dependency of the average pressure force on the time step value was observed, however it is proved that such dependency may exist, moreover, too small value of the time step can cause divergence of the solution.

During further investigation of the influence of the time step on the convergence, an attempt on the computation with the changing time step was done. In the beginning of the computations, the time step was set to 0.01s, after about 20 seconds of the simulation it was decreased to 0.0025s. The pressure force history for this simulation was shown in Fig. 4.
In this particular case, changing the time step during the simulation did not improve the time of convergence because of some shock appearing after reducing the time step – additional time is necessary to stabilize the flow.

One computation was done with five iterations per time step. The time step value in this case was 0.005s. The convergence history was shown in Fig. 5, together with the convergence history for the simulation with 1 iteration per time step.

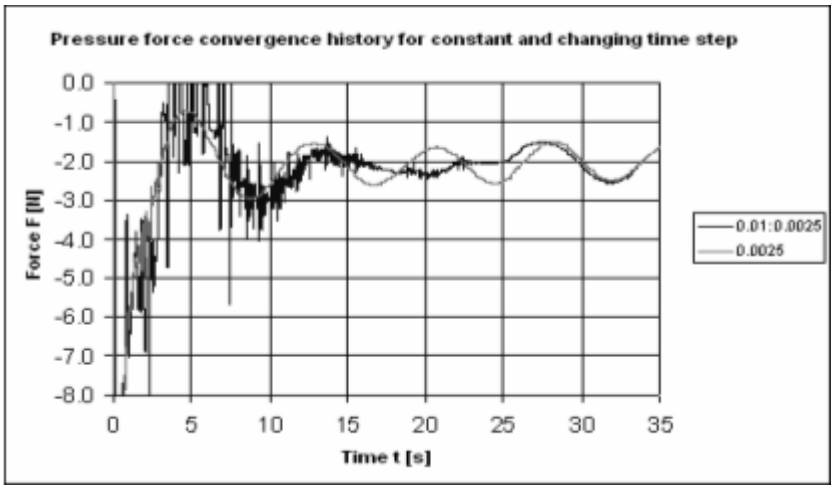

Fig. 4 Pressure force convergence history for constant and changing time step value.

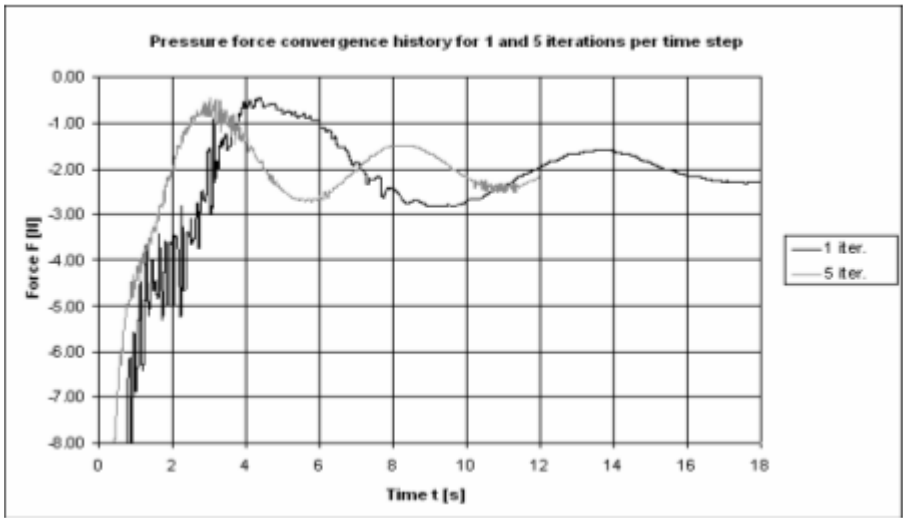

Fig. 5 Pressure force convergence history for 1 and 5 iterations per time step.

The effect of increasing the number of iterations per time step was similar to changing the time scale, but no reduction of the force overshoots was observed. The time necessary to simulate 12 seconds of the flow was given below.

Tab. 5 Computation time for 1 and 5 iterations per time step.

Number of iterations per time step	Time to simulate 12s of the flow, [h]
1	4.52
5	20.04

One can see that the amplitudes of the force overshoots are approximately the same for 1 and 5 iterations per time step, and thus executing 1 iteration per time step seems more reasonable in respect of the convergence speed.

The last parameter investigated in respect of the influence on the drag force convergence was the under-relaxation factor (URF) for the velocity. The URF is a factor used in the iterative algorithm of computing the flow. The velocity field in the current iteration is computed according to the eqn 1.

$$v_i^{new} = \alpha v_i + (1-\alpha) v_i^{n-1}$$

where v_i^{new} - velocity field that will be used in further iterating'

v_i - velocity field calculated in the current iteration'

v_i^{n-1} - velocity field from the previous iteration,

α - under-relaxation factor.

In the previous cases, the URF was equal to 0.5, in this case it was increased to 0.8.
The effect of changing the under-relaxation factor is show in the figure below.

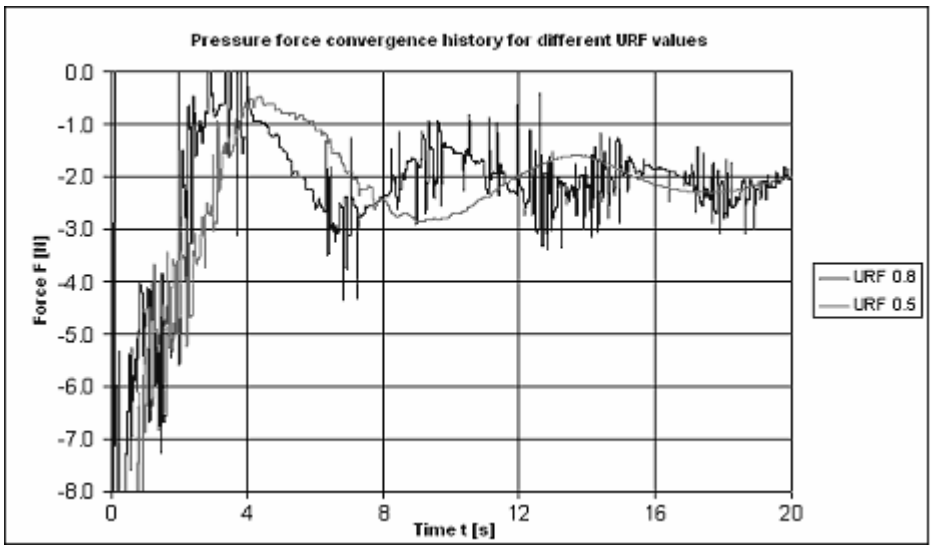

Fig. 6 Pressure force convergence history for different values of the velocity under-relaxation factor.

The effect of increasing the URF value was also similar to changing the time scale, but it also resulted in non-acceptable oscillations of the force.

The discretization scheme is the method of computing the flow parameters values on the cell faces basing on the values in the centre points of the cells. The face values are used in building the equations in the integrated form.
Figures in Tab.6. show the influence of the discretization scheme for convective terms in momentum equations on the wave pattern. "Comet" enables blending two discretization schemes in order to obtain the compromise between the stability and accuracy. In the presented case, the used schemes are First Order Upwind (robust, but diffusive) and Second Order Central (accurate, but causes problems with stability). The blending factor value equal to 0 means using the pure First Order Upwind, 1 means pure Second Order Central.

Tab.7. shows the influence of the discretization scheme for the volume of fluid equation. "Comet" uses special scheme for the volume of fluid, called High Resolution Interface Capturing scheme (HRIC). Due to stability reasons, the HRIC scheme can be blended with the First Order Upwind scheme. The blending factor equal to 1 means using pure HRIC.

Tab. 6 Influence of the discretization scheme for momentum on the wave pattern.

Blend. factor	Wave pattern.
0.0	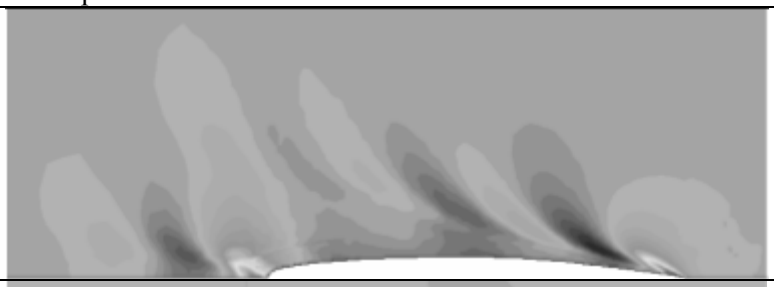
0.6	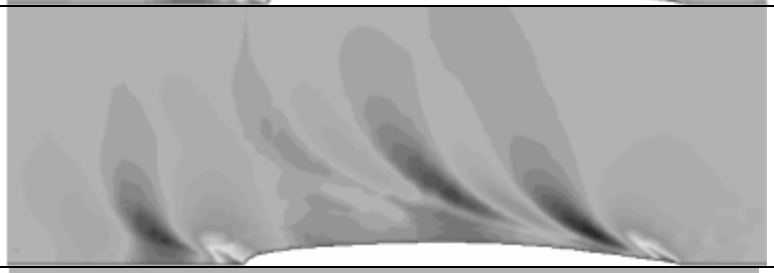
0.9	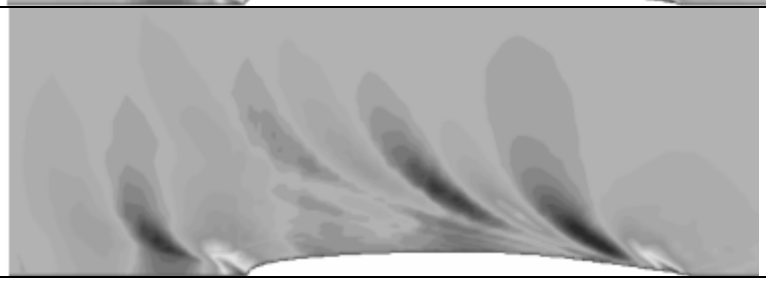

Table 7. Influence of the discretization scheme for VOF on the wave pattern.

Blend. factor	Wave pattern.
0.95	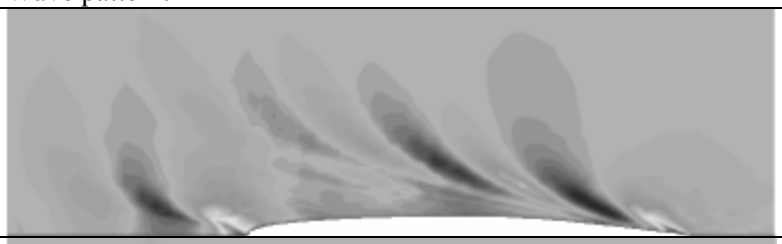
0.975	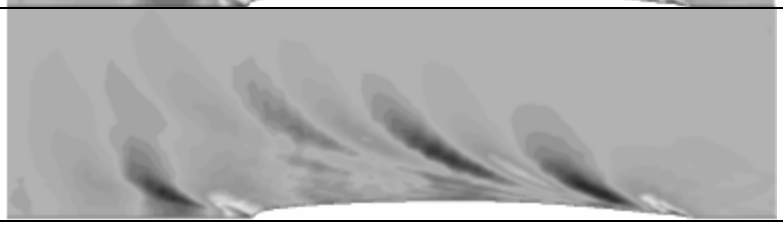
1.0	Solution diverged.

The following conclusions were done:

- The most efficient strategy for fast convergence in the investigated case was as follows: one iteration per time step, constant value of time step throughout the simulation, non-dimensional time step value equal to 0.0007.
- Increasing the under-relaxation factor for the velocity from 0.5 to 0.8 caused strong oscillations of the pressure force.
- The discretization scheme for momentum equations has significant influence on the wave pattern shape. Increasing the blending factor of the discretization schemes in the volume of fluid equation causes slight sharpening of the free surface shape, but using pure HRIC scheme caused divergence of the solution.

CFD Simulation of Oscillating Water Column (OWC)

Stefan Kyulevcheliev, Bulgarian Ship Hydrodynamics Centre, stefan.q@bshc.bg

Introduction

The Oscillating Water Column (OWC) is a wave energy harnessing method considered as one of the best techniques for converting wave energy into electricity.

OWC is economically viable design due to its simple geometrical construction and sufficient strength to withstand waves with different heights and different wave periods and directions.

The Oscillating water column (OWC) device comprises a partly submerged concrete or steel structure, open below the water surface, inside which air is trapped above the water free surface. The oscillating motion of the internal free surface produced by the incident waves makes the air flow through a turbine that drives an electric generator. The axial-flow Wells turbine, invented in the late 1970's, has the advantage of not requiring rectifying valves. It has been used in almost all prototypes.

There are a number of full sized OWC prototypes in Norway, Japan, India, Portugal, UK [1].

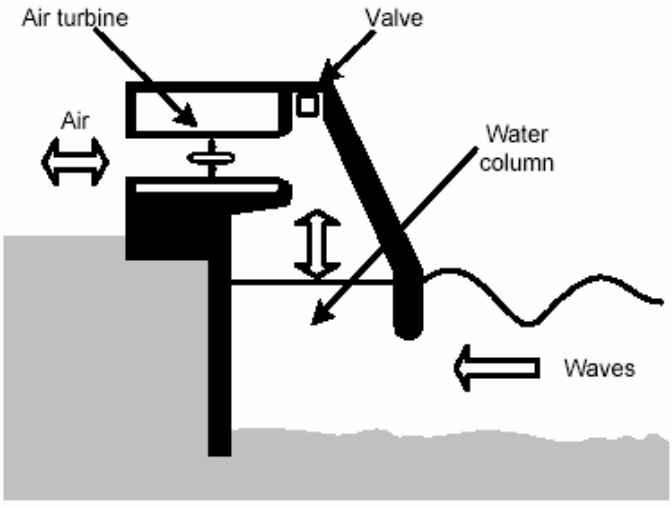

Fig. 1 Principle of OWC operation

In relation with BSHC's participation in a European project: Coordinated Action on Ocean Energy, (www.ramboll-wave.com), we carried out a small feasibility study of applying RANSE solvers to the simulation of Oscillating Water Column hydro- and aerodynamics and their applicability to parametric studies and optimization.

The commercial CFD solver FLUENT has been used. For solving the issue of major importance for the specific problem, i.e. the treatment of the free surface, the Volume of Fluid (VOF) model has been selected out of the multiphase options available in FLUENT.

Alongside all well known advantages of the VOF method, it is very useful for the OWC simulation, where we are interested in both water and air flows and, since the whole domain is considered with VOF, no special measures are needed for coupling or interfacing different models and methods for the two phases.

Simulation set-up

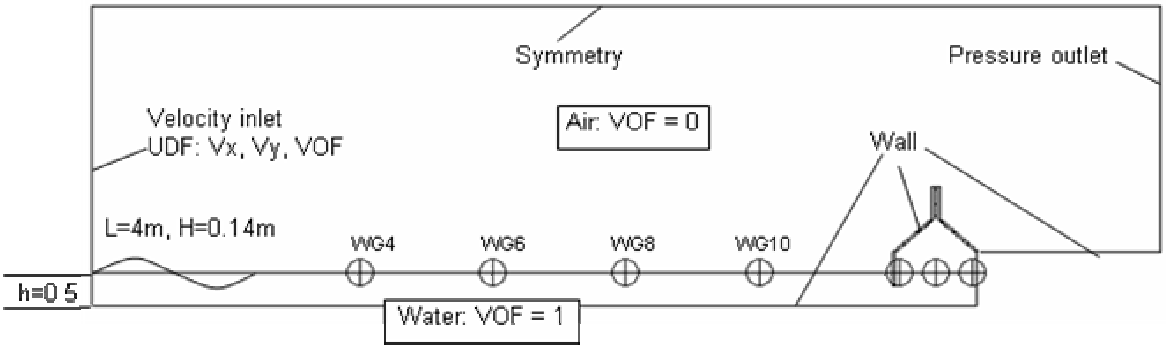

Fig. 2 Simulation set-up

Only 2D cases have been considered so far. The RANSE equations are being solved in transient mode. The classical k-ε turbulence model is used. Figure 2 shows the computational domain and the boundary conditions set.

The wave has been generated by imposing fluid velocities at the inlet boundary according to the wave theory for the corresponding water depth. The velocity profiles should match the instant location of the free surface at the boundary, which is also calculated and set (by prescribing the VOF variable) according to the wave theory.

This boundary conditions are enforced by a user defined function (UDF) called at each time step.

The initialization of the solution includes "patching" hydrostatic pressure and VOF=1 in the still water zone, VOF=0 in the air and gradual increase of the wave height from 0.

In the cases presented here the shown water depth and wave parameters have been considered.

The sketch in Fig 1 shows the "numerical wave gauges", i.e. the positions where the wave elevation has been monitored.

Fig 3. is a more detailed drawing of the first OWC case (called "long").

The dimensions of the OWC are quite arbitrary, constructed studying some publications on the topic [2], [3].

Three wave gauges have been installed inside the chamber and also three sections of the duct defined to monitor the air velocity and pressure in it.

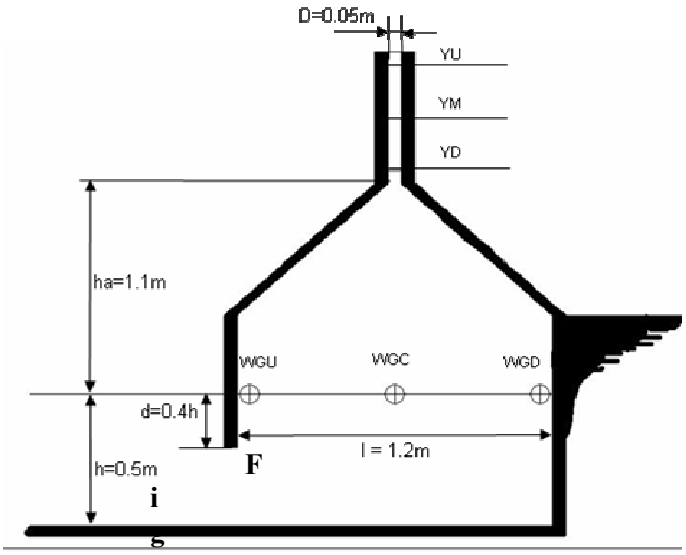

i g . 3 "Long" OWC

The average water level in the chamber has also been monitored. The code allows also monitoring the forces acting on the structure, though this is not discussed here.

Fig. 4 shows a record of the mean water level in the chamber and the incident wave (WG8) throughout 3 wave periods. From it we can deduce the so called capture factor, i.e. their ratio, to be 0.52.

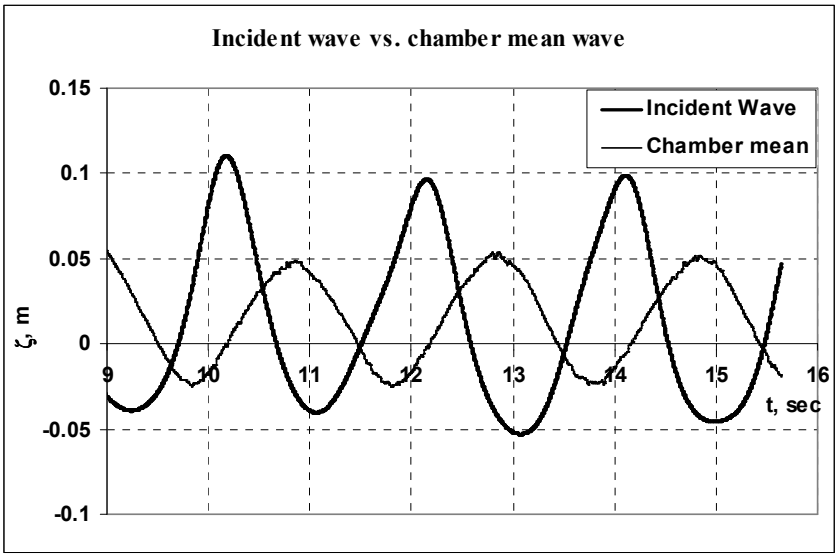

Fig. 4 Incident vs. chamber wave height

Fig. 5 presents the records in the three wave gauges inside the chamber confirming the complicated wave pattern in it: highest and almost sinusoidal wave at the downstream end, while the wave at the upstream end is the lowest and containing higher harmonics.

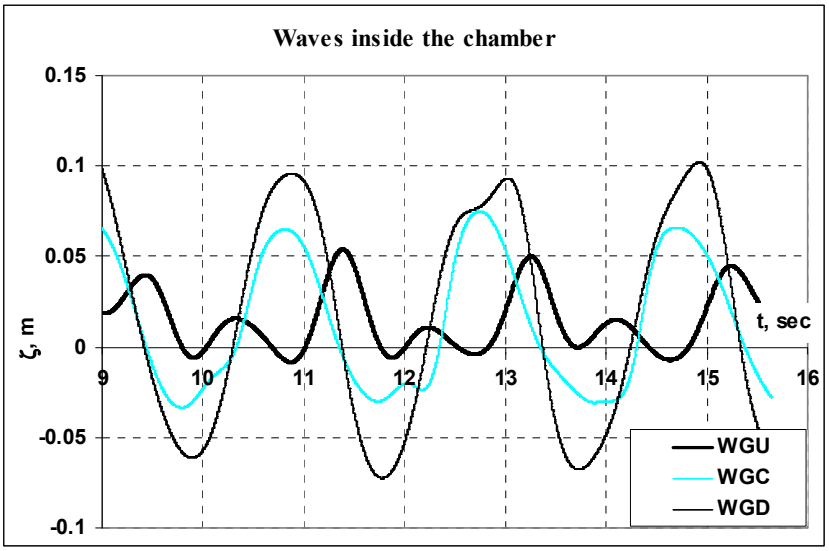

Fig. 5 Wave records inside the chamber

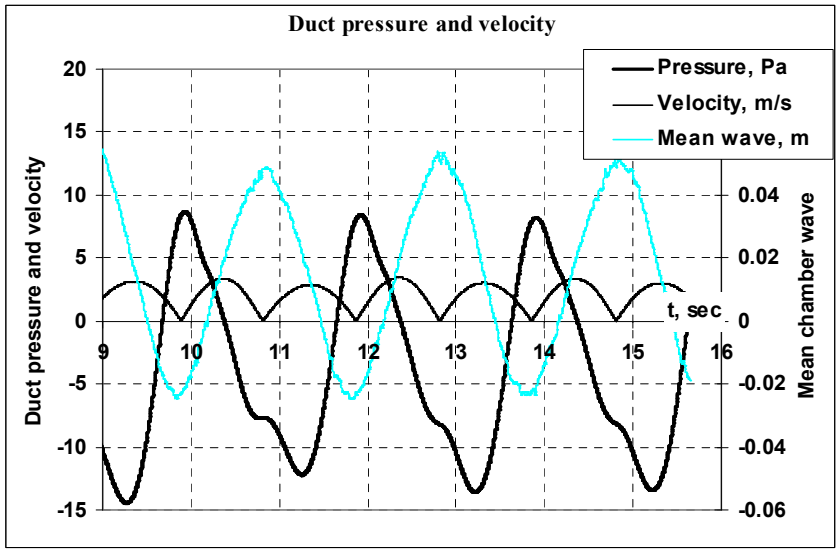

Figure 6 shows the pressure oscillations in the lowest section of the duct and the magnitude of air velocity. The mean wave in the chamber is also shown for referencing the timing of the phenomena.

We can see some signs of higher harmonics in the pressure oscillations as well.

Fig. 6 Pressure and velocity in the air duct

As a trial for a parametric study, a second case has been considered of a "short" chamber, see Fig. 7.

With all other parameters unchanged, the length of the chamber has been reduced by fixing a vertical rear wall and also the submergence of the front wall has been increased. These parameters are specifically indicated in the sketch and, according to [4], are among the most important optimization variables for an OWC.

There are only two wave gauges in that case.

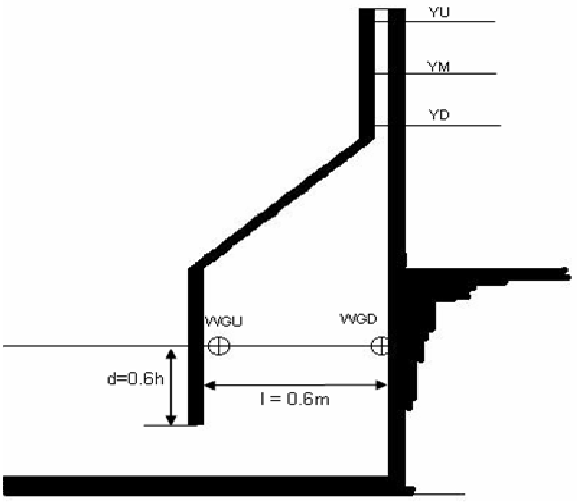

Fig. 7. "Short" OWC

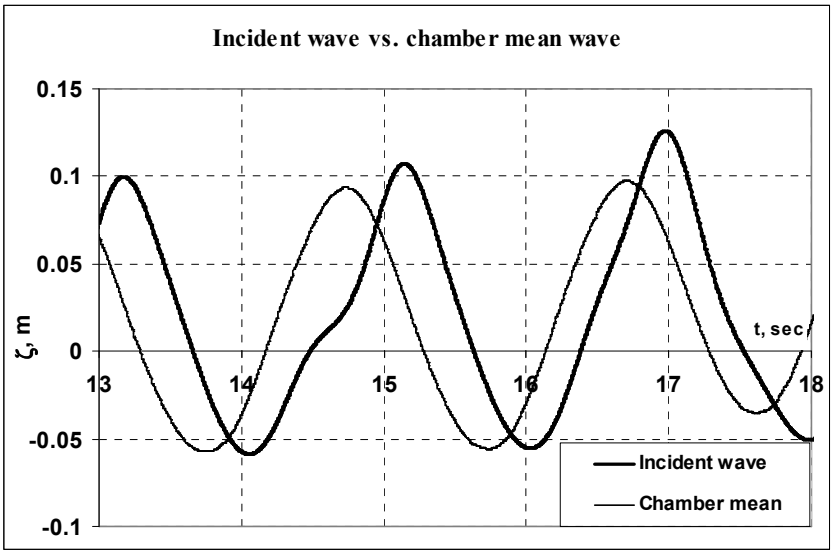

Similar comparison of the incident and internal wave height as in the first case shows a capture factor of 0.94 for this case.

Fig. 8 Incident vs. chamber wave height (short chamber)

The records of the two wave gauges show waves close to sinusoidal and of almost equal height.

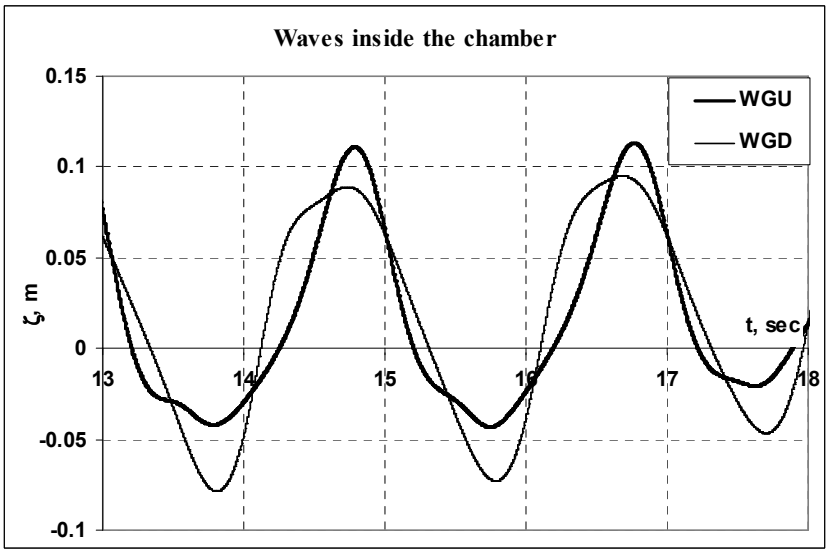

Fig. 9 Wave records inside the chamber (short camber)

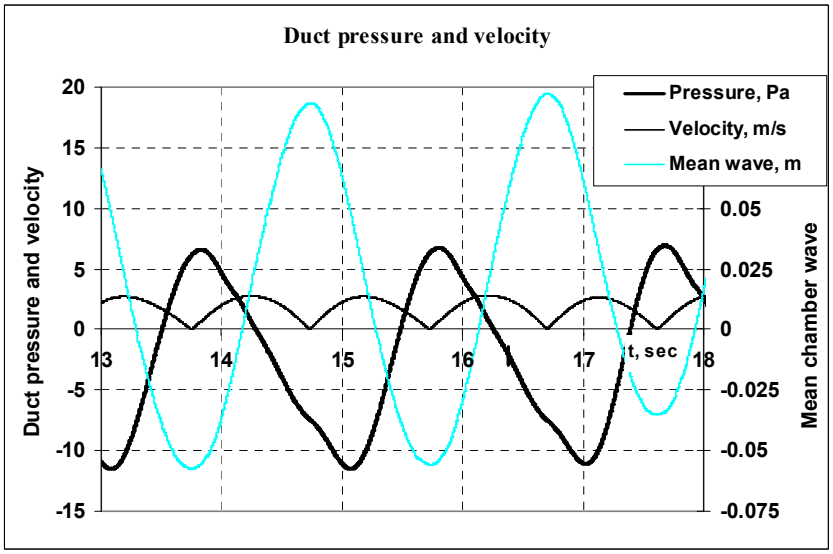

Fig. 10 presents the velocity and pressure oscillations.

One can see smoother (no higher harmonics) pressure oscillations.

Air velocity in the duct and the pressure difference are lower than in the first case, probably due to the higher orifice_diameter – to – chamber_length ratio.

Fig. 10 Pressure and velocity in the air duct (short chamber)

The CFD simulation provides all necessary data to estimate the efficiency of each OWC design.

Following [2], one way to do that is by relating incident wave power to the airflow power in the duct:

$$\eta = \frac{P_D}{P_W} \tag{1}$$

where P_W is the incident wave power

$$P_W = \frac{E_W}{T}$$
$$E_W = \frac{1}{2}\rho g L\left(\frac{H}{2}\right)^2 \tag{2}$$
$$L = \frac{gT^2}{2\pi} th\frac{2\pi h}{L}$$

and P_D is the airflow power in the duct

$$P_D = (p_D + \frac{1}{2}\rho_A v_A^2).|v_A|.D \tag{3}$$

The pressure p_D is taken to be the difference between the mean and the minimum of the calculated pressure.

The efficiency obtained in this way is: 21% for Case 1 and 14% for case 2.

The presented numerical results could be validated only by approximate comparison of the ranges of the obtained values with experimental data from [2] and [3].

Conclusions

The computations with the simple 2D cases demonstrate the feasibility of using CFD solvers and methods like the one presented here for OWC analysis and optimization. CFD simulation provides an abundance of data on the water and air flow difficult or too expensive to obtain experimentally.

Potential further developments on the topic could involve:

- Solving real 3D cases and validation of computational results with experiments;
- Perform systematic parametric studies of the effects of various design parameters and/or wave regimes on OWC performance;
- Incorporate turbine operation in the numerical analysis.

References

1. WaveNet, Results from the work of the European Thematic Network on Wave Energy, EC Project RK5-CT-1999-20001, 2000 - 2003

2. Electricity from Sea Waves, University of Michigan, College of Engineering, Department of Naval Architecture and Marine Engineering, http://www.engin.umich.edu/dept/name/research/projects/wave_device/wave_device.html

3. Graw K.-U., Scale 1:10 Wave Flume Experiments on IIT Oscillating Water Column Wave Energy Device, Bergische Universität Gesamthochschule Wuppertal, Germany

4. Weber J. W., G. P. Thomas, Hydrodynamic Aerodynamic Coupling of An OWC wave energy device: Some Results on System Performance with Wells & Impulse turbine.

ON TIME ACCURATE KINEMATIC BOUNDARY CONDITION IN SURFACE TRACKING CONTEXT

Tommi Mikkola[1]
Ship Laboratory, Helsinki University of Technology

1 INTRODUCTION

In the following, the numerical implementation of time accurate, kinematic free surface boundary condition for a surface tracking flow solver has been studied. Kinematic boundary condition states, that the velocities of the surface and the particles on the surface have to match. Hence, the implementation can be divided into two parts: the discretization of the normal component of the particle velocity on the free surface and the discretization of the velocity of the bounding surface. The former constitutes the steady state part of the equation, whereas the latter has, in principle, signifigance only in time accurate simulations, as in steady state the velocity of the surface vanishes. It is known from several reports, that special measures may be required to ensure a stable discretization of the steady state part of the kinematic boundary condition. In this paper it will be shown, that the implementation of the boundary velocity may in some cases affect the stability of the method as well.

2 NUMERICAL METHOD

A detailed description of the flow solver used is given elsewhere (see e.g. [6], [7]) and therefore only the main features of it are summarized here.

The numerical method is based on 2D unstructured FVM with triangular control volumes. A collocated SIMPLE-type pressure correction scheme is used for the solution of the bulk flow, with velocities and pressures stored at the cell centres. Free surface flows are simulated using a surface tracking approach, in which free surface deformation is solved from the kinematic boundary condition and dynamic boundary condition is coupled to the pressure correction equation. Grid updating is performed with a linear/torsional spring analogy [1], [2], with a Laplacian smoothing or with a combination of these two. Solution of time accurate flows is based on a dual time step approach, in which pseudo time derivatives are added into the unstedy flow equations and solution is iterated in pseudo time for each physical time step until these additional terms vanish.

2.1 Time accurate free surface boundary condition

A common approach with surface tracking methods is to only solve for the vertical movement of the free surface. In order to avoid some of the drawbacks of this approach – especially with extremely steep waves – the free surface is defined as a parametric curve $(h_x(s), h_y(s))$ deforming in the direction of the free surface normals. In the dual time stepping approach used the deformation of the free surface is thus solved from the kinematic boundary condition as

$$\frac{\partial h_i}{\partial \tau} = v_n n_i - \frac{\partial h_i}{\partial t} \,, \tag{1}$$

where h_i are the components of the free surface location defined at the centre of a free surface face. The deformations $\Delta h_i = \Delta h_n n_i$, with Δh_n being the deformation in the normal direction. τ and t are the pseudo and the physical time respectively, n_i are the components of the outward directed normal vector on a free surface face and $v_n = v_i n_i$ is the normal component of the velocity. For each physical time step (Δt) this equation is iterated with the momentum and pressure correction equations in pseudo time (with $\Delta\tau$) until a steady state is reached.

2.2 Discretization of the normal velocity

Several authors have suggested, that some numerical damping is included in the kinematic free surface condition by upwinding the slope of the free surface (see e.g. [3], [8]). Similarly, in this work optional, controlled, numerical

[1]Ship Laboratory, Helsinki University of Technology, Tietotie 1, FIN-02015 Espoo, Finland – E-Mail: Tommi.Mikkola@hut.fi
This work has been funded by the Graduate School in Computational Fluid Dynamics

damping is added into Eq. (1) through upwinding in the first term on the right hand side of the equation. Namely, by a simple manipulation of the first term the equation can be written as

$$\frac{\partial h_i}{\partial \tau} = v_i - v_t \frac{\partial h_i}{\partial s} - \frac{\partial h_i}{\partial t} \ , \tag{2}$$

where v_t is the tangential velocity component on the free surface. As the second term on the right hand side is in a form of a convection term, numerical damping can be introduced into the equation by upwinding the free surface slope $\partial h_i / \partial s$ in this term according to the direction of the tangential velocity.

Previously [7] the upwinding was implemented in the interpolation of the node coordinates from the neighbouring free surface coordinates. A MUSCL-type [10] approach was used, in which MUSCL-interpolation was applied for coordinates normal to the free surface. In tangential direction grid nodes were taken as a weighted average of neighbouring free surface coordinates. The slope of the free surface was then taken from the normal vector of a free surface face. This approach has proven to be somewhat cumbersome, especially in cases, where one tries to avoid wave reflection at boundaries by deliberately adding more numerical damping through lower order interpolation for the node coordinates.

In order to get better control of the numerical damping and a simpler approach, some modifications to the method have been made. In the current method, instead of using the free surface normal vector, slope components $\partial h_i / \partial s$ in Eq. (2) are calculated separately by a simple MUSCL-interpolation of the free surface coordinates, whereas grid points are always taken as weighted averages of neighbouring wave coordinates.

Even though the slope calculation in both the previous and current method is based on MUSCL-approach, one should bear in mind, that this does not rule out the possibility to use central differencing. By an appropriate choice of the MUSCL-parameter the scheme reduces to the central difference.

2.3 Discretization of the free surface velocity

An essential part in the time accurate solution of free surface flows and the main concern in this paper is the approximation of the last term in Eq. (1) representing the velocity of the free surface. In this work two approximations are studied. These are discussed briefly next.

The first approach follows from the natural requirement, that there is no flow through the free surface faces of the computational grid. The velocity of the free surface is therefore defined by the movement of the nodes of the computational grid. This gives

$$\frac{\partial h_i}{\partial t} = v_g n_i \ , \tag{3}$$

for the free surface velocity components, where v_g is the grid normal velocity based on the geometric conservation law (GCL) [4]. The grid velocity is obtained from the time accurate momentum equations by requiring exact conservation in a uniform flow. For the three-level fully implicit scheme (3-LFI) this gives [4]

$$v_g^{n+1} = \frac{1}{\Delta t S^{n+1}} \left(\frac{3}{2} \Delta V^{n+1} - \frac{1}{2} \Delta V^n \right) \ , \tag{4}$$

where ΔV^{n+1} is the volume swept by a face between physical time levels n and $n+1$ and S^{n+1} is the area of the face.

In the second approach the last term in Eq. (1) is replaced directly with the three level difference approximation for the time derivative, that is

$$\frac{\partial h_i}{\partial t} = \frac{1}{\Delta t} \left(\frac{3}{2} h_i^{n+1} - 2 h_i^n + \frac{1}{2} h_i^{n-1} \right) \ . \tag{5}$$

2.4 Semi-implicit treatment of the free surface

Solution of the free surface deformation is based on a semi-implicit treatment [5] of Eq. (2) in pseudo time and 3-LFI in physical time. The scheme is not fully implicit in pseudo time, as the velocities are approximated by the values at the previous pseudo iteration. In the semi-implicit approach the free surface slope is linearised with respect to the previous pseudo iteration k, giving

$$\frac{\Delta h_i}{\Delta \tau}^{n+1,k} = v_i^{n+1,k} - v_t^{n+1,k} \frac{\partial h_i}{\partial s}^{n+1,k} - v_t^{n+1,k} \frac{\partial}{\partial h_i^{n+1,k}} \left(\frac{\partial h_i}{\partial s} \right) \Delta h_i^{n+1,k} - \frac{\partial h_i}{\partial t}^{n,k+1} \ . \tag{6}$$

The third term on the right hand side is then approximated with a first order upwind difference.

The last term on the right hand side of Eq. (6) is linearised as well. The linearisation of this term depends on the approximation used for the velocity of the free surface. When Eq. (3) is used for the velocity, the linearisation gives

$$\frac{\partial h_i}{\partial t}^{n,k+1} = \left(v_g^{n+1,k} + \frac{\partial v_g}{\partial h_i}^{n+1,k} \Delta h_i^{n+1,k} \right) n_i^{n+1,k} = \left(v_g^{n+1,k} + \frac{3}{2\Delta t S} \frac{\partial \Delta V}{\partial h_i}^{n+1,k} \Delta h_i^{n+1,k} \right) n_i^{n+1,k} . \quad (7)$$

The derivative of the swept volume is calculated using the fact, that a grid node coordinate on the free surface is taken as the average of the neighbouring h_i values.

When Eq. (5) is used instead, the linearisation of the last term in Eq. (6) becomes much simpler and can be written as

$$\frac{\partial h_i}{\partial t}^{n,k+1} = \frac{\partial h_i}{\partial t}^{n,k} + \frac{3}{2\Delta t} \Delta h_i^{n+1,k} . \quad (8)$$

For the solution of Eq. (6) the Δh_i terms on the right hand side resulting from the linearisations are transfered on the left hand side. Instead of doing the solution separately for both coordinate directions, the solution is performed only for the normal deformations Δh_n based on the relation $\Delta h_i = \Delta h_n n_i$.

3 TEST RESULTS

The approaches for discretization of the kinematic boundary condition described above are compared using a test case from the ISOPE 2^{nd} Numerical Wave Tank Workshop [9]. The case is wave radiation by sinusoidal heave motion of a 2D wedge in a tank. The wedge has a half breadth a at the still water line and draught $d = 2.5a$. The depth of the tank is $3d$. For the selected case the nondimensional frequency $\omega^2 a/g = 1$ and the nondimensional motion amplitude $A/a = 0.4$. The simulation is inviscid with 100 time steps per oscillation cycle.

The case has been tested using three different grids with 9951, 19975 and 40090 triangles, giving a refinement ratio of approximately $\sqrt{2}$. The number of grid points on the free surface is 235, 333 and 472 respectively with the outflow boundary at $75a$ from the centre line of the wedge.

A comparison of the two free surface velocity discretizations with different grids and free surface slope discretizations is shown in Fig. 1. The time instant and the location have been selected to emphasize the differences.

The most noticeable feature in Fig. 1 is the strong instability in h_i with the grid velocity based discretization of Eq. (3). For the grid nodes, which define the free surface, the instability is not as strong, but still noticeable. Comparison of the results on different grid levels shows, that the instability increases with growing cell size. Similarly, the oscillations are larger on the right hand edge of the graphs, as the cell size grows linearly towards the outflow boundary. On the coarse level the cell size is roughly $0.18a$ at $12a$ and $0.43a$ at $26a$.

On the other hand, the discretization of the time derivative by Eq. (5) leads to a smooth wave profile in every case. A closer examination shows, however, that with sufficiently small cell size, also the grid velocity based discretization converges to the same solution. This can also be seen later in Fig. 2.

Inclusion of numerical damping through the normal velocity discretization has a clear effect on the wave profile for the first approach, due to the large curvature of the oscillations. However, only the first order upwind includes sufficient amount of damping to remove the oscillations, but with a cost of significantly reduced accuracy. The effect of numerical damping is much weaker for the second approach. The wave profiles in this case are practically grid independent for the higher order discretizations upto $12a$ on coarse level and upto $17a$ on medium level, which is roughly equivalent to a cell size of $0.2a$ or 30 points per wave length. With first order upwinding the wave profiles are grid independent only in a very small area next to the wedge. For this particular test case it is actually not necessary to add any additional damping into the kinematic boundary condition and central difference can be used without problems, provided one does not use the grid velocity discretization.

The reason behind the unsatisfactory results for the grid velocity based discretization by Eq. (3) can be explained by studying the modified equation of this approach. For simplicity a case with only a vertical deformation of the free surface and uniform grid spacing is considered. The kinematic boundary condition can then be written as

$$\frac{\partial \Delta h_j}{\partial \tau} = v_{2,j} - v_{1,j} \frac{\partial h}{\partial x_1} - v_{g,j} \quad (9)$$

$$= R_{n,j} - \frac{1}{2} \left(v_{g,j-1/2} + v_{g,j+1/2} \right) \quad (10)$$

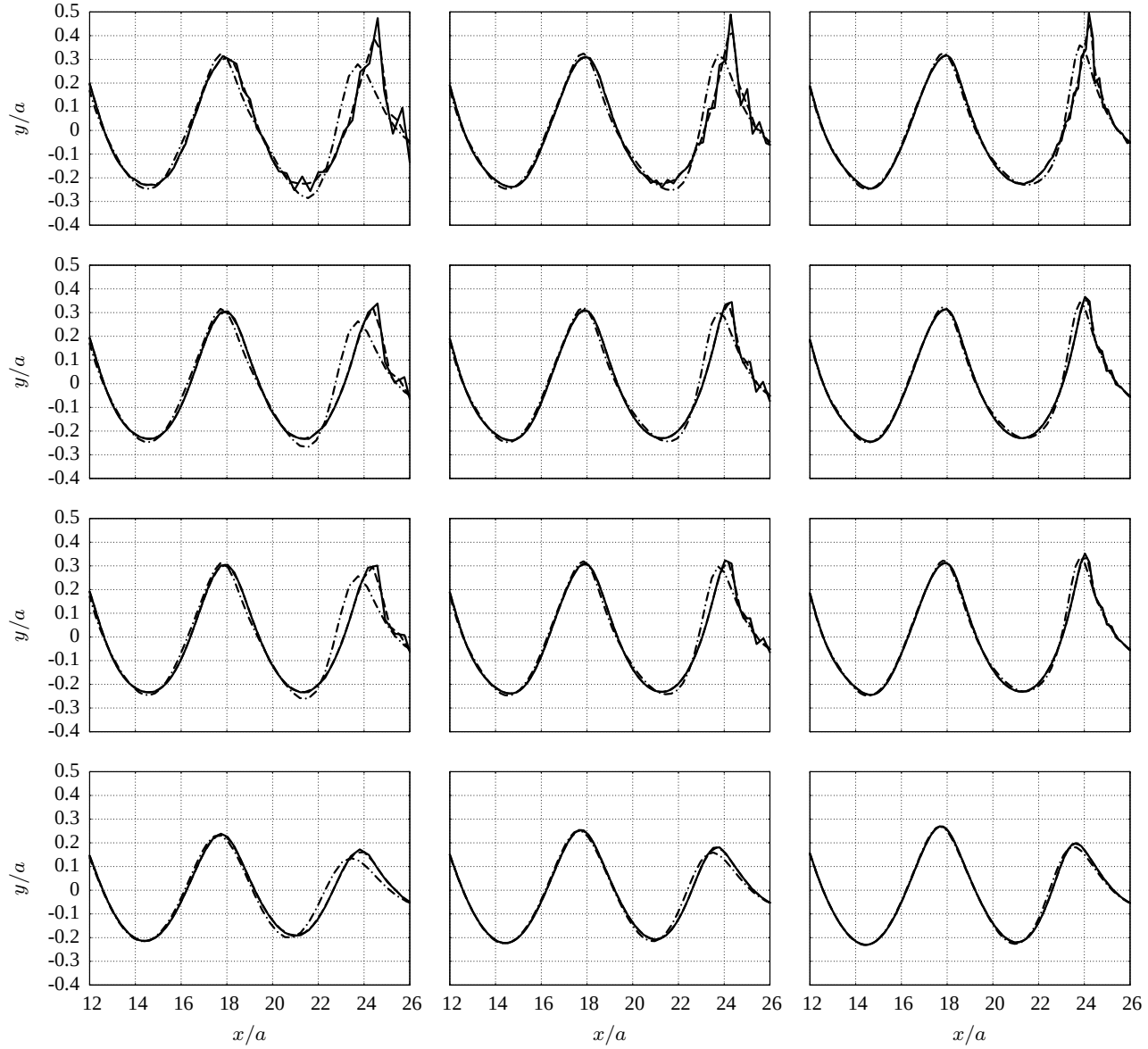

Figure 1: Comparison of wave profiles for different discretizations at $t = 8T$. Solid line: h_i with Eq. (3), dashed line: grid nodes withEq. (3), dot-dashed line: Eq. (5). Discretization of the normal velocity from top to bottom: central, 3^{rd}, 2^{nd} and 1^{st} order upwind. Grid level from left to right: coarse, medium, fine.

$$= \quad R_{n,j} - \frac{1}{4}\left(\frac{\partial h_{j-1}}{\partial t} + 2\frac{\partial h_j}{\partial t} + \frac{\partial h_{j+1}}{\partial t}\right) \tag{11}$$

Taylor approximation for the last form leads to

$$\frac{\partial \Delta h_j}{\partial \tau} = R_{n,j} - \frac{\partial h_j}{\partial t} - \frac{\partial}{\partial t}\left(\frac{1}{4}\frac{\partial^2 h_j}{\partial x_1^2}\Delta x_1^2 + \mathrm{O}(\Delta x_1^4)\right) \tag{12}$$

From Eq. (12) it can be seen, that the modified equation includes an antidiffusion term (the first term in the parenthesis), which has a negative effect on the stability of the iteration. The amount of antidiffusion grows with increasing grid size.

Figs. 2 and 3 show comparisons of the results with numerical reference results from the ISOPE Workshop [9]. The wave profiles for the two free surface velocity discretizations are indistinguishable up to roughly the fifth zero crossing showing the convergence of the approach to the same solution for sufficiently small cell sizes. Largest differences compared to the reference results can be seen at the first and second crests and throughs. In addition to the differences in the height of the crests the shape of these for the present method is unsymmetric, whereas reference results feature symmetric crests. The second through, on the other hand, is flatter and mainly shallower than in the reference cases. It was reported at the workshop, that some methods had problems modelling the intersection of the free surface and the wedge. This explains the differences at the first through.

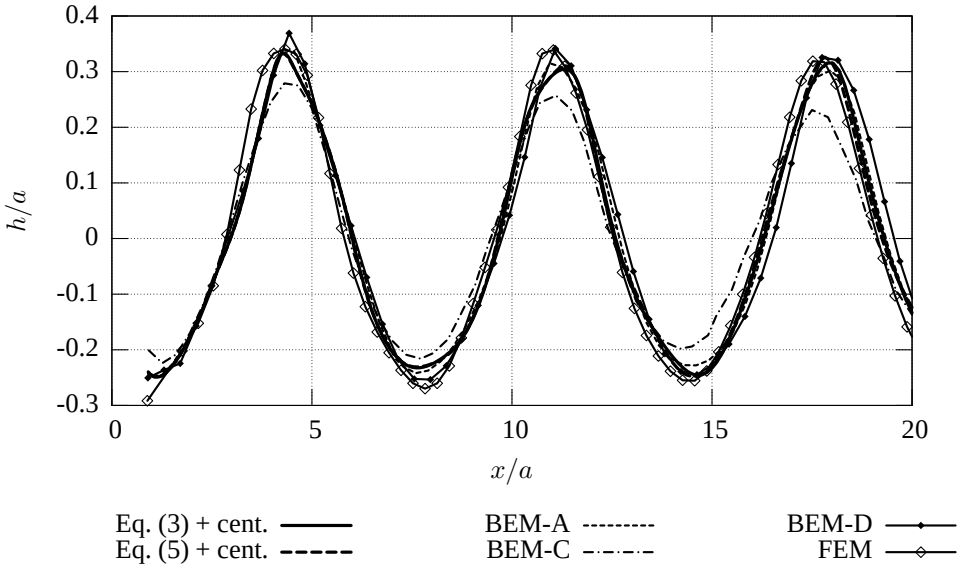

Figure 2: Comparison of wave profiles close to the wedge with wedge at its mean position moving up. Results on fine grid level with central difference for the slope of the free surface. Reference cases from [9].

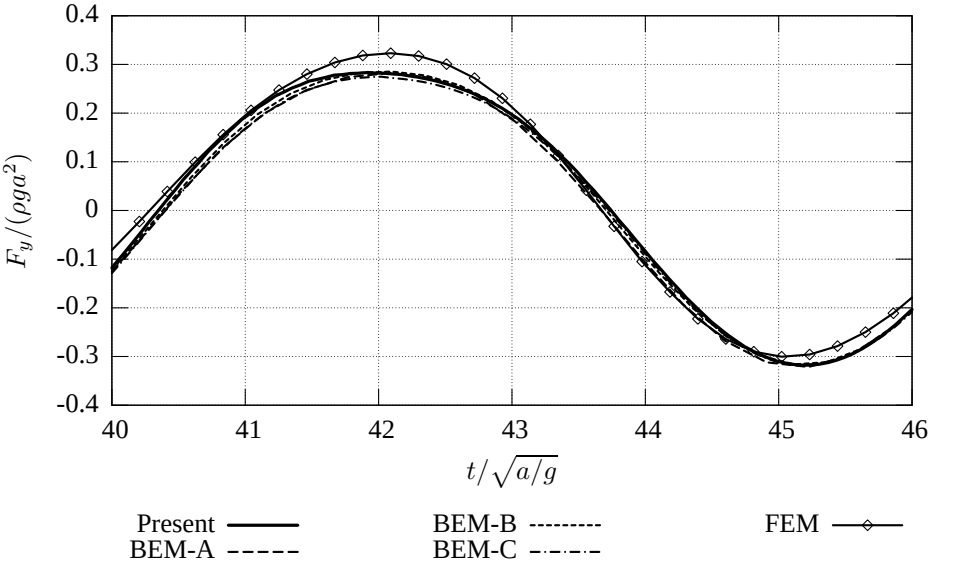

Figure 3: Comparison of the dynamic vertical force on the wedge. Results on fine grid. Reference cases from [9].

The force on the wedge showed no noticeable differences for any of the cases simulated irrespective of the discretizations or the grid level. This is due to the sufficiently small cell size close to the wedge, so that the result there is grid independent already on the coarse grid level. The differences to reference results are also much smaller than for the wave profiles and the agreement is excellent. The only method differing clearly from the other ones is the FEM, but in this case a post-processing error in removing the hydrostatic component can not be ruled out entirely.

4 CONCLUSIONS

Two different approaches for the discretization of the time accurate kinematic free surface boundary condition in surface tracking context have been studied. In the first approach the velocity of the computational grid is used as the velocity of the free surface. The second approach is based on a direct discretization of the physical time derivative in the kinematic boundary condition.

Tests with sinusoidal heave motion of a wedge showed, that depending on cell size the former approach leads to an oscillating free surface. The instability increases with growing cell size. This becomes a problem for example, when one simulates propagating waves, but wishes to use larger cells in areas of lesser importance or when one simulates very steep waves. However, in case of sufficiently small cell size and curvature of the free surface, both approaches give identical results.

In terms of the force on the wedge the results agree extremely well with reference results from the ISOPE workshop. Larger differences were found for the wave profiles close to the wedge, where the present method had horizontally unsymmetric crests, whereas reference cases had symmetric crests.

REFERENCES

[1] BATINA, J. T. Unsteady euler algorithm with unstructured dynamic mesh for complex-aircraft aerodynamic analysis. *AIAA Journal 29*, 3 (1991), 327–333.

[2] FARHAT, C., DEGAND, C., KOOBUS, B., AND LESOINNE, M. Torsional springs for two-dimensional dynamic unstructured fluid meshes. *Computer methods in applied mechanics and engineering 163* (1998), 231–245.

[3] HINO, T., MARTINELLI, L., AND JAMESON, A. A finite-volume method with unstructured grid for free surface flow simulations. In 6^{th} *International Conference on Numerical Ship Hydrodynamics* (Iowa, 1993).

[4] HOFFREN, J. Unsteady Navier-Stokes simulations of airfoil flows. In *Numerical Methods in Laminar and Turbulent Flow*, C. Taylor, Ed., vol. VIII. Pineridge Press, 1993, pp. 1065–1076.

[5] MIKKOLA, T. Implementation of an implicit scheme into a free surface RANS solver in order to improve the convergence. Tech. Rep. M-257, Helsinki University of Technology, Ship Laboratory, 2000. Master's Thesis.

[6] MIKKOLA, T. Numerical simulation of free surface flows in 2D with unstructured finite volume based pressure correction method. In *VIII Finnish Mechanics Days* (Espoo, Finland, 2003), P. Råback, K. Santaoja, and R. Stenberg, Eds.

[7] MIKKOLA, T. Time accurate simulation of free surface flows in 2D using unstructured grids. In 7^{th} *Numerical Towing Tank Symposium* (Hamburg, Germany, 2004), V. Bertram and H. Söding, Eds.

[8] RAVEN, H. C., VAN DER PLOEG, A., AND STARKE, B. Computation of free-surface viscous flows at model and full scale by a steady iterative approach. In 25^{th} *Symposium on Naval Hydrodynamics* (St. John's, Canada, 2004).

[9] TANIZAWA, K., AND CLÉMENT, A. H. Report of the 2nd Workshop of ISOPE Numerical Wave Tank Group: Benchmark Test Cases of Radiation Problem, (Brest, May 1999). In *The Tenth (2000) International Offshore and Polar Engineering Conference* (Seattle, USA, 2000).

[10] VAN LEER, B. Towards the Ultimate Conservative Difference Scheme V: A Second-Order Sequel to Godunov's Method. *Journal of Computational Physics 32* (1979).

Hydro-Elastic Water Entry Simulation using RANSE and FEM

Ciprian MINCU, ATM, Bucharest/Romania, Daniel-Ciprian.Mincu@email.ro
Francois GROSJEAN, Volker BERTRAM, ENSIETA-MSN, Brest/France,
Francois.Grosjean@ensieta.fr, Volker.Bertram@ensieta.fr

We simulated slamming for simple 2-d structures (wedges and cones)[1], using the commercial RANSE solver FLUENT V6. Results are compared with experiments and previous simulations with a potential-flow approach numerically solved using the finite-element code ABAQUS. Our two-phase flow model employed the Volume of Fluids Method (VOF) and a Geometrical Reconstruction (GeoReconstruct) piecewise linear scheme of the water-air interface. After initial parametric studies for wedges, we passed to cones where we could validate against experimental results. ENSIETA intends to repeat experimental tests in its own tank in 2006 and parasite movements were simulated for well-knowing problems involved in process. Since extreme values of pressure were found on the structure, an elastically model was tested, coupling Fluent, Abaqus and mesh generator, Gambit. C++ and FORTRAN were the main programs used to realise the automated code of fluid-structure analyses.

We simulate incompressible flow, but unlike Donguy[2] and Constantinescu[3] we do not restrict ourselves to a potential flow model. The main progress however is the much better treatment of the free surface. While turbulence should have a negligible influence on the pressures in slamming, the additional expense is also negligible in a RANSE simulation, and we included the classical k-ε turbulence model in our computations. On the walls of our structures, we imposed an adherence condition *(u=v=w=0).*

The pressure values (Vertex Average) are recorded using pressure taps in two points situated at 40 and 90 mm from the centre of the body. Three angles (6°, 8°, 14°) were investigated for constant speeds between 2.5 and 8 m/s. We model the water entry in a body-fixed mesh, having the water rise with drop speed. Different mesh configurations were studied for domains sizes between 4.17m x 3.5m (height x length) and 3.17m x 1.17m, mesh cells number between 10 000 and 350 000, boundary layers with 8 to 16 layers and residuum values between 10^{-3} to 10^{-9}. The body radius is 161 mm.

Simulations for wedges were restricted to purely numerical parameter studies and comparisons with other simulation approaches. Table I shows pressures obtained for impact speed of 8 m/s (Re = $1.44 \cdot 10^6$ based on radius) and a wedge angle of 14°, for a mesh of 140000 cells with 16 layers of cells in the boundary layer.

Table I: Computed pressures for entry speed 8 m/s and wedge angle 14°

	Fluent-RANSE	Abaqus-potential	Castem- potential
Point 1	11.38 bar	13.1 bar	12.4 bar
Point 2	11.04 bar	13.3 bar	12.5 bar

An analytical value (12.67 bar) was obtained using a potential model [4] supposing a constant pressure on the body wall and a constant way of touching water (without jet).

$$v_{diedre} = \frac{\pi}{2}\frac{V}{\tan(\beta)} \; ; \qquad P_{\max} = \rho_{fluide}\frac{v_{diedre}^2}{2} \cdot$$

Studies for different angles and speeds showed that pressure values are sensible only on the cell sizes close to the wedge. The turbulent or laminar models, tank size, global size of the mesh, residual value, or time step had no significant influence within the investigated ranges. Starting with a water level close to impact reduced simulation time and had – as expected – no influence on results. For almost all cases the pressure increased with the water penetration. The maximum pressure appears when the water jet detaches from the body. The pressure on the wedge significantly decreases again when the wedge is totally immerged.

For cones, we had experimental validation data. Some discrepancies remain as the experiments did not enforce constant speed as in our computations. We performed first parameter studies for time step and cell adjacent size. The mesh proposed initially offered a cell length of 0,7 mm and 0,1 mm height. In view of the expected long CPU time, we used the Fluent option "Adapt Boundary" of dividing cells in the interesting zones. The calculus was started each time from a position in which the cone was partially immerged into the water and cells length is divided by two. Table II shows the pressures obtained for the first point. A maximum value for the pressure [5] was calculated with $P=\rho_{H2O} \cdot c \cdot U_s$ (c - sonic speed in water, U_s – fall speed). The residuals dropped to values between 10^{-5} and 10^{-7}. We can consider that the pressure obtained by this procedure is an average of the bold values in Table II ($P_{point.1}$=14.61 bar). Previous computations with the potential flow model in Abaqus gives a pressure value of 19 bar for a time step of $2 \cdot 10^{-5}$ and 5µm cell length, with Castem 18.4 bar, while experiments gave 11 bar. Our Fluent results are smaller than those from the finite-element codes.

Since this value is not obtained for the same cell size we created a mesh with a local cell length of 5µm directly from Gambit using an aspect ratio 0.01. The solution on a tandem-processor machine took 3 CPU weeks.

For the two cases studied, the RANSE model (Fluent) and the potential flow model (Abaqus) gave small differences probably related to the fluid models, time step or cell sizes. Tests covered two speeds (2.5 and 5 m/s) and a cone angle of 6°. For 2.5 m/s, pressures were 3.96 bar at point 1 and 4.23 bar at point 2. For 5m/s, the computed pressure at point 1 was 18.7 bar. With classical potential flow theory for small deadrise angle, an analytical value ($v_{cone} = \frac{4}{\pi}\frac{V}{\tan(\beta)}$, $P_{\max} = \rho_{fluide}\frac{v_{diedre}^2}{2}$) results in predicted 18.4 bar. As expected, turbulent and laminar computations resulted in the same pressure values.

Table II: Pressure in first tap for a cone 6° opening angle, 5 m/s entry speed

Time step (s) Cell length (mm)	10^{-5}	10^{-6}	10^{-7}	10^{-8}	10^{-9}
0,7	6,8	8,5	9,5	9,8	9,9
0,4	8,6	**14**	**14,6**	**14,1**	12,6
0,2	diverge	**15**	**15,5**	**14,5**	-

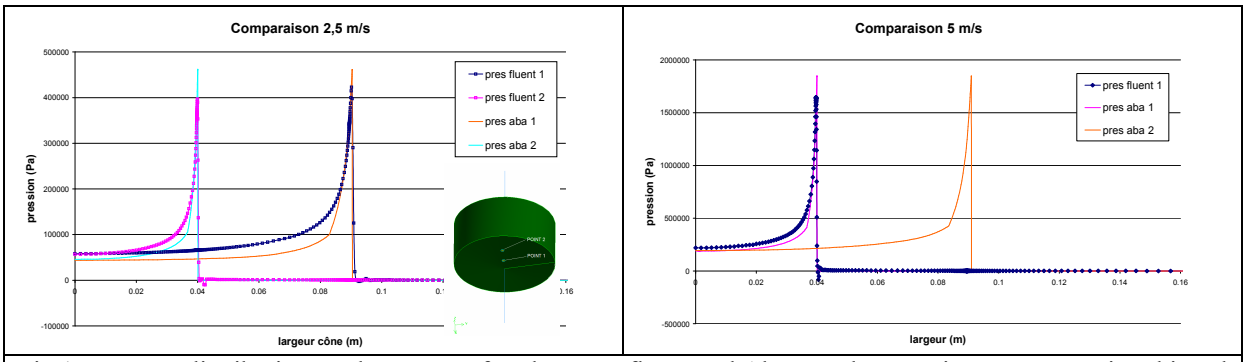

Fig.1: Pressure distribution on the cone surface between fluent and Abaqus when maximum pressure is achieved at pressure taps (deadrise 6°, minimum cell length 5µm), entry speed 2.5 m/s (left) and 5 m/s (right)

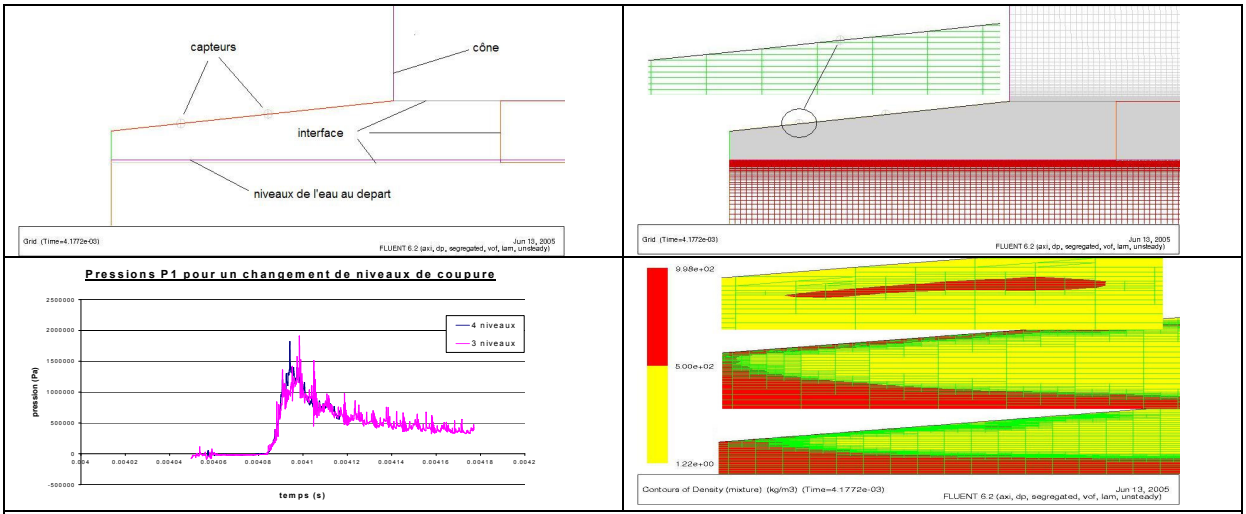

Fig.2: Modified domain (top left); pseudo-structured mesh (top-right); obtained pressures at taps for two studied case (bottom left); remesh models at free surface (bottom right)

Since the global computational time was very high, a new method was tested planning a local re-mesh at the free surface level [6]. This method used a Fluent property which allows splitting cells into same cell type at each time step in regions of changing phase and reassembly in regions of constant phase. Fluent uses a transport equation which allows us to identify the free surface position. Thus we have dynamically adapted cell size and number. Initial tests revealed some problems in the computation of the free surface related to the position and type of cells. The only type of mesh which gave a correct physical response was a pseudo-structural mesh in which all cells have borders perpendicular or parallel with the flow. Because Gambit did not support automatic grid generation for a triangular surface in this way, we created appropriate grids manually. The initial resulting grid had 240 cells over the cone length. Since in this structured mesh, the cell numbers are spread in both ways in the same manner (mirror on cone surface) we chose a new method to reduce the global number of cells. Fluent's boundary condition "Interface" allows to have on one side of this interface cells 4 times bigger that on

the other side. This resulted in good (smooth) free surfaces and reduced global cell count by a factor of 2 to 300000 cells. Using this method we performed two series of tests, cutting the cells 3 or 4 times. In the first case we obtained 19 bar, and in the second 18,2 bar. This is fairly close to the values obtained with the other codes for the same speed and incidence (5 m/s and 6°). Because of the levels of cutting the cells between the two Fluent cases for the moments when the maximal pressure is obtained in the pressure taps, we find a difference of $4.3 \cdot 10^{-6}$ s. In the end, this approach did not reduce global computational time and yielded to similar results as it happened through the standard approach.

Fluid-structure interaction (FSI) involving large deformations requires a hydro-elastic approach. Different numerical methods were developed and applied to solve FSI for steady or unsteady problems [7]. A new domain appeared, numerical hydro-elasticity, where numerical fluid codes (CFD) are coupled structure codes. Most of the proposed methods to solve the fluid-structure interaction are two-domains methods, the fluid domain and the structure one. Different methods like Eulerian-Lagrangian random formulation [8,9], mobile mesh method[10], co-rotational[11,12] or space-time methods[12] can all be reduced to three fundamental components covering the fluid part, the structure part and the mobile mesh part. One of the most popular ways of solving those procedures is the "Conventional Serial Staggered Procedure [11,12]" (CSD), Fig.4, where p represents fluid pressure and U steady state vector of structure $[u, \dot{u}]^T$. We divide our problem in three coupled domains and each one of it is solved independently with different programs, Fig.5[14]. The fluid part is solved with Navier-Stokes program FLUENT V6, the structure calculus with ABAQUS V6.4 and the mesh part with the pre-processor of Fluent, GAMBIT V2.20. Coupling those codes is nothing else but a connection between imported and exported parameters of each program which allows to have at each time-step all parameters that we need. The coupling procedure was written in FORTRAN and C++ and can be used in all fluid-structure interaction for two-phase problems. In order to understand the program better it is important to know the entry parameters "journal" of each program.

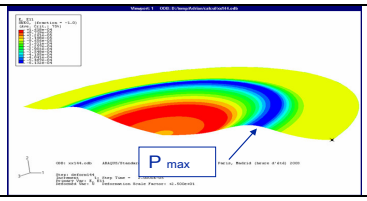

Fig.3: Abaqus deformed model

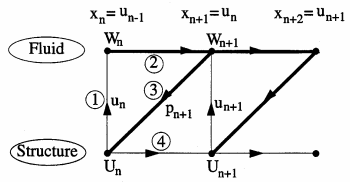

Fig.4: Conventional Serial Staggered Procedure

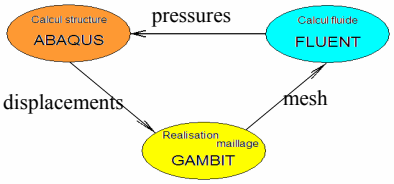

Fig.5: Input and output vectors of each domain

- Deformed surface coordinates
- Domain → **GAMBIT**
- Export mesh

- Read mesh
- Set solver
- Multiphase parameters
- Fluids proprieties
- Operating conditions → **FLUENT**
- Boundary conditions
- Charging user define functions
- Patching the fluid parameters
- Advance solution on time
- Export pressures

- Define structure geometry
  - define nodes
  - define elements
- Define boundary conditions → **ABAQUS**
- Define loads on the structure
- Solve time-dependent problem
  - advance solution in time
  - export structure deformation

The Gambit journal is created based on files used on steady cases. At each time step the new coordinates of the cone surface are renewed and the mesh is automatically created. The new coordinates are output values which Abaqus exports at each time step. Knowing that the computational time is long, the surface below the cone was meshed with 150 nodes and the global domain with 10000 cells.

The Fluent journal is an iterative file based on the same parameters as in the rigid cases (constant speed – 5 m/s). At the beginning, the .msh file created by Gambit is read, the boundary conditions and necessary equations are set, and the iterative calculus begins with the first time step. After each calculus, at each time-step, pressure values are exported in a .txt file and also all fluid parameters: pressure, speed and phases (density) fields using UDF (User Defined Functions). The iterative process is ensured by internal command lines of Fluent (Define Execute Commands). UDFs are procedures which allow to everyone to interact with source code of Fluent. After each new mesh upload the fluid parameters from the last time-step are set on new cells.

The Abaqus journal is also iterative. Initially, an undeformed cone surface is read and elements are chosen. After chosing the boundary conditions, the pressure file exported by Fluent is used to load the structure. The pressure values from this file are cubic spline interpolated before being imported in Abaqus. The geometry of the numerical configuration is created using the axisymmetrical property using shell elements and representing only of the middle fibre. The shell elements (SAX1) used are linear and have 5 integration points in depth. The mesh used 150 cells. Since the fluid reference system was changed, we have to take into account in the same way the fluid computation method for the structure calculus. As boundary conditions, we fixed the right extremity of the cone and for the centre only a movement on the symmetry axis was allowed. Steel mechanical characteristics that were used are: E = 210 GPa, $\nu = 0.3$, $\rho_s = 7800$ kg/m^3. The structure computation is iterative and, at each time step, new points coordinates are exported to a grid file maillage.txt used by Gambit in creation of a new mesh. All those command lines use Python as command language for Abaqus.

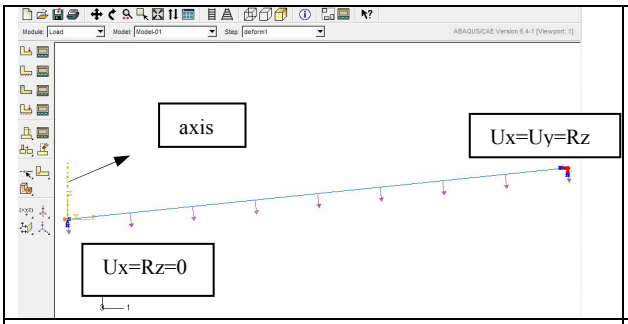

Fig.6: Boundary conditions in structure computation

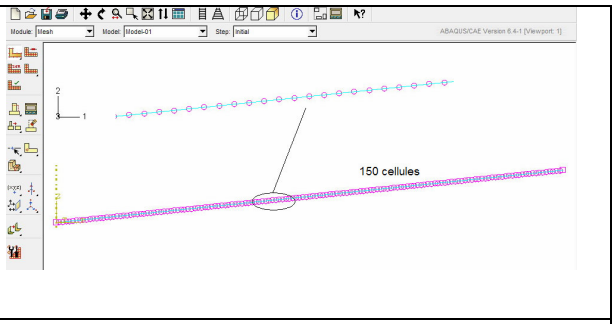

Fig.7: Mesh model use in structure computation

The final program, coupling those three files, can be divided in two main programs: one for the fluid part in which is also included the mesh generator Gambit and other for the structure part. Since the main parameters charged at the beginning of the code are saved in a file, all users can change them in a simple way and use them for some other calculus. After the first pressure file is exported, the code reads automatically the needed files to ensure a continuum computation loop.

References

[1] Mincu, C.; Grosjean, F., Master recherche Rapport, *Etude numérique du slamming de dièdres ou de cônes*, ENSIETA, Brest, 2005

[2] Donguy, B., *Study of the fluid interaction structure at the time of the hydrodynamic impact*, PhD Thesis, Ecole Centrale de Nantes, FRANCE, 2002 (in French)

[3] Constantinescu, A.; Neme, A.; Peseux, B., *Finite element simulations of dihedral and conical shell structures in slamming*, 8th Int. Conf. on Flow-Induced Vibrations, Ecole Polytechnique, Paris, 2004 ??? further authors???

[4] Zhao, R.; Faltinsen, O., *Slamming loads on high-speed vessels*, 19th Symposion on Naval Hydrodynamics, Seoul, KOREA, 1992

[5] Joukovsky, N.E., *Memories of the Imperial Academy of St.Petersburg*, 1898

[6] Alexander, H.; Leroyer, A.; Visonneau, M., *Simulation d'écoulements à surface libre autour de corps en movement avec adaptation locale de maillage*, 10èmes Journées de l'hydrodynamique, Nantes, 2005

[7] Mihaila, A., Grosjean, F., Fuiorea, I., *Simulation numérique des phénomènes d'interaction fluide-structure à l'aide de codes commerciaux*, 30th Int. Scientific Conf. of the Military Technical Academy, Bucarest, 2003

[8] Donea, J., *An arbitrary Lagrangian-Eulerian finite method for transient fluid-structure interactions*, Comput. Methods Appl. Mech. Engrg., 33, 1982

[9] Farhat, C.; Lessione, M.; Maman, N., *Mixed explicit/implicit time integration of coupled aeroelastic problems : three-field formulation, geometric conservation and distributed solution*, Int. J. Numer. Methods Fluids, 21, 1995
[10] Masud, A., *A space-time finite element method for fluid structure interaction*, Ph. D. thesis, Stanford University, 1993
[11] Farhat, C.; Lesoinne, M., *Two efficient staggered algorithms for the serial and parallel solution of three-dimensional nonlinear transient aeroelastic problems*, Comput. Methods Appl. Mech. Engrg., 182, 2000
[12] Farhat, C.; Lesoinne, M., *Fast staggered algorithms for the solution of three-dimensional nonlinear transient aeroelastic problems*, AGARD Report R-807 Special Course of Parallel Computing in CFD, NATO, 1995
[13] Rawson, K.J.; Tupper, E.C.*; Basic Ship Theory 2*, Longman Scientific & Technical, England, 1984
[14] Texier, R., *Modélisation du couplage fluide-structure*, DEA report, Rennes, 2002

Computation of slamming and global loads for structural design using RANSE

Bettar el Moctar, ould.el_Moctar@gl-group.com
Germanischer Lloyd, Hamburg, Germany

Abstract

This paper presents a numerical procedure to predict slamming and global loads by first making use of the potential flow seakeeping code to select design wave and RANSE to determine the corresponding ship motions and the total design loads. RANSE computed motions and bow flare slamming loads were compared to measurements. Global total design loads including slamming and water on deck acting on a Post-Panamax container ship were computed using RANSE and compared to loads obtained with a panel code based on a linear three-dimensional radiation/diffraction Green function formulation in the frequency-domain.

INTRODUCTION

Slamming loads can induce high stresses and cause deformations of local structural components. The accurate assessment of slamming loads is essential for the design of the ship's structure. Classification society rules contain formulas for slamming loads (e.g., *Germanischer Lloyd, 2005*). Generally, these formulas are adequate for conventional ships, as they are based on operational experience. However, for many modern ships it becomes necessary to resort to direct computations of slamming loads.

A satisfactory theoretical treatment of slamming has been prevented so far by the complexity of the problem. Most theories and their numerical procedures were applied on two-dimensional bodies; however, slamming is a strongly three-dimensional nonlinear phenomenon that is sensitive to the relative motion between the ship and the water surface (*Tanizawa and Bertram, 1998*). Slamming is characterized by highly peaked local pressures of short duration. Hence, slamming peak pressures can not be applied on larger areas to estimate structural response to slamming impacts. Moreover, the influence of hydroelasticity, compressibility of water and air pockets may have to be accounted for as well. Mainly because of these phenomena, potential flow methods are not well suited to accurately predict slamming loads (*ISSC, 2003*). Recent progress has been made to develop numerical methods that predict slamming pressures (*ISSC, 2000*). *Kinoshita et al. (1999)* predicted ship motions and loads with a Navier-Stokes solver. Although no extreme load cases were presented, the applied method has the potential to compute slamming loads in extreme wave conditions.

Methods that directly solve the Reynolds-averaged Navier-Stokes equations (RANSE), possibly including the two-phase flow of water and air, are better able to describe the physics associated with slamming. However, the computational effort for a three-dimensional RANSE method to simulate motions and loads on a ship at small, successive instances of time over a long time period appears beyond current computational capabilities.

This paper presents a numerical procedure to predict slamming and global design loads by first making use of the potential flow seakeeping code GLPANEL (*Papanikolaou and Schellin, 1991; Östergaard and Schellin, 1995*) to select design wave and RANSE (*ICCM 1998, Brunswig, el Moctar 2004*) to determine the corresponding ship motions and total design loads.

More Details can be found in (*el Moctar et al, 2004, Brunswig and el Moctar, 2004*)

COMPUTATIONAL PROCEDURE

Slamming loads

The computational procedure is described in more detail in *El Moctar et al. (2004)*. It consists of the following steps:

1. The linear, frequency-domain Green-function panel code GLPANEL, *Papanikolaou and Schellin (1991),* uses zero-speed Green functions and a forward-speed correction based on the encounter frequency approach. GLPANEL computed systematically motions and relative velocities for different forward speeds and wave conditions that subject the ship to slamming loads.
2. Regular design waves were selected on the basis of maximum magnitudes of relative normal velocity between ship critical areas and wave, averaged over the critical areas.
3. Ship motions and slamming loads are computed using the extended RANSE solver COMET (*ICCM 1998, Brunswig and el Moctar, 2004*) that also solve the nonlinear equation of motions

NUMERICAL METHOD

RANSE Solver

The RANSE solver COMET, a code that implements interface-capturing techniques of the volume-of-fluid (VoF) type, proved to be suitable for handling strong nonlinearities. Today, this kind of code is the obvious choice for computing complex free-surface shapes with breaking waves, sprays and air trapping, hydrodynamic phenomena that should be considered to predict slamming pressures. The conservation equations for mass and momentum in their integral form serve as the starting point. The solution domain is subdivided into a finite number of control volumes that may be of arbitrary shape. The integrals are numerically approximated using the midpoint rule. The mass flux through the cell face is taken from the previous iteration, following a simple Picard iteration approach. The unknown variables at the center of the cell face are determined by combining a central differencing scheme (CDS) with an upwind differencing scheme (UDS). The spatial distribution of each of the two fluids is obtained by solving an additional transport equation for the volume fraction of one of the fluids. To accurately simulate the convective transport of the two immiscible fluids, the discretization must be nearly free of numerical diffusion and must not violate the boundedness criteria (*Ferziger and Peric*, *1996*). For this purpose, the high resolution interface capturing (HRIC) scheme is used (*Muzaferija and Peric, 1998*). This scheme is a nonlinear blend of upwind and downwind discretization, and the blending is a function of the distribution of the volume fraction and the local Courant number. The free surface is smeared over two to three control volumes. Fluid structure interaction effects are presently not accounted for, i.e., the body is assumed to be rigid. The fluid is assumed to be viscous and incompressible.

Extended RANSE Solver

The nonlinear equations of the body motions are solved and coupled with the Reynolds averaged Navier-Stokes (RANSE) solver COMET. The computational procedure comprised the following steps:

- The RANSE-solver computes the flow around the body, taking into account the viscosity, flow turbulence and deformation of the free surface. The hydro- and aerodynamic forces and moments acting on the body are then calculated by integrating the pressure and friction stresses over the body surface.
- The nonlinear equations of the rigid body motions are solved in six degrees of freedom (DOF) using all forces acting on the body.
- The motion accelerations, velocities and displacements (translations and rotations) are obtained by time integration.
- The position of the body is updated and the fluid flow is computed again for the new position.

The equations of motion are solved in a non-rotating and non-accelerating Newtonian reference system (G,x,y,z). G is the center of gravity of the body. The coordinate transformation between the Newtonian and the body-fixed local frame of reference (G, ξ, η, ζ) is defined as follows:

$$\vec{x} = \vec{x}_G + S\vec{\xi}$$

where S denotes the transformation matrix, which is the result of three consecutive rotations. First, the rotation around the vertical axis z (yaw angle); second, the rotation about the new transverse axis η (pitch angle); third, the rotation about the new longitudinal axis ξ (roll angle) *(Azcueta, Klemt, 2004)*.
The governing equations of motions can be expressed as:

$$\vec{F} = m \cdot \ddot{\vec{x}}_G$$

$$\vec{M} = SI_L S^T \dot{\vec{\omega}} + \vec{\omega} \times SI_L S^T \vec{\omega}$$

where $\vec{F}$ denotes the resulting force vector, m the mass of the body, $\ddot{\vec{x}}_G$ the translation acceleration vector of G, $\vec{M}$ the resulting moment vector with respect to G, I_L the tensor of inertia of the body about the axes of the body-fixed local frame of reference, and $\vec{\omega}$ the angular velocity vector.
Different time integration methods can be used. In this work the explicit trapezoidal method is used.
More details can be found in *Brunswig (2005).*

FLOW SIMULATION

The numerical volume grids surrounding the ships comprised typically about one and half million hexahedral control volumes. To avoid flow disturbances at outer grid boundaries, these boundaries were located at a distance of one ship length L ahead of the bow, 2L aft, and 1L beneath the keel. The top grid boundary was located above the deck at a distance equal to the length of the ship. The large domain of the mesh, especially above the deck, was chosen to allow large pitch motions in head waves. Near the ship hull and ahead of the ship grid density was high to resolve the wave, whereas aft of the ship the grid became course to dampen the waves.

Front, side, bottom and top flow boundaries were specified as inlets of known velocities and known void fraction distributions defining water and air re-

gions, *Azcueta (2001).* On the hull surface a no-slip condition was enforced on fluid velocities and on the turbulent kinetic energy. The wake flow boundary was specified as a zero-gradient pressure boundary (hydrostatic pressure). All computations were performed using the RNG-k-ε turbulence model with wall functions. The time step size was chosen such that the Courant number was smaller than unity on average. Ship motions were realized by moving the entire grid at each time step. Thus, all boundary conditions were newly computed at each time step.

Volume fractions (*Albina, 2000*) and velocities that initialized the flow field arose from superposition of ship speed and orbital particle velocities of the linear Airy or nonlinear Stokes waves. Numerical diffusion caused by the course grid aft of the ships dampened the incident wave to such an extent that no significant wave reflection occurred at the outlet boundary.

Simulation of the flow field continued until a periodic solution was reached. After a simulation time of two to five encounter periods, depending on ship motions, ship speed, wave height and position of the investigated plate fields, periodically converging solutions were obtained. For each time step up to fifteen outer iterations were needed.

The influence of the used approximation on slamming pressure and hydrodynamic forces was investigated earlier (*El Moctar et al., 2004*). The computation demonstrated that using the higher order approximation increased pressure peaks and decreased vertical forces acting on the vessel. Larger discretization errors result in smaller pitch and heave amplitudes (*Klemt, 2004*)

COMPUTED AND MEASURED SLAMMING LOADS

The Hamburg Ship model basin (HSVA) conducted model tests of a monohull. Table 1 shows main data of the monohull.

The models were constructed with a separated bow segment allowing measurement of forces and moments acting on this segment. Pressure sensors were installed on each side of the bow segment to record local pressures. Loads measured on the segments were corrected for inertial effects. The free-running, self-propelled models were hand operated by the helmsman accommodated on the carriage of HSVA's large towing tank. Tests were run in regular waves of various heights and wave length to ship length ratios ranging from 0.8 to 1.4 at propeller turning rates corresponding to calm water ship speeds of 14 and 16 knots. The added resistance caused the ship to advance at reduced speed. The HSVA test conditions are listed in Table 2.

All pressure and force time histories are presented as non-dimensional values. Pressures were normalized by a maximum value of p_0 = 270 kPa; forces, by the maximum value of F_0 = 2300 kN and time, by the wave encounter period of T_0 = 6.0 s.

Table 1: Principals particulars of the monohull

	Monohull 1
Length	70.0 m
Width	15.0 m
Draft	5.0 m
Speed	16 kn

Table 2: HSVA test runs and design wave conditions

H_w	λ / L_{pp}	Ship speed	Wave direction
3.5 m	1.2	7.1 kn	180°

Pressure sensors were located at a height of 5.0 m above the baseline, with the port one positioned 2.0 m aft and the starboard one 0.5 m aft of the forward perpendicular (Fig. 1).

Ship Motions

Motions of the vessel were determined under characteristic head wave conditions. As head waves were investigated, only pitch and heave motions were considered. Seakeeping model tests yielded experimental data of ship response, including ship motions and accelerations.
To compare the ship motion predictions Table 3 summarizes the motion amplitudes of different methods *(Brunswig, 2005)*. The average value of maximum and minimum heave and pitch motions as well as the accelerations specified their amplitude. The measured motions compared favorably with extended nonlinear RANSE with linear GLPANEL computations.

Slamming Loads and Local Pressures

The RANSE solver performed computations of wave-induced impact-related slamming loads and local pressures acting on the separated bow segment using measured ship motions as part of the input. Simulations of the flow field were performed for two consecutive encounter periods, while the measurements lasted over several periods. Computed forces and pressures hardly changed after the first period; however, the corresponding measurements varied. Over the first two periods, the computed vertical force on the separated bow section compared favorably with the experimental data; see Fig. 2. For the corresponding slamming pressures, shown in Fig. 3, the functional relationship of computed values correlated well

with measurements, whereas computed peak values sometimes deviated from experimental data. This deviation was largely attributed to the relatively strong variation of the measured peaks, most likely caused by the inability of the model to attain steady state conditions during tests in regular waves.

Table 3: Computed and measured ship motions

	Experi-ment	Extended RANSE	GLPANEL
Heave min/max [m]	-/-	-1.1/1.0	-1.6/1.6
Pitch min/max [°]	-7.4/5.2	-6.3/6.0	-6.25/6.25
Acc. at APP min/max [m/s²]	-4.7/3.8	-4.9/3.9	-3.7/3.7
Acc. at FPP min/max [m/s²]	-6.1/7.3	-6.0/7.0	-7.1/7.1

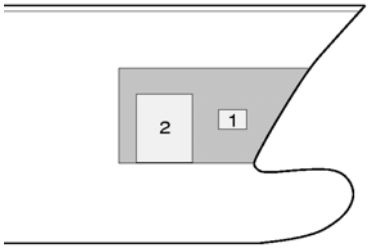

Fig. 1: Selected plate fields for monohull

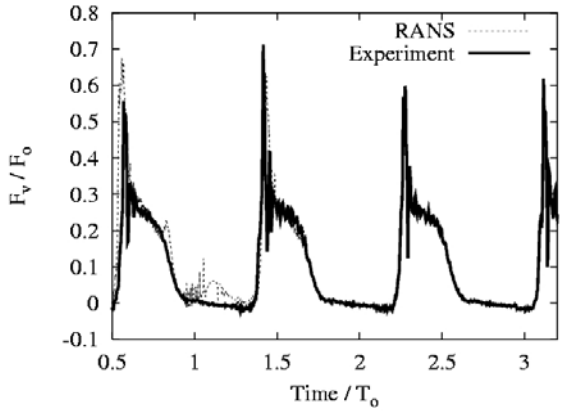

Fig. 2: Time history of vertical force on bow section of monohull

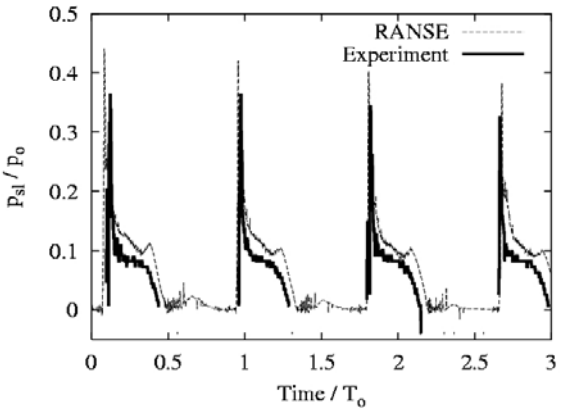

Fig. 3: Time history of pressure on plate field 1 of monohull

GLOBAL LOADS

The sectional loads of a large modern Post-Panamax container ship were computed for design wave conditions using RANSE and the frequency-domain panel code (GLPANEL). Non-linear corrections were applied to the GLPANEL computed loads. An appropriate equivalent design wave was chosen.

Table 4 shows main data of the container ship and the design wave.

Wave-induced sectional loads were computed for the ship avancing at constant forward speed in the midship design wave. For this particular case, the hull girder was subject to a vertical still-water sagging moment. Figures 5 to 8 depict the corresponding envelope curves of maximum and minimum vertical bending moments and shear forces at sections along the length of the ship. Results show that at one-third forward speed, sectional loads from RANSE compared favourably with sectional loads from GLPANEL. However, at two-third forward speed, bending moments as well as shear forces differed significantly in the bow region. These differences were caused by the effects of slamming at at the bow and green water on deck, see Fig.9. As expected, these effects were more pronounced at higher forward speed. The results demonstrate the importance of accounting for the ship's forward speed when computing wave-induced sectional loads.

Table 4 : Principals particulars of Post-Panamx Containership

Ship		Wave	
Length [m]	330	Length [m]	363
Width [m]	48	Height [m]	19
Draft [m]	12	Direction[°]	180
Speed [kn]	27		

Fig.4: Surface grid of Containership

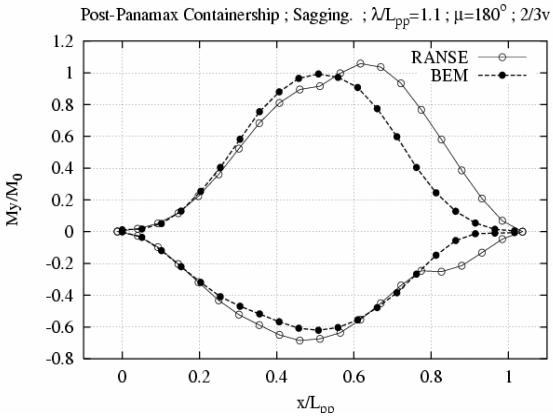

Fig.5: Envelopes of vertical bending moments for 2/3 ship speed at midship design wave condition

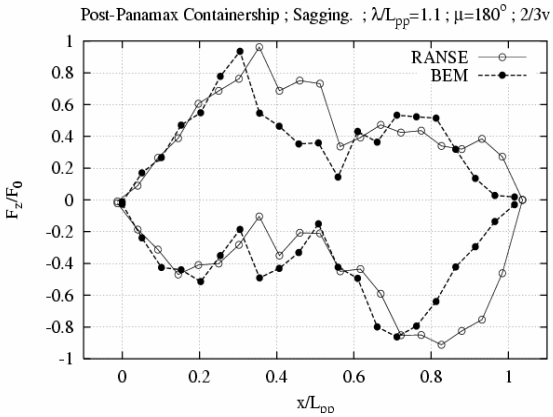

Fig.6: Envelopes of vertical shear forces for 2/3 ship speed at midship design wave condition

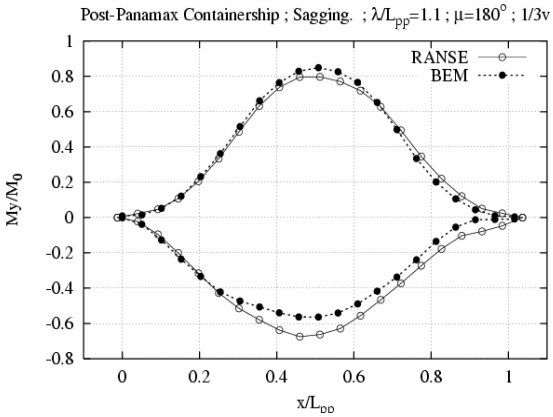

Fig.7: Envelopes of vertical bending moments for 1/3 ship speed at midship design wave condition

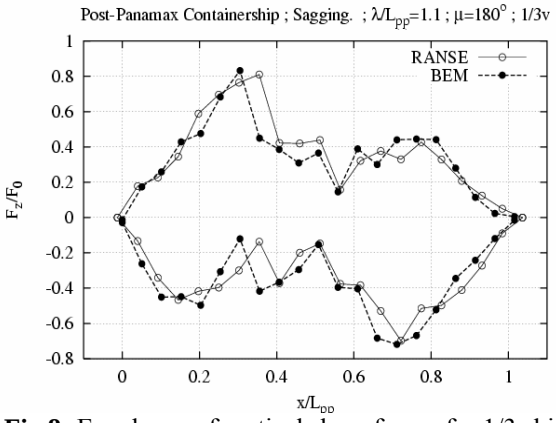

Fig.8: Envelopes of vertical shear forces for 1/3 ship speed at midship design wave condition

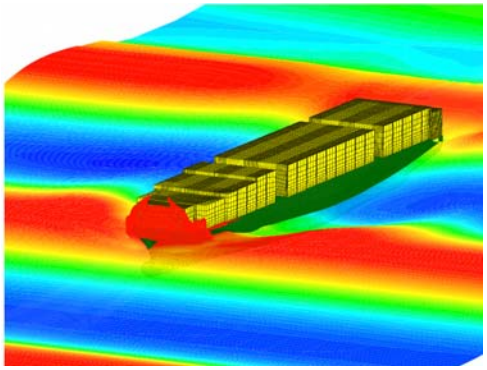

Fig.9: Water on deck

ACKNOWLEDGEMENT

Thanks are due to C. Schiff and A. Brehm for their assistance with the numerical GLPANEL computations and grid generation

CONCLUSION

Computed results of wave-induced slamming loads demonstrated that the procedure presented here was capable of predicting slamming suitable for design of a ship's structure. The generally favorable comparison of computations with model test measurements validated the methods used. The presented procedure relied on the combined use of potential flow codes and a RANSE solver.

The RANSE code COMET was recently modified to also solve the ship motion equations, as described above, so that in future ship motions will no longer have to be supplied as part of the input.

The investigation so far (numerical and experimental) concerned rigid bodies. The effect of hydro-elasticity on slamming loads remains as a topic for further detailed research and development activities.

REFERENCES

ALBINA, F.-O. (2000), *A Procedure to Set Volume Fraction for Calculations with COMET,* TU Hamburg-Harburg.

AZCUETA, R. (2001), *Computation of turbulent free-surface flows around ships and floating bodies*, Ph.D. thesis, TU Hamburg-Harburg (in German).

BRUNSWIG, J., EL MOCTAR, O. (2004), *Prediction of Ship Motions in Waves Using RANSE*, 7th Numerical Towing Tank Symposium, Hamburg.

BRUNSWIG, J. (2005), *Prediction of Ship Motions in Waves Using RANSE*, Diploma thesis, TU Hamburg-Harburg.

EL MOCTAR, O.; BREHM, A.; SCHELLIN, T.E. (2004), *Prediction of slamming loads for ship structural design using potential flow and RANSE codes*, 25th Symp. Naval Hydrodyn., St. John's.

FERZIGER, J. and PERIC, M. (1996*), Computational Methods for Fluid Dynamics*, Springer-Verlag, Berlin.

GERMANISCHER LLOYD (2002), *Rules for Classification and Construction*, I Ship Technology, 1 Seagoing Ships, 1 Hull Structures, Hamburg.

ICCM (1998-2000), *User Manuel COMET Version 2.0*, Institute of Computational Continuum Mechanics GmbH, Hamburg.

ISSC (2000), *Technical Committee I.2 LOADS*, Proceedings of the 14th International Ship and Offshore Structures Congress, Ohtsubo, H. and Sumi, Y., Edts., Vol. 1, Nagasaki, pp. 102-107.

ISSC (2003), *Technical Committee I.2 LOADS*, Proceedings of the 15th International Ship and Offshore Structures Congress, Mansour, A.E. and Ertikin, R.C., Edts., Vol. 1, San Diego, pp. 87-90.

KINOSHITA, T., KAGEMOTO, H., AND FUJINO, M. (1999), *A CFD Application to Wave-Induced Floating-Body Dynamics*, Proceedings of the International Conference on Numerical Ship Hydrodynamics, Nantes.

KLEMT, M. (2004), *Bewegungssimulation schwimmender Körper in viskoser Strömung*, Ph.D. thesis, TU Hamburg-Harburg (in german).

MUZAFERIJA, S. and PERIC, M. (1998), *Computation of Free-Surface Flows using Interface-tracking and Interface-Capturing-Methods,* Nonlinear Water Wave Interaction, Computational Mechanics Publ., Southampton, pp. 59-100.

ÖSTERGAARD, C. AND SCHELLIN, T.E. (1995), *Development of a Hydrodynamic Panel Method for Practical Analysis of Ships in a Seaway*, Transactions of the Schiffbautechnische Gesellschaft, Vol. 89, pp. 561-576.

PAPANIKOLAOU, A.D.; SCHELLIN, T.E. (1991), *A three-dimensional panel method for motions and loads of ships with forward speed*, Ship Technology Research 39, pp.147-156.

TANIZAWA, K. and BERTRAM, V. (1998), *Slamming*, Handbuch der Werften, Vol. XXIV, Hansa-Verlag, pp.191-210.

Alternative boundary-integral representations of 3D flow about a ship advancing through regular waves in finite water depth

Francis Noblesse[1] and Chi Yang[2,3]

[1] NSWCCD, 9500 MacArthur Blvd, West Bethesda, MD 20817, U.S.A.

[2] School of Computational Sciences, George Mason University, Fairfax, VA 22030, U.S.A.

[3] Cheung Kong Scholar, Shanghai Jiao Tong University, Shanghai, China

Introduction

The boundary-integral representations of 3D flow about a ship that advances through regular (time-harmonic) waves given in the literature involve a line integral around the ship waterline. This line integral can be transformed into surface integrals (over the ship surface and the free surface) via Stokes' theorem, as done in numerous studies (mostly for the special case of steady flows), e.g. *Eggers (1966), Brard (1972), Landweber (1972)*. Stokes' theorem is used here to transform the line integral around the ship waterline in the boundary-integral representation given in *Noblesse (2005)*. This boundary-integral representation is a composite of the classical potential representation, used in numerous studies, and the weakly-singular representation given in *Noblesse and Yang (2004a)*. The Stokes' transformations that are performed here yield several variants of the boundary-integral representation given in *Noblesse (2005)*.

Alternative basic potential-flow representations

Nondimensional coordinates, flow velocity, and velocity potential are defined in terms of a reference length L, velocity U, and potential UL. Hereafter, $\widetilde{\mathbf{x}} = (\widetilde{x}, \widetilde{y}, \widetilde{z})$ stands for a point inside a 3D flow region, and $\mathbf{x} = (x, y, z)$ represents a point of the boundary surface Σ of the flow region. The flow-field point $\widetilde{\mathbf{x}}$ and the boundary point $\mathbf{x}$ are associated with a Green function $G(\widetilde{\mathbf{x}}; \mathbf{x})$ that is used to formulate boundary-integral flow representations. The flow potential at a flow-field point $\widetilde{\mathbf{x}}$ or a boundary point $\mathbf{x}$ is represented by $\widetilde{\phi}$ or ϕ, respectively. Furthermore, $d\mathcal{A}$ stands for the differential element of area at a point $\mathbf{x}$ of the boundary surface Σ, $\mathbf{n}$ is a unit vector that points inside the flow region and is normal to Σ at $\mathbf{x}$, and $\nabla = (\partial_x, \partial_y, \partial_z)$.

The potential $\widetilde{\phi} = \phi(\widetilde{\mathbf{x}})$ at a field point $\widetilde{\mathbf{x}}$ within a 3D flow region bounded by a closed boundary surface Σ is defined in terms of the boundary values of the potential ϕ and its normal derivative $\mathbf{n} \cdot \nabla\phi$ by the classical Green boundary-integral representation

$$\widetilde{\phi} = \int_{\Sigma} d\mathcal{A} \, (G \, \mathbf{n} \cdot \nabla\phi - \phi \, \mathbf{n} \cdot \nabla G) \tag{1}$$

The representation (1) defines the potential $\widetilde{\phi}$ in terms of boundary distributions of sources (with strength $\mathbf{n} \cdot \nabla\phi$) and normal dipoles (strength ϕ), and involves a Green function G and the first derivatives of G. The boundary-integral representation (1) holds for a field point $\widetilde{\mathbf{x}}$ inside the flow region, strictly outside Σ. This restriction stems from the well-known property that the potential defined by the dipole distribution in (1) is not continuous at Σ. Indeed, $\widetilde{\phi}$ on the left of (1) becomes $\widetilde{\phi}/2$ at a point $\widetilde{\mathbf{x}}$ of the boundary surface Σ (if Σ is smooth at $\widetilde{\mathbf{x}}$). The boundary-surface integral on the right of (1) is null for a point $\widetilde{\phi}$ located outside the flow region bounded by Σ.

An interesting modification of Green's potential representation (1) is obtained if an integration by parts is performed in the dipole distribution in (1), as accomplished in *Noblesse and Yang (2004a)* using a vector Green function $\mathbf{G}$ that is associated with the scalar Green function G in (1) via the relation

$$\nabla \times \mathbf{G} = \nabla G \tag{2}$$

This relation implies that $\mathbf{G}$ and G are comparable, i.e. that the behaviors of G and $\mathbf{G}$ are comparable in both the nearfield and the farfield. In particular, $\mathbf{G}$ is no more singular than G in the nearfield. The relation (2) between a scalar Green function G and a related vector Green function $\mathbf{G}$ is analogous to the relation

$\nabla\times\boldsymbol{\Psi}=\nabla\phi$ between a velocity potential ϕ and a vector (3D) stream function $\boldsymbol{\Psi}$. The relation (2) does not define a unique vector Green function $\mathbf{G}$. Indeed, if $\mathbf{G}$ satisfies (2), $\mathbf{G}+\nabla H$ also satisfies (2) for an arbitrary scalar function H. Three basic vector Green functions that satisfy (2) are

$$\begin{aligned}
&\mathbf{G}_1=\nabla G^x\times\mathbf{e}_1=(0,G^x_z,-G^x_y) && \mathbf{e}_1=(1,0,0)\\
&\mathbf{G}_2=\nabla G^y\times\mathbf{e}_2=(-G^y_z,0,G^y_x) \quad \text{with} && \mathbf{e}_2=(0,1,0)\\
&\mathbf{G}_3=\nabla G^z\times\mathbf{e}_3=(G^z_y,-G^z_x,0) && \mathbf{e}_3=(0,0,1)
\end{aligned} \tag{3}$$

Here, a subscript or superscript attached to G indicates differentiation or integration, respectively. The three vector Green functions $\mathbf{G}_1$, $\mathbf{G}_2$ and $\mathbf{G}_3$ are related. In particular, $\mathbf{G}_1$ and $\mathbf{G}_2$ can be expressed as $\mathbf{G}_1=\mathbf{G}_3-\nabla G^{zx}_y$ and $\mathbf{G}_2=\mathbf{G}_3+\nabla G^{zy}_x$, i.e. are of the form $\mathbf{G}_3+\nabla H$ as expected. The vector Green function $\mathbf{G}=\mathbf{G}_3$ is used here.

Integration of the identity $[\,\nabla\times(\,\phi\nabla H\,)\,]\cdot\mathbf{n}=(\,\nabla\phi\times\nabla H\,)\cdot\mathbf{n}$ over a closed surface Σ yields

$$0=\int_\Sigma d\mathcal{A}\,(\,\nabla\phi\times\nabla H\,)\cdot\mathbf{n}=\int_\Sigma d\mathcal{A}\,(\mathbf{n}\times\nabla\phi)\cdot\nabla H \tag{4}$$

Similarly, integration of the more general identity

$$\{\,\nabla\times[\,\phi\,(\,\mathbf{G}+\nabla H\,)\,]\,\}\cdot\mathbf{n}=(\,\phi\,\nabla\times\mathbf{G}\,)\cdot\mathbf{n}+[\,\nabla\phi\times(\mathbf{G}+\nabla H\,)\,]\cdot\mathbf{n}$$

over a closed surface Σ and the relation (2) yield

$$-\int_\Sigma d\mathcal{A}\;\phi\,\mathbf{n}\cdot\nabla G=\int_\Sigma d\mathcal{A}\,(\mathbf{n}\times\nabla\phi)\cdot(\mathbf{G}+\nabla H) \tag{5}$$

The identity (4) shows that the transformation (5) is independent of the function H, which may then be chosen at will. The field point $\widetilde{\mathbf{x}}$ in (5) is located inside (or outside) the flow region, strictly off the boundary surface Σ. The transformation (5) expresses a surface integral involving the potential ϕ and the derivative ∇G of a Green function G as an integral that involves $\nabla\phi$ and the vector Green function $\mathbf{G}$, which is comparable to G. Thus, the transformation (5) corresponds to an integration by parts $(\,\phi\,,\nabla G)\longrightarrow(\,\nabla\phi\,,G)$.

Use of the transformation (5), with $H=0$, in Green's classical potential representation (1) yields

$$\widetilde{\phi}=\int_\Sigma d\mathcal{A}\,[\,G\,\mathbf{n}\cdot\nabla\phi+\mathbf{G}\cdot(\mathbf{n}\times\nabla\phi)\,] \tag{6}$$

The identity (4) shows that (6) defines a unique potential $\widetilde{\phi}$, even though (2) does not define a unique vector Green function $\mathbf{G}$. The potential representation (6) involves a Green function G and the related vector Green function $\mathbf{G}$, which is comparable to (in particular, is no more singular than) G as already noted. Thus the potential representation (6) is weakly singular in comparison to the classical representation (1), which involves ∇G. The potential $\widetilde{\phi}$ defined by the weakly-singular representation (6) is continuous at the boundary surface Σ, whereas (1) does not define a potential $\widetilde{\phi}$ that is continuous at Σ.

For the problem of wave diffraction-radiation by a ship, a Green function G that satisfies (approximately or exactly) the related free-surface boundary condition may be used in the potential-flow representations (1) and (6). Such a Green function is defined in terms of two complementary basic solutions: elementary waves $E=\exp\{\,k\,[z+i\,(x\cos\gamma+y\sin\gamma)]\,\}$, where k stands for a wavenumber, and the elementary free-space Rankine source $1/r$ with $r=\|\,\widetilde{\mathbf{x}}-\mathbf{x}\,\|$. These elementary solutions are associated with a wave component (dominant in the horizontal farfield) and a local-flow component (significant in the nearfield and dominant in the vertical farfield), respectively. For the local flow, the dipole term in the Green representation (1) is $O(1/r^2)$, which decays rapidly in the farfield but is strongly singular in the nearfield. The corresponding term in the alternative representation (6) is $O(1/r)$, which is weakly singular in the nearfield but decays slowly in the farfield. The potential representations (1) and (6) are then preferable in the farfield and the

nearfield, respectively. For the wave component, the dipole term in (1) involves ∇E, which is $O(k)$, whereas the corresponding term in (6) involves the $O(1)$ terms E^z_x and E^z_y. The representations (1) and (6) are then preferable for small and large wavenumbers k (i.e. for long and short waves), respectively. Thus, Green's classical representation (1) and the weakly-singular representation (6) are best suited in the farfield and nearfield, and to represent long and short waves, respectively, and clearly are complementary.

It is then useful to consider a composite boundary-integral representation that is equivalent to Green's representation (1) in the limits $r \to \infty$, $k \to 0$ and the weakly-singular representation (6) in the limits $r \to 0$, $k \to \infty$. Such a composite representation is easily constructed, and is given in *Noblesse (2005)*. Specifically, Green's potential representation (1) can be expressed as

$$\widetilde{\phi} = \int_\Sigma d\mathcal{A}\,[\,G\,\mathbf{n}\cdot\nabla\phi - (1-P)\,\phi\,\mathbf{n}\cdot\nabla G - P\phi\,\mathbf{n}\cdot\nabla G\,]$$

where $P = P(\mathbf{x}\,;\widetilde{\mathbf{x}})$ stands for a function of $\mathbf{x}$ and $\widetilde{\mathbf{x}}$. The transformation (5), with ϕ replaced by $P\phi$, applied to the term $P\phi\,\mathbf{n}\cdot\nabla G$ yields

$$\widetilde{\phi} = \int_\Sigma d\mathcal{A}\,[\,G\,\mathbf{n}\cdot\nabla\phi + \mathbf{E}^t\cdot(\,\mathbf{n}\times\nabla\phi\,) - \mathbf{n}\cdot\mathbf{E}^\phi\phi\,] \tag{7}$$

$$\text{with} \qquad \mathbf{E}^t = P\,\mathbf{G} \qquad \mathbf{E}^\phi = (1-P)\nabla G + \mathbf{G}\times\nabla P \tag{8}$$

The potential representation (7) generalizes the classical Green representation (1) and the weakly-singular representation (6), which correspond to the special cases $P = 0$ and $P = 1$, respectively, and thus can be regarded as special cases of the more general family of potential representations (7). For a weight function P chosen so that $P \to 1$ fast enough in the nearfield, the integrands of the boundary-surface integrals in the potential representations (7) and (6) are asymptotically equivalent in the nearfield, and the potential $\widetilde{\phi}$ defined by these weakly-singular representations is continuous at Σ. Similarly, the integrands of the boundary-surface integrals in the representations (7) and (1) are asymptotically equivalent in the farfield if $P \to 0$ sufficiently rapidly in the farfield.

Application to wave diffraction-radiation by a ship

The general flow representation (7) is now applied to free-surface potential flow about a ship (or offshore structure). The z axis is vertical and points upward, and the mean free surface is taken as the plane $z = 0$. For steady or time-harmonic flow about a ship advancing in calm water or in waves, the x axis is chosen along the path of the ship and points toward the bow. The reference length L and velocity U used to nondimensionalize coordinates and the velocity potential may be chosen as the ship length and $\sqrt{gL}$, where g is the acceleration of gravity. An alternative reference velocity is the ship speed $\mathcal{U}$.

Let Σ_B be a surface located outside the viscous boundary layer that surrounds the ship hull. The surface Σ_B includes the outer edge of the viscous wake trailing the ship, or a surface outside the viscous wake. If viscous effects are ignored, Σ_B may be taken as the mean wetted ship hull. For a ship equipped with lifting surfaces, e.g. a sailboat, Σ_B also includes the two sides of every vortex sheet behind the ship hull. For a multihull ship, the hull+wake surface Σ_B consists of several component surfaces, which correspond to the separate hull components of the ship and their wakes. The flow region is bounded by the closed surface

$$\Sigma = \Sigma_B \cup \Sigma_0 \cup \Sigma_D \cup \Sigma_\infty \tag{9}$$

where Σ_0 is the portion of the mean free-surface plane $z = 0$ located outside the "body" surface Σ_B, Σ_D is the sea floor $z = -D/L$ (assumed to be a rigid wall), and Σ_∞ joins Σ_0 and Σ_D in the farfield. The intersection curve between the surfaces Σ_B and Σ_0, i.e. the intersection of the body surface Σ_B with the mean free surface, is identified by Γ hereafter. The unit vector $\mathbf{t} = (\,t^x, t^y, 0\,)$ is tangent to the curve Γ and oriented clockwise (looking down), and (as already noted) the unit vector $\mathbf{n} = (\,n^x, n^y, n^z\,)$ is normal to the boundary surface Σ and points into the flow domain. Thus, $\mathbf{n} = (0\,,0\,,-1)$ at the free surface Σ_0 and $\mathbf{n} = (0\,,0\,,1)$ at the sea floor Σ_D.

The flow representation (7), with the boundary surface (9), yields

$$\widetilde{\phi} = \int_{\Sigma_B} d\mathcal{A}\,[\,G\,\mathbf{n}\cdot\nabla\phi + \mathbf{E}^t\cdot(\mathbf{n}\times\nabla\phi) - \mathbf{n}\cdot\mathbf{E}^\phi\,\phi\,] - \int_{\Sigma_D} dx\,dy\,A_D - \int_{\Sigma_0} dx\,dy\,(G\,\phi_z - A_D) \tag{10}$$

Here, $\mathbf{E}^t$ and $\mathbf{E}^\phi$ are given by (8), with $\mathbf{G} = \mathbf{G}_3$ given by (3), and A_D is defined as

$$A_D = G^z_x\,(P\phi)_x + G^z_y\,(P\phi)_y + (1-P)\,G_z\,\phi \tag{11}$$

The boundary condition $\phi_z = 0$ at the rigid sea floor Σ_D was used in (11). Furthermore, the Green function G in (10) is presumed to vanish sufficiently rapidly in the farfield to nullify the contribution of the farfield boundary surface Σ_∞, which may be taken as a cylindrical surface of radius $h = \sqrt{x^2+y^2}$, as $h \to \infty$. Thus, the contribution of Σ_∞ in (9) is ignored, and the surfaces Σ_0 and Σ_D are unbounded in (10).

The free-surface-flow representation (10) is now considered for diffraction-radiation by a ship that advances (with speed $\mathcal{U}$) through regular waves (with frequency ω). We define the nondimensional wave frequency f, the Froude number F, $\widehat{\tau}$, and the free- surface functions π^ϕ and π^G as

$$f = \omega\,\sqrt{L/g} \qquad F = \mathcal{U}/\sqrt{gL} \qquad \widehat{\tau} = 2\,f\,F = 2\,\omega\,\mathcal{U}/g \tag{12}$$

$$\pi^\phi = \phi_z - f^2\,\phi + i\,\widehat{\tau}\,\phi_x + F^2\,\phi_{xx} \qquad \pi^G = G_z - f^2\,G - i\,\widehat{\tau}\,G_x + F^2\,G_{xx} \tag{13}$$

The integrand of the free-surface integral in (10) can be expressed as $G\,\pi^\phi - A_0 + a_0$ with

$$\begin{aligned} A_0 &= (\pi^G)^{zz}_x\,(P\phi)_x + (\pi^G)^{zz}_y\,(P\phi)_y + (1-P)\,\pi^G\,\phi \\ a_0 &= [\,(1-P)(F^2\,G_x - i\,\widehat{\tau}\,G)\,\phi - F^2\,G\,\phi_x\,]_x - f^2\,[\,(P\,G^{zz}_x\,\phi)_x + (P\,G^{zz}_y\,\phi)_y\,] \\ &\quad + [\,(F^2\,G_x - i\,\widehat{\tau}\,G)^{zz}_y\,(P\phi)_y\,]_x - [\,(F^2\,G_x - i\,\widehat{\tau}\,G)^{zz}_y\,(P\phi)_x\,]_y \end{aligned} \tag{14}$$

Stokes' theorem and (3) can then be used to express the free-surface integral in (10) as

$$\int_{\Sigma_0} dx\,dy\,(G\,\phi_z - A_D) = \int_{\Sigma_0} dx\,dy\,(G\,\pi^\phi - A_0) + \int_\Gamma d\mathcal{L}\,A_\Gamma$$

where A_0 is given by (14) and A_Γ is defined as

$$A_\Gamma = f^2\,\phi\,P\,\mathbf{G}^z\cdot\mathbf{t} + (F^2\,G_x - i\,\widehat{\tau}\,G)^{zz}_y\,\mathbf{t}\cdot\nabla(P\phi) + t^y\,[\,(1-P)(F^2\,G_x - i\,\widehat{\tau}\,G)\,\phi - F^2\,G\,\phi_x\,] \tag{15}$$

with $\mathbf{G}^z = (\,G^{zz}_y\,, -G^{zz}_x\,, 0\,)$ in accordance with (3). In the line integral around the curve Γ, $\mathbf{t} = (\,t^x, t^y, 0\,)$ is a unit vector tangent to Γ (oriented clockwise; looking down), as already noted, and $d\mathcal{L}$ stands for the differential element of arc length of Γ. Substitution of the foregoing Stokes' transformation into (10) yields

$$\widetilde{\phi} = \int_{\Sigma_B} d\mathcal{A}\,[\,G\,\mathbf{n}\cdot\nabla\phi + \mathbf{E}^t\cdot(\mathbf{n}\times\nabla\phi) - \mathbf{n}\cdot\mathbf{E}^\phi\,\phi\,] - \int_\Gamma d\mathcal{L}\,A_\Gamma - \int_{\Sigma_0} dx\,dy\,(G\,\pi^\phi - A_0) - \int_{\Sigma_D} dx\,dy\,A_D \tag{16}$$

where $\mathbf{E}^t$, $\mathbf{E}^\phi$, A_D, A_0 and A_Γ are given by (8), (11), (14) and (15). The potential representation (16) is identical to the representation given in *Noblesse (2005)*. Variants of the representation (16), obtained by using Stokes' theorem to transform the line integral around the boundary curve Γ in (16) into surface integrals, are given below.

Stokes' theorem and (2) yield

$$\int_\Gamma d\mathcal{L}\,\phi\,P\,\mathbf{G}^z\cdot\mathbf{t} = \int_{\Sigma_B} d\mathcal{A}\,\mathbf{n}\cdot[\,P\phi\,\nabla G^z + \nabla(P\phi)\times\mathbf{G}^z\,]$$

Use of this Stokes' transformation in (16), with (8) and (15), shows that A_Γ, $\mathbf{E}^t$ and $\mathbf{E}^\phi$ in (16) become

$$A_\Gamma = (F^2\,G_x - i\,\widehat{\tau}\,G)^{zz}_y\,\mathbf{t}\cdot\nabla(P\phi) + t^y\,[\,(1-P)(F^2\,G_x - i\,\widehat{\tau}\,G)\,\phi - F^2\,G\,\phi_x\,] \tag{17a}$$

$$\mathbf{E}^t = P\,(\mathbf{G} - f^2\,\mathbf{G}^z) \qquad \mathbf{E}^\phi = (1-P)\,\nabla G + f^2\,P\,\nabla G^z + (\mathbf{G} - f^2\,\mathbf{G}^z)\times\nabla P \tag{17b}$$

Expressions (17b) yield

$$\mathbf{E}^t = 0 \qquad \mathbf{E}^\phi = \nabla G \qquad \text{for} \quad P = 0$$
$$\mathbf{E}^t = \mathbf{G} - f^2\,\mathbf{G}^z \qquad \mathbf{E}^\phi = f^2\,\nabla G^z \qquad \text{for} \quad P = 1$$

A useful property of the potential representation defined by (16), (17), (14) and (11) is that, in the special case $F = 0$ (i.e. for wave diffraction-radiation without forward speed; e.g. by an offshore structure) the function A_Γ defined by (17a) is null, whereas the function A_Γ defined by (15) is not null. Thus, no numerical cancellations can occur between the surface integral over Σ_B and the line integral around Γ for the potential representation associated with (17) in the special case $F = 0$.

Another application of Stokes' theorem yields

$$\int_\Gamma d\mathcal{L}\, G_y^{zz}\, \mathbf{t}\cdot\nabla(P\phi) = \int_{\Sigma_B} d\mathcal{A}\, \mathbf{n}\cdot[\,\nabla G_y^{zz} \times \nabla(P\phi)\,]$$

This Stokes' transformation and (17) show that A_Γ, $\mathbf{E}^t$ and $\mathbf{E}^\phi$ in (16) become

$$A_\Gamma = F^2[\,G_{xy}^{zz}\,\mathbf{t}\cdot\nabla(P\phi) - t^y G\,\phi_x\,] + t^y\,(1-P)(F^2 G_x - i\widehat{\tau}\,G)\,\phi \tag{18a}$$
$$\mathbf{E}^t = P\,(\mathbf{G} - f^2\,\mathbf{G}^z - i\widehat{\tau}\,\nabla G_y^{zz}\,) \tag{18b}$$
$$\mathbf{E}^\phi = (1-P)\nabla G + f^2 P\,\nabla G^z + (\mathbf{G} - f^2\,\mathbf{G}^z - i\widehat{\tau}\,\nabla G_y^{zz}\,)\times\nabla P \tag{18c}$$

Yet another application of Stokes'theorem yields

$$\int_\Gamma d\mathcal{L}\, t^y\,(1-P)(F^2 G_x - i\widehat{\tau}\,G)\,\phi = \int_{\Sigma_B} d\mathcal{A}\, \mathbf{n}\cdot\{\,\nabla\,[(1-P)(F^2 G_x - i\widehat{\tau}\,G)\,\phi\,]\times\mathbf{e}_2\}$$

This Stokes' transformation and (18) show that A_Γ, $\mathbf{E}^t$ and $\mathbf{E}^\phi$ in (16) become

$$A_\Gamma = F^2[\,G_{xy}^{zz}\,\mathbf{t}\cdot\nabla(P\phi) - t^y G\,\phi_x\,] \tag{19a}$$
$$\mathbf{E}^t = P\,(\mathbf{G} - f^2\,\mathbf{G}^z - i\widehat{\tau}\,\nabla G_y^{zz}\,) - (1-P)\,\widehat{\mathbf{G}} \quad \text{with} \quad \widehat{\mathbf{G}} = (F^2 G_x - i\widehat{\tau}\,G)\,\mathbf{e}_2 \tag{19b}$$
$$\mathbf{E}^\phi = (1-P)(\,\nabla G + \nabla\times\widehat{\mathbf{G}}\,) + f^2 P\,\nabla G^z + (\mathbf{G} - f^2\,\mathbf{G}^z - i\widehat{\tau}\,\nabla G_y^{zz} + \widehat{\mathbf{G}}\,)\times\nabla P \tag{19c}$$

In the special case $P = 1$, expressions (18) and (19) are identical and become

$$A_\Gamma = F^2(G_{xy}^{zz}\,\mathbf{t}\cdot\nabla\phi - t^y G\,\phi_x\,) \qquad \mathbf{E}^t = \mathbf{G} - f^2\,\mathbf{G}^z - i\widehat{\tau}\,\nabla G_y^{zz} \qquad \mathbf{E}^\phi = f^2\,\nabla G^z \tag{20}$$

The functions A_Γ defined by (20), (19a), (18a) and (17a) are null in the special case $F = 0$, but are not null if $F \neq 0$. Thus, the potential representations associated with these expressions for A_Γ involve a line integral around the boundary curve Γ if $F \neq 0$. A potential representation that does not involve a line integral (in the general case $F \neq 0$) can be obtained if Stokes' theorem is used in (19a). However, this Stokes' transformation does not yield a weakly-singular flow representation and introduces second derivatives of the potential ϕ, whereas the boundary-integral representations obtained previously are weakly singular and only involve ϕ and $\nabla\phi$.

The velocity component ϕ_x in (19a), (18a), (17a) and (15) can be expressed as

$$\phi_x = t^x\,\mathbf{t}\cdot\nabla\phi - n^z t^y\,(\mathbf{n}\times\mathbf{t}\,)\cdot\nabla\phi - t^y\sqrt{1-(n^z)^2}\;\mathbf{n}\cdot\nabla\phi = t^x\,\mathbf{t}\cdot\nabla\phi - t^y\,\mathbf{n}^\Gamma\cdot\nabla\phi \tag{21}$$

where $\mathbf{n}^\Gamma = (-t^y, t^x, 0)$ stands for a unit vector that is normal to the curve Γ in the free-surface plane $z = 0$ and points into the flow region. The first of expressions (21) defines ϕ_x in terms of the velocity component $\mathbf{n}\cdot\nabla\phi$ normal to Σ_B and the velocity components $\mathbf{t}\cdot\nabla\phi$ and $(\,\mathbf{n}\times\mathbf{t}\,)\cdot\nabla\phi$ tangent to Σ_B.

Conclusion

In summary, the potential $\widetilde{\phi}$ (at a field point $\widetilde{\mathbf{x}}$) for 3D flow about a ship advancing through regular waves in finite water depth is defined in terms of the potential ϕ and the velocity $\nabla\phi$ (at boundary points $\mathbf{x}$) by the boundary-integral representation (16), where A_D and A_0 are given by (11) and (14), and A_Γ, $\mathbf{E}^t$ and $\mathbf{E}^\phi$ are defined by four alternative sets of expressions: [1] expressions (8) and (15), [2] expressions (17), [3] expressions (18), and [4] expressions (19). The flow representations [1]–[3] are identical in the special case $f = 0$ (i.e. for steady flow about a ship advancing in calm water). For $P = 1$, the representations [3] and [4] are identical, and the functions A_Γ, $\mathbf{E}^t$ and $\mathbf{E}^\phi$ in (16) are given by the simpler expressions (20).

The potential representations associated with expressions [1]–[4] for A_Γ, $\mathbf{E}^t$ and $\mathbf{E}^\phi$ are mathematically equivalent, and are related to one another by simple Stokes' transformations between a line integral around the boundary curve Γ and a surface integral over the hull surface Σ_B. The alternative flow representations [1]–[4] do not involve functions that are more singular than a Green function G, and thus are weakly singular. The Green function G in the alternative flow representations [1]–[4] may be chosen at will. A practical choice for G is the simple farfield Green function given in *Noblesse and Yang (2004b*).

The potential representation [1] involves a line integral around the boundary curve Γ for all values of F and f, including the special cases $F = 0$ or $f = 0$. The flow representations [2]–[4] do not involve a line integral around Γ in the special case $F = 0$ (for wave diffraction-radiation without forward speed), but involve a line integral if $F \neq 0$. A potential representation that does not involve a line integral (in the general case $F \neq 0$) can be obtained if Stokes' theorem is used in the representation [4]. However, a straightforward Stokes' transformation of (19a) does not yield a weakly-singular boundary-integral representation and introduces second derivatives of the potential ϕ, at variance with the boundary-integral representations [1]–[4] which are weakly singular and only involve ϕ and $\nabla\phi$. A potential representation that does not involve a line integral can be obtained by using a 3D stream function $\mathbf{\Psi}$ and the transformation (5) to perform an integration by parts of the source component $G\,\mathbf{n}\cdot\nabla\phi$ in the Green representation (1) and the related potential representations given above. This approach will be considered elsewhere.

Every one of the alternative potential representations [1]–[4] may in principle be used for numerical purposes, although a representation may be preferable in practice. In particular, the potential representation [2] may be preferable to the representation [1] in the special case $f = 0$ (i.e. for wave diffraction-radiation without forward speed; e.g. by an offshore structure) because the function A_Γ given by (17a) is null (in the special case $F = 0$, whereas the function A_Γ given by (15) is not null. Thus, no numerical cancellations can occur between the surface integral over Σ_B and the line integral around Γ for the potential representation [2] associated with (17) in the special case $F = 0$. The potential representations [3] and [4] may also provide useful alternatives to the representations [1] and [2] in the general case $Ff \neq 0$.

References

Brard R. (1972) "The representation of a given ship form by singularity distributions when the boundary condition on the free surface is linearized", *J. Ship Research*, 16:79-92

Eggers, K. (1966) "On second order contributions to ship waves and wave resistance", *6th Symp. on Naval Hydro.*, Washington DC

Landweber L. (1972) "Contributions on some current problems of ship resistance", *Il Jubilee Meeting, 40th Anniversary Netherland Ship Model Basin*, 32-45

Noblesse F. (2005) "Generalized boundary-integral representation of 3D flow about a ship advancing in regular waves", *10^e Journées de l'Hydrodynamique*, Nantes, France, 379-392

Noblesse F. and Yang C. (2004a) "Weakly-singular boundary-integral representations of free-surface flows about ships or offshore structures", *J. Ship Research*, 48:31-44

Noblesse F., Yang C. (2004b) "A simple Green function for diffraction-radiation of time-harmonic waves with forward speed", *Ship Technology Research*, 51:35-52

Effect of interpolation in interface capturing methods

Roozbeh Panahi, Ebrahim Jahanbakhsh, Mohammad S. Seif
Shrif University of Technology
Roozbeh_Panahi@mehr.sharif.ir

1. Introduction

In many engineering applications, from open channel flow [1] to near interface hydrofoil [2], there are need to simulate the free surface. In general, flow of two immiscible fluids can be classified into three category based on the structure of the interface between them [3]:

- Two fluids separated by a sharp interface, e.g. flows in open channels without wave breaking.
- Transitional flows, in which parts of interface break into regions filled by both fluids, e.g. air bubbles trapped in liquid.
- Dispersed flows, in which two fluids make a suspension without a clearly defined interface, e.g. in rigorously shaken tank.

Numerical methods which are nearly applicable in two first problems can be categorized in two main groups [3]:

- Interface tracking or surface methods
- Interface capturing or volume methods

Interface tracking or moving mesh methods mark and track the interface with calculations only on one phase based on the satisfaction of two conditions [4]:

1. Free surface is a sharp interface between two fluids and there is no flow across it (interface kinematics condition).
2. Forces acting on fluid in free surface are in equilibrium (interface dynamic condition).

Surface methods maintain sharp interfaces for which the exact position is known throughout the calculation, but there is a great disadvantage of treating the large deformation of free surface [5]. However this can be overcome with some modification in mesh movement algorithms [6].

In volume methods, different fluids are marked with massless particles (MAC (Marker And Cell)) [7] or by volume fraction (eq.1). The advantage of such methods is their ability to cope with the arbitrary shaped interfaces and large deformations as well as rupture and coalescence in natural way [5].

$$Volume\ Fraction = \alpha = \frac{Volume\ of\ \ fluid\ 1}{total\ volume\ of\ control\ volume} \tag{1}$$

Considering the value of volume fraction, all properties of the effective fluid will be calculated:

$$\rho = \rho_1\alpha + \rho_2(1-\alpha)$$
$$\mu = \mu_1\alpha + \mu_2(1-\alpha) \tag{2}$$

The SLIC (Simple Line Interface Calculation) is one of the first methods that falls in volume methods category. The fluid distribution of a cell that contains part of the interface is obtained by using the volume fraction distribution of neighboring cells. It approximates the interface in each cell as a parallel line to one of the coordinate axes [8], and can not represent exact interface [9].

The idea of donner-acceptor scheme, in which the volume fraction value of downwind cell (acceptor cell) of a cell face is used to predict the level of volume fraction transported through it during a time step [10], was the basic idea of VoF (Volume of Fluid) scheme. The problem associated with the donner-acceptor formulation is that it causes incorrect steeping on interfaces which are aligned with flow direction. VoF Scheme improved that formulation by including some information on the slope of interface into fluxing algorithm in discretisation of scalar transport equation (eq.3) [11]. It has also been extended to three dimensions [12].

$$\frac{\partial\alpha}{\partial t} + div(\alpha\vec{v}) = 0 \tag{3}$$

In same methods, this equation is used to calculate distance of fluid to interface (level set methods) [13, 14]. Although VoF scheme ensures physical volume fraction values (overall boundedness between zero and one), it doesn't preserve local boundedness; i.e., a volume fraction value which initially lies between the values of its neighbors, does not necessarily preserve this property when advected in the absence of source or sink [9].

In addition to this problem, working with transport equation includes numerical diffusion. Composite schemes have been introduced to solve local boundedness in addition to less numerical diffusion and keeping transitional area through one cell, that all were the deficiencies of simple methods.

In this paper, two high resolution composite schemes will be presented and Differences between their switching (when and where) and its effect on convection results in analyzing of various bench marks will be discussed.

2. Transport equation

The finite volume discretisation of volume fraction transport equation (eq.3) is based on Integration over control volume and the time step. Using the Gauss theorem and Crank-Nicholson scheme in small enough time step for time discretisation result in:

$$\alpha_P^{t+\delta t}\frac{V_P}{\delta t}+\sum_{f=1}^{n}\frac{1}{2}\alpha_f^{t+\delta t}F_f=S_{\alpha_P} \tag{4}$$

Where the source term is:

$$S_{\alpha_P}=\alpha_P^{t}\frac{V_P}{\delta t}-\sum_{f=1}^{n}\frac{1}{2}\alpha_f^{t}F_f \tag{5}$$

This set of equations use the volume fraction values in cell centers as well as faces centers. That is, an interpolation must be applied. As mentioned earlier, popular interpolations, such as central differencing scheme introduce some problems and high resolution composite schemes can resolve them in good manner. Such schemes can be represented with different means such as TVD (Total Variable Diminishing) [15], FCT (Flux Corrected Transport) [16] and NVD (Normalized Variable Diagram) [18]. However, NVD is the most popular concept for applying boundedness criteria (face control), in discretised form of convection equations [9]. NVD can be used to give normal expression for α_D and α_f [Fig. 1]:

$$\tilde{\alpha}_D=\frac{\alpha_D-\alpha_U}{\alpha_A-\alpha_U} \tag{6}$$

$$\tilde{\alpha}_f=\frac{\alpha_f-\alpha_U}{\alpha_A-\alpha_U} \tag{7}$$

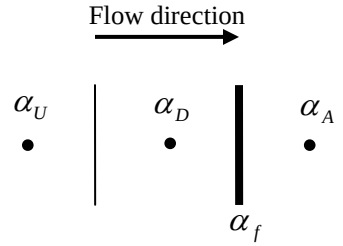

Fig.1. One dimensional control volume

Where in donner-acceptor formulations, donner and acceptor cells are identifying according to the flow direction.

Most composite differencing methods take some information about interface slope into account in different language and properly switch between to high order and low order interpolation schemes in which they use all their benefits to yield a bounded scalar filed with less numerical diffusion.

Two high order differencing methods which are constructed on NVD basis will be discussed in the next sections.

2.1. CICSAM (Compressive Interface Capturing for Arbitrary Meshes)

All Composite differencing methods, switch between different schemes and the main distinction is that how they switch between these schemes. For example, original VoF switches to upwind from downwind, when the angle between the interface and direction of motion is 45^0.

In order to reach less numerical diffusion, CICSAM uses CBC [17] (Convection Boundedness Criteria) as the most compressive scheme that stipulates robust local bounds on $\tilde{\alpha}_f$:

$$\tilde{\alpha}_{f_{CBC}}=\begin{cases}\min\left\{1,\dfrac{\tilde{\alpha}_D}{C_D}\right\} & \text{when } 0\le\tilde{\alpha}_D\le 1\\ \tilde{\alpha}_D & \text{when } \tilde{\alpha}_D\le 0,\tilde{\alpha}_D>1\end{cases} \tag{8}$$

CBC does not actually preserve the shape of interface [5], thus it is necessary to switch to another scheme which will preserve the interface shape better. CICSAM uses UQ (ULTIMATE-QUICKEST) [18] scheme to switch, when is needed to reach its aim, which in explicit form can be represented as:

$$\tilde{\alpha}_{f_{UQ}} = \begin{cases} \min\left\{ \dfrac{8C_f\tilde{\alpha}_D + (1-C_f)(6\tilde{\alpha}_D + 3)}{8}, \tilde{\alpha}_{f_{CBC}} \right\} & when 0 \le \tilde{\alpha}_D \le 1 \\ \tilde{\alpha}_D & when\ \tilde{\alpha}_D < 0,\ \tilde{\alpha}_D > 1 \end{cases} \quad (9)$$

A key issue in composite schemes is how to switch. CICSAM introduces a weighting factor γ_f, based on the angle between the interface and the direction of the motion to predict the normalized face value as:

$$\tilde{\alpha}_f = \gamma_f \tilde{\alpha}_{f_{CBC}} + (1-\gamma_f)\tilde{\alpha}_{f_{UQ}} \quad (10)$$

Finally, face volume fraction value is calculated, using the definitions of NVD and eq.10

In this manner, discretisation of scalar transport equation (eq.3) has been completed by substituting face values with such an interpolation. But as mentioned earlier, all basics of CICSAM method are one dimensional in their original form and extracting such a three dimensional scheme leads to none physical values in some cases. To overcome this problem, a correction step added to volume fraction calculation procedure, which changes the weighting factor β_f implicitly to reach physical distribution, according to mass conservation [5].

2.2. HRIC

This method is also switches between two schemes:

$$\tilde{\alpha}^{**}{}_f = \begin{cases} \tilde{\alpha}_D & \tilde{\alpha}_D < 0 \\ 2\tilde{\alpha}_D & 0 < \tilde{\alpha}_D < 0.5 \\ 1 & 0.5 < \tilde{\alpha}_D < 1 \\ \tilde{\alpha}_D & 1 < \tilde{\alpha}_D \end{cases} \quad (11)$$

$$\tilde{\alpha}^{*}{}_f = \begin{cases} \tilde{\alpha}_f & C_D < 0.3 \\ \tilde{\alpha}_D + (\tilde{\alpha}_f - \tilde{\alpha}_D)\dfrac{0.7 - C_D}{0.4} & 0.3 < C_D < 0.7 \\ \tilde{\alpha}_D & 0.7 < C_D \end{cases} \quad (12)$$

Where C_D is Donner Cell Courant Number.

Here, the switching function is $\sqrt{\cos\theta}$ that includes the effect of two schemes in calculation of normal face value according to the angle between interface and direction of the motion:

$$\tilde{\alpha}_f = \tilde{\alpha}^{*}{}_f \sqrt{\cos\theta} + \tilde{\alpha}_D (1 - \sqrt{\cos\theta}) \quad (13)$$

3. Test Cases

The test cases in this section focus on the interfaces advection of different shapes exposed to translation and shear flow according to CICSAM, HRIC, Hyper-C and UQ (ULTIMATE-QUICKEST) [18] interpolations in developed program. Both Hyper-C and UQ are simple methods besides Hyper-C uses the CBC as its interpolation.

For the purpose of comparison the solution errors, it is defined as:

$$E = \frac{\sum_{i}^{all\ cells} \left\| \alpha_i^n Vol_i - \alpha_i^a Vol_i \right\|}{\sum_{i}^{all\ cells} \alpha_i^o Vol_i} \quad (14)$$

Where α^n is the calculated solution after *n* time steps, α^a the analytical solution and α^o the initial condition.

Two meshes are employed for these benchmarks:

- 100*100 uniformly spaced cells for $x, y \in [0, \pi]$
- 200*200 uniformly spaced cells for $x \in [0,2]$ and $y \in [0,1]$

Time step in all problems have been adjusted to get maximum Courant number of 0.25.

3.1. Constant oblique velocity field

The first test case is the convection of different scalar distributions with a one dimensional velocity field (u,v) = (2,1) which is constant in whole computational domain [Fig.2].

Close-up views of final advected shapes of circle and hollow square are given besides exact scalar distribution which is constant during advection (Figs.3 and 4). CICSAM and Hyper-C methods are of better

performance in preserving the shape of interface besides less numerical diffusion relative to HRIC. This could be predicted because HRIC uses upwind value as one of its switching schemes that is the source of diffusion.

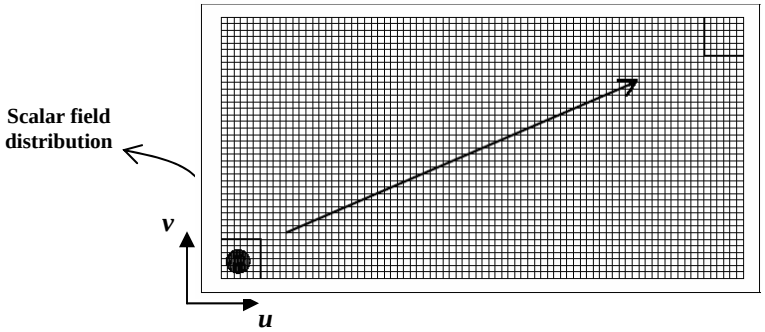

Fig.2. Advection pattern and scalar distribution in computational domain

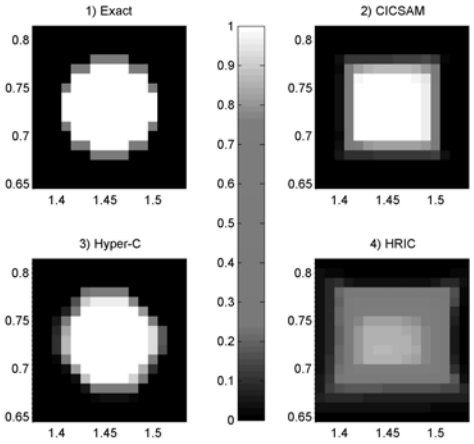

Fig.3. Circle distribution after 500 time steps: (1) exact solution, (2) advection according to CICSAM, (3) advection according to Hyper-C, (4) advection according to HRIC

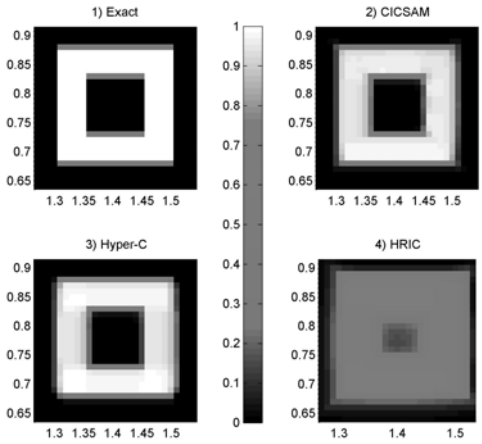

Fig.4. Hollow square distribution after 500 time steps: (1) exact solution, (2) advection according to CICSAM, (3) advection according to Hyper-C, (4) advection according to HRIC

Hyper-C scheme represents less numerical diffusion in comparison with other schemes (Table. 1) in one dimensional flow, however renders wrinkle in interface of complex flows [19]. It has been seen that UQ scheme, has much numerical diffusion, although there is serious disability in shape preservation according to its numerical diffusion.

Table.1. Errors of different methods in scalar transformation

Method	Circle advection	Hollow square advection
CICSAM	0.2009	0.1068
HRIC	0.5147	0.6078
Hyper-C	0.0994	0.957
UQ	1.4152	1.1787

3.2. Shear Flow

Most real two phase flows have shear velocity field. That is, it is important to evaluate the performance of such methods in the presence of shear flow, when interface deforms considerably rather keeping its shape.
In this section a scalar distribution like Fig.5 is encountered to shear velocity field and the ability of mentioned schemes tested with comparison of shape deformations and generated errors. The volume fraction field is exposed to such a velocity field for certain time steps, after which the velocities are reversed for the same time length, in order to return the volume fraction to the initial condition.
The results just before velocities reversation and at the end of the calculation for 1000 and 2000 time steps are given in Fig.6 for CICSAM method and Fig.7 for Hyper-C and HRIC methods.
It seems that CICSAM is the most robust method in preserving actual interface deformation with minimum numerical diffusion, the case that HRIC has serious disadvantage. From numerical diffusion view point,

Hyper-C scheme is more applicable than HRIC, but it has less accuracy in interface shape preservation that comes from its limitation to one dimensional flow rather than HRIC.

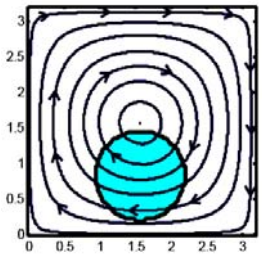

Fig.5. Scalar distribution in shear velocity field

Errors have been calculated according to convected and exact scalar distributions after applying one forward and backward velocity field for 1000 and 2000 time steps and are given in Table 2. However, UQ method represents high numerical diffusion and is not in the order of other methods in shear flow advection.

Table2. Errors of different methods in shear flow advection

Method	Error for 1000 time step forward followed by its backward	Error for 2000 time step forward followed by its backward
CICSAM	0.0316	0.0589
HRIC	0.0763	0.1377
Hyper-C	0.0467	0.1327

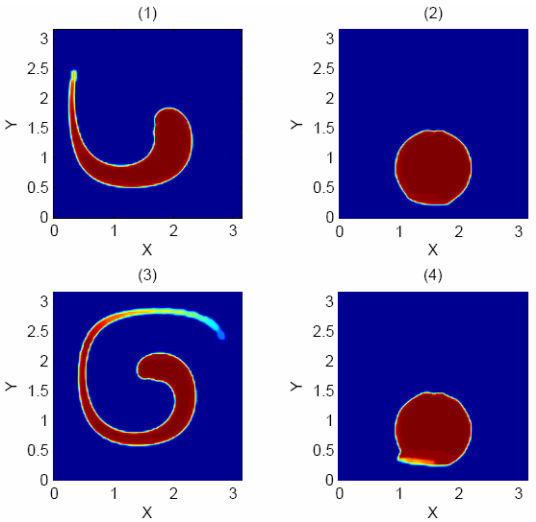

Fig.6. Results for the shear flow case according to CICSAM method: (1) after 1000 step forward, (2) after 1000 step forward followed by 1000 step backward, (3) after 2000 step forward, (4) after 2000 step forward followed by 2000 step backward

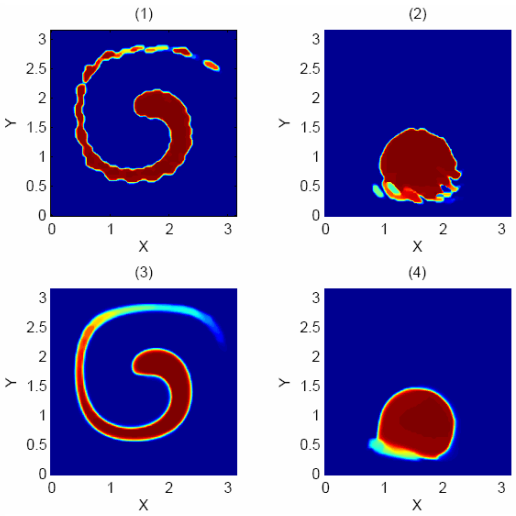

Fig.7 Results for the shear flow case. (1) after 2000 step forward according to Hyper-C, (2) after 2000 step forward followed by 2000 step backward according to Hyper-C, (3) after 2000 step forward according to HRIC, (4) after 2000 step forward followed by 2000 step backward according to HRIC

4. Conclusion

In order to treat the two phase flow, finite volume methods, use different interface schemes that can be categorized as Interface tracking and interface capturing methods. Volume methods has some advantages in complex interface deformations like wave breaking that hold them as the robust and interesting choices, although they must solve an additional scalar convection equation to give volume fraction distribution in all computational domain that exerts more computational effort. One needs a proper interpolation scheme that results in less numerical diffusion and local boundedness preservation in addition to take a real, well defined interface shape to apply on discretised form of volume fraction transport equation. CICCSAM as a high order composite method set an appropriate equilibrium between these challenges and with its correction step, implicitly modifies unphysical volume fraction values in a fully conservative procedure. Although Hyper-C represents less error in one dimensional flows.

References

1. Yamamoto, Y., Kunugi, T, Serizawa, A., *Turbulance statistics and scalar transport in an open-channel flow*, Journal of Turbulence, 2001.
2. Bourgoyne, D. A., Hamel, J. M., Judge C.Q., Ceccio, S.L,.Dowling, D.R., Cutbrith, J.M., *Hydrofoil near-wake structure and dynamic at high Reynolds number*, 24th symposium of naval architecture,2003.
3. Muzaferija, S., Peric, M., *Computation of free surface flows using interface tracking and interface capturing methods*, chap. 2 in O. Mahrenholtz and M. Markiewicz (eds.), Nonlinear Water Waves Interaction, computational Mechanics Publications, Suothahmpton, 1998.
4. ferziger, J. H., Peric, M. *Computational methods for fluid dynamics*, 3rd ed., Springer, 2002.
5. Ubbink, O., *Numerical Prediction of two fluid systems with sharp interfaces*, PhD thesis, Imperial College, Department of Mechanical engineering,1997.
6. Unverdi, S.O., Tryggvason, G., A *front-tracking method for viscous, incompressible, multi-fluid flows*, Comput. Phys, 1992.
7. Harlow, f.H., Welch, J.E., *Numerical Calculations of time-dependent viscous incompressible flow of fluid with free surface*, Phys. Fluids, 1965.
8. Noh, W.F. Woodward, P., *SLIC (Simple line interface Calculations)*, Lecture notes in Physics, Vol. 59, 1976.
9. Ubbink, O., Issa, R. I., *A method for capturing sharp fluid interfaces on arbitrary meshes*, Journal of computational physics, 1999.
10. Ramshaw, J.D., Trapp, J.A., *A numerical technique for low-speed homogenous two-phase flow with sharp interfaces*, J. Comput. Phys. 1976.
11. Hirt, C.W., Nichols, B.D., *Volume of Fluid (VoF) method for the dynamics of free boundaries*, J. Comput. Phys., 1981.
12. Torrey, M.D., Mjolsness, R.C., Stein, L.R., *A three dimensional computer program for incompressible flows with free surfaces*, Los Alomos national laboratory report LA-11009-MS, 1987.
13. Osher, S. Sethian, J.A., *Fronts propagation with curvature-dependent speed: algorithms based on Hamilton-Jacobi formulations*, J. Comput. Phys., 1988.
14. Sussman, M., Smereka P., Osher, S., *A level set approach for computing solutions to incompressible two-phase flow*, J. Comput. Phys. 1994.
15. Van Leer, B., Flux-*vector splitting for the Euler equations*, ICASE Report 82-30, NASA Langley Research Center, USA, 1982.
16. Boris, J. P., Book, D. L., *Flux-Corrected Transport I. SHASTA, A Fluid Transport Algorithm That Works*, Journal of Computational Physics, 1973.
17. Gaskell, H., Lau, A. K. C., *Curvature-compensated convective transport: SMART, a new boundedness-preserving transport algorithm*, International journal of numerical methods in fluids, 1988 .
18. Leonard, B.P., *The ULTIMATE conservation difference scheme applied to unsteady one dimensional direction*, Computational methods in applied mechanic and engineering, 1991.
19. Nielsen, K. B., *Numerical prediction of green water loads on ships*, PhD thesis, Technical University of Denmark, Department of mechanical engineering, 2003.

Simulation of a Solitary Wave Passing a Submerged Reef

VALERI S. PENCHEV
(v.penchev@bshc.bg, val@fi.uni-hannover.de)
JENS M. SCHEFFERMANN
(jens.scheffermann@fi.uni-hannover.de)

1. Introduction

In this paper numerical simulations of Solitary Waves induced by a collapsing water column are presented. Interaction of solitary waves with a submerged coastal reef has been studied. The numerical simulation of the free surface is based on the Volume of Fluid (VOF) Method. Validation of the numerical model has been carried out with results from physical model tests. Main focus is the simulation of water levels and wave induced velocities around an artificial reef.

2. Laboratory Model Tests

The physical model tests were performed in the small flume of the Franzius-Institut, University of Hannover, Germany. The flume has a total length of 8 m, a width of 0,30 m and a height of 0,50 m. Experience from previous laboratory model tests of interaction of waves and reef breakwaters have been used to establish basic reef parameters, as well as initial wave parameters (PENCHEV AT AL., 2001; PENCHEV, 2004). A special technique for generating extreme-height solitary wave at shallow water using a collapsing water column has been developed and used during tests.

Water level variation (wave height), as well as velocity under wave (including near-bottom velocity) have been measured during the tests in front, on top and behind the reef breakwater. Dynamic water level was measured in 4 points along the flume, using resistance type wave-meters. Velocities were measured by means of an ADV (Acoustic-Doppler Velocitymeter) at various points near to water surface, as well as near to the bottom. All test runs have been repeated in order to provide more reliable data for validation of the numerical model.

The experimental set-up is illustrated on Figure 1.

Two types of submerged reefs have been tested, as illustrated on Figure 2.

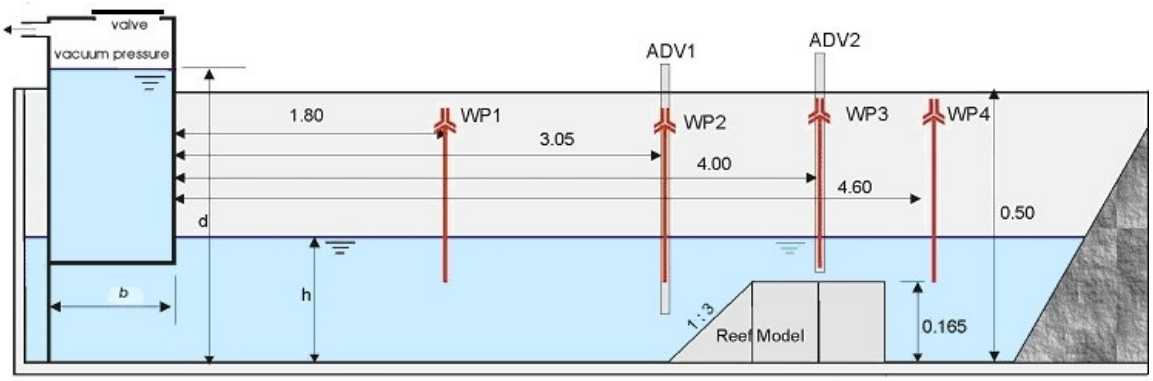

Figure 1: Experimental setup in the small flume in the laboratory Schneiderberg, Franzius-Institut

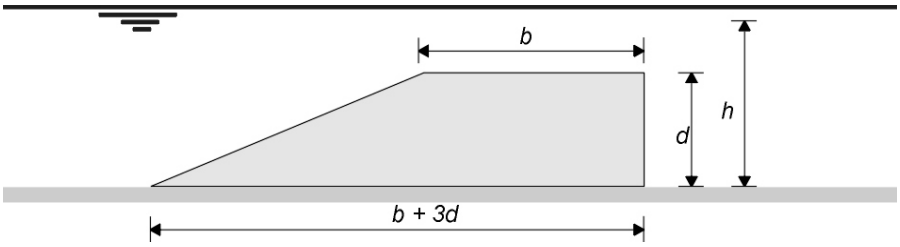

	d/h	b/h
Reef 1	0.75	3.6
Reef 2	0.90	1.8

Figure 2: Two types of reefs tested

3. Basic Numerical Simulation

For the numerical simulations the commercial CFD-Program STAR-CD was used (STAR-CD USER'S GUIDE, 2001). This code applies a three-dimensional CFD-solver system widely used in chemical and mechanical engineering. The numerical model is taking into account a free water surface using the Volume of Fluid (VOF) Method. Basic equations are conservation of mass, momentum and energy. Assuming an incompressible fluid, viscous stresses can be described with the friction approach of Newton, the continuity equation and the NAVIER STOKES Equations. Transposing the differential equation system to a numerical simulation system, a time averaging process results in the time-averaged continuity equation (1) and the time-averaged NAVIER-STOKES Equations (2).

$$\frac{\partial \overline{u_i}}{\partial x_i} = 0 \tag{1}$$

$$\frac{\partial \overline{u_i}}{\partial t} + \overline{u_j}\frac{\partial \overline{u_i}}{\partial x_j} = -\frac{1}{\rho}\left[\frac{\partial \overline{p}}{\partial x_i} - \rho\frac{\partial}{\partial x_j}\left(\nu_t \frac{\partial \overline{u_i}}{\partial x_j}\right) - \overline{u_i' u_j'}\right] + \overline{f_i} \tag{2}$$

where u is the velocity, t is time, p is the fluid pressure, ρ is the fluid density, ν is the viscosity, and f is the body force and the over-bars refer to time averaging of turbulent scales. As a consequence of the averaging process in time additional terms, the so-called REYNOLDS Stresses, appear. The resulting system of equations is commonly referred to as the REYNOLDS-Averaged NAVIER-STOKES Equations (RANSE). The relationship between time-averaged NAVIER-STOKES Equations and REYNOLDS Stresses is described in explicit terms, using a turbulence model. From preliminary numerical simulations the k-ε-standard-model with its standard parameters was chosen as turbulence model.

Evaluation of the VOF-Method with physical model test (MARTIN and MOYCE, 1952) showed the right calculation of water depth in a collapsing water column (for more detailed information please read the extended abstract "Simulation of movable hydraulic structures").

4. Numerical Model of the Flume

The flume was modelled in the numerical model in scale 1:1. Mesh cell size was from 1,5 cm in vertical direction, e.g. direction of the changing water level to 10 cm in horizontal direction, e.g. direction of wave propagation. The total number of cells was around 36.000, depending on the reef type. Time step $\Delta t = 0{,}025$ s was selected (Figure 3).

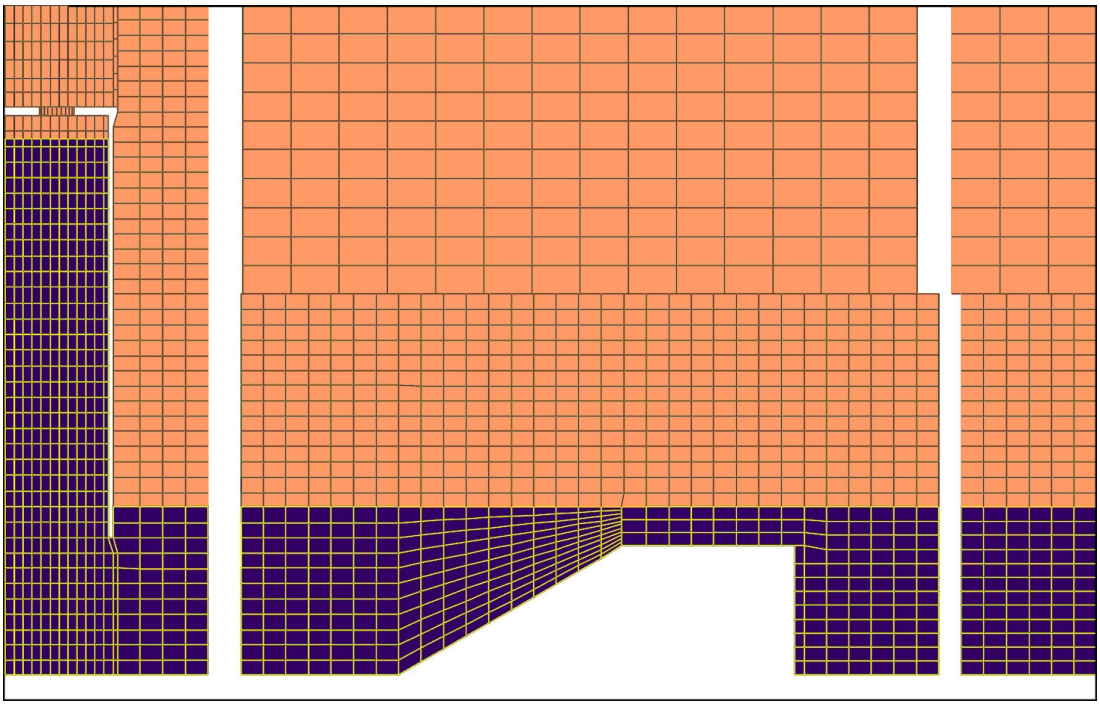

Figure 3: Numerical model of the flume and the submerged reef breakwater

Simulations were transient and with the free surface between water and air filled cells. Bottom and side walls of the flume were "no slip" walls. On top a constant pressure boundary was introduced. The transient RANSE/VOF simulation required approximately 5 hours of computational time for 6 s of laboratory simulation. Numerical model parameters were selected based on previous experience in modelling hydraulic structures and free surface flows (SCHEFFERMANN AND ZIMMERMANN, 2005).

5. Comparison with Water Level Measurements

Numerical simulation results for water level variations (wave height and wave celerity) were compared to physical model test data. Results are illustrated on Figure 4 and 5, respectively for simulations with reef types 1 and 2. Both figures presents wave height transformation along the wave flume, including interaction of wave with the submerged reef. The process of wave-structure interaction leads to breaking of the wave, which is most essential parameter of interaction. The numerical model was expected to simulate creation and development of the solitary wave, but also to track the discontinuous free surface and present some basic parameters of wave breaking, i.e. wave height at breaking (H_B), type/shape of breaking (spilling, plunging, or surging), height of the transmitted wave (H_T).

One can see from the figures presented that a very good simulation of the solitary wave in the flume was reached (Figures 4 and 5, a. and b.). A satisfactory correspondence was observed also for the breaking wave parameters (i.e. wave profile just before wave breaking (Figure 4.c. and 5.c.). A significant deviation was detected in the zone at and after wave breaking (Figure 4.d. and 5.d.). This is a zone with extremely high turbulence and massive aeration, where more attention on boundary layer problem has to be paid, including building of customized turbulence models. It is also obvious that finer grid should be applied to this area.

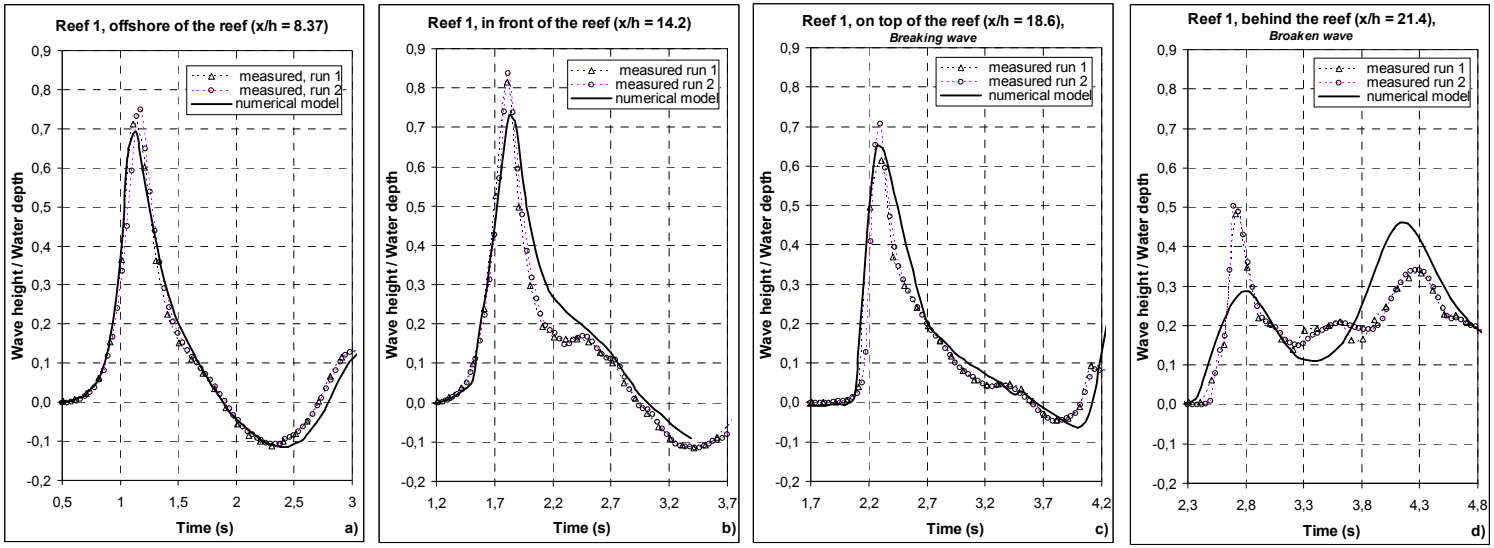

Figure 4: Numerical versus experimental data for water level variation (wave height), Reef type 1

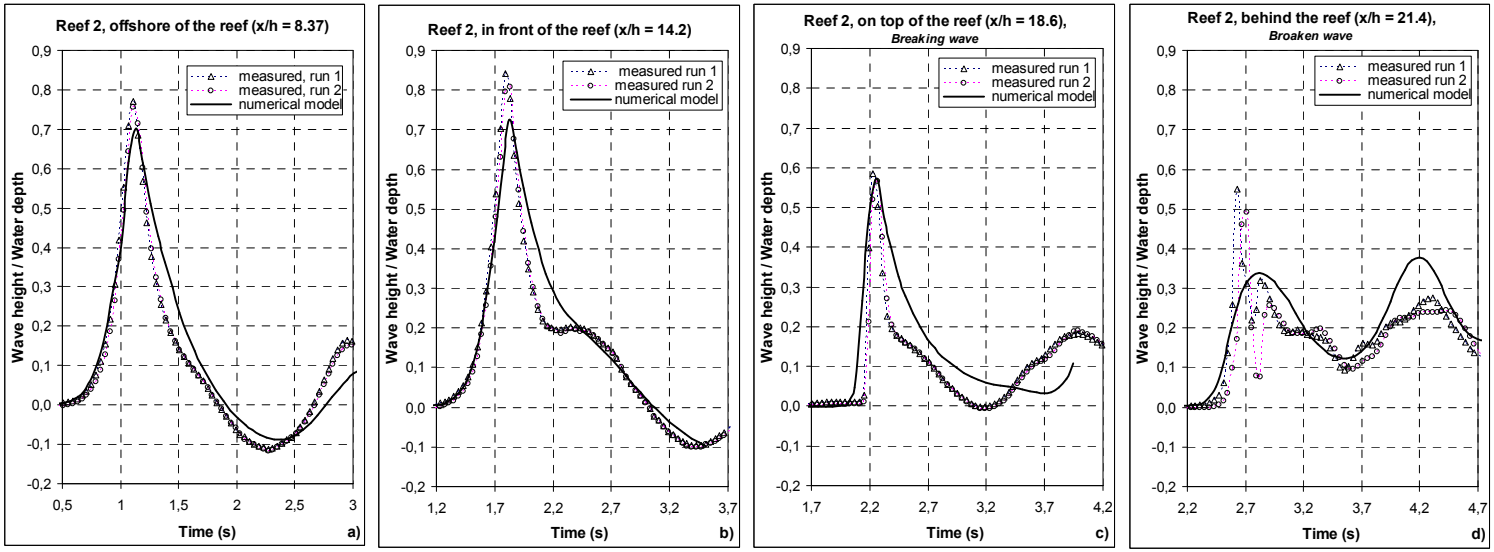

Figure 5: Numerical versus experimental data for water level variation (wave height), Reef type 2

6. Comparison with Velocity Measurements

Results for velocity distribution under the solitary wave from numerical simulations were compared to physical model test data, measured by ADV. Results are illustrated on Figure 6 and 7, respectively for simulations with reef types 1 and 2. Both figures present velocity at various points near to still water surface, as well at the bottom, in front of, on top, and behind the submerged reef.

It can be seen from the figures presented that a very good correspondence has been reached. A higher deviation was detected only when determining velocity on top of the reef (Figure 6.c.) – this again refers to the case of breaking wave, as reported above in it. 5. However, general comparison of data, and the good correspondence encourage authors for further application of the presented model to study similar problems.

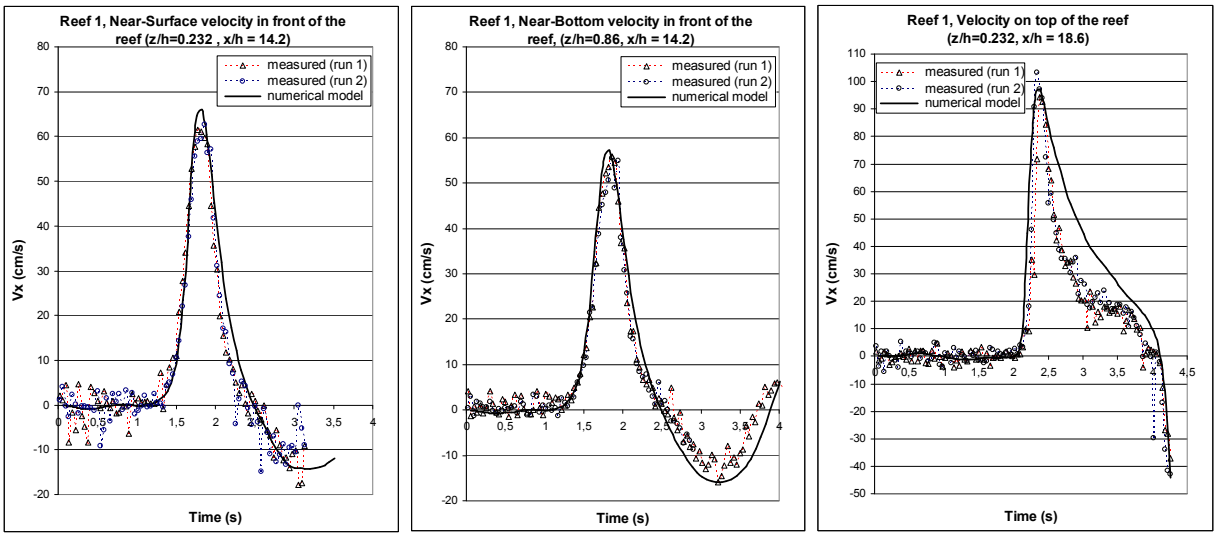

a) b) c)

Figure 6: Numerical versus experimental data for velocity distribution, Reef type 1

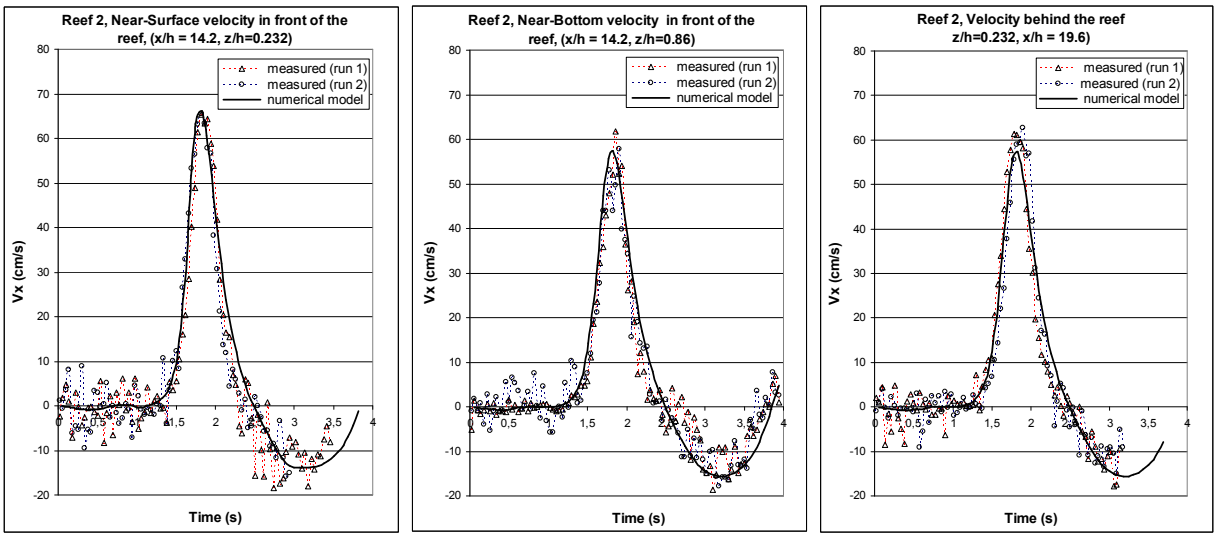

a) b) c)

Figure 7: Numerical versus experimental data for velocity distribution, Reef type 2

7. Conclusion

Comparison of numerical results with test data for two types of reefs tested has shown a very good match that encourages authors for further development and application of the presented CFD model (Figure 4 to 7).

More attention should be paid on the simulation of breaking waves, as indicated above in the paper.

Results obtained demonstrate possibility for using a CFD model as a tool to simulate wave-structure hydrodynamic interaction, and facilitate appropriate design of coastal engineering structures.

References

Martin, J.C., Moyce, W.J., (1952). „Transactions of the Philosophical Society of London", Vol. 244, p. 312.

Penchev, V., (2002). "Interaction of Waves and Reef Breakwaters", Proc. of NATO Advanced Research Workshop Environmentally Friendly Coastal Protection Structures, NATO Science Series, IV - Vol. 53, SPRINGER, pp. 107-127,

Penchev V., Dragancheva D., Matheja A., Mai S., Geils J., (2001). "Combined Physical and Numerical Modelling of an Artificial Coastal Reef", Proc. of 22nd HADMAR 2001 Euro-Conference, Vol.2, Varna, Bulgaria, pp. 325-338

Scheffermann, J. M., Zimmermann, C., (2005). "Simulation of Movable Hydraulic Structures", 8th Numerical Towing Tank Symposium, Varna, Bulgaria

Computational Dynamics Limited (2004). "STAR-CD Methodology." London

Sloshing Simulations inside Floating Bodies

M.Perić, T. Zorn

CD-adapco - Nürnberg Office
Dürrenhofstr. 4, D-90402 Nürnberg, Germany
email: Tobias.Zorn@de.cd-adapco.com

Introduction

For large ship tanks the response of the fluid inside the tanks to ship motion in waves is of great practical relevance. Sloshing in moving tanks can affect the stability of the ship and can also cause serious damage to the tank walls.
The aim of the presentation is to demonstrate the possibilities of predicting loads on partially submerged, moving structures, in particular on tanks in ships. Since tanks can in reality move arbitrarily, we are using the moving grid approach and a Finite Volume solution method designed to cater for arbitrary motions of polyhedral control volumes. The motion of liquid is computed using an interface-capturing scheme which allows overturning and breaking of waves. By performing a coupled simulation of the flow and ship motion, it is possible to obtain a realistic response of the liquid in a tank to external excitation, e.g. by sea waves.
In the past a large number of experimental studies has been performed to determine maximum pressure and forces on tank walls. In all cases known to the authors the tank motion has been prescribed from outside. Normally a regular sinusoidal variation of motion in one or more directions is set. For analyzing the maximum loads on tank walls, it is normally enough to study several "worst-case" scenarios. The real motion of tanks is caused by an interaction between forces exerted by the sea on the vessel and forces exerted by the sloshing liquid on tank walls; thus the motion is usually not regular and the real conditions at sea can never be exactly foreseen. The stability of the ship depends on the interaction of internal and external forces.
To assess the accuracy of the simulation tool to predict pressures on tank walls, test results of the former Ship Research Institute in Tokyo (now National Maritime Research Institute), presented at a workshop in Tokyo in 2001 (Hinatsu et al, 2001), were taken and compared with simulation results.
Then coupled simulations of a ship moving forward in regular head waves with one or more partially-filled tanks located at different positions inside the ship were simulated.
In separate studies the coupled prediction of fluid flow and the motion of floating bodies using the same simulation software has been validated (e.g. Xing-Kaeding, 2005), so that the combined analysis of flow around the vessel and sloshing in its tanks can be considered as reliable in spite of missing experimental data for direct validation.

Numerical Method

The equations for mass, momentum and scalars are solved in their integral form using a finite-volume method. The spatial solution domain is subdivided into a finite number of contiguous control volumes (CVs) which can be of an arbitrary polyhedral shape. The governing equations contain surface and volume integrals, as well as time and space derivatives. These are then approximated for each CV and time level using suitable approximations.

The flow is assumed to be governed by the Reynolds averaged Navier-Stokes equations, in which turbulence effects are accounted for via an eddy-viscosity model like k-ε and k-ω models, which are typically used. Thus, the continuity equation, three momentum equations, and two equations for turbulence properties are solved. In addition, the space-conservation equation has to be satisfied since the CVs will have to move and change their shape due to the adaptation of the mesh to moving walls. The free surface calculation is modelled by a VOF-like method, implemented with the High Resolution Interface Capturing scheme (Muzaferija, S., Perić, M. 1999). The integrals are numerically approximated using the midpoint role.

When the motion of a floating body is also computed, the outer iteration loop within each time step is extended to allow for an update of body position. The equations of body motion are solved first to obtain the velocities using a predictor corrector scheme of second order (equivalent to Crank-Nicolson scheme) and then for displacements and rotations; the grid within flow domain is adjusted to fit the new body position.
Underrelaxation of body motion is used in a similar way as when solving the Navier-Stokes equations; it can be interpreted as adding a virtual mass to the system (Xing-Kaeding, 2005). At the end of each time step, the new body position and the corresponding flow are obtained. The solution method is thus fully implicit and fully coupled, allowing larger time steps and better stability than explicit schemes in which flow and body motion are computed one after another.

When sloshing in rigid tanks is simulated, two approaches are possible:
– The grid is kept fixed, and the equations are solved for a moving reference frame (body forces due to the motion of the coordinate system are added). If the motion is irregular, derivation of expressions for accelerations may become complicated.
– The equations are solved in an inertial coordinate frame and the grid moves as in reality. This approach requires that the grid is updated after every time step; however, it makes animation of flow and comparison with experiments easier and is in particular attractive when the motion is highly irregular or not known in advance, as is the case with floating bodies.

In the present work only the moving-grid approach has been used, since the focus is on tanks attached to floating bodies whose motion has to be computed as part of the global solution.
In the case of moderate motion, like with ships in small amplitude waves, one can move the grid near body rigidly with the body, keeping the grid further away from body fixed and deform the grid in the region between these two, usually done by some kind of algebraic smoothing. A single body in an infinite domain can also been moved, by moving the whole grid with the body. Special treatment for the boundaries needs then to be taken into account. This can be problematic in the case of large motions and waves, because the grid needs to be fine in a larger region in order to capture the free surface and waves properly than would be the case in the first approach.
The third possibility is to use overlapping grids, where one background grid is adapted to the free surface (and possible outside boundaries, like shore or harbor walls), while overlapping grids are attached to floating bodies and move with them without deformation. In this case the grid quality is easier to control and grid motion is also easier to handle, but the solution method needs to account for the coupling of background and overlapping grid solutions.
In the present work the second and the third option have been used. Only the latter is applicable to unlimited motions including capsizing.

Validation of the Solution Method

The validation of the solution method is performed by simulating test cases studied experimentally at the Ship Research Institute in Tokyo in 1999 (see Hinatsu et al, 2001). In these experiments, conducted in cooperation with Nippon Kaiji Kyokai, both amplitudes and periods of periodic motions have been varied in a wide range in order to determine the resonance conditions, i.e. the situation which results in highest loads on tank walls. The aim of the validation study is to determine whether the worst case could have been

identified through numerical simulations and how well can the simulation predict pressures at specified locations. A brief summary of the simulated test cases will be given during the presentation.

Sloshing Application inside Floating Bodies

Since the validation study has shown that the numerical solution method is capable of predicting sloshing phenomena with an acceptable accuracy, several simulations have been performed in which sloshing in tanks mounted on a floating vessel (here a ship model) has been considered. This requires a coupled computation of the flow around the vessel, the flow in tanks, and the vessel motion due to external forces (propulsion force) and flow-induced forces (pressure and shear forces on hull surface and sloshing forces on tank walls). For the time being only heave and pitch motions of the vessel and regular waves are considered; the solution method, however, allows all six degrees of freedom to be activated. The best way to analyze the results of such simulations is through animations; here only two pictures will be shown to demonstrate the main features of the flow and vessel motion.

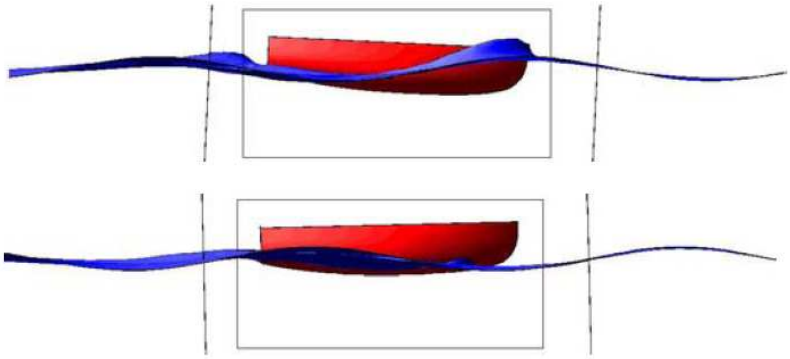

Figure 1: Ship hull position and free-surface shape, using overlapping grid approach.

The ship (Figure 1) is 4.25 m long, 1.6 m wide and has a draught of 0.24 m. The mass of the ship is 800 kg. The vessel moves with a velocity of 2.5 m/s. The waves have a wavelength of 6 m and amplitude of 0.2 m and are generated at the inlet of the solution domain using linear wave theory. Although in the region of grid overlap two solutions exist and both are plotted, no disturbance can be seen in the free surface, indicating that the solution method handles the overlapping region correctly. This method has just been implemented into the software and is undergoing further testing.
Figure 2 shows some pictures from the simulation of ship motion with one partially filled tank located in the center of the ship. In this case the vessel mass is 400 kg and tank mass, liquid included, is 400 kg. The tank is 1.5 m long, 1 m wide, 0.58 m high and 50% filled with a liquid. The tank bottom is at equilibrium flush with undisturbed free surface. Since the tank is located in the center and the pitching motion is moderate, so is the sloshing in the tank.
Figure 3 shows the situation when the tank is located at the rear part of the vessel. In this case the center of mass is moved 1 m towards the stern, which is the reason why the bow points upwards. Again, pitching motion is moderate and the liquid free surface in the tank is almost horizontal most of the time.
The situation becomes different when the frequency of the tank is changed. Here the centrally-located tank has been simply split into two; one half is moved 0.89 m towards bow and the other 1.14 m towards stern. Although both ship velocity and waves are the same as in the previous two cases, now a substantial sloshing takes place in both tanks, as shown in Figure 4.
Figure 5 and Figure 6 shows the variation of the heave and pitch motion of the vessels with the tanks in the middle, back and the split configuration.

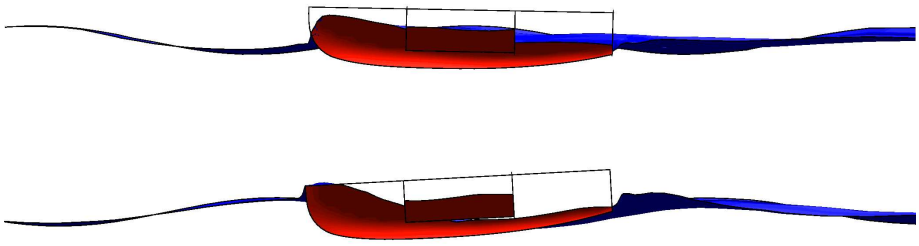

Figure 2: Ship hull position and free-surface shape, tank in CGX = 0 m (MIDDLE).

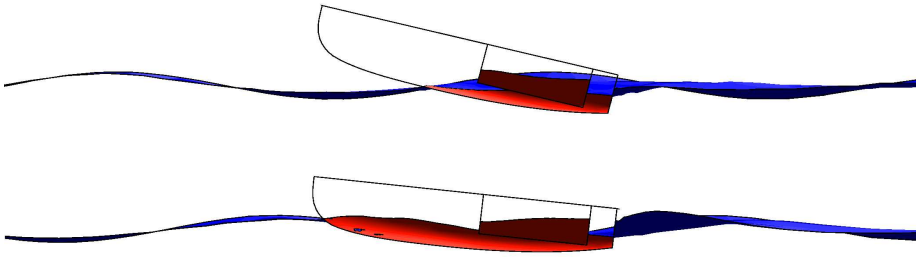

Figure 3: Ship hull position and free-surface shape, tank in CGX = -1 m (BACK).

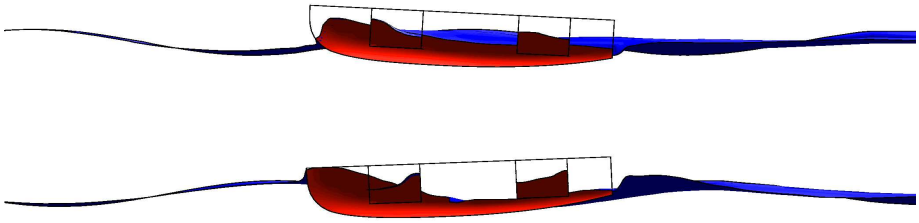

Figure 4: Ship hull position and free-surface shape, tanks in CGX1 = -1.14 m and CGX2 = 0.89 m (SPLIT).

This kind of simulation can be used to study the effect of partial filling of tanks on a multi-tank vessel on the vessel stability, since in the worst case resonance effects can cause either structural damage or capsizing.

We believe that even simulations on relatively coarse grids, which can be performed within relatively short time, can be very useful in the design and optimization stage. A few words about the simulation procedure are worth noticing. It is namely advisable not to start with waves and all degrees of freedom for vessel motion immediately, but to first compute the flow around vessel in a fixed position, starting with undisturbed free surface. This does not have to be forced to full convergence, but once the flow around the vessel has sufficiently developed, one can activate incoming waves and finally the vessel motion. Also, one can keep the critical motions frozen until the others develop, depending on the complexity of the problem.

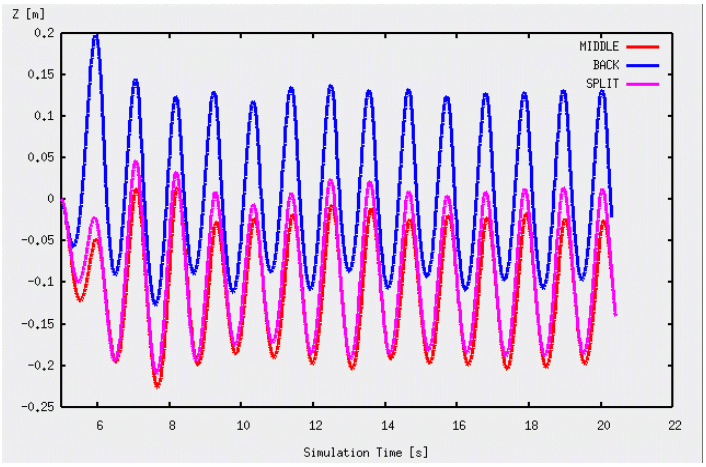

Figure 5: Variation of the heave motion of the vessels with the tanks in the middle, back and the split configuration.

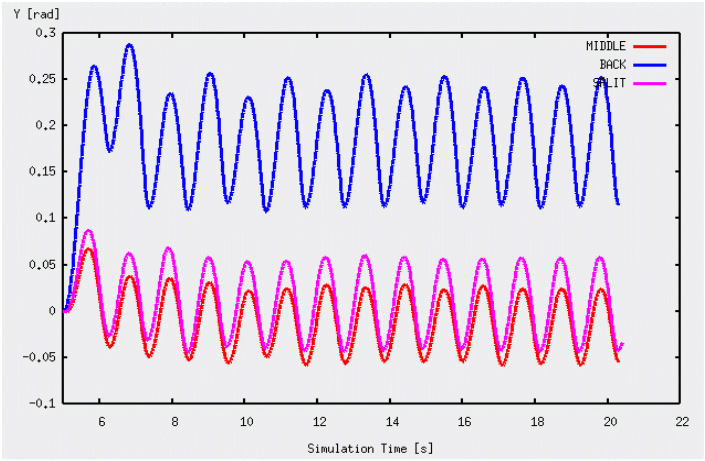

Figure 6: Variation of the pitching motion of the vessel with the tanks in the middle, back and the split configuration.

The vessel motion has been activated after 500 time steps, during which the flow around the vessel and the waves have developed. After an initial phase, the quasi-periodic state has developed. Under different conditions, random components due to severe sloshing could also develop, which could lead to vessel instability in waves.

Conclusions

It has been also demonstrated that a coupled simulation of flow around the floating vessel and in the tanks, and the vessel motion, is now possible and promises to provide simulation capabilities under realistic conditions that can capture all the interaction between sea waves, sloshing in tanks, wind loads on the superstructure, and vessel motion due to all the forces acting on it.

References:

Hinatsu, M., Tsukada, Y., Fukasava, R., Tanaka, Y., Experiments of Two-Phase Flows for the Joint Research, Proc. SRI-TUHH mini-Workshop on Numerical Simulation of Two-Phase Flows, Ship Research Institute, Tokyo, 2001.

Xing-Kaeding, Y., Unified Approach to Ship Seakeeping and Maneuvering by a RANSE Method, Dissertation, TU Hamburg-Harburg, 2005.

Muzaferija, S., Peric, M.: Computation of free surface flows using interface-tracking and interface-capturing methods, chap. 2 in O. Mahrenholtz and M. Markiewicz (eds.), *NonlinearWater Wave Interaction*, pp. 59-100,WIT Press, Southampton, 1999.

Ferziger, J.H., Peric, M., *Computational Methods for Fluid Dynamics*, 3rd ed., Springer, Berlin, 2003.

LES, DES and RANS of High Reynolds Number, Wall Bounded Flows

T. PERSSON*[†], M. LIEFVENDAHL[‡], R.E. BENSOW[†] AND C. FUREBY[‡,†]

[†]Dept. of Shipping and Marine Technology, Chalmers University of Technology, SE 412 96 Gothenburg, Sweden
[‡]Div. of Weapons & Protection, Warheads & Propulsion, The Swedish Defense Research Agency, FOI, SE 147 25 Tumba, Sweden
*Corresponding author. Email: tobias.persson@chalmers.se

1 Introduction

Most Computational Fluid Dynamic (CFD) codes presently used for practical flows are based on the Reynolds Average Navier-Stokes (RANS) equations, [11], together with a statistical turbulence model for modelling the mean effects of turbulence on the mean flow. Although RANS correctly models the mean flow in many cases it often fails when facing more complex flows, or when applied to flows dominated by unsteady effects. The use of CFD in practical applications is increasing, and the demand for accurate and detailed flow information is growing rapidly, and therefore alternatives to RANS are required. Such alternatives are offered by Detached Eddy Simulation (DES), [17], and Large Eddy Simulation (LES), [12]. Both DES and LES are based on the idea of separating scales, and split the flow into two regimes by which all scales larger than the grid are resolved using a space/time accurate algorithm and only the effects of the subgrid scales on the large scales are modeled. The direct computation of the large energy containing eddies (being flow and geometry dependent) gives LES and DES more generality than RANS, although at a higher cost. In the free flow regime, the details of the subgrid models are of less importance as long as it provides sufficient dissipation to emulate the subgrid turbulence and to stabilize the simulation. The main practical difference between DES and LES is the treatment of walls; in DES the subgrid model is designed to switch to a RANS model (e.g. the Spalart-Almares model, [17], as will be used here) close to the wall, whereas in LES either a sufficiently fine grid is required to resolve the near-wall structures, or a separate wall model is required, [12]. There is insufficient understanding of how LES and DES behave when applied to complex wall-bounded flows, and also of the merits and de-merits of both methods with respect to each other. The aim of the paper to be presented is to provide a systematic computational and theoretical study of DES and LES for a few selected cases. Here we have chosen to use the flow over a circular cylinder, flow over a surface mounted hill, and the flow past a bare-hull submarine in model scale.

The first test case is the flow around a circular cylinder at Reynolds number (Re), *Re = 140,000*, which can be characterised as a bluff-body flow. The wake behind a bluff-body is usually spatially complex, often consisting of curved shear layers enclosing a region of extreme complexity characterized by the presence of intense vorticity, but also including the entrainment of irrotational flow elements into the wake from the surroundings. Vorticity is generated by shear around the obstacle and vortices are shed and advected down the wake. If the body is symmetric, as in the case of the circular cylinder, the wake will usually exhibit self-induced periodicity from vortices being shed from alternate side of the body, generating fluctuating forces on the body. During the last two decades there has been a large interest in bluff-body flows, in particular for flow past a circular cylinder.

The second test case is a three dimensional (3D) surface mounted hill experimentally studied by Simpson *et al*, [14], and by Byun *et al*, [3]. The case feature an analytically defined 3D axisymmetric hill of height h, mounted on the floor of a wind tunnel of height $H=3.2h$, at a Reynolds *(Re)* number, based on the height of hill of $Re=130,000$. The test section is wide enough to neglect the influence of the finite spanwise extent of the wind tunnel, and when the hill is not in place, a two-dimensional (2D) zero pressure gradient boundary layer with $Re_\theta=7300$ was reported. The flow contains unsteady separations and reattachments, and is dominated by the combined effects of streamline roll-up on the side of the hill and the splashing of the flow coming over the top of the hill. This creates two flat counter-rotating vortices behind the hill that have their outflow from the centerline close to the wind tunnel floor. This flow have proven to be a real challenge to both LES and DES, but in particular to the engineering models based on RANS that are commonly used in industrial prediction methods.

The third test case consists of the flow past a bare-hull submarine model at a body-length Re-number of $Re=12\cdot10^6$, [7]. The hull has an overall length of L=4.36 m and a diameter of D=0.51 m. Experimental data (based on pressure probes and hot-film techniques) for validation have been provided by David Taylor Model Bassin (DTMB), and computations have been performed using one grid with 3.4 million grid points respectively.

All calculations are performed with no-slip wall boundary condition in conjunction with a wall-model, e.g. [18], and are initiated with quiescent conditions and the unsteady flow evolves by itself.

2. Governing Equations

The governing equations of an incompressible flow consists of the balance equations of mass and

momentum for a linear viscous (or Newtonian) fluid, [8],

$$\begin{cases} \nabla\cdot\mathbf{v}=0, \\ \partial_t(\mathbf{v})+\nabla\cdot(\mathbf{v}\otimes\mathbf{v})=-\nabla p+\nabla\cdot\mathbf{S}+\mathbf{f}. \end{cases} \quad (1)$$

where $\mathbf{v}$ is the velocity, p the pressure, $\mathbf{S}=2\nu\mathbf{D}$ the viscous stress tensor with ν the kinematic viscosity and $\mathbf{D}=\frac{1}{2}(\nabla\mathbf{v}+\nabla\mathbf{v}^T)$ the rate-of-strain tensor and $\mathbf{f}$ the external forces. We must also add initial and boundary conditions to complete the mathematical description. As mentioned in the introduction the numerical simulation of turbulent flows of practical or engineering interest will require too fine computational meshes for present-day computers to handle. Direct Numerical Simulations (DNS), in which all spatial and temporal scales of relevance are fully resolved, may however still be useful for investigating simple and building-block flows to gain additional insight in the flow physics. The alternatives to DNS all involve some degree of modelling and will be summarized next.

3. Turbulence Modeling Approaches

In this Section we will summarize the RANS, DES and LES models and methods used in the present investigation.

3.1. Reynolds Averaged Navier Stokes (RANS) models

The most common turbulence modelling approach is RANS, which is based on a statistical treatment of the fluctuations about a stationary or a slowly varying flow, [11]. The dependent variables are broken into two parts: a mean, time- or ensemble-averaged, part of the flow and a fluctuating component representing deviations from this mean. This approach is only formally correct in the limit of stationary mean flow, otherwise the mean and fluctuating parts cannot be cleanly separated. Following [19] the governing RANS equations are,

$$\begin{cases} \nabla\cdot\langle\mathbf{v}\rangle=0, \\ \partial_t(\langle\mathbf{v}\rangle)+\nabla\cdot(\langle\mathbf{v}\rangle\otimes\langle\mathbf{v}\rangle)= \\ =-\nabla\langle p\rangle+\nabla\cdot(\langle\mathbf{S}\rangle-\mathbf{R})+\langle\mathbf{f}\rangle, \end{cases} \quad (2)$$

where angle-brackets denote the mean, time- or ensemble-averaged part and $\mathbf{R}=\langle\mathbf{v}'\otimes\mathbf{v}'\rangle$ is the Reynolds stress tensor describing the mean influence of the fluctuations on the mean flow. In order to close (2), $\mathbf{R}$ must be modelled from the plethora of available turbulent closure models, e.g. [19]. Here, a cubic eddy viscosity model is used, [4], in which $\mathbf{R}=-2\nu_t\mathbf{A}$, where ν_t is the turbulent viscosity and $\mathbf{A}$ is a tensor field closely related to the mean velocity gradient tensor $\nabla\langle\mathbf{v}\rangle$.

3.2. Large Eddy Simulation (LES)

A promising alternative to RANS for flows of technological interest is LES in which all structures larger than the mesh are resolved using a space and time accurate scheme, and only the effects of the small unresolved eddy scales need to be modelled. The direct computation of the large, energy containing eddies (which are geometry and flow dependent) gives LES more generality than RANS, and possibly also compared to DES, using models for the entire spectrum of turbulent motions. The computational cost of LES, although significant, is becoming manageable with the use of massively parallel computers and subgrid wall models that help to bring down the cost to a level comparable to DES for wall bounded flows. The LES equations are derived from (1) by low pass filtering, using a kernel $G=G(\mathbf{x},\Delta)$, such that,

$$\begin{cases} \nabla\cdot\bar{\mathbf{v}}=m^\rho, \\ \partial_t(\bar{\mathbf{v}})+\nabla\cdot(\bar{\mathbf{v}}\otimes\bar{\mathbf{v}})=-\nabla\bar{p}+\nabla\cdot(\bar{\mathbf{S}}-\mathbf{B})+\bar{\mathbf{f}}+\mathbf{m}^v. \end{cases} \quad (3)$$

Equation (2) introduces three new terms when compared to the raw NSE (1); the unresolved transport term $\nabla\cdot\mathbf{B}$, where $\mathbf{B}=(\overline{\mathbf{v}\otimes\mathbf{v}}-\bar{\mathbf{v}}\otimes\bar{\mathbf{v}})$ is the subgrid stress tensor and the commutation error terms $m^\rho=[G*,\nabla]\mathbf{v}$ and $\mathbf{m}^v=[G*,\nabla](\mathbf{v}\otimes\mathbf{v}+p\mathbf{I}-\mathbf{S})$, where $[G*,\nabla]f=\overline{\nabla f}-\nabla\bar{f}$ is the commutation operator. Although both types of terms contribute to the closure problem, it is customary to neglect the influence of the commutation error terms, since they are usually expected to be smaller than the effect of the unresolved transport.

Modern LES closure strategies can broadly be classified as functional or structural models. Functional models are mainly used to mimic the energy cascade from large to small scales and do not aims at being a good approximation of neither the subgrid stress tensor nor the subgrid flow. Thus they only try to reproduce the global effects of the small, unresolved scales on the resolved ones. The One Equation Eddy Viscosity Model (OEEVM), [13], is a good example of this type of models. Here, $\mathbf{B}=-2\nu_k\bar{\mathbf{D}}$, where the subgrid eddy viscosity ν_k is parameterized in terms of the subgrid kinetic energy, k, which follows from solving the following modelled transport equation,

$$\partial_t(k)+\nabla\cdot(k\bar{\mathbf{v}})=-\mathbf{B}\cdot\bar{\mathbf{D}}+\nabla\cdot(\nu_k\nabla k)-\varepsilon, \quad (4)$$

where $\nu_k=c_k\Delta\sqrt{k}$ and $\varepsilon=c_\varepsilon k^{3/2}/\Delta$. The constants $c_k=0.07$ and $c_\varepsilon=1.03$ are obtained from an inertial subrange behaviour. Moreover, by assuming equilibrium, (4) simplifies to the Smagorinsky model, [15], $k=c_I\Delta^2|\bar{\mathbf{D}}|^2$ and $\nu_k=c_D\Delta^2|\bar{\mathbf{D}}|$, with $c_I=0.13$ and $c_D=0.02$.

Structural models, on the other hand, are designed to retain as much as possible of the overall structure of the

true subgrid stress tensor. However, they have a tendency to not be dissipative enough, which however can be cured by combining a structural model (with high degree of structural correlation) with a functional model to account for the dissipative part. Here, we employ the structural model suggested by Bensow *et al.*, [2], which can be derived by applying the decomposition $\mathbf{v}=\overline{\mathbf{v}}+\mathbf{v}'$ to both components of $\mathbf{B}=\overline{(\mathbf{v}\otimes\mathbf{v}-\overline{\mathbf{v}}\otimes\overline{\mathbf{v}})}$, and takes the form,

$$\begin{aligned}\mathbf{B} &= (\overline{\overline{\mathbf{v}}\otimes\overline{\mathbf{v}}}-\overline{\overline{\mathbf{v}}}\otimes\overline{\overline{\mathbf{v}}})+(\overline{\overline{\mathbf{v}}\otimes\mathbf{v}'}-\overline{\overline{\mathbf{v}}}\otimes\overline{\mathbf{v}'}+\\ &+\overline{\mathbf{v}'\otimes\overline{\mathbf{v}}}-\overline{\mathbf{v}'}\otimes\overline{\overline{\mathbf{v}}})+(\overline{\mathbf{v}'\otimes\mathbf{v}'}-\overline{\mathbf{v}'}\otimes\overline{\mathbf{v}'})= \\ &=\tilde{\mathbf{L}}+\tilde{\mathbf{C}}+\tilde{\mathbf{R}}.\end{aligned} \tag{5}$$

In this expression, the term $\tilde{\mathbf{L}}=\overline{(\overline{\mathbf{v}}\otimes\overline{\mathbf{v}}-\overline{\overline{\mathbf{v}}}\otimes\overline{\overline{\mathbf{v}}})}$ is the scale-similarity term proposed by Bardina *et al.*, [1], as a model for $\mathbf{B}$ based on scale similarity arguments. Hence, $\tilde{\mathbf{L}}$ becomes an explicit part of the LES equations leaving $\tilde{\mathbf{C}}+\tilde{\mathbf{R}}$ to be modelled. Following [2] we here model $\tilde{\mathbf{C}}+\tilde{\mathbf{R}}$ as $-2\nu_k\overline{\mathbf{D}}$, such that $\mathbf{B}=\overline{(\overline{\mathbf{v}}\otimes\overline{\mathbf{v}}-\overline{\overline{\mathbf{v}}}\otimes\overline{\overline{\mathbf{v}}})}-2\nu_k\overline{\mathbf{D}}$, where ν_k is calculated from the OEEVM (4). This LES model is hereafter referred to as the mixed model (MM).

In LES the grid in the near wall region needs refinement in all three directions – particularly in the spanwise direction, [5], to resolve the energetic structures. For most practical flows the required resolution will result in too heavy calculations even for present-day massively parallel computers, and instead subgrid wall modelling is required. Near the wall, the flow is dominated by streaky structures, hairpin vortices and ejection events, i.e. anisotropic flow structures that are usually not reflected in the non-uniform mesh, typically graded towards the wall to catch the wall normal gradients. The most commonly used wall models are based on analytic expressions for the wall shear stress, $\tau_w=\nu(\nabla\overline{\mathbf{v}})|_w$, providing an algebraic relation between τ_w and the tangential velocities at the first layer of cells. These models are however impractical to use for unstructured grids and more practical methods may be devised based on,

$$\partial_y(\nu(\partial_y\overline{v}_i)-B_{iy})=f_i;\ f_i=\partial_i\overline{p}+\partial_t\overline{v}_i+\partial_j(\overline{v}_i\overline{v}_j). \tag{6}$$

Assuming that $f_i=0$, implying that no streamwise pressure gradients affect the boundary layer, and thus (6) can be integrated analytically to give the law-of-the-wall,

$$\overline{\mathbf{v}}^+=\begin{cases}y^+, & y^+<11.225,\\ \kappa^{-1}\ln|y^+|+B, & y^+>11.225,\end{cases} \tag{7}$$

where $\overline{v}_i^+=\overline{v}_i/u_\tau$, $y^+=u_\tau y/\nu$ and $u_\tau=\sqrt{\tau_w}$. Using (7) the friction velocity, u_τ, can be estimated, and by assuming that $\tau_w=\nu_{BC}u_\tau/y$ the subgrid wall viscosity ν_{BC} can be evaluated to enforce the velocity to comply with the law-of-the-wall. This approach has proven effective, [18], and makes sense if the grid is coarse enough to allow multiple structures to coexist.

3.3. Detached Eddy Simulation (DES)

It is well known that wall bounded flows require very high spatial resolution in the near-wall region to capture the dynamically important structures responsible for drag, turbulence prediction etc. LES is known to perform well for free flows, [12], whereas some RANS models have had great success in capturing the mean near-wall flow, [19]. In an attempt to formulate improved prediction methods for technical flows the concept of hybrid RANS-LES methods was born. The concept of DES, [17], can be considered a hybrid RANS-LES method in that the full boundary layer (populated with attached eddies) is assigned to RANS, and only separated regions (detached eddies) are assigned to LES, and is aimed primarily at external flows. The concept of DES is not rigorously justified mathematically in terms of filtering etc. and should therefore be used with some care. However, the approach is appealing from a computational point of view and from the results shown in the literature. The DES equations are essentially identical to the LES equations (3), including the subgrid turbulent stress tensor $\mathbf{B}=\overline{(\mathbf{v}\otimes\mathbf{v}-\overline{\mathbf{v}}\otimes\overline{\mathbf{v}})}$ that requires closure modelling. Following [17] we here use a modified version of the Spalart-Allmaras (S-A) RANS turbulence model, [16]. This model is based on the eddy viscosity concept in which $\mathbf{B}=-2\nu_k\overline{\mathbf{D}}$, where $\nu_k=f_{v1}\tilde{\nu}$ in which f_{v1} is a flow dependent dynamic constant and $\tilde{\nu}$ is the appropriate working variable for which a separate modelled transport equation is solved together with the mass and momentum equations, [17]. In this model, f_{v1} is calculated as $f_{v1}=\chi^3/(\chi^3+c_{v1}^3)$, where $c_{v1}=7.1$ and $\chi=\tilde{\nu}/\nu$. The hybridization between LES and RANS is accomplished by appropriate blending of length scales (or filter widths). In the DES model the characteristic length scale is defined as $\tilde{d}=min(y,C_{DES}\Delta)$, where y is the wall-normal distance, $c_{DES}=0.65$ and Δ is the filter width which is defined as the local maximum grid spacing in the three directions. The intended use of the model is to remove the resolution demands in the wall parallel directions. For a true DES the wall parallel grid resolution should be larger than the boundary layer thickness. If a finer wall resolution is used, the model approaches that of LES with a wall function. Far from the walls, $\Delta<y$, and a balance between the production and the destruction term in the model equation shows that $\tilde{\nu}\propto\Delta^2\,||\,\overline{\mathbf{W}}\,||$,

$\bar{\mathbf{W}}$ being the vorticity tensor, which is similar to the Smagorinsky viscosity model, [15].

4. Result and Discussion

In the following section the global flow patterns will be discussed and a detailed comparison will be made with available laboratory measurement data.

4.1 The Circular Cylinder

The flow past a circular cylinder is examined at sub-critical *Re=140,000*, respectively, using one LES model and one DES model. The computational domain is of rectangular form with a spanwise extent of $1.5\pi D$. The cylinder (of diameter D) is positioned 10D downstream of the inflow plane and 20D upstream of the outflow plane. Moreover, the total vertical extent of the computational domain is 20D. The angular position at which separation occurs is defined clockwise from the upstream side of the cylinder. A block-structured H-grid is used with an O-grid with radius 3D around the cylinder. The number of grid cells in the spanwise direction is 48 and the number of grid cells in each of the planes is about 29,000. This gives a total number of grid cells of about 1.4 millions, see figure 1.

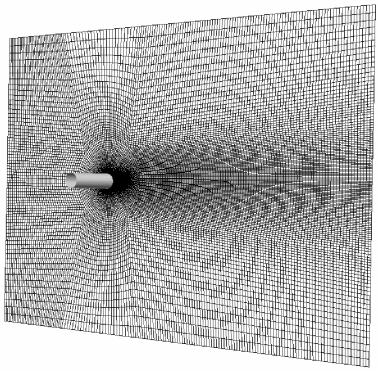

Figure 1. The computational domain for the circular cylinder calculation.

There are some clear differences between the DES and the LES calculations in this case. This is caused by the coarser resolution, forcing the subgrid models to act in a wide range of scales. Along the centerline both models over predicts the recirculation length and the recirculation velocity, especially the DES model, see figure 2a. For the LES results a higher spanwise resolution in the near wall region will improve this prediction, see Persson *et al.* [9]. From the cross-stream profiles, Figure 2b, the over predicted recirculation region is clearly visible, in particular at x/D=1.5. At x/D=1.0, 1.5 and 2.0 both models produce narrower profiles than the experiments, this is clearly improved at x/D=4 and 7.

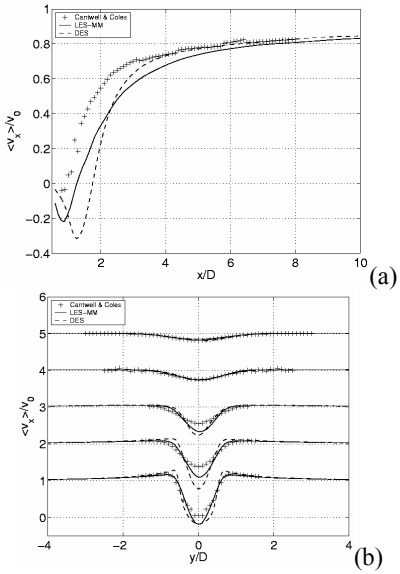

Figure 2. Velocity profiles in the wake of the circularcylinder. (a) Streamwise velocity along the centerline. (b) Streamwise velocity at cross-stream stations located at x/D = 1, 1.5, 2, 4, 7, bottom to top.

4.2 The Axisymmetric Hill

The experiments of Simpson *et al*, [14], and Byun *et al*, [3], features a *h=0.078m* high 3D axisymmetric hill mounted on the centre floor of *H=0.25m* high wind tunnel. The inlet speed is *U*=27.5m/s giving a *Re* number, based on *h*, of *Re=130,000*. The test section is *L=7.6 m* long and *W=3.03 m* wide, and the hill is defined $y/h = -\beta[J_0(\Lambda)I_0(r\Lambda/a) - I_0(\Lambda)J_0(r\Lambda/a)]$, where $\beta=1/6.048$, $\Lambda=3.1926$ and $a=2h$ is the radius of the circular base of the hill, J_0 and I_0 are Bessel and modified Bessel functions, respectively. The computational domain contains a part of the wind tunnel, where no-slip boundary conditions are used on the top and bottom walls and slip conditions are used on the two sides, figure 1. The size of the domain in the streamwise, spanwise and cross-stream directions are *12.0h*, *10.0h* and *3.205h*, respectively and the inlet is located *3.4h* from the top of the hill, see figure 3.

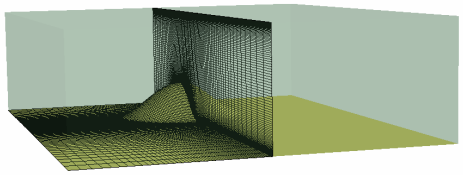

Figure 3. Computational domain, viewed from behind. Baseline grid with 1,008,000 cells

In figure 4 we compare profiles of the time-averaged streamwise and spanwise velocities $\langle v_1 \rangle$ and $\langle v_2 \rangle$. In figure 4a the distribution of the streamwise velocity component $\langle v_1 \rangle$ shows that RANS predict the occurrence of a velocity defect, not present in the

experimental data or in the remaining DES profiles and LES profiles. At the centerline DES somewhat overpredict $\langle v_1 \rangle$, whereas theS calculations show good agreement with data. Between *-0.33<z/h<-1.30* all models, give satisfactory agreement with the data. At *z/h≤-1.30* $\langle v_1 \rangle$ is overpredicted to some extent by all models, which however can be related to the coarser spatial resolution used away from the hill. In figure 2b we find that the spanwise velocity component $\langle v_3 \rangle$ is reasonably well predicted by all DES and LES models. RANS predict a flow towards the centerline instead of away from it close to the wall.

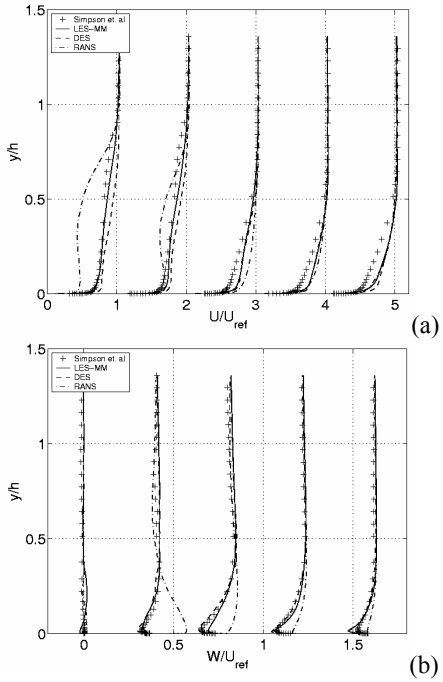

Figure 4. Velocity profiles at *x/h=3.69* and *z/h=0, -0.33*, *-0.81*, *-1.30* and *-1.79*, from left to right, (a) streamwise velocity and (b) spanwise velocity.

4.3 The Darpa Aff1 Configuration

The computational submarine model has been mounted in a cylinder of diameter *d/L = 0.787*, chosen to mimic the cross-section of the wind tunnel, with the inlet placed one hull length *L* upstream of the model and the outlet two lengths *L* downstream. At the inlet, Dirichlet conditions are used for the velocities and *k*, and Neumann conditions are used for *p*. At the outlet, Neumann conditions are used for the velocities and k, and Dirichlet conditions are used for *p*. No-slip conditions are used on the hull together with the wall-model. The computational mesh consists 3,3 million grid cells, with 100 cells in the circumference of the hull. All computations are initiated with quiescent conditions and the unsteady flow evolves by itself.

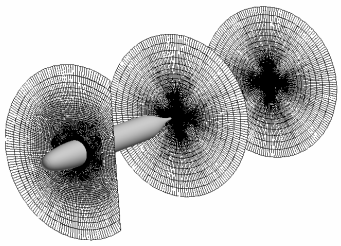

Figure 5. The computational domain for the Darpa Aff1 Configuration

Only the LES calculation is performed for the Darpa Aff1 Configuration, the DES calculation is in progress. The result from the LES calculation is yet very promising and the agreement with the calculations is very good, figure 6. This computational configuration is a very challenging case for all LES based method, due to the large influence of the developing boundary layer on the hull.

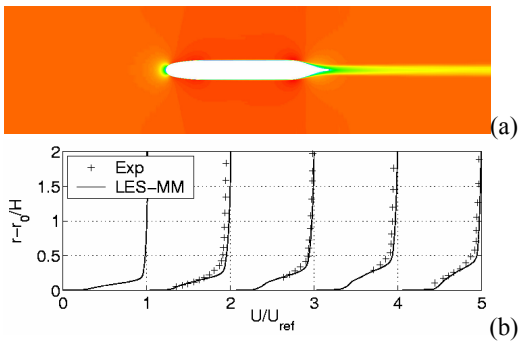

Figure 6. Flow over a bare-hull submarine hull. (a) Time averaged axial velocity contours, and (b) profiles of the axial velocity at x/L=0.875, 0.904, 0.927, 0.956 and 0.978.

5. Concluding Remarks

This study investigates and compares the predictive capabilities of RANS, DES and LES by performing simulations of the flow around a circular cylinder, a surface mounted 3D hill in a channel and the Darpa AFF1 configurartion. The simulation results are compared to the experimental data of, Cantwell and Coles [20], Simpson *et al*, [14], and Byun *et al.*, [3] and Huang *et al.* [7]. A comparative study, such as this, can never be complete or perfect since at some stage models for the turbulent stress tensor or the subgrid stress tensor need to be selected. These sub-models are important to the predicted flow, and its first and second order statistical moments, if applicable (as for DES and LES), although to a higher degree for RANS than for DES and LES. The selection of turbulence and subgrid models made here is based on experience, common availability and practice as well as information and presented results in the open literature. For the RANS model we chose a cubic eddy viscosity model mainly because of its alleged ability to handle streamline curvature in turbulent boundary layers. For DES we

selected the well-known Spalart-Allmares (S-A) model mainly because of its widespread use, and for LES we used two subgrid models: the One Equation Eddy Viscosity Model (OEEVM) and a Mixed Model (MM) consisting of a scale similarity term and the OEEVM. All LES calculations used a wall-model to handle the near wall flow effects. Identical numerical methods and grids were used for LES and DES. For the DES calculations two different viscosity inflow profiles was used – one with low inflow viscosity and one with high inflow viscosity (based on the steady solution of the S-A RANS model).

Both LES and DES make a good prediction of the cylinder flow, yet the recirculation region is highly over predicted. The RANS predictions in the 3D hill case have very poor accuracy when compared to the available experimental data. It appears that this result is not coincidental since other investigators, using different turbulence models, have obtained similar results, e.g. [6]. Both LES and DES makes a much better prediction of the flow, yet the DES results are very sensitive to the inlet conditions of the modified turbulent viscosity $\tilde{\nu}$, see Persson et al. [10]. The Result from the Darpa AFF1 Configuration is very promising for LES, the DES results are under way.

It is evident that the RANS computation fails because RANS removes virtually all of the dynamics of the large energy containing eddy scales, and no turbulence model can alleviate this. The difference between LES and DES can be related to both the wall handling and the subgrid modelling. Both the S-A model and the OEEVM model are one-equation models and relax to a Smagorinsky-like algebraic expression in the equilibrium limit, and therefore we do not think that this part of the modelling is crucial. More important, however, is the inflow profile of the viscosity for the DES S-A model to which the results are very sensitive. Also the wall handling is different, the LES models use a wall model based on the law of the wall, while the DES models try to model the near wall flow in a RANS framework. To use the full potential of the DES wall handling, the wall normal resolution in the near wall region should be larger than the boundary layer thickness, in these cases the grid is adapted to fit the LES wall handling technique, where the wall normal resolution should be as close to wall resolved LES as possible. These reasons can be the major explanation why the LES are slightly more accurate, compared with the measurements, than the DES.

References

[1] Bardina J., Ferziger J.H, and Reynolds W.C., 1980, Improved subgrid scale models for large eddy simulations, AIAA Paper 80-1357

[2] Bensow R., Persson T. and C. Fureby, 2005, Reformulation of the incompressible LES equations with implication on subgrid modeling, Submitted to Phys. of Fluids

[3] Byun G. and Simpson R.L., 2005, Structure of three-dimensional separated flow on a Axisymmetric bump, AIAA Paper 05-0113

[4] Craft T.J., Launder B.E. and Suga K., 1995, Development and application of a cubic eddy-viscosity model of turbulence, Int. J. Heat and Fluid Flow, **17**, 108

[5] Fureby C., Alin N., Wikström N., Menon S., Persson L. and Svanstedt N., 2004, On Large Eddy Simulations of High Re-number Wall Bounded Flows, AIAA.J. **42**, 457

[6] Haase W., Aupoix B., Bunge U. and Schwamborn D., FLOMANIA: Flow-Physics Modelling –An Integrated Approach, 2005, Notes on Numerical Fluid Mechanics and Multidisciplinary Design, (Berlin: Springer Verlag)

[7] Huang T.T., Liu H-L., Groves N.C., Forlini T.J., Blanton J. and Gowing S., 1992, Measurements of Flows over an Axisymmetric Body with Various Appendages (DARPA SUBOFF Experiments), Proc. 19th Symp. On Naval Hydro dynamics, Seoul, Korea.

[8] Panton, R.L., 1996, Incompressible flow, (New York: John Wiley & Sons)

[9] Persson T., Fureby C. and Bensow R., 2005, Large Eddy and Detached Eddy Simulation of turbulent flow around a circular cylinder. Internal Report No 05-98, ISSN 1652-9189

[10] Persson T., Liefvendahl M., Bensow R., and Fureby C., 2005, Submitted to journal of turbulence

[11] Pope, S.B., 2000, Turbulent Flows, (Cambridge University Press)

[12] Sagaut P., 2001, Large Eddy Simulation for incompressible flows, (Berlin: Springer Verlag)

[13] Schumann U., 1975, Subgrid scale model for finite difference simulation of turbulent flows in plane channels and annuli, J. Comp. Phys., **18**, 376

[14] Simpson R.L., Long and C.H. Byun, 2002, Study of vertical separation from an axisymmetric hill, Int. J. of Heat and Fluid Flow, **23**, 582

[15] Smagorinsky J., 1963, General circulation experiments with the primitive equations. I. The basic experiment, Month. Wea. Rev., **91**, 99

[16] Spalart P.R. & Allmaras S.R., 1992, A one-equation turbulence model for aerodynamic flows, AIAA 92-0439

[17] Spalart P.R., Jou W.-H., Strelets M. and Allmaras S.R., 1997, Comments on the Feasability of LES for wings, and on a Hybrid RANS/LES Approach, Advances in DNS/LES, 1st AFSOR Int. Conf. On DNS/LES, Greyden Press, Columbus Oh.

[18] Wikström N., Svennberg U., Alin N and Fureby C., 2004, Large Eddy Simulation of the Flow past an Inclined Prolate Spheroid, J. Turbulence, **5 029**

[19] Wilcox, D.C., 1993, Turbulence modeling for CFD, (DCW Industries)

[20] Cantwell B and Coles D, 1983, An experimental study of entrainment and transport in the turbulent near wake of a circular cylinder, J. Fluid Mech, **136,** 321

Treatment of the free surface boundary conditions in PARNASSOS

Auke van der Ploeg, A.v.d.Ploeg@MARIN.NL

1. Introduction

In this paper we use the iterative method described in (Raven, van der Ploeg, Starke, 2004) to compute the steady viscous flow around a ship including the free surface. For completeness, a brief description of this method is presented in Section 2. In (Raven, van der Ploeg, Starke, 2004) it has been shown that the computational results agree very well with measurements even at a distance from the hull, not only for slender ships like the Series 60, but also for fuller ships like tankers. In (Starke, van der Ploeg, Raven, 2005) it has been shown that the method gives good results also for transom-stern vessels. The method was found to solve the steady free-surface ship viscous flow problem very efficiently. For example, for the Series 60 C_b=0.6 at model scale Reynolds number Rn=3.4x10^6 and Froude number Fn=0.316, the required CPU-time for the RANS/FS computation on a mesh with 1.75M nodes using a PC with a single Intel Pentium IV 2.4 GHz processor is 20 hours.

However, without a special treatment of the boundary conditions near the waterline, the computation is hard to converge. Strong variations in wall-normal direction in the computed wave elevation can occur. This is illustrated by Fig.1, which shows the computed wave elevation near a ship's hull for the Series 60 mentioned above. The computational mesh consisted of 321 x 121 x 45 grid nodes in the streamwise, wall-normal and girthwise direction, respectively. Although the wave pattern is computed accurately in the largest part of the computation domain, behind the bow near the waterline short, sharply diverging waves appear which actually propagate into the wave pattern away from the hull.

Although such waves can have a significant influence on the robustness of the method, they are irrelevant for the wave resistance. It is, therefore, desired and permitted to adjust the formulation such that they are suppressed or filtered out, provided that this does not affect longer wave components and the viscous flow around the hull. In Section 3 we will discuss several ways to deal with these short waves. It will be shown that the short diverging waves are mostly influenced not by the three real boundary conditions at the free surface, but by a 4th equation which is required in order to close the system.

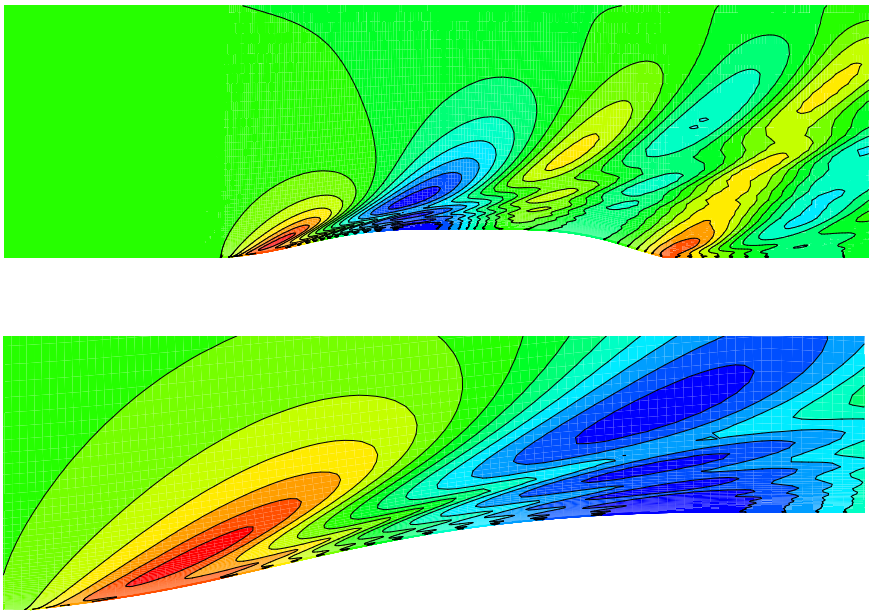

Fig. 1: Isolines of computed wave elevation. Below: wave pattern behind the bow showing short diverging waves near the waterline.

2. Computational method

The viscous flow solver used in this paper is PARNASSOS, a code developed and used by MARIN and IST (Hoekstra, 1999; Van der Ploeg, Eça and Hoekstra, 2000). It solves the discretised Reynolds-averaged Navier-Stokes equations for a steady, 3D incompressible flow around a ship hull. The method can handle body-fitted, generally non-orthogonal HO- or CO-type grids, either single or multi-block structured. No wall functions are used, not even for full-scale computations.

The flow is computed in a relatively small domain, at the outer boundary of which we impose Dirichlet conditions for the pressure and for the velocity components tangential to that boundary; these values are found from a potential-flow solution.

The discretisation is of finite-difference type. All terms in the momentum and continuity equations are discretised by second or third-order accurate difference schemes.

The momentum and continuity equations are solved in fully coupled form. Therefore, the continuity equation need not be recast in a pressure correction or pressure Poisson equation, but can simply be solved as it is. After discretisation and linearisation, the three momentum equations and the continuity equation give rise to a matrix equation containing 4*4 blocks, which is solved using preconditioned GMRES (Saad and Schultz, 1986). This fully coupled solution has been found to be robust and quite insensitive to the mesh aspect ratio.

Free-surface treatment

A surface-fitting approach is used to solve the viscous free-surface flow problem. We use the 'steady iterative formulation' (Raven & Van Brummelen, 1999; Raven & Starke, 2002; Raven, van der Ploeg, Starke, 2004) which, contrary to almost all other RANS/FS methods, involves no time-dependent terms; neither in the momentum equations, nor in the free-surface boundary conditions.

The problem is solved by an iterative procedure, instead of by time integration. This iteration is based on the use of the "combined free-surface boundary condition (FSBC)". If we denote the velocity components (in a *(x,y,z)*-coordinate system fixed to the ship, with x positive aft and z upward) by u,v,w, the hydrodynamic pressure by p and non-dimensionalise all quantities using ship speed U, a reference length L_{pp}, and gravity acceleration g, this combined FSBC reads:

$$Fn^2\left(up_x + vp_y + wp_z\right) - w = 0 \qquad (1)$$

This condition is obtained by substituting the wave elevation from the dynamic condition into the kinematic condition. Together with the dynamic condition it describes exactly the same problem as the original set of conditions; but it has the advantage of permitting a successful iterative procedure. Each iteration consists of the following 2 steps:

I. solve the RANS equations subject to the combined free-surface condition (1) and the two tangential components of the dynamic condition, imposed at the current estimated wave surface.

II. update the wave surface and grid based on the pressure difference at the estimated wave surface, i.e. using the normal component of the dynamic condition. Neglecting surface tension and viscous contributions this reduces to the requirement that the wave height has to equal $Fn^2 p$.

Upon convergence the pressure deviation, normal velocity and shear stress vanish at the wave surface and the solution of the steady RANS/FS problem has been obtained. It has been shown in (Raven, van der Ploeg, Starke, 2004) that only a few steps of this iterative method suffice in order to obtain a converged solution. In the present applications, the 'balanced discretisation' derived in (Raven, van der Ploeg, Starke, 2004) has been used, which reduces the numerical damping of the waves to 5^{th} order in the longitudinal step size Δx, and the numerical dispersion to 3^{rd} order in the vertical spacing Δz. This contributes to a good accuracy of the wave pattern even at a distance from the hull.

3. Treatment of the short, sharply diverging waves

In methods that solve the steady free-surface viscous flow problem by a time-dependent algorithm, the RANS equations are usually solved with a boundary condition p=0 at the free surface, and the free surface is updated using the kinematic FSBC. However, at the wall the no-slip boundary condition would then prevent any free-surface movement, causing stagnation of the iterative process; the well-

known ‘contact line problem’. Therefore, usually some extrapolation towards the waterline is used in the free-surface update.
In our approach, there is no contact-line problem, since the combined FSBC is not violated at the wall and also an update of the free surface using the dynamic FSBC can be applied arbitrarily close to the wall. However, if we solve the FSBC all the way to the wall, short, sharply diverging waves as shown in Fig. 1 are generated near the waterline, and these already occur in the RANS solution. Contrary to the time-dependent approach, we cannot use explicit extrapolation near the waterline, but have to use some implicit correction in the RANS solution itself in order to suppress the spurious short waves.
In order to close the system of equations, in step I of the iterative process described in Section 2 we need a 4th equation at the free surface. This condition should be sufficiently weak and is not a real boundary condition. As a 4th condition we use the momentum equation in the direction normal to the free surface. From numerical experiments it has been found that the implementation of this equation is very important for the way in which the short, diverging waves appear. In order to improve the convergence behavior we normally use a modification of this equation quite close to the waterline: In a small region near this line, at the free surface only, we replace the momentum equation in the direction normal to the free surface by the requirement that the second derivative of p in wall-normal direction has to be zero. Hence we do not modify the three ‘real’ boundary conditions at the free surface, but only the 4th equation which is required in order to close the system. In (Raven, van der Ploeg, Starke, 2004) it is shown that this has the desired effect and reduces the short waves without affecting the rest of the wave pattern. However, the robustness is quite sensitive to the width of the area along the waterline at which this averaging is applied. In this paper we want to investigate the possibilities not to use the above-mentioned averaging, but to use an alternative implementation of the 4th boundary condition. Therefore, we take a grid under a converged wave pattern (which has been obtained using the averaging of the pressure near the waterline), perform one RANS-computation (without this averaging) on this grid and study the resulting estimate of the wave pattern.
First, we will describe the implementation of the 4th boundary condition in more detail. Let (ξ,η,ζ) denote the curvilinear system which is conforming to the boundaries of the domain. Herein ξ is roughly aligned with the streamwise direction, η with the wall-normal direction and ζ with the girthwise direction. A rectangular, uniform mesh in (ξ,η,ζ) space defines the computational grid in physical space. The coordinates in mainstream, wall-normal and girthwise direction are referred to as, i, j and k respectively. The estimate of the free surface is given by the points for which the index k and the coordinate ζ reach their maximum value. Below the free surface, $\partial p/\partial\zeta$ is discretised using a QUICK scheme with a first-order implicit part:

$$(-p_k^{n+1}+p_{k+1}^{n+1})-\left(2p_{k-1}-3p_k+p_{k+2}\right)^n/6 \qquad (2)$$

in which n denotes the iteration number of the viscous flow solver.
At the free surface we use a different discretisation: viscous terms in the ζ-momentum equation are neglected and the pressure derivative in this equation is discretised as

$$(p_k^{n+1}-p_{k-1}^{n+1})-\left(5p_k-12p_{k-1}+9p_{k-2}-2p_{k-3}\right)^n/6 \qquad (3)$$

In the sequel of this paper, the combination of (2) and (3) will be referred to as the ‘p-upward’ discretisation.
We also consider the following alternative: take the bias of $\partial p/\partial\zeta$ in the ζ-momentum equation below the free surface the opposite of the bias in (2), and also reverse the bias of the ζ-derivative in the continuity equation. Hence we use the following discretisation of $\partial p/\partial\zeta$ in the ζ-momentum equation

$$(p_k^{n+1}-p_{k-1}^{n+1})+\left(2p_{k+1}-3p_k+p_{k-2}\right)^n/6 \qquad (4)$$

Furthermore, take as a 4th boundary condition the ζ-momentum equation discretised exactly as below the free surface, including the viscous terms. This will be referred to as the ‘p-downward’ discretisation.
Near midship, the short waves generated near the ship are strongly reduced using the ‘p-downward’ instead of the ‘p-upward’ discretisation. This is demonstrated in Fig. 2, showing a close-up of the isobars in a plane roughly perpendicular to the main stream direction at the intersection of the free surface with the hull. Fig. 3 shows the computed results along wavecuts both quite near the hull

($y = 0.0755 L_{PP}$) and at a larger distance from the hull ($y = 0.2067 L_{PP}$). Also shown in these figures are experimental results from Toda et al (1991). It appears that with the '*p*-downward' discretisation the short waves have been reduced, but right behind the bow they are still present. At a larger distance from the hull, both computed wave patterns are similar.

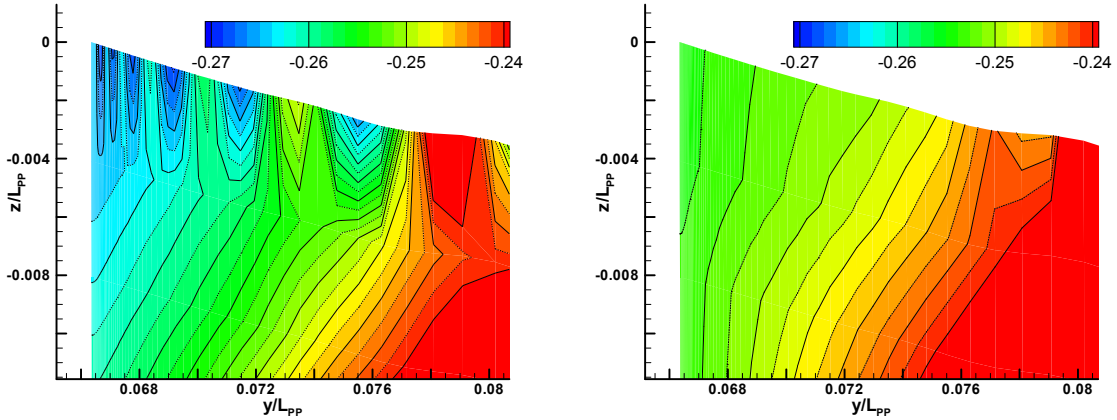

Fig. 2: Isobars near midship in a plane perpendicular to the main stream direction. $h_\zeta \approx 0.004 L_{pp}$ in this area. Left: '*p*-upward' discretisation, right: '*p*-downward' discretisation.

Refinement towards the free surface.

Since we have seen that the discretisation of $\partial p / \partial \zeta$ influences the short waves, we also can expect an influence of reducing the mesh size in ζ-direction towards the free surface. Fig. 4 shows the effect of refinement to the free surface (the '*p*-downward' discretisation has been used to obtain the results shown in this figure). The computed result along the wavecut near the hull improves: the unphysical short waves are reduced and the result is closer to the measurements. Again, at a larger distance from the hull, the effect of refinement to the free surface is smaller.

A possible explanation for the generation of the short waves is the following: the local mesh size in wall-normal direction is extremely small, as required in order to capture the boundary layer and permits to resolve very short waves. Such waves should have a very quick decay in vertical direction, but this decay cannot be resolved on a grid in which the vertical mesh spacing is much larger. Therefore the short waves will be severely distorted, which may explain their occurrence in the computation.

Unfortunately, the computation is harder to converge on a mesh using a refinement towards the free surface.

Extra diffusion in the 4th FSBC

From numerical experiments, it appeared that extra diffusion in wall-normal direction in the 4th FSBC can reduce the short waves quite near the hull, but it also damps the waves further from the hull. We have therefore tried to impose extra diffusion only in those regions where the short waves are present. To detect the short waves, we use the curvature of the free-surface in wall-normal direction. To be more precise: only in those regions where the curvature of the free surface in η-direction is significantly stronger than the average curvature, we use the extra diffusion in the 4th FSBC.

Fig. 5 shows that quite near the waterline, the short waves are damped significantly by the extra diffusion, while it hardly causes extra damping at larger distances from the ships hull.

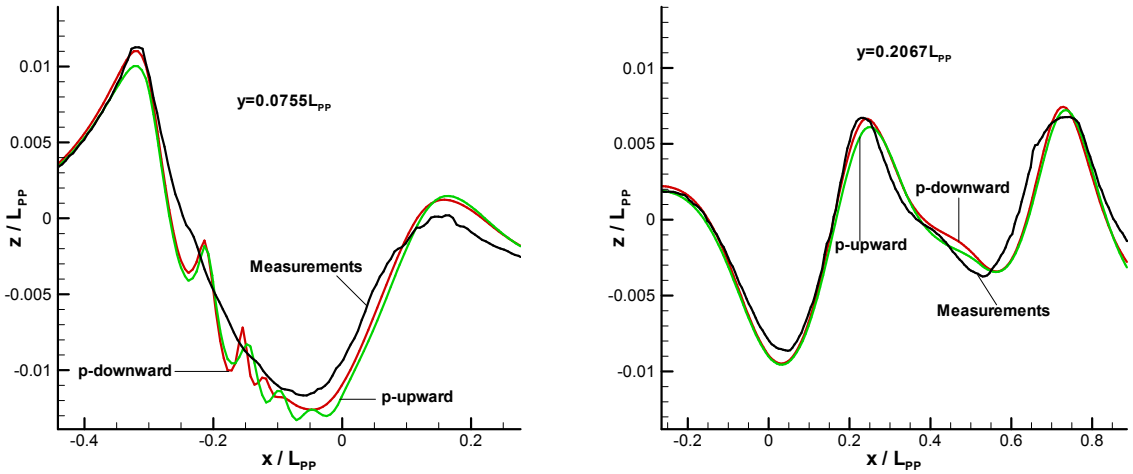

Fig. 3: Measurements and computed solutions along wavecuts.

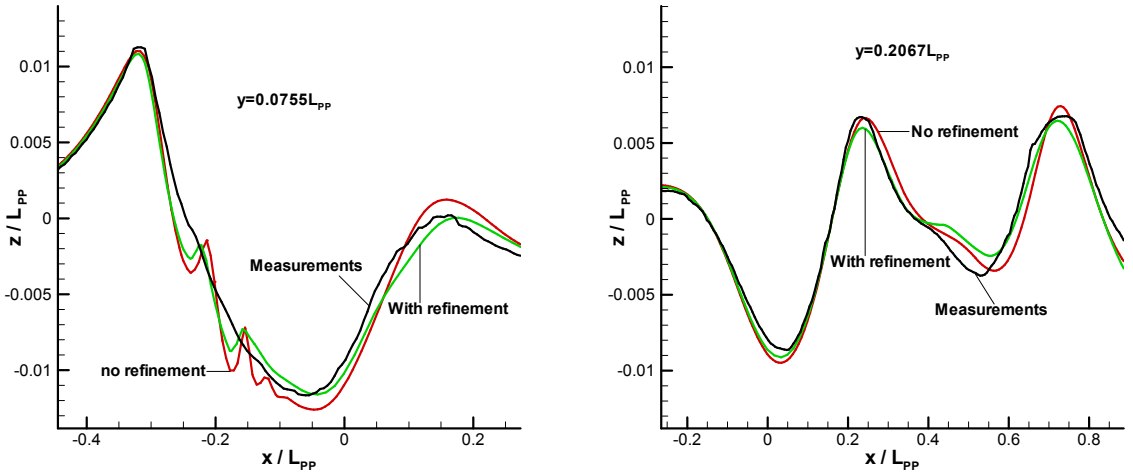

Fig. 4: Measurements and computed solutions both with and without refinement to the free surface.

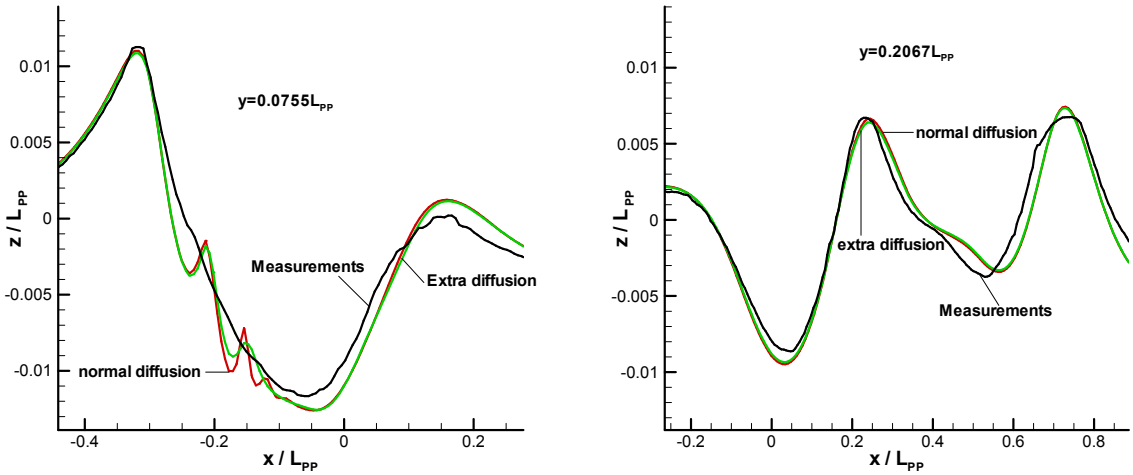

Fig. 5: Measurements and computed solutions both with and without extra diffusion in wall-normal direction in the 4th boundary condition.

4. Conclusions and suggestions for further research

Although the 4th FSBC is only present in order to close the system, and is not a 'real' boundary condition, its implementation strongly influences the short, strongly diverging waves generated quite near the waterline. Although in many cases robustness problems can be avoided by replacing this equation by the requirement that the second derivative of the hydrodynamic pressure in wall-normal direction has to be zero, we have described a better way to deal with these waves: if below the free surface the bias of the discretisation of the pressure derivative in the direction normal to the free surface is reversed, the momentum equation in this direction at the free surface can be used as a 4th 'boundary condition'.

The short waves can be reduced further by adding extra diffusion to the 4th boundary condition in those regions where the curvature of the free surface in wall-normal direction is larger than the average curvature. It has been shown that for the Series 60 this extra diffusion hardly causes extra damping at larger distances from the ships hull. Another way of obtaining modifications only in those regions with strong curvature is to use surface tension. However, for this application, the surface tension forces are not expected to be physically important.

In this paper, only results for the Series 60 have been shown. For the M5415, we have obtained similar results. It has to be checked that similar results can be obtained for other ships as well.

For the Series 60, two grids under a converged wave pattern have been considered, one in which the mesh spacing in the direction normal to the free surface is quite large, and one in which the mesh is refined towards the free surface. The computed results on the latter grid show a further reduction of the short waves generated near the waterline.

However, these short waves do not completely disappear with the modifications mentioned in this paper. It would be ideal to find a way to prevent such unphysical waves even to be generated. Otherwise, a better understanding of the influence of the diffusion in the 4th boundary condition is desirable in order to further reduce these short waves.

REFERENCES

Toda, Y., Stern, F. and Longo, J., "Mean-flow measurements in the boundary layer and wake field of a Series 60 Cb=.6 ship model for Froude numbers .16 and .316," IIHR Report No. 352, Iowa Institute of Hydraulic Research, August, 1991.

Saad, Y. and Schultz, M.H., "A generalized minimal residual algorithm for solving nonsymmetric linear systems", SIAM Jnl. Sci. Statist. Comput., Vol.7, pp. 856-869, 1986.

Hoekstra, M., "Numerical simulation of ship stern flows with a space-marching Navier Stokes method", Thesis, Technical University of Delft, October 1999.

Raven, H.C. and Van Brummelen, E.H., "A new approach to computing steady free-surface viscous flow problems", 1st MARNET-CFD workshop, Barcelona, Spain, 1999.

Eça, L. and Hoekstra, M., "Numerical prediction of scale effects in ship stern flows with eddy-viscosity turbulence models", 23rd Symp. Naval Hydrodynamics, Val de Rueil, France, Sept. 2000.

Van der Ploeg, A., Eça, L. and Hoekstra, M., "Combining accuracy and efficiency with robustness in ship stern flow calculation", 23rd Symp. Naval Hydrodynamics, Val de Rueil, France, Sept. 2000.

Raven, H.C. and Starke, A.R., "Efficient methods to compute ship viscous flow with free surface", 24th Symp. Naval Hydrodynamics, Fukuoka, Japan, 2002.

Raven, H.C., van der Ploeg, A. and Starke, A.R., "Computation of free-surface viscous flows at model and full scale by a steady iterative approach", 25th Symposium on Naval Hydrodynamics, St. John's, Newfoundland, CANADA, August 2004.

Starke, A.R, van der Ploeg, A. and Raven, H.C., "Free-surface viscous flow computations for KCS and 5415 models using the PARNASSOS code" , CFD workshop Tokyo, 2005.

Simulation of Movable Hydraulic Structures

JENS M. SCHEFFERMANN (jens.scheffermann@fi.uni-hannover.de)
CLAUS ZIMMERMANN (claus.zimmermann@fi.uni-hannover.de)

1 Introduction

Prediction and control of water levels and discharges in a river with gates was one of the earliest challenges to the Hydraulic Engineers several hundred years ago. Empirical and semiempirical approaches, including BERNOULLIS energy equation gave a vast number of discharge equations having contraction coefficients in common, which – depending on their definition – depend on gate geometry, stage–discharge relations and which had to comprise unknown roughness and turbulence effects. Such contraction coefficients and discharge coefficients of control gates had to be determinated in hydraulic model tests (GENTILINI, 1941). But there are still problems with the determination of the exact discharge under the gates of weir structures, when downstream water levels are significant larger than the opening height of the gate. For submerged jet flow at several weir structures deviations of 50 % between predicted and measured discharge have been reported (CLEMMENS et al., 2003). Analysis shows that unacceptable deviations are application of experimental coefficients that were obtained under certain boundary conditions, e.g. flat and regular bottom, constant cross sections and/or specific gate orifices or lips. Varying boundary conditions during uplift and downlift of the gate is another reason for inconsistent and unprecise discharge estimations at weirs and gates.

In this paper numerical simulations are presented for one of the 6 vertical lift gates of a storm surge barrier in the tidal river Ems in Germany which can predict unsteady flow conditions at a weir structure with moving boundary, i.e. a lifting gate, using a CFD-Program with a moving mesh. Validation of the numerical model will be with results from physical model tests. Main focus is the simulation of effects during downlift of the gate. For validation results from the numerical model are compared with physical model measurements and results from literature. The approach was then tested at the filling system of a lock.

2 Laboratory Model Tests

A sectional model of a lifting gate of the storm surge barrier in the River Ems, Germany, was installed in a flume (length 20 m, width and depth 1 m) of the FRANZIUS-INSTITUT. This lifting gate is moving with variable velocities along the vertical axis. Wave gauges up- and downstream of the gate recorded the water surface. Velocities behind the moving gate were measured with an ADV-Probe at 8 positions at 20 Hz intervals (Figure 1).

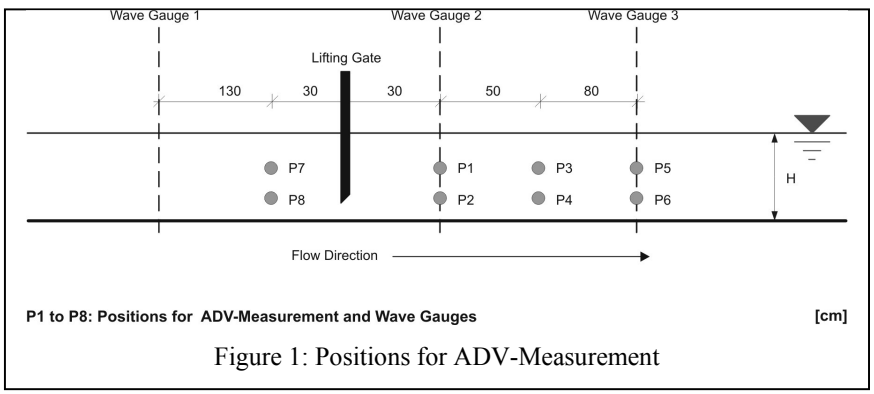

Figure 1: Positions for ADV-Measurement

Tests were with discharges of 25, 50 and 100 l/s at water depths of 40, 50 and 60 cm. The gate velocity was 0,48 (or 0,24) cm/s. The gate was lowered from a starting position above water level in 90 (180) seconds to a final position 10 cm above the flume bottom, where it remained for 20 seconds,

directly after the gate was lifted in 90 (180) seconds to the starting position. Measurements were repeated for each position, assuming constant flow conditions.

3 Basic Numerical Simulation

For the numerical simulations the commercial CFD-Program STAR-CD was used. This code applies a three-dimensional CFD-solver system widely used in chemical and mechanical engineering. The numerical model is taking into account a free water surface using the Volume of Fluid (VOF) Method. Basic equations are conservation of mass, momentum and energy. Assuming an incompressible fluid, viscous stresses can be described with the friction approach of Newton, the continuity equation and the NAVIER STOKES Equations. Transposing the differential equation system to a numerical simulation system, a time averaging process results in the time-averaged continuity equation (1) and the time-veraged NAVIER-STOKES Equations (2).

$$\frac{\partial \overline{u_i}}{\partial x_i} = 0 \tag{1}$$

$$\frac{\partial \overline{u_i}}{\partial t} + \overline{u_j}\frac{\partial \overline{u_i}}{\partial x_j} = -\frac{1}{\rho}\left[\frac{\partial \overline{p}}{\partial x_i} - \rho\frac{\partial}{\partial x_j}\left(\nu_t \frac{\partial \overline{u_i}}{\partial x_j}\right) - \overline{u_i' u_j'}\right] + \overline{f_i} \tag{2}$$

where u is the velocity, t is time, p is the fluid pressure, ρ is the fluid density, ν is the viscosity, and f is the body force and the over-bars refer to time averaging of turbulent scales. As a consequence of the averaging process in time additional terms, the so-called REYNOLDS Stresses, appear. The resulting system of equations is commonly referred to as the REYNOLDS-Averaged NAVIER-STOKES Equations (RANSE). The relationship between time-averaged NAVIER-STOKES Equations and REYNOLDS Stresses is described in explicit terms, using a turbulence model. From preliminary numerical simulations the k-ε-standard-model with its standard parameters was chosen as turbulence model.

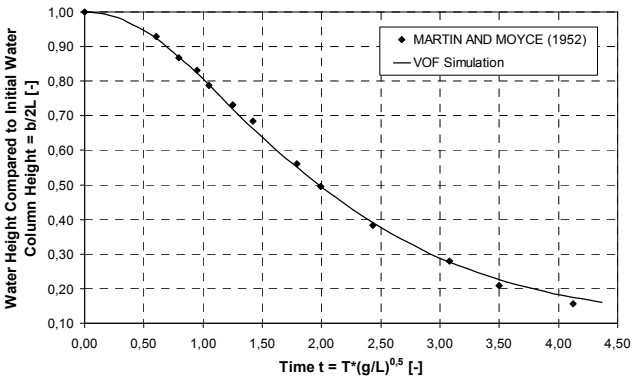

Figure 2: Comparison of VOF-Simulation and Physical Model Tests of a Collapsing Water Column

Evaluation of the VOF-Method with physical model test (MARTIN and MOYCE, 1952) showed the right calculation of water depth in a collapsing water column (Figure 2).

For a simulation with moving meshes, an additional equation called "Space Conservation Law" is solved for the moving coordinate velocity components, which is a form of the Arbitrary LAGRANGIAN-EULERIAN (ALE) Method. This relates the change in the cell volume to the coordinate frame velocity. The application of a moving gate requires a large variation in the solution domain size. If the total number of cells in the solution domain under the gate remains fixed, the cell spacing may become too dense at some stages of the solution and too sparse at others. This is undesirable because the time step required for an accurate solution depends on the mesh COURANT Number. Thus, unwanted small time steps might be necessary when smaller cells are generated during the transient process, leading to extensive computational times and numerical instability problems associated with large aspect ratios of some cells. To avoid these problems, cells can be added under the gate during the transient calculation process.

4 Numerical Model of the Lifting Gate

For this case, the mesh was divided into three different regions (Figure 3). Region #1 includes the flow volume upstream and downstream of the gate. Region #2 includes the gate structure. To generate a motion of this area the vertices of all cells are moved during the transient process. To keep the correct gate geometry all vertices of region #2 are moved by the same value on the y-axis. Due to the gate motion in region #3 the cells have to be deformed.

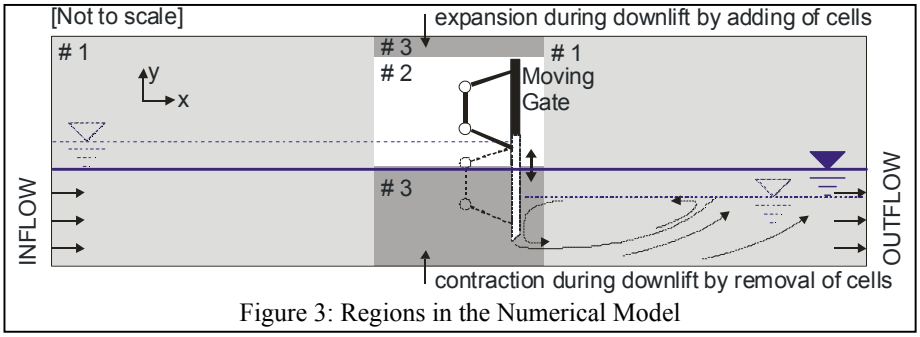

Figure 3: Regions in the Numerical Model

During downlift the cells under the gate are contracted and at specified time steps Δt cells are removed from the cell set. Above the gate cells are expanded and at Δt cells are added to the cell set. Time step is 0,01 to 0,1 sec. (100 to 10 Hz).

The numerical model was built in equal scale with the geometry of the laboratory flume, consisting of approximately 80.000 cells, with the bigger part of cells for meshing the complicated girder structure (**Error! Reference source not found.**). Simulations were transient and with the free surface between water and air filled cells. Bottom and side walls of the flume were “no slip” walls. On top a constant pressure boundary was introduced. The transient RANSE/VOF simulation required approximately 50 hours of computational time for 220 s of laboratory simulation.

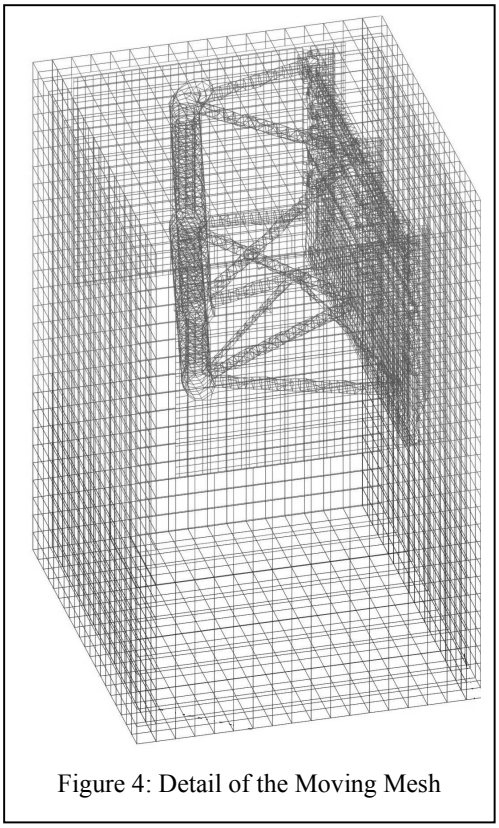
Figure 4: Detail of the Moving Mesh

In Figure 3 the velocities under the gate can be seen. The influence of the girder construction on the flow velocities under the gate is visible. Blockage due to the construction leads to changing discharge on the left and right side of the discharge area under the gate. Normally this effect is neglected, when discharge at gate is calculated by formulae.

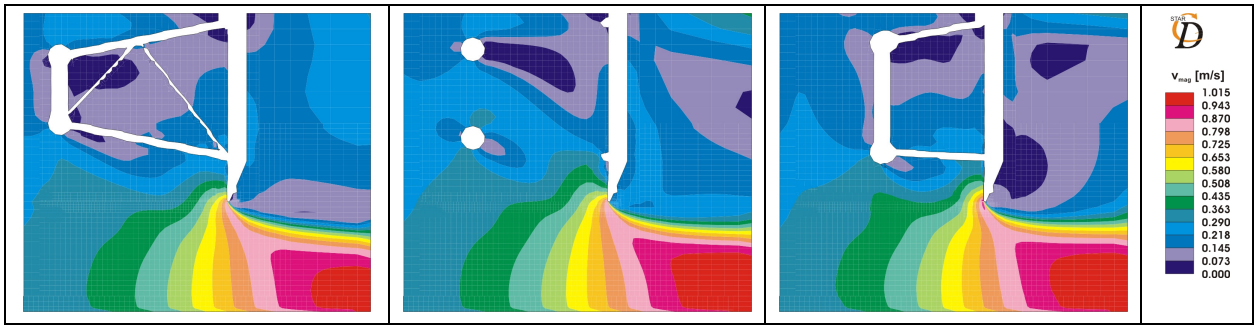

Figure 3: Velocities under the Gate (left side, middle and right side of the gate)

5 Comparison with Velocity-Measurements

In Figure 4 the development of the velocities at various positions of the model is shown. The numerical model is capable to simulate the change from positive to negative velocities near to the water surface downstream the gate (top left and top right), the developing jet velocities (bottom left) and slowing down of the flow upstream of the gate (bottom right). All these effects occur due to the movement of the gate.

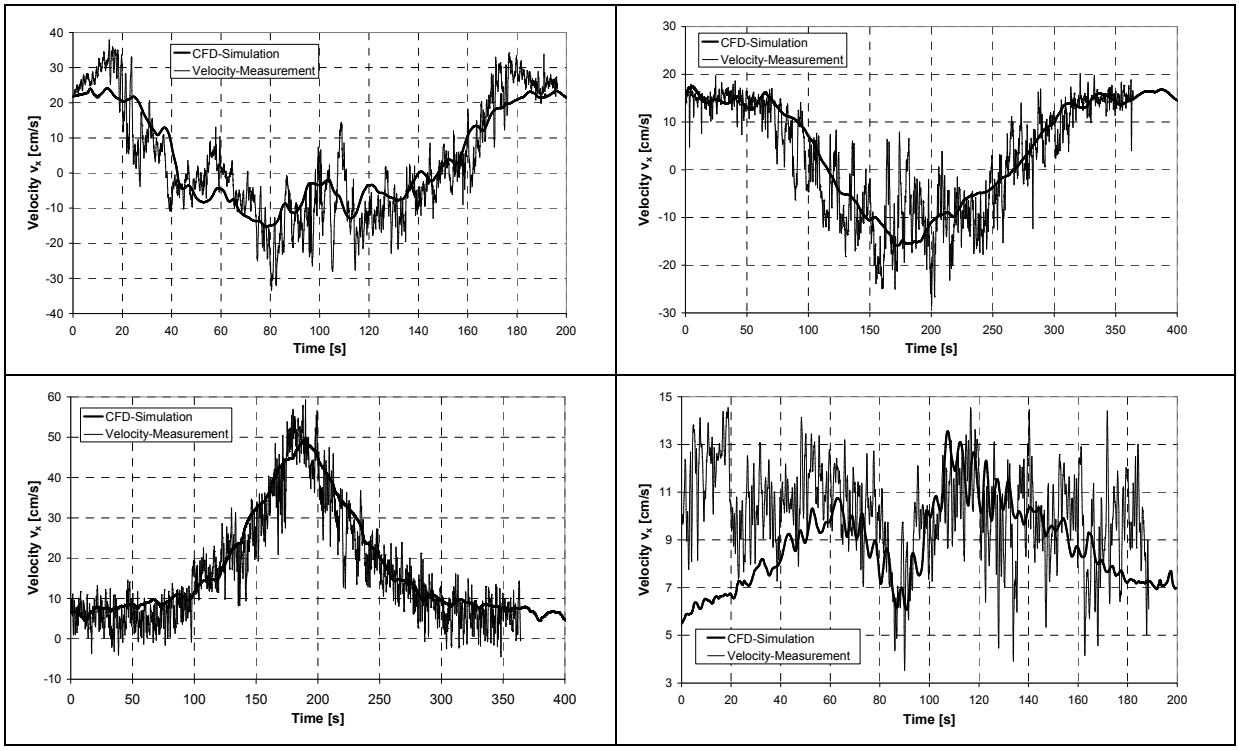

Figure 4: Velocity v_x at different Positions and with different Parameters
Top Left = P1, H = 0,60 m, Q = 50 l/s, t = 90 sec; Top Right = P3, H = 0,40 m, Q = 50 l/s, t = 180 sec
Bottom Left = P2, H = 0,60 m, Q = 25 l/s, t = 180 sec; Bottom Right = P8, H = 0,50 m, Q = 50 l/s, t = 90 sec

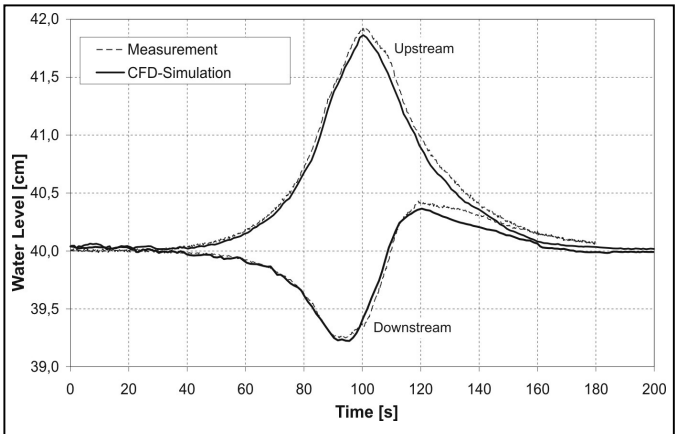

Figure 5: Development of Water Level Upstream
(H = 0,40 m, Q = 50 l/s, t = 100 sec)

The water level in Figure 7 shows the development of the water level upstream and downstream of the gate. The reduced discharge during closing of the gate leads to a higher water level upstream and the jet induces a lower water level downstream, which rises with increasing discharge during opening of the gate.

The results show the possibility of simulating flows with CFD-Programs. Only turbulence induced by microscaled vortices can not be simulated. But the good results show the applicability of the chosen program. A second model should validate the model.

6 Validation of the Moving Mesh Routine

For validation the filling system of a lock was chosen. Temporal and spatial information regarding the pressure in the culverts of a navigation lock is important because in certain locations the pressure can decrease to a level of incipient cavitation. Reasons for low-pressure areas can be the high velocity, which is induced by an opening or closing valve. In most cases the optimum valve speed often has to be defined in physical model tests.

6.1 Physical and Numerical Model Description

The Marmet Locks and Dam project is located on the Kanawha River in the United States. Improvements to the Marmet Locks and Dam include a new lock with a through-the-sill intake, a longitudinal in-chamber filling and emptying system (HITE and STOCKSTILL, 2003), and a conventional sidewall discharge manifold. A physical model study was completed to evaluate different effects at the design lift of 7.315 m. This chapter directs attention to the pressures measured in the culverts during filling operations. During filling operations, the unsteady flow is controlled by vertical lift gates.

A 1:25-scale physical model study (HITE, 1999) was conducted at the COASTAL AND HYDRAULICS LABORATORY (CHL) of the U.S. ARMY ENGINEER RESEARCH AND DEVELOPMENT CENTER. Pressure cells were used to measure instantaneous pressures in the culvert just downstream of the filling valve and to record water-surface elevations within the lock chamber. These pressure cells located within the lock chamber measured the water-surface variations in time at the upstream end, center, and downstream end thus providing the lock-filling curve. The numerical simulations were performed during an assignment of the author at the CHL in Vicksburg, Mississippi during January and February 2005.

The numerical model was built in equal scale with the geometry of the laboratory lock, consisting of approximately 40,000 cells (Figure 8). Sidewalls of the culverts were “no slip” walls. The k-ε model with its standard parameters was again chosen as the turbulence model. The time step was 0.01 sec and an entire lock operation was simulated. To generate a flow through the culvert, pressures were specified at the inlet and the outlet. The inlet pressure was constant, reproducing the water level in the project’s upper pool, and the outlet pressure was specified as time varying, representing a changing water level in the lock chamber.

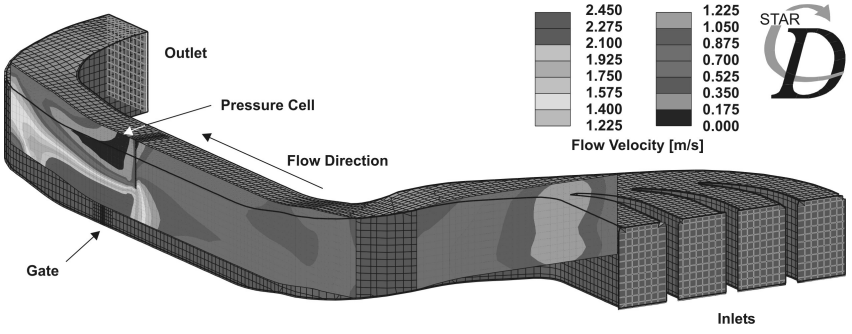

Figure 6: Numerical Model of Marmet Lock System

6.2 Comparison of pressure during valve movement

Valve opening speeds of 2, 4, and 8 min. were tested in the physical model and simulated in this study. For brevity, only the 8-min results are presented here. Figure 9 shows the development of the pressure in the lock (i.e. the water level of the lock chamber), the pressure measured on the culvert roof at a distance approximately one-half a culvert height downstream of the vertical lift valve. The comparison with the

numerical results shows a good agreement between computed and observed pressures with maximum deviations in the range of 5%.

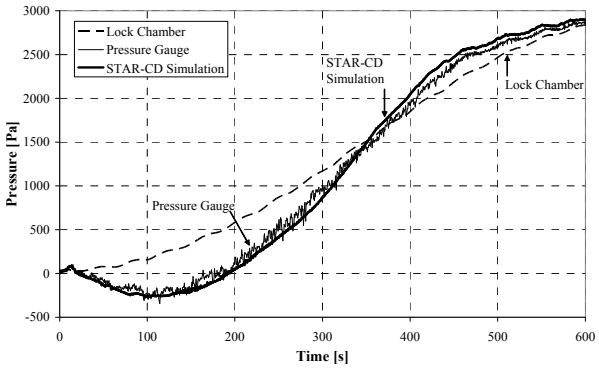

Figure 7: Numerical Model of Marmet Lock System

At the beginning of the valve operation, a pressure increase is noticeable. This is a result of the venting from upstream to downstream of the gate. This effect is quickly overcome and the pressure changes to negative values, because of the developing jet under the gate. As the area under the valve increases, the velocities in this jet decrease and the pressure changes again to positive values. The duration of negative pressure at the culvert ceiling is longer for a valve opening speed of 8 min. than for a 2 or 4 min operation time (results not shown here). The slower valve speed leads to a longer time with a relative small flow area, producing this pressure drop.

Due to energy loss at the filling system in the lock bottom and the inertia of water a higher pressure than in the lock is developing in the culverts. This pressure drop decreases with higher water level in the lock and due to that decreasing discharge. This shows the flatten curve of the hydrostatic pressure at the lock bottom.

7 Conclusion

The results show, that it is possible to simulate pressure and velocity with moving meshes. But the results also show that turbulent fluctuations in the measurements because of micro scaled vortices cannot be computed with the k-ε turbulence model used in this study. But this has no influence on the result quality. If necessary for other problems the grid resolution can be increased.

Given only the specification of pressure as boundary conditions, the RANSE model, together with a moving mesh subroutine for the moving valve, is capable of computing time-varying flow rates and velocity distribution even in the vena contracta. A computational model can be especially useful in areas where measurements are not possible. Accurate calculation of discharge coefficients would require that this model be extended to include the entire lock culvert system and the moving free surface in the lock chamber.

This study shows the promising future of computational application to complicated flow systems with free surface flows and/or moving structures.

8 References

Clemmens, A. J., Strelkoff, T. S., Replogle, J.A., (2003). “Calibration of submerged radial gates.“ Journal of Hydraulic Engineering, 129(9), 680-687

Gentilini, B., (1941). „Effluso dalle luci soggiacenti alle paratoie piane inclinate e a settore“. L’Energia Elettrica, Auszug in: Wasserkraft Wasserwirtschaft Heft 6 und 7 (1942, 37. Jg.)

Hite, J. E. Jr., Stockstill, R. L. (2004). „Hydraulic Design of a Longitudinal Culvert for Lock Filling and Emptying Systems.” Journal of Hydraulic Engineering, Vol. 130 (5)

Martin, J.C., Moyce, W.J., (1952) „Transactions of the Philosophical Society of London,„ Vol. 244, p. 312.

Comparison of Windtunnel Messurements and computations with RANS-Solver FreSCo

Daniel Schmode, d.schmode@tu-harburg.de
Dieke Havermann, hafermann@hsva.de
AB 3-13 of TU Hamburg-Harburg, D-21071 Hamburg

1 Introduction

TUHH and HSVA are developing a new RANS-Solver called FreSCo. The solver is conceived as a multi purpose solver, but validation is aimed at problems related to maritime industry. In the following we compare wind-tunnel measurements for rudder-force with computations using different turbulence models.

2 Numerical Method

The solver is designed for fully unstructured grids with elements of arbitrary shape. Therefor a finite volume discretization with collocated arrangement is implemented. To avoid checkerboard effects a correction proposed by Rhie and Chow [4] is applied to the mass fluxes. Fore pressure velocity coupling the well proven SIMPLE algorithm is used. To increase robustness in case of strong non-orthogonalities we implemented a cross gradient correction for the pressure-correction like it is described in [1].

2.1 Discretization

Spacial Discretization

The code is designed for fully unstructured grids, therefor discretization schemes with higher than 2nd order accuracy are difficult. We use a blending of central differencing and upwind differencing for convective terms. If the connecting line between the cell centers intersects the face aside the face-center we apply a simple correction using the gradient via deferred correction. More details could be found in [3].

The gradients were computed at the cell-centers with Gauss-theorem. For diffusive terms the cell-centered gradients were interpolated on the faces with CD. A correction for non-orthogonalities is implemented using deferred correction. Both topics are described in detail by [3].

Time Discretization

Because of there stability we have implemented only implicit time discretization schemes. We use a implicit Euler scheme, which is first order accurate, an a implicit three-time-level Euler scheme which is 2nd order accurate, but requires more memory than the IE, because two old time-levels have to be stored.

2.2 Turbulence Modeling

Because of there robustness and there relative simple implementation we are using only simple two-equation turbulence models at the moment. In near future we intent to work on explicit algebraic Reynold stress models, but this has not started jet. At the moment FreSCo supports six turbulence Models:

- Standard k-ϵ
- Wilcox k-ω
- RNG k-ϵ
- Chen's k-ϵ
- Menters BSL k-ω
- Menters SST k-ω

2.3 Parallelization

We use here an domain decomposition approach. Due to the spare character of the coefficient matrix of the linear equation system, this approach has proofed to be good scalable on coarse granular Linux clusters. Such coarse granular clusters with out of the shelf network components are quite cheap and relative easy to administrate. So we believe that in terms of computing-power to cost this approach is the most efficient.
For implementation we use the MPI2-standard with the MPICH implementation [6]. Therefore the code is easy portable to other architectures.
Du to the small grids all computations presented here were carried out serial.

2.4 Linear Equation System Solvers

To solve the LES resulting from the discretized equations we use Different Krylow-Subspace-Methods. For the Possion-Equation resulting from the pressure-correction-equation we use a Conjugate-Gradient solver and for the other equations which result in non-symmetric equation system matrixes we use a Bi-Conjugate-Gradient-Stabilizes solver. We use the PetSc-libraries provided by [7], which supply a couple of paralell Krylow-Subspace-Methods.

3 Verification

We started verification by comparing results for some simple test-case (e.g. lid driven cavity flows) on different grids with results from commercial codes. The overall agreement is satisfying, but some results were surprising. E.g. the implementation off turbulence models seem to vary in different codes. But we will not discuss this here, because this is not scope of this paper.

4 Validation

In the following we present our first steps in validation work. For this purpose we carried out computation for a 3D rudder and compare it with wind-tunnel measurements.

5 Wind-Tunnel Measurements

The test data was obtained in our wind-tunnel in Hamburg. Two models have been measured. The Dimensions are given in the following Table.

profile	cord-leng.	height	shaft pos.
MP7320 large	300 mm	435 mm	40 %
MP7320 small	148 mm	214 mm	40 %

The dimensions of the cross section are $1.05m$ times $1.75m$. The test-section is $3.5m$ long. The maximum speed is approx. 50 m/s.
The rudder profile is given in the following figure.

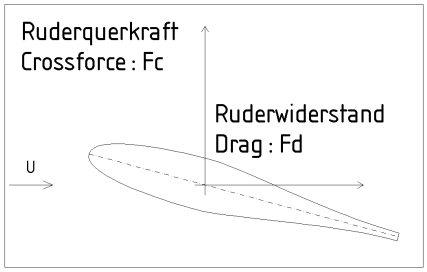

Measurements were carried out at three different speeds: $10\frac{m}{s}$, $20\frac{m}{s}$, $30\frac{m}{s}$.
The rudder model is build of wood and has had a rough surface. After the first measurements were carried out the surface was smoothed and the model was tested again.
The forces are normalized as follows:

$$C_c = \frac{F_c}{\frac{\rho}{2} \cdot U_\infty^2 \cdot c \cdot h}$$

$$C_d = \frac{F_d}{\frac{\rho}{2} \cdot U_\infty^2 \cdot c \cdot h}$$

ρ	:	Density
U_∞	:	Velocity
c	:	cord-length
h	:	rudder height

In the following we refer only on measurements with the large model and a velocity of $30\frac{m}{s}$. The resulting Reynolds-number is $Re = 0.6 \cdot 10^6$. The force coefficients are given in Fig.1.
For the rudder with the rough surface coefficients for measurements of the port and the starboard side are given. In the range between 0 and 17.5^0 the lift-coefficients for the starboard side are slightly larger , at 20^0 the lift is much higher. This may be caused by non symmetries of the model. We present here both measurements to indicate the uncertainty of the experiment. The third set of coefficients given in Fig.1 belongs to the experiment with smoothed surface. Surprisingly the maximum lift is larger then in the experiment with rougher surface. We had expected this vise versa. Again this could be interpreted as uncertainty of the measurements.

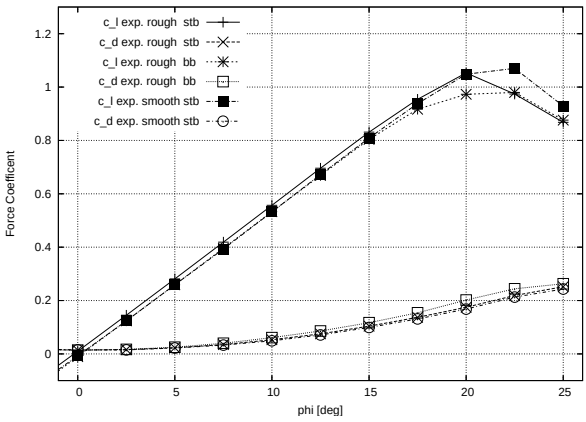

Figure 1: Lift and drag measured in wind-tunnel

6 Computations

Our experience shows that RANS computations coincide the better the higher the Reynolds number is. We believe that this is du to the transition point, which is somewhere on the profile in the wind tunnel model. In RANS computation with standard 2-equation turbulence models, the effect of transition is not captured correct. The computed flow is turbulent on the full cord-length. Thus the viscous drag and the maximum lift is over-predicted.
The error of the mistreatment of the transition increases, with the distance of the transition point and the leading edge. Thus the RANS computation coincides better when the Reynolds-number is increasing. Therfore we decided to use the measurements with the highest Reynolds-number for validation.

Grid

The extension of the computational domain is approx. 10 profile-length in all direction (Fig.2). This has been proposed by [7]. The Grid is block structured and has 110.000 cells (Fig.**??**). Nowadays larger grids are affordable, but we intended to test a couple of turbulence models, each with 8 angles, and therefore we tried to keep the computational effort moderate.

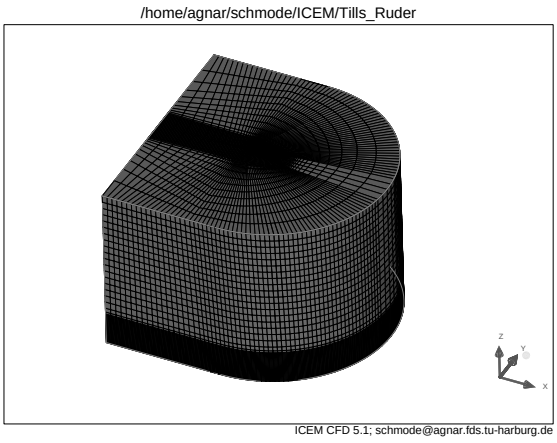

Figure 2: Computational domain used for rudder computation

Results

In Fig. 4 - 7 the results for different turbulence models are given. All turbulence models over-predict the drag, especially at 0^0. This effect can be seen in the work of other author (e.g. [7] and is expected du to the mistreatment of the transition.

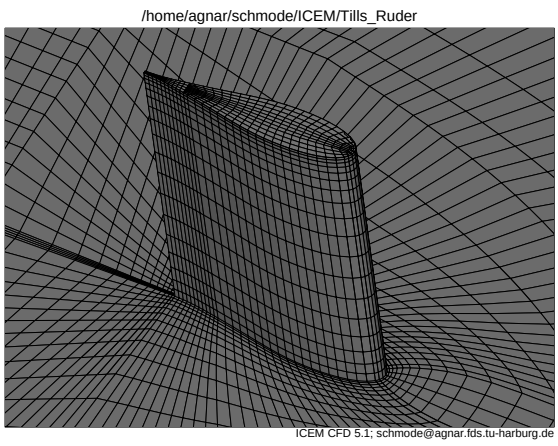

Figure 3: Computational grid used for rudder computation

The standard k-ϵ also over-predicts the lift and the maximum lift angle, while the RNG-k-ϵ model under predicts the lift while the maximum lift angle is predicted good. Both the standard and the SST k-ω model predict better lifts, but over estimate the drag. The difference between standard and SST k-ω model is marginal.
To evaluate the effect of the mistreatment of the transition, we carried out three further computations. Two were we suppressed the turbulence in the first 10% respectively 40% of the cord length, and one compleat laminar one. We implemented this suppression by setting the production term in the k-ϵ-model to zero in a geometrical defined region. This may be a crude approach, but it proofed to be effective and robust.
At the large angles, all three computations did not converge in steady state, but they converge in transient computations. This may be to the transient character of the flow, which could be observed in the experiments too. The forces were averaged over a suitable time.
The coefficients are given in Fig.8 - Fig.10. At large angles the maximum lifts are much smaller than in the standard k-ϵ computation. The effect is the stronger, the larger the laminar part is in the flow. The computation with suppressed transition up to 10% cord-length coincides best with the measurements.

7 Conclusion and Outlook

We have presented first computations with the new RANS-solver FreSCo, and compared them with wind-tunnel-measurements. Considering the small cell number of 110k and the known limitations of the ap-

plied turbulence models, the agreement is satisfying. Thus we judge this first steps towards validation as successful, but of cause a lot more work has to be done. Especially grid-studies an sensitivity studies have to be carried out.
The computations with suppressed transition show that validation of turbulence models with experiments with partly laminar flow maybe questionable. Fortunately ship-rudders operate at much higher Reynolds-number, thus RANS computations for full-scale rudders do not suffer from this effect.

References

[1] A. Cura Hochbaum (1994)
Ein Finite-Volumen-Verfahren zur Berechnung turbulenter Schiffsumstr"omungen
IFS-Report No. 540

[2] OULD A. MOHAMED EL MOCTAR (2001)
Numerische Berechnung von Stroemungskraeften beim Manoevrieren von Schiffen
IFS-Report No. 611

[3] J.H. FERZIGER, M. PERIC (1997)
Computational Methods for Fluid Dynamics
Springer

[4] C.M. Rhie and W.L. Chow (1983)
A numerical study of the turbulent flow past an isolated airfoil with trailing edge separation
AIAA J., 21, 1525-1532

[5] `http://www.cgns.org/`

[6] `http://www-unix.mcs.anl.gov/mpi/mpich/`

[7] `http://www-unix.mcs.anl.gov/petsc`

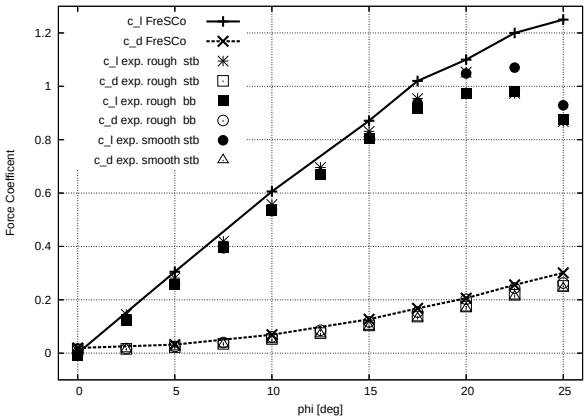

Figure 4: Lift and drag computed wirh k-ϵ model

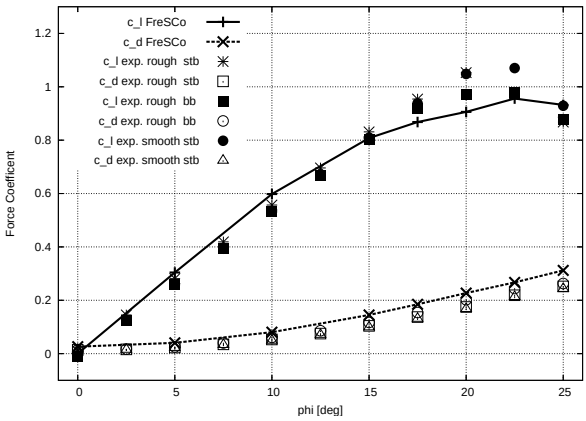

Figure 5: Lift and drag computed wirh RNG-k-ϵ-eps model

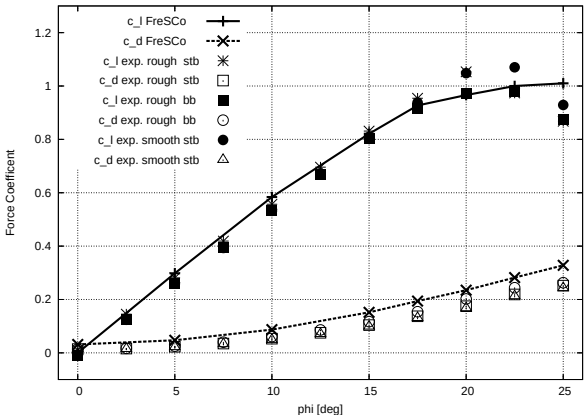

Figure 6: Lift and drag computed wirh k-ω model

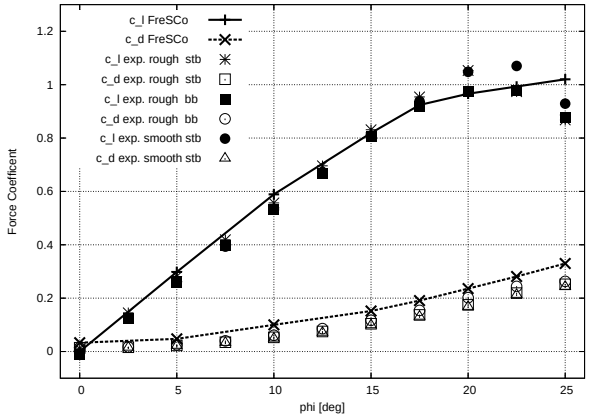

Figure 7: Lift and drag computed wirh SST-k-ω model

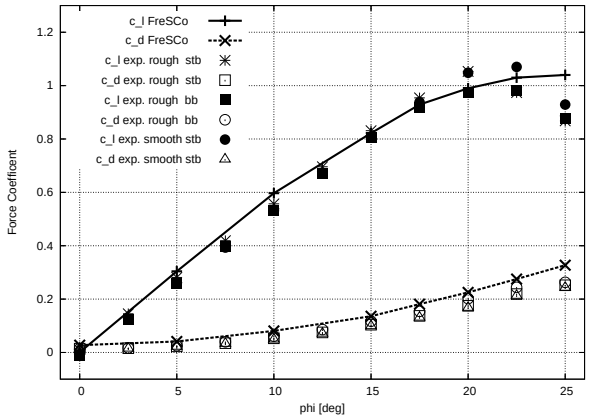

Figure 8: Lift and drag computed wirh k-ϵ model and suppressed transition at first 10% cord-lenghth

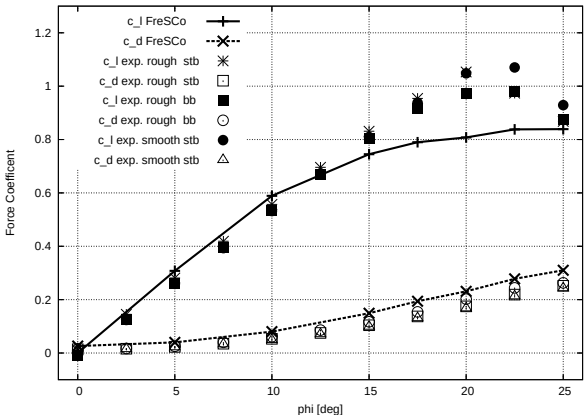

Figure 10: Lift and drag computed laminar

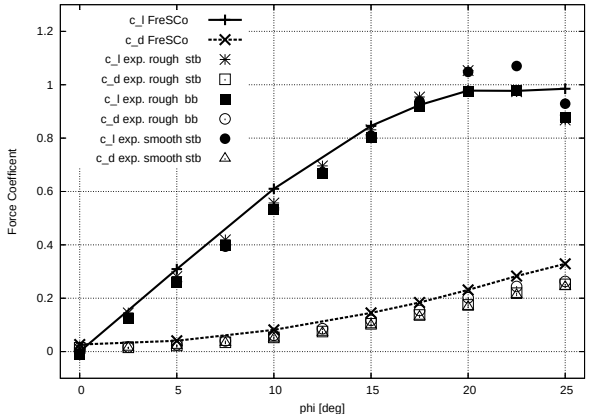

Figure 9: Lift and drag computed wirh k-ϵ model and suppressed transition at first 40% cord-lenghth

Calculation of Hydrodynamic coefficients of a Submerged body with Hull, Sail and Appendages and their length dependence.

M. Sohaib[1] (sohaibaziz@hotmail.com), M. Ayub[2] (mayubakhtar@yahoo.com), S.Bilal[3] (bukharibilal@hotmail.com)
S. Zahir[4] (s.zahir@ccsspak.org) and Mahmood A Khan[5] (rana_mahmood@hotmail.com)

CFD-Chapter, Computational, Modeling, Control & Simulation Society of Pakistan

Abstract

A comprehensive study has been made for the hydrodynamic analysis of the complete submarine DARPA 2, including hull, sail and appendages. The analysis was performed for the submarine hull, with sail on top and four stern appendages. Pressure distribution, forces and moments were calculated over the complete submarine. Comparison of Normal force and pitching moment of complete submarine having mid body length L, shows a reasonable agreement with the experimental results of DARPA 2. Further the study was extended to calculate the yawing moment and drag coefficient for length L. Comparison of Yawing moment at different drift angles shows quite a good agreement with experiment. Drag coefficient was calculated at different angles of attack. The analysis was also performed to study the effects of changing middle body length over the Forces and Moments. Pressure distribution, forces and moments were calculated over the complete submarine for different middle body lengths L-1, L and L+1 at different angle of attacks. The results revealed that by increasing the middle body length of submarine, the Normal force, pitching moment and drag coefficient increases and vice versa. Both quantitative and qualitative analysis of the complete submarine estimate the required design force and moment at different angle of attacks and also demonstrate the flow visualization

Introduction

Applications of computational fluid dynamics (CFD) to the maritime industry continue to grow as this advanced technology takes advantage of the increasing speed of computers. Numerical approaches have evolved to a level of accuracy, which allows them to be used during the design process to estimate the forces and moments acting on the body during steady and unsteady motion and to predict the maneuvering performance of the vehicle moving underwater provided that have been validated to a certain level. Significant progress has been made in predicting flow characteristics around a given ship or marine hull. The marine designers can use this information to improve the submarine and ship's design. Prediction of drag on a ship hull is always a challenging task for a naval architect. At the start of the design process, hull forms are developed given certain requirements. One of the major design tasks is to estimate the powering performance so that propulsion requirements can be determined. Early estimates of resistance and power are often based on simple empirical formulas derived from data for similar ships. As the design process proceeds, a more reliable approach becomes necessary to predict resistance; scale-model testing has been generally adopted for this purpose.

The accuracy of a prediction can be assessed by comparison with model-scale experimental results. The focus of the paper is to validate the CFD for the bodies moving underwater at some speed. In this paper the flow is assumed to be fully wetted as the speed is quiet low in order to avoid the cavitations.Flows over fully appended submarines offer significant challenges for Computational Fluid Dynamics. Our analysis is for submarine DARPA-2.

DARPA 2 consists of a submarine body with sail at zero angle of attack and yaw. The appendages are at right angle to each other.This paper presents the validation results of a CFD Code fluent 6.1 for DAPRA 2.

Geometry

The detail of the geometry is as follows.

DARPA 2 Model

Total Length, $L_t = 4.355$ m

Cylinder body Radius, R =0.2539884 m
Sail Height, h = 0.456 m
Exit Diameter, D (exit) = 0 .0075 m
Appendages height = 0.36 m
Middle body length,L = 1.96 m

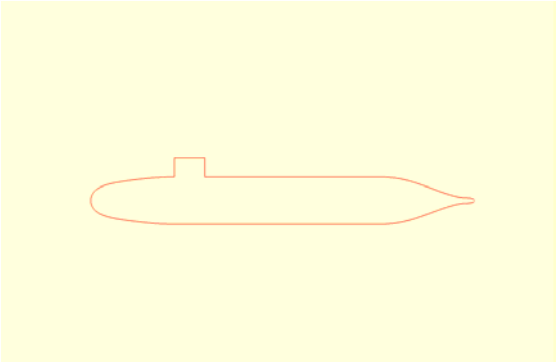

Fig.1 Sketch of Hull with Sail for length L(m)

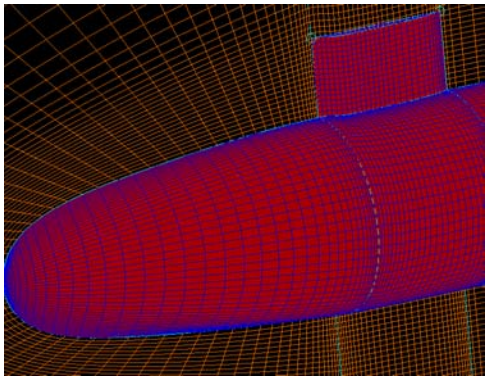

Fig.1 B Sketch of DARPA 2 Nose & Sail

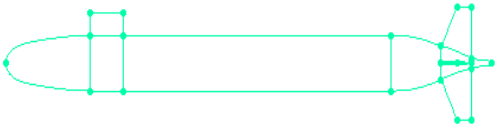

Fig.2 Sketch of DARPA-2 With length L+1 (m)

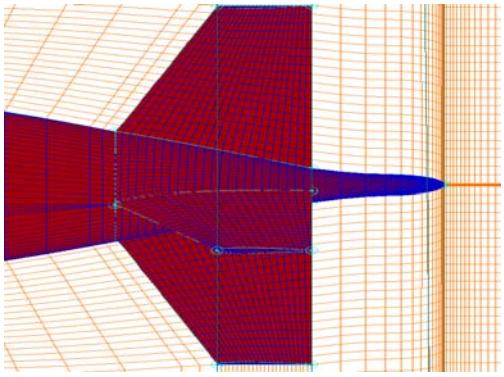

Fig.2a Sketch of DARPA 2 Appendages

Flow conditions

Flow conditions for the submarine DARPA 2 are as follows
Free stream velocity = 9 m/s
Reynolds number = 3.89E07,
Angle of attack = -20, -10, -4, 0, 4, 10, 20 deg
Pressure outlet = 201125 pa
Turbulence model = K-ε model
Depth in water = 10 m
Near wall treatment = Standard wall function
Upwind scheme = Second order upwind scheme

Grid Generation

For 3D simulation, structured grids were modeled for the hull, hull with sail, and appendages. Structured grid was modeled for the complete body configuration that includes hull, sail and appendages. Two different Grid Models were constructed for full body configuration having different number of blocks 10 & 14 respectively. First Grid modeled for the complete configurations of DARPA 2 consist of 10 blocks and by using different grid sizes grid independence was ensured. 3D Half Body was modeled to perform the analysis for the hull, hull with sail and for the complete configuration. Based on the grid independence study conducted the grid size 40 x 45 x 50 points, in the Block-1 containing the Nose section, the Block-2 consists of a sail on top of the model with the

grid size of 30 x 30 x 5 points, the Block-3 is over the sail to the far field of the size of 30 x 45 x 50 points, the Block-4 is over the cylindrical body portion having size 30 x 45 x 50 points, the Block-5 is between the cylinder body and appendages of the size of 20x45x50. Block-6 is between the appendages having points 20,20,18 and Block-7 is between the next two appendages having size 20,20,17.Block-8 is over the appendages to far field having size 20,26,50. Block-9 is at tail of the submarine of size 20,45,50. Block-10 is the last block over the wake of size 40,50,50 points. The grids used for this study were made by using PAKGRID . Grids are shown in Fig3 & Fig3a. below.

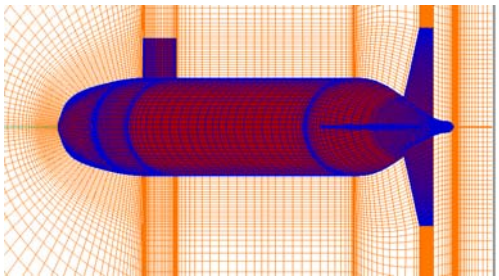

Fig.3 3D 10-Block Structured grid for DARPA2

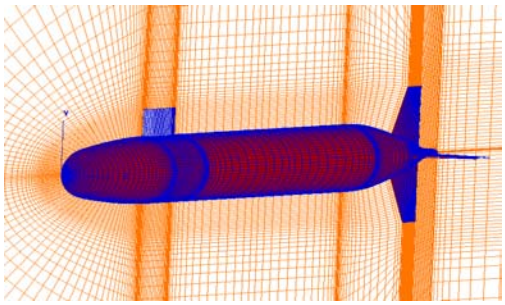

Fig.3a 3D 14-Block Structured grid for DARPA2

Second Grid Model for full body configuration was constructed using 14 –blocks and by using different grid sizes, grid independence was ensured.

Boundary Conditions

Velocity Inlet conditions were imposed on the far field domains, while the pressure outlet condition was imposed at the exit of the submarine assembly. At the submarine walls, no-slip adiabatic Wall condition was imposed. For the interfaces between the different blocks, the contiguous interface boundary condition was used. 3-Dimensional half-body plane was taken as symmetry plane condition and Axis condition was applied on the nose and tail centerline.

Results and Discussions

Emphasis has been given to the analysis of standard DARPA 2 using CFD Code Fluent. The DARPA2 was modeled with structured grid and the Fluent software was used to investigate the flow field qualitatively and quantitatively. The pressure coefficient results were compared for the DARPA 2 Configuration for the hull form and are found to be in good agreement with the predicted CFD results of Feflo solver [4]. The same were also compared with the experimental results and are found to be in a reasonable agreement. These results are shown in Fig. 4 for the two predicted CFD Codes and published CFD and experimental results. The comparison of tangential velocity with the experimental results of DARPA-2 is shown in Fig.5.While pressure contours for hull with sail are shown in Fig.6.

The study has been further extended to the hull with the sail on top and four stern appendages right angled to each other. Fig 7 shows the pressure distribution over the wall of the submarine; while Fig 8 depicts the XY-plot of static pressure over the wall of submarine. Also Figs 9 shows the pressure contours over the symmetry plane of DARPA 2.While Fig. 10 Shows the pressure contours for full body configuration of DARPA-2 at drift angle of 4 Degree. These Figures demonstrate the flow visualization across the full body configuration.

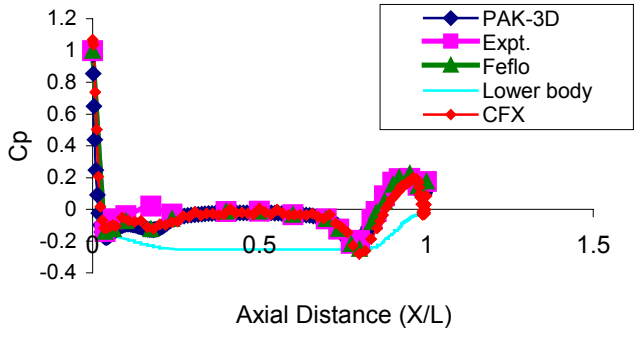

Fig.4 Comparison of Pressure Coefficients for DARPA-2

Comparison of Normal Force and Pitching Moment Coefficients shows a reasonable match with the experimental results of DARAPA-2 having middle body length L as shown in Fig.11.Plot indicates that the Normal force shows a reasonable agreement with the experiment. It matches fairly at low angels of attacks but it deviates slightly from experiment at high angles of attack. Fig. 12 shows the comparison of Pitching Moment Coefficient with the experiment at different angles of attack. The deviation is within 15 %.

Graph shows that Pitching Moment Coefficient matches fairly good at angles of attack between –10 to 10 degrees but it deviates from experiment beyond these angles. The study was finally extended to calculate the Normal force and Pitching moment coefficients for the varying lengths of submarine i.e L-1 & L+1.The pitching moment and Normal force coefficients increase by increasing length of the body and vice versa as shown in Fig.13 & 14.

Drag coefficient is also calculated for the varying lengths of the submarine at different angles of attacks as shown in Fig.15. Finally Yawing moment is calculated for the submarine having length L ,at different drift angles.The graph of yawing moment coefficient is shown in Fig.16.

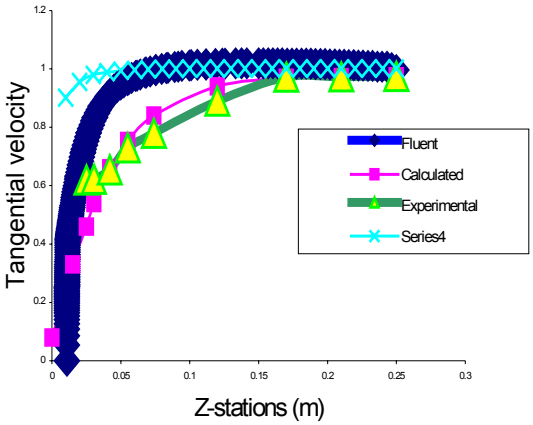

Fig.5 Comparison of tangential velocity distribution at x=0.433 , x=0

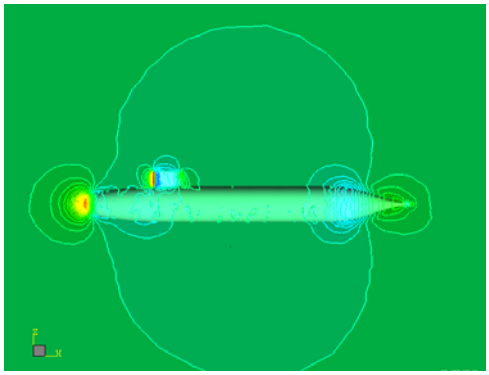

Fig.6 Pressure Contours for hull and Sail of DARPA2

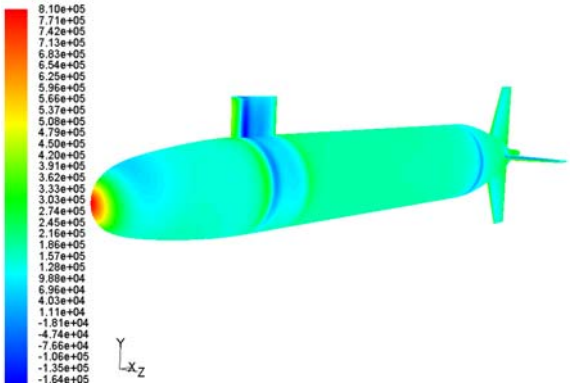

Fig.7 Pressure Contours Over the Submarine wall at angle of Attack = 4 Degree

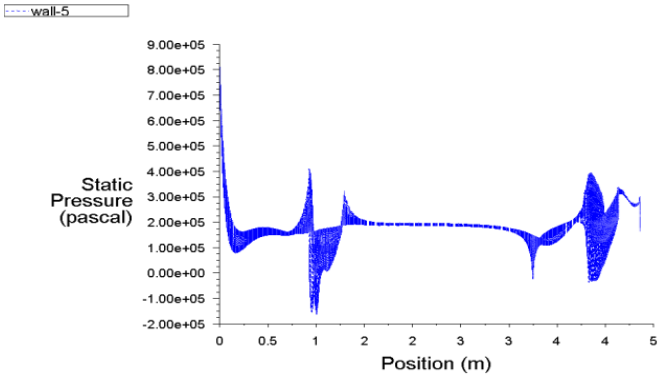

Fig.8 XY-Plot of Static Pressure Over Submarine DARPA 2 at Speed 9 m/s, Angle of Attack = 4 deg

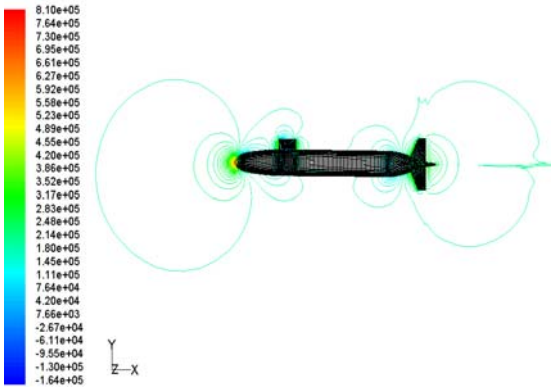

Fig.9 Pressure Contours Over the symmetry plane of Submarine DARPA 2 at Speed 9 m/s, Angle of Attack =4 deg

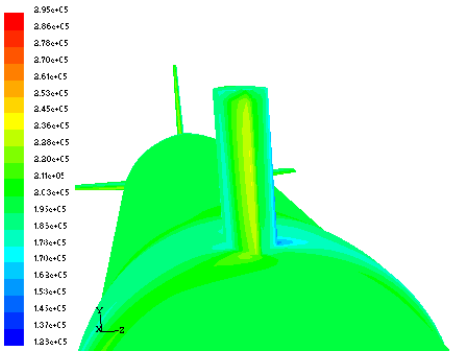

Fig.10 Pressure Contours over wall of Submarine DARPA 2 at Speed 9 m/s, Angle of Drift =4 deg

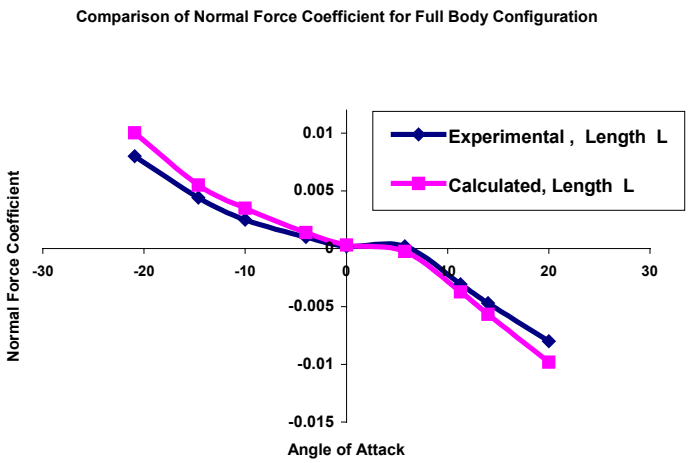

Fig.11 Comparison of Normal Force, Mid-body length L, Stern Appendages +Sail on Top

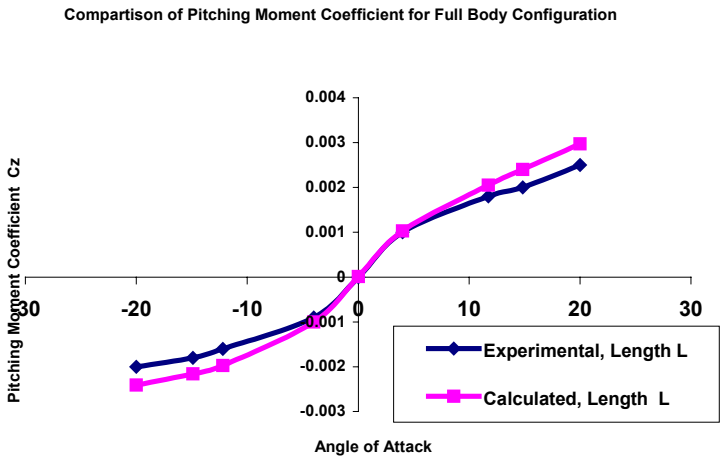

Fig.12 Comparison of pitching Moment, Mid-body Length L, Stern Appendages +Sail on Top

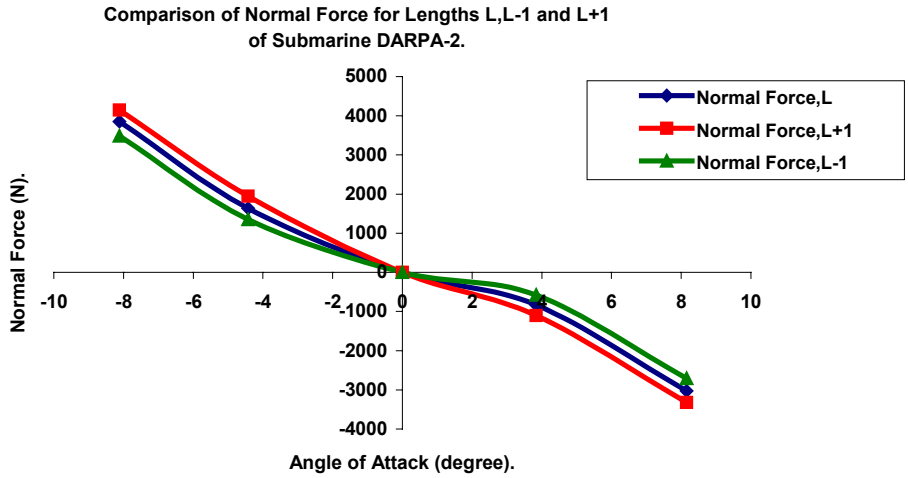

Fig.13 Comparison of Normal Force, for Mid-body length L, L-1 & L+1 of submarine DARAP-2.

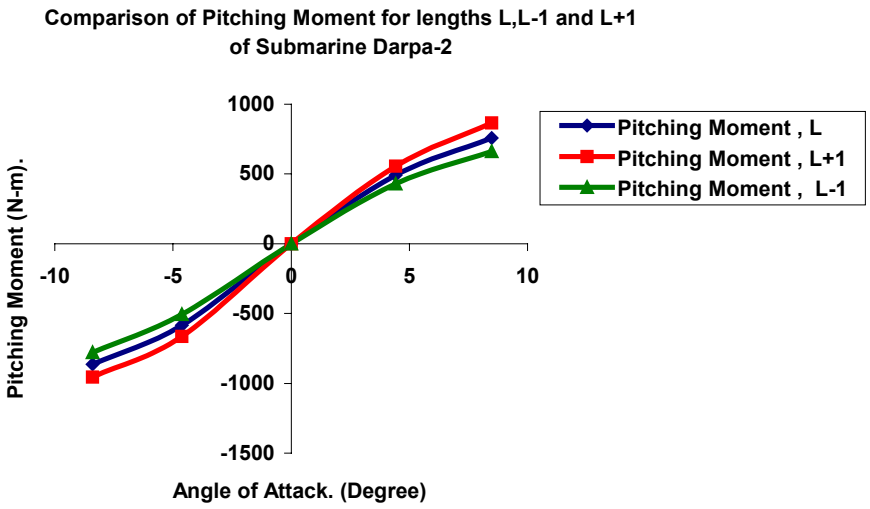

Fig.14 Comparison of Pitching Moment, Mid-body length L,L-1 & L+1 Stern Appendages +Sail on Top

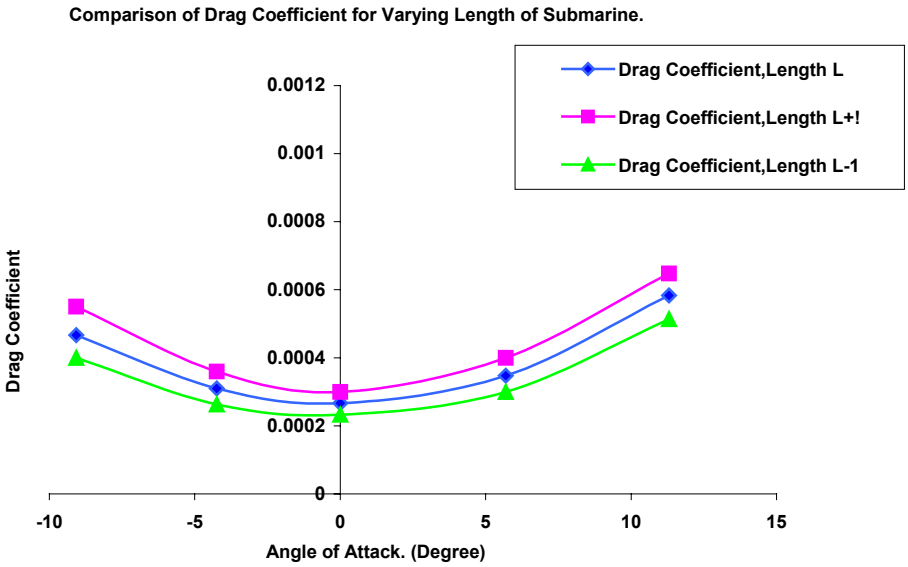

Fig.15 Comparison of Drag Coefficient, Mid-body length L-1, L and L+1, Stern Appendages +Sail on top

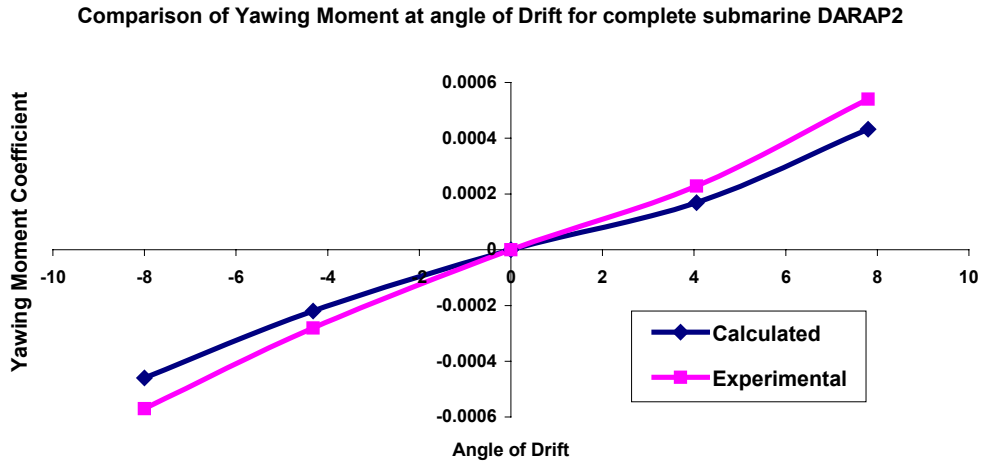

Fig.16 Comparison of Yawing Moment, Mid-body length L, Stern Appendages +Sail on top

Towards gradient-based shape optimisation using adjoint CFD

Arthur Stück, arthur.stueck@tu-harburg.de
Gerhard Jensen, g.jensen@tu-harburg.de
AB 3-13 Fluid Dynamics and Ship Theory, TU Hamburg-Harburg, Germany

1 Introduction

CFD methods are widely used in maritime industry to investigate the performance of given design configurations. In contrast, CFD-based automatic shape optimisation is rarely applied in practice, as the implementation of "real-life" optimisation problems can be a cumbersome task and computational costs often are prohibitive.

Gradient-based shape optimisation can be a very efficient approach, if the design space is sufficiently smooth. Then, it usually has performance advantages over gradient-free methods, e.g. when searching for local optima around a sound reference design.

Flow gradients, also referred to as sensitivities, may support a design process in different ways: Providing flow gradients beside "standard" CFD analysis can facilitate manual shape optimisation [12], or flow sensitivities can be taken into account in automatic optimisation. For practical shape design, interactive optimisation approaches can be a reasonable compromise. This means that user input, such as knowledge about the global cost function distribution or non implemented practical design constrains, is supplied during the optimisation process if necessary.

The performance of a design configuration is assessed by cost functions. Their gradients with respect to the design parameters indicate the direction of steepest slope of the cost function in a certain design point. In single criteria optimisation a gradient vector holds n derivatives of the cost function with respect to the shape parameters; in case of m cost functions the derivatives are allocated in the Jacobian matrix. A key factor to gradient-based shape optimisation is the efficient calculation of accurate flow sensitivities.

Finite differencing of the cost function is a simple approach for calculating flow sensitivities; it only requires a CFD software solving the state equations. In multiple parameter design this technique becomes prohibitively expensive, when the evaluation of the cost function is computationally costly. It is also prone to generate inaccurate gradients depending on the perturbation size.

Alternatively, there are different strategies to calculate flow sensitivities about a solution of the state equations analytically. According to perturbation theory, the state equations can be differentiated prior to the discretisation in a continuous approach – either in a direct or an adjoint way [5]. In the former way, computational costs for the calculation of the Jacobian scale with the number of parameters: In addition to one solution of the original state equations, the derived linearised state equations must be solved once per parameter. The computational work is independent of the number of cost functions. In the latter way, computational costs roughly scale with the number of cost functions: An arbitrary number of derivatives per cost function can be evaluated by a single adjoint solve, in addition to one solution of the original state equations. This is realised introducing Lagrange multipliers defined by the linear adjoint state equations.

In a so-called discrete approach the state equations are differentiated after discretisation, either directly or in an adjoint manner. Recent work is published in [7, 8]. Due to identical discretisation in the primal code (solving the state equations) and the sensitivity code, consistency between the results is ensured.

Manual construction and maintenance of sensitivity code (continuous or discrete) can be a tedious and error prone task. Alternatively, sensitivity code can be generated by automatic differentiation (AD), i.e. by automatic source-to-source precompilation of an existing input code [1, 4]. Depending on the AD precompiler this is possible in direct (referred to as forward) or adjoint (reverse) mode. As the sensitivity code is derived from the primal input code, AD can be classified as a discrete approach. According to Laporte and Le Tallec [6], a combination of hand-coding and AD is an efficient approach to generate complex adjoint solvers.

This paper addresses the calculation of flow sensitivities using AD in forward and reverse mode. In a feasibility study the incompressible steady RANS equations are used as state equations to calculate the cost functions and its gradients. Different cost functions are considered and the state equations are derived with respect to local shape perturbations superimposed on a NACA0025 foil section. To avoid a

crude and too constrictive shape parametrisation, a huge set of design parameters is necessary – especially when it comes to 3D shape optimisation. For most practical optimisation problems the number of design parameters clearly exceeds the number of cost functions: In this case, efficient sensitivity computation should be carried out in adjoint mode.

2 Basics on automatic differentiation

AD precompilation generates a derivative code directly from an existing input code: The model code (state equation solver, here a RANSE solver) is decomposed into a sequence of elementary functions, corresponding to the individual code statements. These elementary functions are differentiated by simple calculus [3]. According to the chain rule, the product of all the elementary function derivatives yields the derivative of the composite model function.

Computational costs strongly depend on the order of execution. In forward (direct) mode the product of the elementary function derivatives is calculated in the order in which the statements are carried out in the model code. Then, computational resources are roughly proportional to the number of independent variables.

In reverse (adjoint) mode, the product of the adjoint elementary function derivatives is calculated in the opposite order. Computational costs are roughly independent of the number of design parameters then, increasing with the number of cost functions.

AD precompilers are usually tied to a specific programming language. Depending on the AD software, certain code constructions should be avoided or replaced in the input code. The performance of the derived sensitivity code depends on the input code [1]. Sensitivity code generated by TAF [2] is easily readable, allowing manual code tuning and modification.

3 Computational method

Sensitivity flow solvers are generated by the AD software TAF. The RANSE solver CAFFA [10], written in Fortran 77, is used as input code. It is a 2D incompressible SIMPLE-based RANSE solver, using k-ϵ turbulence modelling and wall functions. It is based on a finite volume discretisation on collocated structured grids. Investigations are restricted to steady flow. The results presented here are calculated in forward mode. Development and validation of an adjoint solver is underway.

The cost functions are derived with respect to the independent design parameters which are defined as shape perturbations normal to a NACA0025 section (see Figure 1). The surrounding boundary nodes

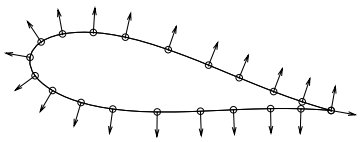

Figure 1: Normal vectors in the design points, each carrying an offset defined by a design parameter. Two design parameters are located at the trailing edge – tangential and normal to the chord.

on the foil contour are connected to the design parameters according to a cubic spline function superimposed on the original shape (Figure 2). Zero-

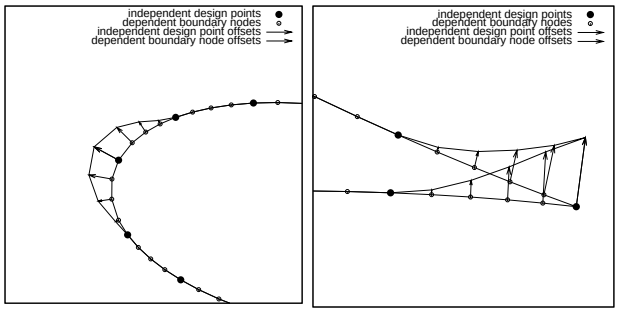

Figure 2: Parametrised shape perturbation around the leading edge (left) and the trailing edge (right) of a NACA0025 section. The boundary nodes are displaced normal to the section curve according to a local offset function.

gradients are declared for the spline functions in the design points and the curvature is noncontinuous there. Then, the perturbations have a local character avoiding overshoots which cubic splines of a continuous curvature would cause.

Assuming the interior grid to be independent of the shape perturbations, i.e. only adapting the boundary nodes to the perturbations, is a straight-forward approach; only the adjacent cell layer is affected by the boundary perturbations, keeping the interior grid fixed. Then, the computed sensitivities contain a contribution originating from the sensitivity of the approximation error (due to a local variation of the grid quality). These gradients indicate the direction of steepest slope of the sum "intended cost function + approximation error". They may be dominated by the gradient of the approximation error with respect to sensitive near-wall grid parameters, such as the non-dimensional wall distance y^+ in case of wall function modelling.

To overcome these difficulties, the inner grid is connected to the shape perturbations by an explicit grid

deformation scheme: Approximate Green functions are used to calculate each nodal displacement based on the distance between the considered node and the boundary perturbation [6]. Figure 3 shows a grid deformation caused by shape modification superimposed on a NACA0025 section.

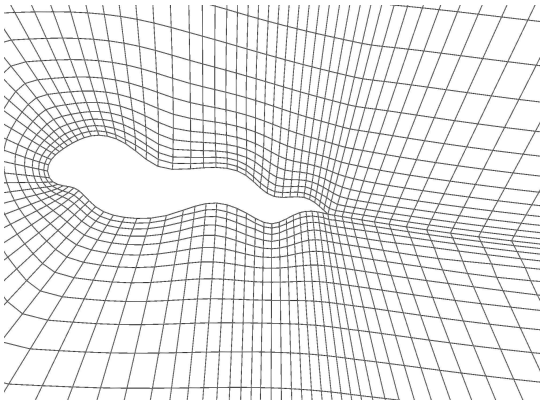

Figure 3: Grid deformation by explicit Green-functions. The NACA0025 section has been modified by superimposing a cubic spline on the original foil contour. The algorithm proved to be robust and capable of substantial grid deformations.

4 Flow case and first results

A NACA0025 foil section is investigated in incompressible flow, at $Re = 1000$ in laminar flow and at $Re = 10^6$ using k-ϵ turbulence modelling and wall functions. It operates in free stream at $\alpha = 10°$ angle of incidence. The computational grid for the laminar case is shown in Figure 4. Different cost functions have been declared to evaluate the usability of the computed sensitivities for practical shape design (Figures 5 to 8, $Re = 1000$ (left) and $Re = 10^6$ (right)). The flow sensitivities are analytical derivatives of the cost function with respect to infinitesimal shape perturbations. The gradients have been validated against divided differences based on the results of the primal CFD solver.

The lift (Figure 5) shows very high sensitivities with respect to trailing edge (TE) perturbations: Accordingly, a slight increase in camber along the rear foil yields a significant lift increment. Sensitivities are pointing outwards along most of the suction side, along the pressure side they are directed inwards.

Negative drag gradients are plotted in Figure 6. Bending the TE upwards will decrease the drag. Slenderising the leading suction side and turning the nose downwards into the direction of the incoming flow should also reduce the resistance.

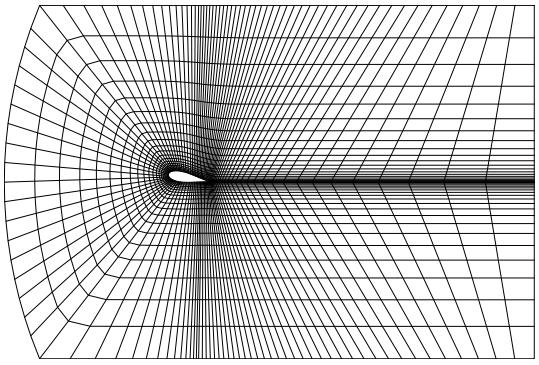

Figure 4: Structured C-grid around a NACA0025 section at $Re = 1000$ and $\alpha = 10°$ angle of incidence. The grid has approx. 3200 cells.

Glide ratio (or lift/drag ratio) sensitivities are displayed in Figure 7. Increasing the camber along the rear foil will improve the glide ratio; the nose should be slenderised and turned downwards.

Towards inverse design, the difference between a target pressure distribution (Figure 8, dashed lines) and the pressure distribution around the original NACA0025 section (continuous line) is declared as cost function; the pressure differences in the corresponding boundary grid nodes i are added up along the foil contour

$$F_{cost} = -\sum_i |c_p^{\mathrm{trg}}(i) - c_p^{\mathrm{org}}(i)|.$$

The cost function is derived with respect to the design parameters. The major gradients can be observed along the forward suction side and around the TE of the foil section. The inward directed strong gradients on the upper nose correspond to the pointed suction peak of the NACA0025 section. Levelling off the upper nose will minimise the pressure differences. Bending the TE downwards will accelerate the flow on the suction side of the NACA0025 and reduce the pressure differences.

Generally, the sensitivities predicted for the laminar case are smoother than those in the turbulent case. Some sensible "global" shape deformations can hardly be guessed directly from the calculated gradients, such as shown in Figure 8: The shape differences between the NACA0025 and the reference foil are maximum at about half chord-length, but the corresponding shape sensitivities remain small as the flow is rather nonsensitive in that area. However, using iterative optimisation algorithms the TE will probably be turned downwards in the early iterations and the resulting hump on the rear suction side might be smoothed in the subsequent steps.

5 Conclusions

As indicated by this feasibility study, AD is a suitable tool for deriving CFD sensitivity code efficiently. A RANSE solver has been differentiated in forward mode and the results have been validated against finite differences of the results of the primal solver. An adjoint version of the code is currently being developed.

In adjoint mode, computational costs are almost independent of the number of parameters. That makes it highly attractive for 3D cases, allowing for a fine shape parametrisation.

In the subsequent step, the method has to be integrated within an optimisation environment. Gradient-based shape optimisation is restricted to local optimisation and the success will strongly depend on the nature of the cost function. However, providing user directives interactively it may be an efficient design approach to support practical shape design.

References

[1] P. Cusdin and J.-D. Müller, *Generating efficient code with automatic differentiation*, European Congress on Computational Methods in Applied Sciences and Engineering (ECCOMAS), 2004

[2] FastOpt, *Transformation of Algorithms in Fortran (TAF)*, http://www.fastopt.de

[3] R. Giering and T. Kaminski, *Recipes for Adjoint Code Construction*, Technical Report 212, Max-Planck-Institut für Meteorologie, 1996 http://www.fastopt.com

[4] R. Giering, T. Kaminski and T. Slawig, *Generating efficient derivative code with TAF: Adjoint and tangent linear Euler flow around an airfoil*, Preprint submitted to Elsevier Science, April 2004 http://www.fastopt.com

[5] A. Jameson, *Aerodynamic Design via Control Theory*, Journal of Scientific Computing, Vol. 3, 1988

[6] E. Laporte and P. Le Tallec, *Numerical Methods in Sensitivity Analysis and Shape Optimisation*, Birkhäuser 2003

[7] A. Le Moigne, *A discrete Navier-Stokes adjoint method for aerodynamic optimisation of Blended Wing-Body configurations*, Ph.D. Dissertation, Cranfield University, December 2002

[8] S.K. Nadarajah, *The discrete adjoint approach to aerodynamic shape optimization*, Ph.D. Dissertation, Stanford University, January 2003

[9] J.C. Newman, A.C. Taylor, R.W. Barnwell, P.A. Newman and G.J.-W. Hou, *Overview of Sensitivity Analysis and Shape Optimization for Complex Aerodynamic Configurations*, Journal of Aircraft, Vol. 36, No. 1, January-February 1999

[10] M. Peric, *Computer Aided Fluid Flow Analysis (CAFFA Ver. 1.2)*, Institut für Schiffbau der Universität Hamburg, October 1996, ftp://ftp.springer.de/pub/technik/peric

[11] J.J. Reuther, A. Jameson, J.J. Alonso, M.J. Rimlinger and D. Saunders, *Constrained Multipoint Aerodynamic Shape Optimization Using an Adjoint Formulation and Parallel Computers, Part 1 and 2*, Journal of Aircraft, Vol. 36, No. 1, January-February 1999

[12] H. Söding, *Resistance Decrease by Computer-Aided Hull Shape Improvements*, 2nd High-Performance Marine Vehicles Conference (HIPER), 2001

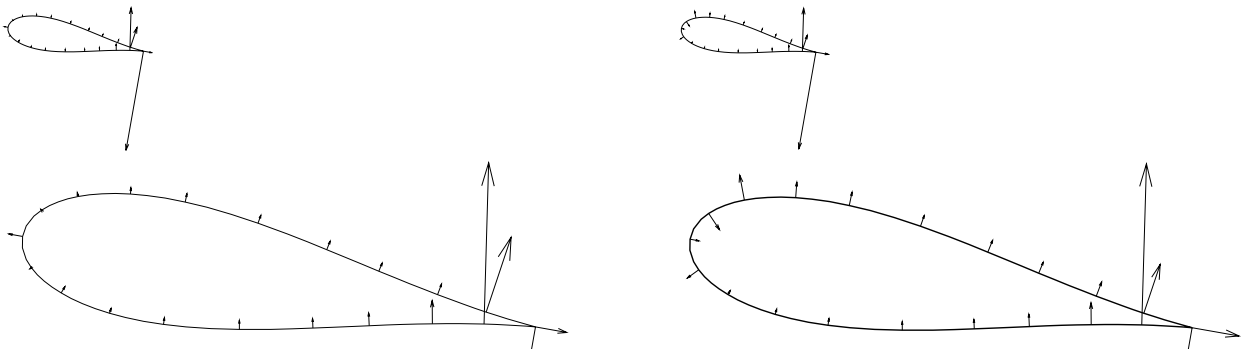

Figure 5: Lift sensitivities with respect to the shape perturbations for a NACA0025 at $\alpha = 10^\circ$ angle of incidence. Laminar at $Re = 1000$ (left); $Re = 10^6$ using k-ϵ turbulence modelling and wall functions (right). The small scale plots on top show the whole scope of the gradients.

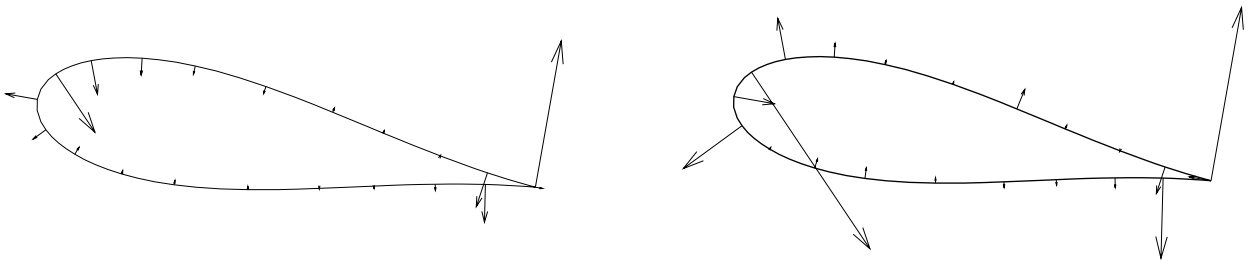

Figure 6: Negative drag sensitivities with respect to the shape perturbations for a NACA0025 at $\alpha = 10^\circ$ angle of incidence. Laminar at $Re = 1000$ (left); $Re = 10^6$ using k-ϵ turbulence modelling and wall functions (right).

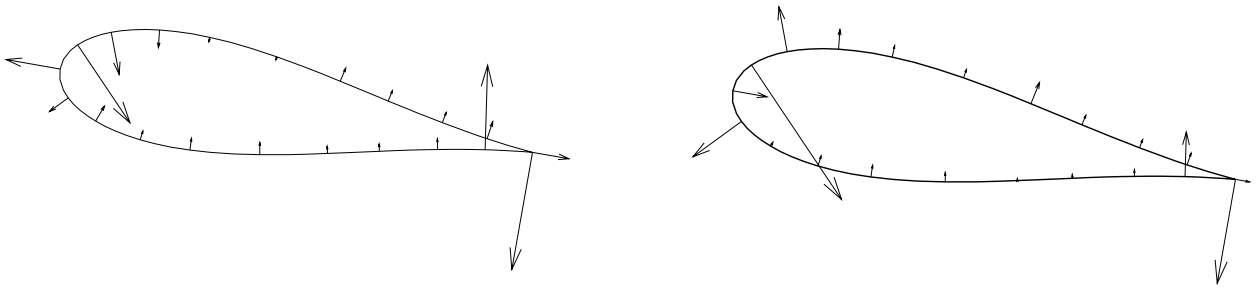

Figure 7: Glide ratio sensitivities with respect to the shape perturbations for a NACA0025 at $\alpha = 10^\circ$ angle of incidence. Laminar at $Re = 1000$ (left); $Re = 10^6$ using k-ϵ turbulence modelling and wall functions (right).

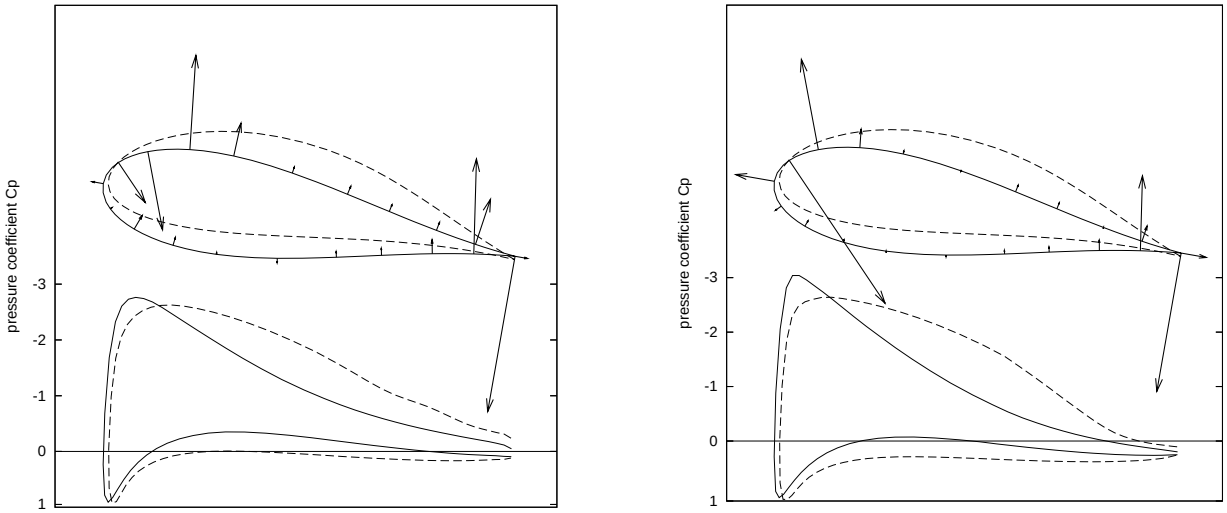

Figure 8: Towards "inverse design": The difference between a target pressure distribution (dashed lines) and the pressure distribution around the original NACA0025 section (continuous line) is declared as cost function. The target foil has been generated by superimposing a cubic spline on the original NACA0025 contour. The original grid has been adapted by the described algorithm. The pressure differences in the corresponding boundary grid nodes i of the target foil and the original foil are added up along the foil contour: $F_{cost} = -\sum_i |c_p^{\mathrm{trg}}(i) - c_p^{\mathrm{org}}(i)|$. This cost function is derived with respect to the shape perturbations. The sensitivities then indicate how to manipulate the NACA0025 section to obtain the target pressure distribution. The section operates at $\alpha = 10^\circ$ angle of incidence, $Re = 1000$ in laminar flow (left); $Re = 10^6$ using k-ϵ turbulence modelling and wall functions (right).

Computation of Bowthrusters with RANS-Solver FreSCo

Martin Thomas, mlrthomas@web.de
Daniel Schmode, d.schmode@tu-harburg.de
AB 3-13 of TU Hamburg-Harburg,Schwarzenbergstraße 95, 21073 Hamburg

1 Introduction

The maximum crossforce, which can be generated by a latteral thruster is dependant on multiple parameters. As design parameters there are the geometry of the ships hull and the thruster tunnel as well as the thruster arrangement within the tunnel. Besides the design parameters there are the operational parameters such as the relative velocity between the ship and the water or the narrowing of the waterway, e.g. due to harbour manoeuvering. Investigating the interactions between the design- and the operational parameters by means of Rans-Computations, the understanding of the underlying physical effects could be improved.

To carry out comparative studys, numerous calculations have to be carried out. Therfore a bodyforce approach was choosen to model the thruster propeller, thus limiting the necessary CPU and memory requirements. An important question is how suitable this approach is for modeling the different effects. As a first step we will investigate the influence of different tunnel geometries on the performance of a bowthruster at zero ship speed in this work.

2 Hydrodynamic effects

The jet reaction force T created by the acceleration of water in a thruster is

$$T = \dot{m}\, v_j' \,, \tag{1}$$

where $\dot{m}$ is the massflux through the thruster tunnel and $v_j{}'$ is the nominal jet velocity [3]. T can be measured at the propeller shaft of the thruster. Besides this force there are the pressure force F_p and friction force F_f acting on the ships hull due to the thruster operation. The resulting crossforce F_c on the ship caused by the thruster is then:

$$F_c = T + F_p + F_f. \tag{2}$$

While the friction force is orders of magnitude smaller than the jet reaction force, the pressure force can be sicnificant.

At the inlet of the thruster tunnel the flow is accelerated, resulting in a low pressure region. This low pressure causes a force on the hull, directed in the same direction than the jet reaction force and is thus favourable [3]. The design of the inlet has a significant influence on this force. A smooth shaped inlet for example will result in low pressure losses at the inlet and thus yield relatively high velocitys and corresponding low pressure fields. A sharp edged inlet will cause seperation at the inlet, impeding high water velocitys at the ships hull and thus generating only a relatively small force (figure 1).

At the outlet the jet extends, generating vortices which cause dissipation of energy [3]. This extension is also influenced by the shape of the outlet as indicated in figure 1.

Another effect of the sharp edged inlet and the resulting flow seperation is a inhomogenious wakefield within the tunnel which will decrease the propeller efficiency.

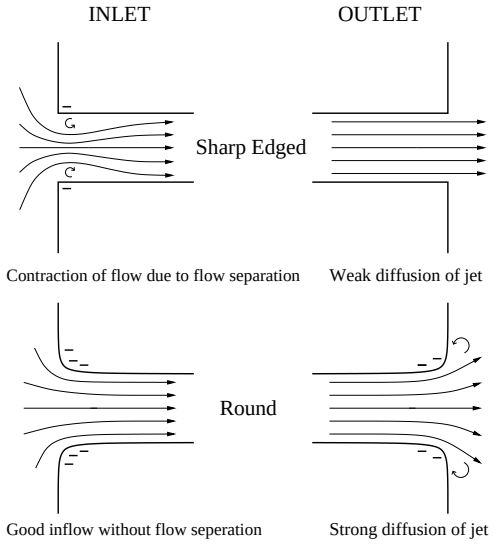

Figure 1: Hydrodynamic effects

3 Geometries

The shape of the shipbow is simplified by a cylindrical body with a crossection as shown in figure 2.

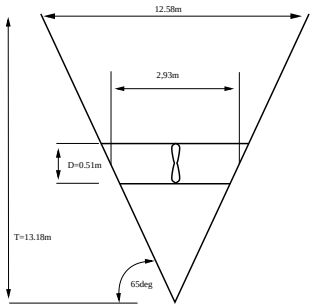

Figure 2: Schematic crosssection

We compared three different shapes of the tunnel ends as shown in figure 3.

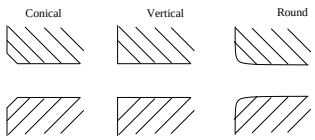

Figure 3: Used geometries

4 Numerical Method

Computations have been carried out with the Rans-Solver FreSCo, developed at TUHH and HSVA. The method is described in [1]. The propeller is modeled using bodyforces which are kept constant over the radius and only have a component parallel to the tunnel.

Neglecting free surface effects, the water surface was modeled using a symmetric boundary condition (BC). At the ships hull, including the tunnel, a wall BC has been applied.

The k-epsilon turbulence model has been used. This model is not suitible for the modeling of free jet turbulence so that we have to take into account an error which mainly influences the dissipation of the jet energy at the outlet.

The domain extends six times the ships width to the inlet side, 13 times to the outlet side and ten times the ships draft downwards. 150000 cells were used for the grid.

The calculations were carried out transient using large timesteps untill steady state was reached. Thus the time resolution was not meant to describe the transient development of the flow and only the results from the steady state are meaningfull.

5 Results

For all calculations the bodyforce BF was prescribed, ranging from $1kN$ to $30kN$. The bodyforce represents the jet reaction force T. The power is calculated using the bodyforce BF_i applied to the cell i and the velocity (in the direction of the bodyforce) v_i:

$$P = \sum_i bf_i \, v_i. \tag{3}$$

As expected, the rounded shape results in the highest average velocity within the tunnel, followed by the conical shape (figure 4).

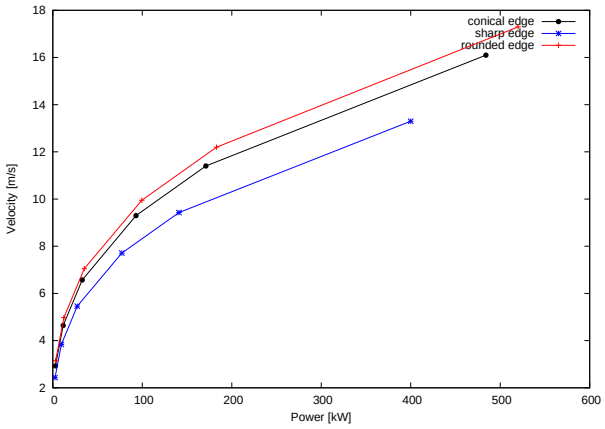

Figure 4: Average velocity within the tunnel

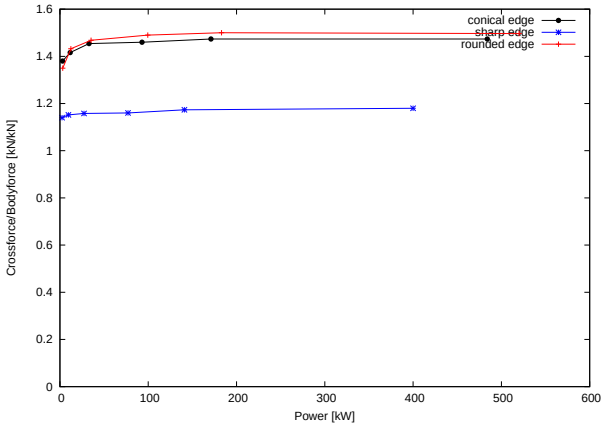

Figure 5: Ratio of crossforce and applied bodyforce

Concidering the ratio of the crossforce F_c and the applied bodyforce BF, the round shape seems to perform best, causing a crossforce up to 1.5 times the applied bodyforce. The conical shape causes up to 1.47 BF and the sharp edged reaches 1.17 BF (figure 5).

For the manoeuvering of the ship only the crossforce F_c is of importance which is shown in figure 6. Here the conical shape yields the highest crossforce, closely followed by the round shape. The difference in the crossforce between the sharp edged geometry and the other two is also not as significant as figure 5 might suggest. This is due to the fact that the geometries which yield a small ratio F_c/BF also yield smaller velocitys. At the same power level a smaller velocity implies a bigger Bodyforce, which compensates the small ratio F_c/BF when considering the crossforce.

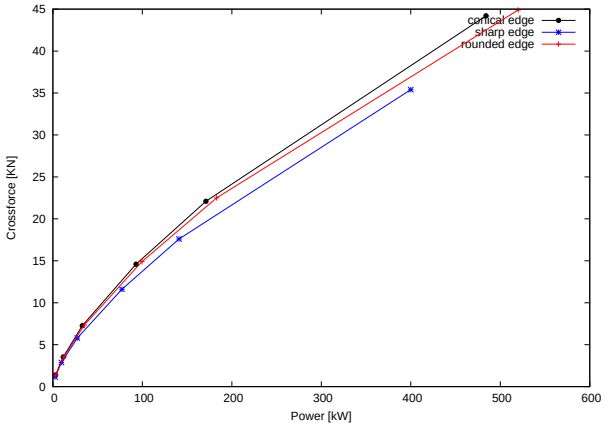

Figure 6: Crossforce on the ship

Taking a look at the wakefield in the propeller plane of the thruster, the round shape has a considerably more homogenious distribution than the conical shape. Due to the strong flow separation caused at the inlet of the sharp edged geometiy, the wakefield turns out to be very inhomogenious.

6 Conclusion

The results presented above give an interesting insight on the different effects causing the crossforce on the ship. But they have to be interpreted carefully since other effects, such as the interaction between the flow and the propeller are not modelled.

In the above diagrams the power is the power used to accalerate the water. In reality the power that is applied to the thruster engine is of importance and therefore the propeller efficiency has to be considered. Taking into account that the propeller efficiency will increase with the homogenity of the wakefield, the round shape might provide a higher crossforce compared to the conical shape. The sharp edged shape on the other hand will perform worse in the comparrison of the crossforces.

The results show that even if the calculated crossforces do not differ significantly, the composition of the crossforce does. The applied bodyforce is equivalent to an applied pressure difference. Figures 5 and 6 show that the sharp edged geometry needs a much bigger bodyforce to reach the same crossforce than the other geometries, thus building up a higher pressure difference. In reality this will result in a higher pressure load on the propeller blades.

References

[1] D. SCHMODE (2005)
First Results with the new RANS-Solver FreSCo
NuTTS 05

[2] J.H. FERZIGER, M. PERIC (1997)
Computational Methods for Fluid Dynamics
Springer

[3] BRIX, JOACHIM E. [Editor] (1993)
Manoeuvring technical manual
Seehafen-Verlag

Wind tunnel test of a winglet keel and how it can be used for CFD validation

Sofia Werner[1], Lars Larsson[1], Björn Regntröm[2]

[1]Chalmers University of Technology, Sweden, sw@na.chalmers.se
[2]Flowtech International AB, Sweden

1 Introduction

Validation data from experiments are invaluable tools for improving CFD methods, as well as for judging the ability of different methods for a given type of application. The goal of our work is to produce a public validation test case of a sailing yacht keel with bulb and winglets, as the ones used on the America's Cup yachts. This is a very specific case, as not many other types of marine vessels use that appendage configuration. In spite of that, we believe that this case can be of general interest. The complex vortex system in the keel wake presents an interesting challenge to advanced tools such as RANS and LES codes. At the same time, the case is simple enough to allow cheaper methods such as panel codes to be able to predict forces and trends.
The current paper describes the results from a wind tunnel test of an America's Cup keel model, where the flow details of the wake as well as the over-all forces are measured. A first test session with the same model has been performed earlier and was reported in [1]. In this second session the measurements have been extended to also include force measurement, more geometrical variations and improved intrumentation. These experiments will be followed by CFD work, where different kinds of numerical methods will be validated against the test results. The aim of this paper is to give some examples of how the experimental results can be used for CFD validation.

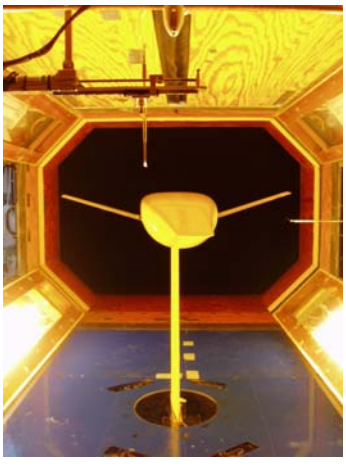

Figure 1: Wind tunnel set-up.

2 Test model and set-up

The test model is a 1:4 model of an America's Cup yacht keel with a bulb and two winglets, as shown in Figure 1. The complete geometrical description can be provided by the first author on request. The fin is a Naca 0012 wing of aspect ratio 2.4 with a trim tab at 75% of the chord. The bulb has a flat bottom and a beave tail tip. The winglets are Naca 0012 wings with a mean chord of 77 mm and a taper ratio of 0.7. The dihedral angle is 18 degrees, which leaves the winglet tips on the same vertical position as the lowest point of the bulb. The span, 3 m full scale, is quite short in order to reduce the blockage. This is compensated by a larger winglet chord length which results in small aspect ration winglets (2.5) and unrealistically bad efficiency of the winglets themselves, but on the other hand they will create a decent level of lift and produce large effects to study.
The winglets can rotate $\pm 2°$ around their span

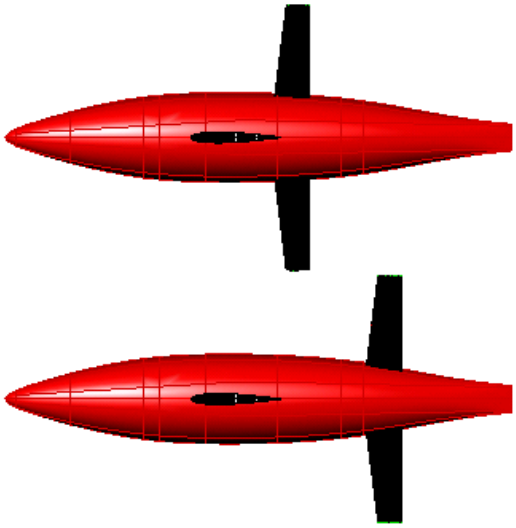

Figure 2: Winglets fitted at the two longitudinal positions.

wise axis (i.e. variable pitch) and they can be fitted to the bulb at two different longitudinal positions, one just behind the trailing edge of the fin and one further aft, as shown in Figure 2. At the aft position, the vortex on the bulb is stronger due to the reduced diameter of the bulb, so the effect of the winglets could be more

pronounced here. On the other hand, with a smaller bulb diameter the geometrical span of the winglets will be smaller for the same wetted surface, compared to the forward position. It is not obvious which one of those two positions is the most advantageous one.
The intention was to make the test resemble the full scale case as much as possible. However, in some aspects it was necessary to compromise between good testing premises and a realistic set-up. To ensure a sufficient clearance to the wind tunnel walls, no heel angle could be applied. Moreover, because of the difficulties to accurately set the model trim tab, it was decided not to deflect the trim tab at all.
By testing at zero heel and zero trim tab angle, the test case deviates from the realistic situation. However, this will not decrease its value as a validation test. The missing trim tab can be somewhat compensated by testing at 4° of yaw angle, which is larger than what is typical for upwind sailing. Obviously, this will affect the profile drag, but here the main interest is the lift-induced tip vortex from the fin. Hence, it is more interesting to have a realistic lift force than a realistic profile drag.
The maximum speed in the wind tunnel with a model of this size is 39 m/s, which give a Reynolds numbers (Re) that is 1/7.5 of the full scale Re. To compensate for this a zig-zag shaped tape was used to trig transition at 10% of the chord length for the winglets, 25% for the fin and and the bulb.
The wind tunnel is situated at the Department of Thermo and Fluid Mechanics, Chalmers. The tunnel has a closed, atmospheric pressure test section of 1.8 m x 1.25 m x 2.7 m. The free stream turbulence intensity is 0.3%.

3 Experimental method

Forces. Lift, drag and lift moment were registered with force gauges under the wind tunnel floor. The model was attached straight to the gauges through a slot in the floor.
For each run the forces were measured at four velocities ranging from 35 m/s to 39 m/s so that they could be corrected for the small variations of the inlet dynamic pressure. This procedure is necessary since the dependency of C_L and C_D with Reynolds number is large enough to disturb the trends if only one velocity would be used (and assuming constant force coefficients).
For each velocity 5x600 samples were taken with a sampling frequency 100 Hz and 1 seconds between the five groupes.

Wake survey. The velocity and pressure in the wake were measured using a 5-hole pressure probe in a plane perpendicular to the free stream at a distance of 323 mm behind the bulb.

Winglet position	Winglet pitch	Forces	Wake survey	Hot wire
Forward	$-2°$	x	x	
Forward	$-1°$	x		
Forward	$0°$	x	x	
Forward	$1°$	x		
Forward	$1.5°$	x		
Forward	$2°$	x	x	
Aft	$-1°$	x		
Aft	$0°$	x		
Aft	$1°$	x		
Aft	$1.5°$	x		
Aft	$2°$	x		
No wings		x	x	x

Table 1: Summary of test configurations.

For each configuration, around 3400 points in the wake were measured. In each point 5000 samples were taken with a sampling frequency of 1kHz. The probe was moved automatically between the measuring points. The points are separated by 2.5 mm in the vertical and 2.5 mm in the horizontal direction in the vortex wakes. In the wake of the fin and the winglets between the main vortices measurements are taken at every 20 mm in the span wise direction and 2 mm in the profile thickness direction.

Hot-wire. In order to study the turbulence intensity in the wake, the fluctuating velocity was measured with a hot-wire. The probe was of single-wire type and it was directed horizontally and perpendicular to the free stream. Around 1300 points we measured with a sampling frequency of 1000 Hz and sampling time 1 s. Only one configuration was tested, namely the bulb with no winglets.
Table 1 summarises the different configurations that were tested with the various methods.

4 Results for validation

Trend validation of total forces. Users of CFD codes for engineering purposes may be interested in validating their codes, may it be RANS or potential methods, against force values or force trends. While the absolute values of the forces might be difficult to predict accurately, it is sometimes sufficient to verify that the code is able to correctly predict the ranking of similar design configurations.
The trends of the lift and the drag forces for varying winglet pitch and position are shown in Figure 3 and 4. The values are shown in percentage of the values for the case without winglets, which is denoted the reference level. The error bars represent the precision error (as defined in the ITTC recommendations [2]) based on two successive runs with the tunnel stopped in between, but without touching the model. It can be seen that the precision error

	Lift	Drag
Reference value [N]	42.2	3.11
Error, force gauges [N]	0.5	0.05
Error, dynamic pressure [Pa]	30	30
Systematic error of ref.level [N]	1.58	0.12
Precision error [N]	0.18	0.03
Uncertainty of ref.level [N]	1.59	0.12
Uncertainty of ref.level [%]	3.8	3.9

Table 2: Reference forces and estimation of systematic errors. The forces are corrected to inlet dynamic pressure 820 Pa and 26° C.

is too large to verify the trends. Increasing the number of tests should decrease this error. For a trustworthy estimation of the repeatability the winglets pitch should really be re-set between the tests. The systematic error (biased error) is assumed to be "subtracted out", as according to the ITTC recommendations [2] is a commonly accepted practice, even though it is not generally true. The absolute value of the reference level is given in Table 2 together with an estimation of the biased error. This error estimate is larger than what is desirable. It stems mainly from a large drift in the manometer recording the free stream velocity. In order improve the estimation of the precision and the systematic errors , the force tests will be repeated in the wind tunnel in the near future, using a better manometer.

Friction drag. The friction drag and the transition are important issues in sailing yacht design for two reasons: 1) Delaying transition reduces the total drag with a relatively large amount (compared to large commercial vessels). 2) The friction drag takes part in several critical trade-off in the design, for example the trade-off between larger frictions drag and improved stability for a larger keel bulb, or reduced induced drag by fitting winglets to the keel. Numerical predictions of the friction drag and the transition of a curved body can be done with many different tools; various types of boundary layer codes, RANS, LES and hybrid-LES. Irrespective of the method, it is a very challenging task and validation data is needed.
As mentioned before the model was equipped with trip tape to trigger transition. In one test the tape on the bulb was removed and the forces were measurements. This result can be compared with the result for the model with the trip tape still fitted. The differences in drag force, given in Table 3, will mainly come from the delayed transition for the case without tape. The drag of the trip tape itself will of course also contribute to the difference. A crude estimation based on the drag of two-dimensional strips [3] show that the drag of the removed tape is around 5% of the

	Increment [%]
Drag	-23.5±1.5
Lift	-0.5±0.6

Table 3: Increment of forces for the model *without* trip tape compared to the model *with* trip tape for the case without winglets.

reference drag, and that the drag of all tapes together is about 18% of the reference drag! This is certainly something that needs to be investigated further.
An attempt to determine the transition line of the case without trip tape was done by using coloured glycerin oil. The first result, show in Figure 5a), displayed a clear transition line on the flat, horizontal, bottom side of the bulb (topside in the wind tunnel). However, when the test was repeated with less paint on the forward part of the model, the transition line moved further aft, as seen in Figure 5b). It is likely that the paint caused instabilities in the boundary layer that triggered the transition. Even though the position of the free natural transition could not be determined with this test, the result can anyway be used for validation purpose in the way that we know that transition should not occur *ahead* of the line found in the test.

Flow details of a free vortex. For keel flow simulations it is important to correctly predict the tip vortex as it can be the key to understanding the vortex drag and how to minimise it. The measurements of the velocities behind the keel in Figure 6-8 show clearly the tip vortices from the fin and winglets and the complex viscous wake of the bulb. These results could be useful for validation of any codes that can handle production and interaction of vortices. Figure 9 shows the turbulence intensity in the wake, which is interesting for comparison with predictions from different turbulence models and LES codes.

5 Conclusion and Discussion

Wind tunnel tests of a winglet keel model have been performed. The results can be used for validation and comparison of different types of CFD methods. The winglets pitch and longitudinal position were varied during the tests and the results revealed differences in the keel performance. However, the precision error and the systematic error were both too large. Until the force measurements have been repeated the force data should be treated as preliminary. The complete test result together with a formal uncertainty analysis will be given in a later report.

References

[1] Werner S. Larsson L. Regnstrom B. Towards a validation test case - wind tunnel test of a winglet keel. In *The Numerical Towing Tank Symposium*, 2004.

[2] International Towing Tank Conference. *ITTC - Recommended Procedures 7.5-02,01-01*, 1999.

[3] Hoerner. S.F. *Fluid-dynamic drag*. Published by the author, 1965.

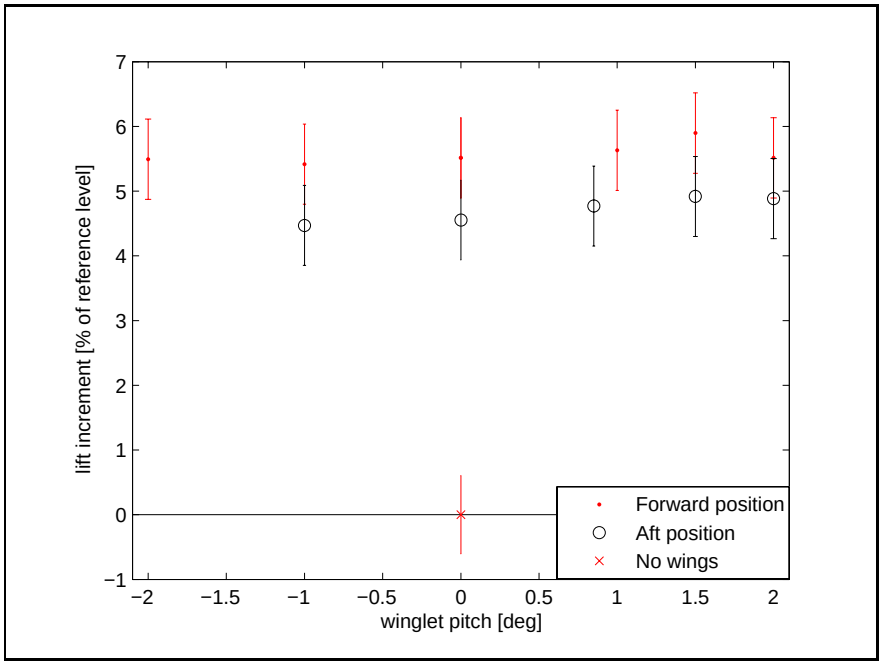

Figure 3: Increment of lift force compared to the case without winglets.

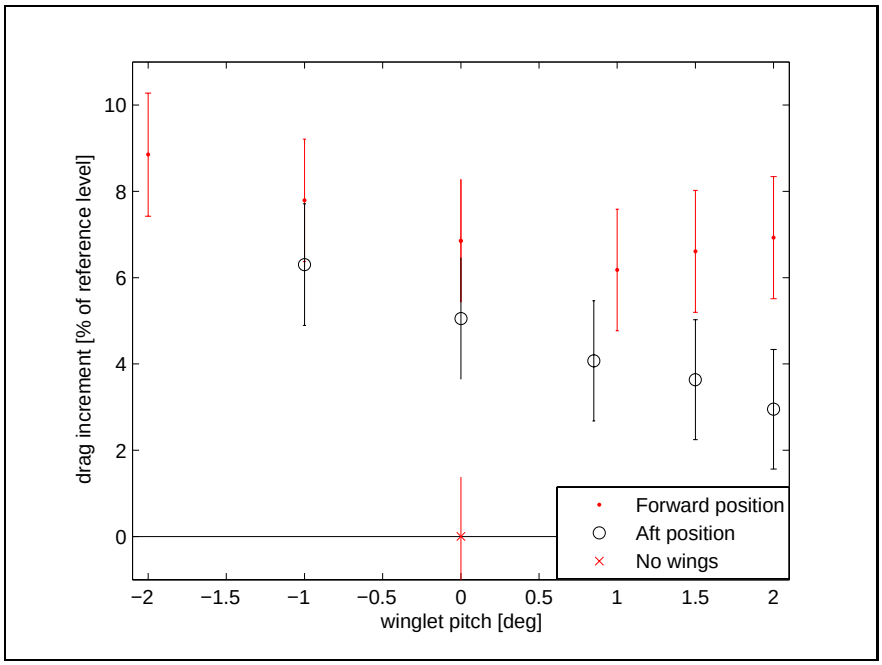

Figure 4: Increment of drag force compared to the case without winglets.

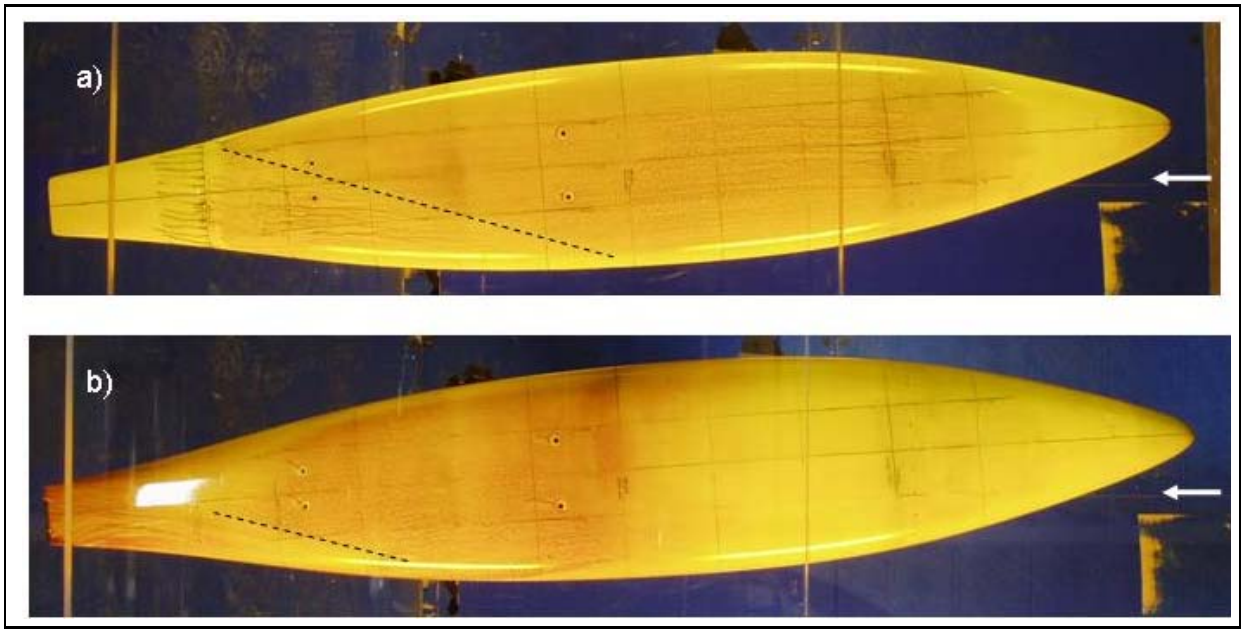

Figure 5: a) Paint test with transition line. b) Less paint used gives a delayed transition line

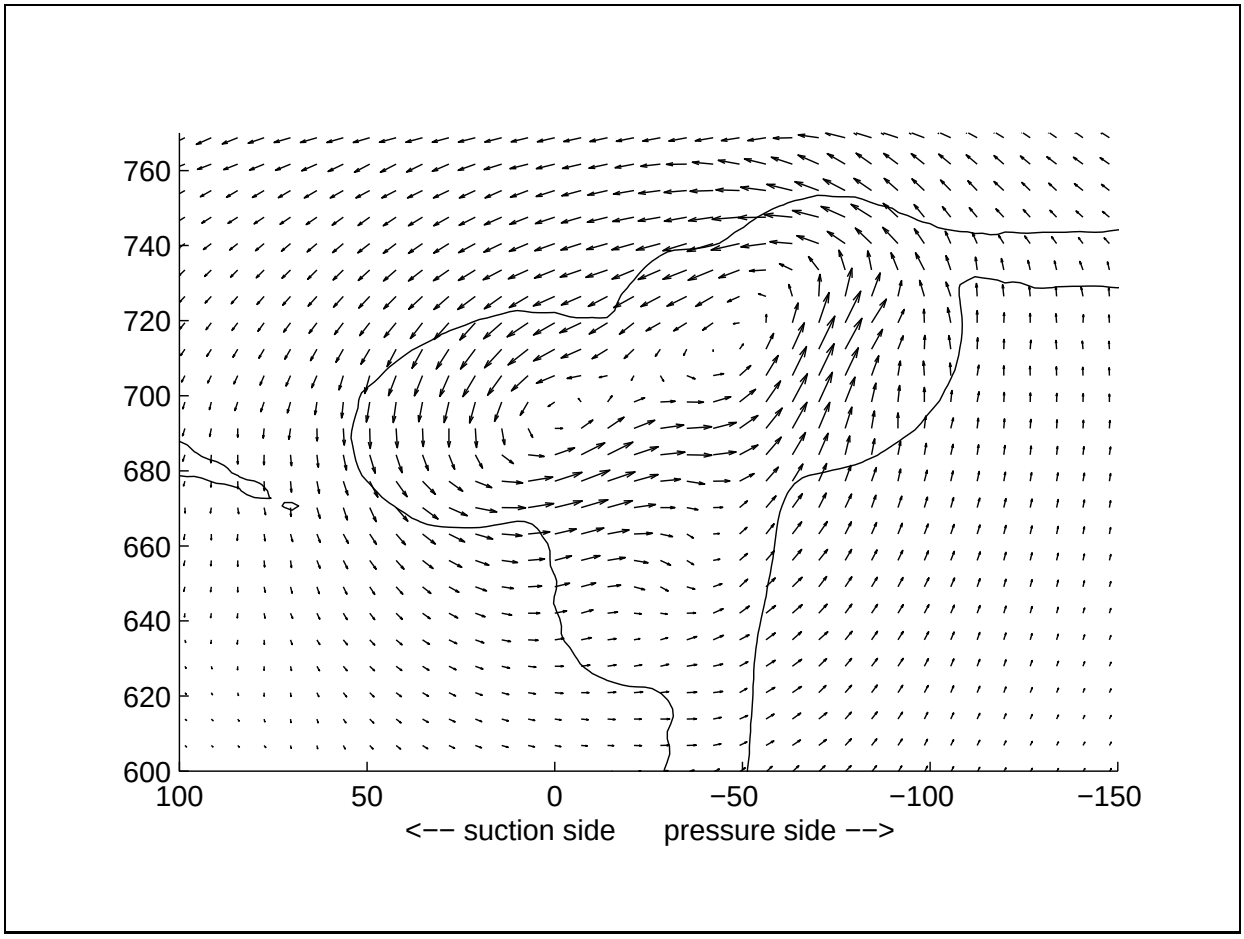

Figure 6: Cross flow components. Wake cut seen from aft. Pressures side to the right.

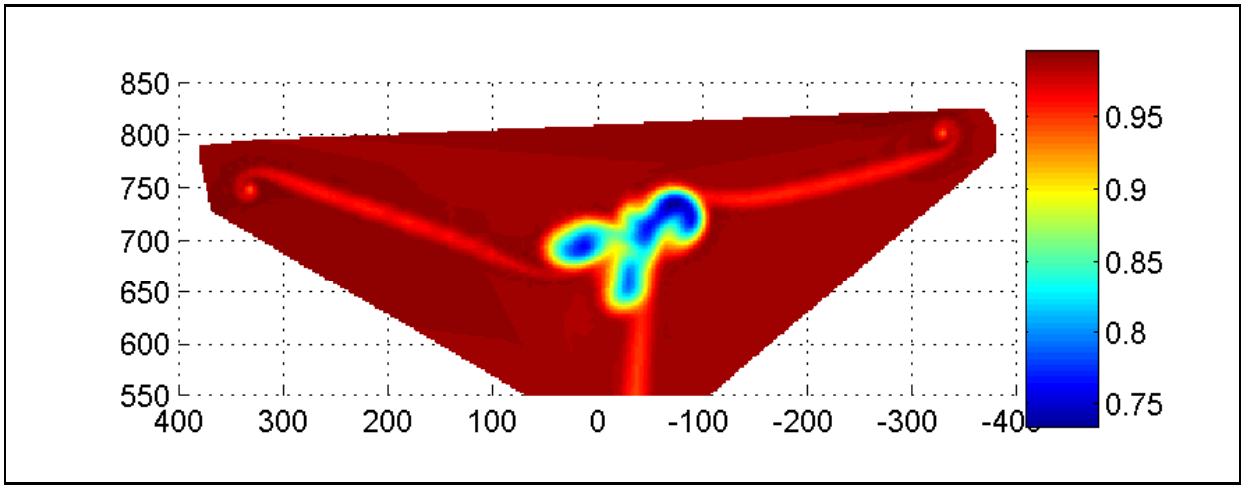

Figure 7: u/u_∞. Winglets in forward position, zero pitch. Wake cut seen from aft. Pressures side to the right.

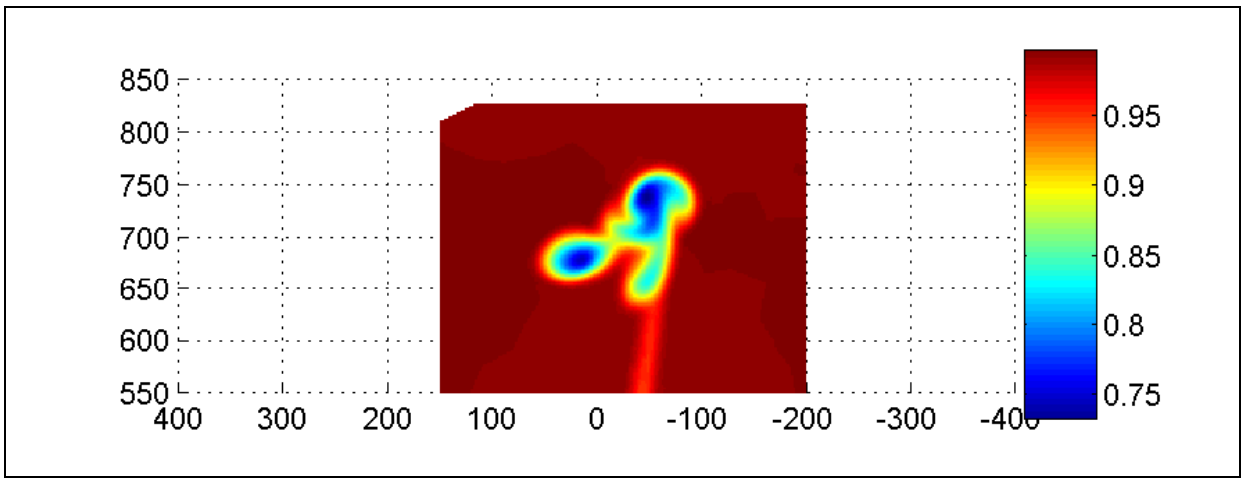

Figure 8: u/u_∞. No winglets. Wake cut seen from aft. Pressures side to the right.

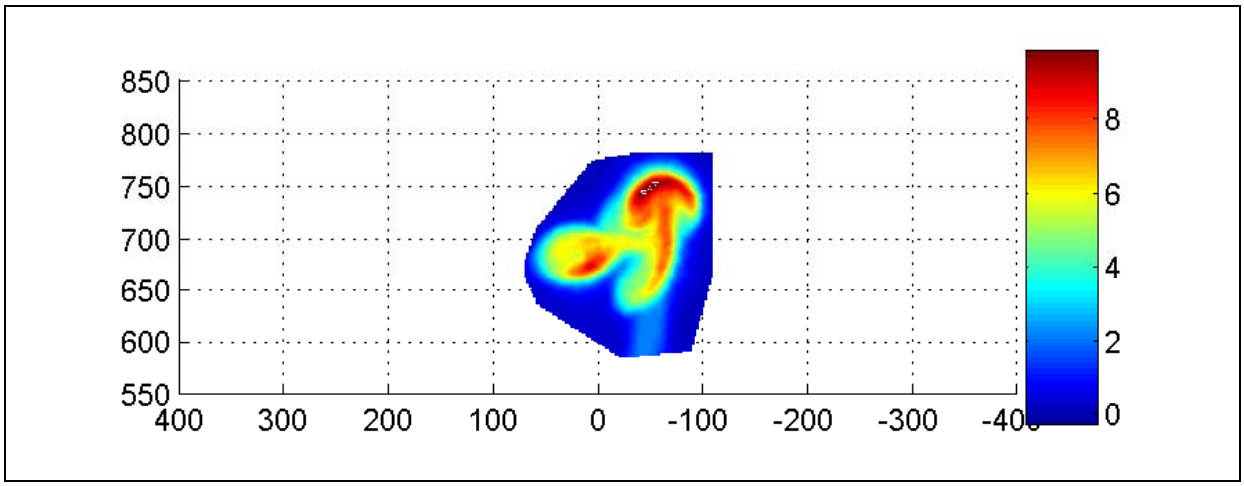

Figure 9: Turbulence intensity [%]. Wake cut seen from aft. Pressures side to the right.

Investigation on the viscous flow behind transoms

Katja Wöckner (katja.woeckner@tu-harburg.de), Florian Kluwe

1 Introduction

Fast ships are typically equipped with a barge like transom. The wave resistance of such ships is significantly influenced by the design of the transom. Especially the transverse wave system can be influenced by parameters like transom immersion and steepness of the buttock-lines. These parameters have been systematically variated, using a 2-D RANS-calculation.

2 Grids

For this computations the solver COMET is used. The stern is modelled in 2-D as a backward facing step. The free-surface flow is modeled by applying a VOF method. For this method the grid has to be very fine in the area of the free surface and near to the stern. This is necessary to keep a sharp interface between water and air during the simulation. In order to achieve a numerical wave damping, the cell size is expanded towards the outlet. This is necessary to avoid wave reflection at the outlet boundaries. The grid near the stern can be seen in Figure 1

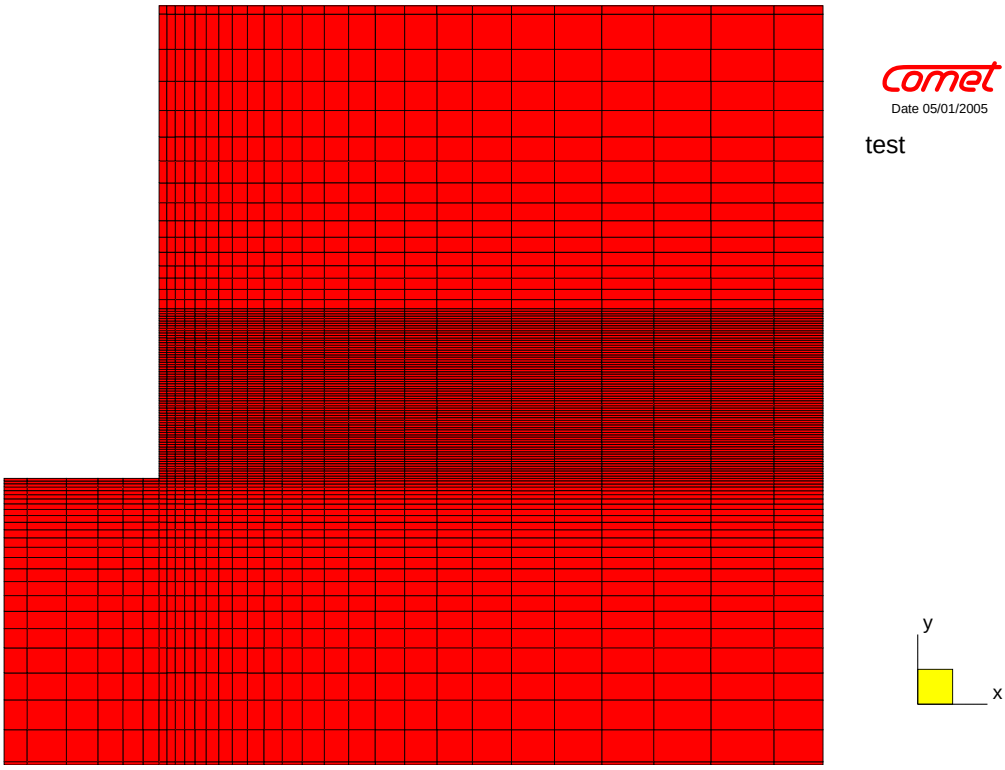

Figure 1: refined grid near the transom

It is necessary to simulate in the time domain, because of the unsteady flow behind the stern due to wave breaking.

3 Investigated Parameters

To investigate the effects of different parameters, various computations are made, varying for example the transom immersion. To compare the different results the specific pressure resistance coefficient and the specific frictional resistance coefficient of the stern are calculated. The calculated coefficients are shown in Figure 2 and 3 as a function of the Froude number. In this specific case the Froude number is defined as $F_n = \frac{v}{\sqrt{g \cdot I}}$, where v is the inflow-velocity , g is the constant of gravitation and I the transom immersion. The resistance coefficients are defined as $c_x = \frac{F_x}{\rho/2 v^2 A}$. For the frictional resistance coefficient the bottom of the ship is used as reference

area A, whereas for the pressure resistance coefficient the transom is used. F_x is the force acting on this areas during the simulation.

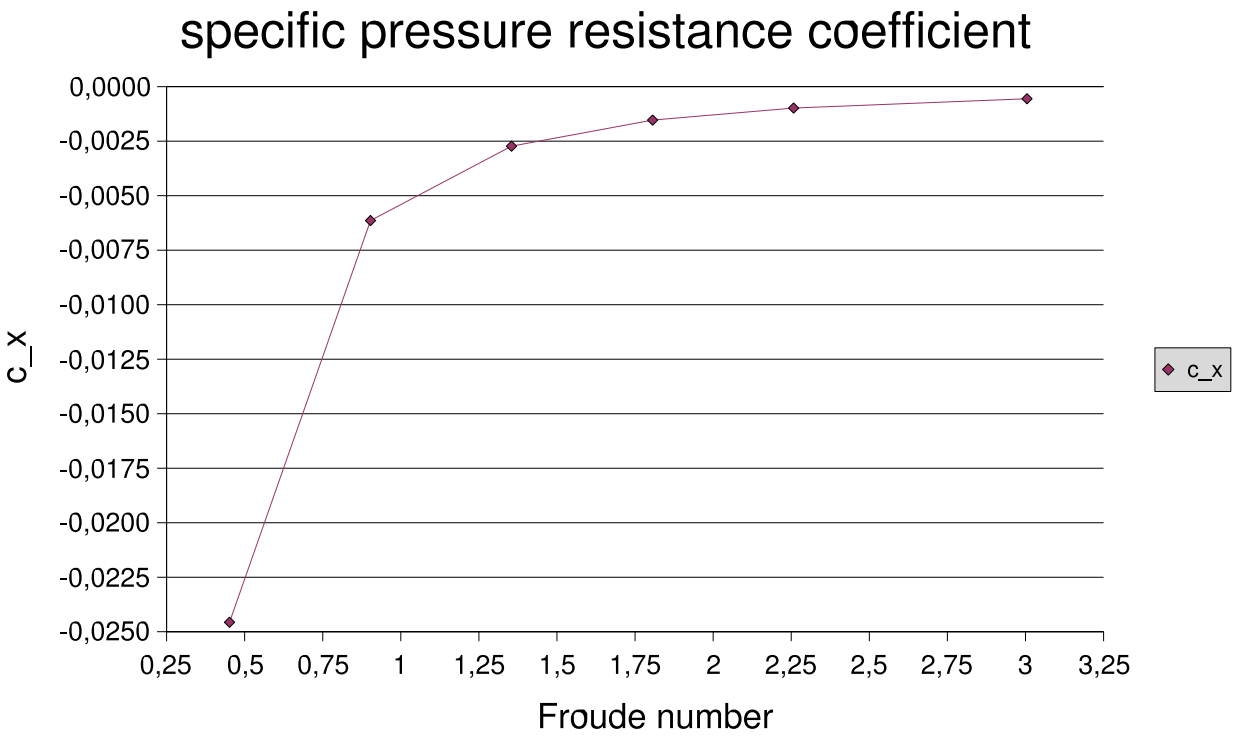

Figure 2: Shape of the specific pressure resistance coefficient, varying the Froude number

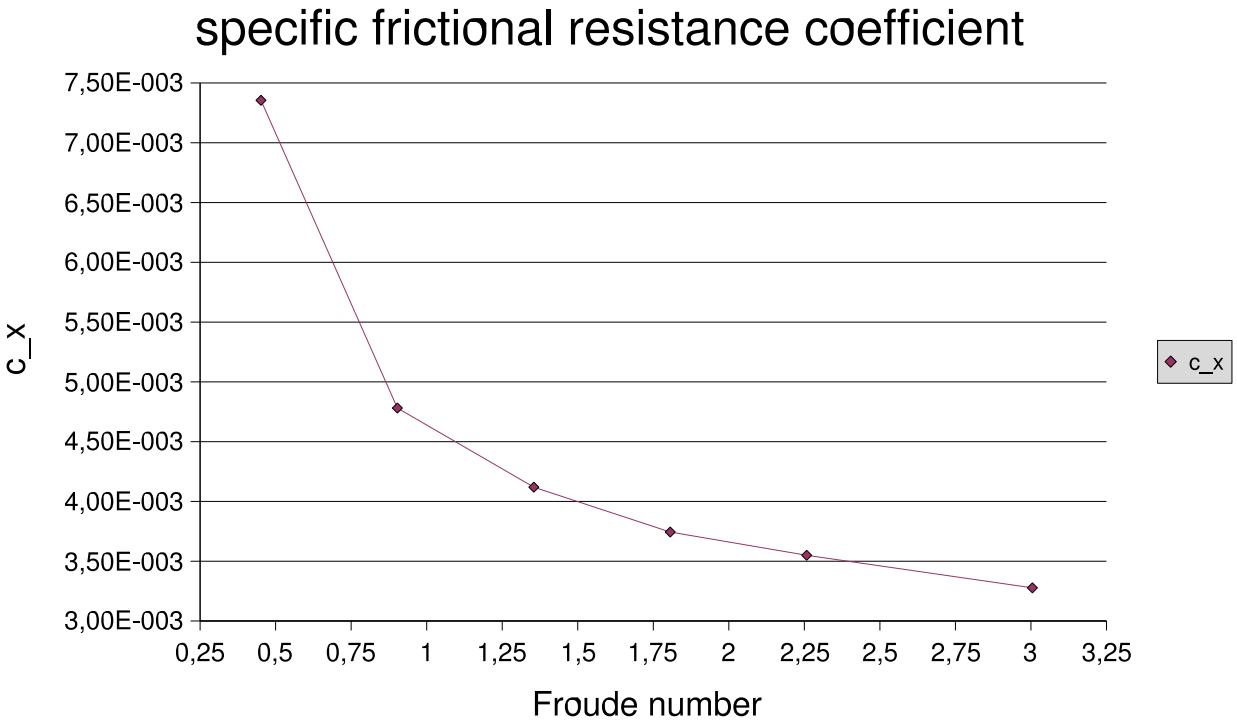

Figure 3: Shape of the specific frictional resistance coefficient, varying the Froude number

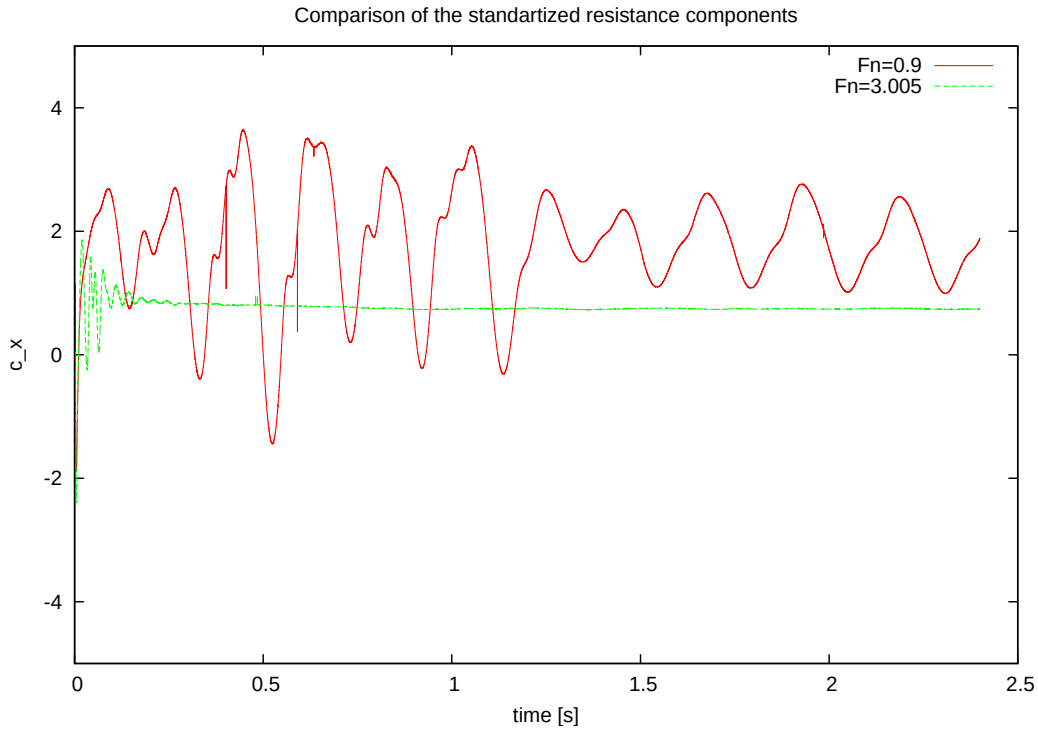

Figure 4: Shape of the standardised dissipation of the momentum

This example shows that the absolute values for the resistance coefficients are getting smaller with increasing Froude number. This means for the frictional resistance coefficient that a higher Froude number results in a smaller resistance. But the pressure coefficient is negative, and the absolute values are bigger at smaller Froude numbers. A negative resistance is a force acting in the direction of motion, which means that the ship is pushed forward. This could lead to the assumption that a wetted transom is beneficial for the ship's resistance. This is not the case, because for breaking waves at small Froude numbers (Figure 5) the dissipation of the momentum along the aft ship is larger than in the case of a clear break off at the transom (Figure 6). This dissipation is calculated as the difference of the momentum at the inlet boundary and at the transom cross-section:

$$(\sum_{A_Q} \rho v^2 S)_{ein} + (\sum_{A_Q} pS)_{ein} - (\sum_{A_Q} \rho v_A^2 S)_{aus} + (\sum_{A_Q} pS)_{aus} = \Delta I \tag{1}$$

This results in a resistance component, as shown below:

$$F = \frac{\Delta I}{\Delta s} \cdot v_A - pA_S \tag{2}$$

In Figure 4 this component of the resistance is shown for two different Froude numbers ($F_n = 0.9$ and $F_n = 1.331$). The resistance component is standardised with $\frac{F}{\rho/2v^2 A_Q}$, where ρ is the water density, v the inflow-velocity and A_Q the area of cross-section from the bottom of the ship to the bottom. It can be seen that the dissipation of the momentum is smaller for the larger Froude number, which results in a smaller overall resistance in case of a clear break off at the transom.

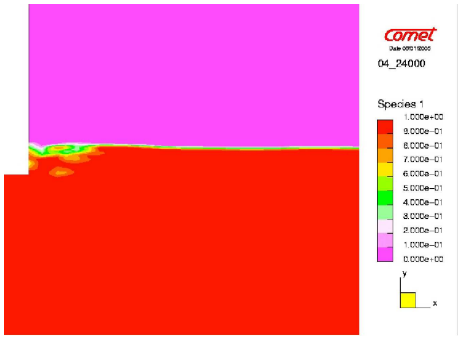

0.6s

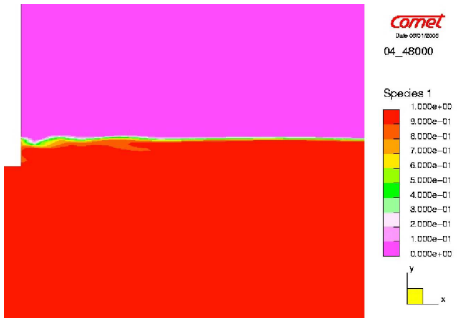

1.2s

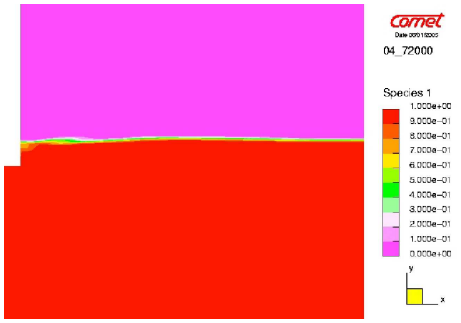

1.8s

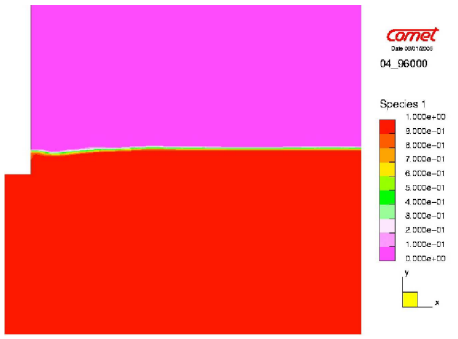

2.4s

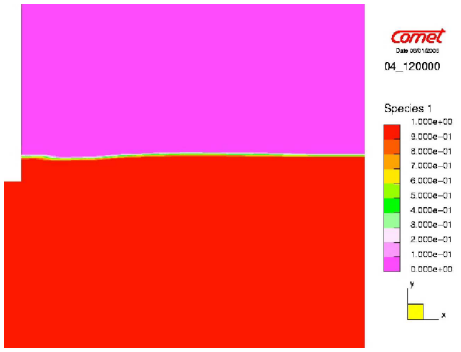

3s

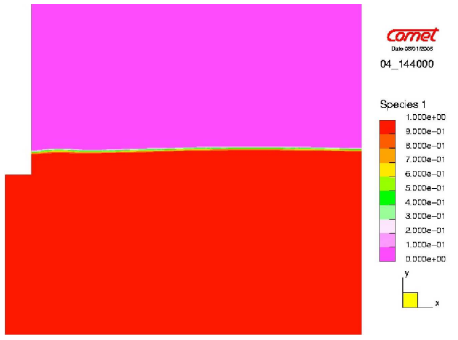

3.6s

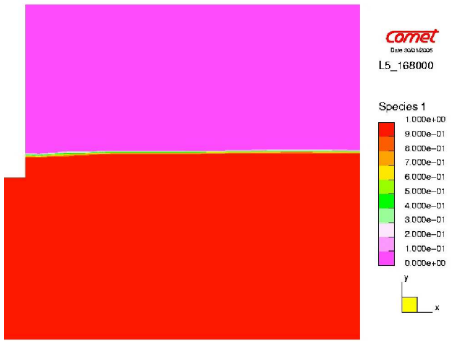

4.2s

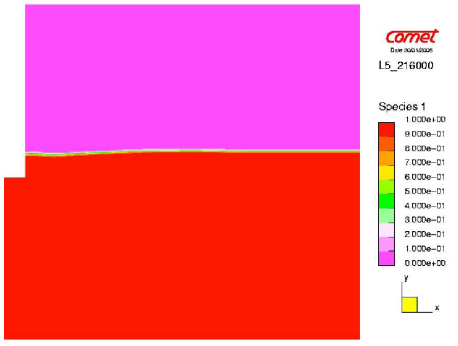

5.4s

Figure 5: Shape of the stern wave after 0.6(top left); 1.2, 1.8, 2.4, 3, 3.6, 4.2, 5.4(bottom right) seconds, $F_n = 0.9$

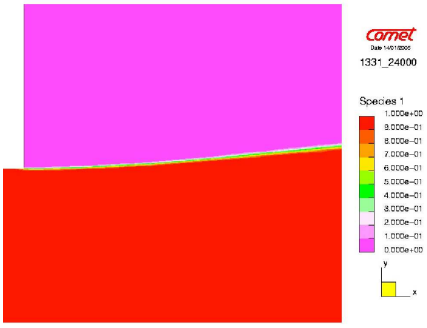

0.6s

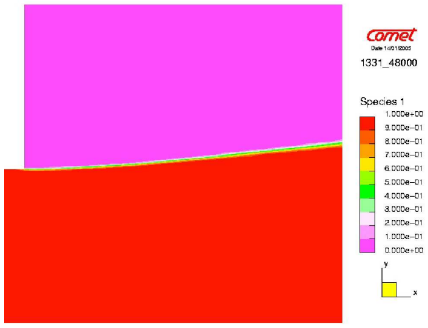

1.2s

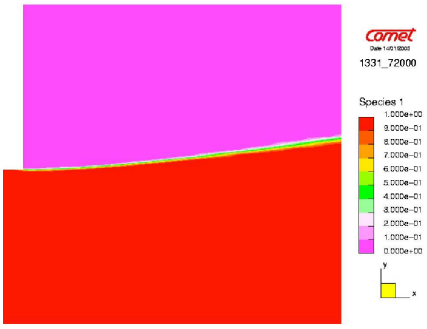

1.8s

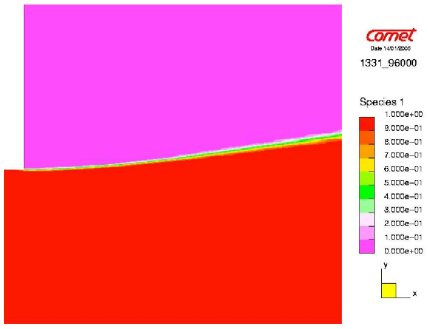

2.4s

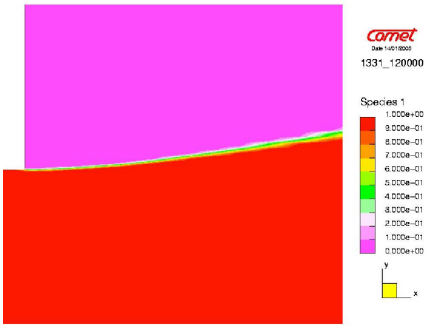

3s

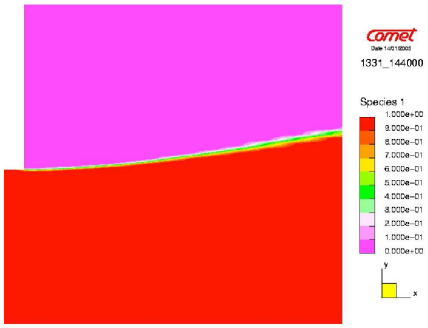

3.6s

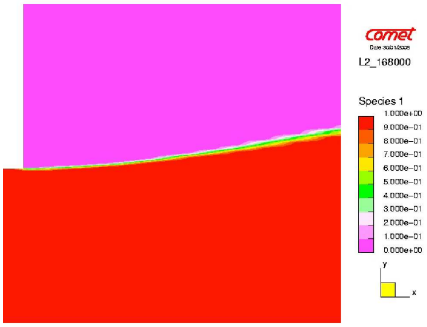

4.2s

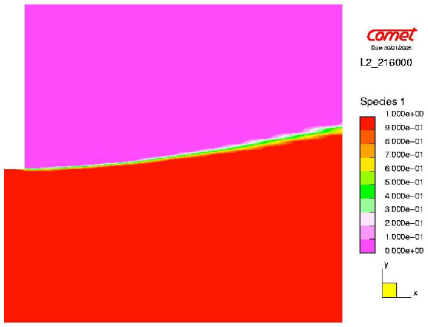

5.4s

Figure 6: Shape of the stern wave after 0.6(top left); 1.2, 1.8, 2.4, 3, 3.6, 4.2, 5.4(bottom right) seconds, $F_n = 3.005$

References

[1] Tadao Yamano, Naoki Hibino, Fumiyaso Kuratani: *On scale Effect of the Resistance due to wave breaking just behind a transom stern*, Hyogo University of Teacher Education, Japan

[2] Schäfer, Michael: *Numerik im Maschinenbau*, Springer 1999

[3] Perić, Milovan: *Numerische Berechnungsmethoden der Strömungsmechanik*, TU Hamburg-Harburg, Vorlesungsmanuskript

[4] ICCM Institute of Computational Continuum Mechanics GmbH: *COMET User Manual*, 2001

[5] Krüger, Stefan: *Strömungsmechanische Grundlagen zum Glattwasserwiderstand von Schiffen*, TU Hamburg-Harburg, Vorlesungsmanuskript, 2002

[6] Krüger, Stefan: *Schiffsformentwurf mit CFD*, TU Hamburg-Harburg, Vorlesungsmanuskript, 2001

[7] Saunders, H.E.: *Hydrodynamics in Ship Design*, SNAME, 1957

RANSE CALCULATIONS FOR THE HYDRODYNAMIC ANALYSIS OF A MARINE PROPELLER

C. Pittaluga,
CETENA - Hydrodynamic Dept., ITALY,
Chiara.Pittaluga@cetena.it

G.Cresta,
FINCANTIERI Naval BusinessUnit-Hydrodynamic and Acoustic Dept., ITALY,
Giacomo.Cresta@fincantieri.it

SHORT ABSTRACT

The present paper is focused on a comparison between experimental data and RANSE calculations for an high skewed propeller which was performed within the scope of work of the European-founded project "LEADING EDGE" (Contract No: G3RD-CT-2002-00818). In particular the paper shows that RANSE solvers are an effective tools to investigate the detailed flow around the especially for tip vortex, trailing vortex and streamlines over the blade.

INTRODUCTION

The scope of the shipyards is obviously to build a ship, to minimize the cost and to satisfy the performances; one of the main requirements in today's shipbuilding industry is a highly efficient and quiet operation of the ship at a relatively high speed or at high power. This operating condition increase the risk of vibration and noise mainly due to propeller cavitation. The study of the propeller is a priority research theme for naval hydrodynamics owing to the complexity of the related physical phenomena and its impact on the overall ship design. For this reason the propeller design have to be carried out taking into account the ship shape, shaft line and brackets, rudder, engine design. The optimal propeller's operation conditions depends on significant aspects such as the contractual ship speed, the fuel and bearing consumption, noise and vibration level, etc.

Today's approach to the propeller design is a combination of all the available methodologies, both physical and numerical models, in order to have a prevision of the propeller performance operating in full scale:

- *1st phase* – theoretical computer aided optimisation
  In the 1st phase the main characteristic of the propeller are chosen by numerical tool based on lifting surface theory, the number of blades, revolution rates and diameter come out in order to have a first estimation of efficiency, advance ratio, thrust and torque coefficient (Kt, Kq), minimum chord length distribution, estimated cavitation pattern, strength characteristics, propeller geometry and rotating direction, a preliminary estimate of fluctuating forces
- *2nd phase* – model aided experimental optimisation
  In the 2nd phase the hull wake is already settled, therefore the propeller geometry can be optimised by Steady/Unsteady Lifting-Surface approach and by Panel Method, this phase is also in the scope of detailed propeller performance and cavitation pattern. The optimised geometry is verified by experimental test in towing tanks and cavitation tunnel (interaction between experiments and numerical models)
- *3rd phase* – verification by full scale experiments
  In the 3rd phase the ship is built and the prevision have to be tested in full scale
- *4th phase* – data base generation
  In the 4th phase, from the shipyards experience in sea trials a database is produced, 4thphase, to scale numerical and experimental data from model to full-scale as a guidelines for the future constructions.

Nowadays the weak point of this procedure is the prediction of cavitation in full-scale, mainly the tip vortex cavitation, thus new procedure are required and RANSE solvers seem to be an useful tool. Thus the firs step is the validation against experiments in model scale and then full-scale computation.
The work presented in this paper regards a validation study developed for a highly-skewed propeller in open water condition: a commercial RANSE solver (CFX5.7) was validated, the assessment of the reliability of CFD calculations as regards the determination of the 3D wake around this propeller was carried out under the support of the EU project LEADING EDGE, devoted to the study of leading edge and tip flow for the design of quiet and efficient screw propellers.
The paper is organised as follows: the first section describes the propeller geometry; the second section details the computational method, both the potential and the viscous approach, the subsequent sections describe the experimental data and the last section the verification and validation procedure.

PROPELLER GEOMETRY

The propeller geometry used in this work is a four bladed, high skew, controllable pitch propeller; the main propeller geometry data in model scale are:

Propeller diameter:	0.233 m
Boss/diameter:	0.32
Number of blades:	4
Rotational Speed:	14 Hz
Maximum Skew:	27°
AE/AO:	0.7

The propeller was analysed at an off-design pitch.

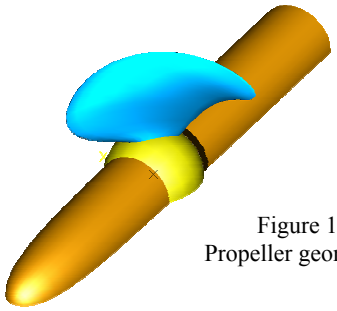

Figure 1 – Propeller geometry

CFD TOOLS AND COMPUTATION SETTINGS

The computation has been performed with a general purpose RANSE code, CFX 5.7 [1], on a structured multi-block mesh. For the present study the steady viscous flow around the propeller has been investigated in open water condition. The flow around the propeller is computed in a rotating reference system attached to the propeller, a K-e turbulence model in conjunction with a scalable wall function method has been adopted in order to keep the grid dimensions and thus reduce the computational time.
The propeller has been tested onto three different operating conditions, corresponding to J = 0. 736, J = 0.5, J = 0.2. The different J value was achieved by tuning the advance velocity value, and keeping fixed the revolution number. All the calculation has been performed in model scale.
A sensitivity analysis has carried out: since a scalable wall function was adopted the grid of computation was set up for J = 0. 736 that correspond to the case with smallest thickness of boundary layer.

DOMAIN OF COMPUTATION

The domain of computation for a propeller in open water conditions is a cylinder shaped domain located around the propeller and co-axial with the propeller axis, moreover, considering the periodicity of the propeller flow, only one blade can been modelled and so the computational domain contains the flow around a single blade. The influence of the other blades is taken into account by the application of a periodic boundary condition.
To employ the periodic boundary condition allows to limit the mesh size but as drawback requires the CAD model of the periodic surface, this requirement led to increment of the time required in the pre-processing phase. For this reason Cetena is developing a methodology for the numerical generation of the periodic surface generation starting from the blade section geometry with Cetena's Panel Code PROPACE, see figure 2.

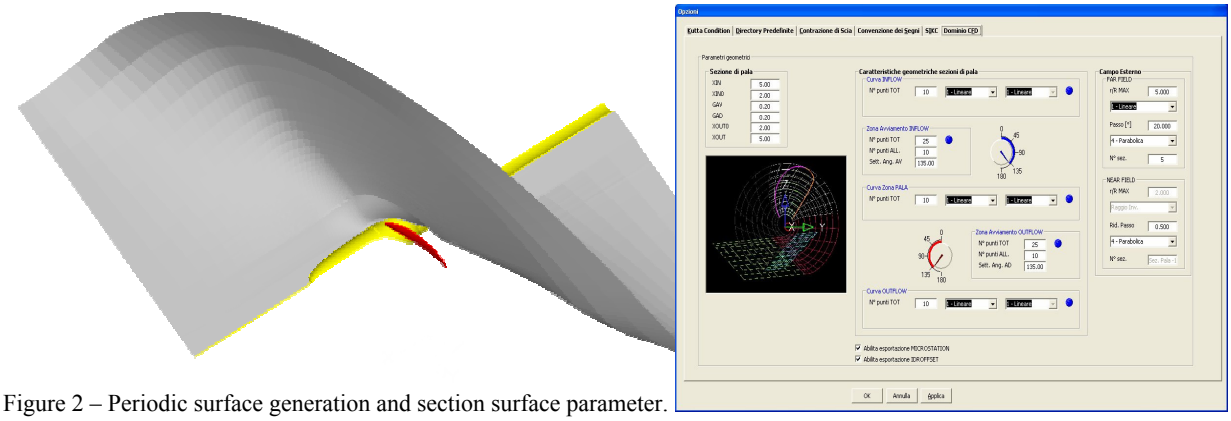

Figure 2 – Periodic surface generation and section surface parameter.

The mathematical model consist of several law to connect the chord line with the axial direction, in the 2D cylindrical section along several given blade section; stating from the leading and trailing edge three curves are defined towards respectively the inflow and outflow zone: first a linear distribution, a connection zone that could be build with different distribution laws a final linear distribution up to the farfield region. From the blade up to the farfield cylindrical zone the skew is reduced along the radius, allowing make a choice amongst several laws in order to select the best distribution on the basis of the skew of the blade.
In order to supply the unperturbed boundary condition the section where the flow is directed inward the domain has to be located at about 2D ahead the propeller blade, the outflow section at about 4D behind and, and cylindrical external border at about 5D. The skew of the whole domain is 270°.

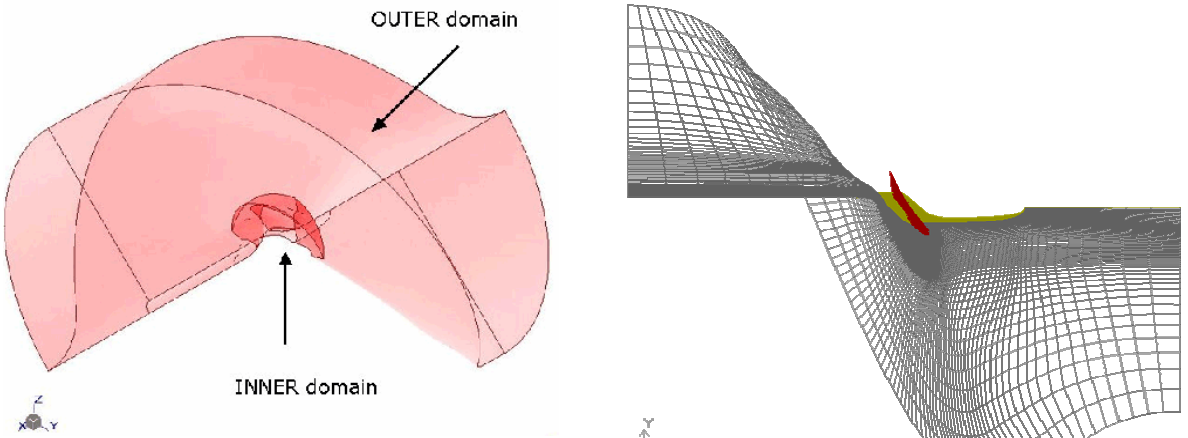

Figure 3 – Periodic surface generation and section surface parameter.

MESHING APPROACH

The code employed for the mesh generation is the structured multi-block code ICEM CFD - Hexa[2]. The domain of computation adopted, to investigate a propeller in open water conditions, is a cylinder shaped domain located around the propeller and co-axial with the propeller axis. Considering the periodicity of the propeller flow, only one blade can been modelled, the influence of the other blades is taken into account by the application of a periodic boundary condition.

CFX 5.7 can perform analysis onto a domain made by a group of sub-domains therefore calculation domain has been divided into 2 sub-domain in order to create a finer grid near the propeller:

- Inner domain, that includes the fluid close to the propeller blade and a part of the shaft line, the flow is solved in the rotating reference system, (propeller reference system)
- Outer domain, that includes the fluid between the inner domain and the domain boundary, the flow is solved in a steady reference system.

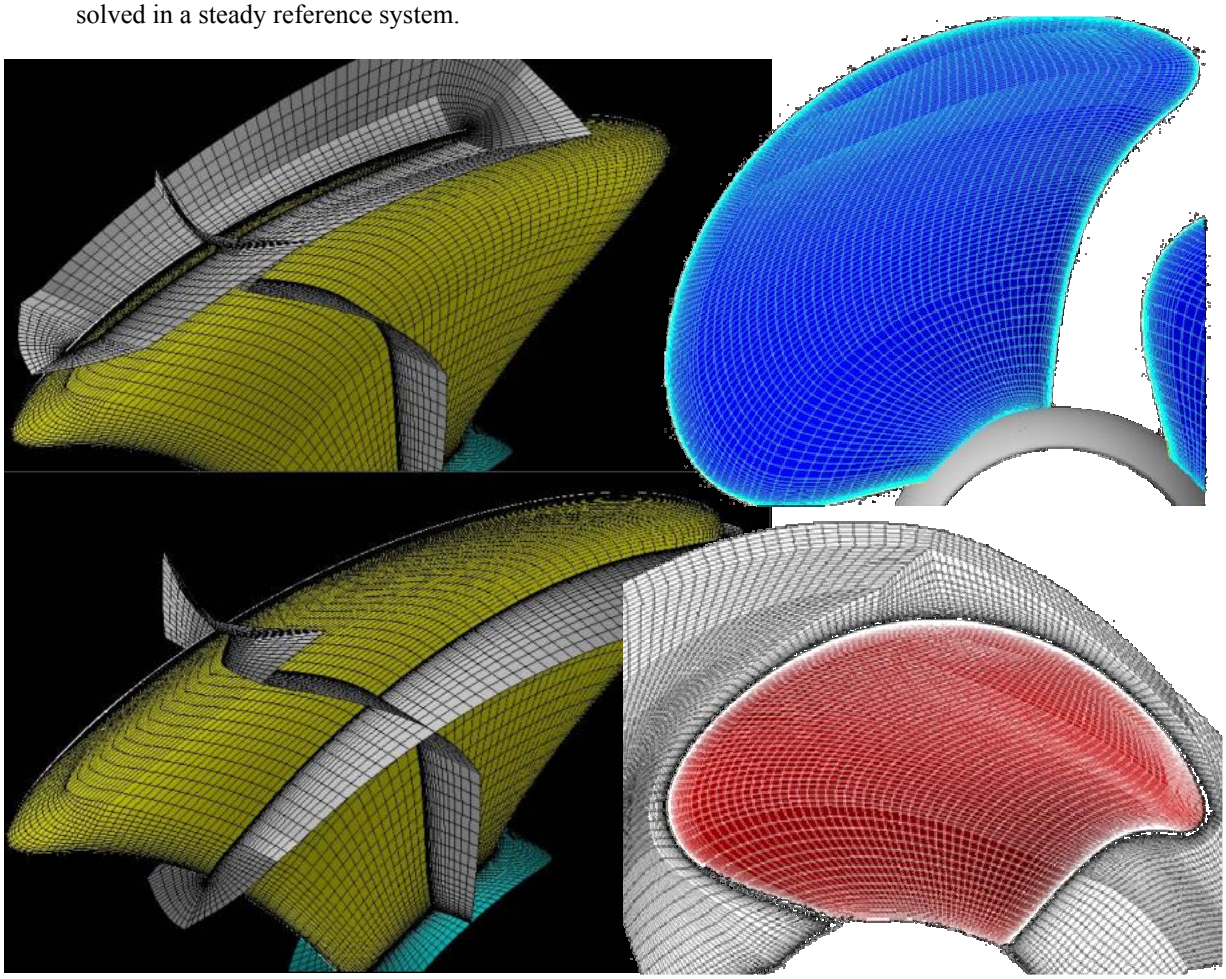

Figure 4 – Viscous mesh

The different domain are connected by General Grid Interface Algorithm (GGI), this tools allow to use non-matching node distribution for the surface grid of adjacent region, but if the number of nodes differs too much the algorithm couldn't perform properly. For this reason first volume grid for inner domain has been generated and then volume grids for outer domain have been built up as a coarse distribution of the former, with coefficient 1:3 or 1:4. No requirements are made by the solver at the periodic surface interface that means that it is possible to have a connection with different node distribution on the two side.

Inner Domain : an H-Grid topology is applied to split the volume, so the initial block is subdivided in 6 blocks; then into the inner domain, close to the blade, an O-Grid topology is applied with the generation of 5 new blocks: two blocks are applied along the leading and trailing edge (from the hub till about 0.8÷0.9 of the radius), one along the tip region, the last two are applied respectively for the pressure side and suction side. The O-Grid is again divided to reflect the characteristic features of the blade geometry. About 830,000 nodes. As an example, the computation J =0.736, pointed out that the y+ parameter is in the range 5÷55.

Outer Domain: Total grid size of this region is about 200.000 nodes, made up by 16 blocks organised in two O grid index. The first O-grid is located around the inner domain to build up the grid at the domain interface as a coarse distribution of the inner domain one, (reduction coefficient 1:3 or 1:4). The second O-grid is applied to generate a radial distribution from the hub to the farfield zone.

The RANS study has been carried out for the Leading Edge EU Project, particular attention was given to key features of this the project: the flow around the centre and the tip region of the propeller in order to capture the incipient tip vortex structure The taking advantage of domain subdivision the size of the grid is increased close to the blade whilst the domain size is decreased away from propeller region. The total mesh Size is a 1.130.000 nodes structured multiblock.

RANSE SOLVER SETTINGS

The commercial code CFX 5 was used to perform the simulations. The governing equations of the viscous flow are solved for the mass and momentum conservation. In order to simulate a propeller operating in open water, steady calculation is carried out in a Multiple Frame of Reference System (MFR), the Rotating reference frame is applied to the fluid domain close to the propeller blade in order to add additional terms compared to those in the inertial system. A Frozen Rotor algorithm with a GGI interface guarantees the conservation of the fluid properties at the domain connection. An algebraic multi-grid algorithm is employed to accelerate the convergence of the linear solver. For brevity, some information about the solver configuration is shown in table 2, for further information refer to the CFX User's guide [1].

The K-e turbulence model with a scalable wall function was used to keep the grid dimensions and thus the computational time. The final mesh size is about 1.130.000 nodes, and satisfy the requirement 5< y+<55 for the mesh spacing of the first point near the wall, in the higher J (=0.736). The boundary condition applied to the domain border correspond to: at the inflow section and the Far-field region the undisturbed velocity is applied, at the outflow section a "zero" pressure gradient, a Periodic boundary condition (GGI) is given at the Periodic surface. The convergence has been achieved with 3100 iterations and has been carried out using different resolution scheme up to the second accurate scheme order, the residual (RMS) are below 10E-06.

Velocity formulation	Absolute velocity dependent
Spatial discretisation	Finite-volume colloc.
Convection Terms Discr	Upwind stnd
Order of acc. Conv. Terms	Second
Diffusion Terms Discr	Upwind
Order of acc. Diff.Terms	Second
Pressure-velocity Coupling	Fully coupled
Type of turb. model	Two-eq., K-ε
Wall function	Wall func without press.grad.
y^+	(5 ÷ 55)
Criteria: Residual	No. of iterations 3100

Table 1: solver configuration

PROPELLER ANALYSIS AND VALIDATION

The first validation step, in order to assess the reliability of numerical results, is the comparison of the measured and calculated values of the *Trust* and *Torque Coefficients*. In Figure 6 and Table 2 it is presented, respectively in graphical and numerical format, the comparison of two experimental data sets in open water condition (SSPA and HSVA in LE Project) with the numerical results of Cetena's potential flow code PROPACE [3], [4] and CFX 5.7 RANSE solver. The accuracy of the viscous flow results is in a range of 0.18÷3.80 % for the thrust coefficient and of 3.88÷6.40 % for the torque coefficient.

A more detailed description of the hydrodynamic behaviour of the propeller is provided in terms of the *Pressure Coefficient* (C_P) distribution over the blade at three different radial sections (both potential and RANSE), in Figure 6a 6f.

The C_P contour map, obtained by the RANSE, shows a typical low pressure distribution close to the leading edge area: it is associated with a vortex at the leading edge, shed on the back at about r/R=0.900, as shown in Figure 6c. On the other hand the potential flow results near the leading edge are clearly affected by numerical instability. At the trailing edge, the pressure distribution is affected by a local peak due to the tip vortex transit.

The distribution of the Cp along the tip vortex allows to evaluate whether or not it is cavitating. In particular by comparing the numerical Cp iso-surfaces against the experimental value of the tip vortex cavitation inception it can be seen (figure 6e), from the thin white trace close to the tip (at about 0.9, trailing edge), that the vortex should be cavitating. These findings are confirmed by figure 6b, which show an acceptable agreement between model-scale calculations and cavitation inception tests in terms of tip vortex structure and strength with exception of the downstream area, where an increasing of the minimum Cp was expected the computations showed a decreasing.

J	Kt		
	Exp 2 / Exp 1	Cet / Exp 1	Cet / Exp 2
0.2	0.15 %	2.12 %	2.28 %
0.5	1.00 %	3.35 %	2.32 %
0.734	4.14 %	0.18 %	3.80 %

J	10 Kq		
	Exp 2 / Exp 1	Cet / Exp 1	Cet / Exp 2
0.2	0.14 %	4.03 %	3.88 %
0.5	1.36 %	6.15 %	4.73 %
0.734	1.81 %	6.40 %	4.05 %

Table 2 -Difference between experimental data and CFX 5.7 results

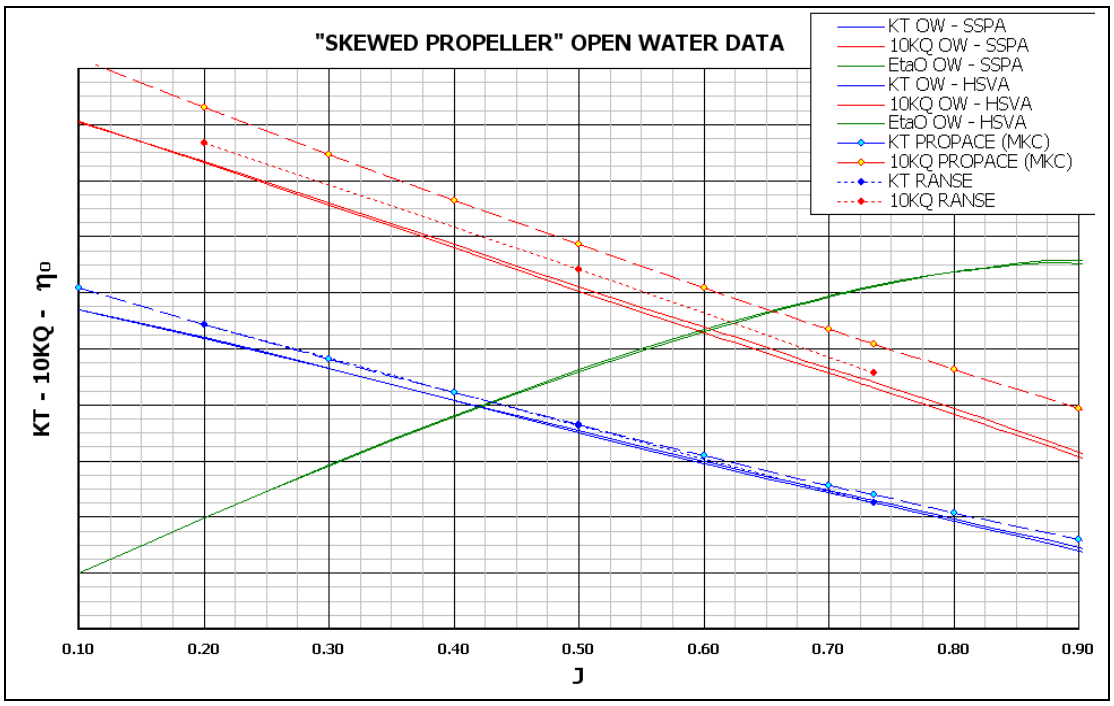

Figure 5 – Open water characteristics

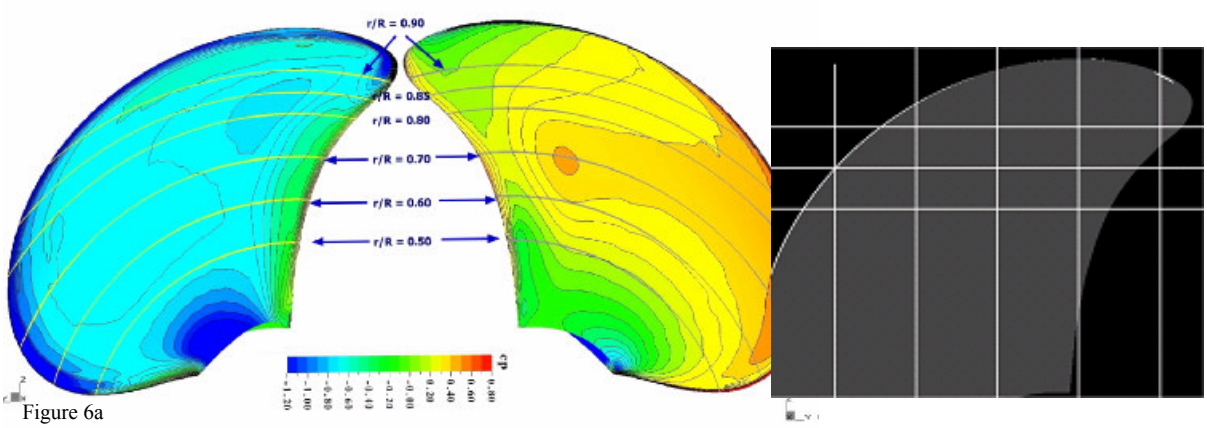

Figure 6a

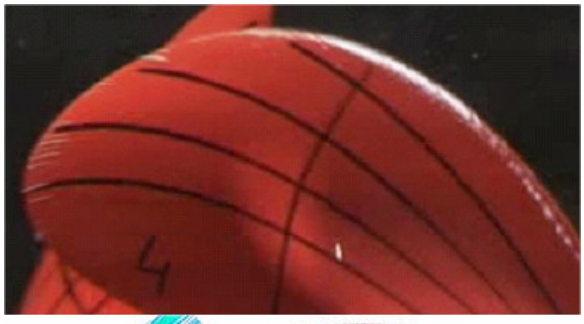

Figure 6b

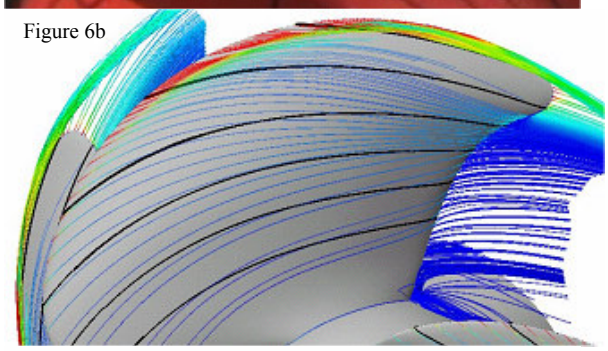

Figure 6c

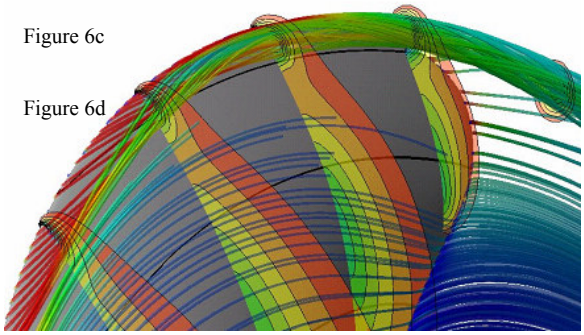

Figure 6d

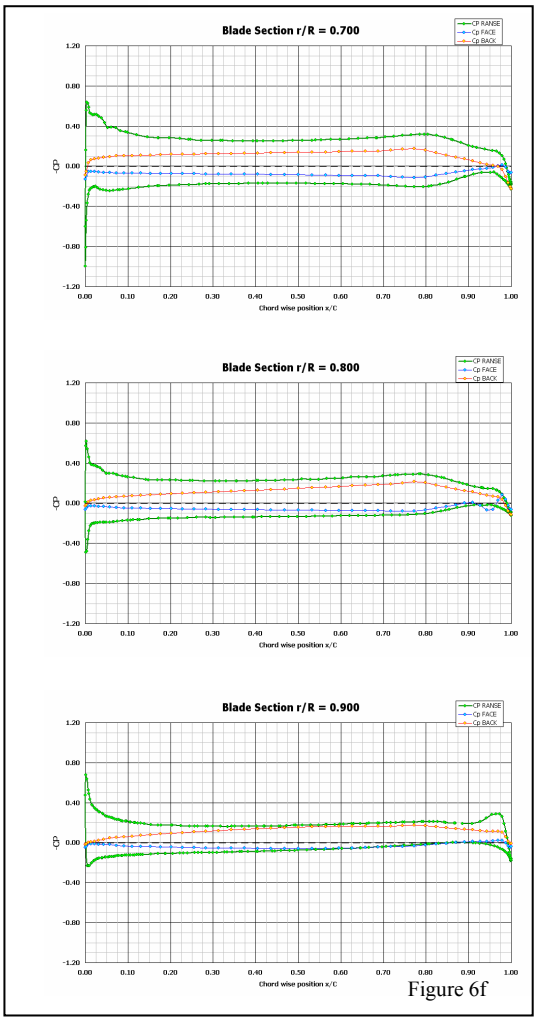

Figure 6f

Figure 6 – Flow fisualization

ACKNOWLEDGEMENTS

The work presented in this paper has been partly funded by the EC though the project LEADING EDGE, prediction of leading edge and tip flow for the design of quiet and efficient screw propellers.
Contract No: G3RD-CT-2002-00818

REFERENCES

1. CFX-5.7 Theory Manual', www.ansys.com/cfx
2. '2000 ICEM CFD Engineering, ICEM CFD Version 4.3, Berkeley, USA
3. P. Becchi - A. Traverso, 'Manuale Utente programma PROPACE Vers. 3.4', Report CETENA 8420
4. P. Becchi - A. Traverso, 'Analisi di sensibilità sul programma PROPACE', Report CETENA 8020

CALL FOR PAPERS

9th Numerical Towing Tank Symposium (NuTTS'06)

Le Croisic, France, 1 - 3 October 2006

Topics:

- Nonlinear flows around marine structures (LES, RANSE, Euler with or w/o free surface)
- Free-surface flows around marine structures (3-d ship seakeeping, free-surface viscous flows)
- Related topics (validation experiments, numerical techniques, grid generation, etc)

Deadlines:	Early feedback:	30 April 2006
	Extended Abstracts received:	28 July 2006
	Last possible update:	1st September 2006

You are invited to participate in the above event. The objective of the event is to provide a forum for informal discussions among experts in the field and to disseminate latest results. Younger workers and Ph.D. students are especially encouraged to participate. The event will be held at a seaside resort near Nantes directly connected with Paris by train. All participants stay and have meals together to maximize interaction and discussion.

The extended abstracts of the proposed talk will be directly reproduced in the proceedings. Proceedings will be in black and white. Work in progress, encountered problems, etc. should be discussed in an open, informal atmosphere (no ties!) among colleagues. The first page of the extended abstract should be headed with the title and authors' names and address (incl. email) in a compact form to economize on space. Academic titles and page numbers shall be omitted. The extended abstract shall neither contain an abstract of the abstract, nor keywords, nor further headers. Font size shall not be less than 10pt Times New Roman. Extended abstracts should be limited to 6 pages in A4 format with 2.5 cm margin.

An early reply will help us in organizing the event better. For the early feedback, a tentative title or topic will suffice.

Following the tradition of previous NuTTS events, the fees will be kept low to allow a maximum number of scientists to attend. The fees including accommodation and meals during the symposium will be:

250 Euro PhD candidates and students (expected to share double)
350 Euro authors (in single room)
450 Euro others (in single room)

Contact: Gerard Delhommeau, Gerard.Delhommeau@ec-nantes.fr